Structure-activity Relationships in Organic Photocatalysts for Hydrogen Production from Water

Catherine M. Aitchison

August 2020

Thesis submitted in accordance with the requirements of the

University of Liverpool for the degree of Doctor of Philosophy

Structure-activity Relationships in Organic Photocatalysts for Hydrogen Production from Water

Catherine M. Aitchison

Hydrogen produced from water by photocatalysis has the potential to be a cheap, sustainable and low-carbon 'solar fuel'. Conjugated organic semiconductors are particularly interesting as photocatalysts as material properties can be tuned through easy modification of chemical structure. However, the relationships between specific material properties and photocatalytic activity are not yet well defined, posing a challenge to the design of new photocatalysts and the development of existing ones. The most widely studied organic semiconductors for solar fuel production are organic-solvent-insoluble bulk polymers with a low degree of order. The inability to process such materials after synthesis means that i) characterisation and ii) optimisation of secondary and tertiary structures are not facile. In this work, alternative conjugated organic materials are investigated as photocatalysts for hydrogen production from water. In each, a degree of control can be exerted during or post synthesis to give a desired or quantifiable material structure.

First, a series of polymers synthesised by emulsion polymerisation were studied. The optimised microstructure of these materials, in comparison to bulk analogues synthesised in precipitation polymerisations, lead to increased photocatalytic activity with EQEs of up to 20% at 420 nm. The ability to generate polymers from the same monomers but with different particle size also allowed the relationship between catalyst surface area and catalytic activity to be investigated.

Next, a series of oligomers were tested for photocatalytic hydrogen evolution. The well-defined chemical structure, conformation and packing of these oligomers was used to determine how properties such as chain length and backbone twisting affect photophysical properties and photocatalytic activity of the materials.

Finally, a hydrogen-bonded organic framework and related materials were studied. By comparing the activity of the same molecule in ordered and amorphous phases it was shown unambiguously that crystal packing can have orders of magnitude effect on photocatalytic activity. The high activity of some of the oligomers and this hydrogen-bonded framework indicates that molecular materials can be as active for photocatalytic hydrogen production as polymers, significantly expanding the scope of organic semiconductors that should be considered for further study.

Acknowledgements

Thank you to Professor Andy Cooper for the chance to carry out this work, for providing a supportive research environment and the opportunity to explore.

I would like to acknowledge my research coordinator Seb for his continuous help over the course of my PhD. Your support and encouragement have been invaluable. Thank you for being such a reliable guide through the past four years.

I want to thank all those I have collaborated with throughout my PhD but especially Martijn at UCL and Michael at Imperial, for their insight, advice and crucial contributions. In Liverpool; Marc, thank you for looking at all of my crystals (and not crystals) and for patiently helping me with an area I knew little about. Rob C, I suspect you are mentioned in a lot of PhD acknowledgments but I'm adding my name to that list, thank you for all the fixes and always knowing what to do. Thanks to all of 'team photocat'; Duncan, Christian, Yang, Xiaoyan and many more for help, discussion and inspiration.

Thank you to Rachel for the many debriefs and all the fun. You, Andy M and all of those cups of coffee kept me sane throughout. To the above and all the other members of the Cooper group who have made this a lot more than a lab - Ammar, Craig, Briggs, Chris, Hui, Ai and the rest - thank you for the many Friday night AJs, Mr Chilli trips, terrible karaoke renditions, badminton battles and mountain trudging trips.

Mum and Dad, thank you for putting up with me during the last few months of writing this and for every piece of encouragement and support you have given me over 26 years.

Finally, Duncan, I can't imagine what the past four years would have been like without you. Thank you for everything.

List of Publications

Articles relevant to this thesis

- **C. M. Aitchison**, M. Sachs, M. A. Little, L. Wilbraham, N. J Brownbill, C. M. Kane, F. Blanc, M. A. Zwijnenburg, J. R. Durrant, R. S. Sprick and A. I. Cooper, Investigating Structure-Activity Relationships in Well-defined Oligomer Photocatalysts for Hydrogen Production from Water. *Chem. Sci,* 2020, *advance article*.
- M. Sachs, H. Cha, J. Kosco, **C. M. Aitchison**, L. Francàs, S. Corby, C. Chiang, A. A. Wilson, R. Godin, A. Fahey-Williams, A. I. Cooper, R.S.Sprick, I. McCulloch, J. R. Durrant, Tracking Charge Transfer to Residual Metal Clusters in Conjugated Polymers for Photocatalytic Hydrogen Evolution, *J. Am. Chem. Soc.,* 2020, *advance article*
- **C. M. Aitchison,** C. M. Kane, D. P. McMahon, P. R. Spackman, A. Pulido, X. Wang, L.Wilbraham, L. Chen, R. Clowes, M. A. Zwijnenburg, R. S. Sprick, M. A. Little, G. M. Day and A. I. Cooper**,** Photocatalytic Proton Reduction by a Computationally Identified, Molecular Hydrogen-Bonded Framework, *J. Mater. Chem. A*, 2020, **8**, 7158-7170.
- **C. M. Aitchison**, R. S. Sprick and A. I. Cooper, Emulsion polymerization derived organic photocatalysts for improved light-driven hydrogen evolution, *J. Mater. Chem. A*, 2019, **7**, 2490–2496.

Also published

- R. S. Sprick, Z. Chen, A. J. Cowan, Y. Bai, **C. M. Aitchison**, Y. Fang, M. A. Zwijnenburg, A. I. Cooper, X. Wang, Water Oxidation with Cobalt-Loaded Linear Conjugated Polymer Photocatalysts, *Angew. Chem – Int. Ed.*, 2020, **583**, 237–241
- B. Burger, P. M. Maffettone, V. V. Gusev, **C. M. Aitchison**, Y. Bai, X. Wang, X. Li, B. M. Alston, B. Li, R. Clowes, N. Rankin, B. Harris, R. S. Sprick and A. I. Cooper, A Mobile Robotic Researcher, *Nature*, 2020, **583**, 237–241
- R. S. Sprick, Y. Bai, A. Guilbert, M. Zbiri, **C. M. Aitchison**, L. Wilbraham, Y. Yan, D. J Woods, M. A Zwijnenburg, A. I. Cooper Photocatalytic Hydrogen Evolution from Water Using Fluorene and Dibenzothiophene Sulfone-Conjugated Microporous and Linear Polymers, *Chemistry of Materials* **31**, 305-313
- R. S. Sprick, **C. M. Aitchison**, E. Berardo, L. Turcani, L.Wilbraham, B. M. Alston, K. E. Jelfs, M. A. Zwijnenburg and A. I. Cooper, Maximising the hydrogen evolution activity in organic photocatalysts by co-polymerisation, *J. Mater. Chem. A*, 2018, **6**, 11994-12003.

Table of Contents

List of Abbreviations

ε	Molar extinction coefficient
λ_{exc}	Excitation wavelength
λ_{em}	Emssion maxima wavelength
AM1.5G	Air mass 1.5 global filter
C_3N_4	Carbon nitride
CB	Conduction band
CMP	Conjugated microporous polymer
COF	Covalent organic framework
CTF	Covalent triazine-based framework
dbts	Dibenzo[*b*,*d*]thiophene sulfone
EA	Electron affinity of photocatalyst's ground state
EA*	Electron affinity of photocatalyst's excited state
EQE	External quantum efficiency
FT-IR	Fourier transform infrared
GC	Gas chromatography
HEP	Hydrogen evolution photocatalyst
HER	Hydrogen evolution rate
HOMO	Highest occupied molecular orbital
ICP-MS	Inductively coupled plasma-mass spectrometry
ICP-OES	Inductively coupled plasma-optical emission spectrometry
IP	Ionisation potential of photocatalyst's ground state
IP*	Ionisation potential of photocatalyst's excited state
LUMO	Lowest unoccupied molecular orbital
MALDI-TOF MS	Matrix-assisted laser desorption/ionization high-resolution time-of-flight mass spectrometry

NMR	Nuclear magnetic resonance
OEP	Oxygen evolution photocatalyst
OER	Oxygen evolution rate
OWS	Overall water splitting
PIA	Photoinduced absorption
PXRD	Powder X-ray diffraction
PV	Photovoltaic
ROS	Reactive oxygen species
SEM	Scanning electron microscopy
STEM	Scanning transmission electron microscopy
SHE	Standard hydrogen electrode
SMR	Steam methane reforming
STH	Solar-to-hydrogen
$T_{50\%}$	Time for 50% of photoinduced absorption at *ca.* 1 ps to decay by 50%
TAS	Transient absorption spectroscopy
TCSPC	Time-correlated single photon counting
(TD)-DFT	Time-dependent density functional theory
TEA	Triethylamine
TEAR	Triethylamine radical
TeOA	Triethanolamine
TGA	Thermogravimetric analysis
UV	Ultraviolet
UV-vis	Ultraviolet-visible
VB	Valence band

List of Figures

Chapter 1

Chapter 2

Chapter 3

Chapter 4

Chapter 5

Chapter 6

List of Tables

Chapter 2

Chapter 3

“Is fossil solar energy the only one that may be used in modern life and civilization? That is the question.”

(The Photochemistry of the Future, G. Ciamician, *Science,* **1912**, *36,* 385.)

Chapter 1: Introduction

On the 23rd of August 1856, '*the circumstances affecting the heat of the Sun's rays'* was read before the American Association for the Advancement of Science.[1] The author, Eunice Foote, was the first person to demonstrate a link between *'carbonic acid gas'* and the '*thermal action of the rays of light that proceed from the Sun.'*. *'An atmosphere of that gas'* she noted *'would give to our Earth a higher temperature'*.

In the 164 years since this initial observation anthropogenic carbon dioxide emissions have amounted to 2 trillion tonnes[2–4] and humanity now faces a climate emergency.[5,6] In 2018, a United Nations special report stated that without a sharp decline in greenhouse gas emissions is by 2030, '*global warming will surpass 1.5 °C in the following decades, leading to irreversible loss of the most fragile ecosystems, and crisis after crisis for the most vulnerable people and societies.*'[7] In the last few years consensus amongst scientists[8] and the public[9–11] have solidified; an alternative source of energy is required.

1.1 ‘Clean’ Energy Sources and Solar Energy

Global energy consumption in 2018 was 19 TW. 80% of this energy was derived from fossil fuels, coal, oil and gas, the combustion of which led to the production of 33,000 Mt of carbon dioxide.[12] The use of alternative energy sources, that do not generate greenhouses gases, is now higher than at any point in history but their uptake will have to increase substantially over the next 10–30 years to meet the commitments outlined in the Paris climate deal.[13] Alternative sources of energy, shown in Figure 1, include harnessing the kinetic energy of wind, waves, tides, and other flowing water, as well as the heat stored in the earth’s surface or in oceans.

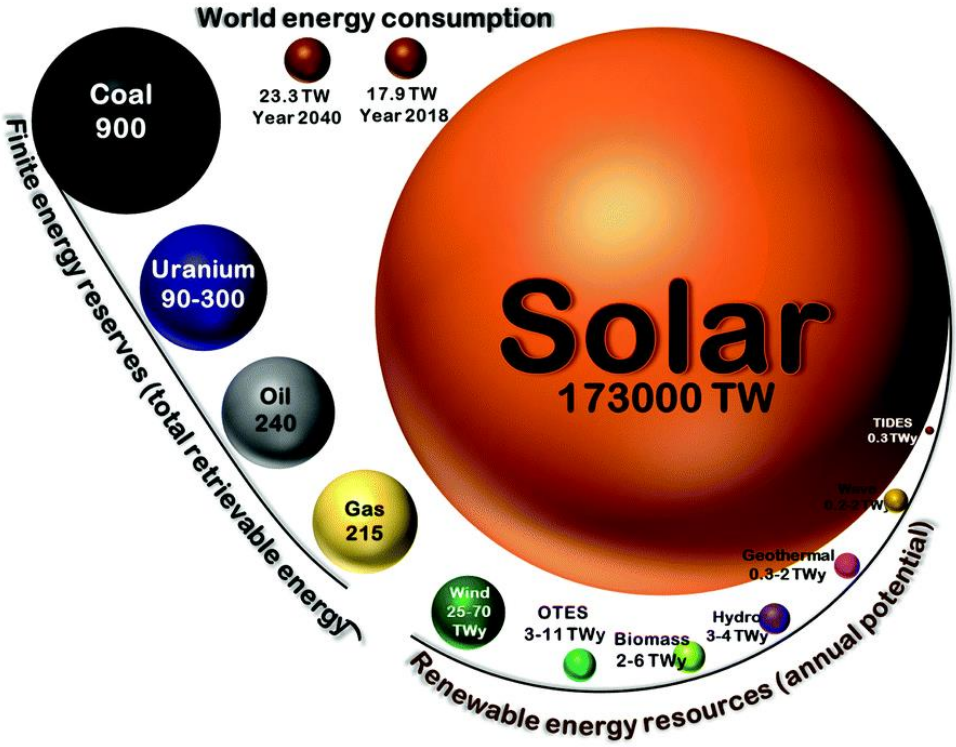

Figure 1: Comparison of renewable energy sources’ annual potentials, total fossil fuel reserves and global energy consumption in 2018 and predicted in 2040. *Reproduced with permission from reference [63].*

Whist nuclear energy does not produce significant amounts of greenhouse gas compared to fossil fuels,[14] it is often separated from other ‘clean’ energies because it can be viewed as non-renewable; the majority of energy generated by fission requires uranium, a finite resource. The process of mining and enriching uranium is highly energy intensive and has significant health and environmental impacts.[15] High profile, public-image-damaging accidents and the high cost and frequent delays associated with power plant construction means investment of nuclear energy has slowed significantly in the last decade.[16] This is in

contrast to newer renewable energy sources, where investment and uptake have grown significantly; wind power for example has gone from a 0% share of electricity production in 2000 to 5% in 2018, with 12% growth in the last year.[12]

The size of the different renewable energy sources vary dramatically and are represented in Figure 1. Solar energy dwarfs all other energy sources; harnessing less than 0.02% of the solar radiation that that hits the Earth's surface would be sufficient to meet current energy demands. The huge potential of solar energy can be exploited in a number of different ways. Figure 2 shows the different routes through which solar energy can be converted into useful forms.

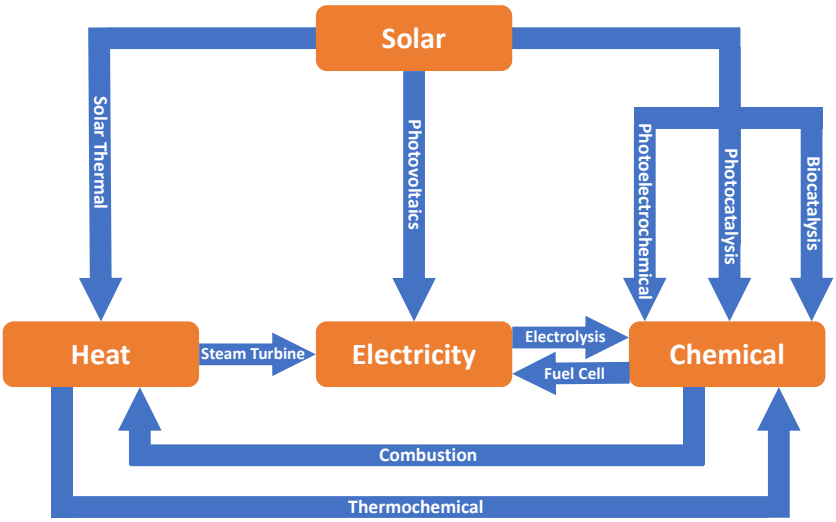

Figure 2: Solar energy conversion processes.

Solar thermal systems can provide low level heat energy for residential, public and commercial buildings and solar water heating collectors now have capacity of 480 GW across 130 countries.[13] Aside from space and water heating, a large proportion of the world's heat demand is industrial processes such as steel and cement manufacturing.[17] Directly powering these with solar energy has not been possible so far because of the high temperatures required. However, recent reports of solar concentrators reaching more than 1000 °C[18] indicate that it may be possible to utilise sunlight for some of these energy intensive industrial processes. Concentrated solar thermal energy can also be used to generate electricity in the same way as traditional fossil fuel power stations; *i.e.*, by heating water to drive a steam turbine. This is now a significant industry with a global capacity of 5.5 GW, accounting for more than 2% of electricity supply in certain countries, notably Spain.[13]

Despite advances in solar thermal technology, photovoltaics constitute most of solar electricity supply. Capacity has increased rapidly over the past 10 years to 505 GW in 2018.[13] Advances in efficiency and scale-up of production have allowed the price of solar electricity to become competitive with fossil fuel-derived electricity.[1920] Even replacing existing coal plants with new PV is becoming increasingly cost-effective.[21] These advances mean that PV technology is on track to meet a Sustainable Development Scenario consistent with the Paris Climate Change Agreement,[2223] but as discussed below, solar electricity alone cannot meet the complex energy requirements of modern society.

1.2 Energy Storage and Hydrogen

Hydrogen has the highest energy per unit mass of any chemical fuel. Its production from and conversion to water allows for an emissions-free energy storage cycle. The idea of a 'Hydrogen Economy' has existed since the 1970s[24] and envisages the use of hydrogen as an energy vector, enabling energy to be stored, transported and used in a similar way to fossil chemical fuels in our current systems, but without the emission of greenhouse gases.

Aside from production—which is discussed in the next section—the realisation of a hydrogen economy faces a number of significant challenges; the low volumetric energy density of hydrogen means substantial compression is required for many applications.[25] This makes distribution and storage more difficult, increasing the cost and complexity of materials and infrastructure.[26,27]

Nevertheless, hydrogen is likely to play a significant role in future energy systems.[2825] Some of the applications in which hydrogen may be useful are outlined below.

1.2.1 Storage for Electrical Grid Systems

A significant issue with many 'clean' energy sources is the temporal and spatial inconsistency of supply; hydroelectric, wind, wave, tidal and solar-derived power all require specific climatic or geographic locations and all but the first of these methods fluctuates on timescales of months, days or (for wind) minutes. Electricity demand is equally variable and grid systems must be capable of covering both seasonal and short-term peaks. In Saudi Arabia, for example, air conditioning requirements mean that daily electricity consumption in August can be more than twice that in January,[29] whilst in the UK a 1990 post-World Cup semi-final penalties tea-making exercise caused a 2800 MW spike in electricity demand in less than five minutes.[30,31] This mismatch between renewable supply and demand means that a comprehensive energy storage solution is required for future electricity provision.

As of 2012, 99% of global energy storage capacity for electricity grids was pumped hydro energy storage (PHES). PHES uses electrical energy to pump water from a low lying to a high lying location. When needed, the stored potential energy is converted back to electricity by allowing the water to flow back downhill and drive a turbine. The advantages to this method of storage is the ability to scale up to large gigawatt-scale plants with long lifetimes and reasonable 75% energy conversion efficiencies.[32] Compressed air energy storage (CAES) is one alternative to water pumping. CAES can be scaled to high (hundreds of MW) capacity plants and, despite lower efficiency from associated thermal energy changes, is still predicted to have lower costs than both PHES and batteries with similar capacity.[33]

Both PHES and CAES require specific geographical locations which limit the applicability of these methods in certain countries. In addition, hour-scale discharge times mean that whilst these technologies are suitable for bulk power management, other systems are required for short term demand changes. Battery technology is an increasingly cost effective solution to this[34] but storing energy as hydrogen could also play a role in modulating energy supply.[25] So-called power-to-gas systems, which use electricity to drive hydrogen production from water (see section 1.1.3), are predicted to become more affordable as electricity and electrolyser costs decrease.[35] Hydrogen could also be burnt to heat water and drive turbines for electricity production.[36] Whilst this process has lower electrical energy conversion efficiency than hydrogen fuel cells it could provide a high level of supply flexibility and provide a short-term route to carbon reductions using existing gas-power stations.[25]

1.2.2 Storage for Fuel Applications

Conversion from and to electricity is only one aspect of the worlds energy storage requirements; 60% of global energy demand is in fact fuel-based, rather than electrical.[37,38] The majority of non-electrical energy is used for heating buildings, transport and industrial processes.[25,38]

Batteries can provide a portable energy storage system for some transport applications and there have been large advances in battery energy density and affordability in recent years.[39] Battery-powered electric vehicles do face challenges with respect to charging time, range and weight limitations which are particularly limiting towards public transport and freight vehicles such as trucks and buses.[40–42] Electric road vehicles powered by on-board hydrogen fuel cells are viewed as viable competitors by some[25,40] and, despite lower global interest than battery-powered vehicles, certain countries, notably Japan, are investing significant resources in creating a hydrogen-based transport infrastructure.[43,44]

Global heating requirements are larger than both electricity and transport and account for 40% of greenhouse gas emissions. Demand is split roughly equally between industrial processes and heating air and water in buildings.[45] In the UK, more than 70% of domestic heating is provided by natural gas.[25] Electrical heat pumps are one low carbon alternative to this but their limited heat output may not be sufficient to meet peak demand in countries with colder winters. Widespread adoption could also require significant upgrades to electrical grid systems to meet demand.[46] Replacing natural gas with hydrogen in traditional condensation boilers is another option and hydrogen can also be used to supply heat using fuel cell combined heat and power (CHP) systems. The cost of these systems are currently high but are decreasing rapidly and could be competitive with other residential heating systems between 2025 and 2050.[47]

Decarbonising heat for industrial processes is one of the most urgent requirements if nations are to meet greenhouse gas emission commitments. Very little progress has been made thus far, partly due to long equipment and investment cycles.[25] Hydrogen burns at a similar temperature to coal and so could be used to heat cement kilns, which is currently a particularly emissions-heavy process. Hydrogen is also capable of reducing iron oxide so could replace carbon-based coke reductants in steel manufacturing. Current limitations to these technologies are the costs associated with furnace replacement, the high price of hydrogen and a lack of hydrogen infrastructure.[48]

1.3 Hydrogen Production Methods

1..3.1 Current Hydrogen Production Methods

Arguably the biggest feasibility problem with the 'Hydrogen Economy' is fuel production; currently 95% of the hydrogen is produced from fossil fuels (Figure 3).[49]

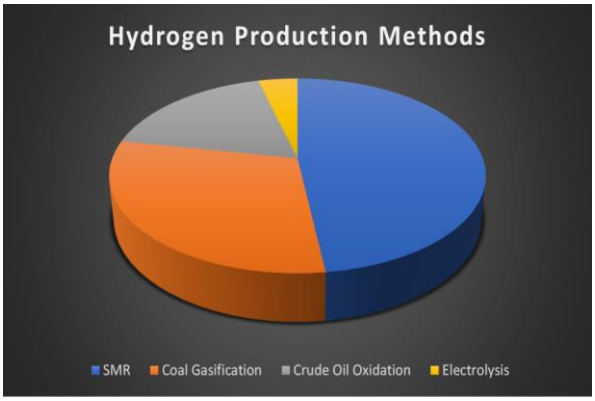

Figure 3**:** Breakdown of global hydrogen production methods. Data from reference [49].

Currently, the primary use of hydrogen is in the production of ammonia for fertiliser but hydrogen is also increasingly used in oil refining and other chemical processing.[50] Production in 2017 was 60 million tonnes, so decarbonisation is an important goal irrespective of the level of uptake of hydrogen into the new technologies and applications discussed in section 1.2.

The most common way of producing hydrogen is through steam methane reforming (SMR), an endothermic process that requires high temperatures that are normally produced via fossil fuel burning.[50] The reaction of methane and water produces a mixture of hydrogen and carbon monoxide, but the latter is often reacted further to produce CO_2 and more hydrogen in the gas-shift reaction.[51] As such, SMR is associated with significant direct and indirect greenhouse gas emissions. Oxidation of other crude oil products and coal gasification makes up the remainder of fossil fuel generated hydrogen, whilst the production of hydrogen from water makes up just 4%.

Hydrogen can be derived from water by electrolysis. This process uses electrical current to drive the otherwise non-spontaneous 'splitting' of water into hydrogen and oxygen. (Section 1.2). Electrolysis is regarded as a feasible route to 'clean' hydrogen as it can be powered with electricity generated by renewables.[50] Systems using solar as the energy source for water splitting have the potential, according to the United States Department of Energy[52] and others,[53] to be a commercially viable if solar to hydrogen (STH, see Section 1.7.1) conversion efficiencies of 10% can be reached.

Water splitting can also be achieved by thermolysis. However, this process requires temperatures exceeding 2500 °C[54] and so is not currently economically viable, even using fossil fuels as heat sources. Coupled processes involving multiple thermochemical reactions, such as Sn(II)/Sn(IV) oxide cycling, lower the required temperature to around 500 °C but introduce reagent and reactor durability issues[55]

1.3.2 Solar Hydrogen Production

1.3.2.1 Two-step Solar Hydrogen Production

Figure 4 shows how water, CO_2 and N_2 can be electrochemically converted into value-added products, such as hydrogen,[56] CO,[57] methanol[58] and ammonia[59] all of which can be used as renewable chemical fuels. By coupling solar-derived electricity with electrolysis it is thus possible to produce 'solar fuels'—such as hydrogen—in two steps using current commercial technologies. Most solar panels have efficiencies of around 15–20% and electrolysers for large-scale alkaline hydrolysis are currently around 60% efficient.[25] These values are

currently not sufficient to make PV-electrolysis-derived hydrogen cost-effective compared to hydrogen produced *via* steam reforming. However, prices are predicted to fall below fossil fuel-based routes in the next 10 years, primarily through a drop in the price of solar electricity.[5335] The development of alternative polymer electrolyte membranes (PEMs) and solid oxide electrolysis could also give efficiency improvements, [532560] as well as further progress of commercial solar panels towards the 40% efficiencies[61] achieved by lab-scale test cells with multiple junctions and solar concentrators.

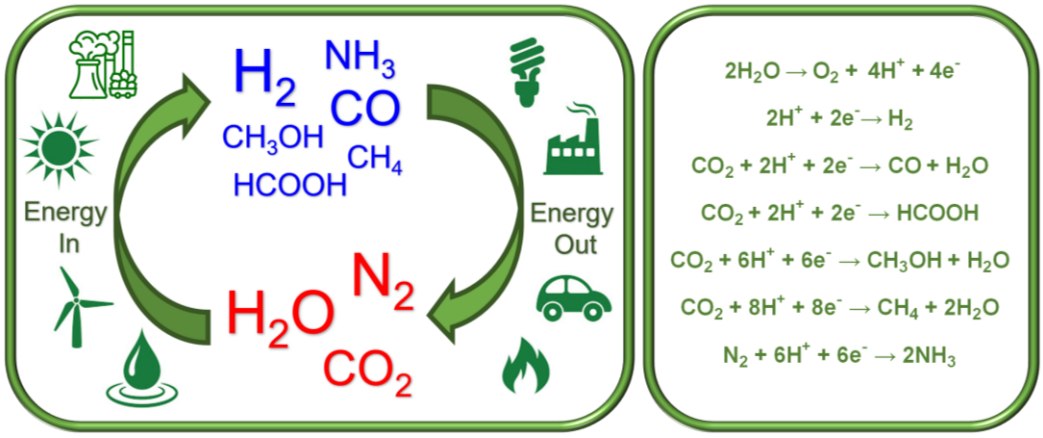

Figure 4: Cartoon of chemical fuel conversion. Electrochemical half reactions for the production of chemical fuel from low value feedstocks.

Whilst it is possible, using a grid system, to conduct these two processes separately, there is also significant interest in integrated modules that could provide localised energy storage or fuel at source. STH efficiencies of 30% have been achieved using a solar concentrator and InGaP/GaAs/GaInNAsSb triple-junction solar cell in series with two high efficiency PEM electrolysers,[62] but STH efficiencies of large scale cells with feasible stability are currently significantly lower.[63]

Hydrogen can also be produced from biomass. Solar fuels research is often dubbed ‘artificial photosynthesis’ as it aims to use man-made materials to mimic the largest chemical conversion process on the planet—photosynthesis. The Earth’s terrestrial and oceanic biosphere produce around 100 billion tonnes of ‘solar fuel’ every year in the form of new biological carbon[64] but this process is significantly less efficient than current synthetic mechanisms. Most plant life has solar-to-biomass conversion efficiencies of less than 1% and the most effective biofuel crops are still below 4%.[65,66] Whilst these sources can be cheap, the sugar cane, maize and palm oil crops most commonly used to make biodiesel and bioethanol, require large amounts of land and water in tropical and equatorial regions. This

means these ‘carbon neutral’ fuels are often associated with considerable environmental and emissions costs through land clearing.[67–70] Biofuel produced from agricultural and urban waste could provide a more sustainable route and countries such as India produce hundreds of megawatts of power from waste.[71] The conversion of biomass to ‘useful chemicals’ make this a two-step solar fuel route. For hydrogen, this processing step can have efficiencies between 50 and 100% depending on the nature of the biomass feedstock. For example, low grade lignocellulosic materials require biomass gasification whist more efficient aqueous reforming or fermentation techniques can be used to make hydrogen from sugars and alcohols.[72]

The focus of this thesis is the direct conversion of solar energy to chemical fuel and the different one-step routes for this are outlined in more detail below. The discussion focusses on hydrogen production from water although similar materials and set-ups can be used for the production of other chemical fuels[7374] as shown in Figure 4.

1.3.2.2 Biological Hydrogen Production

The direct production of hydrogen from sunlight and water—biophotolysis—is a naturally occurring biological process. In photosynthesis, the oxidation of water to produce oxygen, protons and electrons is photocatalysed by photosystem II (Figure 5). In CO_2 reducing photosynthetic systems, electrons are transferred to FNRase for carbon fixation, but a number of other reductases are present in some organisms and can catalyse alternative reduction reactions.[75] Hydrogenases catalyse the reduction of protons to dihydrogen molecules and are present in a number of cyanobacteria and algae.[76] In cyanobacteria, this process is simultaneous with oxygen production but in algae anaerobic conditions are usually required for hydrogen production.[77] Sulfur deprivation can generate the required oxygen-depleted conditions but a number of bioengineering techniques have also been employed to generate strains of microalgae with lower oxygen sensitivity[78] and improved hydrogen evolution rates.[79,80]

Whilst cheap, biophotolysis mechanisms have very low STH conversion efficiencies in comparison to artificial systems.[72] This is due to the inefficient utilisation of the full solar spectrum but is also thought to be related to complex electron transfer pathways of biophotosynthesis which, it is sometimes argued, makes them better suited for the generation of more complex building blocks than for producing hydrogen as a fuel.[81]

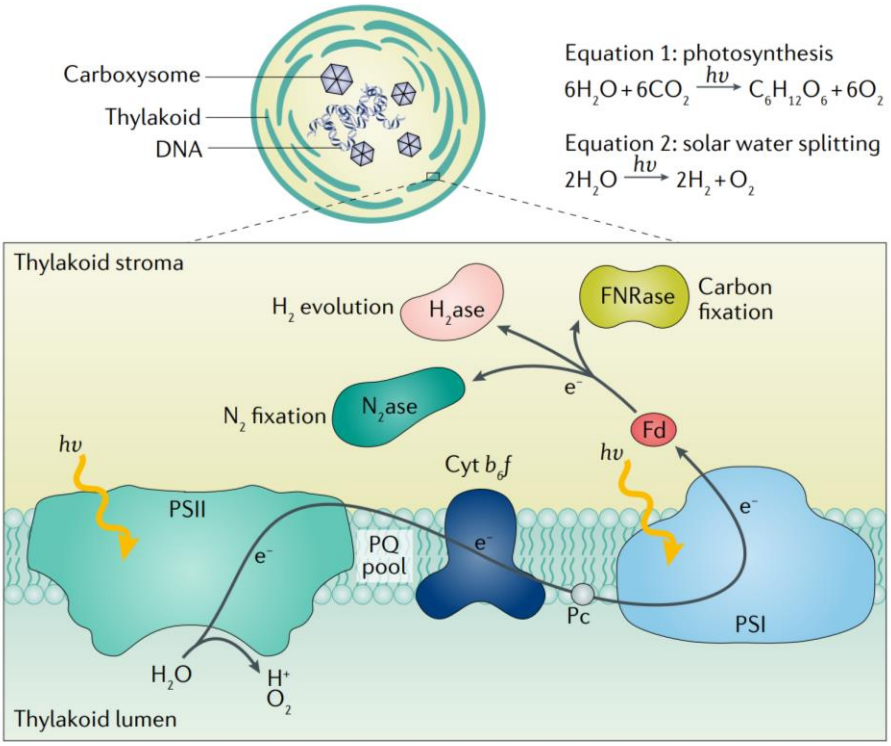

Figure 5**:** Cartoon mechanism of photosynthesis and biophotolysis. Oxidation of water by photosystem II (PSII) is followed by various electron transfer steps and the reduction of ferredoxin (Fd). Fd can donate electrons to various reductases to drive carbon dioxide, nitrogen or proton reduction. *Reproduced with permission from reference [75] - Published by Springer*

An alternative approach is so called semi-artificial photosynthesis which aims to utilise the strengths of both natural and man-made photoabsorbers and catalysts. There is a growing interest in wiring bioderived components such as PSII and various hydrogenases into PV-electrochemical or photoelectrochemichal systems, but the removal of the biological 'housing' of these components often results in low stability.[75] At this relatively early stage of development there are few examples of unbiased systems capable of overall water splitting and STH efficiencies above 0.5% are yet to be reported[82–85]

1.3.2.3 Photoelectrochemical Hydrogen Production

In 1972, Fujishima and Honda were the first to show that water could be split into hydrogen and oxygen using light and a man-made photoelectrochemical (PEC) cell.[86] Whilst electrolysis applies an external voltage across a pair of electrodes to drive a non-spontaneous reaction, PEC cells replace one or more of the electrodes with a photoactive semiconductor electrode, thus replacing some or all of the external bias with the potential generated from

photoexcitation. Photoelectrochemical cells can have three configurations, shown in Figure 6, with a) a photoanode coupled with a 'normal' cathode counter electrode, b) a photocathode with an anodic counter electrode or c) both a photoanode and photocathode.[87]

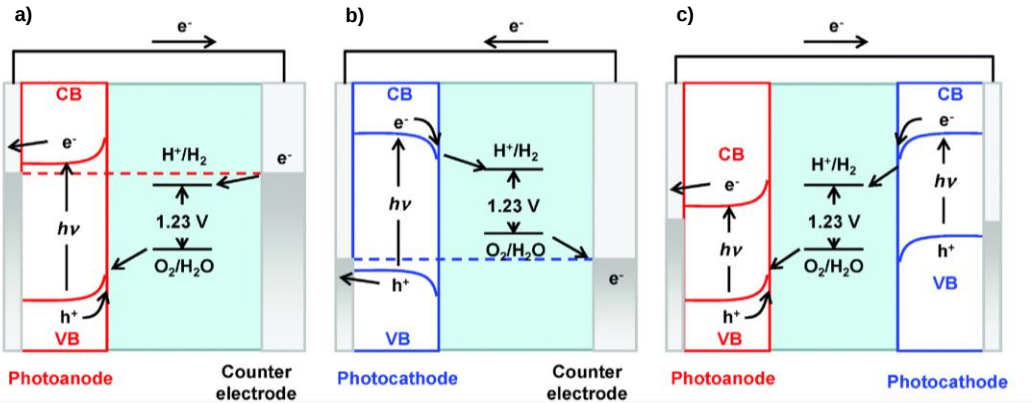

Figure 6: PEC water splitting using (a) a photoanode, (b) a photocathode, and (c) a photoanode and photocathode in tandem configuration. The bandgaps are depicted smaller in (c) to emphasise that semiconductors with a narrow bandgap can be employed. *Reproduced from reference [87] with permission from The Royal Society of Chemistry.*

Configurations a) and b) in Figure 6 rely on a single semiconductor. As such, to drive overall water splitting, the potentials of the conduction and valence bands must sit above and below the potentials for proton reduction and water oxidation, respectively. Splitting water thus requires a minimum photoexcited potential of 1.23 V, equivalent to absorption of a photon with a maximum wavelength of 1009 nm. Figure 7a shows the American Society for Testing and Materials AM 1.5 G standard for solar irradiance by wavelength of radiation.[88] This defined as the solar irradiance received on an inclined plane at 37° tilt toward the equator, an angle chosen—along with the particular temperature, pressure and ozone levels—to approximate average annual conditions across the US's 48 contiguous states.

Considering the proportion of irradiance that has sufficient energy to satisfy this thermodynamic limit and the energy 'wasted' by overly energetic photons gives maximum single-absorber STH efficiencies of around 30–32%.[63,89,90] In reality overpotential requirements mean that feasible bandgaps are significantly larger than the 1.23 V minimum and internal device losses mean that reactor EQEs (see section 1.7.1) will be less than 100%. Figure 7b shows the maximum STH values for different device efficiencies as a function of usable light wavelength. For example, a single semi-conductor with a 2 eV bandgap should be able to utilise wavelengths up to 600 nm and, thus, to reach the 10% STH target an internal device EQE of just over 60% is required.[89]

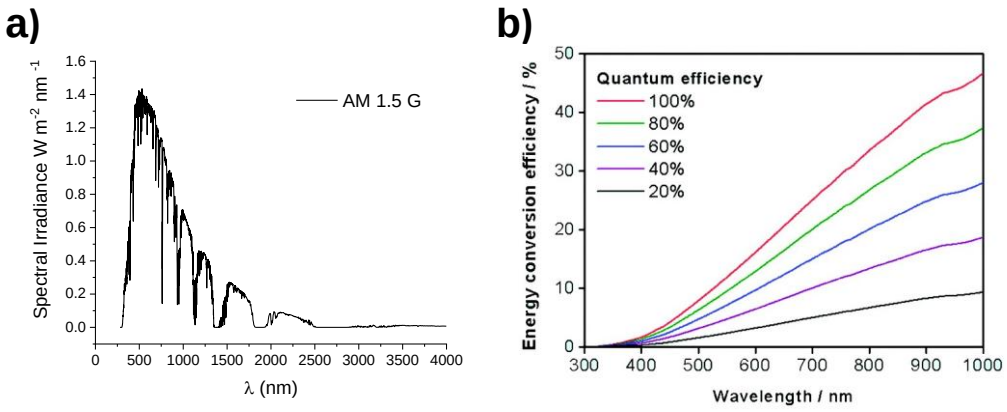

Figure 7**:** a) American Society for Testing and Materials AM 1.5 G standard for solar irradiance by wavelength of radiation, data from reference [88]. b) Calculated solar energy conversion efficiency as a function of wavelength for overall water splitting using photo- catalysts with various quantum efficiencies. *Reproduced with permission from reference [89]. Copyright (2010) American Chemical Society.*

Configuration c) in Figure 6 is the most promising set-up to give overall PEC water splitting as the use of two absorbers means that smaller bandgap semi-conductors can be employed. Dual-absorber systems have a larger thermodynamic STH limit of ~40%[63,90] meaning lower, more achievable device efficiencies could produce the desired 10% target; Feasible bandgaps for a stacked system (whereby a small bandgap absorber sits behind a lager bandgap absorber and hence only receives photons that are too low in energy to be absorbed by the top material) of 1.84 and 1.23 eV are predicted to require device EQEs of less than 44% to give 10% STH.[90] In comparison to PV, PEC water splitting is a relatively undeveloped area of research[53] and experimental results are yet to hit the aforementioned efficiencies. To date, one of the highest reported STH efficiencies for a tandem PEC cell is 3.7%. This was reported in 2018 by Kobayashi and co-workers, who used a $CuIn_{1-x}Ga_xSe_2$ (CIGS) photocathode coupled with a CdS buffer layer and Pt co-catalyst stacked behind a $BiVO_4$ photoanode with Fe/Ni oxide oxygen evolution catalyst.[91] CIGS-based photocathodes such as this are gaining increasing attention for water splitting applications[92,93] due to their wide bandgaps but these materials have significant issues with stability and require full protective layers to separate the materials from the electrolyte.[94] For example, the Kobayashi cell only reports solar to hydrogen conversion over a ten minute period and during this a 19% drop in activity is observed. Photocathodes based on metal oxide semi-conductors show lower photocurrents but are more robust.[63] Cu_2O cathodes are the most widely studied of these and have been shown to be capable of maintaining photocurrents of ~ 5–10 mA cm^{-2} over 120 hours.[95]

As the front layer in stacked systems, and with typically larger overpotential requirements for water oxidation, photoanodes utilise wider bandgap semi-conductors than photocathodes. TiO_2 was the first photoanode material shown to be capable of water oxidation[86] however, as a UV-only absorbing semi-conductor this material has quickly been replaced by other oxides such as $BiVO_4$ and Fe_2O_3 capable of absorbing visible wavelengths.[96] The advantage of these materials is their high stability in water, thus operating times of more than 1000 hours are achievable[97] and simpler cell design can be used. Higher photocurrent densities can be achieved using group 5 and 13 metal nitrides and oxynitrides[9899,100] but these materials are less stable and require surface protection.

The thermodynamic requirements of single absorber systems and device losses mean there are few single semi-conductor PEC systems (configurations a) and b), Figure 6) that show unassisted production of hydrogen and oxygen from water.[101,102103] However, if the photoelectrode band positions do not provide sufficient driving force for the two redox reactions, it is possible to alter the potential across the counter electrode using an external power source. External bias must be taken into account when considering overall efficiency[104] but this provides an easy mechanism for controlling thermodynamic driving force and allows individual photoanode or photocathode materials to be studied in isolation before combination into tandem systems as in Figure 6c).

Alternatively, external bias can be provided by an integrated photovoltaic cell in a PV-PEC hybrid. Here, incoming radiation must be shared between two absorbers, the photoelectrode and the photovoltaic component, but this type of system is significantly more efficient than pure PEC cells with STH of around 8% demonstrated.[105,106]

A final cell type, and one which combines elements of both PEC and PV-electrolysis, is 'buried' systems. Instead of applying a coating to a photoelectrode, buried systems protect a PV junction such as silicon, perovskites or CIGS so that the material can be used in contact with water.[63] On the surface of the protected photoabsorber, electrocatalyst components provide an active site for proton reduction and water oxidation, respectively. The more advanced efficiencies of PV materials mean that these systems can reach solar to hydrogen values of up to 19%,[107108,109] approaching the best unconcentrated solar PV-electrolysis systems.[110,111]

Whilst currently more efficient than the purely catalytic routes discussed below, a significant issue with many PEC, PV-PEC and buried systems is that of reactor complexity and the associated manufacturing costs.[63] Panels often have highly developed designs with up to 6 material layers for a single electrode[98] or more than 10 for full 'artificial leaf' devices,[112]

often requiring multiple finely-tuned coating methods. The many contact points between components means that crystallinity and microstructure is often crucial for optimum efficiency[113] and so energy intensive, high cost techniques such as vapour and atomic layer deposition are employed in the most active systems.[114] An additional issue with panel and electrode systems is that of scale up. The drop off in photocurrent and potential on moving a typical tandem PEC system from 0.1 cm^2 lab-scale test cell to a commercial 10 m^2 panel have been predicted to be at least 33% and 0.15 V respectively, leading to a one third reduction in overall STH efficiency.[63] This is due to a combination of ohmic losses associated with increased substrate resistance and spatial defects, the generation of chemical gradients, such as H^+ ions, and the requirement of a membrane to sperate hydrogen and oxygen. These issues are also evident in experimental results; one of the largest PEC-PV systems tested to date is a 1.6 m^2 $BiVO_4$ photoanode coupled with silicon PV which had 3% STH,[115] considerably lower than smaller panels with similar active components. These manufacturing and scale up issues contribute to the high hydrogen costs calculated for PEC and PV combined systems.[11653]

1.3.1.4 Photocatalytic Hydrogen Production

Several reports analysing the technoeconomics of solar fuels production have indicated that photocatalytic hydrogen production could provide the cheapest route to renewable hydrogen production.[52,90] This is mainly due to the low capital cost of the simple reactor designs possible for this wireless process, as shown in Figure 8 below. Photocatalyst powders suspended in plastic-bag reactor systems could provide hydrogen for US$1.6 and US$3.2 kg^{-1} for the single and dual bed systems shown in a) and b) of Figure 8, significantly lower than the US$4–10 costs predicted for PEC panel set-ups c) and d).[90]

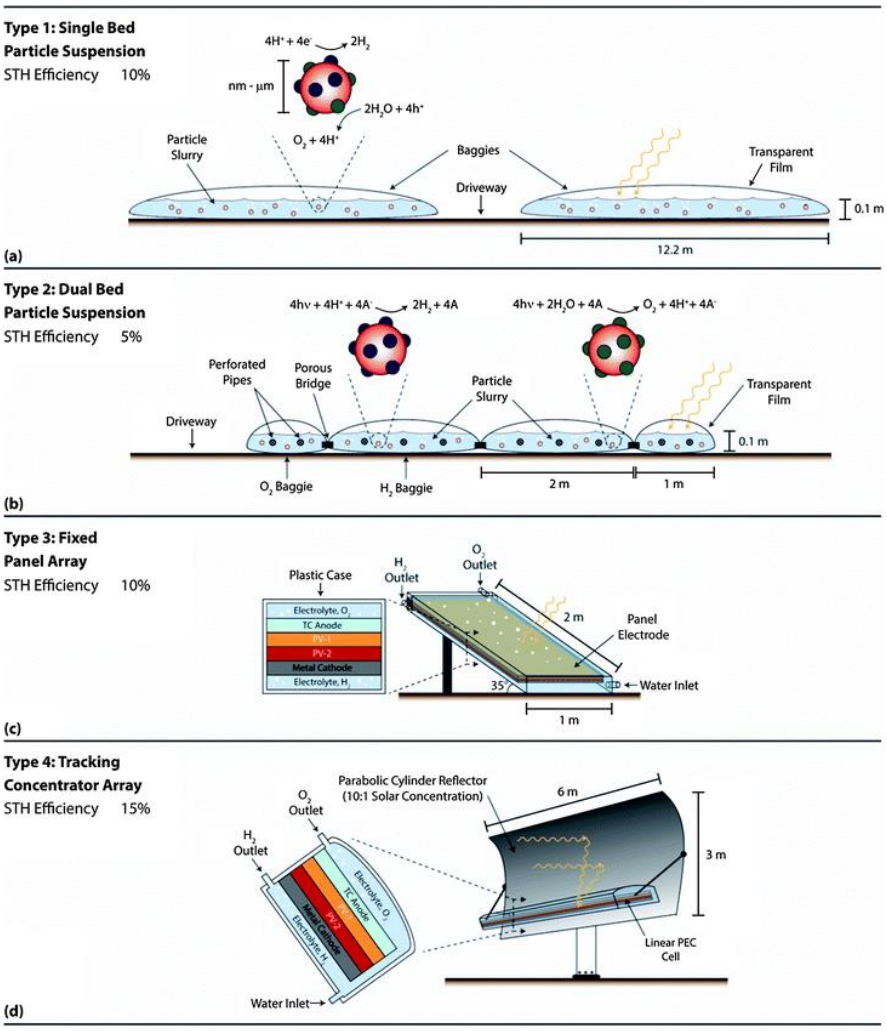

Figure 8: Schematic of four reactor types including (a) Type 1 reactor cross-section showing the particle slurry contained within baggies separated by an access driveway, (b) Type 2 reactor cross-section showing the particle slurries contained within baggie assemblies consisting of an alternating arrangement of a full size and half-size baggie each for O2 and H2 evolution, (c) Type 3 reactor design showing the encased composite panel oriented toward the sun with buoyant separation of gases, and (d) Type 4 reactor design with an offset parabolic cylinder receiver concentrating light on a linear PEC cell.. *Reproduced with permission from reference [90] - Published by The Royal Society of Chemistry*

These calculations assume STH efficiencies of 5–15%, which means significant improvements must be made to current state of the art systems. PC systems are significantly behind PEC and PV-electrolysis in this respect; Currently the maximum STH reported for photocatalytic systems is 5% for inorganic[117] and 2% for metal-free semiconductors[118] but these studies, 6 and 5 years ago respectively, have had little follow-up work. A more representative efficiency of around 0.4% STH was achieved for a 1 m^2 panel, which sustained 60% of its maximum activity after 1000 hours of illumination.[119] This corresponds to nearly 6 months of 6-hour AM 1.5 G days, a substantially shorter timescale than the 5

year reactor lifetime assumed in the aforementioned costings, but longer than has been demonstrated for unbiased PEC overall water splitting (OWS) systems.[63] The panel uses the one-step mechanism shown in Figure 9a, with an alternative design of photocatalyst particles dropped onto a silica substrate, covered with a thin layer of water and enclosed in acrylic that avoids the need for stirring. Gas was collected by tilting the panel by 10–20° and bubble accumulation could be prevented by using a hydrophilic top panel that sits above the thin layer of water. The panel showed a small drop in efficiency compared to a lab-scale reactor, which was attributed to uneven photocatalyst distribution, but cracks in the photocatalyst sheets were found to have no effect on activity, demonstrating the inherent robustness of a system that does not rely on long-range charge transfer. Whilst this system does rely on small amounts of Rh co-catalyst, the semiconductor synthesis and cocatalyst loadings can be achieved through relatively cheap molten salt synthesis. As with PEC systems, significantly higher STH of 3.3%[120] can be achieved using more complex photocatalyst architectures but these rely on expensive, high vacuum techniques such as plasma-assisted molecular beam epitaxy which are not suited to scale-up.

Unlike single photoelectrode PEC, there are numerous examples of unbiased OWS by one-step excitation systems, including those above, that rely on a single semiconductor to provide the driving force for both half reactions as shown in Figure 9a.[121] STH efficiencies exceeding 1% have also been demonstrated with these so-called 'Z-scheme' systems[122] (Figure 9b) but these are yet to be demonstrated in long-term or scaled-up experiments. As with tandem PEC Z-schemes, use of dual absorbers allows semi-conductors with smaller overlapping bandgaps and increased light absorption without compromising driving force. Typically the hydrogen evolution photocatalyst (HEP) is made up of a visible light absorbing semi-conductor whose conduction band sits at a negative potential relative to NHE, and can thus drive proton reduction, combined with a cocatalyst as the active site for reaction. Similarly, the oxygen evolution photocatalyst (OEP) must include a semiconductor with a valence band below 1.23 V relative to NHE and have photoexcited holes that can oxidise water, normally with the assistance of a cocatalyst.

The use of two semi-conductors is only effective if charge transfer can be facilitated between the two, as shown in Figure 9c. A small number of systems have reported OWS though particle collision in suspension[123,124] or by generating fused particles[125] but systems that rely on a solid or solution-based electron mediator are far more common.[121] Solid electron mediators have been found to give high efficiency[63] but the advantage of a solution redox shuttle is the possibility of separating the production of hydrogen and oxygen as shown in Figure 8b.

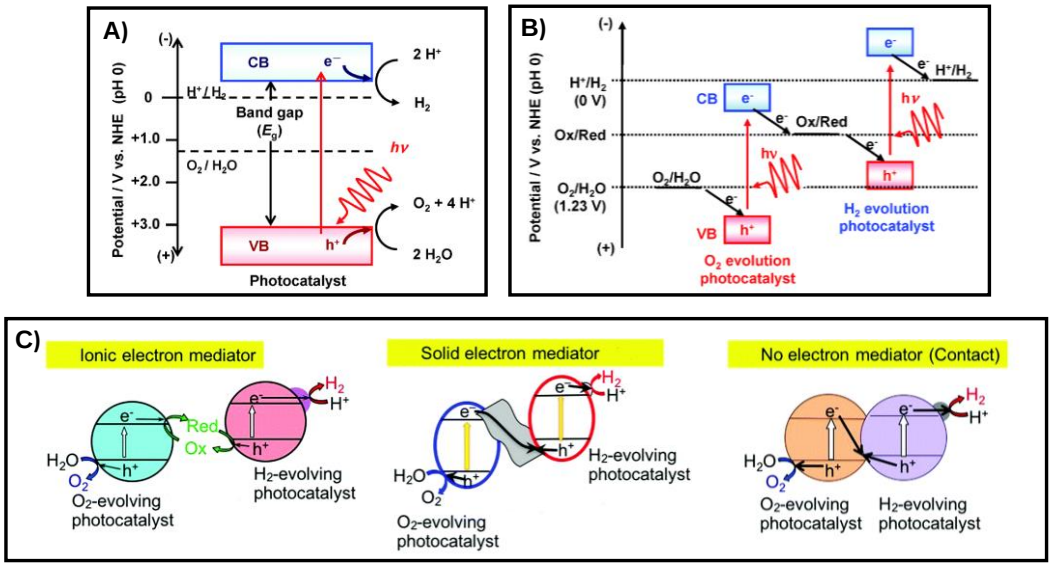

Figure 9: PC water splitting using A) a single absorber, one-step system, B) dual absorber, two-step "Z-scheme" system. C) Strategies for electron transfer in Z-scheme systems. *Adapted with permission from references [87] and [124] - Published by The Royal Society of Chemistry*

The Gibbs free energy of separating a 2:1 mixture of hydrogen and oxygen is less than 1% that of the OWS process[126] and gas separation by pressure swing absorption has been modelled to be achievable at relatively low cost.[90] However, this process involved compression of the H_2/O_2 mix to 300 psi before separation, which some argue constitutes a significant explosive risk.[127] Gas separation membranes can be used at lower pressures which is also thought to be more consistent with current OWS photocatalysts that often require reduced pressure to give optimal performance and avoid back reaction.[119,127] Achieving a suitable balance of permittivity and selectivity using membrane systems may be challenging, however, and increase cost and processing times compared to pressure swing methods.

The mechanism of photocatalytic water splitting, and the different materials studied as photocatalysts are discussed in the following sections.

1.4 The Process of Photocatalytic Water Splitting

The splitting of water into hydrogen and oxygen (equation 1) has a Gibbs free energy of 237 kJ mol^{-1} at 298 K. The overall reaction can be split into two half reactions which occur at separate sites. The two electron reduction of protons to molecular hydrogen (0 V vs. NHE, pH = 0) and the four hole oxidation of water to molecular oxygen (1.23 V vs. NHE, pH = 0) as shown in equations 2 and 3.[121]

$$H_2O \rightarrow H_2 + \frac{1}{2}O_2 \qquad \Delta G_r° = 237 \text{ kJ mol}^{-1} \text{ (1)}$$

$$2H^+ + 2e^- \rightarrow H_2 \qquad E° = 0.00 \text{ V (2)}$$

$$2H_2O \rightarrow 4H^+ + 4e^- + O_2 \qquad E° = +1.23 \text{ V (3)}$$

The energies associated with these reactions are the thermodynamic difference between reactants and products but do not consider any kinetic barriers to reaction, or energy loss incurred in the various stages of photocatalytic reaction. To understand how these might affect the rate of reaction it is necessary to look in more detail at the steps involved.

i) Light Absorption

Electromagnetic (EM) radiation can interact with matter in a number of ways but absorption processes, as opposed to scattering phenomena, involve "*the transfer of energy from an electric field to a material or molecular entity"*.[128] This energy transfer can be thought of as the perturbation of a system of charged particles from a ground state to an excited state. Whilst electromagnetic radiation can be treated as a continuous wave in many instances, the photoelectronic effect indicates that light can also be treated as discrete 'quanta' or photons whose energy is determined by the frequency at which they oscillate, according to the Plank-Einstein relation.[129] The discrete energy of photons limits the transitions that (EM) radiation can drive such that interaction with lower frequency radiation, such as microwaves, can only induce perturbation between states that are relatively close in energy, such as molecules in different rotational states, whilst higher frequency UV and X-ray frequencies can drive transitions between states with different electron configurations.[130] Solar radiation consists of frequencies from $4 – 8 \times 10^{14}$ Hz and thus lies somewhere between these examples. It has insufficient energy to drive electron transitions in atomic orbitals but the reduced energy gap between electronic states in some molecules and materials means absorption of solar radiation can result in excitation.

Absorption will only occur if interaction between the electromagnetic field and the material results in a change in dipole moment but there are a number of other selection rules that govern the probability of transition between two electronic states.[129] The spin conservation rule, or Wigner rule, states that only transitions that do not change the spin state of the system are allowed.[128] Thus, for materials with a singlet ground state S_0 (*i.e.*, with electron spins paired in anti-parallel configurations) the lowest energy 'allowed' transition is to the

first excited singlet state, S_1 (Figure 10). This is the excitation that occurs in the majority of photocatalysts although S_0 to S_n transitions and the T to T transitions of triplet state materials can contribute towards light absorption. Spin-orbit coupling also means that spin-forbidden transitions also occur in some materials.

The absorbance of a material at a particular wavelength is determined by the probability that a transition with energy equal to a photon of that wavelength will occur. This probability is determined by the transition oscillator strength, *f*. As well as spin considerations, the oscillator strength for a particular electronic transition is dependent on the spatial overlap between the two states as well as the change in dipole moment from transition.[130] The S_0 to S_1 absorption spectrum of a material encompasses a range of wavelengths as absorption corresponds to electronic transitions that can also be accompanied by a change in the vibronic and rotational energy levels of the system.[131] Absorption occurs on a femtosecond timescale, much faster than the timescale involved in molecular or lattice vibrations, and so transitions between vibrational states with highly overlapping vibrational wavefunctions – ones that involve little change to the position of nuclei – are the most likely to occur. This approximation, the Franck-Condon principle, governs the vibrational fine structure observed in the electronic absorption spectra of some materials.

The electronic energy levels in molecular systems can be described by molecular orbitals which may be delocalised across several atoms within a molecule. The S_0 to S_1 transition corresponds to an electron moving from the highest occupied molecular orbital (HOMO) to the lowest unoccupied molecular orbital (LUMO) and thus the transition energy is related (although not identical) to the energy difference between those two orbitals and the oscillator strength is dependent on their symmetry and spatial overlap. Many semiconductors are not molecular materials, however, and have electronic energy levels that are best described as bands of states delocalised across an extended lattice. The occupied states of these materials, the valence band (VB), lie at energies up to 4 eV below the unoccupied conduction band (CB) states and thus photoexcitation by visible and UV wavelengths can promote electrons from the VB to the CB.

Regardless of where a semiconductor lies on the spectrum of orbital-like or band-like energy states, electronic transitions result in the formation of an exciton- an unpaired electron in an excited electronic energy level that is bound to a certain degree with the ‘hole’ generated in the ground state energy level by its promotion

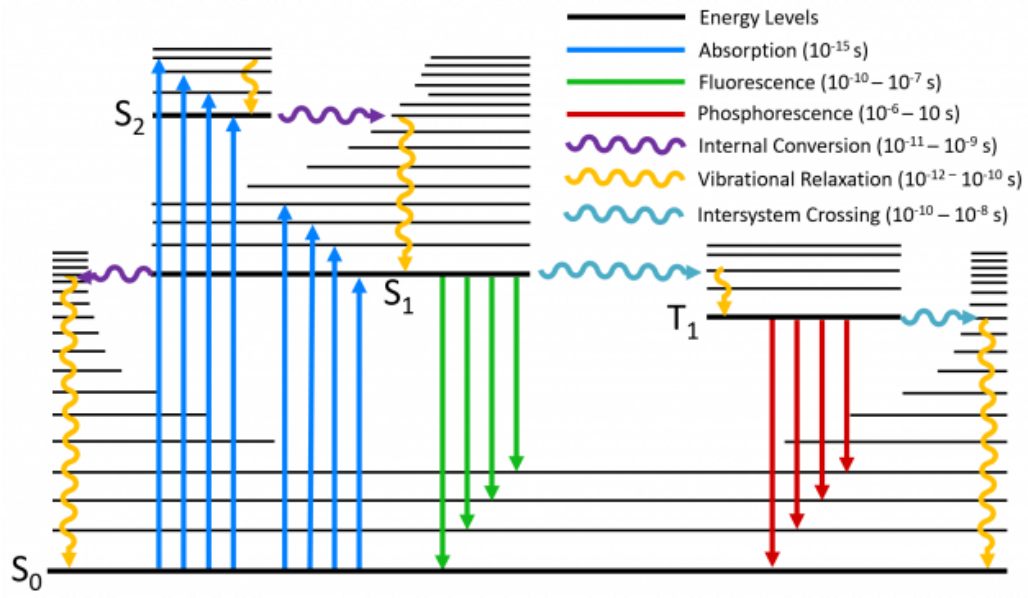

Figure 10: Jablonski diagram showing excitation and possible radiative and non-radiative transitions along with typical timescales of these processes.

ii) Charge carrier generation and separation

The excitonic electron-hole pair are bound by coulombic interactions but the strength of this interaction, the exciton binding energy, is strongly dependant on the relative permittivity of the semiconductor – how significantly the electric field of other electrons in the system can 'screen' the attractive force between charges. The relative permittivity of semiconductors is measured by the dielectric constant and can vary by several orders of magnitude depending on the material. Ionic, inorganic semiconductors typically have high dielectric constants leading to weak coulombic interaction and low (~ 10 meV) exciton binding energies. These are known as Wannier-Mott excitons (Figure 11b) and have a radius larger than the lattice spacing such that the electron and hole components may be located several unit cells apart.[132] In contrast, organic molecular crystals and polymers generally have substantially lower dielectric constants and therefore photoexcitation of these materials generates strongly bound, Frenkel-type, excitons (Figure 11a).[133] These are localised and have binding energies of the order of 0.3–0.5 eV.

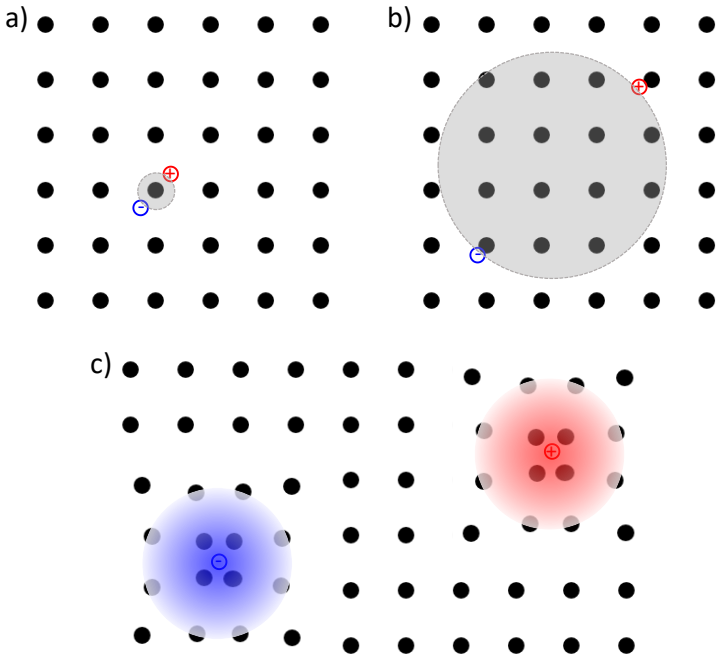

Figure 11: a) Strongly bound Frenkel exciton. b) Weakly bound Wannier-Mott exciton. c) Separated electron polaron and hole polaron. Dots represent lattice points in the crystal.

After formation, excitons will ultimately decay or separate. Radiative decay is most commonly fluorescence – the recombination of electron and hole in an excited state of the same multiplicity as the ground state with the emission of a photon – although phosphorescence after intersystem crossing to an accessible triplet state can occur in some materials. Decay can also be non-radiative, i.e. internal conversion, which is the transition from S_n states to lower singlet states (in reality this is predominantly S_1 to S_0 and, if it occurs, S_2 to S_1), or vibrational deactivation within a state, where energy is lost through heat.[131] These decay processes are summarised in Figure 10 and occur on a range of different timescales, although all are slower than excitation. Vibrational relaxation within an electronic state is very fast and in molecular systems generally occurs in about 10^{-12} s; before fluorescence takes place.[131] The rate of spontaneous fluorescence and other non-emissive routes that depopulate the S_1 state determine the exciton lifetime. In solid semiconductors the rates of these processes are highly dependent on lattice structure as impurities and defects can act as recombination centres and reduce the excited state lifetime.[130]

Photocatalysis relies on the separation of excitons into non-geminate charge carriers before these recombination routes can occur. This thesis focuses on organic molecular crystals and polymers, and separated charges in these systems cause strong, atomic scale lattice

deformations, known as polarons (Figure 11c), which differ substantially from 'free' electrons or holes.[130] Exciton dissociation occurs spontaneously in many inorganic materials[134] but organic semiconductors are generally thought to require donor-acceptor type electronic structures[135,136] or homojunctions between ordered and disordered domains[137] to stabilise polaron formation. Charge separation can also be driven by exciton interaction with an 'external' species; Noble metal cocatalysts, such as Pt, with Fermi levels below the semiconductor conduction band can aid in charge separation by acting as an electron sink.[138,139] Similarly, redox shuttles in Z-scheme systems can facilitate polaron formation by donating electrons or holes to excitons.

When studying HEPs and OEPs individually for incorporation into Z-scheme systems it is common to use sacrificial electron donors or acceptors and these can facilitate charge separation analogously to redox shuttles. Photocatalysts for the oxygen evolution half reaction are commonly studied with $AgNO_3$, which irreversibly scavenges an electron from the photoexcited semiconductor. HEPs are studied with a variety of electron donors[140] and these can facilitate electron polaron formation from reductive quenching of excitons.[141] Triethylamine (TEA), ascorbic acid, and mixtures of sodium sulfite and sulfide are all employed as electron donors in this work and their proposed degradation schemes following oxidation are shown in Figure 12.[140,142]

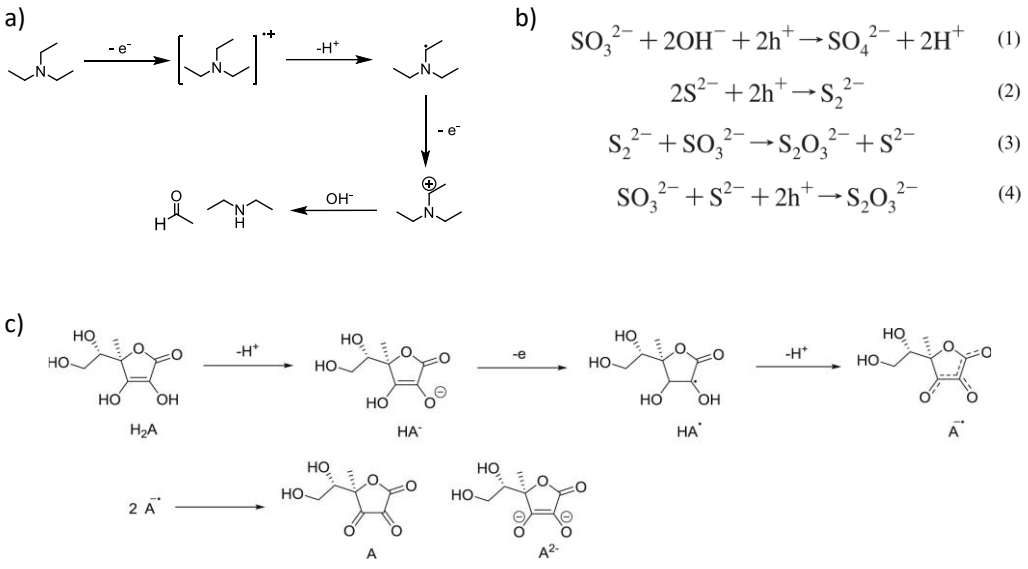

Figure 12: a) Oxidation of triethylamine to acetaldehyde. b) Na_2S / Na_2SO_3 donates electrons via oxidation of sulfate and sulfide via (1-4), *reproduced with permission from reference [142. Copyright (2008) American Chemical Society*. c) Oxidation of ascorbic acid, *reproduced from reference [140]*.

The scientific validity of using sacrificial electron donors as a proxy for OWS is complicated by the fact that most scavengers are thermodynamically 'easier' to oxidise than water (*i.e.*, they have less positive oxidation potential). The risk in these systems is that improvements to hydrogen evolution rate may in fact be facilitated by improvements to the hole scavenging process, a step which ultimately must be removed in OWS systems. In recent years there have been some moves toward donors, such as cysteine[143] that might ultimately act as reversible redox shuttles. An alternative approach is to pair proton reduction with a useful, or at least sustainable, oxidation reaction. Reisner and co-workers have developed CdS quantum dots that could photocatalyse the oxidation of lignocellulose or plastic waste to facilitate the reduction of protons to hydrogen.[144,145]

iii) Charge transfer

Efficient transport of charge carriers from the point of initial excitation to redox active sites on the material surface are required for successful hydrogen and oxygen production. In organic semiconductors, energy transfer can occur both before and after charge separation and thus correspond to the movement of bound excitons or separated electron and hole polarons through the material. In organic polymers and molecular crystals excitons migrate through non-radiative dipole-dipole interactions best modelled as a Forster resonance energy transfer process.[146] This transfer occurs between neighbouring molecules or chains, but the strength of resonance interactions decreases rapidly with distance and is dependent on the mutual orientation of the donor and acceptor dipole moments. This means that the conformation and packing of polymer chains or molecules has a large effect on how far excitons can diffuse through the material.[147] This diffusivity, along with the excited state lifetime, determines exciton diffusion length, which is typically 5–10 nm in organic semiconductors. As this is significantly shorter than the tens to hundreds of nanometres that light can penetrate into semiconductors, exciton migration to sites of charge separation on the material surface may limit photocatalysis.[146]

Charge separation, proton reduction and water oxidation do not typically occur at the same site on the photocatalyst and thus transfer of separated charge carriers through the semiconductor may also be required for hydrogen or oxygen production. Mechanisms vary substantially between inorganic and organic materials. The band structure of the former means that the wavefunctions of charge carriers can be thought of as delocalised, leading to coherent transport and high (10^2–10^4 cm^2 V^{-1} s^{-1}) mobilities. In contrast, the more localised orbitals of organic semiconductors means polaron transport is best described as a hopping mechanism between sites, typically resulting in lower charge carrier mobilities of 10^{-10}–10^1 cm^2 V^{-1} s^{-1}.[148]

The mobility of polarons is dependent on the coupling between the starting and ending electronic states; *i.e.*, a charge localised on one molecule to a charge localised on its neighbour.[149] The distortion of the lattice surrounding the separated charge makes a significant contribution to the polaron energy so the displacement of surrounding atoms or molecules from equilibrium, as the charge moves from site to site, can also act as a kinetic barrier to charge mobility. As with excitons, the polaron diffusion lengths are a function of this mobility versus the lifetime of the separated state, and are reduced by the presence of traps or recombination centres.[148]

iv) Proton reduction and water oxidation

Some semiconductors possess surface groups that act as the active site for either proton reduction or water oxidation.[150] However, most semiconductors capable of photocatalytic water splitting require the addition of a cocatalyst. Whilst the role of the semiconductor is to generate and transport charges at the correct potential to drive the reaction, the role of the cocatalyst is to lower the activation energy of the redox reactions. Water oxidation is particularly kinetically challenging, as it is a four-electron process and can require millisecond to second timescales,[151] but proton reduction can also benefit from the presence of cocatalysts. It has been shown that, in certain materials, 'trapped' photogenerated electrons can exist on a timescale of hours yet be unable to facilitate hydrogen production until a cocatalyst is added.[152]

The cocatalysts deposited on semiconductors for water oxidation and proton reduction are typically heterogeneous nanoparticles or clusters rather than well-defined molecular catalysts. As such the mechanisms by which these materials facilitate redox processes are often not well understood. Most proposed mechanisms for water oxidation catalysts involve the coordination of water to metal centres followed by oxygen–oxygen bond formation.[153–155] Similarly HE catalysts involve transfer of an electron from a metal centre to a proton to form M-H bonds followed by H-H bond formation. This means cocatalysts with higher Fermi energy levels are the most active catalysts whilst an intermediate M-H bond strength facilitates both absorption and desorption steps.[138,156,157] Cocatalysts can also lower the activation energy of unwanted reactions such as the reduction of oxygen. Coating methods, as shown in Figure 13, can be used to disfavour such competing back reactions by blocking gas diffusion to the active site surface.[121]

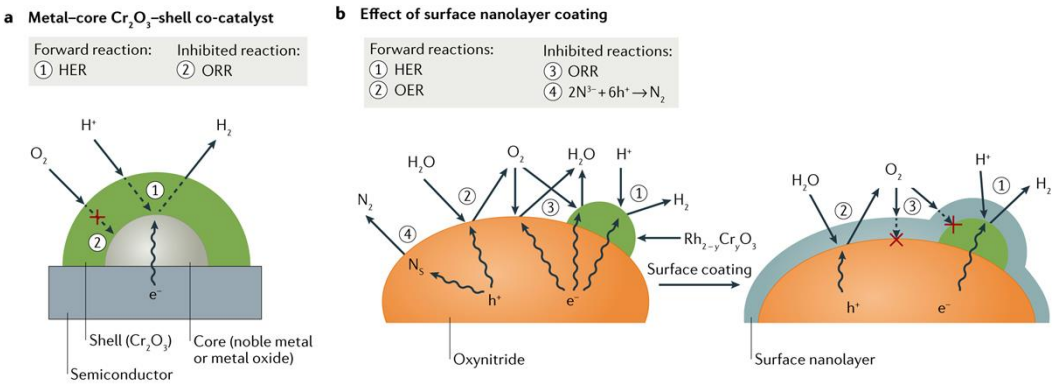

Figure 13: Schematic model of the functioning of a metal–Cr_2O_3 core–shell cocatalyst during the promotion of photocatalytic OWS. The surface nanolayer coating promotes proton reduction—hydrogen evolution reaction (HER)—and water oxidation—oxygen evolution reaction (OER)—over oxygen reduction reaction (ORR). *Reproduced with permission from reference [121].*

Depending on the rate of redox reaction versus charge carrier generation, holes and electrons may accumulate on cocatalyst sites or may be 'used' immediately. The amount and distribution of cocatalyst present on the semiconductor is thus often crucial to optimising hydrogen production. There is often a 'volcano' type relationship between cocatalyst loading and activity; at low catalyst loadings increasing content leads to an increase in activity up to an optimum level but above this value increasing content results in lowered activity. Low loading behaviour is dominated by the reduction in diffusion length required of charge carriers as cocatalyst content increases, whilst at higher levels cocatalysts can facilitate charge recombination or block light absorption.[158,159]

1.5 Photocatalyst Design

Materials chemistry papers frequently talk about 'design'[160–163]; the idea that a material's properties and performance for a given application can be accurately predicted based on the chemical groups or processing used. In order to successfully employ this strategy for hydrogen-producing photocatalysts, a thorough understanding of how different structural properties affect photocatalytic activity is needed. In this relatively new field these 'design rules' are not well defined. However, considering the mechanism of photocatalysis outlined above, it is possible to identify some of the factors that might affect hydrogen evolution rate:

Driving Force: The potential difference between the excited electron or hole and the redox potentials gives the thermodynamic driving force, or overpotential, for reaction. The positioning of semiconductor orbitals (or bands), and thus excited electron and hole

energies, are dictated by the chemical composition and bonding present in the semiconductor. The frontier molecular orbitals of organic semiconductors are typically aromatic π orbitals and thus conjugation along a polymer backbone or extended molecule can also significantly affect the orbital energies. As such, chain length and the angles between units—determined by substitution pattern and backbone twisting—can be as important as monomer structure or the functional groups present.

Light Absorption: The number of photons absorbed by the semiconductor depends on both the fraction of solar wavelengths that can interact with the material—the absorption onset—and the magnitude of the absorption; that is, the extinction coefficient of the material. The former depends on the band gap or HOMO-LUMO energy gap of the semiconductor and is thus affected by the same factors that govern driving force; the latter is a function of the material oscillator strength. Oscillator strength depends on a variety of factors including spatial overlap of the orbitals involved in the transition. Reactor design and the microstructure and dispersibility of the photocatalyst can also significantly affect the proportion of light that is transmitted through or scattered by a system.

Charge carrier lifetime, separation and mobility: This encompasses a number of processes, but all are affected by material properties such as the conformation of monomer units, the distances between and the relative orientation of molecules or chains (packing). In general, charge carrier lifetime and mobility are increased by more ordered systems with fewer defects that could encourage recombination.[164] Such properties may be affected by molecular structure or chain length but synthesis or processing methods can also govern the degree of crystallinity and the particular polymorph present in a material.

Surface Area: The area of the photocatalyst that is in contact with water or scavenger is dependent on the particle size of a suspension photocatalyst, or the roughness of a film. Porosity can also affect accessible surface area and, like external surface properties such as particle size and roughness, can depend on the chemical groups present but is often also altered by synthesis or processing methods. The ability of water or scavenger to permeate a material determines any internal surface area and is different to porosity. Although affected by pore size and distribution, the presence of hydrophilic functional groups is often key and can facilitate an increase in active area by pore wetting or by swelling otherwise non-porous structures.

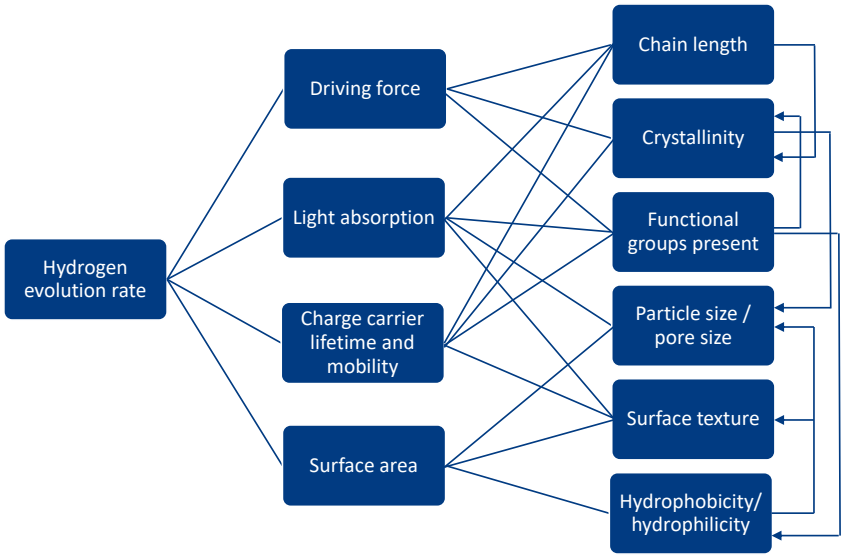

Figure 14: Scheme representing the factors and material properties that may influence photocatalytic hydrogen evolution rate and the complex cause-effect relationships between them.

Figure 14 shows the complex relationship between material properties, such as chain length or crystallinity, and the factors that dictate photocatalytic activity. Isolating individual structure-activity relationships in real-world materials is particularly hard due to the difficulty in changing only one property and affecting only one of these factors. Without an understanding of why a particular material has a high or low hydrogen evolution rate it is hard to identify the features that should be kept or enhanced when designing the next photocatalyst iteration and those that we should attempt to remove.

Indeed, one relatively new approach that has risen out of the expansion of high throughput workflows and automation is that of materials discovery.[165,166] This strategy relies less on design or control of material properties and instead relies on the testing of vast numbers of different materials to identify the best candidates for a particular application.[167] An increasing variety of material properties can also be measured in high throughput workflows, meaning large datasets can be used to see whether particular properties correlate with photocatalytic activity. Such post-rationalisation could provide significant insights into structure-activity relationships, especially when paired with machine learning techniques, which have been shown to be capable of using material datasets to predict hydrogen evolution rate to a reasonable degree of accuracy.[168]

Whilst high throughput screening of photocatalysts for hydrogen production can cover a lot of chemical space and frequently do find highly active ‘hits’, the search space has mostly been limited to testing ready-made materials or altering testing conditions.[169] Synthesising

and processing new materials still carry significant resource and labour costs. It is thus important to focus high throughput searches into feasible areas of investigation, a process that ultimately relies on some understanding of structure-activity relationships.

1.6 Materials Used for Photocatalytic Hydrogen Production

1.6.1 Inorganic Semiconductors

Five years after Fujishima and Honda first used TiO_2 as a photoelectrode for water splitting, Schrauzer and Guth showed that when a suspension of the same compound in water was irradiated with UV-light, hydrogen and oxygen were evolved in a 2:1 stoichiometric ratio.[170] This was the first example of light-driven OWS though a purely photocatalytic mechanism. Small amounts of hydrogen and oxygen were produced without the addition of a co-catalyst but the authors noted an improvement in hydrogen evolution by the addition of a Fe_2O_3 dopant. Soon after, it was reported that the addition of a RuO_2 cocatalysts was required for sustained oxygen production[171] whilst early studies using $SrTiO_3$ relied on Ni and Pt cocatalysts.[172,173]

TiO_2 provides a good example of how crystal structure can influence photocatalytic activity, as the rutile phase of the TiO_2 semiconductor in these initial studies was crucial for hydrogen and oxygen production. Anatase and brookite phases show little or no water-splitting activity, which has been attributed to the presence of trap states near to the valence bands of these two phases, which lowers the driving force for water oxidation.[174] TiO_2 and $SrTiO_3$ are some of the most widely studied semiconductors for overall water splitting and photocatalysts based on these materials can reach very high (> 30%) EQEs at UV wavelengths.[175,176] However, a fundamental issue with using these materials to produce solar fuels is their inability to absorb wavelengths greater than 400 nm. Metal oxides of many d^0 and d^{10} cations, [177–180] such as Ti^{4+}, were investigated in the 30 years following the initial report of OWS but in general these materials have valence bands composed of O *2p* orbitals with potentials around 3 V (vs NHE). Thus, if the conduction bands (normally metal cation *d* orbitals) of these compounds are to lie at a more negative potential than the proton reduction potential then the bandgap must be greater than 3 eV, precluding the absorption of most visible light.[121]

One strategy for raising VB potential and thus increasing visible light absorption is to replace the oxygen anions in metal oxides with less electronegative nitrogen or chalcogen anions. These have occupied orbitals (N *2p*, S *3p* and Se *4p*) that lie at higher energies than O *2p* and thus introduce valence bands that sit at less negative potentials. This concept was

applied in 2006 by Domen *et al* to give the first example of visible light driven photocatalytic water splitting.[181] Their $(Ga_{1-x}Zn_x)(N_{1-x}O_x)$ semi-conductor uses aliovalent substitution of Zn^{2+} for Ga^{3+} to tune the O/N ratio of the solid solution and give an absorption onset at 510 nm and EQEs of up to 2.5% between 420 and 440 nm. Further 'red-shift' can be achieved with perovskite structures based on $LaMg_xTa_{1-x}O_{1+3x}N_{2-3x}$ [182] or oxysulfides such as $Y_2Ti_2O_5S_2$[183] that can split water at wavelengths up to 600 nm. However, the efficiency of these materials is significantly lower than wider bandgap semiconductors and many oxynitride materials are not stable to photodegradation unless coated with an oxyhydroxide nanolayer.[121]

The addition of dopants with partially filled *d* orbitals is a less widely used technique for raising VB energy, as such transition metal centres tend to act as recombination centres. One example of this is Rh/Sb doped $SrTiO_3$ which uses Sb^{5+} in Ti^{4+} sites to stabilise the formation of Rh^{3+}.[184] Rh 4*d* orbitals effectively provide a higher energy VB and enable absorption up to 520 nm but the EQEs of this system are limited to 0.1% at 420 nm.

Several visible light absorbing photocatalysts, such as Fe_2O_3, WO_3 and $BiVO_4$, show high activity as water oxidation catalysts but have conduction bands with insufficient potential to drive proton reduction.[185–187] Bismuth-containing materials have been modified to increase the bandgap and allow for overall water splitting. This was first achieved by Yttrium doping,[188,189] but much higher activity has been reported for simultaneous substitution of In^{3+} and Mo^{6+} into $BiVO_4$. These dopants induce a partial phase transition in the semiconductor lattice from monoclinic to tetragonal which results in a raised conduction band energy and a 'greenish' $BiVO_4$ with an EQE of 3.2% under overall visible light (420–800 nm) (Figure 15).[190]

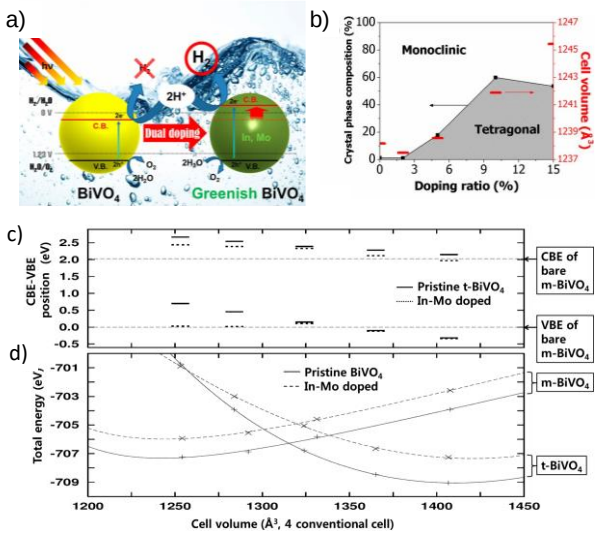

Figure 15: $BiVO_4$ modification to facilitate proton reduction. Doping with In and Mo induces a phase transformation which raises the CB energy. *Reproduced with permission from reference [190].*

Above are examples of single absorber/one-step excitation, as shown in Figure 9a. Z-scheme arrangements with two absorbers were first shown to be active for visible light driven water splitting in 2001.[191] This initial study used a platinised $SrTiO_3$-based HEP coupled with platinised WO_3 for photocatalytic oxygen evolution and a IO_3^-/I^- redox shuttle to enable electron transfer between the two. Similar Pt/WO_3-based OEPs have been paired with more efficient Ta and Zr oxynitrides,[192] as well as a variety of oxysulfides[193] to generate tandem systems with EQEs of up to 6.8% at 420 nm.[194] To date, one of the most active Z-schemes using a solution phase redox shuttle used $[Fe(CN)_6]^{-3/-4}$ with a $CoO_x/BiVO_4$ OEP and a Rh/Cr_2O_3 loaded Zn/Ta oxynitride HEP to achieve STH of 0.5% (Figure 16).[195]

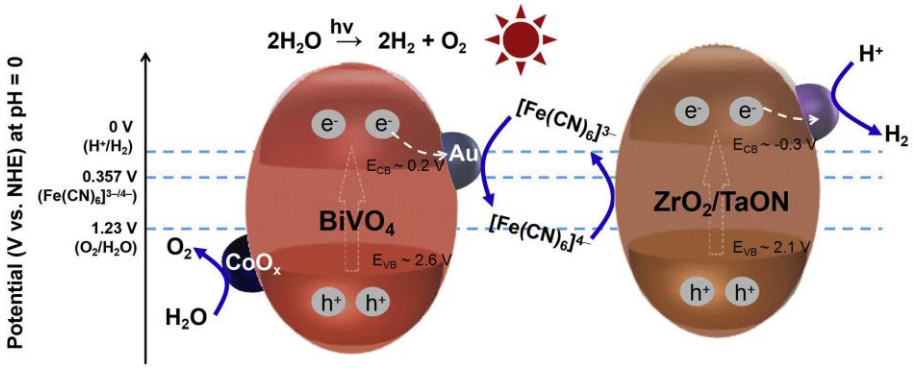

Figure 16: Z-scheme overall water splitting with tandem $BiVO_4$ and ZrO_2/TaON semiconductor absorbers with CoO_x water oxidation catalyst, Au to catalyse reduction of the $[Fe(CN)_6]^{3-}$ redox shuttle and Rh/CrO_x for proton reduction. *Reproduced with permission from reference [195].*

Z-scheme systems have been reported for separate particulate systems without any redox shuttles,[123] but higher efficiency (> 1% STH) systems rely on photocatalyst particles immobilised on a solid state electron mediator. Commonly these are expensive noble metals[196–199] but reduced graphene oxide[200] and carbon[122] have also been shown to be effective conducting layers, improving the scalability of these sheet-type systems.

The contact between particles and mediator is crucial to photocatalytic activity in these systems and has been improved by annealing,[199] but an alternative approach is to generate fused heterostructures.[201,202]. These often rely on HEP and OEP crystal phases that can grow off one-another's surfaces such as Ta_3N_5 and $BaTaO_2N$,[125] whose similar octahedral structural units allow for lattice alignment (Figure 17) and an improved charge transfer interface. A similar concept has also been applied to InGaN embedded in GaN nanowires, although this is stated to be a 'one-step' system rather than a Z-scheme heterostructure.[203] A follow up study improved activity significantly by introducing an electric field along the wire by Mg-doping.[120] This was thought to provide a driving force for charge separation and resulted in a STH of 3.3%. Aside from a similar InGaN heterostructure that was reported recently[204] and the aforementioned Co_xO single component system[117] (which both claim > 5% efficiency), this is the highest reported STH for any OWS photocatalyst.

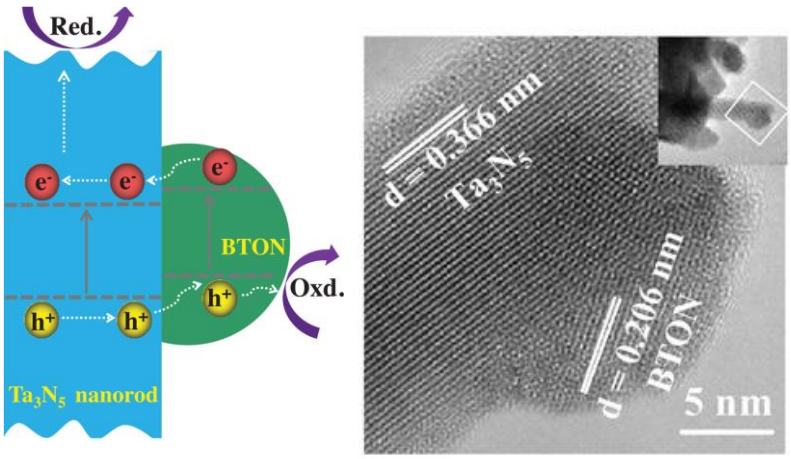

Figure 17: Z-scheme overall water splitting with fused Ta_3N_5 HEP and $BaTaO_2N$ OEP. *Reproduced with permission from reference [125].*

The above overview focuses on semiconductor modification but nearly all of these examples utilise one or more co-catalyst components. Transition metal oxides, such as IrO_x, MnO_x, RuO_x and CoO_x, are the mostly widely utilised oxygen evolution catalysts whilst metal nanoparticles of Pt, Pd, Rh and Ni, as well as sulfides and phosphides, have been shown to facilitate proton reduction.[205] Cocatalysts can also reduce semiconductor photodegradation

and are thought to aid in interfacial charge transfer.[138] These factors are dependent on the chemicals chosen but can also be controlled through modification to the co-catalyst surface and interface.[205] Very recently, Domen and co-workers optimised their $SrTiO_3$:Al photocatalyst by doping the oxygen and hydrogen evolving cocatalysts on separate crystal facets to promote 'one-way' charge separation within particles and achieve EQEs of 96%.[206] This, however, was only achieved using high energy wavelengths (< 360 nm) and it may be that such high efficiency is much more difficult to achieve with smaller bandgap semiconductors; at a rudimental level, charge separation processes always rely on a degree of 'downhill' potential to get from the initial excitation to a successful redox reaction. Nevertheless, the fact this result represents efficiencies of close to unity across the multi-step processes of light absorption; charge carrier generation, separation and transfer to active sites; proton reduction and water oxidation is quite remarkable. This study proves photocatalytic systems can realise OWS close to the theoretical limits described in Figure 7b.

1.6.2 Metal-Free Semiconductors

The above examples all rely on metal-based inorganic semiconductors. However, in 2009, Wang *et al.* reported visible light-driven hydrogen production from water using a metal-free carbon nitride semiconductor and a Pt co-catalyst in the presence of a triethanolamine (TeOA) sacrificial electron donor.[207] Carbon nitrides, shown in various forms in Figure 18, are a class of polymers based on triazine and heptazine units and had been previously shown to be active as a heterogeneous catalysis.[208] The 2009 study created a huge amount of interest in graphitic carbon nitride ($g\text{-}C_3N_4$)[1] as a cheap, stable and earth-abundant alternative to metal-oxide semiconductors for solar fuel photocatalysis.

[1] note this abbreviation is literature convention and often does not represent the elemental composition of photocatalyst materials.

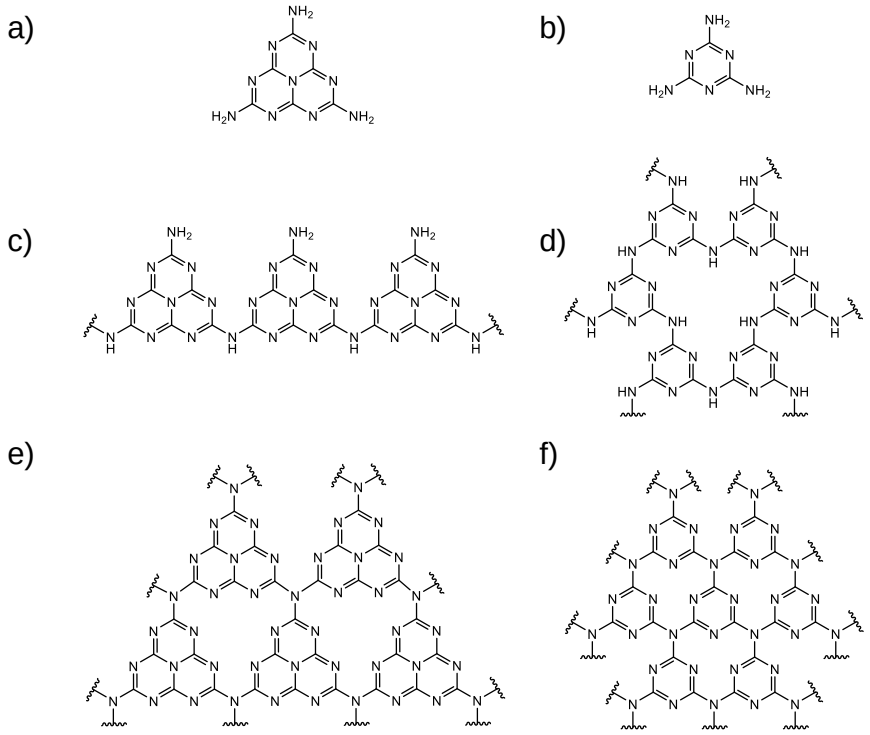

Figure 18: Carbon nitride and related materials. a) melamine, b) triaminotriazine, c) melon, d) poly(triazine imide), e) heptazine-based C_3N_4, f) triazine-based C_3N_4.

Unmodified g-C_3N_4 is usually formed through condensation of dicyandiamide or melamine precursors at temperatures of 450–600 °C, which gives a melon-type structure (Figure 18c) with a bandgap of 2.6–2.7 eV, substantially larger than the 2.1 eV bandgap of the theoretical infinite sheet of fully condensed g-C_3N_4.[207,209] Nitrogen p_z orbitals are primary components of the materials' HOMO levels and thus form the valence band, whilst the LUMOs are derived from mostly carbon p_z orbitals and make up the conduction band. These have been calculated by density functional theory (DFT) to give oxidation and reduction potentials of approximately 1.5 and -1.2 V versus NHE and thus indicate the material has an appropriate band structure to drive proton reduction and water oxidation.[207] These potentials have subsequently been supported by cyclic voltammetry and photoelectron and inverse photoemission spectroscopy measurements.[210,211] The materials absorption onset is correspondingly around 460 nm and a common strategy for optimising g-C_3N_4 photocatalysts is to narrow the bandgap through atomistic doping. S, P, C, I, O, F and B, as well as many metal cations have been doped into g-C_3N_4-based photocatalysts[212] and, whilst this can significantly extend the materials absorption spectrum, doping can also increase charge carrier recombination[213] possibly through increased disorder.[212] To avoid this, strategic and controlled doping is required, for example O-doping at bridging positions has been shown to give materials with absorption up to 800 nm and high 10% EQEs.[214]

Dye loading has also been employed to extend the absorption spectra of carbon nitride materials. Organic molecular dyes such as Eosin Y and indole-based donor acceptor structures, as well as organometallics such as zinc and manganese phthalocyanine complexes have been added to carbon nitrides to produce composites with higher HER than unmodified materials.[215–217] Mesoporous carbon nitrides and small dye loadings are commonly employed in such systems to prevent the blocking of the semiconductor or cocatalyst interface with water. Composite materials with onsets and activity in the near-IR region can be formed but these are yet to be combined with the highest EQEs, possibly due to poor charge transfer across the photosensitiser/semiconductor interface.

Possibly the most common strategy for improving the photocatalytic activity of carbon nitrides is to employ microstructuring techniques to increase the semiconductor active surface area.[218] These morphological approaches are covered in more detail in the next chapter, Section 2.1.

Precursor selection is an important factor in the activity of carbon nitride photocatalysts. Using urea instead of dicyandiamide or melamine precursors has been found to give increased HER on a number of occasions.[219–221] This has been attributed to higher degrees of polymerisation[221] but it has also been suggested that persistent unreacted end-groups can improve hydrogen evolution rates in carbon nitrides[222] meaning the role of amine, cyanamide and other protonated groups is still somewhat unclear. Another strategy has involved the use of 'pre-organised' materials such as melamine/cyanuric acid which form self-assembled supramolecular structures before heating to convert to g-C_3N_4. This can give a variety of nanostructures[223] with increased dispersibility and surface area but is also thought to increase order within the semiconductor and improve charge transport.[224]

The most active carbon nitrides are fabricated using ionothermal molten salt procedures. These are employed after the initial melon-forming calcination and give significantly more crystalline materials. In 2016, Wang and co-workers produced a highly ordered carbon nitride photocatalyst using this method. The material had reduced electron-hole recombination due to a low density of defect sites and so could reach EQEs of above 50% at 405 nm for the first time.[225] Zhang *et al.* subsequently increased efficiencies even further by switching to a urea/oxamide precursor which gave a reduced bandgap for improved light absorption and smaller interlayer stacking distances thought to aid exciton dissociation and charge transport between layers.[226] Most recently the same authors reported EQEs of 60%, the highest of any carbon nitride, by optimising the salt mix used for ionothermal treatment. NaCl /KCl mixtures were found to avoid the formation of less active poly(triazine imide)

(Figure 18d), compared to lower melting point Li salts, and encourage the formation of a triazine-heptazine donor-acceptor structures which may aid charge separation.[220]

The headline efficiency above was tested over 16 hours but sustained hydrogen production has also been reported for platinised g-C_3N_4 in a scaled-up 0.7 m^2 reactor across 30 days of operation albeit with much lower EQEs[227]

Carbon nitride has primarily been examined for proton reduction or water oxidation under sacrificial conditions but OWS has been achieved though the loading of g-C_3N_4 with appropriate H_2 and O_2 producing cocatalysts.[228] There are a small number of reports of carbon nitride and carbon-based materials for OWS without metal cocatalysts, which often attribute their activity to heterojunction type nanostructures.[229] A 2015 study on g-C_3N_4 loaded with carbon quantum dots which reported an EQE of 16% at 420 nm and STH of 2%.[118] However, to date no follow-up studies have been reported that reproduced these results. There are significantly more reports of OWS by carbon nitrides incorporated into Z-scheme systems with inorganic semiconductors and loaded with appropriate cocatalysts.[230–233]

Aside from carbon nitride, mixed main-group semiconductors based on boron carbides, B_6O, BP, BN, borocarbonitrides[234] and $C_3N_3S_3$[235] have been shown to be active for hydrogen production from water under sacrificial conditions although with low (< 1%) EQEs. Although elemental carbon is not a semiconductor, N-and P-doped graphene can have visible light compatible bandgaps and show moderate activity as hydrogen production photocatalysts,[236,237] as can nanostructured silicon[238] and red phosphorus.[239] In recent years, black phosphorus has become a particular material of interest for proton reduction,[240241] and Z-scheme[242] OWS, due to its near-IR absorption onset and the ability to create high surface area nanosheets.

1.6.3 Organic Semiconductors

Organic materials are generally considered to contain C-H bonds. Whilst the idealised structure of graphitic carbon nitride is C_3N_4, the real-world materials used as photocatalysts also contain significant amounts of hydrogen[243] and thus could be considered organic. The carbon nitride-based materials above are differentiated from other organic materials, below, primarily due to synthetic considerations; carbon nitrides are prepared through low-yield, high-temperature reaction of a small number of precursor materials and thus the chemical diversity achievable through modern organic chemistry cannot be fully employed. A range of cross coupling techniques including Sonogashira, Kumada, Negishi, Stille and Suzuki

polymerisation,[244] as well as reversible low-temperature condensation and cyclisation reactions mean a huge range of functional groups can be tolerated and incorporated into extended conjugated materials.

1.6.3.1 Conjugated Linear Polymers

The 2009 paper by Wang *et al.* on carbon nitride began a new era of interest in carbon-based semi-conductors as hydrogen producing photocatalysts, but this was not the first 'metal-free' semiconductor shown to be capable of light driven hydrogen production from water. In 1985 Yanagida *et al.* showed that, upon irradiation with light of $\lambda > 290$ nm and using triethylamine or diethylamine sacrificial electron donor, poly(*p*-phenylene) (**PPP** Figure 19) was capable of photocatalysing proton reduction to molecular hydrogen.[245] No metal cocatalysts were added in these initial experiments although the polymers were formed by Kumada-type coupling so likely contained residual Ni. Subsequent studies by the same authors showed that the addition of Ru^0 increased the HER of poly(*p*-phenylene) by a factor of 7 and provided the first evidence that noble metal particles could aid in the transfer of electrons from polymer to protons.[246]

Easy modification of monomer chemical structure is perhaps organic semiconductors' greatest advantage in comparison to inorganic materials and can result in huge changes to a polymers physical and optoelectronic properties.[160] Again, this was first shown in the context of photocatalytic proton reduction by Yanagida when his group demonstrated the order of magnitude increase in HER on moving from the homopolymer of phenylene (**PPP**) to the 2,5-homopolymer of pyridine (**PPy** Figure 19).[247] The bandgap of **PPy** was found to contract by 0.5 eV in comparison with its phenylene analogue, leading to an absorption onset reaching further into the visible region. This extended light absorption range does not, however, fully explain the increased activity of **PPy** observed at wavelengths less than 400 nm. Instead, the authors suggest the heterocycle provides an effective interface for charge separation and electron transfer through radical intermediates that are not accessible to **PPP**. This is stated to be partially due to the more coplanar chain of **PPy**, whereby reduced steric clash from the absence of the 6-proton results in a less twisted backbone geometry and increased stabilisation of radical anions by delocalisation. Whilst subsequent studies have also invoked the importance of hydrophilicity to explain the activities of these particular materials,[248] this concept of planarisation has also been used in more recent studies on linear polymers for photocatalysis; In 2016 Sprick *et al.* synthesised a series of planarised fluorene-type co-polymers shown in Figure 19 **P2-7**. [249] The fused fluorene unit in **P2** and **P3** was found to give HERs between 3 and 4 times greater than the freely rotating phenylene units in **P1**. Importantly this was despite equivalent synthesis methods and similar palladium

contents across the polymers. Interestingly, the optical gaps of the planarised materials, particularly **P2**, were not significantly different to **P1.** Oligomeric analogues with equivalent chain lengths did show slightly red-shifted absorption spectra for fluorene-containing materials but it does appear that planarisation benefits photocatalytic activity beyond improving light absorption properties.

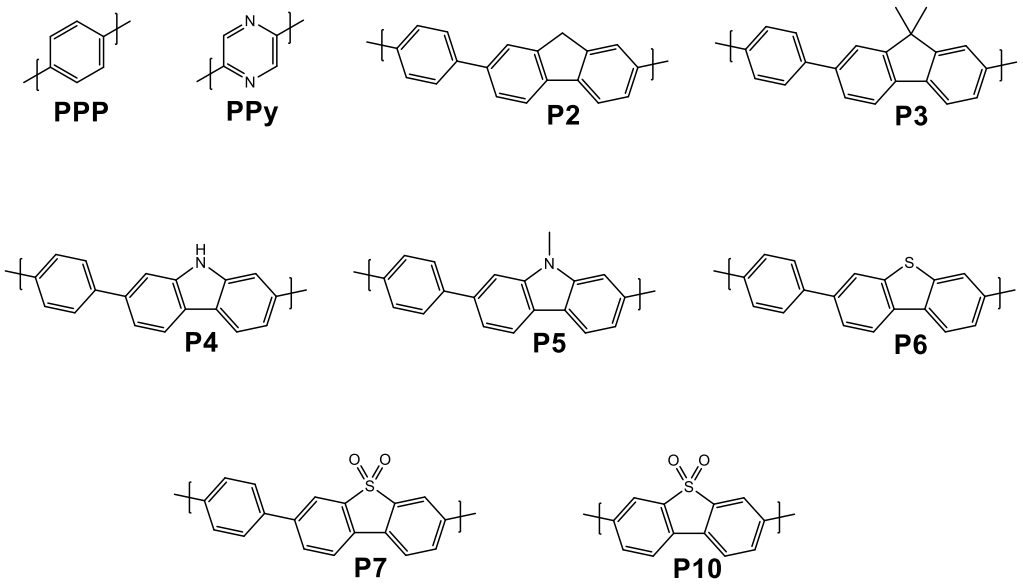

Figure 19: Linear polymer photocatalysts for hydrogen production.

Even more significant improvements in activity were found when replacing the bridgehead carbon atom of the fused ring with alternative heteroatom based functional groups such as in the carbazole, dibenzo[*b,*d]thiophene and dibenzo[*b,d*]thiophene sulfone bearing polymers **P4-7**. Of these, **P7** is the most active hydrogen producing photocatalyst with a rate of 2,352 μmol h^{-1} g^{-1} under broad spectrum irradiation, which was higher than platinised TiO_2 tested on the same set-up. Significantly, the slightly contracted 2.70 eV bandgap of **P7** allows for absorption of visible wavelengths of light meaning that, unlike TiO_2, **P7** has a significant external quantum efficiency of 7.2% at 420 nm.

Since this initial finding, the dibenzo[*b,*d]thiophene sulfone (dbts) unit has become one of the most widely studied monomers in organic photocatalysts for hydrogen production and has been incorporated into various linear polymers, CMPs, COFs and CTFs, some of which are detailed below. Insights into dbts-bearing materials' high activity were elucidated using a combination of modelling and spectroscopic measurements on the highly active dbts homopolymer **P10**.[141] Transient absorption spectroscopy (technique outlined in Section 1.7.3) showed that, upon excitation in the presence of a triethylamine sacrificial electron

donor, **P10** gives a long-lived absorption signal at 630 nm assigned to an electron polaron, indicating hole transfer from a polymer-based exciton to TEA. This feature was found to have significantly smaller amplitude in polymers with decreasing dbts content. Modelling suggested the increased polaron yield of **P10** was the result of increased thermodynamic driving force for electron transfer due to the increased localisation of water around this material. Dbts units have a permanent dipole of 5.7 D which makes **P10** significantly more hydrophilic than phenylene based materials, with smaller, sub-60°, contact angles with water. Aside from stabilising charge carrier generation, this increased wettability may also influence the polymer microstructure and dispersibility, resulting in increased polymer surface area in contact with the reaction medium or exposed to light.

Benzothiadiazole is another acceptor monomer with a substantial permanent dipole[250] and has also been shown to form linear polymers with high HERs.[251,252] The co-polymer of benzothiadiazole and phenylene has an EQE of 5.38% at 420 nm whilst, on an identical set-up, the equivalent dbts/phenylene co-polymer, **P7**, has a similar EQE of 6.61%.[251] Modelling of a high activity benzothiadiazole/fluorene co-polymer concluded, similarly to the dbts study described above, that the heteroatoms in the benzothiadiazole unit, may facilitate hydrogen-bond formation and thus could improve interaction with water molecules or protons.[253]

The above examples increase wettability by altering the polymer backbone but it is also possible to add hydrophilic side chains such as ethylene glycol to conjugated linear polymers. This was first done in 2016 by Yu and co-workers who added triethylene glycol (TEG) chains to a benzodithiophene/bipyridine co-polymer.[254] Despite decreased contact angles with water, this material was outperformed substantially by a perylenebisimide-based polymer with hydrophobic alkene chains, most likely due to perylene based materials redshifted absorption spectra and subsequently improved light absorption properties. More surprising was the fact that an analogous benzodithiophene/bipyridine co-polymer with hydrophobic dodecyl side chains had almost identical activity to the TEG-bearing material. This is in direct contrast to more recent studies that have shown TEG side chains can improve the photocatalytic activity of fluorene/phenylene co-polymers by a factor of 40 compared to hydrocarbon sidechains.[255] Even polymer backbones with polar dbts groups were found to have double the activity moving from hexyl to TEG side chains. This, and other studies,[256] suggest the hydrophilic chains improved dispersibility compared to the alkane analogues with evidence of reduced suspension particle sizes and increased swelling leading to increased catalytically active area. TEG side chains have also been associated with increased photogenerated electron lifetime,[255] improved interaction with Pt cocatalysts

and reduced interlayer stacking distance,[256] highlighting the complex effect changes to molecular structure can have on the various factors shown in Figure 14.

At the extreme of polar hydrophilic polymers are polyelectrolytes. In these materials full wetting would be represented by fully dissolved single chains of polymer. Recently, Wu *et al.* synthesised an alkyl ammonium bromide-bearing polyelectrolyte with a conjugated fluorene/phenyl/ethyne backbone that does appear to fully dissolve in aqueous solution at 0.05 mg mL^{-1} concentrations. However, this material had very low activity for photocatalytic hydrogen evolution.[257] Interestingly, adding fluorine or cyano-substituents to the polymer backbone appeared to induce partial aggregation of the polymer chains and lead to an order of magnitude increases in HER suggesting maximising interactions with water must be weighed against maintaining interchain interactions which could aid charge separation and transport.

Linear polymers have also been used to demonstrate the importance of chemical structure in tailoring the VB and CB energies. Polythiophene is a low-bandgap material which absorbs up to 800 nm but subsequently has a 0.8 eV driving force for proton reduction, in contrast to **PPP**'s 1.5 eV overpotential and limited visible light absorption. Sprick *et al.* showed that co-polymerisation with varying proportions of thiophene and phenylene monomers resulted in materials with bandgaps intermediate between that of the homopolymer end points and with up to six times the photocatalytic activity.[258] This study demonstrates the balance between using a small enough semi-conductor bandgap to allow for a significant proportion of solar irradiation to be absorbed whilst also maintaining sufficient thermodynamic driving force for the reduction of protons and oxidation of the scavenger respectively.

Several studies on heterogeneous linear co-polymers credit the combination of donor and acceptor monomers with improving charge separation in the excited state[253,254] and charge transfer has also been explored through physical mixtures of separate donor and acceptor polymers. Cao and co-workers used triphenylamine-bearing polymer donors with benzothiadiazole-bearing polymer acceptors and showed that mixtures of the two materials, and particularly nanostructures formed by blending the two materials, had activity that outperformed the individual polymers.[259] The authors ascribe this effect to photoinduced charge transfer between the two polymers reducing recombination. More recently, Kosco *et al.* showed a similar concept could be applied to produce heterostructures with very high activity (60 mmol h^{-1} g^{-1} using an ascorbic acid SED and wavelengths from 350 to 800 nm).[260] The donor and acceptor polymers used in this study are shown in Figure 20 and showed the importance of the interface between the materials and with water, as

photocatalytic activity varied by an order of magnitude moving from core-shell assemblies to an intermixed blend. This allows high EQEs of up to 6.2% at red-shifted 700 nm wavelengths.[260]

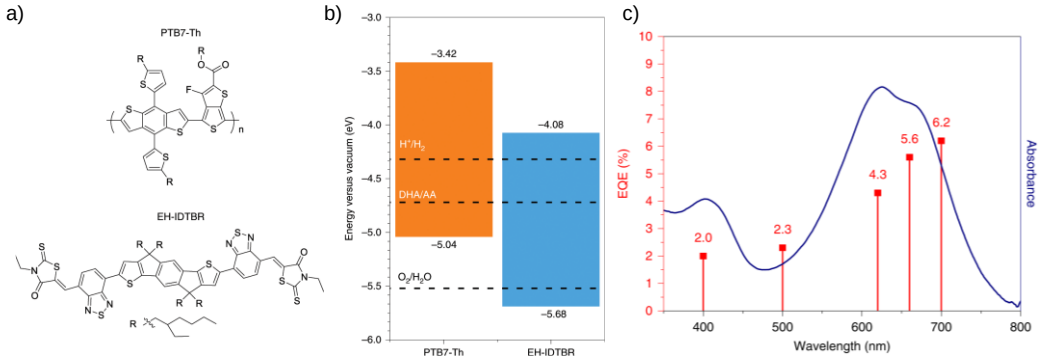

Figure 20: Heterostructure polymer nanoparticles for photocatalytic proton reduction. *Reproduced with permission from reference* [260].

1.6.3.2 Conjugated Polymer Networks

Aside from carbon nitride, the first polymeric networks to be shown to be active for hydrogen production were a series of polyazomethine networks developed by Schwab *et al*.[261] These highlighted the effect that linker regioisomerism can have on photocatalytic activity, with order of magnitude increases in HER upon moving from a 9,10-substituted anthracene dialdehyde, to 2,6-substituted anthracene and naphthalene dialdehydes. In this instance twisting of the anthracene linker out of the plane of the network was thought to interrupt charge carrier transport but similar effects have also been observed for flat tridentate linkers, particularly 1,3,5-phenylene,[251,262] the *meta*-substitution pattern of which is thought to reduce polymer conjugation length.

As with linear polymers, forming CMPs with varying proportion of two optoelectronically contrasting monomers, phenylene and pyrene in this case, has been found to be an effective method for tuning polymer bandgap.[263] An intermediate bandgap of 2.33 eV, between those of the two homogeneous end points, was again found to be the most active photocatalysts for proton reduction. Interestingly, varying monomer content also had a large effect on porosity, with BET surface areas ranging from 597 – 1710 m^2 g^{-1}, but in line with several subsequent CMP studies,[251,262,264] this did not appear to correlate at all with catalytic activity. This is not to say that microstructure and porosity have no effect on HER; it may be that their significance is masked by other optoelectronic factors. Systems where porosity is found to correlate with photocatalytic activity, often contain significantly more heteroatom groups

and it has been suggested that hydrophilic pores are crucial in enabling full wetting of open network structures.[265,266] Without this, accessible surface areas measured by gas sorption do not necessary translate into catalytically active surface area where contact between polymer and water (or SED) enables reaction to occur. This and other microstructural effects are reviewed in more detail in Chapter 2 and Chapter 4.

The hydrophilic, acceptor-type benzothiadiazole and dbts monomers have been used in a CMP structures by a number of groups[251,266,267] but Yu and co-workers have focused on more red-shifted aromatic linkers based on perylene and thiophene.[268,269] They, and others,[270,271] have shown that, when co-polymerised with phenylene-type linkers, these strong donor units tend to have low activity. However, significantly higher HERs can be achieved when they are combined with pyridyl-based acceptors, shown in Figure 21, which are thought to give improved charge separation. The most active material, **PCP11**, which is also stated to have an optimised dipole moment as well as improved wettability and crystallinity, has a moderate EQE of 1.93% at 400 nm.

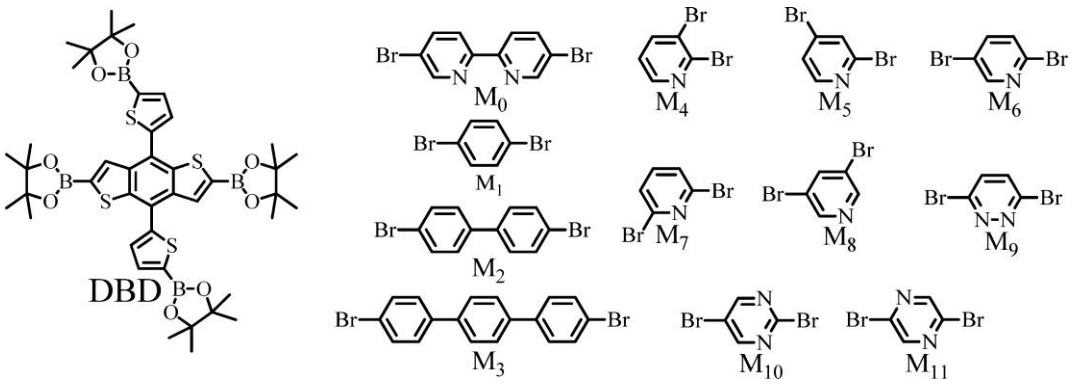

Figure 21: Structures of comonomers (M0−M11) used for the preparation of **PCP0−PCP11**, by Suzuki Coupling. *Reproduced with permission from reference [269]. Copyright (2016) American Chemical Society.*

Like many CMP and linear polymers synthesised through Pd-catalysed cross coupling these materials show photocatalytic hydrogen production without the addition of Pt cocatalysts. It is widely accepted the carbon nitride materials require a metal co-catalyst to achieve significant hydrogen evolutions rates but the role of residual palladium in organic polymers had, until recently, been less widely studied. The insoluble nature of most of the photocatalysts in question make complete removal of Pd nanoparticles very difficult and CO poisoning experiments show little change in activity.[263] The materials shown in Figure 21, and several other studies[251,263,272] showed no particular correlation of Pd content with HER

across different polymer structures. However, the authors showed that their **PCP0** polymer synthesised with increasing Pd contents did have higher activity, up to around 0.8 wt. % Pd when the HER appeared to plateau.[268] More recent studies on the role of palladium on photocatalytic activity are discussed in Section 3.8, where the topic is investigated in detail.

CMPs containing triazine units, often referred to as covalent triazine-based frameworks (CTFs), are often differentiated from other CMP photocatalysts, perhaps because they can be formed though nitrile trimerisation reactions[273–275] rather than carbon-carbon bond forming reactions. In reality, many CTFs studied for photocatalysis could be, and sometimes have been,[265,276] formed through metal catalysed cross coupling reactions to give chemically (if not microstructurally) analogous materials. One of the first examples of CTFs as a hydrogen production photocatalysts was in 2015 when CTF-1, the network formed by trimerization of 1,4-dicyanobenzene, was shown to have visible light activity comparable to g-C_3N_4.[277] Shortly after, Lotsch and co-workers, reported an oligomeric phenyl-triazine material, formed from the same starting materials but using lower synthesis temperatures. These were thought to have higher activity than more condensed structures, possibly due to increased crystallinity and hydrophilicity.[278]

Increasing the length of phenyl linkers was found to increase the HER of CTFs to a certain extent,[279,280] but higher activities have been achieved through the introduction of heteroatom-containing functional groups such as carbazoles or nitriles.[276,281] Donor-acceptor structures have been used in CTFs in an analogous way to other CMPs. Bodjys and co-workers used fused thiophene donors and found that triazine/benzotrithiophene CTFs gave particularly high HERs, which were assigned to strong charge transfer interactions through short donor-acceptor distances. The authors also suggest that push-pull type spatially separated orbital structures can provide an alternative route to reducing bandgaps as opposed to increasing conjugation lengths through extended aromatic synthons.[282]

Huang *et al.* took a slightly different approach and aimed to create co-block polymer-type structures by introducing a second monomer 30 minutes into the polymerisation reaction.[283] This heterostructure was found to show significantly longer PL lifetimes and higher activity than the separated components suggesting that the junction does improve charge separation. The authors state that the fully covalent interface is important for this and enables a high 7% EQE under visible wavelengths.

Most CMP and CTF materials are amorphous but recently an alternative CTF synthesis method using *in situ* oxidation of alcohols to aldehydes was developed by Tan *et al.* which produced more crystalline, highly active materials at relatively low temperatures. It is

thought that the slow production of the aldehyde reagent in this method results in a more controlled polymerisation with a low nucleation rate and thus highly ordered structures.[284]

Aside from carbon nitride-based materials, CTFs were also the first polymeric semiconductors shown to be active for the water oxidation half reaction. The initial report of the photocatalytic activity of CTF-1 demonstrated that, in addition to HE activity, when loaded with an RuO_x co-catalyst the material had low activity for photocatalytic oxygen evolution.[277] The reduced carbonisation of low-temperature CTF synthesis compared to high-temperature salt-melts, is often cited as crucial to photocatalytic activity and the CTF-1/RuO_x combination was also found to have significantly higher OE activity (up to 140 μmol g^{-1} h^{-1} using an $AgNO_3$ electron scavenger, $\lambda > 420$ nm), when the polymer was synthesised under mild microwave conditions, which the authors suggest gives a highly ordered structure.[285] Whilst several CTFs have been shown to be active for oxygen evolution, and generally show higher rates than carbon nitride,[279,286] one of the most active organic water oxidation photocatalysts to date is an alternative aza-CMP formed from the condensation of 1,2,4,5-benzenetetramine and hexaketocyclohexane.[287] This material's headline visible-light OER of 572 μmol g^{-1} h^{-1} was achieved using a $Co(OH)_x$ co-catalyst ($AgNO_3$ electron scavenger, $\lambda > 420$ nm) and interestingly the low 1.22 eV bandgap of this material allowed limited photocatalytic activity to persist up to near-IR wavelengths (> 800 nm).

There are a few reports of OWS by CMP photocatalysts. In 2017 Xu and co-workers reported overall water splitting using nanosheets of 1,3-diyne linked CMP.[288] Surprisingly, this single component catalyst was stated to reach STH efficiencies of 0.6% without the addition of any metal cocatalysts (and importantly was not synthesised using noble metal-catalysed cross-coupling). It should be noted that no follow-up studies have been reported to date that reproduce these remarkable results. The evolution of hydrogen and oxygen in these systems was dependant on sonication of the photocatalyst after illumination. The authors state this is to release gas trapped in the pores of the material, but this processing raises questions about the possibility of mechano-chemical water splitting in this set-up.[289] That said, the same authors have also reported OWS using a Z-scheme of two aza-fused CMPs that does not rely on sonication.[290] In this instance, a van der Waals heterostructure of weakly interacting interlayered HEP and OEP sheets was thought to be crucial to the material's activity. The authors demonstrate increased photocurrent in the composite material versus the separate components so claim the heterostructure enables efficient charge separation and migration.

1.6.3.3 Covalent Organic Frameworks

Covalent organic frameworks (COFs) were first developed in 2005 by Yaghi and co-workers.[291] COFs are a class of extended networks held together by reversible covalent bonds, such as those in boronate esters, imines and hydroazones.[292] This contrasts with CMPs that have monomers joined by strong, irreversible covalent bonds.[293] The reversibility of COF network linkages allows for reorganisation of defects during synthesis, moving the system from kinetic to thermodynamic control and allowing the formation of single crystals with order up to μm-scale domains.[294] COFs have the potential to combine crystallinity, porosity, and extended conjugation with molecular tunability and thus are particularly attractive for photocatalytic hydrogen production.

In 2014, Lotsch and co-workers developed hydrazone-based **TFPT–COF** (Figure 22) which, when loaded with a Pt cocatalyst, was shown to be active for visible light driven hydrogen production under sacrificial conditions.[295] The same authors followed this with an azine linked triazine-bearing material, **N_3–COF**, which was found to have higher activity than related pyrimidyl, pyridyl or phenyl-bearing analogues. This was thought to be due to the higher planarity of the triazine-linked units giving decreased disorder and lateral offset between layers and higher surface areas.[296] Whilst these materials show reasonable, 2-3 day, retention of photocatalytic activity over time, the inherent instability of many COF linkages make them unsuitable for prolonged exposure to water or non-neutral pH which often leads to collapse of the low-density ordered structure.

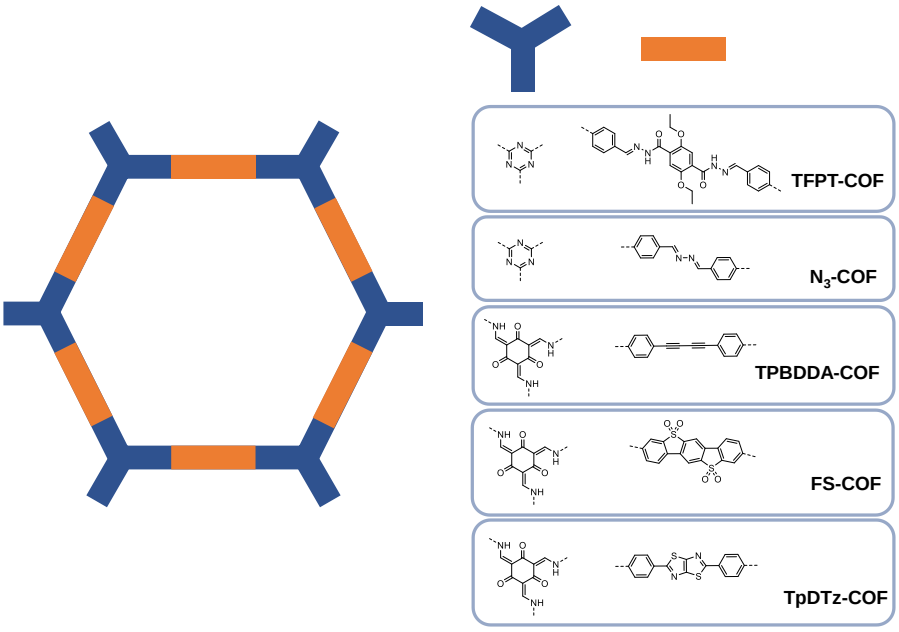

Figure 22: Structures of selected COFs used for photocatalytic proton reduction.

Kandambeth *et al*. had previously developed a versatile strategy of COF linkage stabilisation using 1,3,5-triformylphloroglucinol.[297] This aldehyde could undergo reversible Schiff-base reaction with amine linkers to give imine-linked networks, but these linkages also contained enols. After reversible formation of the order network, enol-keto tautomerisation occurs and is rendered essentially irreversible by the presence of a strong intramolecular hydrogen bond in this form. This approach allows a diverse set of aromatic di and tri-amines to be used in the synthesis of stable COFs and was utilised in 2018 to give a diacetylene-bearing COF, **TP-BDDA COF**, which retained crystallinity in a variety of organic solvents as well as water and HCl (3M).[298] The EQE of this material was found to be 1.3% at 420 nm. Interestingly the activity of this **TP-BDDA COF** was over ten times that of an analogous monoacetylated material with a similar absorption spectrum, surface area and stacking arrangement. The difference was assigned to improved charge transport characteristics of the diacetylene linkers but demonstrates that COFs, like CMPs and linear polymers, are highly dependent on molecular structure, even when favourable packing in terms of order and porosity are present.

Wang *et al*. showed that very active photocatalysts could be generated by combining the 1,3,5-triformylphloroglucinol linker with a fused benzothiophene sulfone-based diamine linker. This material, **FS-COF**, has an EQE of 3.2% at 420 nm but it has an absorption onset that stretches well into the visible region, meaning EQEs of 0.6% were obtained at 600 nm. The hydrophilic groups of this material line the pore walls of the low-density structure and

enable high water uptake into the network, increasing the catalytically active surface area. A similarly stable, hydrophilic COF, **TpDTz-COF**, was obtained using polar thiazolo[5,4-*d*]thiazole linkers and was shown to display high activity with an earth abundant Ni catalyst instead of the usual Pt or Pd.[299]

One major disadvantage of COFs is the difficulty of synthesis. Generation of COF crystals often involves low yielding reactions over extended time periods that are difficult to scale to even 100 mg levels.[300] This is a relatively new field in comparison to cross coupled polymerisations, however, and recent developments in COF synthesis, such as using electron beam irradiation, suggest these materials could be made on larger scales.[301]

More specific overviews of microstructured, oligomeric and crystalline molecular photocatalysts are given at the start of Chapters 2-4.

1.7 Techniques and Concepts

Non-standard concepts and techniques used in this work are outlined below.

1.7.1 Measurement of photocatalyst efficiency

1.7.1.1 Solar to Hydrogen

Solar to hydrogen (STH) efficiency is a measure of the percentage of solar energy that is successfully converted into chemical energy, in the form of hydrogen, and is defined by equation 4. It should be noted that this measure is only relevant to overall water splitting as sacrificial electron or hole donors introduce other chemical energy considerations.

$$STH = \left[\frac{HER \times \Delta G_R}{I \times A_d}\right]_{AM\ 1.5\ G} \times 100\ \% \qquad (4)$$

Chemical energy is given as the rate of hydrogen production in mol s^{-1} multiplied by the Gibbs free energy change of the reaction (237,000 J mol^{-1} at 25 °C). Solar energy is given by the intensity, I (in J $m^{-2}S^{-1}$), of the Air Mass 1.5 Global (AM 1.5 G) G173 standard (as shown in Figure 7a) multiplied by the device area, A_d (in m^2).[104]

1.7.1.2 External Quantum Efficiency

External Quantum Efficiency (EQE) measures the percentage of photons incident on a device that result in a successful photocatalytic reaction.[104] Two absorption events are required to produce one molecule of hydrogen, hence EQE is given by two times the number of molecules of hydrogen produced (n_{H_2}) divided by the number of incident photons ($n_{photons}$) (equations 5 and 7). In practice, $n_{photons}$ is measured using a power meter. These display a power reading (P_s) which can be divided by the area of the sensor (A_s) to give a light intensity at the position of the device. This light intensity can in turn be multiplied by the area of the device exposed to light (A_s) to give the power hitting the device (A_d), and further multiplied by the time (t) over which the hydrogen is produced to give the total energy hitting the device (E_d). Finally the number of photons is calculated by dividing this total energy by the energy of a photon (E_{photon}), defined by the Plank-Einstein relation[302] as the product of the photons speed (c) and Planks constant (h), divided by its wavelength (λ) (equation 6).

$$EQE = \frac{2\, n_{H_2}}{n_{photons}} \times 100\ \% \tag{5}$$

$$n_{photons} = \frac{E_d}{E_{photon}} = \frac{P_d\, t\, \lambda}{hc} = \frac{P_s A_d\, t\, \lambda}{A_s hc} \tag{6}$$

$$EQE = \frac{2\, n_{H_2}\, N_A A_s\, hc}{P_s A_d t \lambda} \times 100\ \% \tag{7}$$

1.7.2 Particle Size Analysis Using Light Scattering

1.7.2.1 Dynamic Light Scattering

Solid particles suspended in fluids undergo Brownian motion. This is the random movement of suspended particles due to collision with the thermally excited molecules of the fluid and is generally only significant in systems with particles of less than 1 μm. The translational diffusion coefficient of particles (D) defines the velocity of Brownian motion and is

inversely related to hydrodynamic diameter (d_H) according to the Stokes-Einstein equation (8), such that smaller particles move more rapidly than larger ones.[303]

$$d_H = \frac{kT}{3\pi\eta D} \tag{8}$$

Dynamic light scattering (DLS) is non-invasive particle sizing technique that relies on this relationship. When a laser is passed through a suspension the Brownian movement of particles causes light to be scattered at different intensities. The frequency of these intensity fluctuations can be used to determine particle size for materials of around 1 nm up to several μm,[304] as shown in Figure 23. The oscillating intensity signal is converted into a particle size distribution using a correlation function. This extracts the time dependency of the signal by measuring how quickly the correlation between a signal at time t and a signal at time $t + \tau$ is lost. The resulting correlation curve is analysed to give the intensity-weighted mean diameter, Z_{av}, as well as polydispersity index which measures the broadness of the particle size distribution.[305]

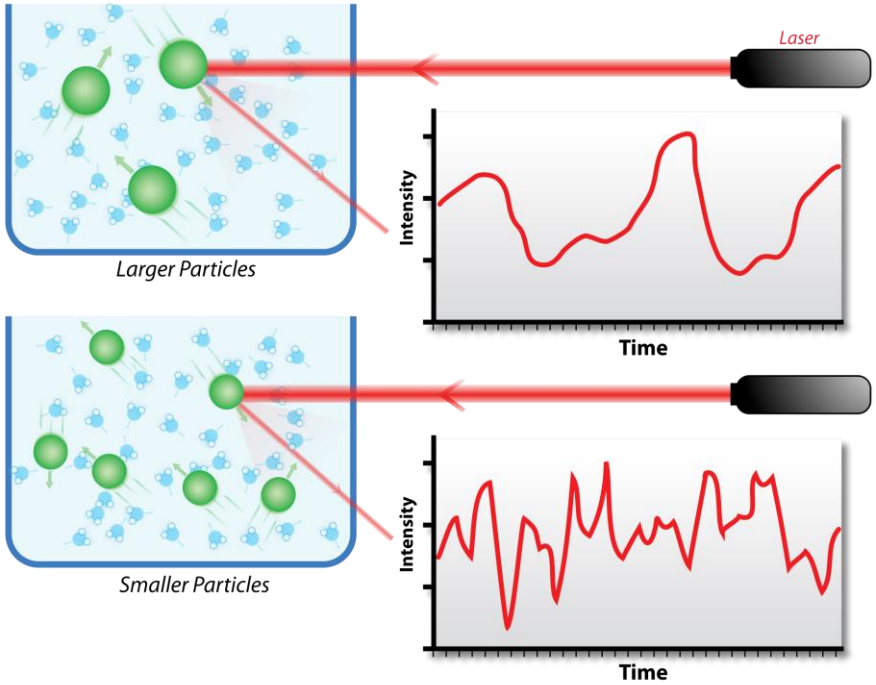

Figure 23: Light scattering by different particle sizes. Differences in diffusion coefficient results in different frequency fluctuations in light intensity. *Copyright CC BY-SA 3.0 Mike Jones.*

1.7.2.2 Static Light Scattering

Whilst DLS measures fluctuations in the intensity of scattered light at one fixed angle, static light scattering (SLS, also known as laser diffraction) measures the time-independent intensity of light scattered across a range of angles. The scattering of light by particles sized from hundreds of nanometres up to 50 μm is dominated by diffraction and is best described using Mie theory.[306] This model estimates the intensity of light diffracted by a particle, at a particular angle, based on the size of the particle and the difference in refractive index between the particle and the liquid medium. The smaller the particle the larger the angle of light diffraction.[307]

SLS involves the illumination of a suspension with a laser (typically 400 – 700 nm) and uses up to 100 detectors to measure how the intensity of diffracted light varies with angle. This signal is then compared to a Mie theory-based predicted optical model for an initial 'best guess' particle size distribution. This size distribution is refined in an interactive process to give the best fit to the measured signal.[308]

The accuracy of the particle size distributions predicted by static light scattering can be negatively affected by multiple scattering events, particularly for higher concentrations or smaller particle sizes. SLS is also less suited to particle sizes significantly below the wavelength of the laser because in these systems Rayleigh scattering makes up a significant component of measured light intensity¸ reducing the appropriateness of the Mie scattering model. Fitting can also be affected by the material refractive index and absorbance used for the optical model and so care should be taken if these parameters are estimated rather than measured.[309]

There are a number of parameters that can be extracted from particle size distributions. In the context of photocatalysis, particle size is important because it affects the active surface area. As such, the most relevant information from particle size distributions is the Sauter mean diameter, (*D[3,2]*).[310] This is defined by equation 9, where particle sizes are divided into *n* channels in a histogram. The geometric mean particle diameter associated with each channel, D_i, is defined as the square root of the product of the upper and lower channel bounds. the percentage of the distribution in each channel is v_i. (*D[3,2]*) represents a surface area-weighted mean diameter and is thus strongly influenced by the presence of small particle fractions. A suspension of uniform particles with diameters equal to *D[3,2]* would have the same surface area as the measured distribution.[311]

$$D[3,2] = \frac{\sum_{i=1}^{n} D_i^3 \nu_i}{\sum_{i=1}^{n} D_i^2 \nu_i} \quad (9)$$

1.7.3 Time-resolved Spectroscopy Techniques

1.7.3.1 Time-Correlated Single Photon Counting

Time-correlated single photon counting (TCSPC) is a spectroscopic method that can be used to determine fluorescence lifetimes, amongst other applications. Samples are excited with a single wavelength pulsed light source and emission is measured perpendicular to excitation. A photomultiplier is usually employed so that single photons hitting the detector can be measured. Fluorescence timescales are determined by comparing the time delay between photons arriving at the detector, via emission from the sample, and a reference pulse which travels directly from light source to the detector. This gives an emission count signal with respect to time.[131]

Fluorescence lifetimes are estimated by fitting this signal to a decay model in the form of equation 10. Decay of the excited state may be through a single process or multiple processes and so signal intensity ($I(t)$) is made up of one or more components each with a corresponding lifetime (τ) and coefficient representing contribution to overall decay, (α_i). An instrument response signal is usually measured using a non-luminescent standard and subtracted from the sample signal to account for photons that reach the detector through scattering or other non-emissive processes. After fitting, average fluorescence lifetime (τ_{av}) can be calculated according to equation 11 and are useful for comparing trends between materials and are related to the steady state emission.[312]

$$I(t) = \sum_{i=1}^{n} \alpha_i e^{t/\tau_i} \quad (10)$$

$$\tau_{av} = \sum_{i=1}^{n} \alpha_i \tau_i \quad (11)$$

1.7.3.2 Transient Absorption Spectroscopy

Transient absorption spectroscopy (TAS) is a pump-probe technique used to investigate the excited state of molecules or materials. Samples are excited with a laser pulse (pump) and the UV-visible absorption spectrum recorded (probe) after a certain time delay. Difference spectra are generated by comparison to the ground state sample absorption profile.

Depopulation of the ground state can give a negative signal, or bleach, whilst excited state species give separate positive absorption features. These can be characterised by the specific wavelengths of the absorption and the magnitude can provide information about the yield of exciton or polaron formation. Analysis of how these features grow in or decay over time can also be used to establish the timescale of active species formation and their lifetime. This is particularly useful since, unlike TCSPC, the lifetime of states that decay by non-radiative pathways can be analysed as well as those that are fluorescent. Another advantage is that ultrafast TAS can probe samples significantly less than 1 ps after the initial excitation meaning even short-lived species can be detected.[313]

1.7.3.3 Photoinduced Absorption Spectroscopy

Whilst the short laser 'pump' used in TAS can generate excited state species and provide valuable insight into the decay processes, this excitation method is not analogous to conditions used in photocatalysis, where materials are continuously illuminated. Photoinduced absorption spectroscopy (PIAS), is an alternative time resolved spectroscopy technique, where quasi steady-state conditions can be achieved using a LED pulse of up to several seconds duration as the excitation source (Figure 24a). This is an important difference as excited state species will accumulate on a material if photo-generation is more rapid than the combined rate of decay or reaction processes.[314] The concentration of charged species can also affect the rate of these different process, with recombination rates higher at increased charge carrier concentrations.[149] This limits charge accumulation and typically leads to a saturation point a short time after the light source is turned on, as shown in Figure 24b.

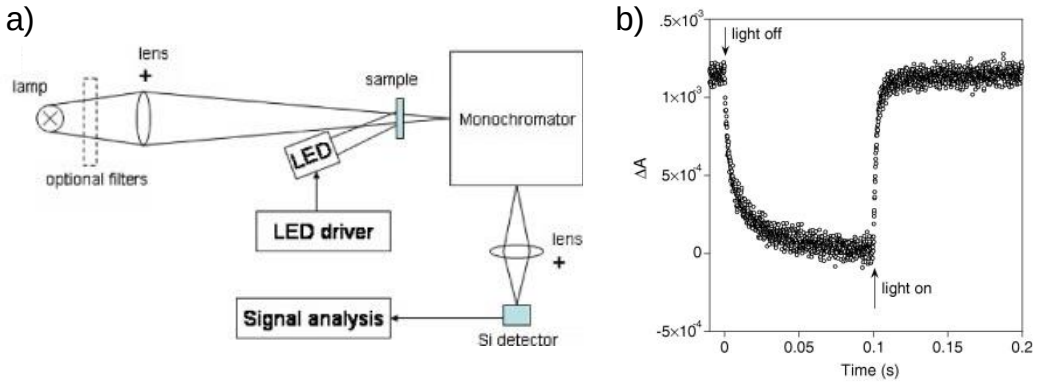

Figure 24: a) Set-up for PIAS. b) Typical PIAS spectrum showing the build-up and saturation of charge carriers on a TiO_2 semi-conductor. *Adapted with permission from reference [314].*

1.8 Project Aims

To deconvolute structure-activity relationships in organic photocatalysts (Section 1.3), we need to vary one property while keeping others as constant as possible. This is inherently difficult (Fig. 14) in the specific context of organic materials, discussed in section 1.6, most of which are insoluble polymers synthesised in bulk precipitation reactions. As such, purification and indeed atomistic-level characterization for these materials is challenging. Also, changes to the molecular structure of the monomer unit may alter not just the orbital energies of the polymer but also properties such as molecular conformation, crystallinity, and particle size. These properties are then difficult to change post-synthesis because the materials cannot be dissolved in organic solvents for processing. The smaller range of characterisation techniques possible for these types of insoluble materials also makes it difficult to measure whether, or how much, properties have changed as a result of the synthetic variation.

This work examines materials where a degree of control can be exerted during synthesis or by processing, with the aim of gaining a greater understanding of how various material properties affect photocatalytic hydrogen production. To do this, we use a battery of different characterization methods.

Chapter 2 examines the effect of microstructure on photocatalytic activity by synthesising polymers comprised of the same monomer units but with differing particle sizes. This was accomplished by employing emulsion polymerisation techniques that allow nanoparticle analogues of unprocessable bulk materials to be produced. The absorption properties of these materials was measured to compare the relative degrees of polymerisation achieved through these two synthesis routes. The hydrogen production activities of the nanoparticle and bulk systems were measured under a number of different photocatalytic conditions, using different SEDs and catalyst concentrations. The differing aggregation behaviour of the samples in these systems was characterised using microscopy and the light scattering techniques described in Section 1.7.2, to gain further insight into the relationship between particle size or particle-dispersant interaction and photocatalytic activity. In Chapter 3, oligomeric semiconductors based on fluorene or dibenzothiophene sulfone are investigated as proton reduction photocatalysts. Oligomers with differing numbers of repeat units or substituent groups were synthesised, and characterised by single crystal X-ray diffraction. The aim was to use the well-defined photocatalyst structures to investigate how particular features, such as chain length or backbone twisting, affect the absorption properties of the material and photocatalytic activity. In addition, the effect of chain length and palladium

content on charge carrier generation and lifetime were investigated using the time resolved spectroscopy techniques described in Section 1.7.3. These kinetics were used, along with hydrogen production rates, to gain insight into the mechanism and rate limiting steps of photocatalysis.

Hydrogen-bonded organic frameworks (HOFs) were investigated as hydrogen production photocatalysts in Chapter 4. One aim of this section was to exploit the solubility of HOF materials in polar organic solvents to grow single crystals. The packing of these materials, particularly their propensity to form extended π-π stacking columns is investigated. In particular, the processability of a pyrene-based HOF was used to generate crystalline and amorphous versions of the same molecule. This isolates the effect, if any, of crystal packing on photocatalytic activity from the effect of changing chemical structure. These materials were also compared to a number of related pyrene-based compounds with different degrees of order or different porosities. Finally, the feasibility of forming photocatalytically active HOFs from a wider range of materials is assessed by initial studies incorporating alternative aromatic core groups.

1.9 References

1 E. Foote, *Am. J. Sci. Arts*, 1856, **22**, 382–383.

2 P. Friedlingstein et al., *Earth Syst. Sci. Data*, 2019, **11**, 1783–1838.

3 R. K. Pachauri, L. Meyer, S. Hallegatte France, W. Bank, G. Hegerl, S. Brinkman, L. van Kesteren, N. Leprince-Ringuet and F. van Boxmeer, *Climate Change 2014: Synthesis Report.*, IPPC, Geneva, 2014.

4 M. Rocha, M. Krapp, J. Gutschow, L. Jeffery, B. Hare and Schaeffer Michiel, *Historical Responsibility for Climate Change – from countries emissions to contribution to temperature increase*, Climate Analytic, London, 2015.

5 J. Rankin, *Guard.*, 2019. https://www.theguardian.com/world/2019/nov/28/eu-parliament-declares-climate-emergency

6 *Climate emergency declarations in 1,488 jurisdictions and local governments cover 820 million citizens*, Climate Emergency Declaration, 2020. https://climateemergencydeclaration.org/climate-emergency-declarations-cover-15-million-citizens/, (accessed 7 May 2020).

7 V. Masson-Delmotte et al. *Global warming of 1.5°C An IPCC Special Report on the impacts of global warming of 1.5°C above pre-industrial levels and related global greenhouse gas emission pathways, in the context of strengthening the global response to the threat of climate change, sustainable development, and efforts to eradicate poverty*, IPCC, Paris, 2019.

8 J. Cook, et al. *Environ. Res. Lett.*, 2016, **11**, 048002.

9 M. Smith, *International poll: most expect to feel impact of climate change, many think it will make us extinct*, YouGov, 2019.

10 A. Revkin, *Natl. Geogr. Mag.*, 2019. https://www.nationalgeographic.com/environment/2019/01/climate-change-awareness-polls-show-rising-concern-for-global-warming/

11 H. Christine, F. Moira, *A look at how people around the world view climate change*, Pew Research Centre, Washington DC, 2019.

12 *Global Energy & CO2 Status Report 2019*, IEA, Paris, 2019.

13 *Renewables 2019 Global Status Report*, REN21, Paris, 2019.

14 M. Pehl, A. Arvesen, F. Humpenöder, A. Popp, E. G. Hertwich and G. Luderer, *Nat. Energy*, 2017, **2**, 939–945.

15 R. R. Srivastava, P. Pathak and M. Perween, in *Uranium in Plants and the Environment*, Springer, Cham, 2020, ch.3, pp. 69–89.

16 *Nuclear Power in a Clean Energy System*, IEA, Paris, 2019.

17 *Cement – Tracking Industry – Analysis*, IEA, Paris, 2019.

18 *Press Release: Heliogen achieves breakthrough temperatures from concentrated sunlight for industrial processes*, Heliogen, Pasadena, 2019.

19 *Renewable Power Generation Costs in 2018*, IRENA, Abu Dhabi, 2019.

20 *Future of Solar Photovoltaic Deployment, investment, technology, grid integration and socio-economic aspects A Global Energy Transformation paper*, IRENA, Abu Dhabi, 2019.

21 Gray Matt, Sundaresan Sriya, B. Udomchaiporn, Lavelle Stefan and Chau Lily, *How to waste over half a trillion dollars: The economic implications of deflationary renewable energy for coal power investments*, Carbon Tracker Initiative, London, 2020.

22 *Solar PV – Tracking Power – Analysis*, IEA, Paris, 2019.

23 *Paris Agreement FCCC/CP/2015/L.9/Rev.1*, IPCC, COP21, Paris, 2015.

24 J. O. M. Bockris, *Int. J. Hydrogen Energy*, 2013, **38**, 2579–2588.

25 I. Staffell, D. Scamman, A. Velazquez Abad, P. Balcombe, P. E. Dodds, P. Ekins, N. Shah and K. R. Ward, *Energy Environ. Sci.*, 2019, **12**, 463–491.

26 J. Yang, A. Sudik, C. Wolverton and D. J. Siegel, *Chem. Soc. Rev.*, 2010, **39**, 656–675.

27 G. Sdanghi, G. Maranzana, A. Celzard and

V. Fierro, *Renew. Sustain. Energy Rev.*, 2019, **102**, 150–170.

28 N. P. Brandon and Z. Kurban, *Philos. Trans. R. Soc. A Math. Phys. Eng. Sci.*, 2017, **375**, 20160400.

29 N. Howarth, N. Odnoletkova, T. Alshehri, A. Almadani, A. Lanza and T. Patzek, *Climate*, 2020, **8**, 4.

30 J. Torriti, *Peak Energy Demand and Demand Side Response*, Routledge, Abingdon, 2016.

31 *Football trouble brewing for National Grid*, BBC News, http://news.bbc.co.uk/1/hi/uk/109355.stm, (accessed 17 May 2020).

32 G. Strbac, M. Aunedi, D. Pudjianto, P. Djapic, F. Teng, A. Sturt, D. Jackravut, R. Sansom, V. Yufit and N. Brandon, *Strategic Assessment of the Role and Value of Energy Storage Systems in the UK Low Carbon Energy Future*, Carbon Trust, London, 2012.

33 D. Rastler, *Electricity Energy Storage Technology Options*, Electric Power Research Institute, Palo Alto, CA, 2010.

34 S. Comello and S. Reichelstein, *Nat. Commun.*, 2019, **10**, 1–9.

35 G. Glenk and S. Reichelstein, *Nat. Energy*, 2019, **4**, 216–222.

36 P. Chiesa, G. Lozza and L. Mazzocchi, *J. Eng. Gas Turbines Power*, 2005, **127**, 73–80.

37 *BP Statistical Review of World Energy, 67th edition*, BP, 2018.

38 *World Energy Balances 2019 – Analysis*, IEA, Paris, 2019.

39 J. Deng, C. Bae, A. Denlinger and T. Miller, *Joule*, 2020, **4**, 511–515.

40 Z. P. Cano, D. Banham, S. Ye, A. Hintennach, J. Lu, M. Fowler and Z. Chen, *Nat. Energy*, 2018, **3**, 279-289.

41 G. Zhu, C. Zhao, J. Huang, C. He, J. Zhang, S. Chen, L. Xu, H. Yuan and Q. Zhang, *Small*, 2019, **15**, 1805389.

42 P. Morrissey, P. Weldon and M. O'Mahony, *Energy Policy*, 2016, **89**, 257–270.

43 *The Future of Hydrogen – Analysis*, IEA, Paris, 2019.

44 *Basic Hydrogen Strategy-Key Points-English-Press*, Japanese Ministry for Economy Trade and Industry, Tokyo, 2017.

45 *Heat – Renewables 2019 – Analysis*, IEA, Paris, 2019.

46 I. Staffell and S. Pfenninger, *Energy*, 2018, **145**, 65–78.

47 P. E. Dodds and A. Hawkes, *The role of hydrogen and fuel cells in providing affordable, secure low-carbon heat.*, H2FC SUPERGEN, London, 2014.

48 D. Hart, J. Howes, F. Lehner, P. Dodds, N. Hughes, B. Fais and M. Crowther, *Scenarios for deployment of hydrogen in contributing to meeting carbon budgets and the 2050 target*, E4tech, UCL energy institute, Kiwa Gastec, London, 2015.

49 *Options for producing low-carbon hydrogen at scale POLICY BRIEFING*, The Royal Society, London, 2018.

50 Editorial, *Nat. Mater.*, 2018, **17**, 565.

51 D. Sadler, A. Cargill, M. Crowther, A. Rennie, J. Watt, S. Burton, M. Haines, J. Trapps, M. Hand, R. Pomroy, K. Haggerty, I. Summerfield and M. Evans, *100% hydrogen conversion feasibility study*, H21 Leeds City Gate, Leeds, 2016.

52 B. D. James, G. N. Baum, J. Perez and K. N. Baum, *Technoeconomic Analysis of Photoelectrochemical (PEC) Hydrogen Production*, Directed Technologies Inc (for US Department of Energy), 2009.

53 R. J. Detz, J. N. H. Reek and B. C. C. Van Der Zwaan, *Energy Environ. Sci.*, 2018, **11**, 1653–1669.

54 J. E. Funk, *Int. J. Hydrogen Energy*, 2001, **26**, 185–190.

55 P. Nikolaidis and A. Poullikkas, *Renew. Sustain. Energy Rev.*, 2017, **67**, 597–611.

56 K. Scott, in *Electrochemical Methods for Hydrogen Production*, The Royal Society of Chemistry, 2020, pp. 1–27.

57 C. Chen, J. F. Khosrowabadi Kotyk and S. W. Sheehan, *Chem*, 2018, **4**, 2571–2586.

58 Y. Wu, Z. Jiang, X. Lu, Y. Liang and H. Wang, *Nature*, 2019, **575**, 639–642.

59 B. H. R. Suryanto, H. L. Du, D. Wang, J. Chen, A. N. Simonov and D. R. MacFarlane, *Nat. Catal.*, 2019, **2**, 290–296.

60 O. Schmidt, A. Gambhir, I. Staffell, A. Hawkes, J. Nelson and S. Few, *Int. J. Hydrogen Energy*, 2017, **42**, 30470–30492.

61 M. A. Green, E. D. Dunlop, J. Hohl-Ebinger, M. Yoshita, N. Kopidakis and A. W. Y. Ho-Baillie, *Prog. Photovoltaics Res. Appl.*, 2020, **28**, 3–15.

62 J. Jia, L. C. Seitz, J. D. Benck, Y. Huo, Y. Chen, J. Wei, D. Ng, T. Bilir, J. S. Harris and T. F. Jaramillo, *Nat. Commun.*,2016, **7**, 13237.

63 J. H. Kim, D. Hansora, P. Sharma, J.-W. Jang and J. S. Lee, *Chem. Soc. Rev.*, 2019, **48**, 1908–1971.

64 C. B. Field, M. J. Behrenfeld, J. T. Randerson and P. Falkowski, *Science*, 1998, **281**, 237–240.

65 X. G. Zhu, S. P. Long and D. R. Ort, *Curr. Opin. Biotechnol.*, 2008, **19**, 153–159.

66 R. E. Blankenship et al., *Science*, 2011, **332**, 805–809.

67 M. C. Rulli, S. Casirati, J. Dell'Angelo, K. F. Davis, C. Passera and P. D'Odorico, *Renew. Sustain. Energy Rev.*, 2019, **105**, 499–512.

68 K. Kleiner, *Nat. Clim. Chang.*, 2008, **1**, 9–11.

69 J. Fargione, J. Hill, D. Tilman, S. Polasky and P. Hawthorne, *Science*, 2008, **319**, 1235–1238.

70 L. Ferrante and P. M. Fearnside, *Nature*, 2020, **577**, 170.

71 N. Gaurav, S. Sivasankari, G. S. Kiran, A. Ninawe and J. Selvin, *Renew. Sustain. Energy Rev.*, 2017, **73**, 205–214.

72 I. Z. Boboescu, V. D. Gherman, G. Lakatos, B. Pap, T. Bíró and G. Maróti, *Bioresour. Technol.*, 2016, **204**, 192–201.

73 Z. Yan, M. Ji, J. Xia and H. Zhu, *Adv. Energy Mater.*, 2020, **10**, 1902020.

74 J. L. White et al., *Chem. Rev.*, 2015, **115**, 12888–12935.

75 J. Z. Zhang and E. Reisner, *Nat. Rev. Chem.*, 2020, **4**, 6–21.

76 W. Lubitz, H. Ogata, O. Rüdiger and E. Reijerse, *Chem. Rev.*, 2014, **114**, 4081-4148.

77 K. Kumar and D. Das, in *Natural and Artificial Photosynthesis: Solar Power as an Energy Source*, John Wiley & Sons, London, 2013, ch.6, pp. 173–215.

78 S. Wu, L. Xu, R. Huang and Q. Wang, *Bioresour. Technol.*, 2011, **102**, 2610–2616.

79 A. Scoma, D. Krawietz, C. Faraloni, L. Giannelli, T. Happe and G. Torzillo, *J. Biotechnol.*, 2012, **157**, 613–619.

80 S. N. Kosourov, M. L. Ghirardi and M. Seibert, *Int. J. Hydrogen Energy*, 2011, **36**, 2044–2048.

81 H. Michel, *Angew. Chemie Int. Ed.*, 2012, **51**, 2516–2518.

82 K. P. Sokol, W. E. Robinson, J. Warnan, N. Kornienko, M. M. Nowaczyk, A. Ruff, J. Z. Zhang and E. Reisner, *Nat. Commun.*, 2018, **3**, 944–951.

83 R. I. Pinhassi, D. Kallmann, G. Saper, H. Dotan, A. Linkov, A. Kay, V. Liveanu, G. Schuster, N. Adir and A. Rothschild, *Nat. Commun.*, 2016, **7**, 1–10.

84 W. Wang, H. Wang, Q. Zhu, W. Qin, G. Han, J. Shen, X. Zong and C. Li, *Angew. Chemie Int. Ed.*, 2016, **55**, 9229–9233.

85 Z. Li, W. Wang, C. Ding, Z. Wang, S. Liao and C. Li, *Energy Environ. Sci.*, 2017, **10**, 765–771.

86 A. Fujishima and K. Honda, *Nature*, 1972, **238**, 37-38.

87 T. Hisatomi, J. Kubota and K. Domen, *Chem. Soc. Rev.*, 2014, **43**, 7520–7535.

88 *Solar AM 1.5 G Standard: G173, 2003e1, in Standard Tables for Reference Solar Spectral Irradiances: Direct Normal and Hemispherical on 37 Tilted Surface*, American Society for Materials Testing, West Coshohocken, PA.

89 K. Maeda and K. Domen, *J. Phys. Chem. Lett.*, 2010, **1**, 2655–2661.

90 B. A. Pinaud et al., *Energy Environ. Sci.*, 2013, **6**, 1983–2002.

91 H. Kobayashi, N. Sato, M. Orita, Y. Kuang, H. Kaneko, T. Minegishi, T. Yamadaac and K. Domen, *Energy Environ. Sci*., 2018, **11**, 3003-3009.

92 Y. F. Tay et al., *Joule*, 2018, **2**, 537–548.

93 T. Yao, X. An, H. Han, J. Q. Chen and C. Li, *Adv. Energy Mater.*, 2018, **8**, 1800210.

94 D. Bae, B. Seger, P. C. K. Vesborg, O. Hansen and I. Chorkendorff, *Chem. Soc.*

Rev., 2017, **46**, 1933–1954.

95 L. Pan, J. H. Kim, M. T. Mayer, M. K. Son, A. Ummadisingu, J. S. Lee, A. Hagfeldt, J. Luo and M. Grätzel, *Nat. Catal.*, 2018, **1**, 412–420.

96 D. K. Lee, D. Lee, M. A. Lumley and K. S. Choi, *Chem. Soc. Rev.*, 2019, **48**, 2126–2157.

97 Y. Kuang, Q. Jia, G. Ma, T. Hisatomi, T. Minegishi, H. Nishiyama, M. Nakabayashi, N. Shibata, T. Yamada, A. Kudo and K. Domen, *Nat. Energy*, 2017, **2**, 1–9.

98 G. Liu, S. Ye, P. Yan, F. Xiong, P. Fu, Z. Wang, Z. Chen, J. Shi and C. Li, *Energy Environ. Sci.*, 2016, **9**, 1327–1334.

99 S. Chu, S. Vanka, Y. Wang, J. Gim, Y. Wang, Y. H. Ra, R. Hovden, H. Guo, I. Shih and Z. Mi, *ACS Energy Lett.*, 2018, **3**, 307–314.

100 J. Seo, T. Hisatomi, M. Nakabayashi, N. Shibata, T. Minegishi, M. Katayama and K. Domen, *Adv. Energy Mater.*, 2018, **8**, 1800094.

101 A. Martinez-Garcia, H. B. Russell, W. Paxton, S. Ravipati, S. Calero-Barney, M. Menon, E. Richter, J. Young, T. Deutsch and M. K. Sunkara, *Adv. Energy Mater.*, 2018, **8**, 1703247.

102 Y. Wang, Y. Wu, J. Schwartz, S. H. Sung, R. Hovden and Z. Mi, *Joule*, 2019, **3**, 2444–2456.

103 A. Paracchino, V. Laporte, K. Sivula, M. Grätzel and E. Thimsen, *Nat. Mater.*, 2011, **10**, 456–461.

104 Z. Chen et al., *J. Mater. Res*, 2010, **25**, 3-16.

105 Y. Pihosh et al., *Sci. Rep.*, 2015, **5**, 1–10.

106 J. H. Kim, J. W. Jang, Y. H. Jo, F. F. Abdi, Y. H. Lee, R. Van De Krol and J. S. Lee, *Nat. Commun.*, 2016, **7**, 1–9.

107 W. H. Cheng, M. H. Richter, M. M. May, J. Ohlmann, D. Lackner, F. Dimroth, T. Hannappel, H. A. Atwater and H. J. Lewerenz, *ACS Energy Lett.*, 2018, **3**, 1795–1800.

108 J. Gao, F. Sahli, C. Liu, D. Ren, X. Guo, J. Werner, Q. Jeangros, S. M. Zakeeruddin, C. Ballif, M. Grätzel and J. Luo, *Joule*, 2019, **3**, 2930–2941.

109 J. L. Young, M. A. Steiner, H. Döscher, R. M. France, J. A. Turner and T. G. Deutsch, *Nat. Energy*, 2017, **2**, 1–8.

110 W. J. Chang et al., *ACS Omega*, 2017, **2**, 1009–1018.

111 S. A. Bonke, M. Wiechen, D. R. MacFarlane and L. Spiccia, *Energy Environ. Sci.*, 2015, **8**, 2791–2796.

112 S. Y. Reece, J. A. Hamel, K. Sung, T. D. Jarvi, A. J. Esswein, J. J. H. Pijpers and D. G. Nocera, *Science*, 2011, **334**, 645–648.

113 S. C. Warren, K. Voïtchovsky, H. Dotan, C. M. Leroy, M. Cornuz, F. Stellacci, C. Hébert, A. Rothschild and M. Grätzel, *Nat. Mater.*, 2013, **12**, 842–849.

114 Y. He, T. Hamann and D. Wang, *Chem. Soc. Rev.*, 2019, **48**, 2182–2215.

115 K. Tolod, S. Hernández and N. Russo, *Catalysts*, 2017, **7**, 13.

116 M. R. Shaner, H. A. Atwater, N. S. Lewis and E. W. Mcfarland, *Energy Environ. Sci*, 2016, **9**, 2354.

117 L. Liao et al., *Nat. Nanotechnol.*, 2014, **9**, 69–73.

118 J. Liu, Y. Liu, N. Liu, Y. Han, X. Zhang, H. Huang, Y. Lifshitz, S.-T. Lee, J. Zhong and Z. Kang, *Science*, 2015, **347**, 970-974.

119 Y. Goto et al., *Joule*, 2018, **2**, 509–520.

120 F. A. Chowdhury, M. L. Trudeau, H. Guo and Z. Mi, *Nat. Commun.*, 2018, **9**, 1707.

121 S. Chen, T. Takata and K. Domen, *Nat. Rev. Mater.*, 2017, **2**, 17050.

122 Q. Wang, T. Hisatomi, Y. Suzuki, Z. Pan, J. Seo, M. Katayama, T. Minegishi, H. Nishiyama, T. Takata, K. Seki, A. Kudo, T. Yamada and K. Domen, *J. Am. Chem. Soc*, 2017, **139**, 24.

123 Y. Sasaki, H. Nemoto, K. Saito and A. Kudo, *J. Phys. Chem. C*, 2009, **113**, 17536–17542.

124 A. Kudo, S. Yoshino, T. Tsuchiya, Y. Udagawa, Y. Takahashi, M. Yamaguchi, I. Ogasawara, H. Matsumoto and A. Iwase, *Faraday Discuss.*, 2019, **215**, 313–328.

125 B. Dong, J. Cui, Y. Gao, Y. Qi, F. Zhang and C. Li, *Adv. Mater.*, 2019, **31**, 1808185.

126 T. Hisatomi and K. Domen, *Nat. Catal.*, 2019, **2**, 387–399.

127 T. Setoyama, T. Takewaki, K. Domen and T. Tatsumi, *Faraday Discuss.*, 2017, **198**,

509-527.

128 S. E. Braslavsky, *Pure Appl. Chem.*, 2007, **79**, 293–465.

129 K. T. Hecht, *Quantum Mechanics*, Springer Science and Business Media LLC, New York, 2000.

130 M. Grundmann, *The Physics of Semiconductors*, Springer Science and Business Media LLC, Heidelberg, 2016.

131 J. R. Lakowicz, *Principles of fluorescence spectroscopy*, Springer Science and Business Media LLC, New York, 3rd edn., 2006.

132 S. R. Forrest, *Phil. Trans. R. Soc. A*, 2105, **373**, 20140320

133 J. Frenkel, *Phys. Z. Sowjetunion*, 1936, **9**, 158–186.

134 J. B. Baxter, C. Richter and C. A. Schmuttenmaer, *Annu. Rev. Phys. Chem.*, 2014, **65**, 423–447.

135 T. Shimazaki and T. Nakajima, *Phys. Chem. Chem. Phys.*, 2015, **17**, 12538–12544.

136 Y. Wang, A. Vogel, M. Sachs, R. S. Sprick, L. Wilbraham, S. J. A. Moniz, R. Godin, M. A. Zwijnenburg, J. R. Durrant, A. I. Cooper and J. Tang, *Nat. Energy*, 2019, **4**, 746–760.

137 H. Wang, X. Sun, D. Li, X. Zhang, S. Chen, W. Shao, Y. Tian and Y. Xie, *J. Am. Chem. Soc.*, 2017, **139**, 2468–2473.

138 J. Yang, D. Wang, H. Han and C. Li, *Acc. Chem. Res.*, 2013, **46**, 1900-1909.

139 J. Kosco, M. Sachs, R. Godin, M. Kirkus, L. Francas, M. Bidwell, M. Qureshi, D. Anjum, J. R. Durrant and I. McCulloch, *Adv. Energy Mater.*, 2018, **8**, 1802181.

140 Y. Pellegrin and F. Odobel, *Comptes Rendus Chim.*, 2017, **20**, 283–295.

141 M. Sachs, R. S. Sprick, D. Pearce, S. A. J. Hillman, A. Monti, A. A. Y. Guilbert, N. J. Brownbill, S. Dimitrov, X. Shi, F. Blanc, M. A. Zwijnenburg, J. Nelson, J. R. Durrant, A. I. Cooper, *Nat. Commun.*, 2018, **9**, 4968.

142 N. Bao, L. Shen, T. Takata and K. Domen, *Chem. Mater.*, 2008, **20**, 110–117.

143 K. Sakimoto, S. Zhang and P. Yang, *Nano Lett*., 2016, **16**, 5883-5887.

144 T. Uekert, M. F. Kuehnel, D. W. Wakerley and E. Reisner, *Energy Environ. Sci.*, 2018, **11**, 2853–2857.

145 D. W. Wakerley, M. F. Kuehnel, K. L. Orchard, K. H. Ly, T. E. Rosser and E. Reisner, *Nat. Energy*, 2017, **2**, 1–9.

146 S. Dimitrov, B. Schroeder, C. Nielsen, H. Bronstein, Z. Fei, I. McCulloch, M. Heeney and J. Durrant, *Polymers*, 2016, **8**, 14.

147 Y. Tamai, H. Ohkita, H. Benten and S. Ito, *J. Phys. Chem. Lett.*, 2015, **6**, 3417–3428.

148 L. Alcácer, *Electronic Structure of Organic Semiconductors: Polymers and small molecules*, IOP Publishing, 2018.

149 V. Coropceanu, J. Cornil, D. A. da Silva Filho, Y. Olivier, R. Silbey and J. L. Brédas, *Chem. Rev.*, 2007, **107**, 926–952.

150 A. Kudo and Y. Miseki, *Chem. Soc. Rev.*, 2009, **38**, 253–278.

151 J. Tang, J. R. Durrant and D. R. Klug, *J. Am. Chem. Soc.*, 2008, **130**, 13885–13891.

152 V. W. Lau, D. Klose, H. Kasap, F. Podjaski, M.-C. Pignié, E. Reisner, G. Jeschke and B. V. Lotsch, *Angew. Chemie Int. Ed.*, 2017, **56**, 510–514.

153 A. I. Nguyen, M. S. Ziegler, P. Oña-Burgos, M. Sturzbecher-Hohne, W. Kim, D. E. Bellone and T. D. Tilley, *J. Am. Chem. Soc.*, 2015, **137**, 12865–12872.

154 M. Busch, E. Ahlberg and I. Panas, *J. Phys. Chem. C*, 2013, **117**, 288–292.

155 R. R. Rao et al., *Nat. Catal.*, 2020, **3**, 516–525.

156 S. Trasatti, *J. Electroanal. Chem.*, 1972, **39**, 163–184.

157 J. K. Nørskov, T. Bligaard, A. Logadottir, J. R. Kitchin, J. G. Chen, S. Pandelov and U. Stimming, *J. Electrochem. Soc.*, 2005, **152**, 23–26.

158 K. Maeda, X. Wang, Y. Nishihara, D. Lu, M. Antonietti and K. Domen, *J. Phys. Chem. C*, 2009, **113**, 4940–4947.

159 B. Ohtani, K. Iwai, S.I. Nishimoto and S. Sato, *J. Phys. Chem. B*, 1997, **101**, 3349-3359.

160 H. Bronstein, C. B. Nielsen, B. C. Schroeder and I. Mcculloch, *Nat. Chem. Rev.*, 2020, **4**, 66-77.

161 S. A. Benner, *Science*, 1993, **261**, 1402–1403.

162 A. Travesset, *Science*, 2011, **334**, 183-184.

163 T. P. Lodge, *Science*, 2008, **321**, 50–51.

164 S. J. Tang, S. J. A. Moniz, S. A. Shevlin, D. J. Martin, Z.-X. Guo and J. Tang, *Energy Environ. Sci.*, 2015, **8**, 731–759.

165 S. Curtarolo, G. L. W. Hart, M. B. Nardelli, N. Mingo, S. Sanvito and O. Levy, *Nat. Mater.*, 2013, **12**, 191–201.

166 A. Ludwig, *npj Comp. Mat.*, 2019, **5**, 70.

167 R. J. Kearsey, B. M. Alston, M. E. Briggs, R. L. Greenaway and A. I. Cooper, *Chem. Sci.*, 2019, **10**, 9454–9465.

168 Y. Bai, L. Wilbraham, B. J. Slater, M. A. Zwijnenburg, R. S. Sprick and A. I. Cooper, *J. Am. Chem. Soc.*, 2019, **141**, 9063–9071.

169 B. Burger et al., *Nature*, 2020, **583**, 237–241.

170 G. N. Schrauzer and T. D. Guth, *J. Am. Chem. Soc.*, 1977, **99**, 7189–7193.

171 T. Kawai and T. Sakata, *Chem. Phys. Lett.*, 1980, **72**, 87–89.

172 F. T. Wagner and G. A. Somorjai, *J. Am. Chem. Soc.*, 1980, **102**, 5494-5502.

173 K. Domen, S. Naito, M. Soma, T. Onishi and K. Tamaru, *J. Chem. Soc. Chem. Commun.*, 1980, **12**, 543–544.

174 R. Li, Y. Weng, X. Zhou, X. Wang, Y. Mi, R. Chong, H. Han and C. Li, *Energy Environ. Sci.*, 2015, **8**, 2377–2382.

175 Y. Ham, T. Hisatomi, Y. Goto, Y. Moriya, Y. Sakata, A. Yamakata, J. Kubota and K. Domen, *J. Mater. Chem. A*, 2016, **4**, 3027–3033.

176 Y. Goto et al., *Joule*, 2018, **2**, 509–520.

177 A. Kudo, A. Tanaka, K. Domen, K. ichi Maruya, K. ichi Aika and T. Onishi, *J. Catal.*, 1988, **111**, 67–76.

178 Y. Inoue, T. Niiyama, Y. Asai and K. Sato, *J. Chem. Soc. Chem. Commun.*, 1992, **7**, 579–580.

179 J. Sato, N. Saito, H. Nishiyama and Y. Inoue, *J. Phys. Chem. B*, 2001, **105**, 6061–6063.

180 Y. Inoue, *Energy Environ. Sci.*, 2009, **2**, 364–386.

181 K. Maeda, K. Teramura, D. Lu, T. Takata, N. Saito, Y. Inoue and K. Domen, *Nature*, 2006, **440**, 295–295.

182 C. Pan, T. Takata, M. Nakabayashi, T. Matsumoto, N. Shibata, Y. Ikuhara and K. Domen, *Angew. Chemie. Int. Ed.*, 2015, **54**, 2955–2959.

183 Q. Wang, M. Nakabayashi, T. Hisatomi, S. Sun, S. Akiyama, Z. Wang, Z. Pan, X. Xiao, T. Watanabe, T. Yamada, N. Shibata, T. Takata and K. Domen, *Nat. Mater.*, 2019, **18**, 827–832.

184 R. Asai, H. Nemoto, Q. Jia, K. Saito, A. Iwase and A. Kudo, *Chem. Commun.*, 2014, **50**, 2543–2546.

185 M. J. Katz, S. C. Riha, N. C. Jeong, A. B. F. Martinson, O. K. Farha and J. T. Hupp, *Coord. Chem. Rev.*, 2012, **256**, 2521–2529.

186 J. R. Darwent and A. Mills, *J. Chem. Soc. Faraday Trans. 2 Mol. Chem. Phys.*, 1982, **78**, 359–367.

187 A. Kudo, K. Ueda, H. Kato and I. Mikami, *Catal. Letters*, 1998, **53**, 229–230.

188 H. Liu, J. Yuan, W. Shangguan and Y. Teraoka, *J. Phys. Chem. C*, 2008, **112**, 8521–8523.

189 H. Liu, J. Yuan, Z. Jiang, W. Shangguan, H. Einaga and Y. Teraoka, *J. Mater. Chem.*, 2011, **21**, 16535–16543.

190 W. J. Jo, H. J. Kang, K. J. Kong, Y. S. Lee, H. Park, Y. Lee, T. Buonassisi, K. K. Gleason and J. S. Lee, *Proc. Natl. Acad. Sci.*, 2015, **112**, 13774–13778.

191 K. Sayama, K. Mukasa, R. Abe, Y. Abe and H. Arakawa, *Chem. Commun.*, 2001, **1**, 2416–2417.

192 K. Maeda, M. Higashi, D. Lu, R. Abe and K. Domen, *J. Am. Chem. Soc.*, 2010, **132**, 5858–5868.

193 G. Ma, S. Chen, Y. Kuang, S. Akiyama, T. Hisatomi, M. Nakabayashi, N. Shibata, M. Katayama, T. Minegishi and K. Domen, *J. Phys. Chem. Lett.*, 2016, **7**, 3892–3896.

194 S. Chen, Y. Qi, T. Hisatomi, Q. Ding, T. Asai, Z. Li, S. S. K. Ma, F. Zhang, K. Domen and C. Li, *Angew. Chemie Int. Ed.*, 2015, **54**, 8498–8501.

195 Y. Qi, Y. Zhao, Y. Gao, D. Li, Z. Li, F. Zhang and C. Li, *Joule*, 2018, **2**, 2393-2402.

196 R. Kobayashi, T. Takashima, S. Tanigawa, S. Takeuchi, B. Ohtani and H. Irie, *Phys. Chem. Chem. Phys.*, 2016, **18**, 27754–

27760.

197 Q. Wang, Y. Li, T. Hisatomi, M. Nakabayashi, N. Shibata, J. Kubota and K. Domen, *J. Catal.*, 2015, **328**, 308–315.

198 Q. Wang, T. Hisatomi, S. S. K. Ma, Y. Li and K. Domen, *Chem. Mater.*, 2014, **26**, 4144–4150.

199 Q. Wang et al., *Nat. Mater.*, 2016, **15**, 611–615.

200 A. Iwase, Y. H. Ng, Y. Ishiguro, A. Kudo and R. Amal, *J. Am. Chem. Soc.*, 2011, **133**, 11054–11057.

201 H. Li, Y. Zhou, W. Tu, J. Ye and Z. Zou, *Adv. Funct. Mater.*, 2015, **25**, 998–1013.

202 Q. Jia, A. Iwase and A. Kudo, *Chem. Sci.*, 2014, **5**, 1513–1519.

203 M. G. Kibria, H. P. T Nguyen, K. Cui, S. Zhao, D. Liu, H. Guo, M. L. Trudeau, S. Paradis, A.-R. Hakima and Z. Mi, *ACS Nano*, 2013, **7**, 7886-7893.

204 Y. Wang, Y. Wu, K. Sun and Z. Mi, *Mater. Horizons*, 2019, **6**, 1454–1462.

205 S. Bai, W. Yin, L. Wang, Z. Li and Y. Xiong, *RSC Adv.*, 2016, **6**, 57446–57463.

206 T. Takata, J. Jiang, Y. Sakata, M. Nakabayashi, N. Shibata, V. Nandal, K. Seki, T. Hisatomi and K. Domen, *Nature*, 2020, **581**, 411-414.

207 X. Wang, K. Maeda, A. Thomas, K. Takanabe, G. Xin, J. M. Carlsson, K. Domen and M. Antonietti, *Nat. Mater.*, 2009, **8**, 76–80.

208 A. Thomas, A. Fischer, F. Goettmann, M. Antonietti, J.-O. Müller, R. Schlögl and J. M. Carlsson, *J. Mater. Chem.*, 2008, **18**, 4893.

209 B. V. Lotsch, M. Döblinger, J. Sehnert, L. Seyfarth, J. Senker, O. Oeckler and W. Schnick, *Chem. - A Eur. J.*, 2007, **13**, 4969–4980.

210 P. Wu, J. Wang, J. Zhao, L. Guo and F. E. Osterloh, *J. Mater. Chem. A*, 2014, **2**, 20338–20344.

211 K. Akaike, K. Aoyama, S. Dekubo, A. Onishi and K. Kanai, *Chem. Mater.*, 2018, **30**, 2341–2352.

212 L. Jiang, X. Yuan, Y. Pan, J. Liang, G. Zeng, Z. Wu and H. Wang, *Appl. Catal. B Environ.*, 2017, **217**, 388–406.

213 T. Xiong, W. Cen, Y. Zhang and F. Dong, *ACS Catal.*, 2016, **6**, 2462–2472.

214 Y. Wang, M. K. Bayazit, S. J. A. Moniz, Q. Ruan, C. C. Lau, N. Martsinovich and J. Tang, *Energy Environ. Sci.*, 2017, **10**, 1643–1651.

215 K. Takanabe, K. Kamata, X. Wang, M. Antonietti, J. Kubota and K. Domen, *Phys. Chem. Chem. Phys.*, 2010, **12**, 13020–13025.

216 S. Min and G. Lu, *J. Phys. Chem. C*, 2012, **116**, 19644–19652.

217 X. Zhang, T. Peng, L. Yu, R. Li, Q. Li and Z. Li, *ACS Catal.*, 2015, **5**, 504–510.

218 J. Wen, J. Xie, X. Chen and X. Li, *Appl. Surf. Sci.*, 2017, **391**, 72–123.

219 Y. Zhang, J. Liu, G. Wu and W. Chen, *Nanoscale*, 2012, **4**, 5300–5303.

220 G. Zhang, L. Lin, G. Li, Y. Zhang, A. Savateev, S. Zafeiratos, X. Wang and M. Antonietti, *Angew. Chemie - Int. Ed.*, 2018, **57**, 9372–9376.

221 D. J. Martin, K. Qiu, S. A. Shevlin, A. D. Handoko, X. Chen, Z. Guo and J. Tang, *Angew. Chemie - Int. Ed.*, 2014, **53**, 9240–9245.

222 V. W. Lau, I. Moudrakovski, T. Botari, S. Weinberger, M. B. Mesch, V. Duppel, J. Senker, V. Blum and B. V. Lotsch, *Nat. Commun.*, 2016, **7**, 12165.

223 Y. S. Jun, J. Park, S. U. Lee, A. Thomas, W. H. Hong and G. D. Stucky, *Angew. Chemie - Int. Ed.*, 2013, **52**, 11083–11087.

224 M. Shalom, S. Inal, C. Fettkenhauer, D. Neher and M. Antonietti, *J. Am. Chem. Soc.*, 2013, **135**, 7118–7121.

225 L. Lin, H. Ou, Y. Zhang and X. Wang, *ACS Catal.*, 2016, **6**, 3921–3931.

226 G. Zhang, G. Li, Z.-A. Lan, L. Lin, A. Savateev, T. Heil, S. Zafeiratos, X. Wang and M. Antonietti, *Angew. Chemie - Int. Ed.*, 2017, **56**, 13445–13449.

227 M. Schröder, K. Kailasam, J. Borgmeyer, M. Neumann, A. Thomas, R. Schomäcker and M. Schwarze, *Energy Technol.*, 2015, **3**, 1014–1017.

228 G. Zhang, Z.-A. Lan, L. Lin, S. Lin and X. Wang, *Chem. Sci.*, 2016, **7**, 3062–3066.

229 W. Che, W. Cheng, T. Yao, F. Tang, W. Liu, H. Su, Y. Huang, Q. Liu, J. Liu, F. Hu, Z. Pan, Z. Sun and S. Wei, *J. Am.*

Chem. Soc., 2017, **139**, 3021-3026.

230 D. J. Martin, P. J. T. Reardon, S. J. A. Moniz and J. Tang, *J. Am. Chem. Soc.*, 2014, **136**, 12568–12571.

231 Z. Pan, G. Zhang and X. Wang, *Angew. Chemie - Int. Ed.*, 2019, **131**, 7176–7180.

232 J. Yan, H. Wu, H. Chen, Y. Zhang, F. Zhang and S. F. Liu, *Appl. Catal. B Environ.*, 2016, **191**, 130–137.

233 X. She et al., *Adv. Energy Mater.*, 2017, **7**, 1700025.

234 M. Z. Rahman, M. G. Kibria and C. B. Mullins, *Chem. Soc. Rev.*, 2020, **49**, 1887-1931.

235 Z. Zhang, J. Long, L. Yang, W. Chen, W. Dai, X. Fu and X. Wang, *Chem. Sci.*, 2011, **2**, 1826–1830.

236 B. C. M. Martindale, G. A. M. Hutton, C. A. Caputo, S. Prantl, R. Godin, J. R. Durrant and E. Reisner, *Angew. Chemie - Int. Ed.*, 2017, **56**, 6459–6463.

237 M. Latorre-Sánchez, A. Primo and H. García, *Angew. Chemie - Int. Ed.*, 2013, **52**, 11813–11816.

238 F. Dai, J. Zai, R. Yi, M. L. Gordin, H. Sohn, S. Chen and D. Wang, *Nat. Commun.*, 2014, **5**, 1–11.

239 Z. Hu, L. Yuan, Z. Liu, Z. Shen and J. C. Yu, *Angew. Chemie - Int. Ed.*, 2016, **55**, 9580–9585.

240 S. K. Muduli, E. Varrla, Y. Xu, S. A. Kulkarni, A. Katre, S. Chakraborty, S. Chen, T. C. Sum, R. Xu and N. Mathews, *J. Mater. Chem. A*, 2017, **5**, 24874–24879.

241 B. Tian, B. Tian, B. Smith, M. C. Scott, R. Hua, Q. Lei and Y. Tian, *Nat. Commun.*, 2018, **9**, 1–11.

242 M. Zhu, Z. Sun, M. Fujitsuka and T. Majima, *Angew. Chemie - Int. Ed.*, 2018, **57**, 2160–2164.

243 A. B. Jorge, D. J. Martin, M. T. S. Dhanoa, A. S. Rahman, N. Makwana, J. Tang, A. Sella, F. Corà, S. Firth, J. A. Darr and P. F. McMillan, *J. Phys. Chem. C*, 2013, **117**, 7178–7185.

244 Y. Mikhaylov, Y. H. Budnikova, S. Xu, E. H. Kim, A. Wei and E. I. Negishi, *Sci. Technol. Adv. Mater.*, 2014, **15**, 044201.

245 S. Yanagida, A. Kabumoto, K. Mizumoto, C. Pac and K. Yoshino, *J. Chem. Soc. Chem. Commun.*, 1985, **8**, 474.

246 S. Matsuoka, H. Fujii, T. Yamada, C. Pac, A. Ishida, S. Takamuku, M. Kusaba, N. Nakashima and S. Yanagida, *J. Phys. Chem.*, 1991, **95**, 5802–5808.

247 S. Matsuoka, T. Kohzuki, Y. Kuwana, A. Nakamura and S. Yanagida, *J. Chem. Soc. Perkin Trans. 2*, 1992, **4**, 679.

248 R. S. Sprick, L. Wilbraham, Y. Bai, P. Guiglion, A. Monti, R. Clowes, A. I. Cooper and M. A. Zwijnenburg, *Chem. Mater.*, 2018, **30**, 5733–5742.

249 R. S. Sprick, B. Bonillo, R. Clowes, P. Guiglion, N. J. Brownbill, B. J. Slater, F. Blanc, M. A. Zwijnenburg, D. J. Adams and A. I. Cooper, *Angew. Chemie - Int. Ed.*, 2016, **55**, 1792–1796.

250 F. L. Tobiason, L. Huestis, C. Chandler, S. E. Pedersen and P. Peters, *J. Heterocycl. Chem.*, 1973, **10**, 773–778.

251 C. Yang, B. C. Ma, L. Zhang, S. Lin, S. Ghasimi, K. Landfester, K. A. I. Zhang and X. Wang, *Angew. Chemie - Int. Ed.*, 2016, **55**, 9202–9206.

252 L. Wang, R. Fernández-Terán, L. Zhang, D. L. A. Fernandes, L. Tian, H. Chen and H. Tian, *Angew. Chemie - Int. Ed.*, 2016, **55**, 12306–12310.

253 P. B. Pati, G. Damas, L. Tian, D. L. A. Fernandes, L. Zhang, I. B. Pehlivan, T. Edvinsson, C. M. Araujo and H. Tian, *Energy Environ. Sci.*, 2017, **10**, 1372–1376.

254 L. Li, R. G. Hadt, S. Yao, W.-Y. Lo, Z. Cai, Q. Wu, B. Pandit, L. X. Chen and L. Yu, *Chem. Mater.*, 2016, **28**, 5394–5399.

255 D. J. Woods, S. Hillman, D. Pearce, L. Wilbraham, L. Flagg, W. Duffy, I. Mcculloch, J. Durrant, A. Guilbert, M. Zwijnenburg, R. S. Sprick, J. Nelson and A. Cooper, *Energy Environ. Sci.*, 2020, **13**, 1843-1855.

256 Z. Hu, Z. Wang, X. Zhang, H. Tang, X. Liu, F. Huang and Y. Cao, *iScience*, 2019, **13**, 33–42.

257 Y. Wu, X. Zhang, Y. Xing, Z. Hu, H. Tang, W. Luo, F. Huang and Y. Cao, *ACS Mat. Lett.*, 2019, **1**, 620-627.

258 R. S. Sprick, C. M. Aitchison, E. Berardo, L. Turcani, L. Wilbraham, B. M. Alston, K. E. Jelfs, M. A. Zwijnenburg and A. I. Cooper, *J. Mater. Chem. A*, 2018, **6**,

11994–12003.

259 X. Zhang, F. Shen, Z. Hu, Y. Wu, H. Tang, J. Jia, X. Wang, F. Huang and Y. Cao, *ACS Sustain. Chem. Eng.*, 2019, **7**, 4128–4135.

260 J. Kosco et al., *Nat. Mater.*, 2020, **19**, 559–565.

261 M. G. Schwab, M. Hamburger, X. Feng, J. Shu, H. W. Spiess, X. Wang, M. Antonietti and K. Müllen, *Chem. Commun.*, 2010, **46**, 8932.

262 R. S. Sprick, B. Bonillo, M. Sachs, R. Clowes, J. R. Durrant, D. J. Adams and A. I. Cooper, *Chem. Commun.*, 2016, **52**, 10008–10011.

263 R. S. Sprick, J. X. Jiang, B. Bonillo, S. Ren, T. Ratvijitvech, P. Guiglion, M. A. Zwijnenburg, D. J. Adams and A. I. Cooper, *J. Am. Chem. Soc.*, 2015, **137**, 3265–3270.

264 Y. Xiang, X. Wang, L. Rao, P. Wang, D. Huang, X. Ding, X. Zhang, S. Wang, H. Chen and Y. Zhu, *ACS Energy Lett.*, 2018, **10**, 2544-2549.

265 Y. S. Kochergin, D. Schwarz, A. Acharjya, A. Ichangi, R. Kulkarni, P. Eliášová, J. Vacek, J. Schmidt, A. Thomas and M. J. Bojdys, *Angew. Chemie - Int. Ed.*, 2018, **57**, 14188–14192.

266 R. S. Sprick, Y. Bai, A. A. Y. Guilbert, M. Zbiri, C. M. Aitchison, L. Wilbraham, Y. Yan, D. J. Woods, M. A. Zwijnenburg and A. I. Cooper, *Chem. Mater.*, 2019, **31**, 305–313.

267 Y. Zhao, W. Ma, Y. Xu, C. Zhang, Q. Wang, T. Yang, X. Gao, F. Wang, C. Yan and J. X. Jiang, *Macromolecules*, 2018, **51**, 9502–9508.

268 L. Li, Z. Cai, Q. Wu, W.-Y. Lo, N. Zhang, L. X. Chen and L. Yu, *J. Am. Chem. Soc.*, 2016, **138**, 7681–7686.

269 L. Li, W. Lo, Z. Cai, N. Zhang and L. Yu, *Macromolecules*, 2016, **49**, 6903–6909.

270 Y. Xu, N. Mao, S. Feng, C. Zhang, F. Wang, Y. Chen, J. Zeng and J. X. Jiang, *Macromol. Chem. Phys.*, 2017, **218**, 1700049.

271 L. Li and Z. Cai, *Polym. Chem.*, 2016, **7**, 4937–4943.

272 R. S. Sprick, B. Bonillo, R. Clowes, P. Guiglion, N. J. Brownbill, B. J. Slater, F. Blanc, M. A. Zwijnenburg, D. J. Adams and A. I. Cooper, *Angew. Chemie Int. Ed.*, 2016, **55**, 1792–1796.

273 D. R. Anderson and J. M. Holovka, *J. Polym. Sci. Part A-1 Polym. Chem.*, 1966, **4**, 1689–1702.

274 S. Ren, M. J. Bojdys, R. Dawson, A. Laybourn, Y. Z. Khimyak, D. J. Adams and A. I. Cooper, *Adv. Mater.*, 2012, **24**, 2357–2361.

275 P. Kuhn, M. Antonietti and A. Thomas, *Angew. Chemie - Int. Ed.*, 2008, **47**, 3450–3453.

276 C. B. Meier, R. Clowes, E. Berardo, K. E. Jelfs, M. A. Zwijnenburg, R. S. Sprick and A. I. Cooper, *Chem. Mater.*, 2019, **31**, 8830–8838.

277 J. Bi, W. Fang, L. Li, J. Wang, S. Liang, Y. He, M. Liu and L. Wu, *Macromol. Rapid Commun.*, 2015, **36**, 1799–1805.

278 K. Schwinghammer, S. Hug, M. B. Mesch, J. Senker and B. V. Lotsch, *Energy Environ. Sci.*, 2015, **8**, 3345–3353.

279 Z.-A. Lan, Y. Fang, Y. Zhang and X. Wang, *Angew. Chemie - Int. Ed.*, 2018, **57**, 470–474.

280 C. B. Meier, R. S. Sprick, A. Monti, P. Guiglion, J.-S. M. Lee, M. A. Zwijnenburg and A. I. Cooper, *Polymer*, 2017, **126**, 283-290.

281 L. Guo, Y. Niu, H. Xu, Q. Li, S. Razzaque, Q. Huang, S. Jin and B. Tan, *J. Mater. Chem. A*, 2018, **6**, 19775–19781.

282 Y. S. Kochergin, D. Schwarz, A. Acharjya, A. Ichangi, R. Kulkarni, P. Eliášová, J. Vacek, J. Schmidt, A. Thomas and M. J. Bojdys, *Angew. Chemie - Int. Ed.*, 2018, **57**, 14188–14192.

283 W. Huang, Q. He, Y. Hu and Y. Li, *Angew. Chemie - Int. Ed.*, 2019, **58**, 8676–8680.

284 M. Liu, Q. Huang, S. Wang, Z. Li, B. Li, S. Jin and B. Tan, *Angew. Chemie - Int. Ed.*, 2018, **57**, 11968–11972.

285 J. Xie, S. A. Shevlin, Q. Ruan, S. J. A. Moniz, Y. Liu, X. Liu, Y. Li, C. C. Lau, Z. X. Guo and J. Tang, *Energy Environ. Sci.*, 2018, **11**, 1617–1624.

286 D. Kong, X. Han, J. Xie, Q. Ruan, C. D. Windle, S. Gadipelli, K. Shen, Z. Bai, Z. Guo and J. Tang, *ACS Catal.*, 2019, **9**,

7697-7707.

287 L. Wang, Y. Wan, Y. Ding, Y. Niu, Y. Xiong, X. Wu and H. Xu, *Nanoscale*, 2017, **9**, 4090–4096.

288 L. Wang, Y. Wan, Y. Ding, S. Wu, Y. Zhang, X. Zhang, G. Zhang, Y. Xiong, X. Wu, J. Yang and H. Xu, *Adv. Mater.*, 2017, **29**, 1702428.

289 S. Ikeda, T. Takata, T. Kondo, G. Hitoki, M. Hara, J. N. Kondo, K. Domen, H. Hosono, H. Kawazoe and A. Tanaka, *Chem. Commun*, 1998, 2185–2186.

290 L. Wang, X. Zheng, L. Chen, Y. Xiong and H. Xu, *Angew. Chemie - Int. Ed.*, 2018, **57**, 3454–3458.

291 A. P. Côté, A. I. Benin, N. W. Ockwig, M. O'Keeffe, A. J. Matzger and O. M. Yaghi, *Science*, 2005, **310**, 1166–1170.

292 C. S. Diercks and O. M. Yaghi, *Science*, 2017, **355**, 923-931.

293 A. I. Cooper, *Adv. Mater.*, 2009, **21**, 1291–1295.

294 A. M. Evans, L. R. Parent, N. C. Flanders, R. P. Bisbey, E. Vitaku, M. S. Kirschner, R. D. Schaller, L. X. Chen, N. C. Gianneschi and W. R. Dichtel, *Science*, 2018, **361**, 52–57.

295 L. Stegbauer, K. Schwinghammer and B. V. Lotsch, *Chem. Sci.*, 2014, **5**, 2789–2793.

296 V. S. Vyas, F. Haase, L. Stegbauer, G. Savasci, F. Podjaski, C. Ochsenfeld and B. V. Lotsch, *Nat. Commun.*, 2015, **6**, 8508.

297 S. Kandambeth, A. Mallick, B. Lukose, M. V. Mane, T. Heine and R. Banerjee, *J. Am. Chem. Soc.*, 2012, **134**, 19524–19527.

298 P. Pachfule, A. Acharjya, J. Roeser, T. Langenhahn, M. Schwarze, R. Schomäcker, A. Thomas and J. Schmidt, *J. Am. Chem. Soc.*, 2018, **140**, 1423–1427.

299 B. P. Biswal, H. A. Vignolo-González, T. Banerjee, L. Grunenberg, G. Savasci, K. Gottschling, J. Nuss, C. Ochsenfeld and B. V. Lotsch, *J. Am. Chem. Soc.*, 2019, **141**, 11082-11092.

300 K. Geng, T. He, R. Liu, S. Dalapati, K. T. Tan, Z. Li, S. Tao, Y. Gong, Q. Jiang and D. Jiang, *Chem. Rev.*, 2020.

301 M. Zhang et al., *J. Am. Chem. Soc.*, 2020, **142**, 9169-9174.

302 A. P. French and E. F. Taylor, *An Introduction to Qunatum Physics*, W. W. Norton & Company, London, 1978.

303 F. Gensdarmes, in *Nanoengineering: Global Approaches to Health and Safety Issues*, Elsevier, 2015, pp. 55–84.

304 T. Misono, in *Measurement Techniques and Practices of Colloid and Interface Phenomena*, Springer Singapore, 2019, pp. 65–69.

305 J. Stetefeld, S. A. McKenna and T. R. Patel, *Biophys. Rev.*, 2016, **8**, 409–427.

306 G. B. J. de Boer, C. de Weerd, D. Thoenes and H. W. J. Goossens, *Part. Part. Syst. Charact.*, 1987, **4**, 14–19.

307 D. J. Lockwood, in *Encyclopedia of Color Science and Technology*, Springer New York, 2016, pp. 1097–1107.

308 *A basic guide to particle characterization - Whitepaper*, Malvern Instruments Limited, 2015.

309 C. M. Keck and R. H. Müller, *Int. J. Pharm.*, 2008, **355**, 150–163.

310 J. Sauter, *Die Grössenbestimmung der im Gemischnebel von Verbrennungskraftmaschinen vohrhandenen Brennstoffteilchen*, VDI-Verlag, 1926.

311 P. B. Kowalczuk and J. Drzymala, *Part. Sci. Technol.*, 2016, **34**, 645–647.

312 A. Sillen and Y. Engelborghs, *Photochem. Photobiol.*, 1998, **67**, 475–486.

313 R. Berera, R. van Grondelle and J. T. M. Kennis, *Photosynth. Res.*, 2009, **101**, 105–118.

314 G. Boschloo and A. Hagfeldt, *Inorganica Chim. Acta*, 2008, **361**, 729–734.

Chapter 2: Microstructuring of Polymer Photocatalysts to Enhance Hydrogen Production

All materials in this chapter were prepared, characterised, and tested by the author apart from the thermogravimetric analysis and nitrogen sorption measurements, which were performed by Dr Reiner Sebastian Sprick.

2.1. Introduction

Whilst the optimal morphology of a photocatalyst is as yet unknown, increasing active surface area would be expected to increase catalytic rate as a general rule for heterogeneous catalysts. In conjugated organic polymers, exciton diffusion typically occurs on the length scale of 5–20 nm;[1–3] that is, potentially significantly less far than the depths into which light can penetrate into the material.[4] Polymeric photocatalysts are typically made by precipitation polymerisation reactions to give 'bulk' particles in the micron size range. Hence, for bulk photocatalysts, a portion of photogenerated excitons will typically be unable to reach the material surface and react. In the case of photocatalytic proton reduction, the "active area" should therefore consider the area that is exposed to light and the area that is in contact with water or sacrificial electron donor. This surface area can be either extrinsic or intrinsic, which gives two potential approaches for microstructuring: pores and nanoparticles.

Generating different microstructures is relatively simple if using monomers with different chemical structures. For example, a series of fluorene and dibenzothiophene sulfone based CMPs using 1,3,5- and 1,2,4,5-phenyl crosslinkers were compared to linear 1,4- and 1,3-phenyl linked polymer analogues to investigate the effect of porosity on hydrogen production rates.[5] In this study, the most active material was found to be a highly porous network, which was shown by water uptake measurements and quasi-elastic neutron scattering to be capable of hydration up to 52 wt. % with indications of good mass transport in the material. However not all of the porous polymers in this study outperformed their linear analogues suggesting that porosity may only be beneficial to photocatalytic hydrogen production if the pores are accessible to water. Indeed, a previous study by Yang *et al.* investigating benzothiadiazole based polymer photocatalysts for hydrogen production[6] found no correlation between BET surface area and hydrogen production rates, with the one linear polymer tested—one of the least porous materials in the study—found to be more active than all eight CMP materials. Clearly, variation in chemical structure can sometimes outweigh potentially beneficial features in tertiary structure. A further fundamental question is the impact of porosity on exciton transport.

Instead of comparing different material classes that have inherently different microstructures, actively microstructuring a material and measuring the effect on photocatalysis allows structural properties to be separated from other chemical or electronic effects—that is, only the microstructure varies, and not the chemistry. In the context of organic polymers, different microstructures can be obtained if a material is soluble in organic solvents and thus solution processable. In 2017, Woods *et al* showed that the

addition of a solubilising 2-ethylhexyl side chain to a carbazole based polymer did not significantly alter hydrogen production rate in the bulk but it did allow a highly active thin film to be cast, using significantly less material whilst maintaining a very high hydrogen production rate.[7] The hydrophobic aliphatic chains used in this work may be not be ideal for generating a highly wetable photocatalyst. In recent years, there have been examples of photocatalysts with hydrophilic[8,9] or ionic[10] side chains that couple good processability with higher photocatalytic activities. Casting films also allows for measurement of a number of different photoelectronic properties. For example, photoelectron spectroscopy in air (PESA)[11] can be employed to calculate energy levels in organic thin films.[12–14] Similarly, many conductivity and charge transport techniques such as impedance spectroscopy[15] and time of flight[16] require polymer-electrodes most easily achieved through films. In photocatalytic applications, soluble polymers have also been cast onto glass fibres which has allowed for photocatalysis in flow[17] and in scale-up experiments.[9]

Nanoparticles of solution processable conjugated polymers have been shown to have some of the highest hydrogen evolution rates per gram of catalyst in the literature.[18] In 2016, polymer 'dots' of approximately 60 nm were reported using PFBT and a polysterene/PEG based co-polymer (Figure 1) and were found to have unprecedented initial hydrogen evolution rates of 8.3 mmol h^{-1} g^{-1}, 5 orders of magnitude higher than the bulk polymers under equivalent conditions.[19]

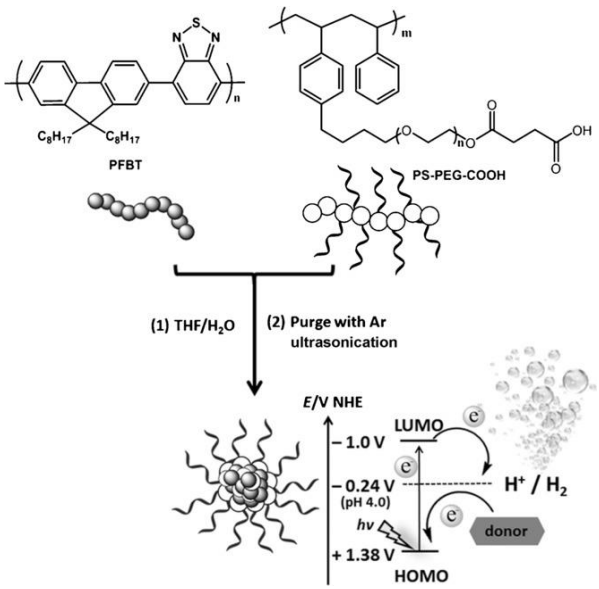

Figure 1: Preparation of PFBT-Pdots and a diagram for light-driven hydrogen generation. *Image reproduced from reference [19] with permission of the rights holder, John Wiley & Sons, Inc.*

However, this initial rate was sustained for less than 20 minutes and after 80 minutes the hydrogen evolution rate had been reduced to almost zero. The same group improved the activity and longevity of this material by introducing a thiophene unit into the backbone leading to initial rates as high as 50 mmol h^{-1} g^{-1} and an increased 4-hour hydrogen production lifetime.[20] Similar results were also found for 'hollow' polymer dots[21] and for nanoparticles with blends of two different polymers.[22] These materials are most active when loaded with photodeposited platinum which is thought to act as an active centre for proton reduction. An alternative approach by Tseng *et al.* was to create polymer nanoparticles with a cycloplatinated monomer unit, which displayed high activity and longevity, with up to 12 hours of hydrogen production.[23] In general, these materials are tested at very low concentrations (10–20 μg mL^{-1}) and hence, whilst the mass normalised hydrogen evolution rates are very high, the EQEs (see Section 1.7) are low in comparison with bulk polymer photocatalysts in literature.[18] From a practical perspective, the amount of hydrogen produced per unit irradiated area is a better measurement of performance than the mass-normalized hydrogen production rate. EQEs are a direct incident light to hydrogen calculation and therefore dilute systems tend to have low values due to transmission of light through the sample. Developing systems with increased longevity that are active at more practicable concentrations is crucial to the progress of this field. A recent example by McCulloch *et al.* also used a blending technique and showed that with appropriate choice of donor and acceptor polymers and an intermediate 0.1 mg mL^{-1} concentration, EQEs of 6.2% could be reached at wavelengths up to 700 nm.[24]

The most widely studied organic material for hydrogen production is graphitic carbon nitride[18,25,26] and this, along with some of the most active and stable organic polymer photocatalysts,[18,27,28] is insoluble in organic solvents. Optimising the microstructure of these materials is therefore significantly more challenging and often energy intensive. Techniques such as ball milling[29,30] and exfoliation[31,32] have been used to create nanostructured versions of carbon nitride and other 2-D networks that have improved photocatalytic activity over the bulk materials. Similarly reducing particle size through delamination has been used to obtain sheets of only a few molecules thick in a variety of acetylene,[33] hydrazone[34] and boronate ester[35] bearing covalent organic frameworks but this technique is not suited to linear or 3-dimensional polymers.

Materials can also be microstructured through a variety of *in-synthesis* methods. Polymers are particularly suited to this approach as, although conjugated polymers containing aromatic groups without aliphatic sidechains are commonly insoluble, the monomer units from which they are made are often significantly more processable. For example, the surface

areas of otherwise non-porous or low porosity polymers can be increased by polymerising in the presence of a silica template which is then removed post synthesis, to yield permanent cavities in the material. This technique has been widely used in the high temperature synthesis of carbon nitride[26,36,37] but has also been shown to give increased surface areas for polymers synthesised by solution-based carbon carbon cross coupling[38] as well as in acid catalysed vapour phase synthesis of hollow polytriazine networks (Figure 2).[39]

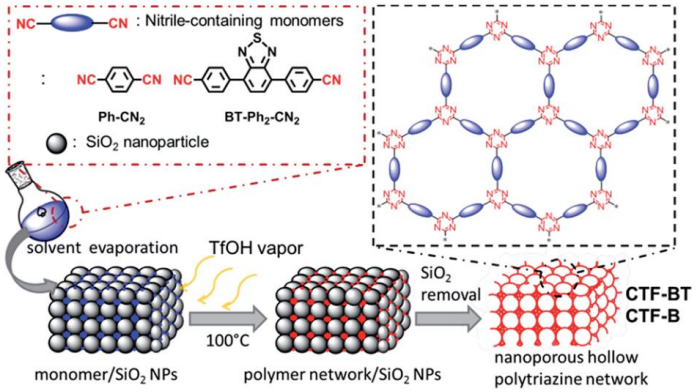

Figure 2: Schematic of solid vapor synthesis and idealized structures of the nanoporous hollow polytriazine networks. *Reproduced from reference [39], published by the Royal Society of Chemistry.*

Whilst effective, the removal of the silica templates often involves hazardous chemicals such as NH_4F or HF which are highly environmentally damaging and not compatible with the chemical linkages of some organic photocatalysts. Aside from carbon nitride, the first polymers tested for hydrogen production were primarily based on cross coupled carbon-carbon bonds[40] but the current field of organic photocatalysts now includes a range of covalent organic frameworks with triazine,[30,41] immine,[27,42,43] hydrazone[44] and azine[45,46] linkages. Recently Karak *et al.* developed a new method for creating low-density COF foams by adding sodium bicarbonate to the reaction mixture (Figure 3). The resultant effervescence was frozen in by freeze drying before heating to polymerise by β-ketoenamine formation.[47] It remains to be seen whether this approach would be applicable to many other materials but the chemical diversity of organic photocatalysts means microstructuring approaches with broad scope are particularly attractive.

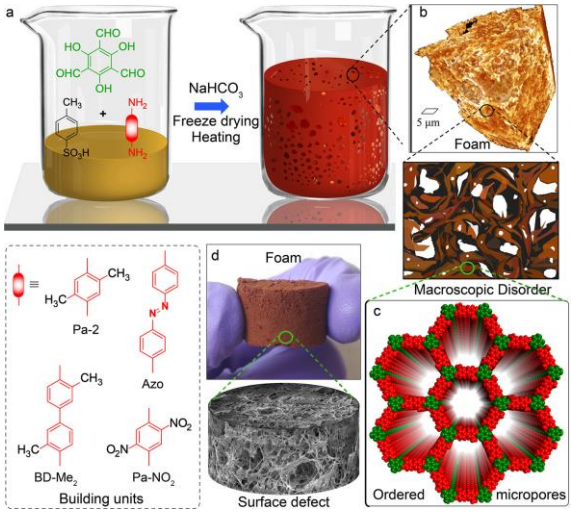

Figure 3: (a) Schematic representation of COF−foam synthesis using an *in-situ* gas-foaming technique. (b) 3D volume rendered X-ray computed tomographic image of COF foam and cartoon representation of disordered macropores present in the foam matrix. (c) Space-filled model of ordered micropores of the 2D crystallites of the COF foam. (d) Digital image of COF−foam and scanning electron microscopy (SEM) image of the surface of the foam. *Image reproduced from reference [47], with permission of the American Chemical Society.*

The concept of introducing porosity using a two-phase synthetic medium has also been widely studied in the context of polyHIPEs (Figure 4). Polymers synthesised in high internal phase emulsions have been used in a number of different applications including membrane separations, reaction supports, tissue engineering scaffolds and photocatalysis[48,49] but often utilise non-conjugated monomers with large alkyl chains and the technique has not been studied for less soluble groups.

Figure 4: Schematic of polyHIPE synthesis. *Image reproduced from reference [49], with permission of Elsevier.*

Polymers can also be synthesised in 'normal' oil in water emulsions, where the aqueous continuous phase makes up the majority volume with a minor dispersed organic phase, resulting in colloidal polymer particles.[50] This approach to limiting particle size has been widely applied for biomedical applications[51–53] where the polymer nanoparticles produced can encapsulate biomolecules or drugs.[54–57] It is also an easy method of synthesising magnetic polymer nanoparticles[58,59] which have applications in imaging[60] and magnetic separation[61] and for encapsulating fluorescent molecules, which can help to improve loading concentrations and stability.[62,63] In these examples, the polymer produced is primarily a matrix for another material. As such, acrylate-based polymers are most commonly used with polymerisation through both radical and anionic routes.[52,53,64–67] Emulsion polymerisation can also be used for coordination-based polymerisations such as metathesis reactions[68,69] and cross coupling techniques including Glaser,[70,71] Songashira[72,73] and Suzuki coupling reactions.[72] These routes allow for the easy synthesis of aromatic polymer backbones and as such the formation of nanoparticles where the polymer itself is the functional component.

The above are primarily examples of mini-emulsion polymerisation where the oil droplet size ranges from 50 to 1000 nm and where polycondensation occurs only within pre-existing droplets.[50] Mini-emulsions are created by applying a shear stress to a mixture of two immiscible liquids.[74] Although not a thermodynamic energy minimum, these systems are kinetically stabilised on a timescale of hours to years by the addition of surfactants. This is in contrast to macro-emulsions where droplet sizes are 1–100 µm and which exist on a timescale of seconds to hours.[50] Most mini-emulsions use surfactants that are soluble in the continuous phase and therefore, for oil in water emulsions, ionic surfactants such cetrylbutylammonium bromide (CTAB) or sodium dodecylsulfate (SDS) are commonly used. This approach is particularly attractive for the large aromatic groups normally associated with good photoredox activity as highly solubilising solvents such as toluene can be used as the dispersed phase.

It has previously been shown that a benzothiadiazole bearing CMP synthesised in mini-emulsion can outperform the bulk analogue for the photocatalytic degradation of Rhodamine-B (Figure 5)[72] but to date emulsion polymerisation derived materials have not been investigated for hydrogen production.

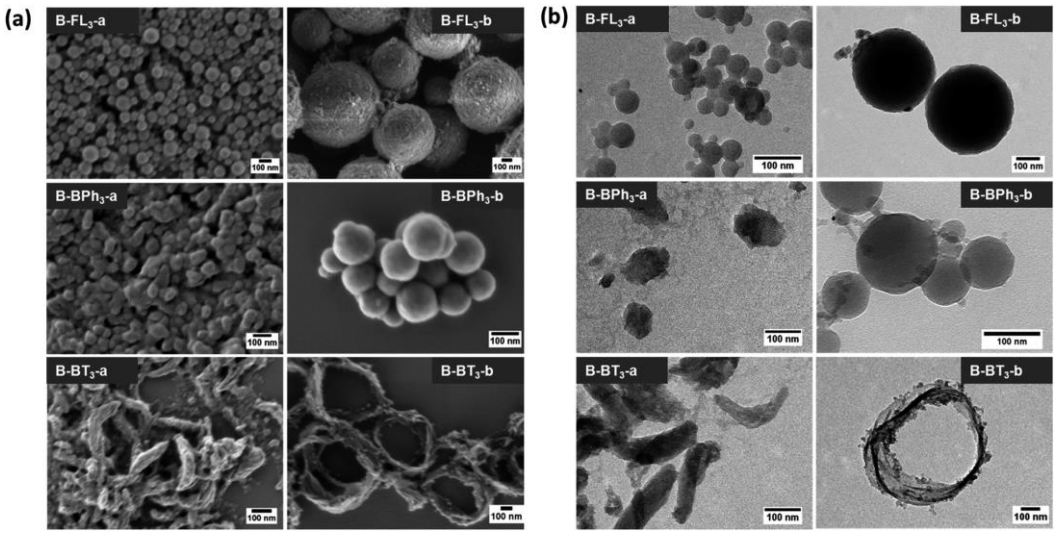

Figure 3: (a) SEM and (b) TEM images of differently shaped benzothiadiazole bearing CMP nanoparticles made in mini-emulsion. *Reproduced from reference [72], published by the Royal Society of Chemistry.*

In this chapter, three polymers synthesised in mini-emulsions were tested for photocatalytic proton reduction and compared to bulk analogues to measure the effect of particle size on activity. The phenyl-based network **ME-CMP** (Figure 6) was deemed to be a good candidate as it has been shown to be a moderately active hydrogen production photocatalyst under UV irradiation[75] and has been made in mini-emulsion before.[72] Introducing dibenzothiophene sulfone units into the polymer backbone has been previously shown to increase photocatalytic activity by increasing hydrophilicity and charge carrier lifetime.[28] Therefore, the dibenzothiophene sulfone analogue of **ME-CMP**, **S-CMP1** was also tested as well as the linear homopolymer **P10** (Figure 6). These materials also allow us to compare CMP networks to linear polymers.

2.2. Emulsion polymerisation derived polymers

2.2.1. Synthesis and Characterisation

Bulk polymers **ME-CMP**, **S-CMP1** and **P10** were synthesised by Suzuki coupling in precipitation polymerisations according to literature methods.[5,28,75] A single-phase DMF/water solvent system was used and refluxed at 145° C for 48 hours. **ME-CMP-e**. **S-CMP1-e** and **P10-e**, in contrast, were synthesised by Suzuki coupling in toluene/ water mini-emulsions via a modified literature procedure.[72] These were necessarily conducted at a lower temperature and a shorter reaction time of 17 hours (See experimental section 2.4.2 for full details).[76]

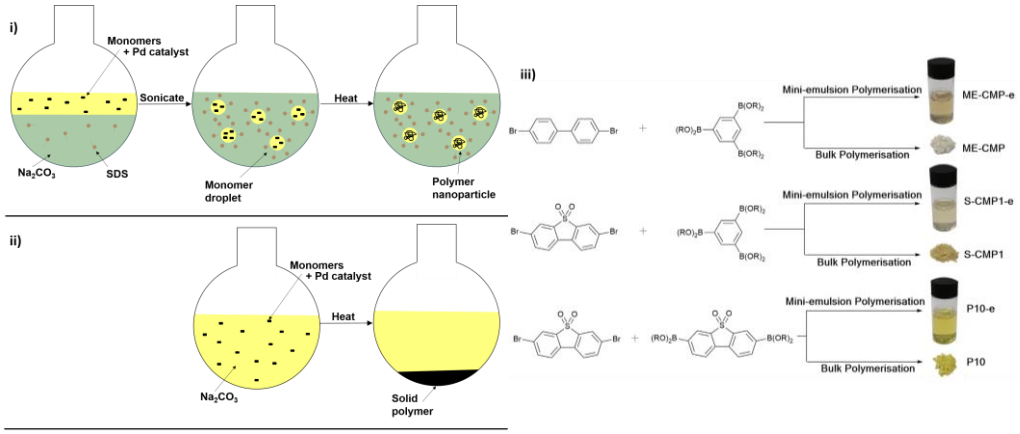

Figure 4: i) Cartoon of emulsion polymerisation. ii) Cartoon of precipitation polymerisation. iii) Synthesis routes of the polymers. Image reproduced from reference [71], published by the Royal Society of Chemistry

Dynamic light scattering (DLS) measurements on the emulsion-derived materials indicted all samples were exclusively made up of particles less than one micrometer with average hydrodynamic diameters (Z-average) of 248, 180 and 156 nm for **MECMP-e**, **S-CMP1-e** and **P10-e** respectively (Figure 7A). These particle sizes are consistent with polymerisation occurring within the toluene droplets of the mini-emulsion.[50] The CMP particles, **ME-CMP-e** and **S-CMP1-e**, showed no signs of aggregation over 11 days without stirring, with minimal (< 15%) changes in average particle diameter or size polydispersity as measured by DLS (Figure 7E). By contrast, the linear **P10-e** particles flocculated over 9 days to give an average diameter of 400 nm. When sonicated, these 400 nm agglomerates could be redispersed and a hydrodynamic radius of 169 nm was found by DLS, close to the original size of the particles directly after synthesis.

Scanning electron microscopy (SEM) of the emulsion particles agreed well with the DLS measurements, showing particle sizes from 50 nm up to 500 nm for all samples. Aside from size, the different materials had different shapes; **ME-CMP-e** and **S-CMP1** showed a more elongated, tendril-like morphology compared to **P10-e**, which comprised roughly spherical particles. This variation in morphology has previously been observed in emulsion polymerisation derived materials[72] (Figure 7 B-D) and could be due to the developing particle forming within a droplet or at the interface.

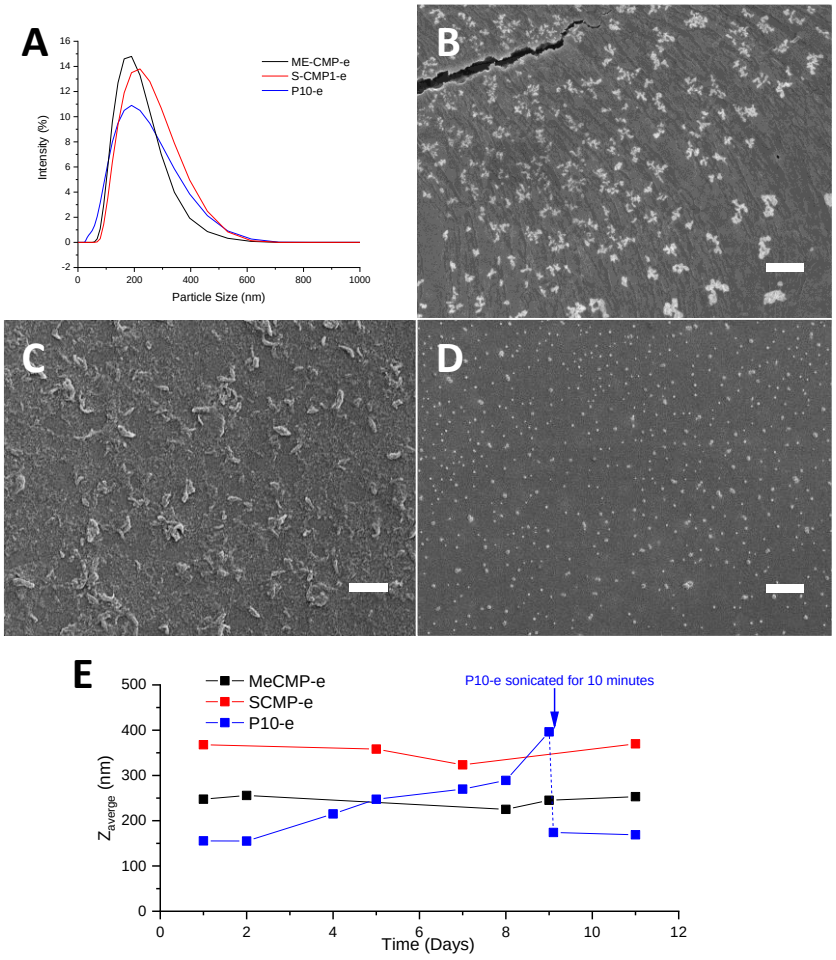

Figure 7: (A) Distribution of particle sizes for the emulsion-derived materials by DLS. SEM images of **ME-CMP-e** (B), **S-CMP1-e** (C) and **P10-e** (D) recorded at 3 keV, scale bars are 1 µm. (E) Stability of the average particle size of the emulsion derived materials, as measured by DLS.

Due the dependence of emulsion droplet size on oil content,[67,77] smaller particle sizes could be generated by altering the water: toluene ratio of the emulsion used for synthesis. However, these reactions gave diminished poly-condensation yields as assayed by UV-visible spectroscopy and so this was not chosen as a means for increasing photocatalyst

surface area. Increasing sonication time and power did not result in smaller particle sizes, indicating the conditions used provided sufficient energy for the mini-emulsion to reach a pseudo steady state.[67] Attempts to remove the sodium dodecylsulfate surfactant by dialysis after synthesis resulted in increased flocculation of the samples and so the emulsion-derived materials were used without further purification.

It has been shown that residual palladium from the cross coupling catalyst used in synthesis, can play a role in photocatalytic hydrogen production from water[78,79] and this is discussed further in Chapter 3. The residual palladium content of the polymers was determined by inductively coupled plasma - optical emission spectrometry (ICP-OES) (emulsion-derived materials) or by inductively coupled plasma – mass spectrometry (ICP-MS) (bulk materials). **ME-CMP-e**, **S-CMP1-e** and **P10-e** had levels of 0.542, 0.420 and 0.403 wt. % with respect to the polymer, similar to the levels of Pd found in their corresponding bulk polymers (0.363, 0.332 and 0.650 wt. %).

Table 1: Palladium contents and optical properties of the bulk and emulsion-derived materials.

Material	Pd content from ICP (wt. %)	Absorption onset[a] (nm)	Emission maxima[b] (nm)
ME-CMP	0.363 ± 0.006[c]	404	432
ME-CMP-e	0.542 ± 0.002[d]	358	396
S-CMP1	0.332 ± 0.007[c]	439	465
S-CMP1-e	0.420 ± 0.003[d]	409	441
P10	0.650 ± 0.02c[b]	481	508
P10-e	0.403 ± 0.001[d]	466	513

[a] See section 2.4.1 for how onset is extracted from spectra. [b] λ_{ex} = 325 nm. [c] Pd content measured by ICP-MS, average and standard deviation of 3 repeats. [d] Pd content measured by ICP-OES, average and standard deviation of 5 repeats.

UV-Vis spectroscopy (Figure 8) revealed significant differences between the absorption profiles for the CMP emulsion-derived particles and their bulk analogues. Bulk **ME-CMP** has an absorption onset of 404 nm while in **ME-CMP-e**, this is shifted further into the UV (358 nm). Similarly, bulk **S-CMP1** has an absorption onset of 439 nm, compared to 409 nm for **S-CMP1-e**. It is possible that the lower temperature of the emulsion polymerization resulted in a reduced degree of polycondensation compared to the bulk synthesis at higher temperature. Lower molecular weights have been observed previously for CMPs that were prepared in nonpolar solvents such as toluene at lower temperatures, as compared to the same CMP synthesised in aprotic polar solvents, such as DMF, at higher temperatures.[80] The linear polymers **P10** and **P10-e** showed a smaller difference between their absorption profiles with onsets of 481 nm and 466 nm, respectively.

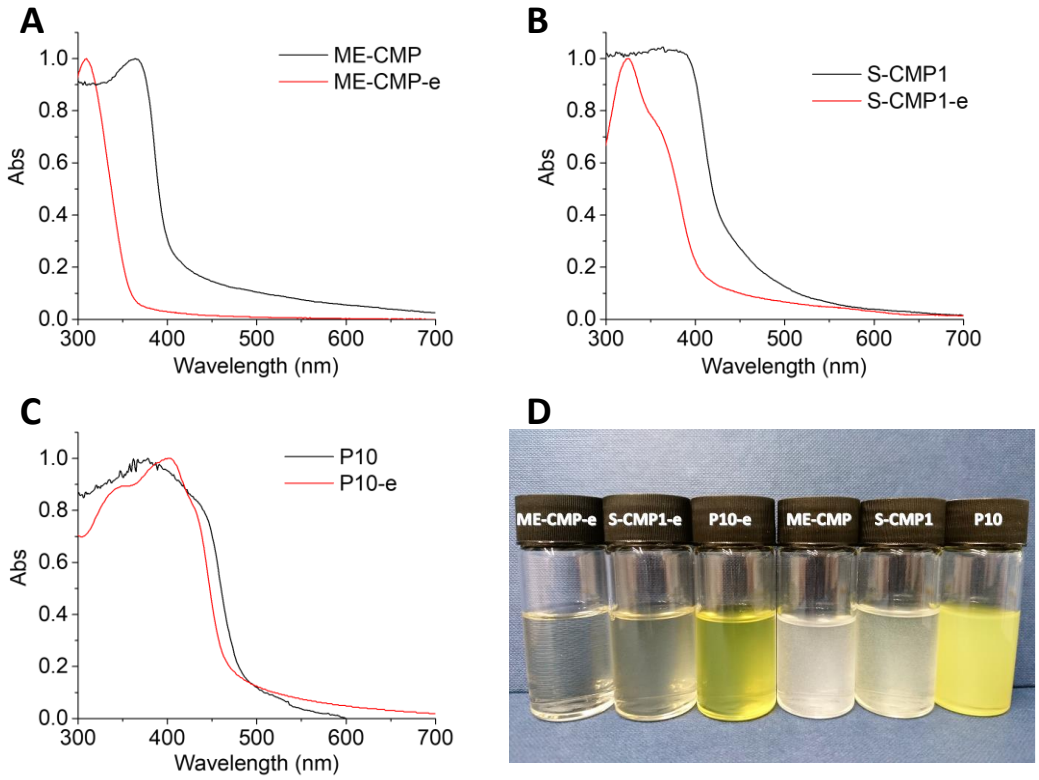

Figure 8: UV-Vis spectra of the bulk and emulsion-derived materials, **ME-CMP** and **ME-CMP-e** (0.006 mg mL^{-1}) (A), **S-CMP1** and **S-CMP1-e** (0.007 mg mL^{-1}) (B) and **P10** and **P10-e** (0.010 mg mL^{-1}) (C), emulsion particles were measured in suspension, bulk samples are measured by DRS, all spectra are normalised. Photograph of all materials as photolysis suspensions (D).

For linear systems, it has been shown previously that low molecular weight oligomers can have similar absorption on-sets to their respective polymer.[7] It is possible, therefore, that differences in chain length between the linear polymers **P10** and **P10-e** have a more limited

effect on the absorption on-set as compared to the two CMPs. The insoluble nature of the polymers meant full analysis of chain length was not possible, but the effect of chain length on absorption and catalytic properties of these materials is discussed in more detail in Chapter 3. Photoluminescence spectroscopy was employed to measure the emission characteristics of the materials and again showed significant differences between the bulk and emulsion-derived materials. The emission maximum of **ME-CMP** was 432 nm whilst the maximum for **ME-CMP-e** was blueshifted 38 nm to 396 nm. Similarly, the emission of **S-CMP1** was 465 nm compared to 441 nm for **S-CMP1-e**. Again, **P10** and **P10-e** were the most similar with emission maxima of 508 and 513 nm respectively.

A sample of **P10-e** was collected from dispersion by high frequency centrifugation, washed with water and dried under vacuum for thermogravimetric and nitrogen sorption analysis. Whilst bulk **P10** is not a porous polymer, its nitrogen isotherm does show some surface adsorption and it has an apparent BET surface area of 56 m^2 g^{-1} (Figure 9). In contrast, the dried **P10-e** material showed negligible adsorption and gave a nominal BET surface area of just 7 m^2 g^{-1}. This difference may be due to more optimal packing of the small, regularly shaped emulsion-derived particles in comparison with the large bulk particles that are fused into irregular shapes. The collection and drying of sufficient sample for sorption analysis required scale up of the emulsion synthesis by a factor of 10 and samples could not be redispersed. Analysis was therefore only performed on the highly active **P10-e** material.

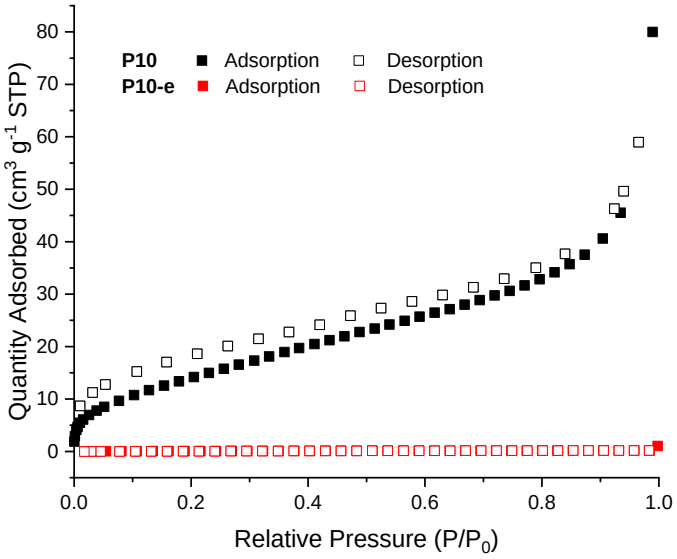

Figure 9: Nitrogen sorption isotherms of **P10** and **P10-e** measured at 77.3 K to 1 bar (desorption curves shown as open symbols).

Thermogravimetric analysis of **P10** and the dried **P10-e** samples also showed a difference between the two materials; **P10-e** was significantly more stable, with a 50 wt.% loss at a temperature of 565 °C, compared to 518 °C for **P10**. This is perhaps surprising given the assumption, discussed above, that **P10-e** has a shorter chain length than bulk **P10** and indicates that the secondary or tertiary structure of **P10-e** is stabilising the material. This may be the result of electrostatic interactions of the dibenzothiophene sulfone units on the particles surface or may be due to different chain stacking in the emulsion derived materials. The interaction of the material with the pan and the subsequent effect on heat transfer could also be responsible.

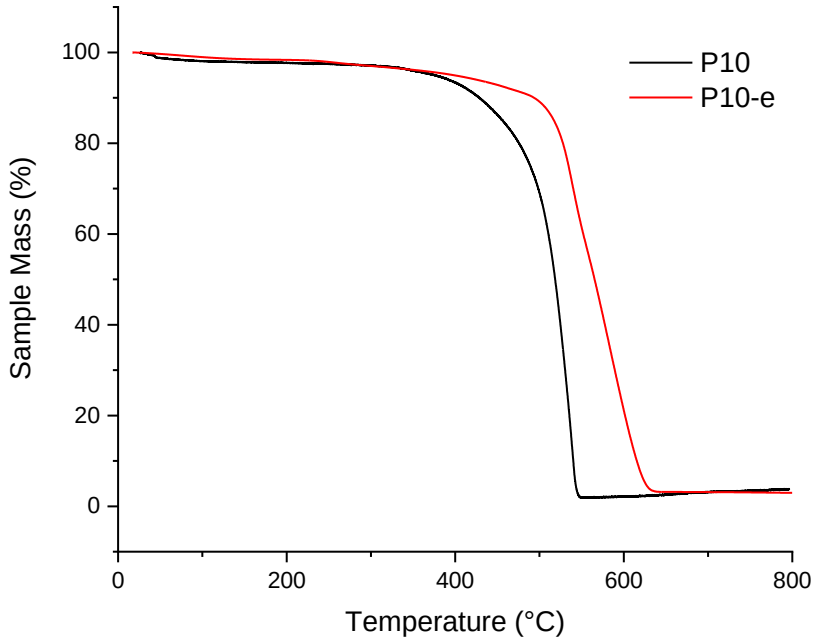

Figure 10: Thermogravimetric analysis of **P10** and **P10-e** heated at 10 °C min^{-1} in air.

2.2.2 Photocatalytic hydrogen production using triethylamine

2.2.2.1 Hydrogen evolution experiments

The emulsion-derived and bulk polymers were first tested for photocatalytic proton reduction using a triethylamine (TEA) sacrificial electron donor as well as a methanol co-solvent to aid miscibility with the aqueous phase.[28] The concentrations of the emulsion-derived samples were calculated assuming full conversion of the monomer into polymer. The emulsion-derived samples (8.3 mL) were added to equal parts TEA and methanol (16.7 mL), sonicated for 10 minutes and degassed by N_2 bubbling for 30 minutes before

illuminating with a 300 W Xe lamp fitted with either a $\lambda > 295$ nm or $\lambda > 420$ nm filter. The amount of hydrogen produced was measured by gas column chromatography at approximately hourly intervals. The concentration of photocatalyst can be highly influential to mass normalised hydrogen evolution rates[81] (as is discussed further below) and so the bulk materials were tested at the same concentration as their emulsion-derived analogues. In addition, to account for any surfactant effects, the bulk materials were tested in identical conditions to those used in the preparation of the emulsion-derived material; that is the appropriate mass of bulk polymer was dispersed in water / toluene (9:1), SDS (10 mg mL^{-1}) and K_2CO_3 (3.5 mg mL^{-1}). To this suspension (8.3 mL) was added equal parts TEA and methanol (16.7 mL) to give identical photolysis conditions to those used for emulsion-derived materials.

Table 2: Photocatalytic activity of the bulk and emulsion-derived materials.

Material	Polymer concentration (mg mL^{-1})	HER[a] $\lambda > 295$ nm (mmol h^{-1} g^{-1})	HER[a] $\lambda > 420$ nm (mmol h^{-1} g^{-1})
ME-CMP	0.06	1.72 ± 0.04	0.046 ± 0.002
ME-CMP-e	0.06	4.40 ± 0.25	0.052 ± 0.001
S-CMP1	0.07	5.92 ± 0.18	2.59 ± 0.07
S-CMP1-e	0.07	8.54 ± 0.11	1.84 ± 0.01
P10	0.1	9.54 ± 0.26	6.13 ± 0.22
P10-e	0.1	29.46 ± 0.38	14.52 ± 0.31

[a]Hydrogen evolution rate (HER) determined with catalyst in 25 mL aqueous/methanol/triethylamine 1:1:1 (aqueous phase containing water: toluene (9:1), SDS surfactant (10 mg mL^{-1}) and Na_2CO_3 (3.5 mg mL^{-1}) irradiated by 300 W Xe light source fitted with the specified band pass filter. HERs were determined from a linear regression fit over 5 hours and the error is given as the standard deviation of the amount of hydrogen evolved.

Under broadband illumination ($\lambda > 295$ nm), all emulsion-derived materials were more active than their bulk counterparts. **ME-CMP-e** was the least active with a hydrogen

evolution rate (HER) of 4.4 mmol h^{-1} g^{-1}, over twice that of the bulk material **ME-CMP** (1.72 mmol h^{-1} g^{-1}) under equivalent conditions. **S-CMP-e** was more active, producing hydrogen at a rate of 8.54 mmol h^{-1} g^{-1} however the improvement over the bulk material was smaller (44 %) in this case as the bulk material **S-CMP1** had a HER of 5.92 mmol h^{-1} g^{-1}. **P10-e** was the most active, with a HER of 29.46 mmol h^{-1} g^{-1} and was over three times as active as the bulk analogue **P10** (9.54 mmol h^{-1} g^{-1}).

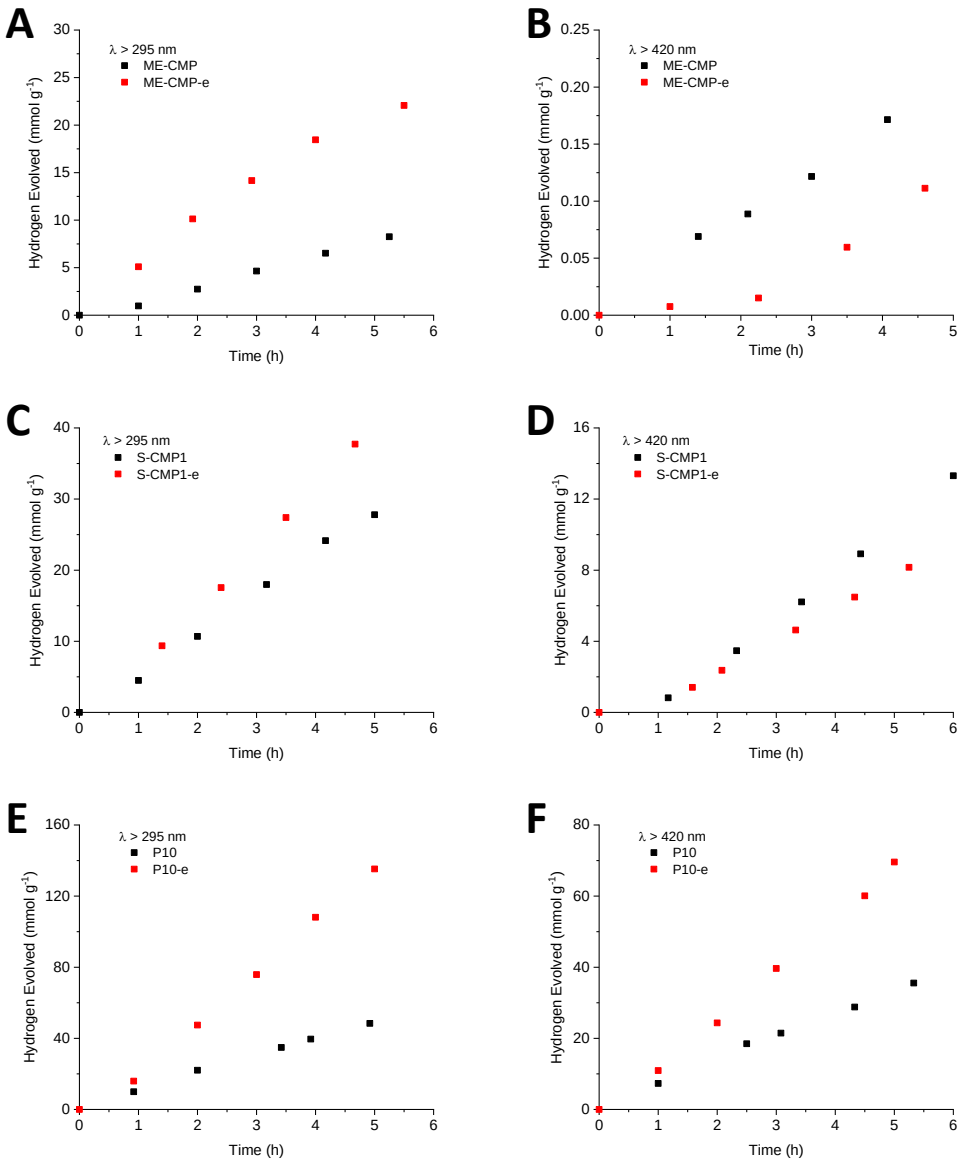

Figure 11: Hydrogen evolution of emulsion-derived and bulk materials over time in 25 mL aqueous/methanol/triethylamine (1:1:1) (aqueous phase containing water: toluene (9:1), SDS surfactant 10 mg mL^{-1} and Na_2CO_3 3.5 mg mL^{-1}). **ME-CMP** and **ME-CMP-e** (0.06 mg mL^{-1}) using λ > 295 nm (A) or λ > 420 nm (B), SCMP-1 and SCMP-1-e (0.07 mg mL^{-1}) using λ > 295 nm (C) or λ > 420 nm (D), **P10** and **P10-e** (0.1 mg mL^{-1}) using λ > 295 nm (E) or λ > 420 nm (F).

Using only visible light (λ > 420 nm filter) the photocatalytic behaviour was significantly different; neither **ME-CMP-e** and **ME-CMP** absorb visible wavelengths and this was reflected in very low hydrogen evolution rates of 0.052 mmol h^{-1} g^{-1} and 0.046 mmol h^{-1} g^{-1} respectively. **SCMP-1** has a more red-shifted light absorption onset and has a correspondingly greater HER of 2.59 mmol h^{-1} g^{-1} but under these conditions **SCMP-1-e** has lower activity than the bulk (1.84 mmol h^{-1} g^{-1}). It appears that any increase in active surface area in the emulsion-derived material in this instance, is outweighed by the blue shift in absorption onset and correspondingly smaller fraction of usable light. Again, **P10-e** was the most active material with a HER of 14.52 mmol h^{-1} g^{-1} and, importantly, retained a 2.4-fold increase compared to the bulk (6.13 mmol h^{-1} g^{-1}). It is probable that the smaller blueshift on moving from bulk to emulsion-derived material allows the increased surface areas to dominate.

2.2.2.2 Aggregation

It was noted that the turbidity of the emulsion-derived material dispersions increased when under the conditions described for photolysis and indeed post-photocatalytic DLS measurements indicated the presence of material with a hydrodynamic diameter of greater than a micrometre. Control experiments (Figure 12). revealed that aggregation is not a function of light irradiation but occurs within minutes of adding TEA and methanol to the emulsion-derived materials.

For example, the average particle size of a sample of **S-CMP1-e** increased from 180 nm to 1937 nm within 2 minutes of adding TEA and methanol to make up the (1:1:1) photolysis medium. It should be noted that this latter hydrodynamic radius is not precise as the sample contains particle sizes above the measurable range by DLS.[82] A similar result was found upon addition of methanol only or TEA only.

Addition of TEA and methanol to the nanoparticle mixtures also resulted in a slight red-shift of the UV-Vis absorption spectra of the emulsion derived particles (Appendix, Figure 12).

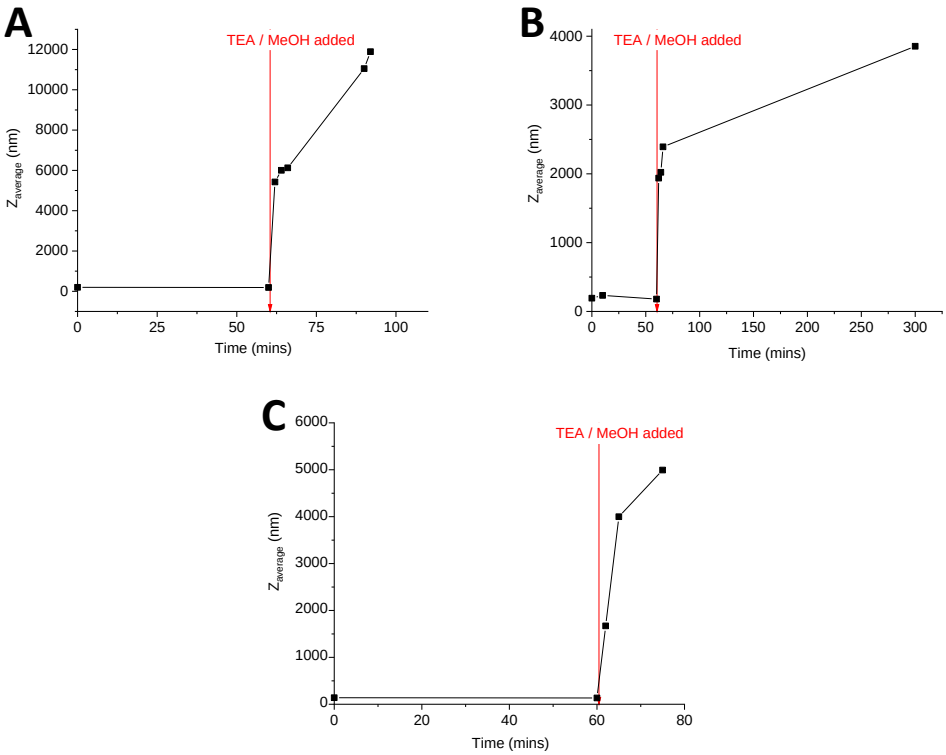

Figure 12: Aggregation of **ME-CMP-e** (A), **S-CMP1-e** (B) and **P10-e** (C) upon addition of TEA (1 mL) and methanol (1 mL) to the 'as synthesised' nanoparticle dispersions (1 mL). $Z_{average}$ (hydrodynamic radius) measured by DLS.

To enable more accurate measurement of larger particles, analysis on the aggregated materials was also carried out by static light scattering (SLS, see section 1.7). This also allowed comparison with the bulk materials. Although the emulsion-derived materials had aggregated in the photolysis medium, they were still smaller than the bulk materials under equivalent conditions; Bulk **ME-CMP** had particle sizes ranging from 2–100 µm while the aggregated **ME-CMP-e** particles were 1–40 µm. Perhaps more significantly, the surface area weighted Sauter mean diameter,[83] D[3,2] (Section 1.7), decreased from 16.6 µm for the bulk polymer to 7.94 µm for **ME-CMP-e** (Figure 13 and Table 3).

Table 3: Particle sizes of the bulk and emulsion-derived materials in the photolysis medium

Polymer	*D*[3,2][a,b] (μm)	Relative Surface Area[a,c] (m^2 kg^{-1})
ME-CMP	16.6	361
ME-CMP-e	7.94	756
S-CMP1	20.7	290
S-CMP1-e	3.69	1625
P10	2.06	2911
P10-e	0.37	16390

[a]Bulk and emulsion-derived particle sizes as measured by static light scattering under catalytic conditions; polymer dispersed in aqueous/methanol/triethylamine (1:1:1) (aqueous phase containing water: toluene (9:1), SDS surfactant 10 mg mL^{-1} and Na_2CO_3 3.5 mg mL^{-1}). [b]Sauter mean diameter (see Equation 1 in Chapter 1, Section1.7.2). [c] Relative surface area calculated from the total particle surface area divided by total particle mass assuming a density of 1 g cm^{-3}.

Likewise, bulk **S-CMP1** ranged from 1 μm to over 100 μm, with a D[3,2] of 20.7 μm, while the emulsion-derived particles, **S-CMP1-e**, had a maximum size of 20 μm with sub-micrometer material also present, giving a smaller D[3,2] of 3.69 mm (Figure 13 and Table 3). The **P10** materials gave more multi-modal SLS plots: both the bulk and the emulsion-derived materials had a large fraction of particles in the 1–20 μm range but the emulsion system showed a particularly significant nanoscale fraction ranging from 30 nm to 500 nm. This resulted in a lower D[3,2] value of 0.37 μm for **P10-e** compared to 2.06 μm for bulk **P10** (Figure 13 and Table 3). Table 1 also shows the relative surface areas of the different samples according to their particle distributions. This is not an absolute measure and is only valid for comparison between materials since the density of the materials has not been measured. The values stated are calculated assuming an arbitrary density of 1 g cm^{-1}.

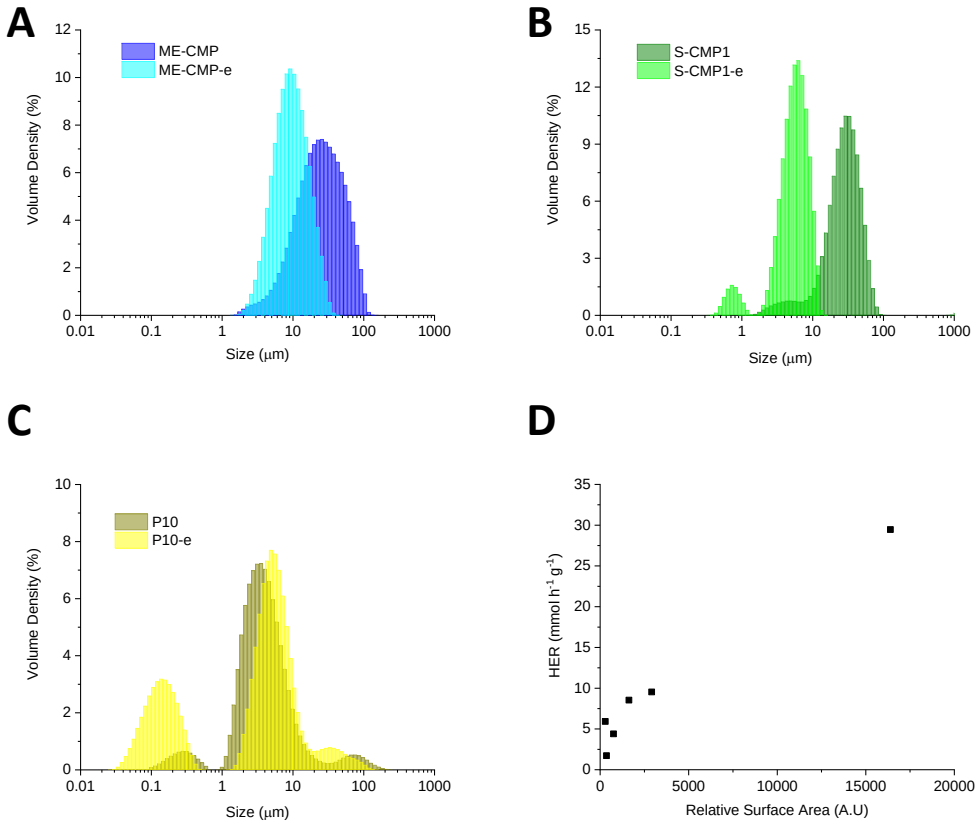

Figure 13: Particle size distributions of **ME-CMP** and **ME-CMP-e** (A), **S-CMP1** and **S-CMP1-e** (B), **P10** and **P10-e** (C) by static light scattering under catalytic conditions; polymer dispersed in aqueous/methanol/triethylamine 1:1:1 (aqueous phase containing water: toluene (9:1), SDS surfactant 10 mg mL^{-1} and Na_2CO_3 3.5 mg mL^{-1}). Plot of relative surface area as determined by SLS, against HER at $\lambda > 295$ nm for the different materials (D).

The aggregated particles were also analysed by SEM. Samples of **ME-CMP-e**, **S-CMP1-e** and **P10-e** collected from the photolysis mixtures contained a polydisperse mixture of particle sizes (Figure 14). All emulsion-derived materials showed microscale aggregates but smaller 'free' nanoparticles from 50 nm – 1 μm were also present in all three materials. These free nanoparticles were not observed in the SLS distributions of **ME-CMP-e** and (to a lesser extent) **S-CMP1-e** suggesting the limitations of SLS for such polydisperse materials (see section 1.7) and indicates that the relative surface areas of the emulsion-derived materials in Table 1 are likely to be underestimates compared to the bulk. Even allowing for this, we can still see a strong correlation between the measured surface areas and HER (Figure 13D); it seems that this factor, coupled with absorption onset, is crucial in determining photocatalytic activity in these systems.

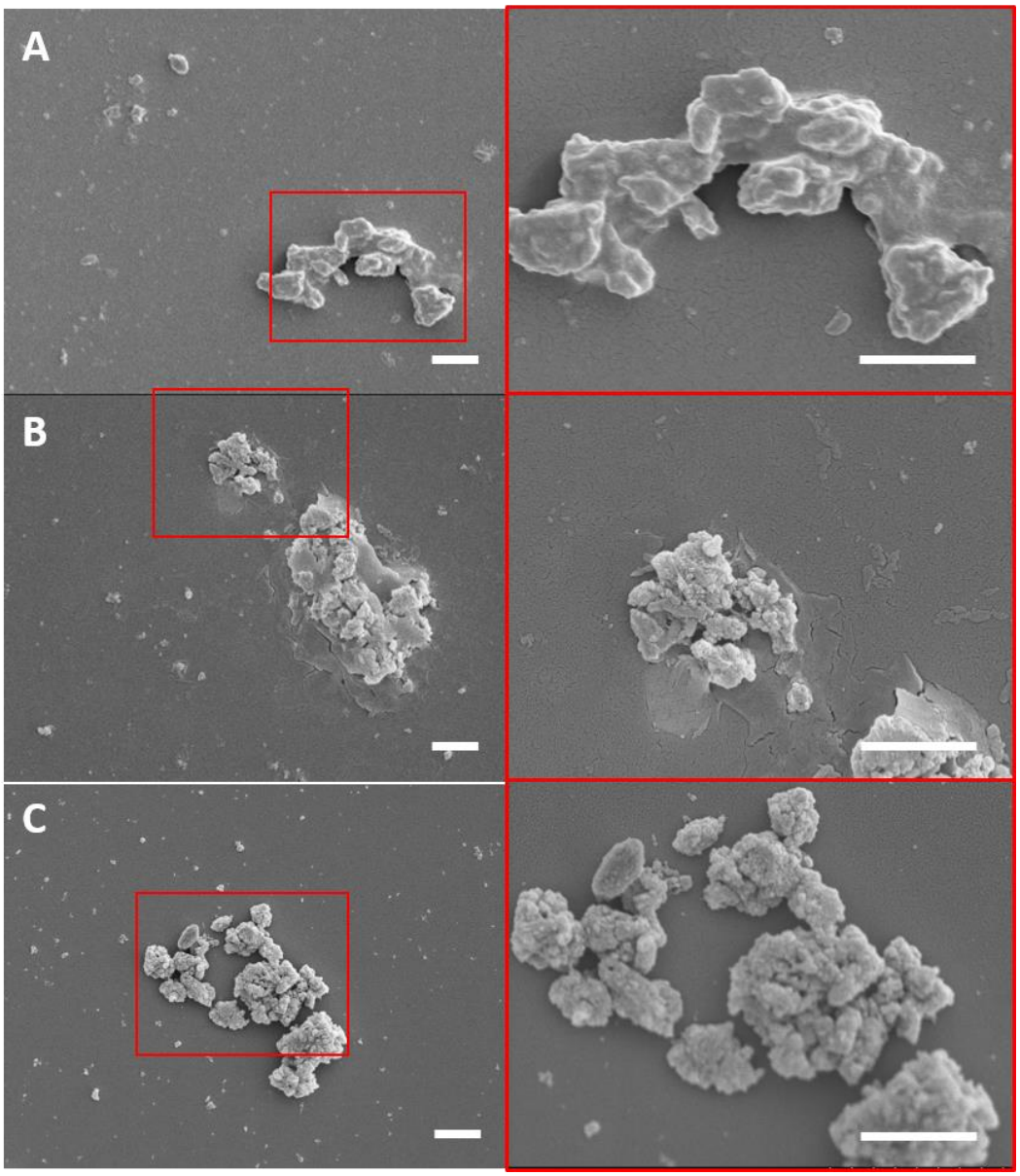

Figure 14: SEM images of **ME-CMP-e** (A), **S-CMP1-e** (B) and **P10-e** (C) collected from the photolysis mixture recorded at 3 keV. Scale bars are 1 µm.

2.2.2.3 Effect of concentration on mass normalised hydrogen evolution rates

Thus far, the concentration of the polymer used in photocatalytic testing was simply one third that of the emulsion polymerisation synthesis concentration. In order to compare the emulsion-derived material to other polymer nanoparticles used for photocatalytic hydrogen production in literature[19,20,23] **P10-e** was also tested at a concentration of 13 µg mL^{-1}. This led to a greatly increased mass normalised hydrogen evolution rate of 60 mmol h^{-1} g^{-1}, similar to the highest reported values for polymer nanodots in the literature. Comparing the actual amounts of hydrogen produced across the 13 µg mL^{-1} and the original 100 µg mL^{-1}

experiments (Figure 15), it is clear to see that the latter is within the saturated regime of catalyst concentration whereby increasing the amount of photocatalyst does not lead to a corresponding linear increase in hydrogen evolution rate. As argued by Kisch in 2010,[81] care must therefore be taken when comparing mass normalised hydrogen evolution rates as a small difference in the concentrations used for testing can lead to vastly different mass normalised rates. Although these mass normalised rates are interesting in understanding the inherent activity of a material, the field is arguably yet to reach a stage where amount of catalyst required is a limiting factor, rather than more immediate issues such as lifetime, low rates and the requirement for sacrificial agents. Given that we are yet to reach the 10% solar to hydrogen target discussed in Section 1.7, an arguably more practical measure might focus on the total amount of hydrogen produced by a system for a given number of incident photons. This is the basis of external quantum efficiencies.

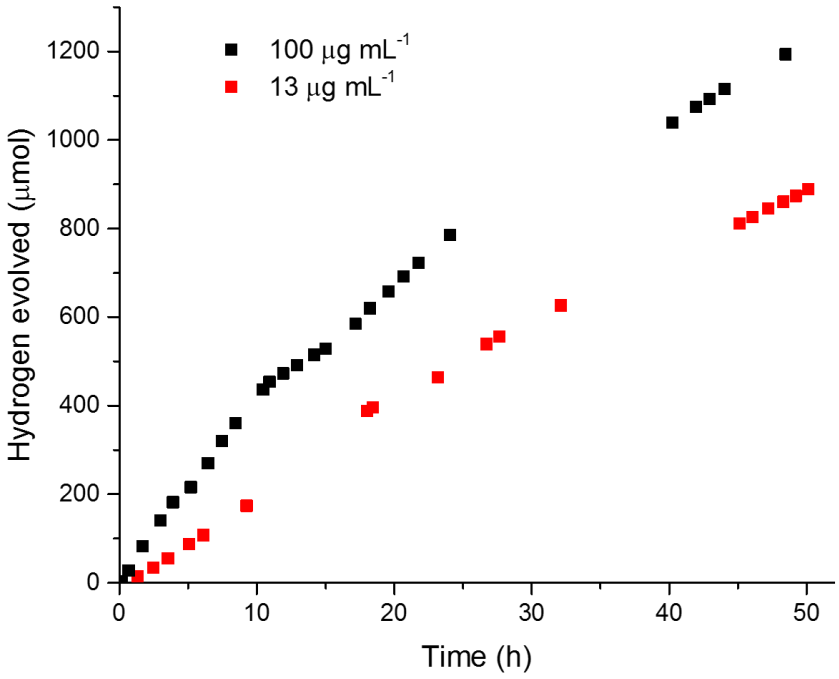

Figure 15: Hydrogen evolution of **P10-e** at different concentrations.

2.2.2.4 External Quantum Efficiency

External quantum efficiency (EQE) is defined in Chapter 1 Section 1.7.1 and represents the percentage of photons incident on a device that are absorbed by the semi-conductor catalyst and go on to successfully reduce a proton. Two such events are required to produce one

molecule of hydrogen. At a concentration of 0.1 mg mL^{-1}, using a pathlength of 1 cm, **P10-e** had an EQE at 420 nm of 5.8 ± 0.2%, over twice that of the bulk material under equivalent conditions (2.3 ± 0.1%). However, this was significantly lower than the maximum EQE for bulk **P10**, measured previously as 11.6%.[28] It was presumed this drop was due to the much lower ($^1/_{10}$) concentration of catalyst and therefore **P10-e** was also measured at a concentration of > 1 mg mL^{-1}. Under these conditions, **P10-e** had a similar activity to **P10**, with an EQE = 12.7%. It was noted, however, that the suspension of **P10-e** remained significantly more transparent than the bulk equivalent, potentially allowing a significant fraction of the light incident on the device to pass straight through. EQE does not take into account any light lost by transmission through the sample. **P10-e** was therefore also measured in cells with increased path lengths of 2 cm and 5 cm (previously 1 cm) to investigate the effect of reduced transmission. As expected, the EQE of **P10-e** increased with the path length of cell used (Table 4) such that a maximum EQE of 20.4 % was determined. This is amongst the highest EQE of any polymer photocatalyst[18] although significantly lower than the most active carbon nitride materials, which can reach greater than 50% efficiency.[84,85]

Table 4: External Quantum Efficiencies of **P10** and **P10-e** at 420 nm

Material	Concentration (mg mL^{-1})	Path Length (cm)	EQE[a] (%)
P10	0.1	1.0	2.3 ± 0.1
P10-e	0.1	1.0	5.8 ± 0.2
P10-e	0.1	2.0	10.5 ± 1.0
P10-e	0.1	5.0	14.2 ± 0.2
P10-e	> 1	1.0	12.7 ± 0.8
P10-e	> 1	5.0	20.4 ± 0.4

[a] Average EQE over a 5 hour experiment error given by the standard deviation.

2.2.3 Photocatalytic hydrogen production using alternative sacrificial electron donors

2.2.3.1 Particle size in different systems

If the emulsion-derived particles could be prevented from aggregating under photocatalytic conditions, it was thought that the resulting increase in surface area might lead to even higher hydrogen evolution rates. To explore this possibility, the particle sizes of the emulsion-derived materials was measured using a number of different sacrificial electron donors.

Triethanolamine (TeOA) has been used as sacrificial electron donor for many organic photocatalysts[86] and, unlike triethylamine, is fully miscible with water so can be utilised without a methanol co-solvent. The 'as synthesised' emulsion-derived materials (1 mL) added to a 10 vol.% TeOA solution (2 mL) were stable to aggregation. In fact, particle sizes reduced. This could be due to the 1/3 dilution, or the amphiphilic structure of TeOA could facilitate a surfactant-like effect, preventing flocculation. DLS indicated **ME-CMP-e** had a hydrodynamic diameter of 94 nm compared to 248 nm as synthesised. Similarly, **S-CMP1-e** reduced from 180 nm as synthesised to 88 nm in the TeOA solution. As previously, **P10-e** had the smallest particles; 59 nm (verses 156 nm as synthesised).

(L)-Ascorbic acid is also commonly used as a sacrificial electron donor[27,86] and the emulsion-derived materials (1 mL) added to a solution of ascorbic acid (2 mL, 0.1 M) appeared to be stable to aggregation. Particle sizes were similar to those 'as synthesised'; hydrodynamic diameters by DLS were 209, 226 and 160 nm for **ME-CMP-e**, **S-CMP1-e** and **P10-e** respectively (Figures 16).

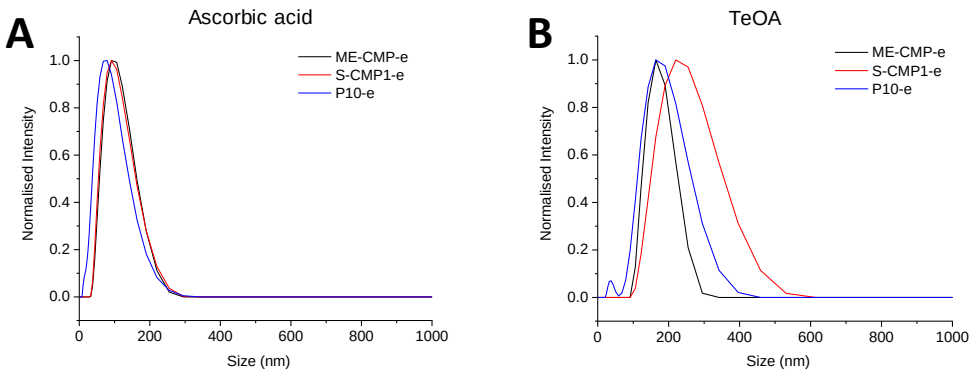

Figure 16: Distribution of particle sizes for the emulsion-derived materials by DLS in the presence of a TeOA (A) or ascorbic acid (B) sacrificial electron donor.

Table 5: Particle sizes of the emulsion-derived materials in various sacrificial electron donors.

Material	Size as synthesised[a] (nm)	Size in TeOA solution[b] (nm)	Size in ascorbic acid solution[c] (nm)
ME-CMP-e	248	94	209
S-CMP1-e	180	88	226
P10-e	180	59	160

[a]Hydrodynamic diameter (Z_{av}) from DLS of the emulsion-derived materials at the concentrations used for synthesis. [b]Hydrodynamic diameter (Z_{av}) from DLS of the emulsion-derived material (1 mL) added to 10 vol. % TeOA (2 mL). [c]Hydrodynamic diameter (Z_{av}) from DLS of the emulsion-derived material (1 mL) added to ascorbic acid solution (2 mL, 0.1 M).

2.2.3.2 Hydrogen evolution using ascorbic acid as an electron donor

The emulsion-derived materials were tested using an ascorbic acid donor, at the same polymer concentration as described in section 2.2.2.1 Table 2. The emulsion-derived samples (8.3 mL) were added to ascorbic acid solution (0.1 M, 16.7 mL), sonicated for 10 minutes and degassed by N_2 bubbling for 30 minutes before illuminating with a 300 W Xe lamp. **ME-CMP-e** and **S-CMP1-e** were tested using a $\lambda > 295$ nm filter and had HERs of 148 and 2662 µmol h^{-1} g^{-1} respectively. These values were similar to the bulk materials under equivalent conditions (218 and 1818 µmol h^{-1} g^{-1}) and considerably lower than the rates of the materials using a triethylamine donor (Table 2). **P10-e** was tested under visible light ($\lambda >$ 420 nm) and showed a hydrogen evolution rate of 2089 µmol h^{-1} g^{-1}, less than half that of the **P10** bulk under the same conditions. It appears that the reduced size of the emulsion-derived materials in this system does not lead to increased performance.

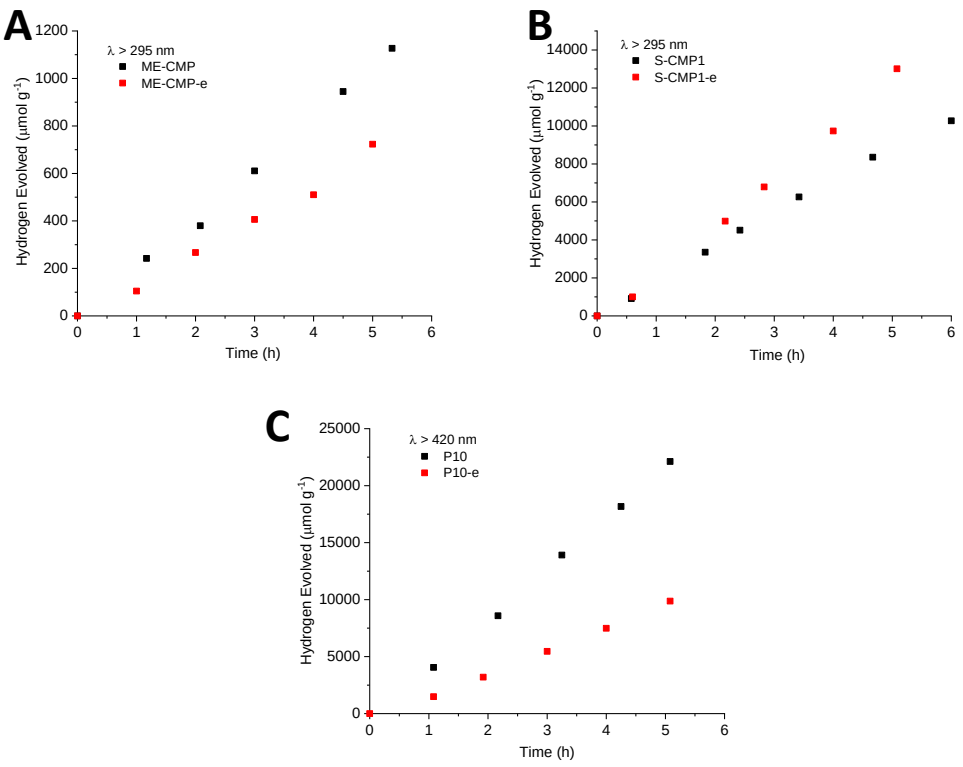

Figure 17: Hydrogen evolution of emulsion-derived and bulk materials over time in 25 mL, made up of 'synthesis liquor' (8.3 mL) added to ascorbic acid solution (16.7 mL, 0.1 M), '(synthesis liquor' containing water: toluene (9:1), SDS surfactant 10 mg mL^{-1} and Na_2CO_3 3.5 mg mL^{-1}). (A) **ME-CMP-e** and **ME-CMP** using λ > 295 nm. (B) **S-CMP1-e** and **S-CMP1** using λ > 295 nm. (C) **P10-e** and **P10** using λ > 420 nm.

2.2.3.3 Hydrogen evolution using a TeOA electron donor

The polymer photocatalysts were tested using a triethylamine sacrificial electron donor; the as synthesised suspensions (8.3 mL) were added to triethanolamine solution (16.7 mL, 10 vol. %) sonicated for 10 minutes and degassed by N_2 bubbling for 30 minutes before illuminating with a 300 W Xe lamp. **ME-CMP-e** and **S-CMP1-e** were again tested using a λ > 295 nm filter, whilst **P10-e** was tested using only visible light (λ > 420 nm). Under these conditions, the emulsion-derived materials performed much worse than their bulk analogues with HERs of 34, 102 and 501 μmol h^{-1} g^{-1} compared to 82, 3583 and 6832 μmol h^{-1} g^{-1} for the corresponding bulk polymers. This was despite the significantly smaller particle sizes of the emulsion-derived materials in this system.

Based on these results, it appears that the relationship between particle size and overall photocatalytic rate is complex and not solely determined by surface area. This indicates that reducing particle size indefinitely may not increase activity and that other factors such as light transmission and light scattering need to be considered.

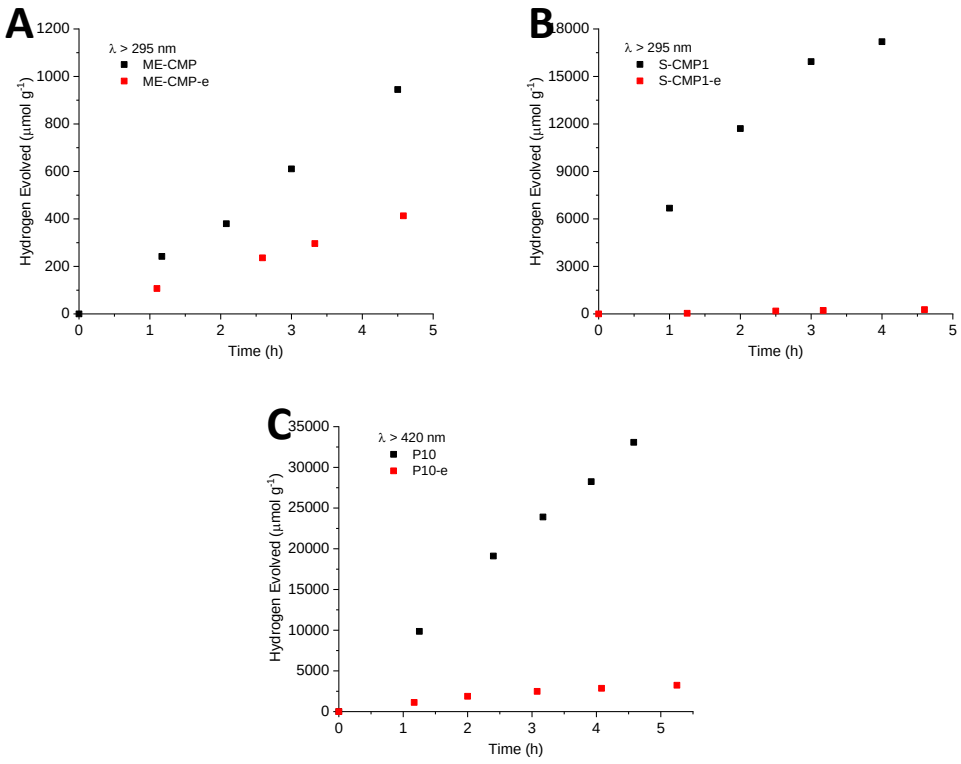

Figure 18: Hydrogen evolution of emulsion-derived and bulk materials over time in 25 mL, made up of 'synthesis liquor' (8.3 mL) added to triethanolamine solution (16.7 mL, 10. vol %), '(synthesis liquor' containing water: toluene (9:1), SDS surfactant 10 mg mL^{-1} and Na_2CO_3 3.5 mg mL^{-1}). (A) **ME-CMP-e** and **ME-CMP** using λ > 295 nm. (B) **S-CMP1-e** and **S-CMP1** using λ > 295 nm. (C) **P10-e** and **P10** using λ > 420 nm.

Table 6: Photocatalytic activity of the bulk and emulsion-derived materials using alternative donors

Material	Polymer concentration (mg mL^{-1})	HER Ascrobic Acid donor[a] (mmol h^{-1} g^{-1})	HER Triethanolamine donor[b] (mmol h^{-1} g^{-1})
ME-CMP	0.06	0.22 ± 0.01 [c]	0.082 ± 0.003 [c]
ME-CMP-e	0.06	0.15 ± 0.01 [c]	0.034 ± 0.003 [c]
S-CMP1	0.07	1.82 ± 0.04 [c]	3.58 ± 0.62 [c]
S-CMP1-e	0.07	2.66 ± 0.05 [c]	0.10 ± 0.02 [c]
P10	0.1	4.53 ± 0.07 [d]	6.83 ± 0.26 [d]
P10-e	0.1	2.09 ± 0.02 [d]	0.50 ± 0.06 [d]

[a]Hydrogen evolution rate (HER) determined with suspension (25 mL), made up of emulsion-derived material (8.3 mL) added to ascorbic acid solution (16.7 mL, 0.1 M), or [b] Hydrogen evolution rate (HER) determined with suspension (25 mL), made up of emulsion-derived material (8.3 mL) added to triethanolamine solution (16.7 mL, 10 vol. %), irradiated by 300 W Xe light source. [c] $\lambda > 295$ nm filter. [d] $\lambda > 420$ nm filter.

2.2.4 Aggregation and solvent effects

Across the previous experiments, the most successful photocatalytic system was a mixture of free nanoparticles and aggregated material; the emulsion-derived **P10-e** added to a 1:1 mixture of TEA and methanol. It has been shown previously that an induction period with an accompanying degree of aggregation was required for photocatalysis in nanoparticle systems[19] albeit over much smaller particle sizes than described here. It is therefore possible that the aggregates in the TEA / methanol system are crucial to improved evolution rate, possibly due to light scattering effects;[87] that is, reflection within the polymer suspension leads to greater catalytically productive capture of light, rather than unproductive transmission.

2.2.4.1 Salt induced aggregation

Increasing the concentration of ions of water is known to induce aggregation in some nanoparticle systems.[88] An attempt was therefore made to induce aggregation in the, otherwise stable, TeOA donor system by adding sodium chloride. Visible aggregation occurred within 30 minutes upon addition of 1 g of sodium chloride to 25 mL of the TeOA donor system (as described in section 2.2.4.3). Before salt addition, the average **P10-e** hydrodynamic radius was measured as 59 nm by DLS. The particle size of the mixture was too large for analysis by DLS, but SLS measurement indicated an average particle size of 4 μm (Figure 19).

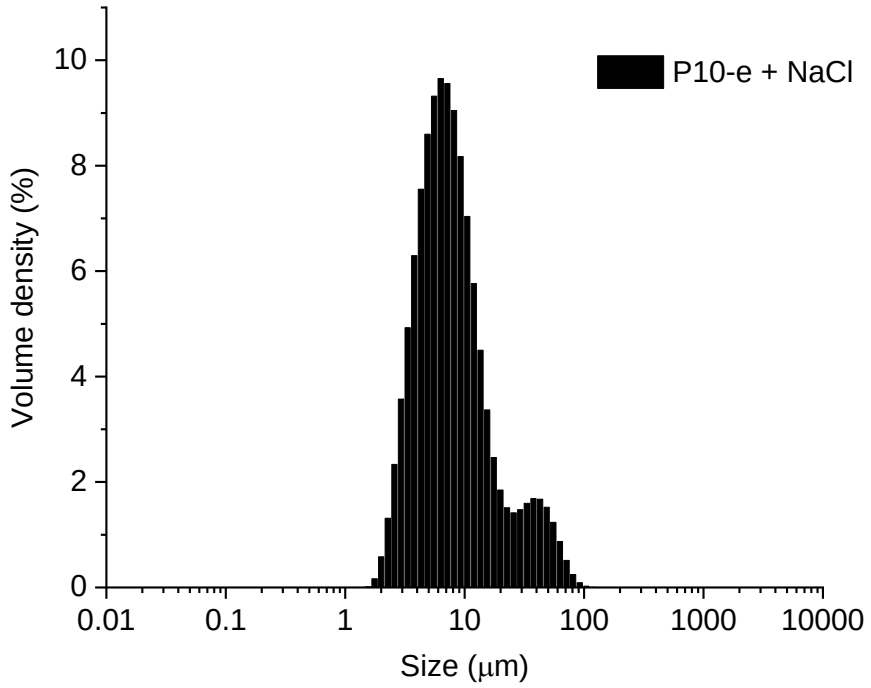

Figure 19: Particle size distribution of **P10-e** in the TeOA donor system (Section 2.2.3.3) after the addition of NaCl (40 mg mL^{-1}) by static light scattering.

The hydrogen evolution rate of the system with salt added was found to increase to 1223 μmol h^{-1} g^{-1}; that is, more than twice that of the un-aggregated system (Figure 20A). The ionic content of water has also been shown to influence the photocatalytic activity of some carbon nitride systems, possibly due to interaction between photogenerated electrons and ions.[89] However, a control reaction of bulk **P10** under the same conditions showed minimal variation with and without salt added (Figure 20B). This suggests that the

difference in activity between **P10-e** with and without salt is indeed an aggregation effect, rather than stemming from the medium conductivity.

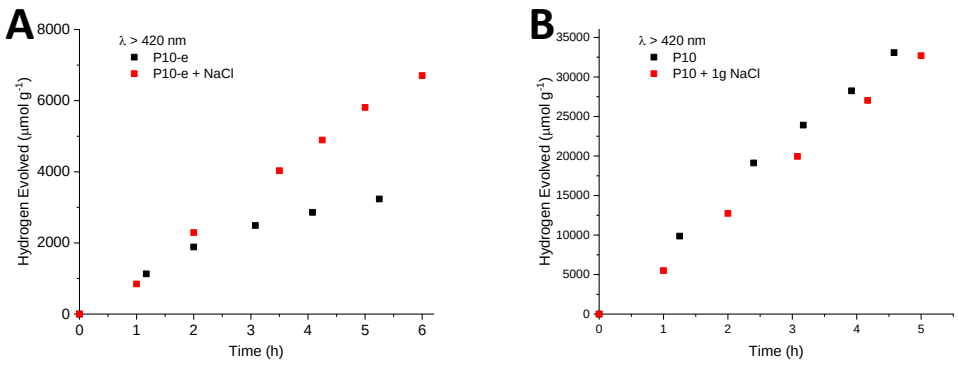

Figure 20: Hydrogen evolution of **P10-e** (A) and **P10** (B), with and without the addition of NaCl (40 mg mL^{-1}).

2.2.4.2 Removal of toluene

In relating particle size to active area of a photocatalyst, it is often assumed or left implicit that there is perfect contact between the polymer and the water or sacrificial electron donor. Dibenzothiophene sulfone-bearing polymers, such as **P10**, are among the most widely studied materials for hydrogen evolution[5,27,28,90] and it has been suggested that the hydrophilicity of this monomer is particularly important for its generally high activity.[28] However, in a two-phase toluene in water system, these polymers may still show a strong affinity for the oil phase. In principle, residual toluene could therefore be limiting proton reduction in the TeOA system by coating the polymer photocatalyst and inhibiting interaction with the aqueous phase. The amphiphilic structure of TeOA may exacerbate this effect by stabilising a two-phase system. This would not be an issue in the TEA system due to the addition of large amounts of miscibilising methanol. To investigate this effect, a sample of **P10-e** was treated by high speed centrifugation several times to remove all residual toluene. When redispersed in 10 vol.% TeOA by sonication, these particles showed a very similar size to 'as synthesised' (66 nm vs 59 nm Figure 21A). This sample was then tested for hydrogen evolution in the TeOA system and activity was found to increase 13-fold

from 0.5 to 6.9 mmol h^{-1} g^{-1}. This was, however, still less than half the rate of the TEA/MeOH based system.

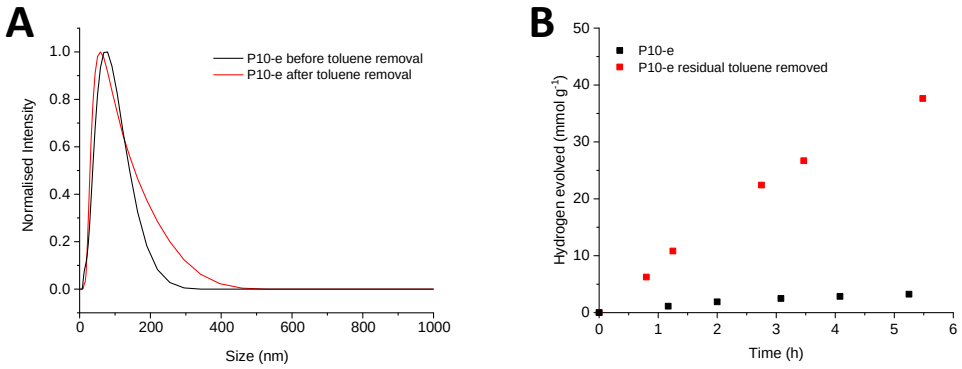

Figure 21: (A) Particle size distribution and (B) Hydrogen evolution of **P10-e** before (black) and after (red) full removal of toluene.

2.2.4.3 Deposition onto silica

Although the improvement upon toluene removal is significant, the rate of **P10-e** is still very similar to that of the bulk, despite its vastly reduced particle size, and is significantly lower than the TEA system. To better mimic the aggregated material in the high-performing TEA system, a sample of toluene-free **P10-e** was deposited onto silica colloids. Elemental analysis of this material indicated 33% **P10-e** by mass and analysis by SLS showed a highly polydisperse sample with particle sizes from 300 nm to 200 µm (Figure 22A). Photocatalytic testing in the TeOA system showed an increased HER of 9.0 mmol h^{-1} g^{-1} (normalised to the mass of the polymer) indicating that larger particle sizes may be beneficial for light capture which in this case seems to outweigh any decrease in particle size (Figure 22B). A control reaction of silica colloids in the TeOA system produced no hydrogen upon irradiation. Given that silica is an insulator, we suggest that this effect stems from light scattering by the silica colloids, suggesting strategies where inert, scattering colloids might be used to enhance the HER of colloidal catalysts for water splitting.

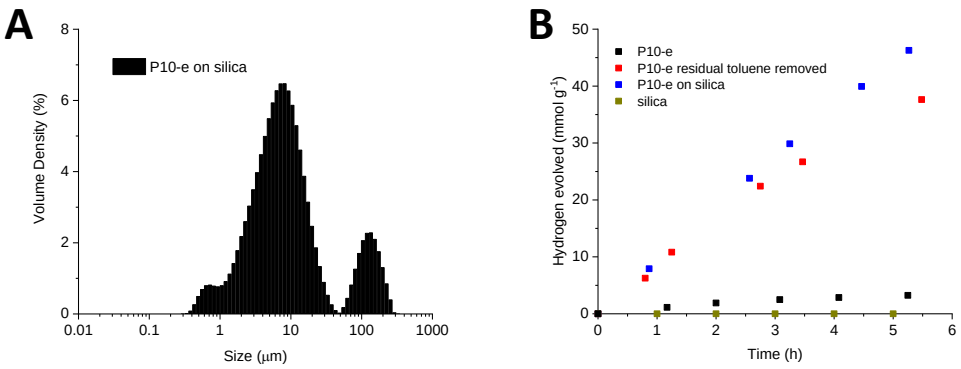

Figure 22: Particle size distribution by SLS (A) and hydrogen evolution (B) of **P10-e** deposited onto silica colloids.

2.3 Conclusions

In summary, the work in this chapter suggests that reducing particle size is an effective way of increasing the photocatalytic activity of polymer particles, at least up to a point. Mini-emulsion polymerisation was shown to be an effective method of synthesising small particle analogues of otherwise unprocessable, insoluble bulk polymers but there were some drawbacks to using this method; Polymerisation appeared to be inhibited by the mini-emulsion conditions, resulting in materials with shorter chain lengths and correspondingly blue shifted absorption profiles. This appeared to be particularly significant in CMP materials where the reduced light absorption of **ME-CMP-e** and **S-CMP1-e** led to reduced hydrogen evolution rates under visible light compared to the bulk materials. This was in contrast to HERs for these materials when including UV light ($\lambda > 295$ nm), where they outperformed the bulk materials—presumably because, under these conditions, the increased surface area of the emulsion-derived materials outweighs their inferior absorption characteristics. The polymerisation of the linear material, **P10**, seemed to be less affected by the emulsion conditions with only a small blue-shift in absorption onset from the bulk material. Whether this is due to **P10-e** reaching higher molecular weights than the CMPs or whether the absorption profile of **P10** is more similar to its shorter chain length analogues is currently unknown,although this point is explored further in Chapter 3. In either case, it appears that mini-emulsion polymerisation may be better suited for the synthesis of organic photocatalysts that contain visible light absorbing chromophores. This could reduce the reliance on high polycondensation yields to give sufficiently red-shifted absorption spectra.

Perhaps unsurprisingly, it was found that interactions between the polymer and water or polymer and scavenger are particularly important for catalytic activity and that the residual toluene from the emulsion synthesis could inhibit hydrogen production. Whilst this could be avoided by the careful removal of toluene through repeated centrifugation, it highlights the potentially detrimental effect of hydrophobic groups or molecules that could 'coat' photocatalysts or otherwise render them more hydrophobic, inhibiting contact with water. This suggests great care should be taken when modifying materials with, for example, alkyl chains to improve solubility, that improvements in processability do not come at the cost of wettability. Similarly, the selection of components for more complex systems involving dye sensitisation or redox shuttles should consider these colloidal interactions.

Interestingly, studies of photocatalysts in different scavenger systems found that the relationship between decreased particle size and increased hydrogen production rate was not a simple linear correlation. Whilst increased surface area was in general beneficial, the most active system studied here contained a highly polydisperse mixture of large, micron-sized aggregates and 'free' nanoparticulate material. The reason for this is not clear but may in part be due to light scattering effects. Scattering layers have been widely employed in solar cells to increase the proportion of light that interacts with a photoactive layer.[87] In these materials, particles with sizes equivalent to the wavelength of light scatter incoming photons, reducing the fraction that pass through the device without being absorbed. It is possible the particle sizes of the emulsion-derived photocatalysts using a TeOA scavenger (*circa.* 60 nm for **P10-e**) are too small to provide optimal interaction with the $\lambda > 295$ nm irradiation, with a significant proportion of the light passing straight through the suspension. This would be consistent with the EQE measurements whereby increasing the path length of the measurement cell increased the hydrogen production efficiency for a given incident light. Maximising light absorption has been considered in photoelectrochemical cell design for many years, with the reduced exciton diffusion lengths of thin films, or nanoscale materials being balanced against optimal interaction with light.[91,92] It also possible that the presence of polydisperse aggregates provides some advantages in term of electronics. It has been claimed that a composite material of small and large particles of the same crystalline TiO_2 phase can take advantage of the differing band positioning in the bulk and nanoparticulate material to form a so called 'homojunction'.[93] This was thought to aid spatial charge separation and reduce recombination resulting in an increased hydrogen evolution rate of the composite material over the individual small and large components.

Nanoparticles can be used as a model system to investigate the relationship between structure and activity, but the high hydrogen evolution rates achieved here, and in other

systems, suggests that polymer nanoparticles also have the potential to be used in practical solar fuels applications. One issue with previous polymer nanoparticle systems is that of longevity; some of the most active materials in the literature based on mass-normalized HERs[20,22,23] have been shown to produce hydrogen for just 2–12 hours before significant or total loss of activity occurred. These are significantly shorter timescales than many bulk organic materials such as benzothiadiazole-bearing polymers,[38] most carbon nitride photocatalysts[26] or even many crystalline materials such as COFs.[27,45,94,95] The reason for the loss of nanoparticle activity has often not been explored but in some cases deactivation has been ascribed to aggregation.[19,20] Whilst aggregation occurs rapidly in the TEA/MeOH system, it did not seem to inhibit photocatalysis. Alternatively, chemical breakdown of the catalyst may occur: indeed, the difference in hydrogen production longevity between **ME-CMP-e**, **S-CMP1-e** and **P10-e** (see appendix Figure 23 and 24) does suggest that chemical differences may play a role in the photocatalysts' stability to irradiation or scavenging conditions. Clearly, the maximised active surface areas and small catalysts loadings of nanoparticle systems would be particularly affected by chemical instability but, at least in the case of **P10-e**, the timescale for photocatalytic activity is similar to that of **P10**. Its sustained hydrogen production over 50 hours shows that polymer nanoparticles can be as stable photocatalysts as bulk materials. It is perhaps significant that some of the short-lived examples in literature[19,20] use polymers that show limited stability (< 2 hours) even in the bulk. This suggests that carefully choosing the chemical structure of a photocatalyst may be the most important factor in determining catalyst longevity, rather than there being an inherent instability associated with nanoparticle-based systems.

Another potential issue with nanoparticle photocatalysts is concentration. Polymer nanoparticles are often tested at very low catalysts loadings. This, as discussed above, can lead to very high hydrogen evolutions rates when normalised to catalyst mass, but very little hydrogen actually being produced per unit area irradiated. **P10-e**, however, shows good activity when tested at higher concentrations meaning that very high optimised EQE values of 20.4% can be achieved.

2.4 Experimental

2.4.1 General Procedures

Nuclear Magnetic Resonance Spectroscopy

Solution state ^{1}H and $^{13}C\{^{1}H\}$ Nuclear magnetic resonance spectra were recorded at 400 and 75 MHz respectively using a Bruker Avance 400 NMR spectrometer.

Mass Spectrometry

High resolution mass spectrometry was performed on an Agilent Technologies 6530B accuratemass QTOF mixed ESI/APCI mass spectrometer (capillary voltage 4000 V, fragmentor 225 V) in positive-ion detection mode.

Thermogravimetric Analysis

Thermogravimetric analysis was performed on an EXSTAR6000 by heating samples at 10 °C min^{-1} under air in open platinum pans from room temperature to 800 °C.

Sorption Analysis

Surface areas were measured by nitrogen adsorption and desorption at 77.3 K. Powder samples were degassed offline at 110 °C for 15 hours under dynamic vacuum (10^{-5} bar) before analysis. Isotherms were measured using Micromeritics 2420 volumetric adsorption analyser. Surface areas were calculated in the relative pressure (P/P_0) range from 0.07 to 0.35 of the adsorption branch.

Inductively Coupled Plasma Mass Spectrometry

Palladium contents were determined by by ICP-MS using a Perkin Elmer ICP MS NexION 2000. Samples (5 mg) were digested in nitric acid (70 wt. %, 10 mL) using a Perkin Elmer Microwave Titan prior to analysis and diluted to a minimum volume of 50 mL. Instrument has 1 ppb (0.0000001 wt. %) baseline with respect to the digested sample solution, therefore 'useable' limit is 10 ppm (0.001 wt. %) with respect to the sample

Dynamic Light Scattering

Dynamic light scattering measurements were performed on a Malvern Zetasizer Nano Particle Sizer, at 25 °C, in aqueous solutions or with the addition of triethylamine (TEA), methanol (MeOH) or triethanolamine (TeOA) as described. Three measurements, each of 12 scans, were taken for each sample and the average calculated. A polymer refractive index of 1.59 and absorbance of 0.01 was used for all samples. Measurements in aqueous solution

were fitted using the Malvern 'Generic latex' standard operating procedure with solvent refractive index of 1.330 and viscosity 0.8872 cP. Measurements in Water/MeOH/TEA mixtures were fitted with a modified operating procedure with solvent refractive index of 1.337 and viscosity 1.646 cP. Measurements in a 10% TeOA mixture were fitted with a modified operating procedure with solvent refractive index 1.013 and viscosity of 1.347 cP.

Static Light Scattering

Static light scattering measurements were performed on a Malvern Mastersizer 3000 Particle Sizer, polymers were dispersed in water/methanol/triethylamine (1:1:1) mixture by 10 minutes of ultrasonication and the resultant suspensions were injected into a stirred Hydro SV quartz cell, containing more of the Water/MeOH/TEA mixture, to give a laser obscuration of 2 – 8%. Particle sizes were fitted according to Mie theory, using the Malvern 'General Purpose' analysis model, for non-spherical particles with fine powder mode turned on. A polymer refractive index of 1.59, polymer absorbance of 0.1 and solvent refractive index of 1.337 were used for fitting.

Scanning Electron Microscopy

Imaging of the polymer morphology was achieved on a Hitachi S4800 Cold Field Emission SEM, with secondary electron and backscatter detectors. SEM samples of the bulk were dropped as powder, whilst nanoparticles were dropped from aqueous dispersion onto conductive carbon, and coated with gold using a sputter coater. SEM images were recorded at 3 keV.

Fluorescence Spectroscopy

The fluorescence spectra of the oligomers were measured with a Shimadzu RF-5301PC fluorescence spectrometer at room temperature. Bulk samples were measured as powders in the solid state whilst the emulsion particles were measured as suspensions.

UV-Visible Absorption Spectroscopy

The UV-Visible diffuse reflectance spectra of bulk samples were measured as powders in the solid state and the absorption spectra of the emulsion particles were measured as suspensions at room temperature on a Shimadzu UV-2550 UV-Vis spectrometer. Absorption onset was measured from the intersection of a tangent to the steepest slope of the onset with a tangent to the scattering tail, as shown in Figure 23.

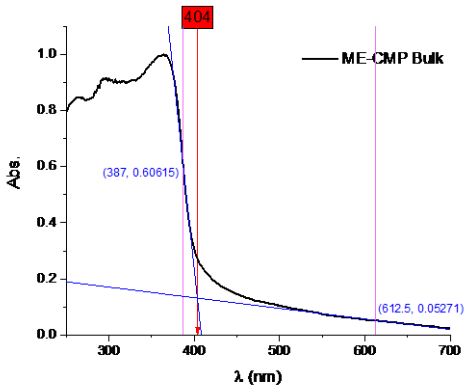

Figure 23: Measurement of absorption onset.

Hydrogen Evolution Experiments

Water for nanoparticle synthesis and hydrogen evolution experiments was purified using an ELGA LabWater system with a Purelab Option S filtration and ion exchange column (ρ = 15 MΩ cm) without pH level adjustment. A quartz flask was charged with the catalyst and dispersants as described and sealed with a septum. The resulting suspension was ultrasonicated until the photocatalyst was dispersed before degassing by N_2 bubbling for 30 minutes. For standard measurements, the reaction mixture was illuminated with a 300 W Newport Xe light-source (Model: 6258, Ozone free) for the time specified. The lamp was cooled by water circulating through a metal jacket. Gas samples were taken with a gas-tight syringe, and run on a Bruker 450-GC gas chromatograph equipped with a Molecular Sieve 13X 60-80 mesh 1.5 m × ⅛” × 2 mm ss column at 50 °C with an argon flow of 40.0 mL min-1. Hydrogen was detected with a thermal conductivity detector referencing against standard gas with a known concentration of hydrogen. Hydrogen dissolved in the reaction mixture was not measured and the pressure increase generated by the evolved hydrogen was neglected in the calculations.

External Quantum Efficiency

EQEs were measured using a 420 nm (± 10 nm, fwhm) LED. P10-e and dispersant were sonicated for 10 minutes. The mixture was transferred into a quartz cell, sealed with a septum and degassed for 30 minutes before illuminating with the LED. Light intensity was measured at the front of the cell using a ThorLabs probe and the hydrogen produced was measured as above. Efficiency was calculated as the incident photon to hydrogen conversion yield. Illuminated area was 8 cm and light intensity varied from 15-19 W m^{-2} between experiments.

2.4.2 Synthesis

All reagents were obtained from Sigma-Aldrich or Key Organics and used as received. Water for nanoparticle synthesis was purified using an ELGA LabWater system with a Purelab Option S filtration and ion exchange column (ρ = 15 MΩ cm) without pH level adjustment. Reactions were carried out under nitrogen atmosphere using standard Schlenk techniques.

3,7-Dibromodibenzo[b,d]thiophene sulfone

Dibenzo[*b,d*]thiophene sulfone (20.0 g, 92.5 mmol) in sulfuric acid (98%, 600 mL) was heated in a nitrogen purged flask to 70 °C. In the dark *N*-bromosuccinimide (35.6 g, 200 mmol) was added in several portions and the solution stirred for 24 h. The mixture was carefully added to water with cooling and then extracted with chloroform, washed with brine, dried with magnesium sulfate and filtered. After evaporation a mixture of 3,7-dibromodibenzo[*b,d*]thiophene sulfone and 3-bromodibenzo[*b,d*]thiophene sulfone was obtained. 3,7-dibromodibenzo[*b,d*]thiophene sulfone was isolated by crystallisation from chlorobenzene as a white powder (22.5 g, 60.2 mmol, 65%). ^{1}H NMR (400 MHz, $CDCl_3$): δ(ppm) = 7.94 (d, J 2.0 Hz, 2H), 7.78 (dd, J 7.5, 2.0 Hz, 2H), 7.64 (d, 7.5 Hz, 2H). ^{13}C {^{1}H} NMR (75 MHz, $CDCl_3$): δ(ppm) = 138.93 (quaternary), 137.14, 129.63 (quaternary), 125.62, 124.64 (quarternary), 122.94. Anal. Calcd for $C_{12}H_6Br_2O_2S$: C, 38.53; H, 1.62; S, 8.57 %; Found: C, 38.48; H, 1.71; S, 8.67 %. HR-MS Calcd for [$C_{12}H_6Br_2O_2S$ + Na]+: m/z = 394.8353, 396.8333, 398.8312; found: m/z = 394.8342, 396.8333, 398.8297.

3,7-Dibenzo[b,d]thiophene sulfone diboronic acid bis(pinacol) ester:

3,7-Dibromodibenzo[*b,d*]thiophene sulfone (935 mg, 2.5 mmol), bis(pinacolato)diboron (1.50 g, 5.9 mmol), potassium acetate (586 mg, 6.0 mmol) and [Pd(dppf)Cl_2] (27.4 mg, 0.038 mmol, 1.5 mol%) were added to a dried flask, dried under vacuum for 5 minutes and then purged with N_2. *N,N*-Dimethylformamide (25 mL) was added via syringe and the

solution was stirred under nitrogen at 90 °C overnight. The solution was added to water (100 mL) and the product extracted with ethyl acetate. The organic phase was washed with hydrochloric acid (1 M, 50 mL), dried with magnesium sulfate and filtered. After evaporation the crude product was recrystallised from acetonitrile to give light brown crystals of 3,7-dibenzo[*b,d*]thiophene sulfone diboronic acid bis(pinacol) ester (564 mg, 1.2 mmol, 48%).^{1}H NMR (400 MHz, $CDCl_3$): δ(ppm) = 8.28 (s, 2H), 8.05 (d, J 7.5 Hz, 2H), 7.80 (d, 2H), 1.36 (s, 24H). ^{13}C {^{1}H} NMR (75 MHz, $CDCl_3$): δ(ppm) = 140.07, 137.53 (quaternary), 133.78 (quaternary), 128.42, 121.07, 84.57, 24.88. Signals for carbons bonded to boron were not observed due to C-B coupling. Anal. Calcd for $C_{24}H_{30}B_2O_6S$: C, 61.57; H, 6.46; S, 6.85 %; Found: C, 61.58; H, 6.43; S, 6.75 %. HR-MS Calcd for [$C_{24}H_{30}B_2O_6S$ + Na]+: m/z = 491.1847; found: m/z = 491.1855.

Representative synthesis of mini-emulsion particles:

The monomers were dissolved in toluene (16 mL) and degassed by nitrogen bubbling for 30 minutes. An aqueous solution (144 mL) of sodium *n*-dodecyl sulfate (10 mg $mL^{-1)}$ and sodium carbonate (3.5 mg mL^{-1}) was degassed by nitrogen bubbling for 30 minutes. [$Pd(PPh_3)_4$] (5 mg, 6.83 µmol) was added to the organic phase followed by the aqueous solution. The mixture was sonified with a Branson 550 W digital sonifier at 40% power for 2 minutes. The emulsion was then degassed for a further 10 minutes before heating to 90 °C for 16 hours. The emulsion was filtered through paper (Whatman® general use) and the nanoparticles used as synthesised.

ME-CMP-e

Monomers: 1,3,5-phenyl triboronic acid tri(pinacol) ester (40.1 mg, 0.88 mmol) and 4,4'-dibromobiphenyl (41.2 mg, 0.132 mmol).

S-CMP1-e

Monomers: 1,3,5-phenyl triboronic acid tri(pinacol) ester (40.1 mg, 0.88 mmol) and 3,7-dibromodibenzo[b,d]thiophene sulfone (49.4 mg, 0.132 mmol).

P10-e

Monomers: 3,7-dibenzo[b,d]thiophene sulfone diboronic acid bis(pinacol) ester (51.5 mg. 0.11 mmol) and 3,7-dibromodibenzo[b,d]thiophene sulfone (41.2 mg, 0.11 mmol).

2.5 References

1 A. Bruno, L. X. Reynolds, C. Dyer-Smith, J. Nelson and S. A. Haque, *J. Phys. Chem. C*, 2013, **117**, 19832–19838.

2 J. E. Kroeze, * T. J. Savenije, and M. J. W. Vermeulen and J. M. Warman, *J. Phys. Chem. B*, 2003, **107**, 7696–7705.

3 P. E. Shaw, A. Ruseckas and I. D. W. Samuel, *Adv. Mater.*, 2008, **20**, 3516–3520.

4 S. Dimitrov, B. Schroeder, C. Nielsen, H. Bronstein, Z. Fei, I. McCulloch, M. Heeney and J. Durrant, *Polymers*, 2016, **8**, 14.

5 R. S. Sprick, Y. Bai, A. A. Y. Guilbert, M. Zbiri, C. M. Aitchison, L. Wilbraham, Y. Yan, D. J. Woods, M. A. Zwijnenburg and A. I. Cooper, *Chem. Mater.*, 2019, **31**, 305–313.

6 C. Yang, B. C. Ma, L. Zhang, S. Lin, S. Ghasimi, K. Landfester, K. A. I. Zhang and X. Wang, *Angew. Chemie Int. Ed.*, 2016, **55**, 9202–9206.

7 D. J. Woods, R. S. Sprick, C. L. Smith, A. J. Cowan and A. I. Cooper, *Adv. Energy Mater.*, 2017, **7**, 1700479.

8 Z. Hu, Z. Wang, X. Zhang, H. Tang, X. Liu, F. Huang and Y. Cao, *iScience*, 2019, **13**, 33–42.

9 D. J. Woods, S. Hillman, D. Pearce, L. Wilbraham, L. Flagg, W. Duffy, I. Mcculloch, J. Durrant, A. Guilbert, M. Zwijnenburg, R. S. Sprick, J. Nelson and A. Cooper, *Energy Environ. Sci.*, 2020, **13**, 1843-1855.

10 Y. Wu, X. Zhang, Y. Xing, Z. Hu, H. Tang, W. Luo, F. Huang and Y. Cao, 2020, **7**, 21.

11 M. U. M.Uda, *Jpn. J. Appl. Phys.*, 1985, **24**, 284.

12 R. J. Davis, M. T. Lloyd, S. R. Ferreira, M. J. Bruzek, S. E. Watkins, L. Lindell, P. Sehati, M. Fahlman, J. E. Anthony and J. W. P. Hsu, *J. Mater. Chem.*, 2011, **21**, 1721-1729 .

13 Y. Hashimoto, *Electr. Eng. Japan*, 2014, **188**, 9–17.

14 W. Zhang, J. Smith, R. Hamilton, M. Heeney, J. Kirkpatrick, K. Song, S. E. Watkins, T. Anthopoulos and I. Mcculloch, *J. Am. Chem. Soc*, 2009, **131**, 33.

15 J. F. Rubinson and Y. P. Kayinamura, *Chem. Soc. Rev.*, 2009, **38**, 3339–3347.

16 S. Tiwari and · N. C. Greenham, *Opt Quant Electron*, 2009, **41**, 69–89.

17 W. Huang, B. Chiyin Ma, D. Wang, Z. Jun Wang, R. Li, L. Wang, K. Landfester and K. A. I Zhang, *J. Mat. Chem. A.*, 2017, **5**, 3792-3797

18 Y. Wang, A. Vogel, M. Sachs, R. S. Sprick, L. Wilbraham, S. J. A. Moniz, R. Godin, M. A. Zwijnenburg, J. R. Durrant, A. I. Cooper and J. Tang, *Nat. Energy*, 2019, **4**, 746–760.

19 L. Wang, R. Fernández-Terán, L. Zhang, D. L. A. Fernandes, L. Tian, H. Chen and H. Tian, *Angew. Chemie - Int. Ed.*, 2016, **55**, 12306–12310.

20 P. B. Pati, G. Damas, L. Tian, D. L. A. Fernandes, L. Zhang, I. B. Pehlivan, T. Edvinsson, C. M. Araujo and H. Tian, *Energy Environ. Sci.*, 2017, **10**, 1372–1376.

21 A. Liu, C.-W. Tai, K. Rina Hoí and H. Tian, *J. Mater. Chem. A*, 2019, **7**, 4797-4803.

22 X. Zhang, F. Shen, Z. Hu, Y. Wu, H. Tang, J. Jia, X. Wang, F. Huang and Y. Cao, *ACS Sustain. Chem. Eng.*, 2019, **7**, 4128–4135.

23 P.-J. Tseng, C.-L. Chang, Y.-H. Chan, L.-Y. Ting, P.-Y. Chen, C.-H. Liao, M.-L. Tsai and H.-H. Chou, *ACS Catal.*, 2018, **8**, 7766–7772.

24 J. Kosco, M. Bidwell, H. Cha, T. Martin, C. T. Howells, M. Sachs, D. H. Anjum, S.

Gonzalez Lopez, L. Zou, A. Wadsworth, W. Zhang, L. Zhang, J. Tellam, R. Sougrat, F. Laquai, D. M. DeLongchamp, J. R. Durrant and I. McCulloch, *Nat. Mater.*, 2020, **19**, 559-565.

25 X. Wang, K. Maeda, A. Thomas, K. Takanabe, G. Xin, J. M. Carlsson, K. Domen and M. Antonietti, *Nat. Mater.*, 2009, **8**, 76–80.

26 J. Wen, J. Xie, X. Chen and X. Li, *Appl. Surf. Sci.*, 2017, **391**, 72–123.

27 X. Wang, L. Chen, S. Y. Chong, M. A. Little, Y. Wu, W.-H. Zhu, R. Clowes, Y. Yan, M. A. Zwijnenburg, R. S. Sprick and A. I. Cooper, *Nat. Chem.*, 2018, **10**, 1180–1189.

28 M. Sachs, R. S. Sprick, D. Pearce, S. A. J. Hillman, A. Monti, A. A. Y. Guilbert, N. J. Brownbill, S. Dimitrov, X. Shi, F. Blanc, M. A. Zwijnenburg, J. Nelson, J. R. Durrant and A. I. Cooper, *Nat. Commun.*, 2018, **9**, 4968.

29 Q. Cai, J. Shen, Y. Feng, Q. Shen and H. Yang, *J. Alloys Compd.*, 2015, **628**, 372–378.

30 C. B. Meier, R. S. Sprick, A. Monti, P. Guiglion, J.-S. M. Lee, M. A. Zwijnenburg and A. I. Cooper, *Polymer*, 2017, **126**, 283–290.

31 S. Yang, Y. Gong, J. Zhang, L. Zhan, L. Ma, Z. Fang, R. Vajtai, X. Wang and P. M. Ajayan, *Adv. Mater.*, 2013, **25**, 2452–2456.

32 L. Wang, Y. Wan, Y. Ding, Y. Niu, Y. Xiong, X. Wu and H. Xu, *Nanoscale*, 2017, **9**, 4090–4096.

33 I. Berlanga, R. Mas-Balleste and F. Zamora, *Chem. Commun*, 2012, **48**, 7976–7978.

34 D. N. Bunck and W. R. Dichtel, *J. Am. Chem. Soc.*, 2013, **135**, 14952–14955.

35 I. Berlanga, M. L. Ruiz-González, J. M. González-Calbet, J. L. G. Fierro, R. Mas-Ballesté and F. Zamora, *Small*, 2011, **7**, 1207–1211.

36 F. Goettmann, A. Fischer, M. Antonietti and A. Thomas, *Angew. Chemie - Int. Ed.*, 2006, **45**, 4467–4471.

37 X. Wang, K. Maeda, X. Chen, K. Takanabe, K. Domen, Y. Hou, X. Fu and M. Antonietti, *J. Am. Chem. Soc.*, 2009, **131**, 1680–1681.

38 K. Zhang, D. Kopetzki, P. H. Seeberger, M. Antonietti and F. Vilela, *Angew. Chemie - Int. Ed.*, 2013, **52**, 1432–1436.

39 W. Huang, Z. J. Wang, B. C. Ma, S. Ghasimi, D. Gehrig, E. Laquai, K. Landfester and K. A. I. Zhang, *J. Mater. Chem. A*, 2016, **4**, 7555-7559.

40 R. S. Sprick, J. X. Jiang, B. Bonillo, S. Ren, T. Ratvijitvech, P. Guiglion, M. A. Zwijnenburg, D. J. Adams and A. I. Cooper, *J. Am. Chem. Soc.*, 2015, **137**, 3265–3270.

41 J. Bi, W. Fang, L. Li, J. Wang, S. Liang, Y. He, M. Liu and L. Wu, *Macromol. Rapid Commun.*, 2015, **36**, 1799–1805.

42 M. G. Schwab, M. Hamburger, X. Feng, J. Shu, H. W. Spiess, X. Wang, M. Antonietti and K. Müllen, *Chem. Commun.*, 2010, **46**, 8932.

43 P. Pachfule, A. Acharjya, J. Roeser, T. Langenhahn, M. Schwarze, R. Schomäcker, A. Thomas and J. Schmidt, *J. Am. Chem. Soc.*, 2018, **140**, 1423–1427.

44 L. Stegbauer, K. Schwinghammer and B. V. Lotsch, *Chem. Sci.*, 2014, **5**, 2789–2793.

45 V. S. Vyas, F. Haase, L. Stegbauer, G. Savasci, F. Podjaski, C. Ochsenfeld and B. V. Lotsch, *Nat. Commun.*, 2015, **6**, 8508.

46 T. Banerjee, F. Haase, G. Savasci, K. Gottschling, C. Ochsenfeld and B. V. Lotsch, *J. Am. Chem. Soc.*, 2017, **139**, 16228–16234.

47 S. Karak, K. Dey, A. Torris, A. Halder, S. Bera, F. Kanheerampockil and R. Banerjee, *J. Am. Chem. Soc.*, 2019, **141**, 7572–7581.

48 K. Zhang, Z. Vobecka, K. Tauer, M.

Antonietti and F. Vilela, *Chem. Commun.*, 2013, **49**, 11158.

49 M. S. Silverstein, *Prog. Polym. Sci.*, 2014, 39, 199–234.

50 S. Slomkowski, J. V Alemán, R. G. Gilbert, M. Hess, K. Horie, R. G. Jones, P. Kubisa, I. Meisel, W. Mormann, S. Penczek and R. F. T. Stepto, *Pure Appl. Chem*, 2011, **83**, 2229–2259.

51 K. Landfester, *Angew. Chemie Int. Ed.*, 2009, **48**, 4488–4507.

52 A. Gharieh, S. Khoee and A. R. Mahdavian, *Adv. Colloid Interface Sci.*, 2019, **269**, 152–186.

53 C. Vauthier and K. Bouchemal, *Pharm. Res.*, 2009, **26**, 1025–1058.

54 L. Cabeza, R. Ortiz, J. L. Arias, J. Prados, M. A. R. Martínez, J. M. Entrena, R. Luque and C. Melguizo, *Int. J. Nanomedicine*, 2015, **10**, 1291–1306.

55 J. Duan, H. M. Mansour, Y. Zhang, X. Deng, Y. Chen, J. Wang, Y. Pan and J. Zhao, *Int. J. Pharm.*, 2012, **426**, 193–201.

56 P. Couvreur, B. Kante, M. Roland, P. Guiot, P. BAuduin and P. Speiser, *J. Pharm. Pharmacol.*, 1979, **31**, 331–332.

57 K. Alhareth, C. Vauthier, C. Gueutin, G. Ponchel and F. Moussa, *J. Appl. Polym. Sci.*, 2011, **119**, 816–822.

58 K. Chen, Y. Zhu, Y. Zhang, L. Li, Y. Lu and X. Guo, *Macromolecules*, 2011, **44**, 632–639.

59 C. Kaewsaneha, P. Tangboriboonrat, D. Polpanich, M. Eissa and A. Elaissari, *J. Polym. Sci. Part A Polym. Chem.*, 2013, **51**, 4779–4785.

60 K. Li and B. Liu, *J. Mater. Chem.*, 2012, **22**, 1257–1264.

61 A. R. Mahdavian and M. A. S. Mirrahimi, *Chem. Eng. J.*, 2010, **159**, 264–271.

62 M. Chen and M. Yin, *Prog. Polym. Sci.*, 2014, **39**, 365–395.

63 O. S. Wolfbeis, *Chem. Soc. Rev*, 2015, **44**, 4743.

64 K. Landfester, *Angew. Chemie - Int. Ed.*, 2009, **48**, 4488–4507.

65 C. Limouzin, A. Caviggia, F. Ganachaud and P. Hémery, *Macromolecules*, 2003, **36**, 667–674.

66 I. Bertholon-Rajot, D. Labarre and C. Vauthier, in *Polymer*, Elsevier BV, 2005, vol. 46, pp. 1407–1415.

67 K. Landfester, *Annu. Rev. Mater. Res*, 2006, **36**, 231–79.

68 J. Pecher and S. Mecking, *Macromolecules*, 2007, **40**, 7733–7735.

69 D. M. Lynn, S. Kanaoka and R. H. Grubbs, *J. Am. Chem. Soc.*, 1996, **118**, 784–789.

70 M. C. Baier, J. Huber and S. Mecking, *J. Am. Chem. Soc.*, 2009, **131**, 14267–14273.

71 K. Wu, J. Guo and C. Wang, *Chem. Commun.*, 2014, **50**, 695–697.

72 B. C. Ma, S. Ghasimi, K. Landfester, F. Vilela and K. A. I. Zhang, *J. Mater. Chem. A*, 2015, **3**, 16064–16071.

73 E. Hittinger, A. Kokil and C. Weder, *Angew. Chemie - Int. Ed.*, 2004, **43**, 1808–1811.

74 T. G. Mason, J. N. Wilking, K. Meleson, C. B. Chang and S. M. Graves, *J. Phys. Condens. Matter*, 2006, **18**, 635-666.

75 R. S. Sprick, B. Bonillo, M. Sachs, R. Clowes, J. R. Durrant, D. J. Adams and A. I. Cooper, *Chem. Commun.*, 2016, **52**, 10008–10011.

76 C. M. Aitchison, R. S. Sprick and A. I. Cooper, *J. Mater. Chem. A*, 2019, **7**, 2490–2496.

77 G. G. Badolato, F. Aguilar, H. P. Schuchmann, T. Sobisch and D. Lerche, in *Progress in Colloid and Polymer Science*, Springer, Berlin, Heidelberg, 2007, vol. 134, pp. 66–73.

78 L. Li, Z. Cai, Q. Wu, W.-Y. Lo, N. Zhang, L. X. Chen and L. Yu, *J. Am. Chem. Soc.*, 2016, **138**, 7681–7686.

79 J. Kosco, M. Sachs, R. Godin, M. Kirkus, L. Francas, M. Bidwell, M. Qureshi, D. Anjum, J. R. Durrant and I. McCulloch,

Adv. Energy Mater., 2018, **8**, 1802181.

80 R. Dawson, A. Laybourn, Y. Z. Khimyak, D. J. Adams and A. I. Cooper, *Macromolecules*, 2010, **43**, 8524-8530.

81 H. Kisch, *Angew. Chemie - Int. Ed.*, 2010, **49**, 9588–9589.

82 *A basic guide to particle characterization - Whitepaper*, Malvern Instruments Limited, 2015.

83 J. Sauter, *Die Grössenbestimmung der im Gemischnebel von Verbrennungskraftmaschinen vohrhandenen Brennstoffteilchen*, VDI-Verlag, 1926.

84 G. Zhang, G. Li, Z.-A. Lan, L. Lin, A. Savateev, T. Heil, S. Zafeiratos, X. Wang and M. Antonietti, *Angew. Chemie - Int. Ed.*, 2017, **56**, 13445-13449.

85 G. Zhang, L. Lin, G. Li, Y. Zhang, A. Savateev, S. Zafeiratos, X. Wang and M. Antonietti, *Angew. Chemie - Int. Ed.*, 2018, **57**, 9372–9376.

86 Y. Pellegrin and F. Odobel, *Comptes Rendus Chim.*, 2017, **20**, 283–295.

87 T. G. Deepak, G. S. Anjusree, S. Thomas, T. A. Arun, S. V. Nair and A. Sreekumaran Nair, *RSC Adv.*, 2014, **4**, 17615–17638.

88 F. Gambinossi, S. E. Mylon and J. K. Ferri, *Adv. Colloid Interface Sci.*, 2015, **222**, 332–349.

89 M. Schwarze, D. Stellmach, M. Schröder, K. Kailasam, R. Reske, A. Thomas and R. Schomäcker, *Phys. Chem. Chem. Phys.*, 2013, **15**, 3466–3472.

90 R. S. Sprick, B. Bonillo, R. Clowes, P. Guiglion, N. J. Brownbill, B. J. Slater, F. Blanc, M. A. Zwijnenburg, D. J. Adams and A. I. Cooper, *Angew. Chemie - Int. Ed.*, 2016, **55**, 1792–1796.

91 K. Itoh and M. Bockris, *J. Appl. Phys.*, 1984, **56**, 874.

92 A. Kay, I. Cesar and M. Grätzel, *J. Am. Chem. Soc.*, 2006, **128**, 15714-15721.

93 Y. Bai, Y. Zhou, J. Zhang, X. Chen, Y. Zhang, J. Liu, J. Wang, F. Wang, C. Chen, C. Li, R. Li and C. Li, *ACS Catal.*, 2019, **9**, 3242–3252.

94 B. P. Biswal, H. A. Vignolo-González, T. Banerjee, L. Grunenberg, G. Savasci, K. Gottschling, J. Nuss, C. Ochsenfeld and B. V. Lotsch, *J. Am. Chem. Soc.*, 2019, **141**, 11082-11092 .

95 P. Pachfule, A. Acharjya, J. Roeser, T. Langenhahn, M. Schwarze, R. Schomäcker, A. Thomas and J. Schmidt, *J. Am. Chem. Soc.*, 2018, **140**, 1423–1427.

Chapter 3: Well-defined Conjugated Oligomers for Photocatalytic Hydrogen Production

All materials in this chapter were synthesised by the author except for **PFP**, **PSP** and **MFM**, which were prepared by Dr Reiner Sebastien Sprick. All materials characterisation and testing was carried out by the author apart from single crystal X-ray diffraction, where the data was collected and structures solved by Dr Marc Little. Transient absorption measurements and analysis were carried out by Dr Michael Sachs (Imperial College London) and (TD)-DFT calculations were performed by Dr Liam Wilbraham and Dr Martijn Zwijnenburg (University College London).

3.1. Introduction

3.1.1 Oligomers for hydrogen production

The majority of organic materials investigated for hydrogen production are polymeric materials with extended covalent structures in either one dimension (linear polymers) or two dimensions (gC_3N_4, CMPs, CTFs and COFs). Much effort has been focused on optimising the degree of polymerisation of these materials, particularly gC_3N_4,[1] where it has been shown that materials with a higher degree of polymerisation have narrowed band gaps,[2,3] increased crystallinity[4,5] and improved charge transport properties.[6] Whilst highly condensed carbon nitrides with high C : N ratios have been shown to have some of the highest external quantum yields of any organic photocatalysts,[2,6–8] it is also frequently argued that decreasing the extent of polymerisation can be beneficial to photocatalysis[9] as this leads to an increase in the number of terminating 'defect' groups, which can improve hydrophilicity[10] or may act as the active site for catalysis.[11] Indeed, melamine derived low-molecular weight carbon nitride oligomers have been shown to be more active than their polymer analogues, which was ascribed to an increased number of chain terminating amine groups.[12] These two essentially contradictory approaches underscore the difficulty in designing materials of this type from first principles.

The high temperature conditions employed for carbon nitride synthesis means that it is difficult to control chain length, without also altering the prevalence of defects. The insoluble nature of the final materials also means that they are also difficult to characterise and, thus, the extent of the covalent network as well as the functional groups present are poorly defined. As well as unreacted amine groups, cynamide and oxygen bearing groups can form through thermal depolymerisation or reaction with precursor impurities or trace water during high temperature synthesis in air.[11] As such, limited conclusions can be drawn about the relationship between polymer chain length and photocatalytic activity for carbon nitrides, and this is essentially intrinsic to that chemistry. Conjugated polymers synthesised by lower temperature solution-based methods have reduced potential to form defect groups, although end groups may still persist. Like carbon nitrides, the resulting products are often also insoluble. Well-defined oligomeric materials, by contrast, offer a way of systematically investigating the effects of chain length on photocatalytic activity using materials that can be characterized at the atomistic level – sometimes, as here, by single-crystal X-ray diffraction.

Shortly after their initial investigations into poly(*p*-phenylene),[13] Yanagida *et al.* showed that analogous short chain oligomers (n = 2 – 6) were also (very modestly) active for proton reduction.[14] Despite the extensive use of solid-state single molecules and oligomers in organophotoredox reactions[15–19] and in organic photovoltaics,[20,21] studies into heterogeneous

oligomer photocatalysts for light-driven hydrogen evolution have been limited since this initial work. As for the aforementioned low-molecular weight carbon nitrides,[12] the covalent triazine bearing framework, CTF-1, Figure 1, was shown to be significantly less active than the related phenyl-triazine oligomers produced when its 1,4-dicyano precursor was condensed at a lower synthesis temperature.[22] The increased activity of the shorter chain lengths was again ascribed to the oligomers higher ratio of terminating (in this case) cyano groups, which resulted in a more hydrophilic dispersible material. It was also stated that increased overpotential for proton reduction and increased crystallinity could play a role. Overall, the differing end-group ratio between the oligomers and the polymer meant that it was difficult to deconvolute the effects of extending the materials conjugation length from the effect of altering the functional groups present. On the other hand, the HER of the oligomers (1076 µmol $h^{-1}g^{-1}$) was competitive with melon-type carbon nitrides under the same conditions (3. wt.% Pt, TeOA scavenger, AM 1.5G solar simulator, 380 mW cm^{-2}) and this does indicate that long chain lengths are not necessarily required for high photocatalytic activity.

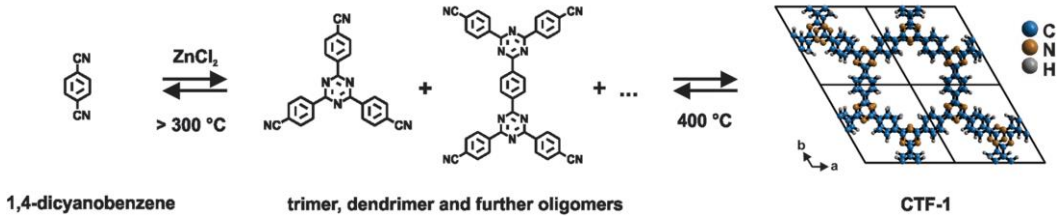

Figure 1: Reaction mechanism of CTF-1 starting from 1,4-dicyanobenzene, which leads to the formation of oligomers via trimerization and, ultimately, to an extended 2D CTF (right). The idealized crystal structure of fully condensed, crystalline CTF-1 is shown in an AA-type eclipsed configuration (viewed along the c-direction). *Reproduced, with permission from reference [22]. Published by the Royal Society of Chemistry.*

More recently, a series of organoborane / thiophene based oligomers was shown to be moderately active for hydrogen evolution.[23] These materials were synthesised *via* Stille polymerisation of difunctionalised monomers and thus their low molecular weights are a function of inefficient polymerisation rather than molecular design. Whilst not particularly active, these oligomers do show that with the correct choice of monomer units, chain lengths of between 5 – 8 repeat units are sufficient to generate materials with excellent visible light absorption up to 700 nm.

A different approach was adopted by Cao and co-workers who synthesised PorFN, a zinc-porphyrin based molecule with extended fluorene arms and quaternary amine salt substituents (Figure 2).[24] The latter enabled PorFN to be dissolved in water, and to form a

homogeneous photocatalytic system with low HER. However, upon addition of NaCl, the PorFN aggregates to form a highly-active heterogeneous photocatalyst. Although this material has a transition metal component, it does not appear that the zinc atom is an active centre for catalysis as its activity, as with nearly all organic photocatalysts, is dependent on the presence of a noble metal co-catalyst. This is thought to be the first example of a (primarily) organic molecular hydrogen-producing heterogeneous photocatalyst, and its very high HER of 10.9 mmol $h^{-1}g^{-1}$ (TeOA hole scavenger, AM 1.5G solar simulator, 100 mW cm^{-2}) demonstrates that such materials can be as active, if not more so, than polymers.

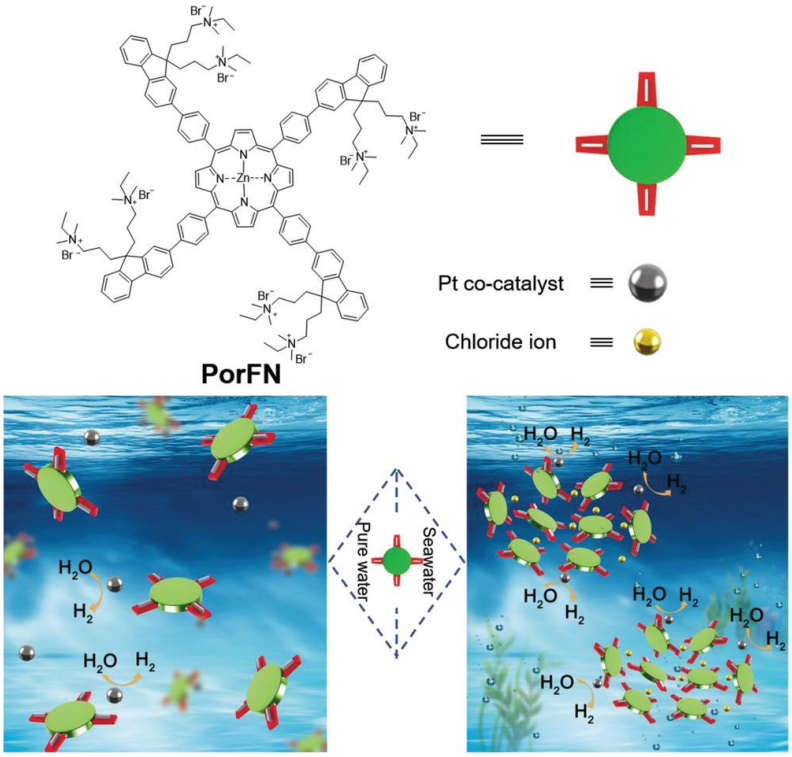

Figure 2: Chemical structure of PorFN and schematic of the proposed supramolecular structure. PorFN solvated in pure water that showed low photocatalytic activity and assembled in seawater leading to high activity *Reproduced with permission from reference [24].*

Aside from investigating the relationship between chain length and activity, a desirable property of many molecular and oligomeric materials is the ability to form single crystals. Increased crystallinity has been found to correlate with increased photocatalytic activity in many different organic systems including carbon nitrides,[1,4,6,25] CTFs[22,26] and COFs[27,28] possibly due to increased charge transport through more ordered structures.[29,30] Increases in catalytic activity are frequently observed upon moving from amorphous to semi-crystalline materials[28] and hence the ability to generate an entirely single-crystalline photocatalyst is particularly attractive.

As well as having a defined primary structure, crystalline materials possess secondary and tertiary arrangement of atoms in space, and these can be determined by X-ray diffraction. This is particularly useful because it enables investigation into how changing structural properties, such as molecular conformation and packing, effects photocatalytic activity. For example, Sprick *et. al*[31] and several others[32–34] have shown that polymers containing fused rings often have higher hydrogen evolution rates than non-planarised analogues. This is thought to be due to reduced twisting of the polymer backbone, which increases conjugation along the chain. However, as these are amorphous or semi-crystalline materials, confirming this is less simple. DFT calculations can be used to predict the lowest energy conformations of such polymeric materials[35,36] but predicting packing between chains is much more computationally expensive—and cannot by definition be definitive, since the experimental amorphous structure is unknown. By contrast, in single crystals of molecular or oligomeric materials these properties can be determined directly from a single crystal structure.

Fluorene and its 9,9´-alkylated analogues are cheap, easily processable monomeric units, that are included in many polymeric photocatalysts[31,34,37–39] and well as in polymers for various organic electronic applications.[40] The more polar, heteroatom-containing dibenzo[*b,d*]thiophene sulfone unit has been less widely studied for electronic applications but is a common emitter in thermally activated delayed fluorescence devices[41,42] and nuclear stains.[43] In addition, as discussed in section 1.4.3, dibenzo[*b,d*]thiophene sulfone based polymers have been repeatedly shown to be amongst the most active organic photocatalysts for hydrogen production.[28,35,38,44] This chapter investigates the effect of chain length on the properties of materials containing these two important units. The monomer, dimer and trimer of 9,9´-dimethyl fluorene (**MeF1-3**) and dibenzo[*b,d*]thiophene sulfone (**S1-3**) were synthesised and investigated as hydrogen producing photocatalysts. In addition, to test the impact of molecular conformation and packing more directly, a series of trimeric catalysts with either phenylene or mesitylene substituents on a fluorene or dibenzo[*b,d*]thiophene sulfone "core", **PFP**, **MFM**, **PSP** and **MSM** was also investigated.

3.2 Dimethyl Fluorene Oligomers

3.2.1 Synthesis and characterisation

The 9,9´-dimethylfluorene monomer, **MeF1**, was obtained commercially and used without further purification. The analogous dimer and trimer, **MeF2** and **MeF3**, were synthesised by Suzuki coupling, as shown in Scheme 1, followed by re-crystallisation in dichloromethane /

n-hexane. The structures of the three materials, obtained by single crystal X-ray diffraction (SCXRD) are shown in Figure 3 (see section 3.10.4 for full details).

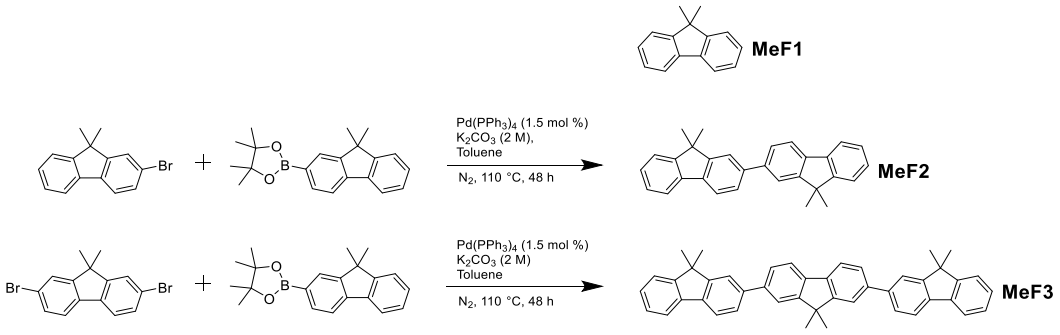

Scheme 1: Structures and synthesis of **MeF1-3.**

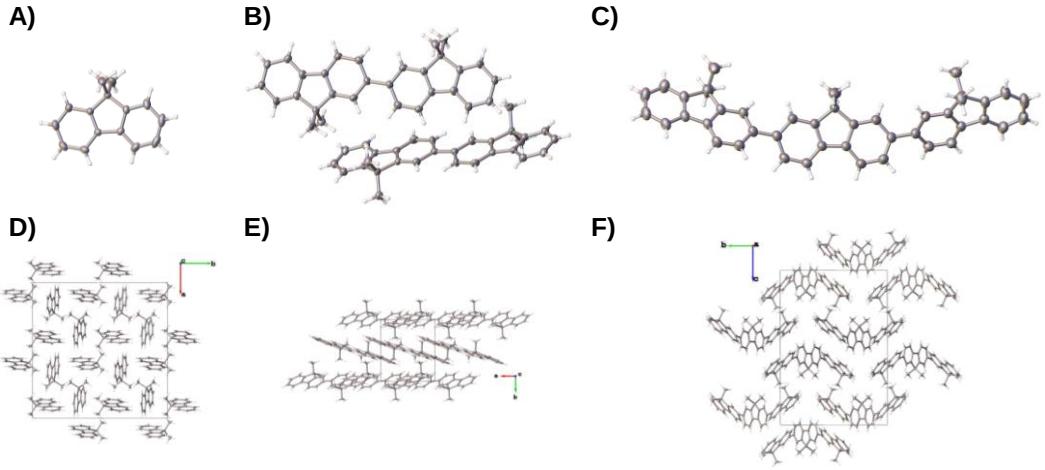

Figure 3: Molecular conformations and crystal packings of **MeF1** (A and D), **MeF2** (B and E) and **MeF3** (C and F) as determined by SCXRD.

Residual palladium in polymers from Suzuki coupling has been found to play a significant role in photocatalytic hydrogen production.[45,46] The palladium content of **MeF1**, **MeF2** and **MeF3** was therefore analysed by ICP-MS. Whilst **MeF1** had palladium levels below the detection limit of the instrument (> 10 ppm with respect to the oligomer, see section 2.4.1 for full details) **MeF2** and **MeF3** were found to contain 0.011 and 0.017 wt. % (110 and 170 ppm) palladium respectively. To allow for fair comparison between the monomer and longer oligomers a sample of **MeF1** was also loaded with 0.02 wt. % Pd by photodeposition of

$Pd(NH_3)_2Cl_4$. When analysed by ICP-MS, this sample was found to contain 0.016 wt. % palladium (160 ppm) similar to that of **MeF2** and **MeF3**

The size of the MeF oligomer particles was measured by SLS (Figure 4). Suspended in water, **MeF1** had particle sizes from 1 to 1000 µm with a Sauter mean diameter of 24.2 µm. **MeF2** had smaller particles from 1 to 300 µm with an average of 13.9 µm, whilst **MeF3** ranged from 1 to 500 µm but had the largest average at 33.4 µm.

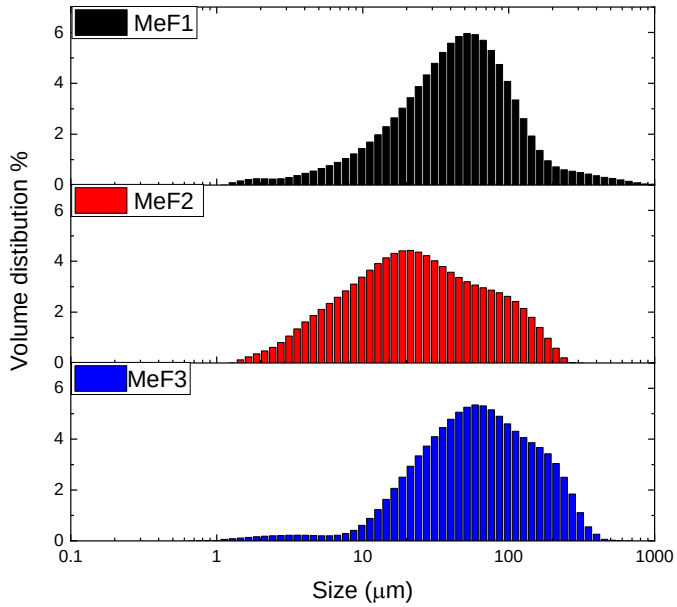

Figure 4: Particle size distributions, by static light scattering, of the **MeF** oligomers suspended in water.

3.2.2 Photophysical properties

The optical properties of the **MeF** oligomers were measured both in the solid state and in chloroform solution. A redshift in absorption spectra with chain length was observed in both states (Figure 5); by solid state DRS, **MeF1** had an absorption onset of 332 nm which increased to 405 nm for **MeF2** and 430 nm for **MeF3,** whilst in solution the absorption maxima redshifted from 269 to 330 to 355 nm on moving from **MeF1-3.** This is to be expected since increased conjugation length leads to contraction of the HOMO and LUMO**. MeF1,** unlike the longer oligomers, also showed weaker $\pi \rightarrow \pi^*$ bands at 291 and 307 nm thought to originate, as in fluorene, [47,48] from short-axis polarized and long-axis polarized states, respectively.

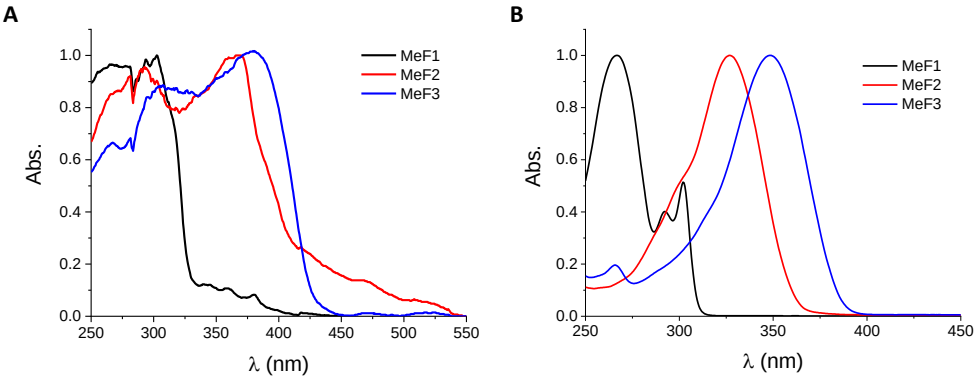

Figure 5: UV-Vis spectra of **MeF1-3** in (A) the solid state (DRS) and (B) in chloroform solution. All spectra are normalised.

The photoluminescent emission spectra of the materials also moved to higher wavelengths on moving from monomer to dimer to trimer, with emission maxima at 312, 363 and 394 nm in chloroform solution, although **MeF2** and **MeF3** both displayed multiple emission peaks. In the solid state, **MeF1-3** showed global emission maxima at 326 nm, 428 nm and 446 nm but all three materials showed three emission peaks, similar to the emission spectra of 9,9-dialklyated fluorene polymers.[49] In addition, **MeF1** showed an addition broad emission at 450 nm. Similar red-shifted emissions have been observed in annealed films of fluorene bearing co-polymers[49] and are thought to be due to excimer formation.

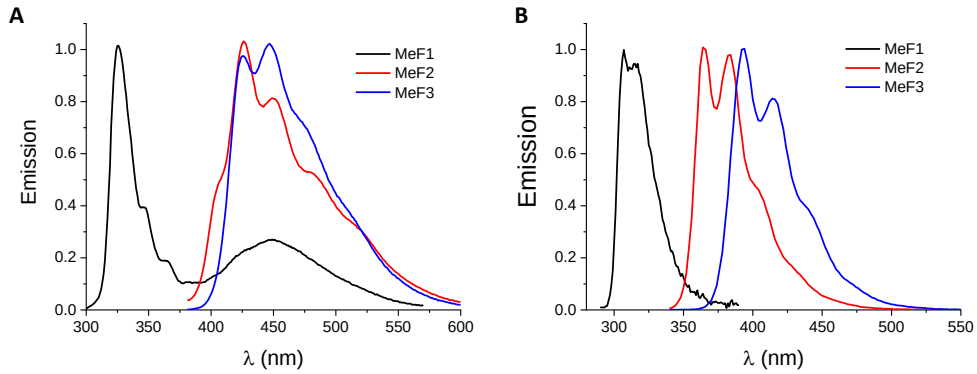

Figure 6: Photoluminescence emission spectra of **MeF1-3** in (A) the solid state and (B) in chloroform solution. Each material was excited at its absorption maxima as described in Table 1. All spectra are normalised.

Aside from the wavelengths of light that each photocatalyst can interact with, it is also important to look at the intensity of these interactions. The molar extinction coefficients and photoluminescence quantum yields (PLQY) (see Section 3.10.3 for full details) were thus

measured for each material in chloroform solution and calculated for each material's maximum absorption (Table 1).

MeF1 had the lowest molar extinction coefficient, ε_{Molar}, of 16,500 M^{-1} cm^{-1}, compared to 42,800 and 71,100 M^{-1} cm^{-1} for **MeF2** and **MeF3**. However, clearly the larger oligomers have increased number of aromatic units per mole and hence the mass extinction coefficient, ε_{Mass}, (Section 3.10.3) is perhaps a more useful comparison here. In this case, **MeF1** has an extinction coefficient of 85.2 cm^2 g^{-1}: closer to but still lower than **MeF2** (111 cm^2 g^{-1}) and **MeF3** (123 cm^2 g^{-1}). As well as the magnitude of light absorption at the maxima, for the purposes on photocatalytic testing, it is interesting to consider the amount of light absorbed across a range of wavelengths. In section 3.2.5, the oligomers are studied in for photocatalytic activity under homogeneous conditions. As such the average extinction coefficient across the 275 – 400 nm range of wavelengths used in that experiment were calculated to approximate the amount of light each material could absorb during photocatalysis (see section 3.10.3 for full details). The average extinction coefficient for **MeF1** from 275 – 400 nm was 9.6 cm^2 g^{-1} indicating the monomer has limited light absorption potential compared to the dimer and timer (44.5 and 54.5 cm^2 g^{-1}) across this range of wavelengths.

The efficiency of radiative emission also increased with chain length; **MeF1** has a photoluminescent quantum yield of 10 %, **MeF2** 94 % and **MeF3** 100 %.

Table 1: Optical properties of the **MeF** oligomers.

	MeF1	**MeF2**	**MeF3**
λ_{onset} solid-state[a] (nm)	332	405	430
λ_{max} chloroform (nm)	269, 307	330	355
λ_{em} solid-state (nm)	326	428	446
λ_{em} chloroform (nm)	312	363	394
ε_{Molar}[b] (M^{-1} cm^{-1})	16,500	42,800	71,100
ε_{Mass}[b] (cm^2 g^{-1})	85	111	123
Average ε_{Molar}[b,c] (M^{-1} cm^{-1})	1,860	17,200	31,500
Average ε_{Mass} [b,c] (cm^2 g^{-1})	9.6	44.5	54.5
Φ[b] (%)	10 ± 1	94 ± 3	100 ± 5

[a]From diffuse reflectance spectroscopy of solid powder. [b] See section 3.10.3 for full definitions and details of how Φ was measured. [c] λ = 275-400 nm

Whilst it is not clear whether emissive excited states are necessarily required for good photocatalysis or whether non-radiative states could also lead to proton reduction, water splitting and proton reduction photocatalysts are often highly photoluminescent.[39,50]

PLQY tells us only about those excitons that recombine radiatively, emitting a photon. Photocatalysis (and OPV) relies on the prevention of this, for example by using an electron donor, co-catalyst, or donor-acceptor structure to separate charges. The lifetime of excited states is thus thought to be crucial in allowing charges to be separated before recombination. Time-correlated single photon counting (TCSPC) was employed to probe the kinetics of the excited states of **MeF1-3**. In each case, the oligomers showed multi-exponent emission decays. Due to the complex solid-state emission spectra for these materials, lifetime was measured for several different emission wavelengths. For example, in the solid state, **MeF3** has emissions at 428nm and 450 nm which gave very short $\tau_{average}$ lifetimes of 0.78 and 1.07 ns respectively. The lifetime of **MeF2** across the same emissions was somewhat longer with $\tau_{average}$ lifetimes of 1.43 and 1.98 ns (Figure 7B). The emission of **MeF1** was measured at 326 and 350 nm and showed significantly longer average lifetimes of 2.87 and 7.15 ns. A sample of **MeF1** loaded with palladium (0.016 wt. %) to similar concentrations as the dimer and trimer showed significantly decreased lifetimes of 1.71 ns and 5.53 ns at 326 nm and 350 nm emissions (Figure 7A). In chloroform solution the lifetimes were shorter and less varied but the overall trend of decreasing lifetime with chain length was preserved, with average lifetimes of 1.15, 1.07 and 0.83 ns for **MeF1-3**.

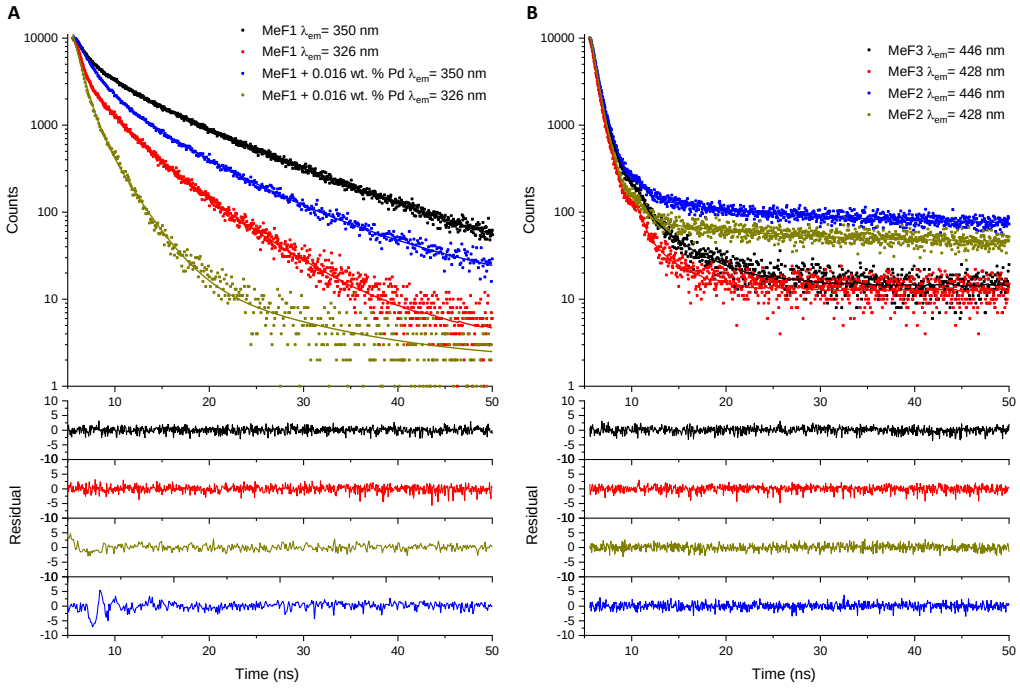

Figure 7: TCSPC spectra of **MeF1** (A), **MeF2** and **MeF3** (B) in the solid state. Data (points), fit (line) and residuals (bottom). Excited with a 295 nm (**MeF1**) or 375 nm (**MeF2** and **MeF3**) laser.

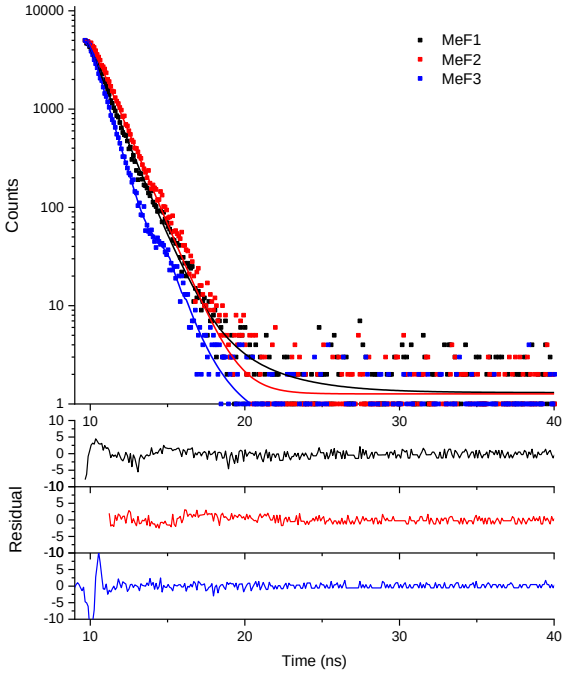

Figure 8: TCSPC spectra of **MeF1-3** in the chloroform solution. Data (points), fit (line) and residuals (bottom). **MeF1** and **MeF2** excited with a 295 nm laser. **MeF3** excited with a 375 nm laser.

3.2.3 Photocatalytic Hydrogen Production in Suspension

A summary of HERs for all photocatalytic testing in this chapter can be found in Section 3.10.6, Table 7. An equal parts mixture of triethylamine, methanol and water has been found to be an efficient sacrificial electron donor medium for hydrogen production.[51] The photocatalysts were therefore tested in this mixture first. The photocatalyst (25 mg) was suspended by sonication in the equal parts mixture of triethylamine, methanol and water (25 mL) in a quartz flask, degassed by nitrogen bubbling for 30 minutes before irradiation by a 300 W lamp. None of the oligomers has significant absorption in the visible light region so a $\lambda > 295$ nm filter was used. Pristine **MeF1** was tested, as well the **MeF1** sample loaded with Pd to approximately equivalent levels as **MeF2** and **MeF3** (see, section 3.2.1). The hydrogen evolution rate was found to increase with chain length; Pristine **MeF1** produced hydrogen at a rate of 5 µmol h^{-1} g^{-1} over the 5 hours testing period and **MeF1** with added Pd had a HER of 10 µmol h^{-1} g^{-1} whilst **MeF2** and **MeF3** had HERs of 13 and 37 µmol h^{-1} g^{-1} (Figure 9A, C and E). This overall trend was preserved upon moving to solely UV light ($275 < \lambda <$ 400 nm filter) albeit with a smaller variation between the oligomers; **MeF1-3** showed rates of 3, 4 and 28 µmol h^{-1} g^{-1} (Figure 9B, D and F) and **MeF1** with added Pd had a HER of

5 μmol h^{-1} g^{-1}. It should be noted that whilst the dimer and trimer were stable as solids, the monomer **MeF1**, dissolved in the mixture meaning a fair and direct comparison between the three materials is perhaps not possible in this system.

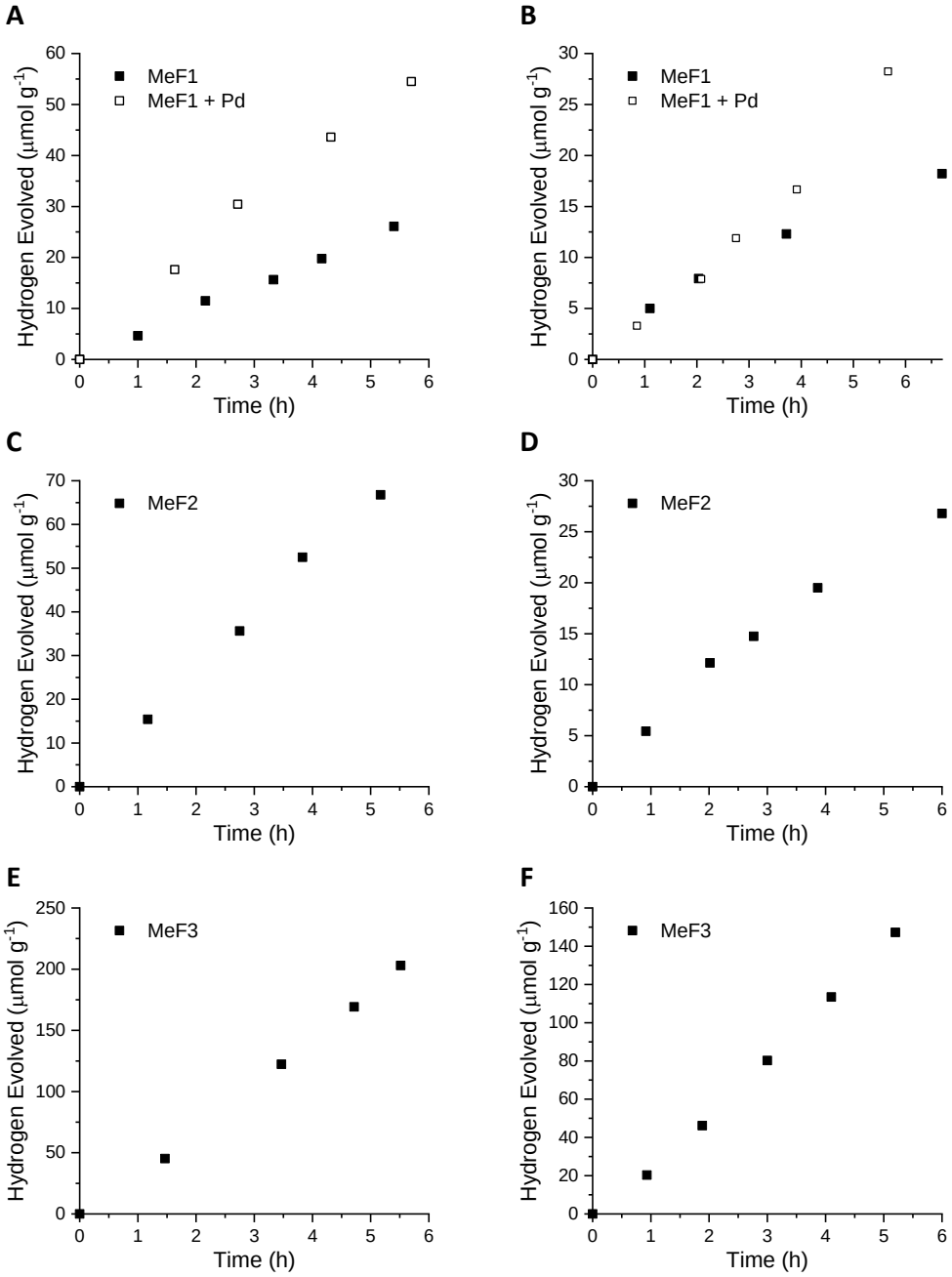

Figure 9: Photocatalytic hydrogen evolution of **MeF1** (25 mg) over λ > 295 nm (A) and 275 < λ < 400 nm (B), **MeF2** (25 mg) over λ > 295 nm (C) and 275 < λ < 400 nm (D) and **MeF3** (25 mg) over λ > 295 nm (E) and 275 < λ < 400 nm (F) suspended in (1:1:1) water/methanol/triethylamine mixtures (25 mL), 300 W Xe light source.

Despite dissolving in the mixture **MeF1** collected post photolysis showed no signs of chemical breakdown by NMR. Similarly, NMR spectra of **MeF2** and **MeF3** showed no evidence of chemical instability (Figure 12).

To allow for direct comparison between all three materials as heterogeneous catalysts, **MeF1-3** were also tested in a fully aqueous system, using an inorganic sodium sulphide scavenger. All three materials were stable as solids and evolved hydrogen upon irradiation. Using the $\lambda > 295$ nm filter **MeF1** had a rate of 4 μmol h^{-1} g^{-1} slightly higher than **MeF2** (3 μmol h^{-1} g^{-1}) whilst **MeF3** was the most active with a HER of 10 μmol h^{-1} g^{-1}. However, the **MeF1** with Pd levels equivalent to the dimer and trimer was significantly more active with a hydrogen evolution rate of 14 μmol h^{-1} g^{-1}. Upon moving to the $275 < \lambda < 400$ nm filter **MeF1** was more active, with a HER of 7 μmol h^{-1} g^{-1}, whilst **MeF2** and **MeF3** showed a rates of 5 and 7 μmol h^{-1} g^{-1}. Again, the **MeF1** with equivalent Pd levels showed the highest rate of 28 μmol h^{-1} g^{-1}.

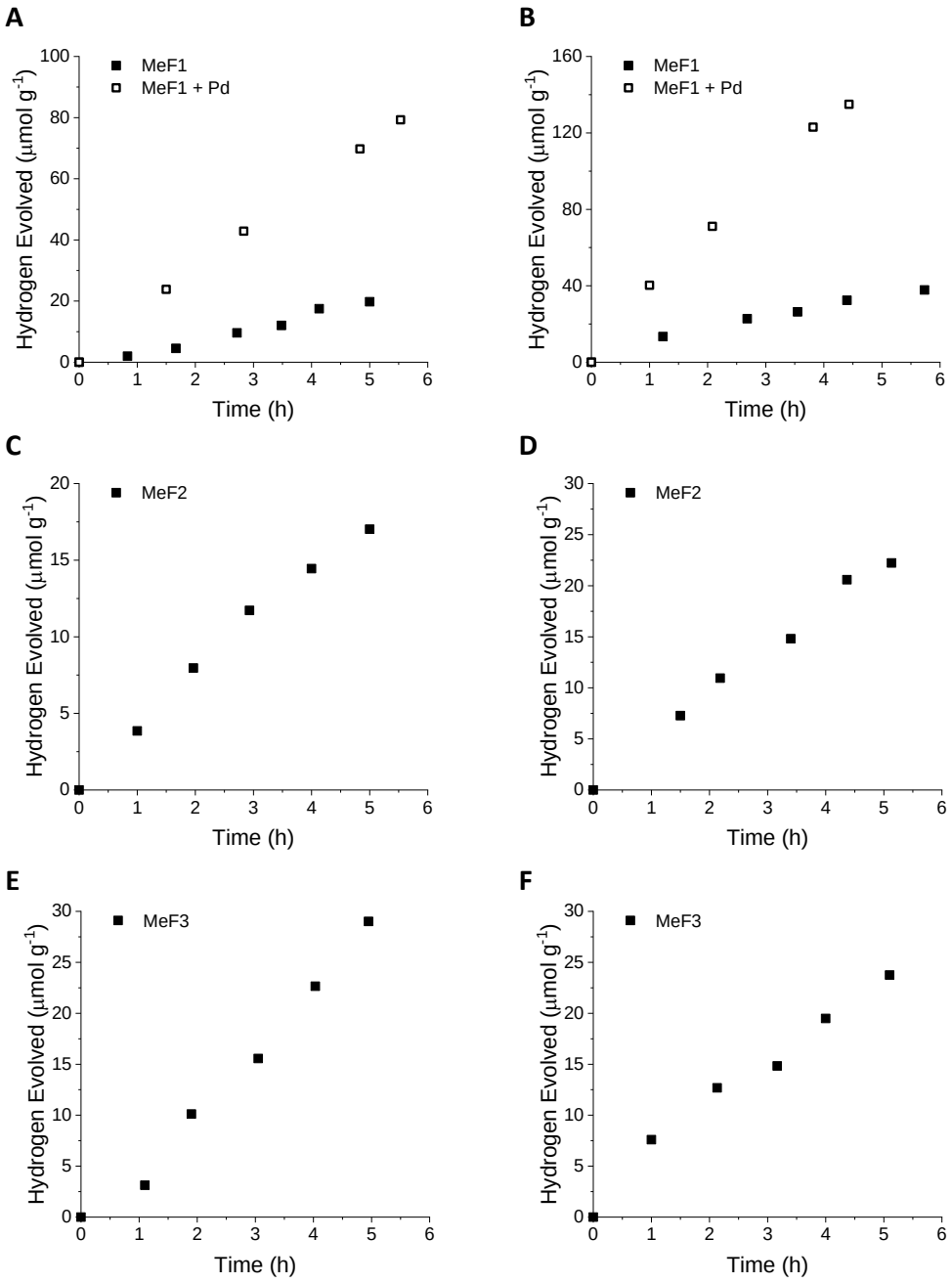

Figure 10: Photocatalytic hydrogen evolution of **MeF1** (25 mg) over λ > 295 nm (A) and 275 < λ < 400 nm (B), **MeF2** (25 mg) over λ > 295 nm (C) and 275 < λ < 400 nm (D) and **MeF3** (25 mg) over λ > 295 nm (E) and 275 < λ < 400 nm (F) suspended in $Na_2S_{(aq)}$ (0.35 M) / $Na_2SO_{3(aq)}$ (0.2 M) (25 mL), 300 W Xe light source.

As with the TEA system, no chemical break down of the oligomers was observed by NMR (Figure 11), with all materials showing identical spectra pre and post photolysis. PXRD patterns of the materials collected after photocatalysis were also similar to those collected before with preservation of the main peaks and no evidence new crystal phases (Figure 12).

This indicates these polymorphs are stable under testing conditions, at least over the periods investigated here.

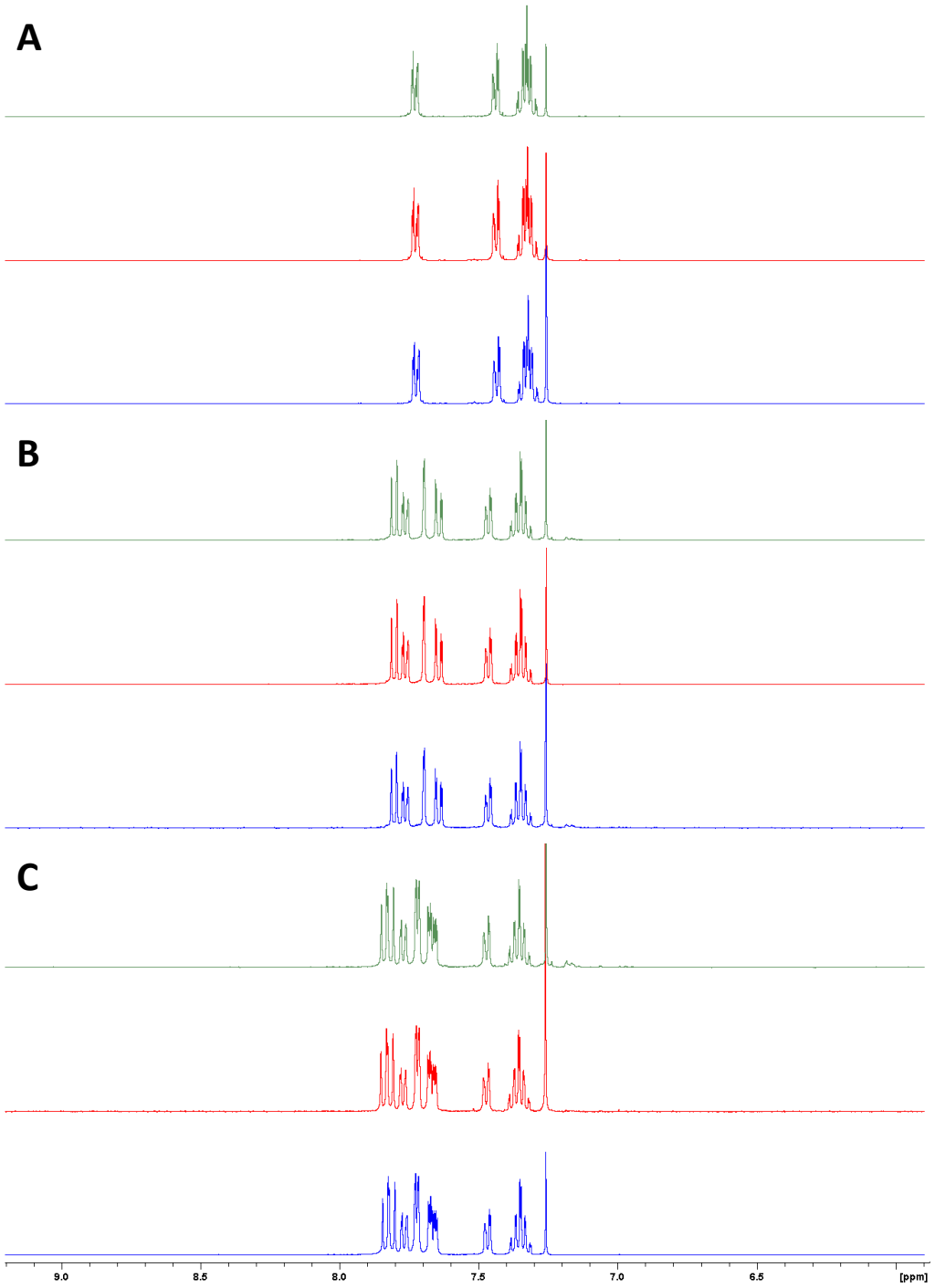

Figure 11: NMR spectra of **MeF1** (A), **MeF2** (B) and **MeF3** (C), pre catalysis (green), post catalysis for 6 hours in $Na_2S_{(aq)}$ (0.35 M) / $Na_2SO_{3(aq)}$ (0.2 M) (red) or in (1:1:1) water/methanol/triethylamine (blue) using a 300 W Xe lamp fitted with a $\lambda > 295$ nm filter.

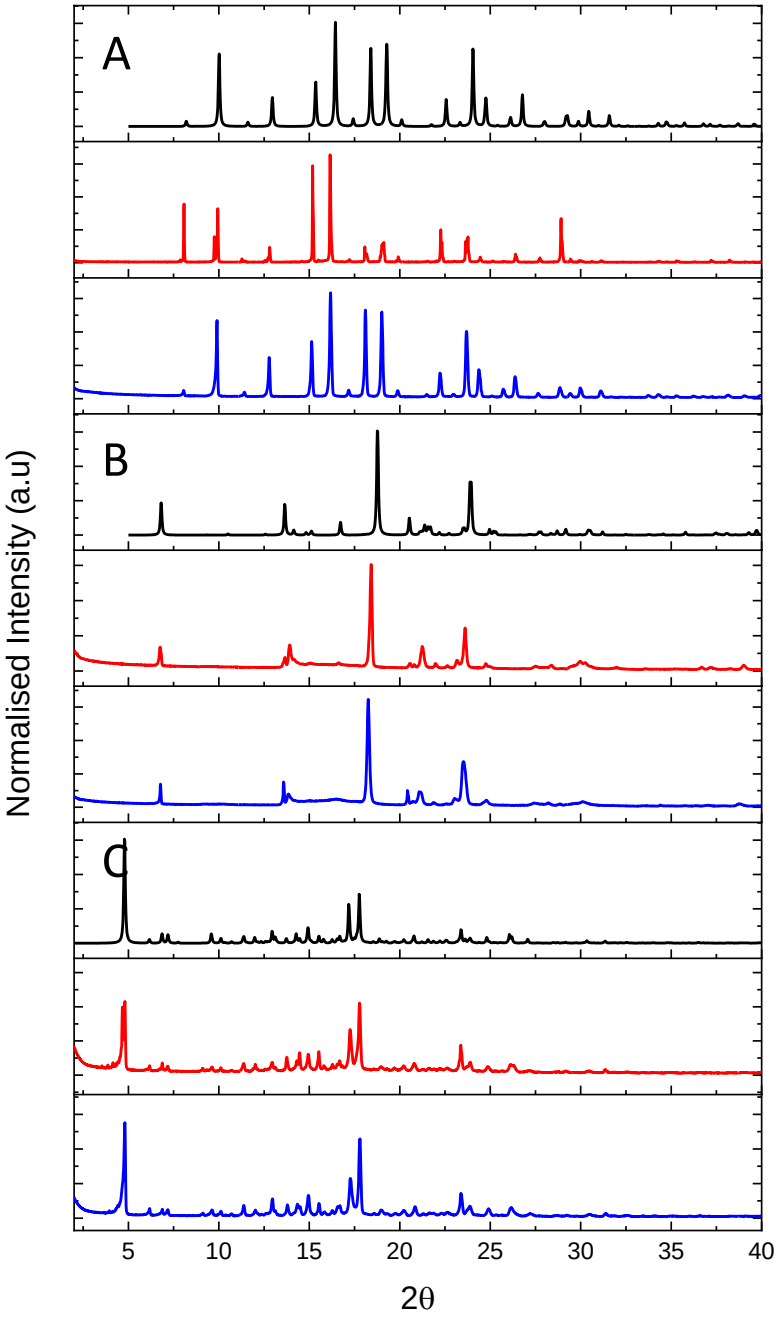

Figure 12: PXRD spectra of **MeF1** (A), **MeF2** (B) and **MeF3** (C). Predicted from single crystal structures (black), pre catalysis (red) and post catalysis (blue) for 6 hours in $Na_2S_{(aq)}$ (0.35 M) / $Na_2SO_{3(aq)}$ (0.2 M) using a 300 W Xe lamp fitted with a $\lambda > 295$ nm filter.

3.2.4 Homogenous Photocatalytic Hydrogen Evolution

Since the **MeF** oligomers are soluble in common organic solvents, it was also possible to test their activity for photocatalytic proton reduction under homogeneous conditions. It is interesting to consider whether the same trends in activity occur in the solution state when the effects of solid-state packing are removed. The oligomers (5 mg) were dissolved in a solution of THF, water and triethylamine (90:5:5) (25 mL). Although none of the oligomers appeared to be chemically unstable under the heterogeneous conditions described previously, the oxidative degradation of polyfluorenes under photolysis has been widely observed in optoelectronic devices.[52] Therefore, a singlet oxygen and super oxide anion scavenger, nickledibutylthiocarbamate[53,54] (1 mg) was added to the solutions to minimise degradation of the oligomers. None of the dissolved oligomers absorbed significantly in the visible region and so the materials were tested using only UV light with the $275 < \lambda < 400$ nm filter. **MeF1** was the most active material under these conditions with a HER 107 µmol h^{-1} g^{-1}, and this decreased with increasing chain length to 93 µmol h^{-1} g^{-1} for **MeF2** and 30 µmol h^{-1} g^{-1} for **MeF3**. Unlike in the solid state, we can use the extinction coefficient of the oligomers in solution to estimate the amount of light absorbed by the materials in these experiments. If we divide the HERs of the oligomers by the average extinction coefficients across the wavelengths of irradiation (as calculated in Table 1) we can define an absorption corrected activity (ACA). In this case, **MeF1** had an ACA of 11.2, whilst **MeF2** and **MeF3** had values of 2.8 and 0.6 respectively.

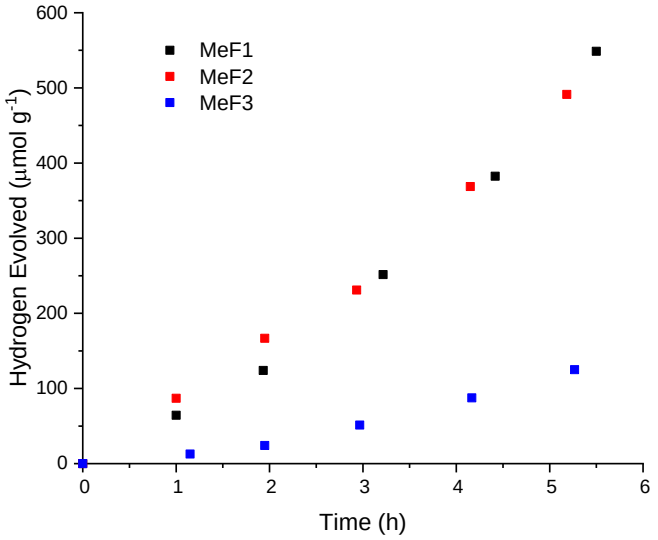

Figure 13: Photocatalytic hydrogen evolution of **MeF1-3** (5 mg) dissolved in a solution of THF, water and triethylamine (90:5:5) (25 mL), irradiated with a 300 W Xe light source fitted with a $275 < \lambda < 400$ nm filter. Nickeldibutylthiocarbamate (1 mg) was added as a singlet oxygen scavenger.

Despite the addition of the reactive oxygen species scavenger, **MeF1-3** collected post photolysis showed small impurity peaks in the aromatic region of the NMR spectra (Figure 14). Substituted fluorene oligomers have previously been shown to form radical cations under electrochemical excitation, these can then couple to form further oligomers[55] or could react with triethylamine to give impurity species. In these experiments the rates of hydrogen evolution are too low to test by isotopic analysis; hence, while we believe that the hydrogen evolved is photocatalytic rather than produced from substrate breakdown, we cannot prove this conclusively at this stage. Line broadening in these spectra is thought to be due to paramagnetic Ni.

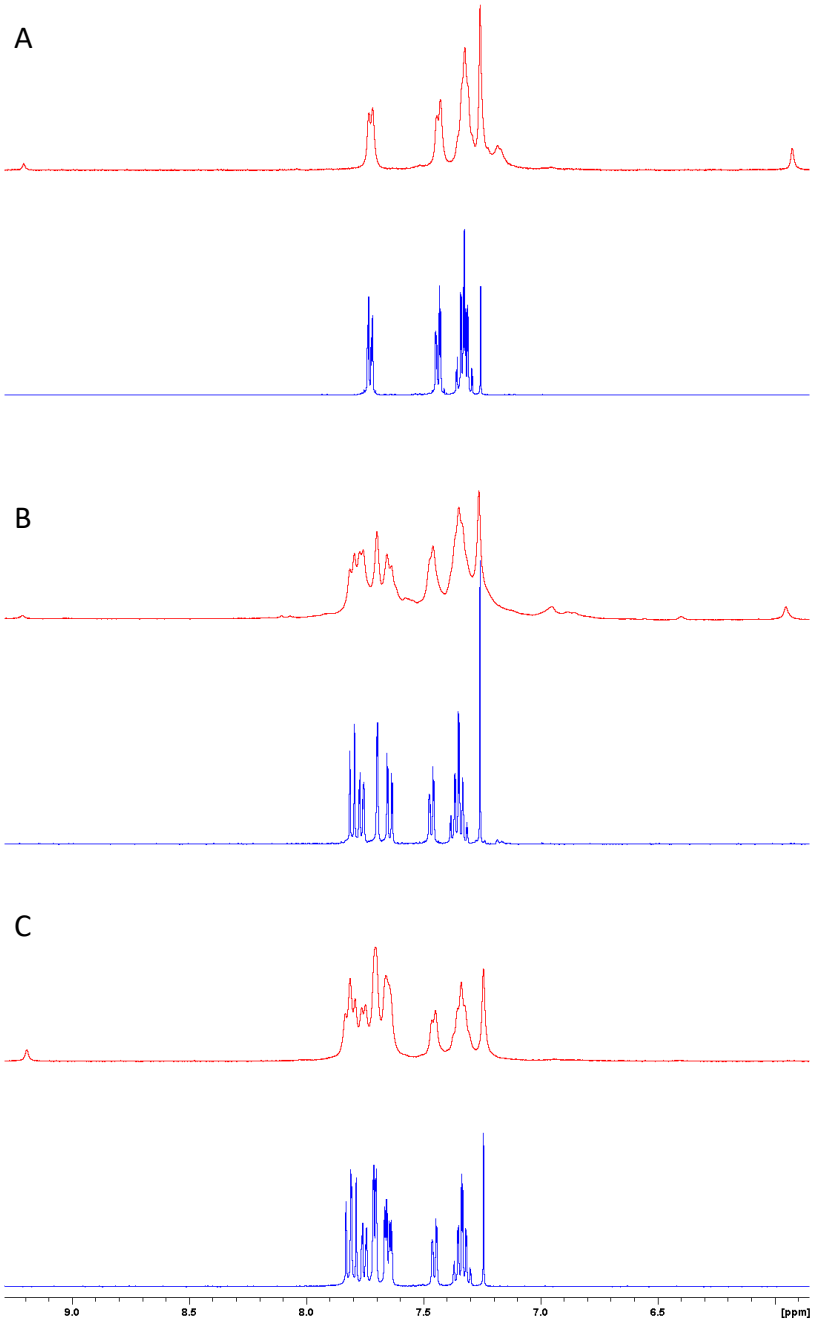

Figure 2: NMR spectra of **MeF1** (A), **MeF2** (B) and **MeF3** (C), pre (blue) and post (red) homogeneous catalysis.

3.3 Phenyl and Mesityl Oligomers

3.3.1 Synthesis and Characterisation

PSP, **MSM**, **PFP** and **MFM** were synthesised by Suzuki coupling, as shown in Scheme 2, **MSM** was purified by column chromatography and all materials were re-crystallised (Section 3.10.4 for full details). The structures of the four materials, obtained by SCXRD are shown in Figure 15. These are notable for the clear backbone twisting effect of replacing the phenyl substituent on **PSP** and **PFP** with a mesityl group; whilst the **PSP** and **PFP** average dihedral angles between rings of 26° and 13°, in **MSM** and **MFM** this is increased to 91° and 97°.

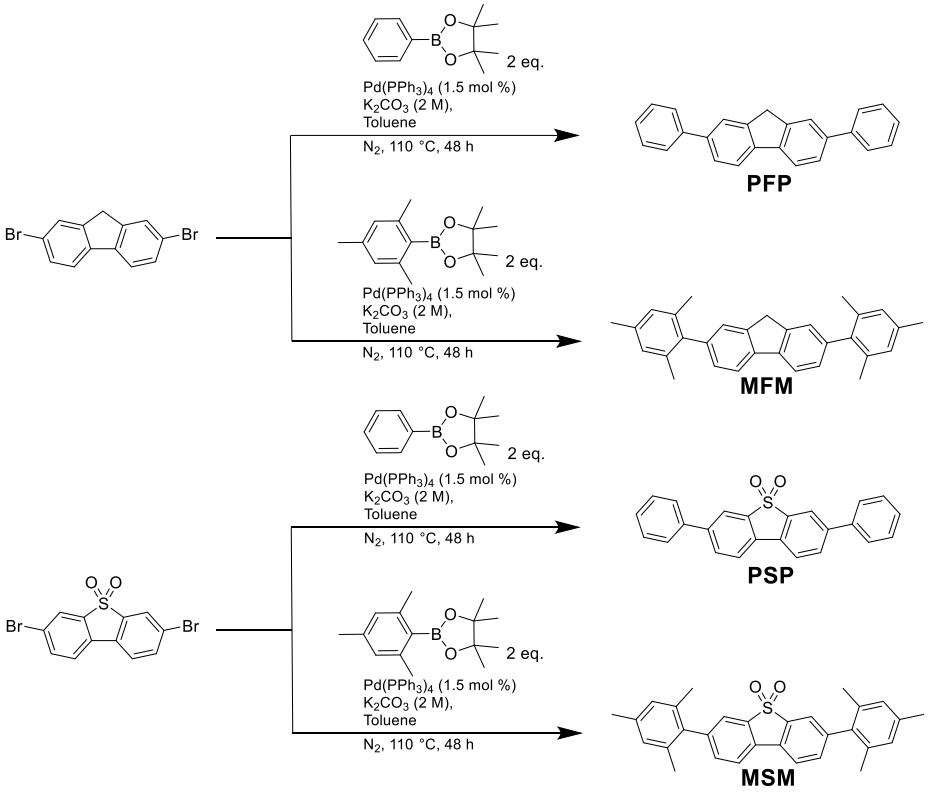

Scheme 2: Structures and synthesis of the phenyl and mesityl oligomers.

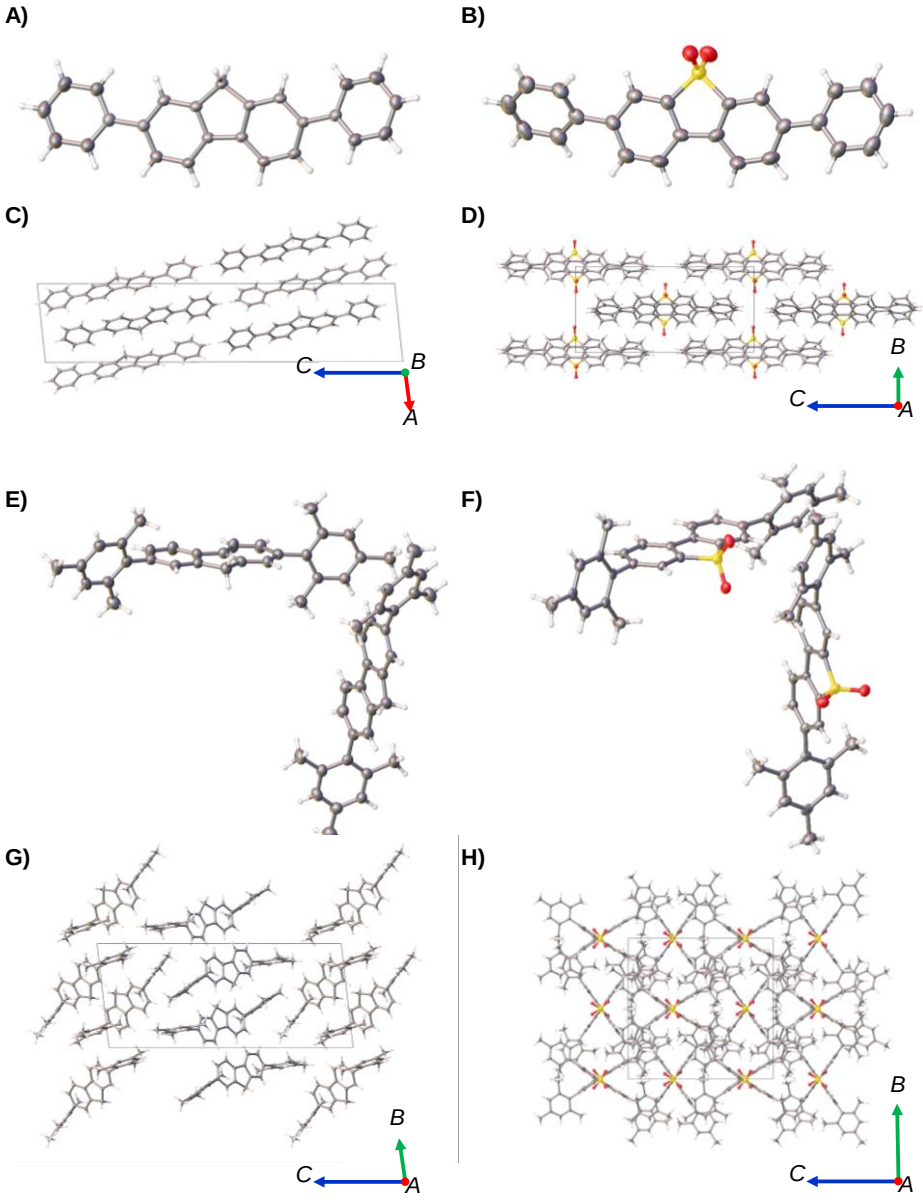

Figure 15: Molecular conformations and crystal packings of **PFP** (A and C), **PSP** (B and D), **MFM** (E and G) and **MSM** (F and H) from SCXRD.

Palladium levels for all materials were measured by ICP-MS, which showed all materials to have very low residual Pd from synthesis. **PSP** had levels below the 10 ppm detection limit of the instrument whilst **MSM** and **PFP** also had very low levels of 15 ppm and 31 ppm, respectively, and **MFM** had a higher level of 140 ppm.

The particle sizes of these oligomers suspended in water were found to be smaller than the **MeF** group of oligomers. SLS measurements (Figure 16) showed all four materials were quite polydisperse with particles of less than 1 micron up to several hundred microns and slight variation in D[3,2] values from 5.3 to 7.3 to 9.3 to 11.6 µm for **PSP**, **MFM**, **MSM** and **PFP** respectively.

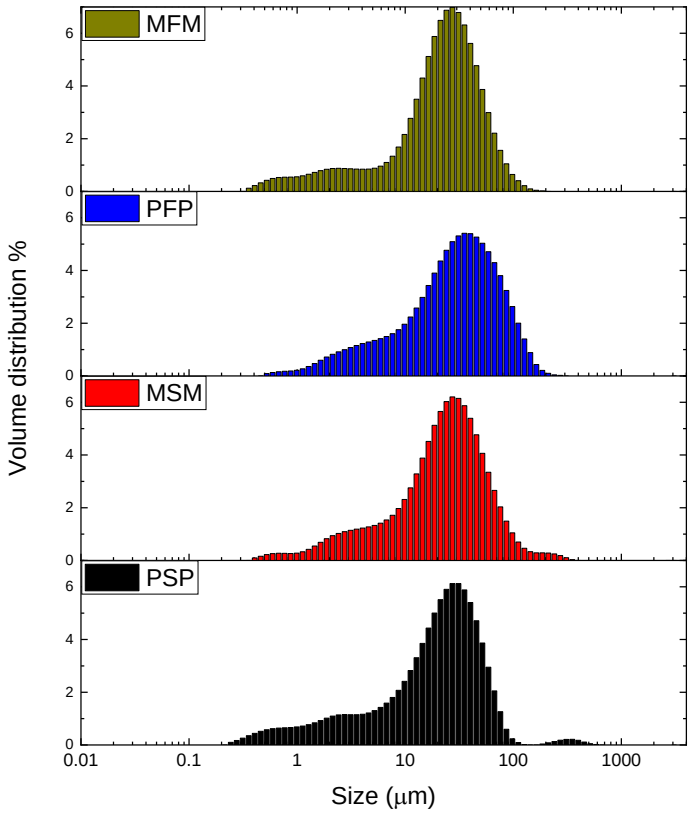

Figure 16: Particle size distributions, by static light scattering, of the phenyl and mesityl oligomers suspended in water.

3.3.2 Photophysical Properties

The optical properties of the phenyl and mesityl substituted oligomers were measured in the solid state and in chloroform solution. In both cases, a blueshift was observed in absorption spectra upon moving from phenyl substituted material to mesityl analogue (Figure 17). This was most evident in the solid-state DRS spectra with a blue shift in absorption onset of 40 nm for the dibenzothiophene sulfone pair and 96 nm for the fluorene pair. This shift is ascribed to the increased backbone twisting observed in the crystal structures of **MSM** and in particular **MFM** and the subsequently reduced conjugation lengths. The spectra in chloroform show less pronounced blueshifts of 22 nm (**PSP** to **MSM**) and 52 nm (**PFP** to **MFM**), which nevertheless indicates that the sterically bulky mesityl groups are causing twisted conformations to be adopted in solution as well as the solid state. Both **PSP** and **MSM** show a shoulder absorption common in dibenzothiophene sulfone bearing molecules, which is ascribed to an n → π* transition. It is also notable that in solution **MFM**, unlike **PFP**, shows a sharp secondary absorption at 312 nm, similar to those of **MeF1**, which is also

thought to correspond to weaker π → π* transitions in addition to the main S – S peak.[47,48] This spectra suggests the backbone twisting of **MFM** causes it to behave, electronically speaking, similarly to an isolated fluorene monomer.

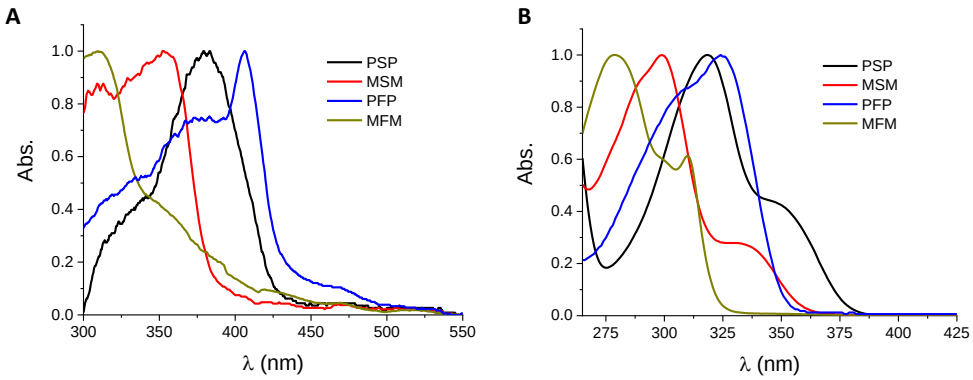

Figure 17: UV-Vis spectra of the phenyl and mesityl substituted oligomers in (A) the solid state (DRS) and (B) in chloroform solution. All spectra are normalised.

The same trend was observed in the photoluminescent emission spectra of the materials; **PSP** and **PFP** had emission maxima at significantly higher wavelengths than their mesityl substituted analogues **MSM** and **MFM**. In the solid state, **PSP** had an emission maxima at 438 nm compared to 387 nm for **MSM**, whilst **PFP** and **MFM** had emission maxima at 423 and 372 nm respectively. Again, **MFM** displayed similar behaviour to the **MeF1** monomer with an additional broad emission at 450 nm thought to be due to excimer formation.[49] Dissolved in chloroform, it was notable that the dominant factor in emission wavelength appeared to be the bridgehead group of the oligomer core, with both **PSP** and **MSM** displaying large stokes shifts and correspondingly higher emission wavelengths (409 and 390 nm) than **PFP** and **MFM** (357 and 334 nm). The only molecule to show multiple emissions in this case was **PFP**, which had a secondary maximum at 373 nm.

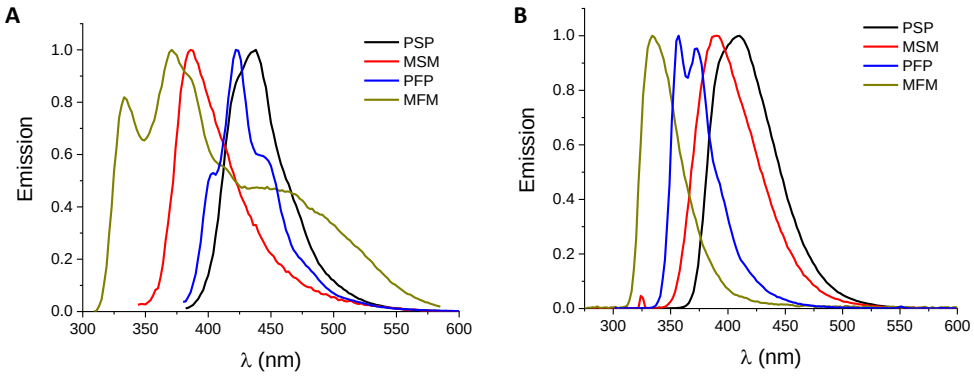

Figure 18: Photoluminescence emission spectra of phenyl and mesityl substituted oligomers in (A) the solid state and (B) in chloroform solution. Each material was excited at its absorption maxima as described in Table 2. All spectra are normalised.

To compare the intensities of these photophysical processes, the molar extinction coefficients and PLQYs were also measured for each material in chloroform solution. **MFM** had the lowest molar extinction coefficient, ε_{Molar}, of 29,800 M^{-1} cm^{-1}, compared to the highest value of 40,300 M^{-1} cm^{-1} for **PFP**. The dibenzothiophene sulfone-based materials showed a similar trend with **MSM** displaying a lower value (18,800 M^{-1} cm^{-1}) than **PSP** (35,300 M^{-1} cm^{-1}). As with the **MeF** oligomers, these materials were tested for photocatalysis across a range of wavelengths, so it is important to consider absorption intensity across the 275 – 400 nm range used (see section 3.3.3). The average extinction coefficient for **MFM** from 275 – 400 nm was 7,400 M^{-1} cm^{-1}, similar to that of **MSM (**6,700 M^{-1} cm^{-1}), whilst the phenylated analogues were over twice as high; 15,700 and 14,300 M^{-1} cm^{-1} for **PFP** and **PSP** respectively.

The efficiency of radiative emission increased dramatically on moving from mesityl substituted fluorene to phenyl with PLQYs of 8 and 94% for **MFM** and **PFP** respectively. Again, the dibenzothiophene sulfone materials were more similar but, like the fluorene-based materials, showed an increased PLQY for the more planar phenyl analogue (65 and 76 % for **MSM** and **PSP**).

Table 2: Optical properties of the phenyl and mesityl substituted oligomers.

	PSP	**MSM**	**PFP**	**MFM**
λ_{onset} solid-state[a] (nm)	426	386	437	341
λ_{max} chloroform (nm)	323	301	331	279, 312
λ_{em} solid-state (nm)	438	387	423	333, 372
λ_{em} chloroform (nm)	409	390	357, 373	334
ε_{Molar}[b] (M^{-1} cm^{-1})	35,300	18,800	40,300	29,800
ε_{Mass}[b] (cm^2 g^{-1})	96	103	127	74
Average ε_{Molar}[b,c] (M^{-1} cm^{-1})	14,300	6,700	15,700	7,400
Average ε_{Mass}[b,c] (cm^2 g^{-1})	39	15	49	18
Φ[b] (%)	76 ± 1	65 ± 3	94 ± 1	8 ± 1

[a]From diffuse reflectance spectroscopy of solid powder. [b] See section 3.10.3 for full definitions and details of how **Φ** was measured. [c] λ = 275-400 nm

Time-correlated single photon counting (TCSPC) measurements indicated that the bridgehead group was a more dominant factor in excited state lifetime than the phenyl or mesityl substituents. In general, the dibenzothiophene sulfone containing molecules were found to have significantly longer lived emissive excited states. All oligomers showed multi-exponent emission decays but the average lifetimes (τ_{av}) were calculated as 2.47 and 2.68 ns for **PSP** and **MSM** in the solid state, compared to 1.02 and 0.58 for **PFP** and **MFM** (Figure 19A). We note that the particularly low value for **MFM** may be a function of its higher Pd content but the general trend does not correlate strongly with Pd levels, for example **MSM** has a longer lifetime than **PSP** despite higher Pd content. The same difference between fluorene and dibenzothiophene sulfone bearing molecules was found in solution measurements (Figure 19B); **PSP**, **MSM**, **PFP** and **MFM** had weighted average lifetimes of 2.42, 3.86, 0.57 and 0.05 ns respectively.

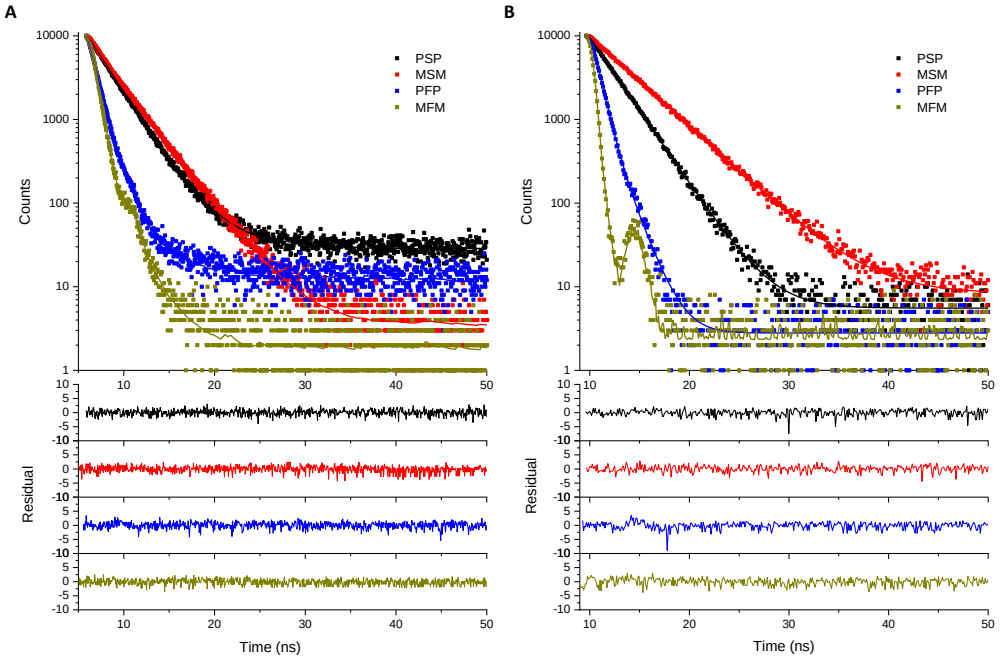

Figure 19: TCSPC spectra of the phenyl and mesityl substituted oligomers in the solid-state (A) and in chloroform solution (B). Data (points), fit (line) and residuals (bottom). Emission of all materials were measured from the emission maxima wavelength as described in Table 2. All measurements used 295 nm laser for excitation apart from the solid-state measurements of **PFP** and **PSP** were excited with a 375 nm laser.

3.3.3 Photocatalytic Hydrogen Production in Suspension

The oligomers were found to be partially soluble in the mixture of equal parts water, triethylamine and methanol and so photocatalytic hydrogen evolution was measured using the sodium sulphide scavenger system (as described in section 3.2.3) to avoid this. All four materials were stable as solids in suspension and evolved hydrogen upon irradiation. Using the $\lambda > 295$ nm filter **PSP** was the most active material with a rate of 24 µmol h^{-1} g^{-1}, followed by **PFP** with HER of 14 µmol h^{-1} g^{-1}, **MSM** HER 6 µmol h^{-1} g^{-1} and **MFM** HER of 5 µmol h^{-1} g^{-1} (Figure 17). Upon moving to the $275 < \lambda < 400$ nm filter **PSP** was still the most active (HER 30 µmol h^{-1} g^{-1}) but **MSM** under these conditions showed an improved rate of 20µmol h^{-1} g^{-1} and in the case of the fluorine based oligomers **MFM** was actually more active than **PFP** (10 versus 9 µmol h^{-1} g^{-1}) (Figure 20).

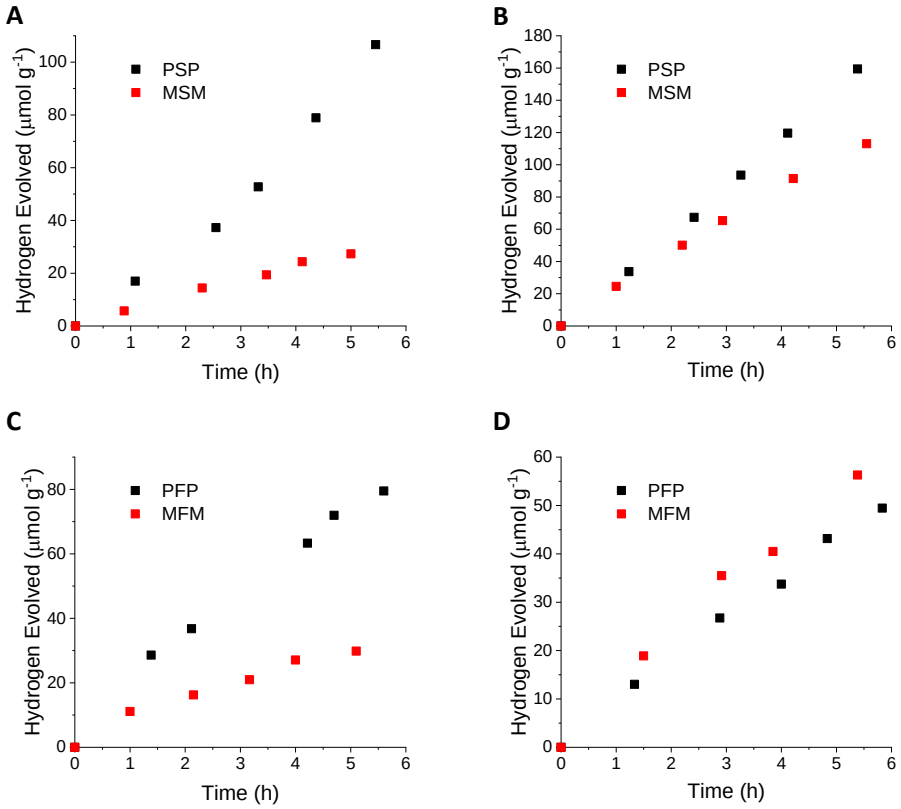

Figure 20: Photocatalytic hydrogen evolution of the phenyl and mesityl substituted oligomers (25 mg) suspended in $Na_2S_{(aq)}$ (0.35 M) / $Na_2SO_{3(aq)}$ (0.2 M) (25 mL), 300 W Xe light source, using a $\lambda > 295$ nm filter (A and C) and using a $275 < \lambda < 400$ nm filter (B and D).

Under these conditions, all of the oligomer polymorphs were found to be stable by PXRD (Figure 21 and 22)—there was no sign of any phase transformation—and these materials showed no signs of chemical degradation by NMR (Figure 24).

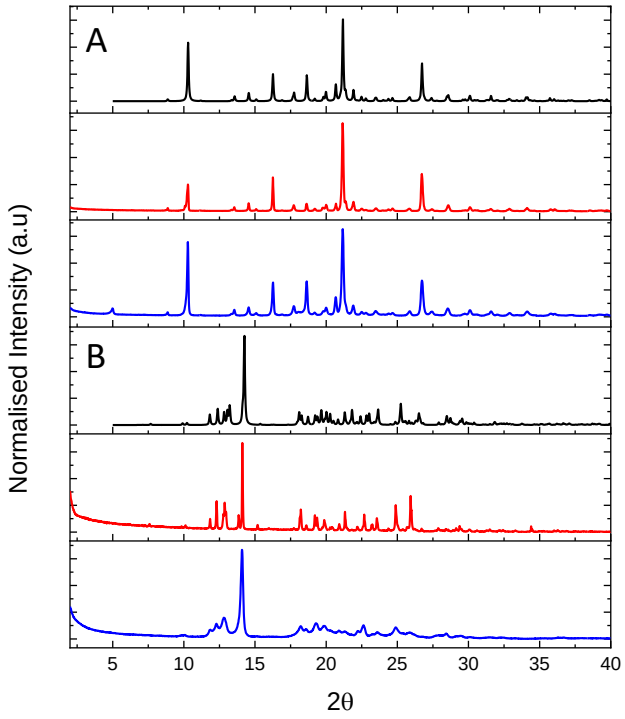

Figure 21: PXRD spectra of **PSP** (A) and **MSM** (B) as predicted from single crystal structures (black), pre catalysis (red) and post catalysis (blue).

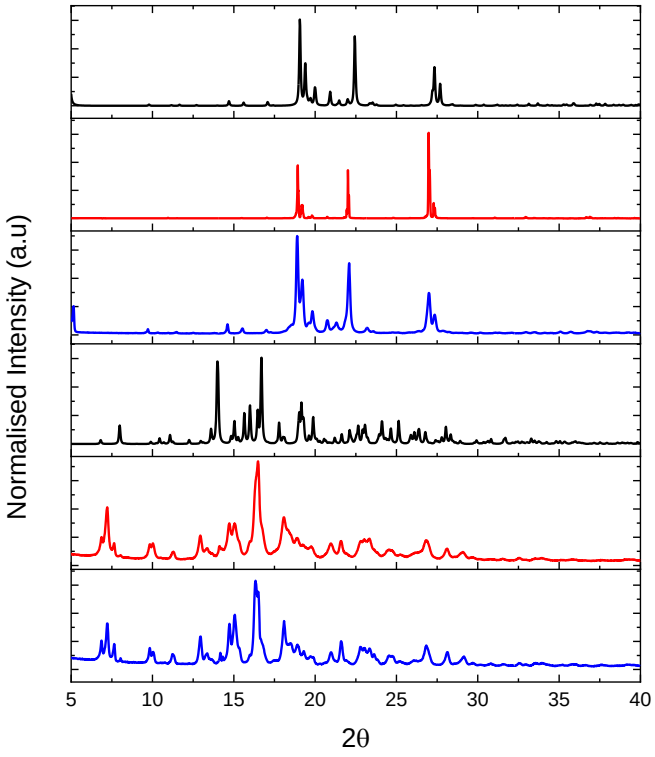

Figure 22: PXRD spectra of **PFP** (A) and **MFM** (B) as predicted from single crystal structures (black), pre catalysis (red) and post catalysis (blue).

3.3.4 Homogenous photocatalytic hydrogen evolution

As with the **MeF** oligomers, **PSP**, **MSM**, **PFP** and **MFM** were soluble in THF and so could be tested for homogeneous proton reduction in solution. The oligomers were tested under the same conditions as described in section (3.2.4). After an initial induction period **PFP** showed a HER of 120 μmol h^{-1} g^{-1}—the highest of the materials under these conditions. **PSP** and **MSM** also evolved hydrogen steadily over 5 hours with rates of 14 and 44 μmol h^{-1} g^{-1} respectively. **MFM** on the other hand showed a slow drop off in activity over time with an average HER 13 μmol h^{-1} g^{-1}. NMR analysis of the materials collected post catalysis showed **MFM** had degraded with complete loss of the signals associated with the original material. **MSM** and to a lesser extent **PFP** also show some chemical decomposition with impurity peaks present in the aromatic region. **PSP** appeared to be stable (Figure 24). Line broadening in the spectra of the materials collected after homogeneous catalysis is thought to be due to paramagnetic Ni. As in section 3.2.4, whilst we believe the hydrogen produced in these experiments is from photocatalytic proton reduction it was not possible to prove this conclusively with isotopic analysis due to the low amounts of gas produced.

Normalising these rates to the absorption spectra of the oligomers over the irradiation period gives us the absorption corrected activity (ACA) values (defined as HER in μmol h^{-1} g^{-1} divided by the mass extinction coefficient, ε_{Mass}, in cm^2 g^{-1}). These showed no clear trend on moving from dibenzothiophene sulfone bridgehead to fluorene or on moving from phenyl substituted to mesityl substituted with ACA values for **PSP**, **MSM**, **PFP** and **MFM** of 0.3, 1.9, 2.4 and 0.7.

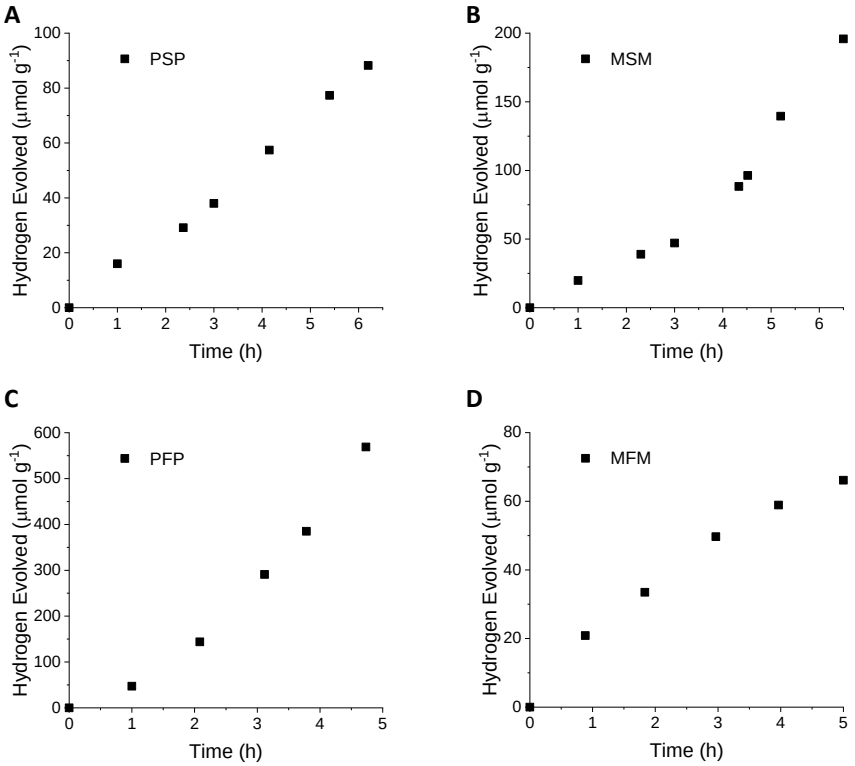

Figure 23: Photocatalytic hydrogen evolution of the phenyl and mesityl substituted oligomers (5 mg) dissolved in a solution of THF, water and triethylamine (90:5:5) (25 mL), irradiated with a 300 W Xe light source fitted with a $275 < \lambda < 400$ nm filter. Nickeldibutylthiocarbamate (1 mg) was added as a singlet oxygen scavenger.

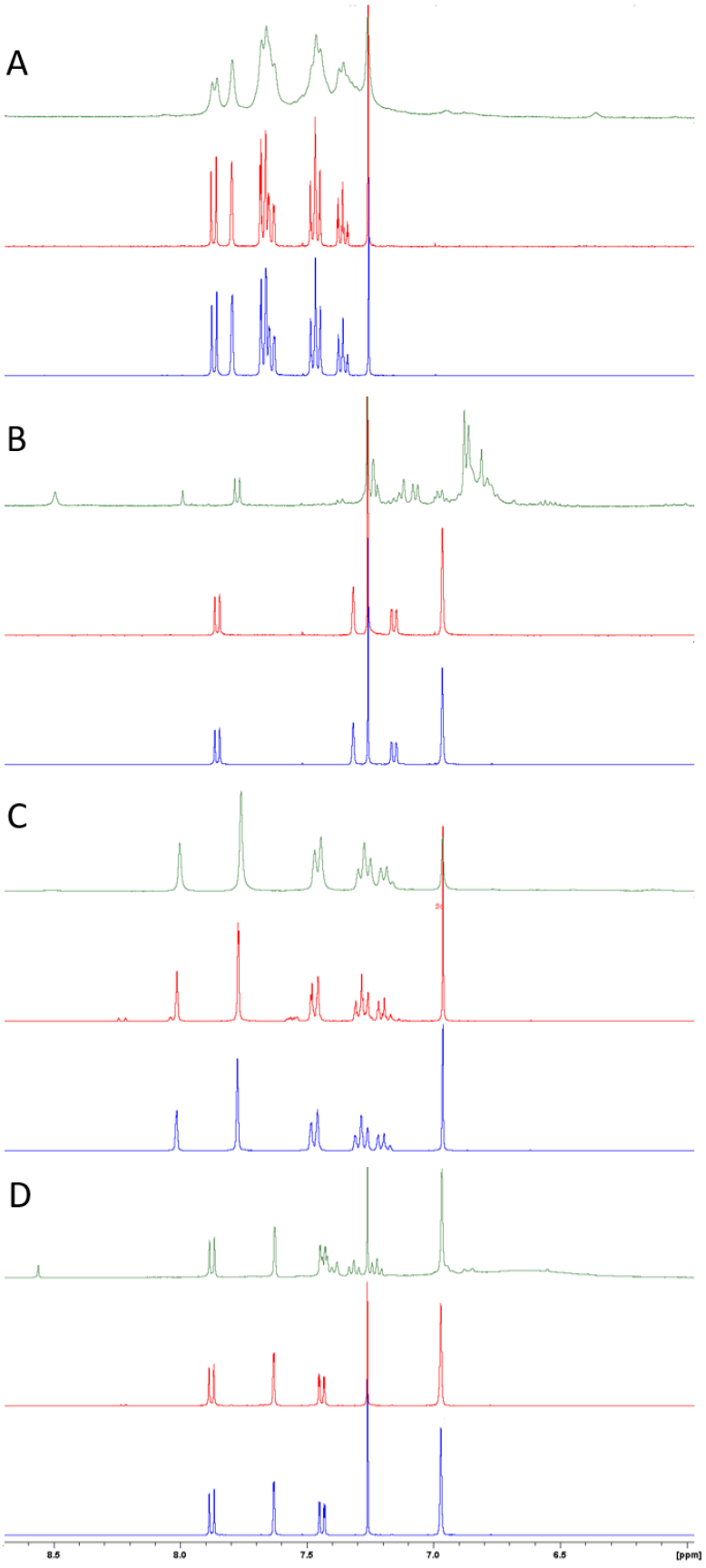

Figure 24: NMR spectra of **PFP** (A), **MFM** (B) **PSP** (C) and **MSM** (D), pre catalysis (blue), post catalysis in $Na_2S_{(aq)}$ (0.35 M) / $Na_2SO_{3(aq)}$ (0.2 M) (red) or post homogeneous catalysis

3.4 Dibenzothiophene Sulfone Oligomers

3.4.1 Synthesis and characterisation

The dibenzo[*b,d*]thiophene sulfone monomer, **S1**, was obtained commercially and was ground before analysis. Bromination of the monomer using NBS yielded primarily 3,7-dibromodibenzo[*b,d*]thiophene sulfone with a small amount of mono brominated 3-bromodibenzo[*b,d*]thiophene sulfone. These were used to synthesis the corresponding boronic acid (pinacol) esters via Pd catalysed Miyaura borylation and subsequently the dimer and trimer of dibenzo[*b,d*]thiophene sulfone, **S2** and **S3**, by Suzuki coupling (Scheme 3).

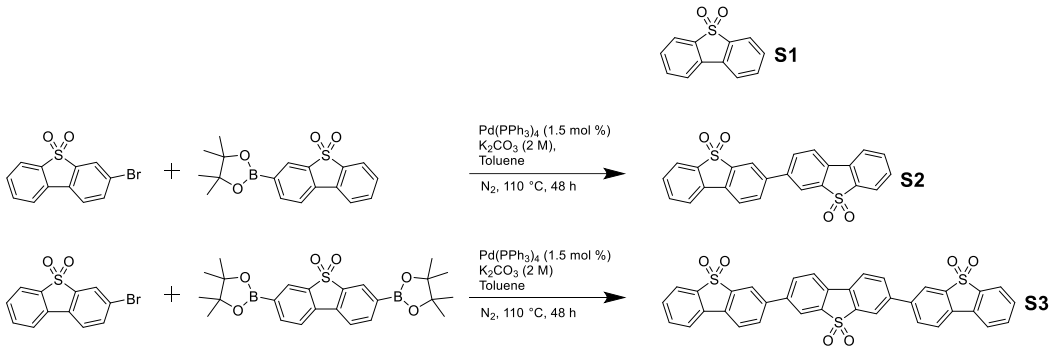

Scheme 3: Structures and synthesis of **S1-3.**

As synthesised, **S2** and **S3** were found to be semi-crystalline by PXRD (Figure 26) but insoluble in common organic solvents tested. Crystals suitable for single crystal-XRD were therefore obtained by sublimation. The crystals structures of **S1**, **S2** and **S3** are shown in Figure 25, The single crystal structures and PXRD patterns of sublimed **S2** and **S3** showed the same phases as the as-synthesised oligomers (Figure 26) but provided insufficient material for analysis. Further characterisation and testing of **S2** and **S3** was therefore performed on the as-synthesised materials.

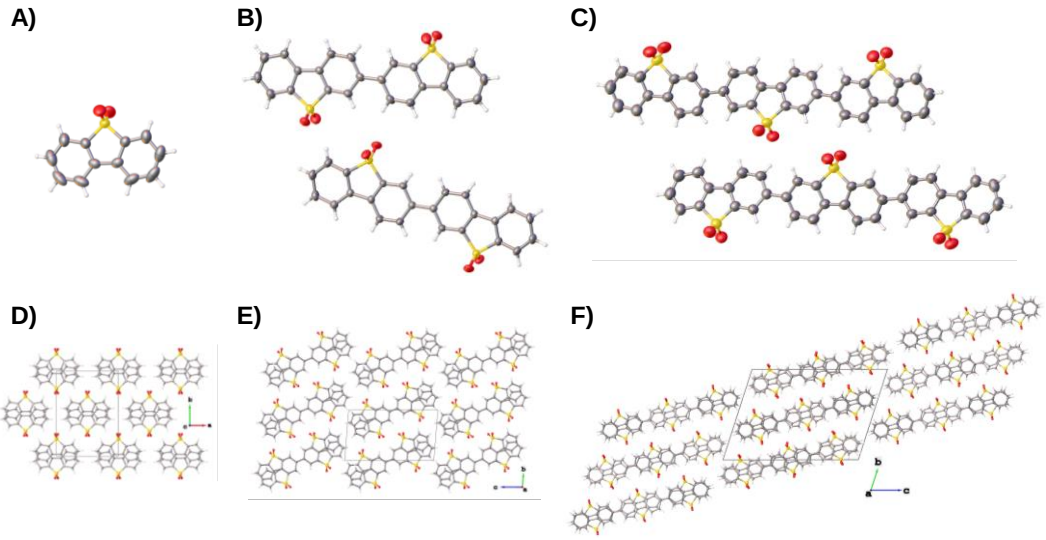

Figure 25: Conformation and packing of **S1** (A and D), **S2** (B and E), and **S3** (C and F) from SCXRD. Crystals of **S2** and **S3** were obtained by sublimation.

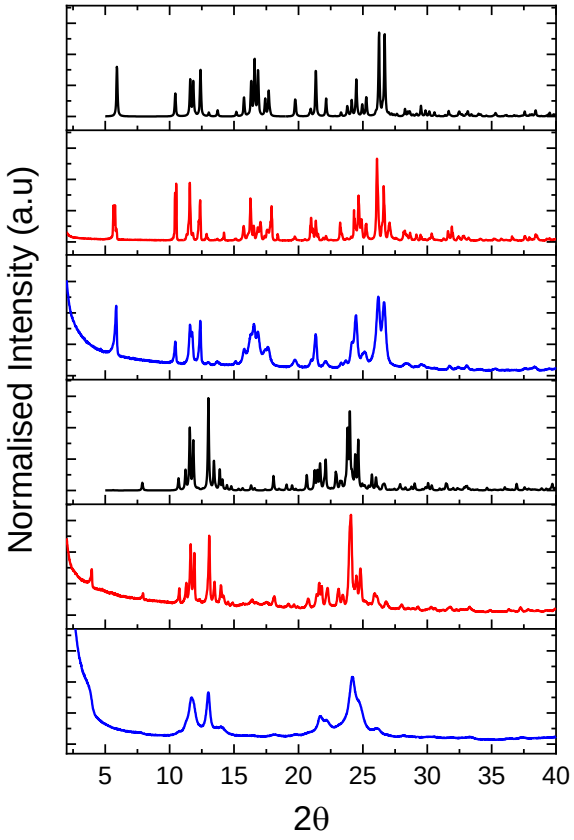

Figure 26: PXRD spectra of **S2** and **S3** as synthesised compared to the sublimed material and to the predicted pattern of the single crystal structure.

Figure 27 show **S1-3** by SEM. **S1** was comprised of large crystals up to 100 µm in size (Figure 27A and B). **S2** on the other hand was made up of very small but well-defined cuboidal crystals of approximately 100 by 500 nm, aggregated in larger micron scale polycrystalline particles. (Figure 27C and D). This is consistent with the sharp peaks observed by PXRD. No obviously crystalline material was found in **S3**, which was instead made of globular particles, although it should be stated here that morphology alone can often

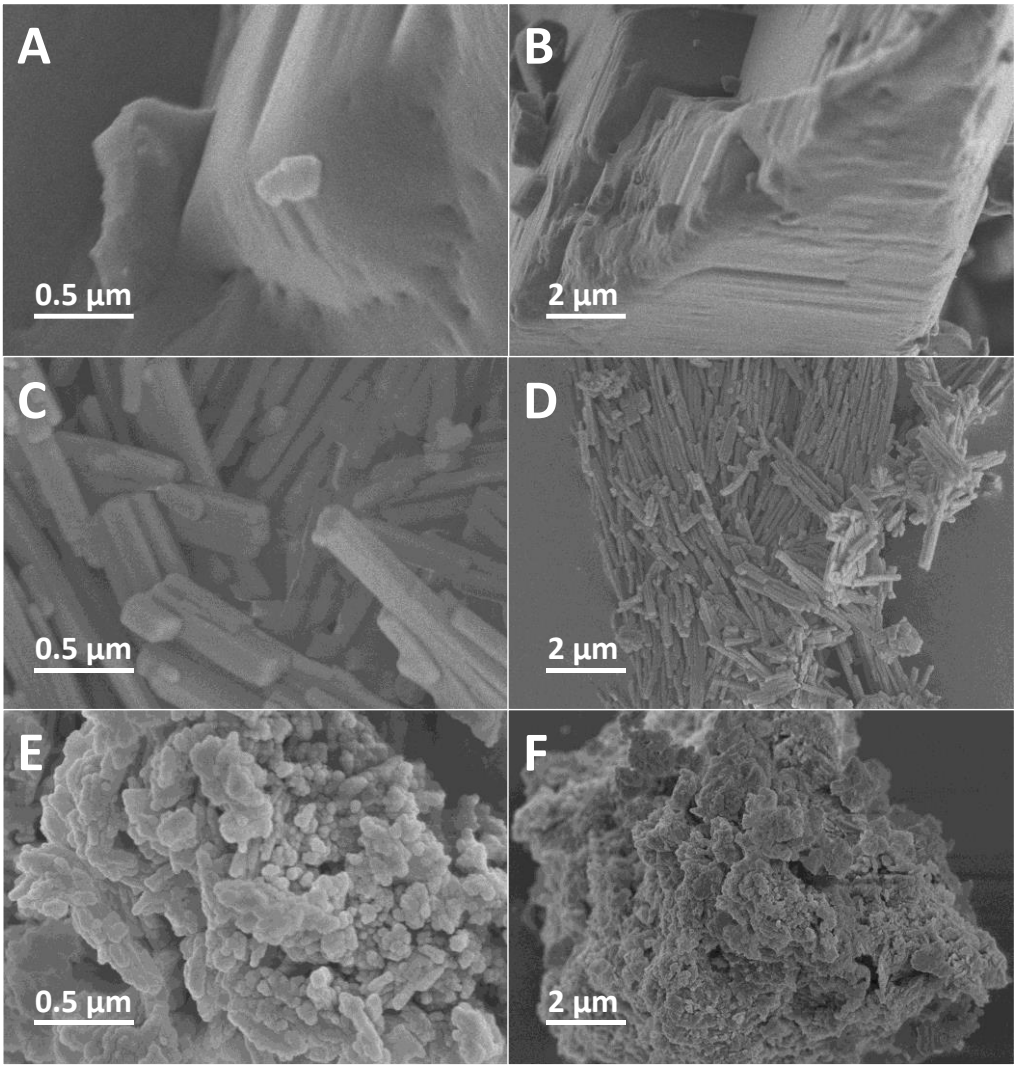

Figure 27: SEM images of **S1** (A and B), **S2** (C and D), and **S3** (E and F), recorded at 3 keV.

be a poor marker for crystallinity. These showed a similar polydispersity to **S2** with very small particles (< 100 nm) mostly fused into larger micron scale aggregates (Figure 27E and F).

Particle size analysis by SLS indicated that the sub-micron particles of **S2** and **S3** could disperse freely to some extent. In water suspensions, both dimer and trimer had significant populations of material between 200 and 1000 nm, along with the larger aggregates up to 10

µm. This gave small D[3,2] values of 0.87 and 1.79 µm for the dimer and trimer. **S1** dispersed in water was made up of generally larger particles with very little material less than a micron and a D[3,2] value of 3.96 µm. As with the **MeF1** monomer, **S1** dissolved in the TEA/MeOH/Water mixture but **S2** and **S3** were also tested as suspensions in this system. Both oligomers dispersed well in this system and had smaller D[3,2] values of 0.68 and 0.57 µm.

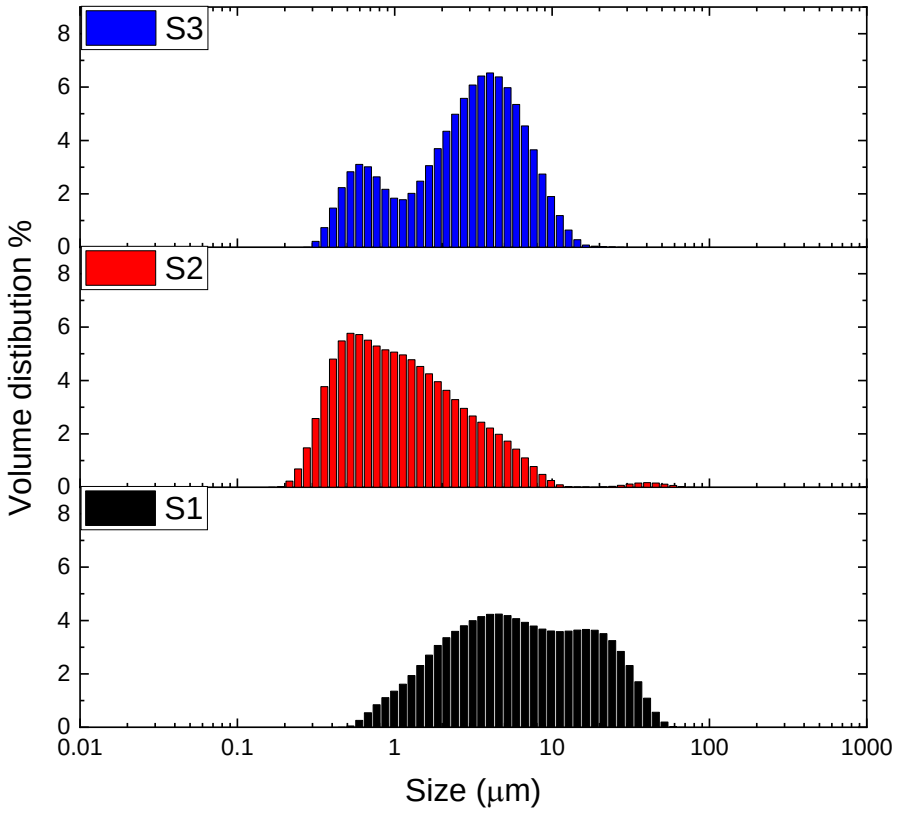

Figure 28: Particle size distributions, by static light scattering, of the **S** oligomers suspended in water.

ICP-MS analysis showed the purchased monomer, **S1**, had palladium levels below the 10 ppm detection level of the instrument whilst **S2** and **S3** both had significant residual palladium from Suzuki coupling at levels of 0.22 and 0.26 wt. % (2200 and 2600 ppm).

3.4.2 Photophysical properties

As expected, the UV-Vis spectra of **S1-3** showed a considerable redshift in absorption onset in the solid state and in absorption maxima in chloroform solution with increasing chain length. Figure 29A shows the solid-state spectra where **S1** has an onset of 382 nm, whilst dimer and trimers absorption spectra reach into the visible; **S2** has an onset of 444 nm and **S3** 471 nm. In solution the oligomers absorb solely in the UV region and there is evidence of multiple transitions. **S1** had two shoulder maxima at 362 and 323 nm, with the global maxima, well into the mid-UV at 285 nm. **S2** had two maxima at 316 and 333 nm whilst **S3** had two at 322 and 344 nm. The extinction coefficient of **S1** in chloroform was calculated to be 7,400 M^{-1} cm^{-1} but **S2** and **S3** were too insoluble to calculate accurate concentrations.

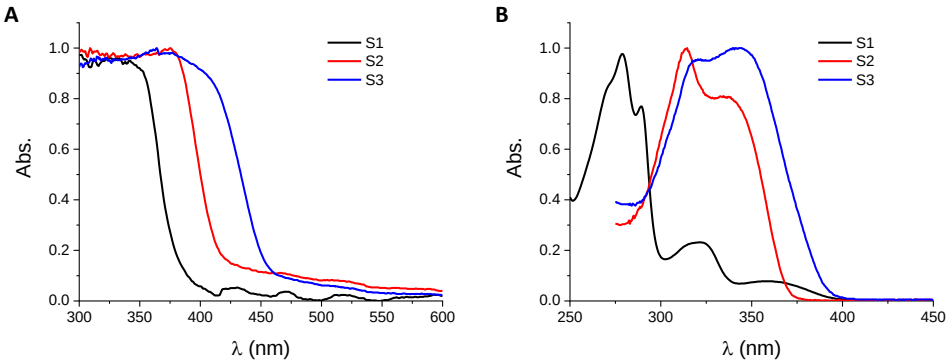

Figure 29: UV-Vis spectra of **S1-3** in (A) the solid state (DRS) and (B) in chloroform solution. All spectra are normalised.

The Stokes shift of the oligomers also increased with chain length; **S1** has a fluorescence maximum in the solid state at 394 nm (Stokes shift 12 nm), **S2** shifted 16 nm and had a maxima at 460 nm whilst **S3** had a fluorescence maxima at 492 nm, a Stokes shift of 21 nm. Dissolved in chloroform **S1** showed fluorescence with an emission maxima at 361 nm but the longer oligomers had more complex emission, with maxima at 373 and 389 nm (**S2**) or 396 and 414 nm (**S3**). **S1** was also found to be significantly less fluorescent with a PLQY of 11%, compared to 73 and 77% for the dimer and trimer.

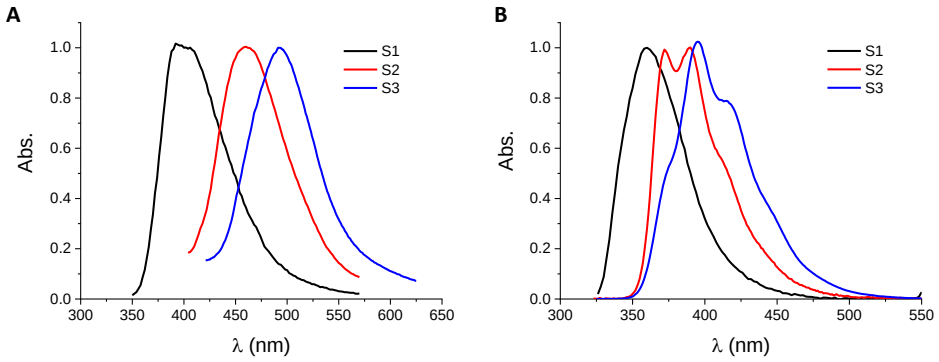

Figure 30: Photoluminescence emission spectra of **S1-3** in (A) the solid state and (B) in chloroform solution. Each material was excited at its absorption maxima as described in Table 3. All spectra are normalised.

Table 3: Optical properties of the **S** oligomers.

	S1	**S2**	**S3**
λ_{onset} solid-state[a] (nm)	382	444	471
λ_{max} chloroform (nm)	285, 323, 362	316, 333	322, 344
λ_{em} solid-state (nm)	394	460	492
λ_{em} chloroform (nm)	361	373, 389	393, 414
ε_{Molar}[b] (M^{-1} cm^{-1})	7,400	- [c]	- [c]
Φ[b] (%)	11 ± 1	73 ± 4	77 ± 5

[a]From diffuse reflectance spectroscopy of solid powder. [b] See section 3.10.3 for full definitions and details of how **Φ** were measured. [c] Too insoluble for accurate concentration.

As with the **MeF** oligomers, the fluorescence lifetimes of **S1-3** were found to decrease with chain length. τ_{Av} of **S1** was 6.08 ns, **S2** was 4.85 ns and **S3** 3.00 ns. Due to its lower Pd content **S1** was also tested loaded with 0.36 wt. % Pd loaded by photodepostion and an almost identical spectrum to pristine **S1** (Figure 28). Similarly, samples of **S2** and **S3** loaded with 3 wt. % Pd showed minimal difference in their TCSPC spectra (Figure 28). **S2** had an identical τ_{Av} of 4.85 ns, whilst **S3** decreased slightly to 2.76 ns.

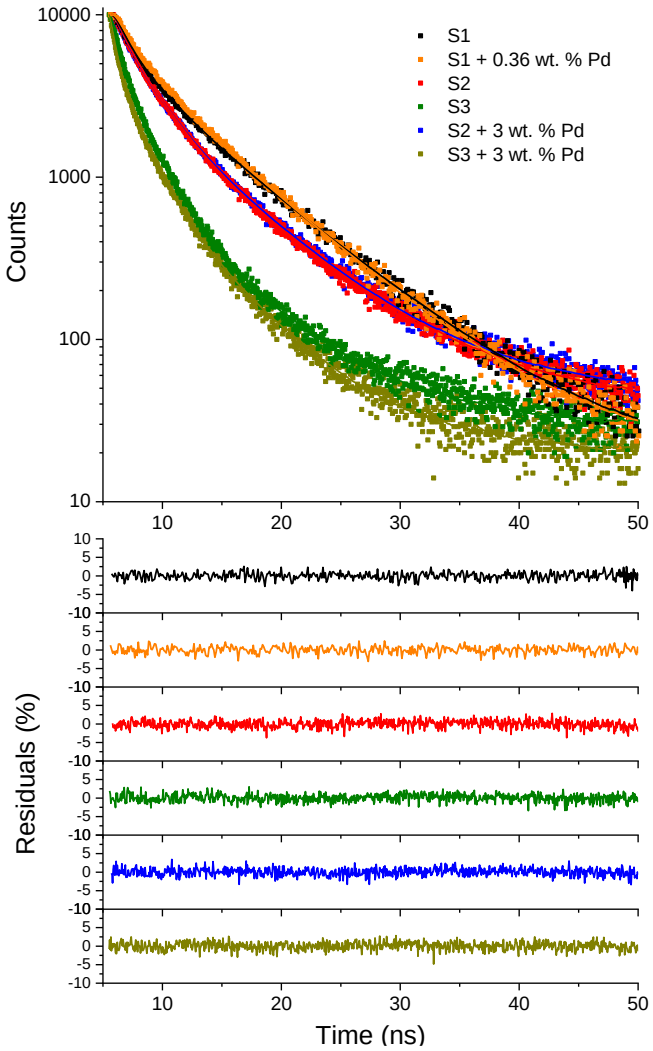

Figure 31: TCSPC spectra of the **S** oligomers in the solid state. Data (points), fit (line) and residuals (bottom). **S1** excited with a 295 nm laser, **S2** and **S3** excited with a 375 nm laser.

3.4.3 Photocatalytic hydrogen production in the solid state

S1, **S2** and **S3** were insoluble in the aqueous Na_2SO_3 / Na_2S scavenger system, as described previously. Hydrogen evolution of pristine **S1** was tested along with a sample with 0.36 wt. % Pd added by photodeposition to give similar loadings to those found in **S2** and **S3**. Using the $\lambda > 295$ nm filter pristine **S1** evolved hydrogen at a rate 8 µmol h^{-1} g^{-1} whilst the sample with added palladium was almost twice as active with a HER of 15 µmol h^{-1} g^{-1}. This, however, was still significantly lower than the dimer and trimer, which had rates of 81 and 286 µmol h^{-1} g^{-1}, respectively. An increase in activity with increasing chain length was also found when using the UV-only $275 < \lambda < 400$ nm filter although to a lesser extent than under broad spectrum radiation; moving from **S1** (with equated Pd levels) to **S2** to **S3** HER

increased from 33 to 50 to 162 µmol h^{-1} g^{-1}. The pristine **S1** with no Pd added showed a slightly lower rate of 25 µmol h^{-1} g^{-1}.

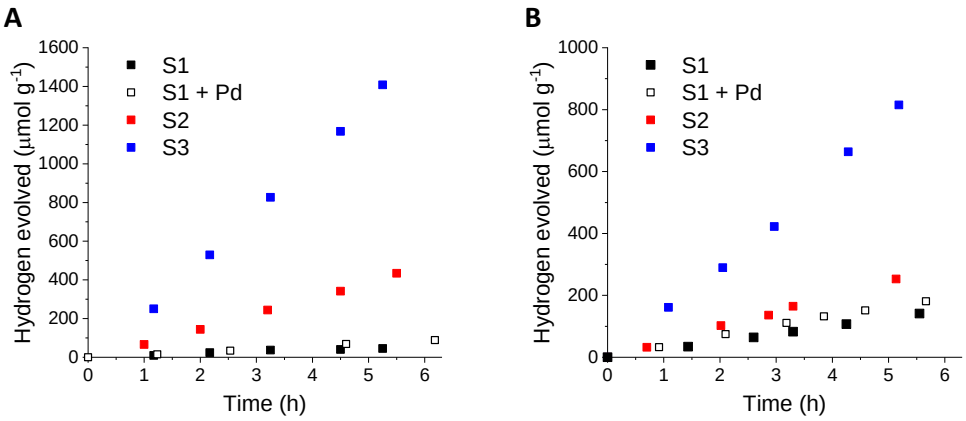

Figure 32: Photocatalytic hydrogen evolution of the **S** oligomers (25 mg) suspended in $Na_2S_{(aq)}$ (0.35 M) / $Na_2SO_{3(aq)}$ (0.2 M) (25 mL), 300 W Xe light source, using a $\lambda > 295$ nm filter (A) and using a $275 < \lambda < 400$ nm filter (B).

Hydrogen evolution was next tested using the TEA/MeOH/Water scavenger system (Figures 30). As with the **MeF** oligomers, the monomer was found to partially dissolve in this mixture and therefore **S1** should not be compared directly with **S2** and **S3**, which were both insoluble and stable as suspensions. Using the $\lambda > 295$ nm filter, pristine **S1** evolved hydrogen at an average rate of 26 µmol h^{-1} g^{-1} over the first 3 hours of irradiation. However, hydrogen evolution did not remain linear, with a sharp decrease to just 8 µmol h^{-1} g^{-1} for hour 5 – 6 (this is discussed further in the next section). Activity increased rapidly with chain length in this system; **S2** had a hydrogen evolution rate of 414 µmol h^{-1} g^{-1} and **S3** 2073 µmol h^{-1} g^{-1}. Again, this trend was preserved on moving to the $275 < \lambda < 400$ nm filter with HERs of 20, 101 and 526 µmol h^{-1} g^{-1} for **S1**, **S2**, and **S3**. Given that both **S2** and **S3** have absorption profiles that stretch into the visible region the **S** oligomers were also tested for hydrogen evolution using a $\lambda > 420$ nm filter. **S1** produced no measurable hydrogen over 5 hours of irradiation but **S2** showed low activity (HER = 26 µmol h^{-1} g^{-1}) and **S3** retained a high rate of 1125 µmol h^{-1} g^{-1}. This was consistent with the EQEs of **S2** and **S3** at 420 nm, which were found to be 0.4 and 8.8%.

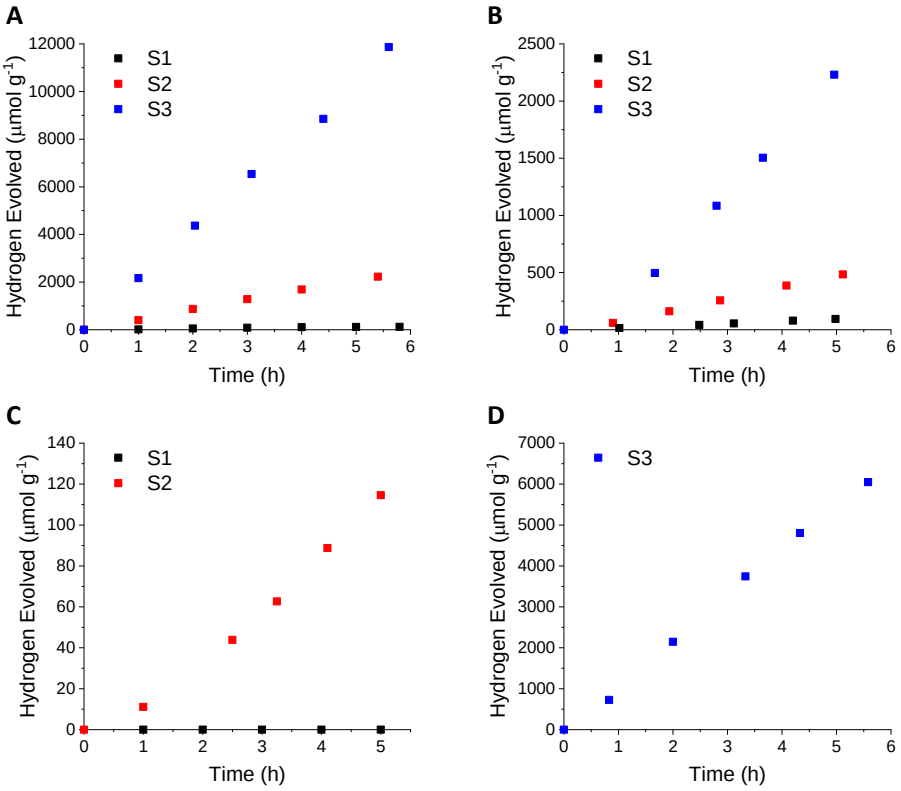

Figure 33: Photocatalytic hydrogen evolution of the **S** oligomers (25 mg) suspended in (1:1:1) water/methanol/triethylamine mixtures (25 mL), 300 W Xe light source, using a $\lambda > 295$ nm filter (A) a $275 < \lambda < 400$ nm filter (B) or $\lambda > 420$ nm (C and D).

Figure 34 shows the activity of **S2** and **S3** tested for photocatalysis over a longer period. Unlike the **S1**, **S2** shows good longevity; a slow drop off in activity was observed but with a reduction in rate of less than 50% over 50 hours. **S3** showed a more rapid drop off in activity with a rate of 576 µmol h^{-1} g^{-1} over hours 50 – 55, compared to an initial rate of 2080 µmol h^{-1} g^{-1}. This reduction in activity could be almost completely reversed by replacing the TEA/MeOH/water dispersant however (Figure 34B), indicating build-up of TEA oxidation products may be inhibiting catalysis, rather than degradation of the photocatalyst.

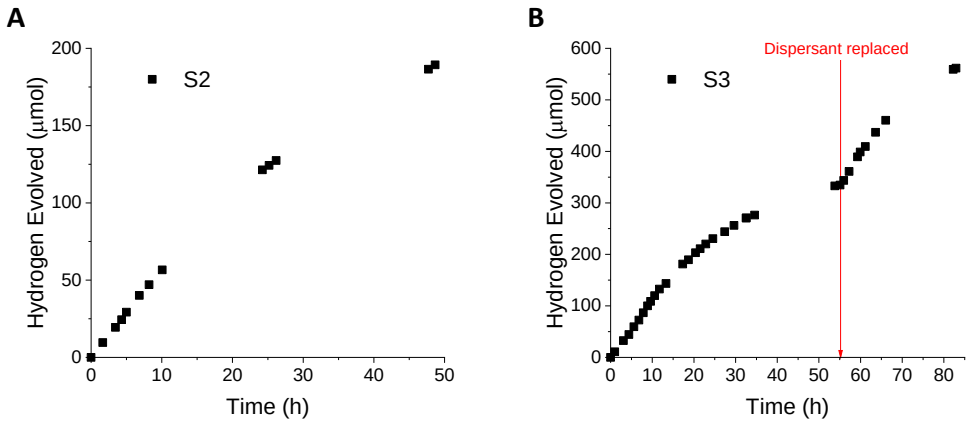

Figure 34: Photocatalytic hydrogen evolution of the **S2** (A) and **S3** (B) (25 mg) suspended in (1:1:1) water/methanol/triethylamine mixtures (25 mL), 300 W Xe light source, using a $\lambda > 295$ nm filter.

Analysis of **S1** collected after photocatalysis in the aqueous Na_2SO_3 / Na_2S scavenger system showed no sign of chemical break down by NMR but the sample collected from the TEA/MeOH/Water scavenger system showed significant impurity peaks (Figure 35C). In order to analyse this chemical breakdown, a sample of **S1** was irradiated for 72 hours in the TEA/MeOH/water photolysis mixture and was found to fully convert to a single product. Analysis by NMR spectroscopy (^{1}H, ^{13}C ATP, ^{1}H COSY and HSQC) and mass spectrometry (Section 3.10.2) indicated this material was the triethylamine salt of [1,1'-biphenyl]-2-sulfonic acid. This transformation was thought to be due to oxidation of **S1** by singlet oxygen or a superoxide anion and therefore a sample of **S1** was also tested in the presence of nickel(II) dibutyldithiocarbamate, which has been shown to act as reactive oxygen species (ROS) scavenger.[53,54] With ROS scavenger the hydrogen evolution of **S1** increased to 53 µmol h^{-1} g^{-1} and was linear over at least 23 hours (Figure 35B). Material collected post photolysis was found to be **S1** by NMR (Figure 35C), indicating oxidation of the substrate was effectively suppressed.

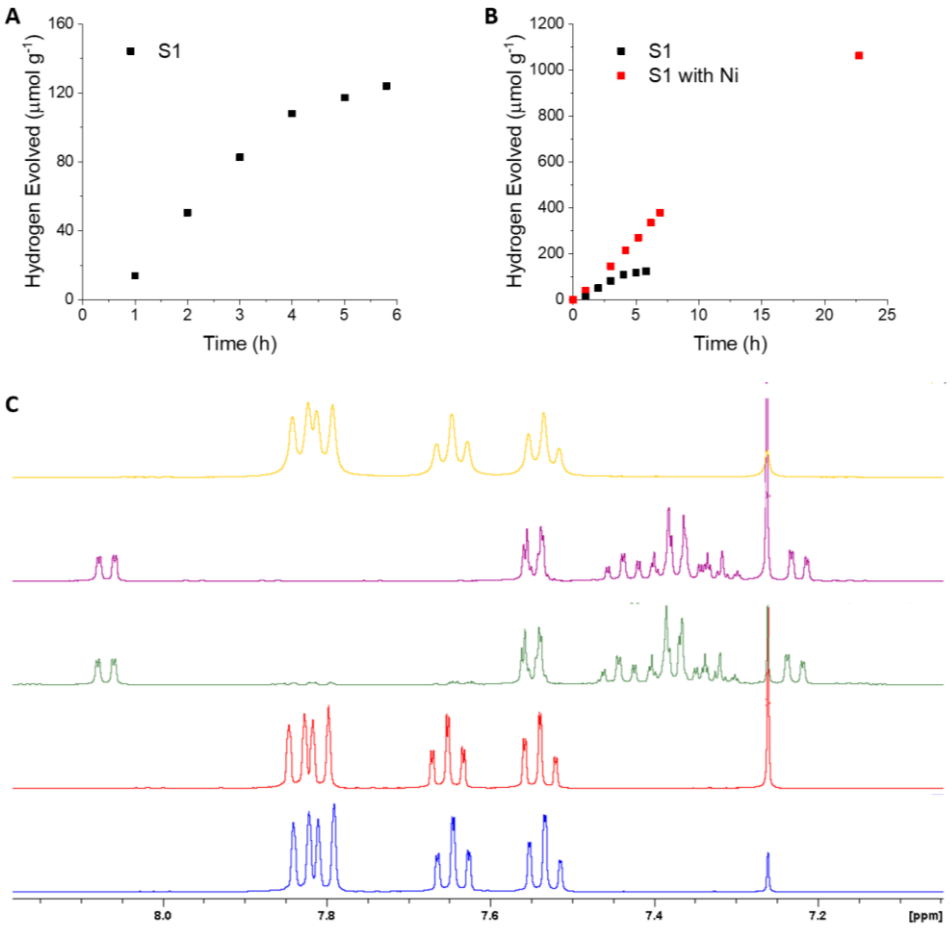

Figure 35: Photocatalytic hydrogen evolution of the **S1** (25 mg) with and without the addition of nickel(II) dibutyldithiocarbamate (1 mg) suspended in (1:1:1) water/methanol/triethylamine mixtures (25 mL), 300 W Xe light source, using a $\lambda > 295$ nm filter over 5 hours (A) and 1 day (B). (C) NMR spectra of **S1** pre photolysis (blue), collected post photolysis in aqueous Na_2S/ Na_2SO_3 for 5 hours (red), collected post photolysis in water/methanol/triethylamine after 5 hours (green), or 72 hours (purple) without nickel(II) dibutyldithiocarbamate, or after collected post photolysis in water/methanol/triethylamine 24 hours with nickel(II) dibutyldithiocarbamate

PXRD and IR spectra of **S2** and **S3** collected after extended photocatalysis were very similar to the as synthesised materials, suggesting they are more stable than the monomer Figure 36. It is possible that **S2** and **S3** also oxidise under photolysis in the TEA/MeOH/water mixture but at a much slower rate than the **S1**. The instability of the monomer may be partially due to the fact it dissolves under these conditions whilst the dimer and trimer are stable as solid suspensions. For example, in aqueous Na_2S/ Na_2SO_3, where all materials are stable as solids, no sign of chemical breakdown was observed.

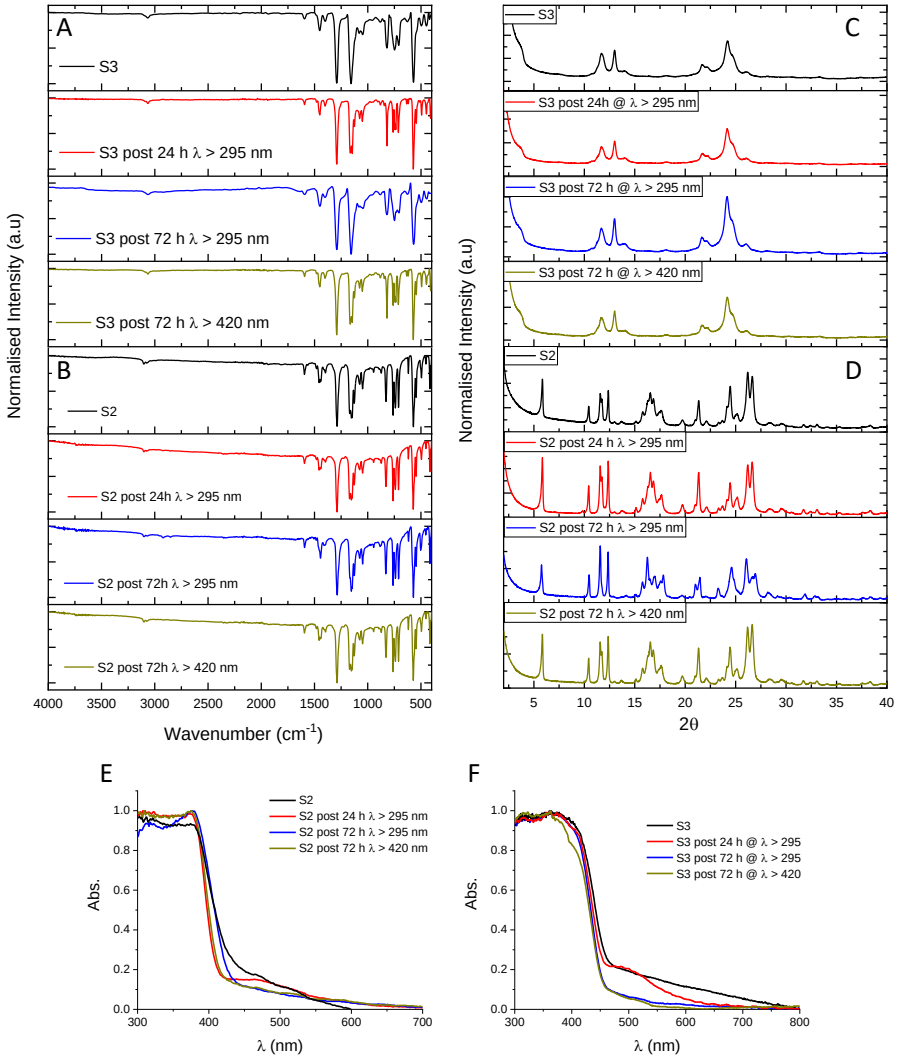

Figure 36: FT-IR spectra of **S2** (A) and **S3** (B), PXRD spectra of **S2** (C) and **S3** (D) and solid-state UV-Vis spectra of **S2** (E) and **S3** (F), collected pre and post photolysis using various filters and illumination times in the water/methanol/triethylamine system.

3.4.4 Time-resolved absorption spectroscopy

The excited state kinetics of **S2** and **S3** were studied in more detail by transient absorption spectroscopy. A suspension of **S2** in the triethylamine/water/methanol mixture probed at 1.0 ps following excitation by 355 nm laser showed a 630 nm exciton absorption peak in the transient spectra (Figure 37A). The exciton peak for **S3** under equivalent conditions was shifted to 710 nm and is itself at a lower wavelength than the corresponding peak found for the polymer equivalent of the **S** oligomers, **P10**.[44] Whilst these peaks are thought to originate from exciton absorptions the presence of an electron donor in the system means that some polaron formation may also occur. This redshift in exciton absorption with increasing chain

length is in good agreement with the corresponding absorption onsets and photoluminescent emission maxima. In line with the TCSPC experiments exciton lifetime was found to decrease significantly moving from **S2** to **S3** (Figure 37B). Interestingly, little change in exciton lifetime was found on moving from the hole scavenger containing triethylamine/water/methanol mixture to a water suspension indicating that, whilst it was possible that polarons could form in the system containing TEA electron donor, the signal is mainly excitonic.

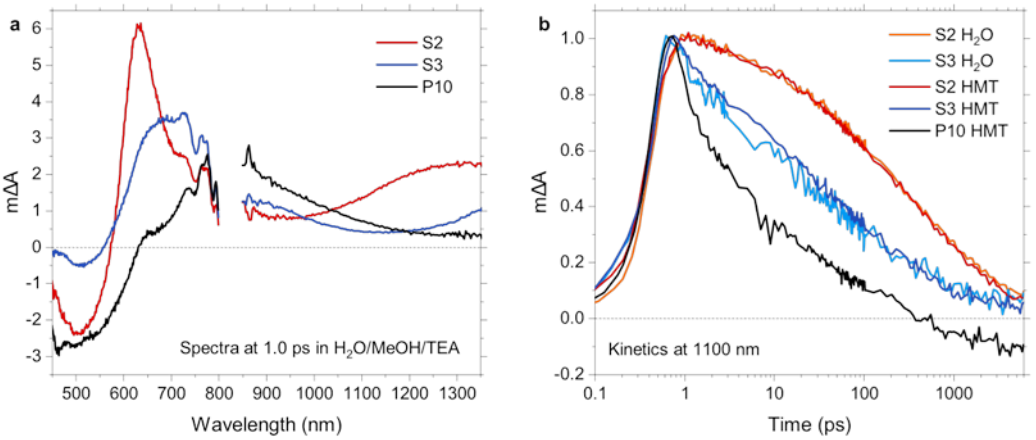

Figure 37: Exciton signatures and dynamics in S2, S3, and P10 suspensions. (a) Transient absorption spectra probed at 1.0 ps using polymer particles suspended in a H_2O/MeOH/TEA mixture, and (b) transient absorption kinetics probed at 1100 nm as obtained from suspensions in H_2O and H_2O/MeOH/TEA. All experiments were performed using an excitation wavelength of 355 nm and a fluence of 0.08 mJ cm^{-2}.

The transient absorption spectra of **S2** and **S3** suspended in TEA/MeOH/water were also probed at 100 µs following 355 nm excitation are shown in Figure 38A. **S3** exhibits a peak around 600 nm. This transient absorption feature is very similar to an electron polaron absorption previously observed for P10,[44] both in spectral shape and spectral position. The inset shows the kinetics when probing the sample at 600 nm following excitation. The feature persists with significant magnitude up to 100 milliseconds, again matching well with long-lived polaron reported for P10. The lifetime of these features are sufficiently long to drive proton reduction.[44] **S2**, on the other hand, does not show a clear polaron absorption peak at these longer timescales with low ΔA across the visible range probed. The most prominent transient absorption feature in this sample, lies above 1000 nm and could be the result of a NIR polaron absorption.

S2 and **S3** were also measured using PIAS (Figure 38B), to give quasi-steady state illumination conditions. 2.7 s pulses of a 365 nm LED were used for excitation. The spectra

of **S3** under these constant illumination condition show the same 600 nm feature found during the transient measurement indicating it is also the results of electron polarons on the sample. The inset shows the accumulation of electron polarons over the timescale of seconds, before the signal reaches a saturation point. This suggests that, at this point, polaron formation is in a steady state with the combined loss processes of polaron decay through recombination and polaron utilisation in proton reduction. **S2** again displays lower signal amplitudes than the trimer with a weak absorption feature towards the NIR. This mirrors the transient measurements and suggests that lower concentrations of electron polarons accumulate on **S2** under constant illumination conditions compared to **S3**.

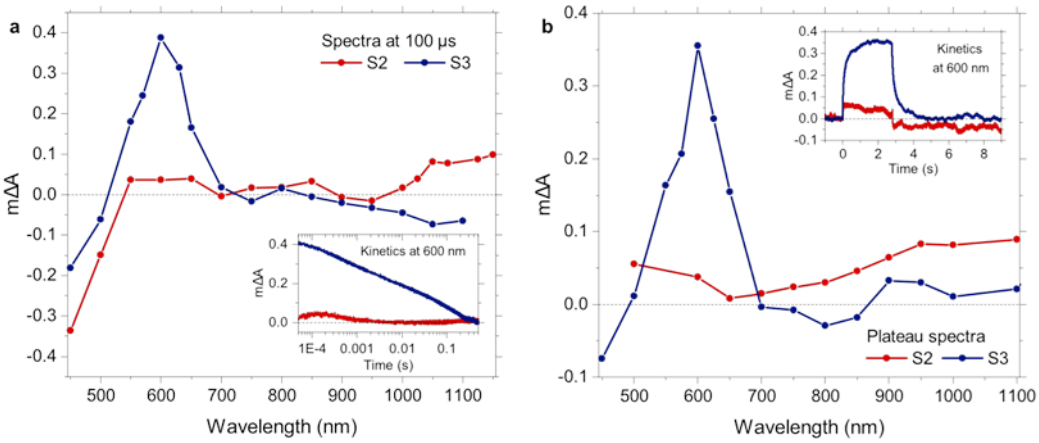

Figure 38: Optical signals from suspensions of **S2** and **S3** in TEA/MeOH/water under transient and steady state conditions. (**a**) Transient absorption spectra obtained upon 355 nm excitation using a fluence of 0.40 mJ cm^{-2}, and (**b**) photoinduced absorption spectra obtained upon 365 nm excitation using a fluence of 5.5 mW cm^{-2}. The insets show the corresponding kinetics probed at 600 nm showing (**a**) the decay of intermediates following a 4-7 ns laser pulse, or (**b**) their accumulation during a 2.7 s LED pulse and their decay after the LED is turned off.

3.4.6 Photocatalytic activity at high Pd contents

The photocatalytic tests above were performed on **S1-3** with palladium levels of 0.2 -0.4 wt. %, but this is significantly below the co-catalyst loading levels found to be optimal for proton reduction in carbon nitrides[56] and other polymer materials.[38,57,58] As such **S1-3** were also tested with the addition of 3 wt. % palladium by photodeposition of $[Pd(NH_3)_2Cl_4]$. The dissolution of **S1** in the photolysis mixture meant accurate determination of deposition yield was not possible but ICP-MS analysis of the **S2** and **S3** materials showed Pd contents of 2.1 and 2.5 wt. % respectively. STEM imaging showed that palladium nanoparticles of *circa* 5 – 30 nm had formed on the surface of **S2** and **S3** (Figure 39 and 40), with reasonable distribution. It is possible smaller nanoparticles of Pd are also present but below the resolution of the STEM instrument.

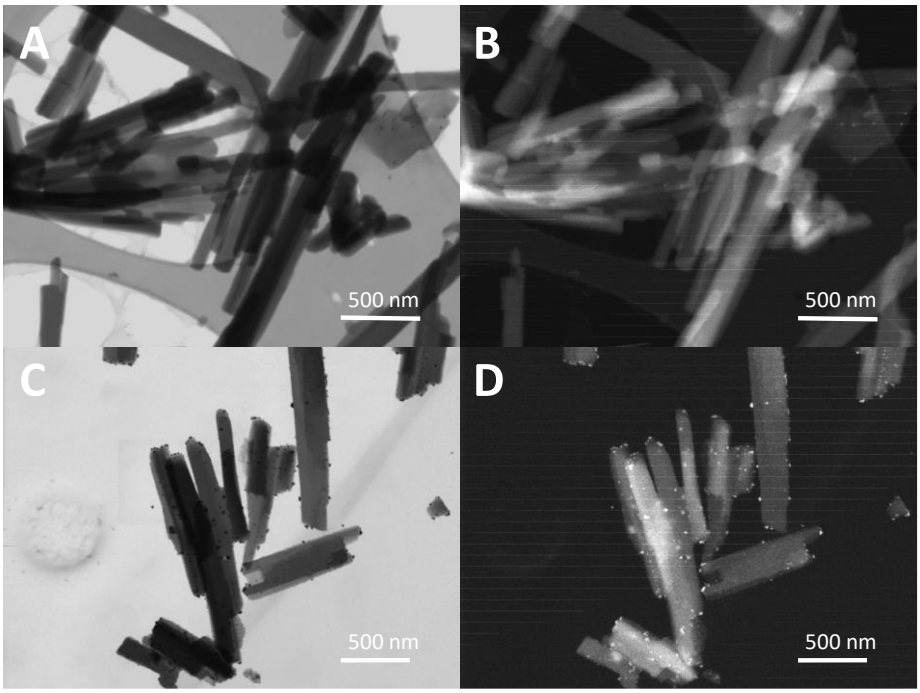

Figure 39: STEM imaging of **S2** as synthesised in bright field (BF) mode (A) and high-angle dark field (HADF) mode (B) and **S2** with 3 wt. % Pd added by photodeposition in BF mode (C) and HADF mode (D).

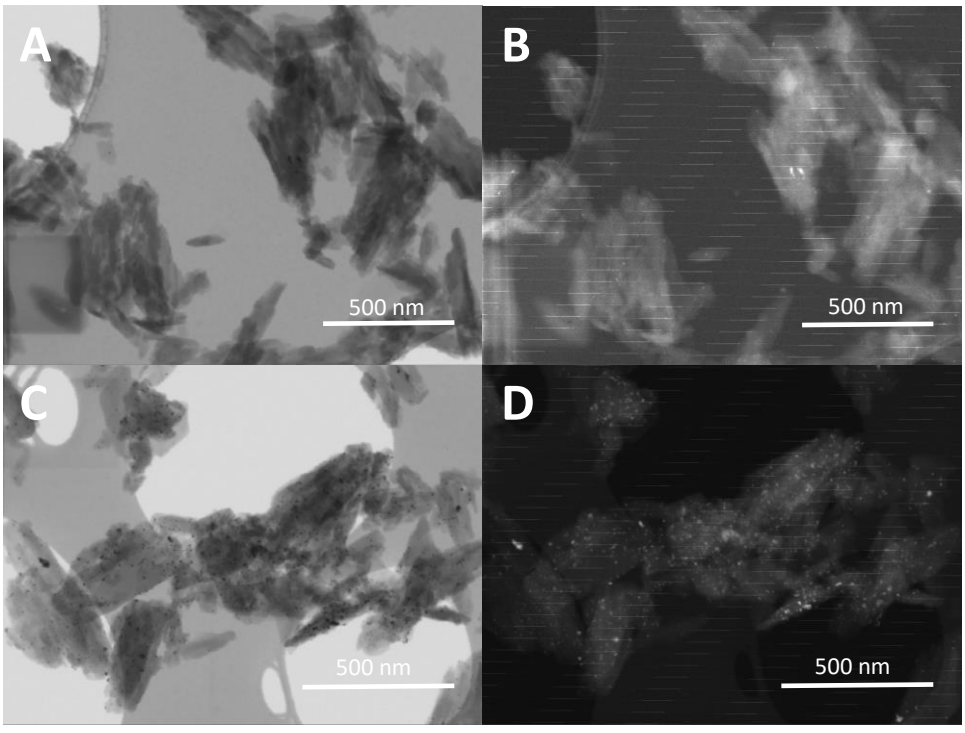

Figure 40: STEM imaging of **S3** as synthesised in BF mode (A) and HADF mode (B) and **S3** with 3 wt. % Pd added by photodeposition in BF mode (C) and HADF mode (D).

The hydrogen evolution of these materials in the water/triethylamine/methanol system is shown in Figure 41 compared to the as synthesised samples. As discussed previously, **S1** was partially soluble and unstable in this solvent system and the sample with 3 wt. % Pd added reached a maximum hydrogen evolution of 86 µmol h^{-1} g^{-1} before decreasing significantly at 3 hours. Again, **S2** and **S3** showed more linear evolution of hydrogen over 5 hours and both showed increases in activity upon addition of 3 wt. % Pd. **S2** with 3 wt. % Pd added had a HER of 1369 µmol h^{-1} g^{-1} , 3.3 times that of pristine **S2**. **S3** showed a similar, 3.2 times increase to 6550 µmol h^{-1} g^{-1} with 3 wt. % Pd.

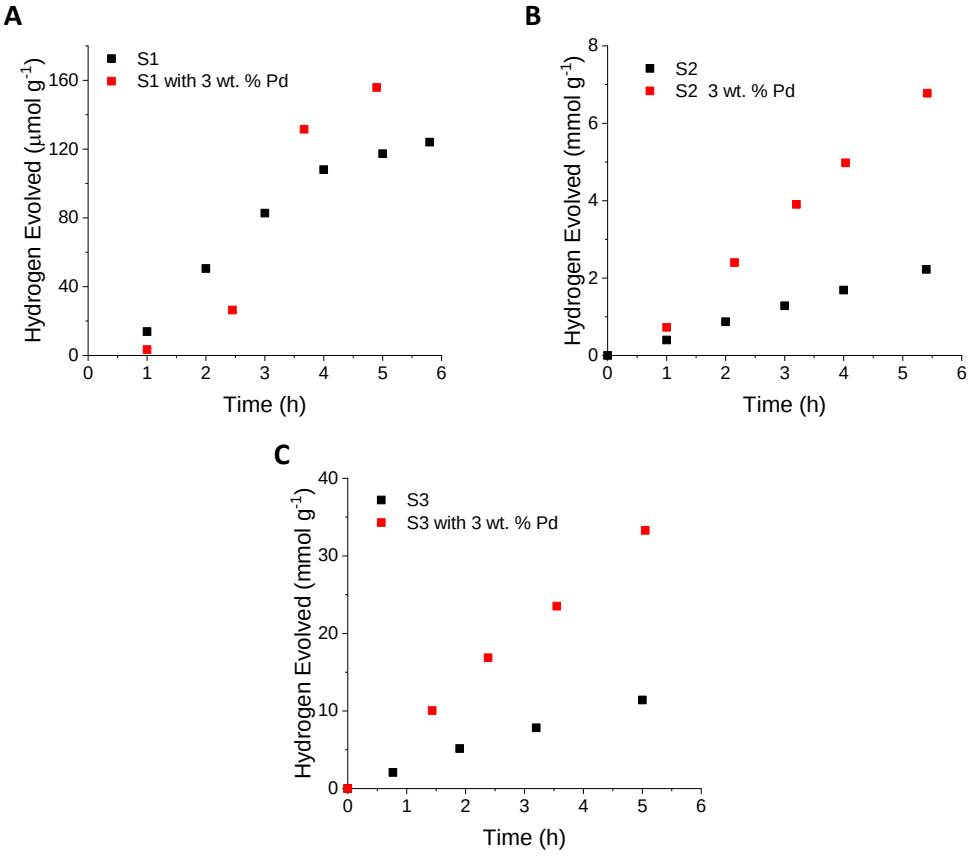

Figure 41: Photocatalytic hydrogen evolution of **S1**(A), **S2** (B) and **S3** (C) (5 mg) with and without the addition of 3 wt. % Pd, from photodeposition of $[Pd(NH_3)_2Cl_4]$, suspended in (1:1:1) water/methanol/triethylamine mixtures (5 mL), 300 W Xe light source, using a $\lambda > 295$ nm filter.

3.5 Predicted optical properties

The systems in this chapter rely on semiconductors that act as the photosensitiser, the transport medium for charged species, and provide the electrochemical potentials required for reaction. As such, whilst increasing the onset wavelength for absorption of a photocatalysts is beneficial up to a point, smaller HOMO-LUMO (or band in extended

systems) gaps also reduce the thermodynamic driving force for redox reactions. UV-Vis measurements can be used to approximate the size of the optical gap in these systems (Tables 1-3) but these do not provide information on the positioning of these energy levels relative to the redox potentials of the two photochemical half reactions examined here; namely, the reduction of protons to molecular hydrogen and the oxidation of the triethylamine or sodium sulphide scavenger. It is clear that if the relevant energy levels of a semi-conductor photocatalyst do not straddle these redox potentials then hydrogen production will not be energetically feasible. It has also been shown previously, that even across systems where proton reduction and scavenger oxidation are energetically favourable, the magnitude of this driving force can have a strong effect on hydrogen production rates. The potentials of the frontier orbitals in the three groups of oligomers discussed above were predicted using (TD)-DFT using previously described methods (Figure 42D).[59] The calculations were performed on gas phase lowest energy conformational structures and the driving force for proton reduction was estimated by comparing the potential required for proton reduction with that of the electron affinity (EA) of the oligomer. Similarly, the driving force for scavenger oxidation was compared with the oligomers ionisation potential (IP), to approximate the driving force for the oxidation half reaction. This gives an indication of the energy levels of the separated charge carriers (i.e. electron and hole) but, to also give an indication of the energy levels associated with the initial oligomer exciton, the IP* and EA* values of the oligomers in the excited state were also calculated. The predicted optical gaps from these band calculations correlated well with the optical gaps observed for the oligomers in chloroform solution (Figure 42B). The observed values were generally slightly higher, possibly due to calculating the optical gap from the maxima in absorption rather than the onset. Alternatively, differences in conformation between the gas phase and chloroform solution could be responsible.

As expected the increased conjugation lengths observed on moving from **MeF1** to **MeF3** leads to a lowering of the oligomer LUMO energy and subsequent shift in EA potential to less negative values (relative to SHE), as well as raising the oligomer HOMO energy which moves the IP potential to less positive values (relative to SHE). As such, the driving force for both proton reduction and for scavenger oxidation decrease with increasing chain length. Whilst all

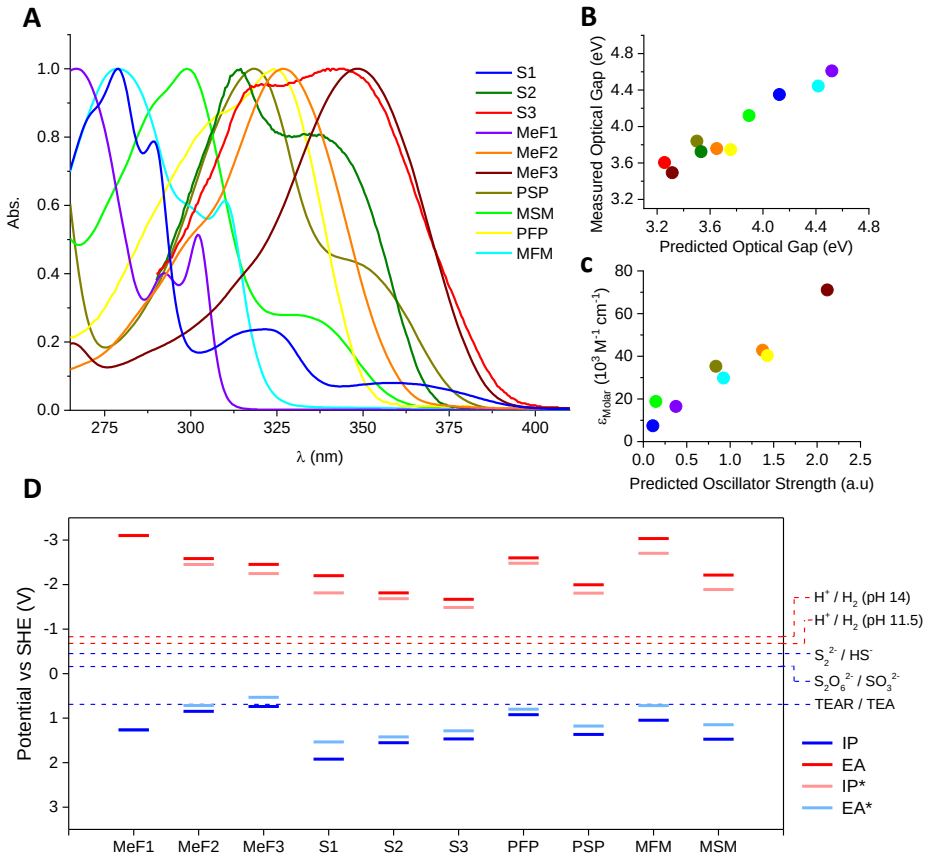

Figure 42: A) Normalised UV-Vis absorption spectra of the oligomers in chloroform; B) Plot of the TD-DFT predicted optical gap versus the value obtained from absorption maxima in chloroform solution;C) Plot of the oscillator strength predicted by TD-DFT versus the measured molar extinction coefficient (ε_{Molar}) in chloroform solution; D) Potentials of the free charge carriers (IP,EA) and excitons (IP*,EA*) oligomers predicted by DFT and relevant solution reactions (at pH 11.5 for the case of using triethylamine as hole scavenger and pH 14.0 in the case of SO_3^{2-} and HS^-). Potential of the 2-hole oxidation of triethylamine to diethylamine and acetaldehyde not shown as it lies in a similar place as the proton reduction potential for pH 11.5. *Reproduced, with permission, from reference [87]- Published by The Royal Society of Chemistry.*

of the **MeF** oligomers have large (>1 V) driving force for proton reduction this result is more significant for the oxidation half reaction; **MeF1** has a 0.56 V driving force for the initial oxidation of TEA but in **MeF2** this is reduced to 0.16 V and just 0.05 V in **MeF3**. The trend is even more significant when examining the excited state EA*, a measure for the potential required for exciton quenching by the scavenger, where the driving force for **MeF2** is reduced to 0.03V and in **MeF3** this process is in fact energetically disfavoured. It should be noted that, without transient absorption spectroscopy of these materials, it is difficult to determine whether scavenger oxidation is performed by an exciton (thus helping the generation of a separated charged species) or by an already separated hole on the oligomer

and thus which of the two driving force values is most applicable. It should also be noted that, whilst the initial step in the oxidation of TEA may provide a kinetic bottleneck for **MeF3**, all of the oligomers have large driving forces for the overall oxidation of TEA to DEA. Both HS^- and SO_3^{2-} are present in the Na_2S/Na_2SO_3 and could act as the hole scavenger. Whilst SO_3^{2-} is the easiest to oxidise overall (2 hole oxidation to SO_4^{2-} has a reported experimental potential of -0.94 V) the initial one-hole oxidation of HS^- to S_2^{2-} is easier (-0.45 V) than that of SO_3^{2-} to $S_2O_6^{2-}$ (-0.16 V).[60] If HS^- anion acts as the hole scavenger then all **MeF** oligomers have overpotentials of at least 1 V for the one hole oxidation.

PSP, **MSM**, **PFP** and **MFM** were all predicted to have large (> 1 V) driving forces for proton reduction and the one hole oxidation of HS^- but the 'acceptor' properties of the sulfone group were apparent in the less negative EA and more positive IP values of **PSP** and **MSM** relative to the fluorene analogues. This means the sulfonated materials had larger driving forces for the scavenger oxidation whilst the fluorene analogues had larger driving forces for proton reduction. Moving from phenylated to mesitylated oligomers the ground state EA and IPs moved further from zero, reflecting the increased optical gaps in these materials, and increasing driving force. Interestingly when looking at the excited state IP* and EA* values the driving force by excitons (rather than separated charge species, as indicated by the ground state EA and IP) was 0.3 V smaller in both mesitylated compounds. This large difference could be due to considerable conformational change in the oligomer backbone on moving from an exciton to separated charge carriers.

The IP of ground state **S1** is predicted to lie 1.23 V below the redox potential for initial oxidation of TEA, whilst the electron affinity of the first excited state (EA*) was estimated to be 0.84 V below, indicating that both a separated hole or an exciton had sufficient driving force for oxidation half reaction. Similarly, the ground state EA and the excited state IP* lie 1.52 and 1.13 V above the proton reduction potential respectively meaning hydrogen evolution should be thermodynamically favourable for a separated electron or an exciton. As expected from the contracted band gaps, the over-potentials for both half reactions decrease with chain length. The difference in ground state and excited state potentials were also smaller for **S2** and **S3**. The excited state potentials give the smaller predicted driving forces but both **S2** and **S3** still have good thermodynamic over-potentials for initial TEA oxidation (0.73 V and 0.6 V) as well as proton reduction (1.00 V and 0.81 V).

In addition to predicting the energy levels involved in redox reactions (TD)-DFT was used to approximate the efficiency of light absorption by calculating the oscillator strengths of the transitions involved in photoexcitation. Oscillator strength depends on a number of factors

including the energy gap between the two states and the spatial overlap between orbitals.[61,62] Figure 42C shows the strong correlation between the predicted oscillator strengths and the measured extinction coefficients in chloroform solutions.

The influence of the energy gap on oscillator strengths is evident on when comparing the oligomers of different chain length. Moving from **MeF1** to **MeF2** to **MeF3** the predicted oscillator strength increases from 0.38 to 1.37 to 2.12 as the band gap decreases from 3.73 to 2.88 V. Accounting for the number of dimethyl fluorene units per molecule this is still an increase in oscillator strength "per fluorene unit in the molecule" of 86%. The same trend is found for the predicted oscillator strengths of the dibenzothiophene sulfone oligomers; values of 0.11, 1.02 and 1.77 are predicted for **S1-3**. The oscillator strengths of the dibenzothiophene sulfone oligomers are significantly lower than the dimethyl fluorene-based analogues. Similarly, both **MSM** and **PSP** are predicted to have smaller oscillator strengths than **MFM** despite their significantly smaller optical gaps. The highly electron withdrawing sulfone group creates a large dipole on dibenzothiophene sulfone units which would be expected to give more spatially separated frontier orbitals, decreasing the probability of transition.

3.6 Discussion of Results from Sections 3.2–3.5

Aside from chain length, it appears that the effective conjugation length, and thus frontier orbital energies and light absorption onsets, of oligomers can be altered by the substitution of phenylene groups for sterically hindered mesitylene groups. Crystal structures show the backbone of **MSM** and **MFM** have average dihedral angles between rings of 91° and 97° compared to 26° and 13° for **PSP** and **PFP**. This lack of planarization limits conjugation giving blue-shifted absorption onsets in the solid-state of 40 nm when comparing **PSP** to **MSM** and 96 nm for **PFP** compared to **MFM** with similar shifts in solution measurements. This twisting also appears to affect the magnitude of absorption as reflected in the significantly higher extinction coefficient of **PFP** and **PSP** versus **MFM** and **MSM**. The loss in light absorption of the mesityl substituted oligomers is reflected in their poorer photocatalytic activity under broad band irradiation. However, when using UV light only, the activities of **PSP** and **MSM** are very similar, as are **PFP** and **MFM**. It seems that the twisting of the oligomer backbone through mesityl substitution is primarily inhibiting photocatalytic activity by limiting light absorption. Under UV light, it appears that the functional group present in the oligomer core is the dominant factor rather than the substituent groups, with the dibenzo[*b*,*d*]thiophene sulfone containing oligomers having at least twice the activity of the fluorene oligomers. It has been previously shown that the hydrophilic nature of dibenzo[*b*,*d*]thiophene sulfone unit is important in its high catalytic

activity as it forms materials with small, easily dispersible particles. However, SLS measurements do not show that the particle sizes of **PSP** and **MSM** are significantly smaller than **PFP** and **MFM**, perhaps due to the high crystallinity of these materials and the fully aqueous scavenger system. Instead improved activity of the dibenzo[*b,d*]thiophene sulfone containing oligomers may be related to improved interaction with the scavenger at the crystal surface or the longer-lived excited states observed by TCSPC.

We do not observe the same trend in catalytic activity in solution; **PFP** displays by far the highest activity of 120 μmol $h^{-1}g^{-1}$, **MSM** has a maximum rate of 44 μmol $h^{-1}g^{-1}$ whilst **PSP** and **MFM** had rates of 14 and 13 μmol $h^{-1}g^{-1}$, respectively. Accounting for differences in absorption gives ACAs of 0.3, 1.9, 2.4 and 0.7 for **PSP**, **MSM**, **PFP** and **MFM** respectively. It appears that the advantages provided by the dibenzo[*b,d*]thiophene sulfone unit are not as dominant in solution. This is perhaps surprising given that the extended PL lifetimes of **PSP** and **MSM** compared to their fluorene analogues were observed in both the solid state and solution TCSPC. It is possible that in a homogenous system, where contact between oligomer, electron donor and water is maximized, the rate limiting factor for hydrogen production may change. Additionally, the crystal packing structures observed for the dibenzo[*b,d*]thiophene sulfone bearing oligomers could improve exciton or polaron mobility between molecules and play a role in their improved activity in the solid state which is not applicable in the homogenous system.

Moving back to the solid state and examining the other two groups of oligomers, increasing oligomer length leads to a red-shift in absorption on-set which we may expect to increase hydrogen production rate. On the other hand, this "positive" effect is accompanied by a predicted decrease in driving-force for proton reduction as well as scavenger oxidation. Looking at the dimethylfluorene oligomers using a triethylamine scavenger, it would appear that the absorption effect dominates as **MeF3** is more active than its shorter chain length analogues. However, the dissolution of the monomer under these conditions could also significantly affect photocatalytic activity. Indeed, when we switch to a system where **MeF1-3** are all stable as solids and normalise the Pd levels then the trend changes significantly; **MeF1** has higher HER than both **MeF2** and **MeF3** using a Na_2S scavenger when using solely UV light, and when using broad spectrum. This is particularly significant considering that **MeF1**, with solid state absorption onset at 322 nm is able to absorb a much smaller fraction of the incoming radiation than **MeF2** and **MeF3**. This trend could be a consequence of **MeF1**'s increased driving force, but this would be unexpected given that all **MeF** oligomers have a > 1 V overpotential for both half reactions in the Na_2S system. Alternatively, the trend in HER also correlates with increased fluorescence lifetimes, suggesting recombination of excitons before quenching by the electron donor could be

limiting the activity of the longer chain length oligomers. This is consistent with the strong decrease in fluorescence lifetime and strong increase in HER of **MeF1** upon addition of palladium. In these materials, palladium may increase activity by reducing losses by radiative exciton recombination. This could explain the differing trends in activity when moving between electron donors; it is possible that improved scavenger interaction in the TEA/MeOH/Water system means reductive quenching occurs faster, reducing recombination, which favours the short lifetime, longer oligomers.

The dibenzo[*b,d*]thiophene sulfone oligomers showed significantly higher photocatalytic activities compared to the dimethylfluorene analogues which is consistent with our previous work comparing related polymer analogues.[63] Unlike the **MeF** oligomers, the **S** family of oligomers maintain the hierarchy of increasing activity with increasing chain length under all tested conditions. The difference however, varied significantly; using Na_2S scavenger **S3** is 20 times more active than **S1** under broad spectrum irradiation whilst under solely UV-light this drops to a factor of 4. This suggests that a majority, but not all, of the longer chain length oligomers superior activity is due to their redshifted absorption onset. The oscillator strengths predicted by DFT for these materials' S_o to S_1 transitions indicate that absorption intensity will also increase significantly with chain length; after accounting for the number of monomer units per molecule the predicted oscillator strength of **S3** is over five times that of **S1**. Particle size could also play a role in the lower activity of **S1** as it has a significantly higher D[3,2] than the dimer and trimer. These factors do not, however, explain the differences in HER between **S2** and **S3** whose particle sizes and oscillator strengths are much closer.

Whilst photoexcitation is important, the next stage towards hydrogen production, exciton separation into charged species, must also be considered. In this transient absorption spectroscopy does indicate a difference between the two materials. Previous studies on the polymer analogue of **S1-3** (**P10**) have found that upon illumination and in the presence of an electron donor, long-lived electron polarons form on the polymer.[44] Whilst **S3** shows a comparable polaron absorption peak at 600 nm when probed at 100 μs, **S2** shows a much smaller absorption. Assuming the materials absorb a comparable intensity of the 355 nm laser, this would indicate the polaron yield of **S2** is significantly lower then **S3**, correlating well with its reduced HER even under exclusively UV irradiation.

As with the **MeF** oligomers, the fluorescence lifetimes of the **S** oligomers decrease with increasing chain length. Unlike dimethylfluorene however, Pd content was found to have little effect on the lifetime of the excited states of **S1, S2** and **S3** as measured by TCSPC, at least over the Pd contents measured. Photocatalytic activity, on the other hand, shows a high

dependence on Pd content. Along with the decreasing lifetime along the **S1**/**S2**/**S3** series (by both TAS and TCSPC); that is, in the order of increasing performance, these contrasting trends suggest that the performance differences observed for these materials are not due to differences in exciton lifetime. This contrasts with the dimethylfluorene-based materials and points to fundamental differences in the excited state behavior of these two families of materials.

Previous studies on the fluorene containing F8BT polymer have shown that Pd promotes exciton separation and acts as an electron sink, thus causing electron polarons to become localised on Pd centres.[37] The behaviour of the **MeF** oligomers would also be consistent with this mechanism but further kinetic analysis would be needed to confirm this. In contrast the steady-state TAS experiments on **S3** (Figure 38B) show that electron polarons accumulate on the oligomer under constant illumination and thus suggests that transfer of the electron from the oligomer to a Pd active center could be limiting hydrogen production. This would be consistent with the high dependence of HER on Pd loading and might be due to a low mobility of electron polarons in the solid, with increasing Pd content reducing the diffusion length required for transfer to an active site.

Crystallinity over large length scales does not appear to be a significant factor in these materials' activity, as hydrogen evolution decreases moving from semi-crystalline **S3** to polycrystalline **S2** to single crystals of **S1**. This is not to say that ordering of dibenzothiophene sulfone units on smaller length scales is not beneficial to activity, indeed examining the crystals structures of **S1** and of sublimed **S2** and **S3** (which appear to be the same polymorph to as synthesised) it is evident that these materials have greater planar overlap of aromatic units and smaller stacking distances than their dimethlyfluorene analogues (Figures 3 and 23). It is possible that this more favourable packing accounts in part for the generally higher activity of the dibenzothiophene sulfone oligomers. The increased hydrophilicity of the more polar dibenzothiophene sulfone units is also thought to play a role as it results in significantly smaller particle sizes in suspension.

Interestingly, the visible light activity of the dibenzo[*b*,*d*]thiophene sulfone trimer **S3** (1125 μmol h^{-1} g^{-1}) is of the same order of magnitude as its polymer analogue, **P10**, under equivalent conditions (2825 μmol h^{-1} g^{-1}). This challenges the general assumption that long chain lengths are required for significant photocatalytic hydrogen production. Only three monomer units are required to generate a material with an EQE of 8.8% at 420 nm, outperforming many polymeric catalysts in literature.

Given the results of sections 3.2 to 3.4, the effects of backbone twisting and the role of palladium on photocatalysis were also investigated using further oligomeric and polymeric materials and this is discussed in the next two sections.

3.7 Substituted Dibenzothiophene Sulfone Oligomers

One example of where structure-activity relationships are important, is in the design of conjugated polymers with alkyl substituents. Alkyl and other side chains are employed extensively in organic photovoltaic materials and increasingly in organic photocatalysts to impart solubility. However, the placement of such chains is highly significant when we think about the backbone twisting observed in **MSM** and **MFM** and resultant negative impact on hydrogen evolution. Whilst co-polymerising dibenzothiophene sulfone units with alkylated fluorenes has been shown to be an effective method for increasing solubility, photocatalytic activity is found to decrease significantly with decreasing dibenzothiophene sulfone content. As such, alkylating the dibenzothiophene sulfone monomer directly has the potential to impart both processability and high activity. To investigate the effect of adding larger, more solubilising hexyl chains directly to this active unit, the un-alkylated polymer **P7** is compared to its hexylated analogue **P7$_6$** whilst **S3** is compared to the increasingly hexylated **SS$_6$S**, **S$_6$SS$_6$** and **S$_6$S$_6$S$_6$** (Scheme 5).

3.7.1 Synthesis and characterisation

Meta-linkages in several phenylene-based polymers have been shown to give shorter effective conjugation lengths.[38,64–66] It was therefore thought to be desirable for photocatalytic activity to maintain para-linkages along the polymer backbone. This theoretically leaves the 1,2 or 4 (and the corresponding 5, 6 or 8) positions of dibenzo[*b*,d]thiophene sulfone free for alkylation, Steric limitations mean the 2 and 6 positions are the most accessible: however, in dibenzothiophene sulfone, these positions are highly electron deficient, making them difficult to functionalise. Alkylation was therefore performed on the thiophene analogue followed by oxidation to the sulfone. Briefly, bromination of dibenzothiophene resulted in 2,6-dibromdibenzothiophene, and was followed by lithium halogen exchange with *n*-hexyl lithium and 1-bromohexane to yield 2,6-dihexyldibenzothiophene before oxidation with peroxide to the sulfone analogue, **S$_6$** (Scheme 4).

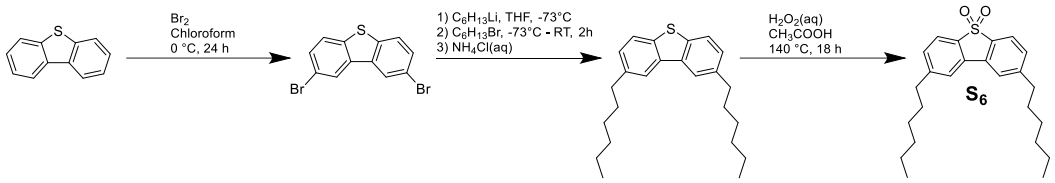

Scheme 4: Synthesis of hexylated dibenzo[*b*,d]thiophene sulfone

NBS bromination of **S$_6$** in H_2SO_4 gave the 3-bromo- and 3,7-dibromo-2,6-dihexyldibenzo[*b*,d]thiophene sulfone monomers. The latter was co-polymerised with 1,4-benzenediboronic acid bis(pinacol)ester to give **P7$_6$** and coupled to 3-dibenzo[*b*,*d*]thiophene sulfone) boronic acid (pinacol) ester to give the partially hexylated trimer **SS$_6$S** both via Pd catalysed Suzuki coupling. Suzuki coupling of 3-bromo-2,6-dihexyldibenzo[*b*,d]thiophene sulfone with 3,7-(dibenzo[*b*,*d*]thiophene sulfone) diboronic acid (bispinacol) ester gave another partially hexylated trimer, **S$_6$SS$_6$**. 3-(2,8-dihexyldibenzo[b,d]thiophene sulfone) boronic acid (pinacol) ester was synthesised through Miayura borylation of 3-bromo-2,6-dihexyldibenzo[*b*,*d*]thiophene sulfone followed by Suzuki coupling with 3,7-dibromo-2,6-dihexyldibenzo[*b*,d]thiophene sulfone to give the fully hexylated trimer **S$_6$S$_6$S$_6$** (Scheme 5).

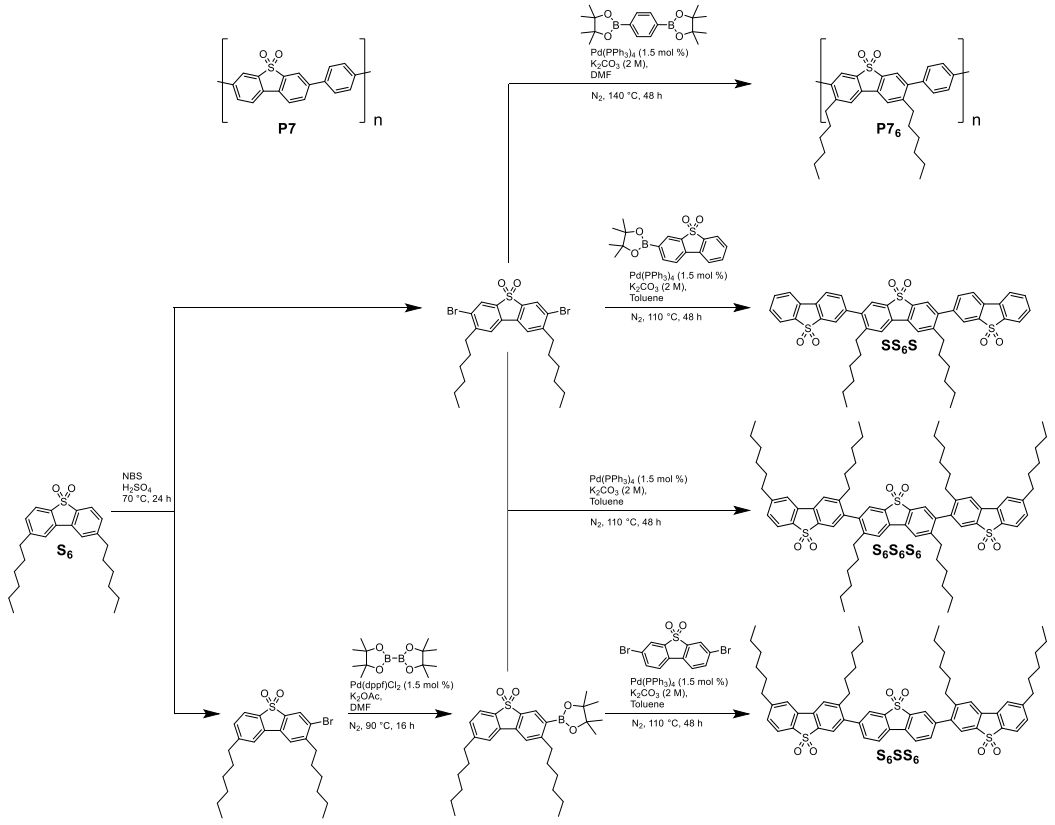

Scheme 5: Synthesis of **P7$_6$** and the hexylated dibenzo[*b*,d]thiophene sulfone trimers.

Analysis of the materials by ICP-MS showed that all contained significant levels of residual palladium. **SS_6S**, **S_6SS_6** and **$S_6S_6S_6$** had Pd contents of 0.34, 0.33 and 0.43 wt.%, all higher than **S3** (0.26 wt.%). **$P7_6$** on the other hand, had a lower Pd content (0.21 wt.%) than its non-hexylated analogue **P7** (0.37 wt.%).

3.7.2 Photophysical properties

The photophysical properties of the hexylated monomer, **S_6**, are very similar to those of its non-hexylated analogue (Figure 43). The absorption maximum in chloroform solution was 284 nm compared to 279 nm for **S1**, whilst emission maximum was 366 nm compared to 361 nm for **S1**. In contrast, **S_6** showed a slightly blueshifted absorption onset (379 nm) and emission maximum (384 nm) in the solid state compared to **S1** (382 nm and 394 nm respectively). The slight reduction in solution state optical gap on moving from **S1** to **S_6** is consistent with the latter's more electron donating alkyl chains, which would be expected to raise the energy of the HOMO. In the solid state, molecular packing may be the more dominant factor on frontier orbital energy levels, whereby reduced intermolecular conjugation in **S_6** gives the slightly blueshifted solid state absorption and emission.

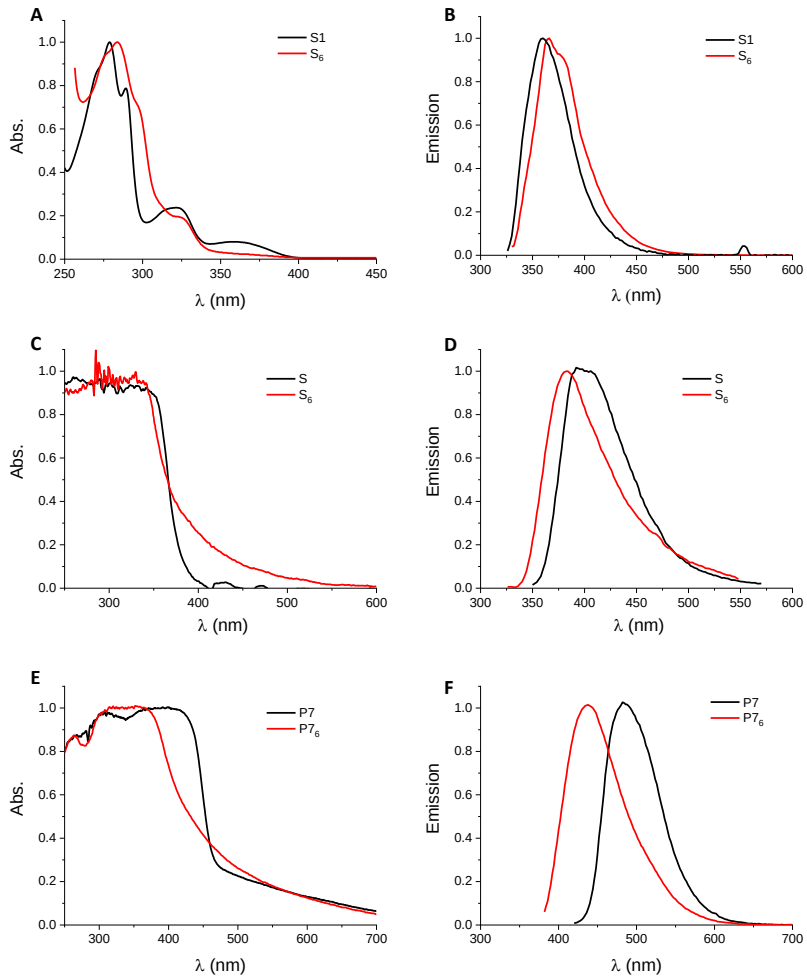

Figure 43: Normalised UV-Vis spectra of **S1** and **S6** in chloroform solution (A) and in the solid-state (C) and **P7** and **P76** in the solid-state (E). Normalised fluorescence spectra of **S1** and **S6** in chloroform solution (A) and in the solid-state (C) and **P7** and **P76** in the solid-state (E). Excitation wavelengths of 275 nm (B), 300 nm (D) and 350 nm (F) were used.

There were larger differences in the absorption and emission spectra of **P7** and **P76** (Figure 43E and F). The solid-state absorption onsets of **P7** and **P76** were 478 nm and 449 nm whilst the solid-state emission maxima were 480 and 446 nm respectively. These larger differences are thought to be due to the twisted conformation of the polymer backbone. As with the mesitylated oligomers in section 3.3, steric clash between alkyl chain substituent and the neighbouring aromatic core may result in a less planar structure, reducing conjugation and causing the blueshift in absorption.

This effect was also observed in the increasingly alkylated trimers. **S3** has an absorption maximum in chloroform solution of 396 nm. **SS6S** and **S6SS6** show almost identical absorption spectra, both with a maxima at 312 nm whilst the fully alkylated trimer **S6S6S6** was further blueshifted to 306 nm. Likewise, in the solid state, absorption onset was

blueshifted from 472 to 449 to 443 to 423 nm with increasing alkylation, with the same trend observed in the emission spectra as well.

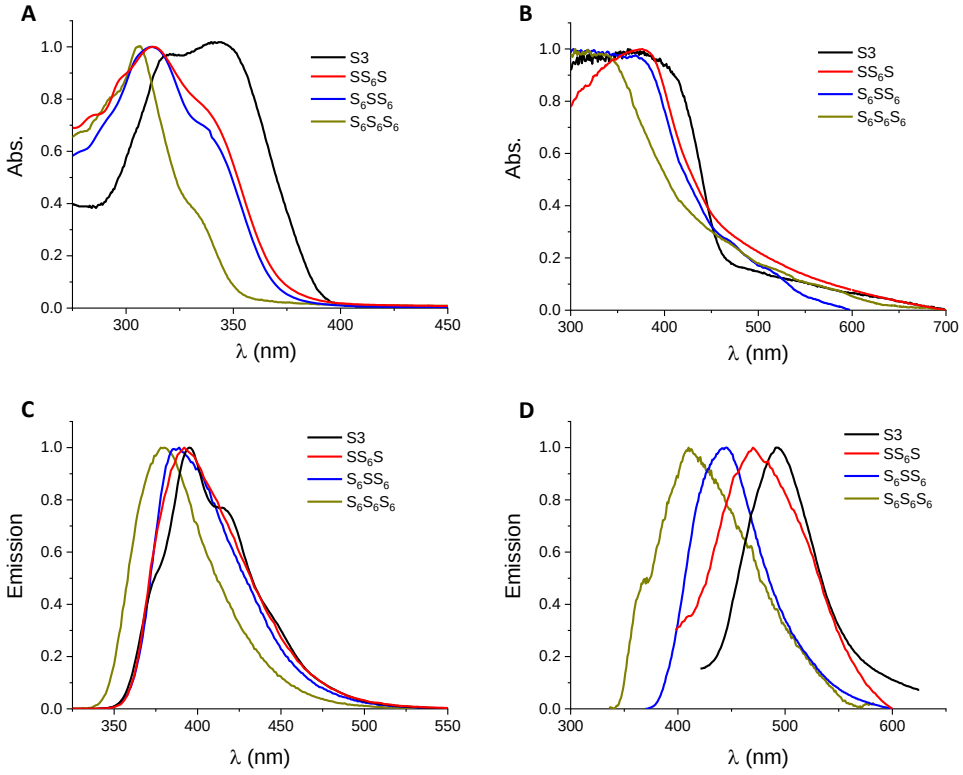

Figure 44: Normalised UV-Vis spectra of **S3** and the hexylated trimers in chloroform solution (A) and in the solid-state (B). Normalised fluorescence spectra of **S3** and the hexylated trimers in chloroform solution (C) and in the solid-state (D).

3.7.3 Photocatalytic hydrogen evolution

Previously, HERs were normalised to the mass of catalyst used in experiments. This assumes activity is related to the concentration of 'active absorbers'; that is, the aromatic ring monomers. In the previous samples, the molecular weight of the oligomers 'per active unit' has been quite similar. However, in these alkylated materials the mass 'per active unit' is as high as 385 g mol^{-1} whilst the unsubstituted materials are 216 g mol^{-1}; as such, the 25 mg of catalyst used for testing contains significantly different numbers of active units. To account for this in this section, the hydrogen evolution rates are also normalised to the number of moles of catalyst used for testing ($mmol_{cat}$). Whilst the mole-normalised rates account for molecular weight differences, they ignore the fact that we are most likely operating in the saturated regime of catalysts concentration[67] and thus the lower number of moles of the hexylated materials may artificially inflate the normalised HER; that is, a

higher number of moles would have produced the same amount of hydrogen and thus given a lower normalised rate. Each method has its problems and which of the two rates gives the fairest comparison between materials is debatable.

The hydrogen evolution rate of **S_6** in the Na_2S/Na_2SO_3 scavenger system (as described in section 3.2) was 5.1 μmol h^{-1} g^{-1} using the λ < 295 nm filter, lower than **S1** under equivalent conditions (8.0 μmol h^{-1} g^{-1}) (Figure 45A). Considering the differences in molecular weight by examining the HER per mole of photocatalyst rather than per gram the rates are much more similar at 1.8 and 1.9 μmol h^{-1} $mmol_{cat}^{-1}$ (Figure 45B). Similarly using the 400 < λ < 275 nm filter the HERs of **S1** and **S_6** were 25 and 18 μmol h^{-1} g^{-1} but normalising per mole of catalysts then **S_6** has the higher rate, 7.0 μmol h^{-1} $mmol_{cat}^{-1}$, compared to **S1**, 5.5 μmol h^{-1} $mmol_{cat}^{-1}$ (Figure 45C and D).

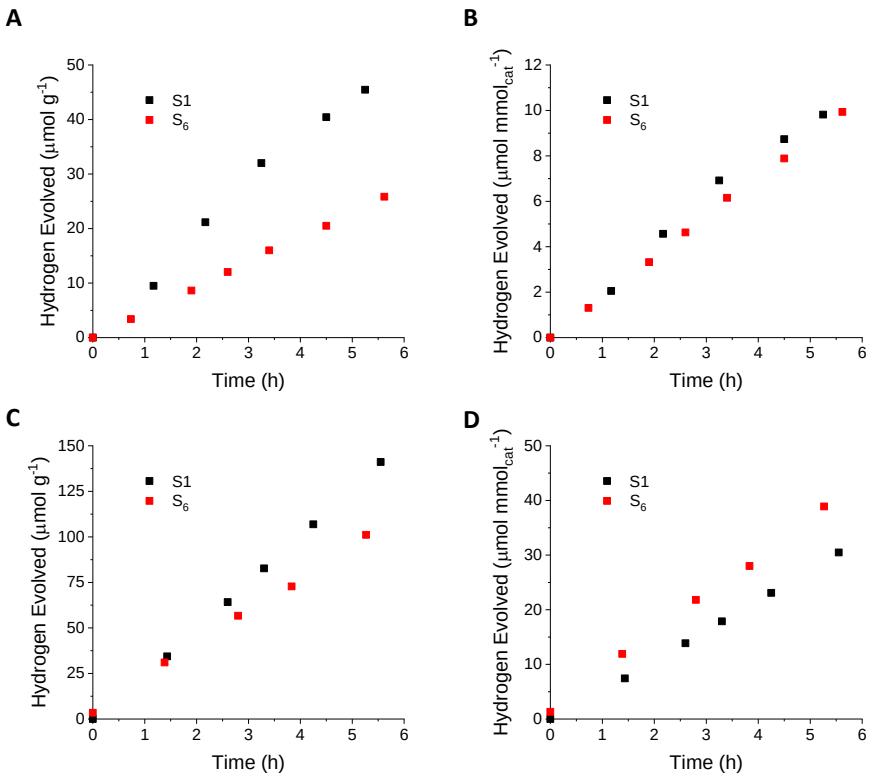

Figure 45: Photocatalytic hydrogen evolution of **S1** and **S_6** (25 mg) suspended in $Na_2S_{(aq)}$ (0.35 M) / $Na_2SO_{3(aq)}$ (0.2 M) (25 mL), 300 W Xe light source, using a λ > 295 nm filter (A and B) and using a 275 < λ < 400 nm filter (C and D). Amounts of hydrogen normalised to the mass of the catalyst (A and C) compared to the moles of catalyst (B and D).

In contrast to the monomers, alkylation of the trimers led to a significant reduction in rate. The HERs of **$S_6S_6S_6$**, **S_6SS_6** and **SS_6S** using the λ < 295 nm filter were 10, 15 and 70 μmol h^{-1} g^{-1} compared to 286 μmol h^{-1} g^{-1} for **S3**. Even taking into account molecular weight differences (Figure 46B) there is a large reduction in rate with increasing alkylation

indicating the blueshifted absorption profiles of hexylated trimers are limiting activity by reducing the proportion of photons with a useable wavelength. Using solely UV irradiation the activities were much more similar with rates of 66, 62, 87 and 162 µmol h^{-1} g^{-1} or 76, 60, 71and 101 µmol h^{-1} $mmol_{cat}^{-1}$ with decreasing alkylation (Figure 46C and D). These results indicate absorption onset is a dominant factor in these materials differing HERs, but, as with the **S1-S3** trend, it appears that another factor, perhaps absorption magnitude or hydrophobicity, is also limiting the alkylated materials.

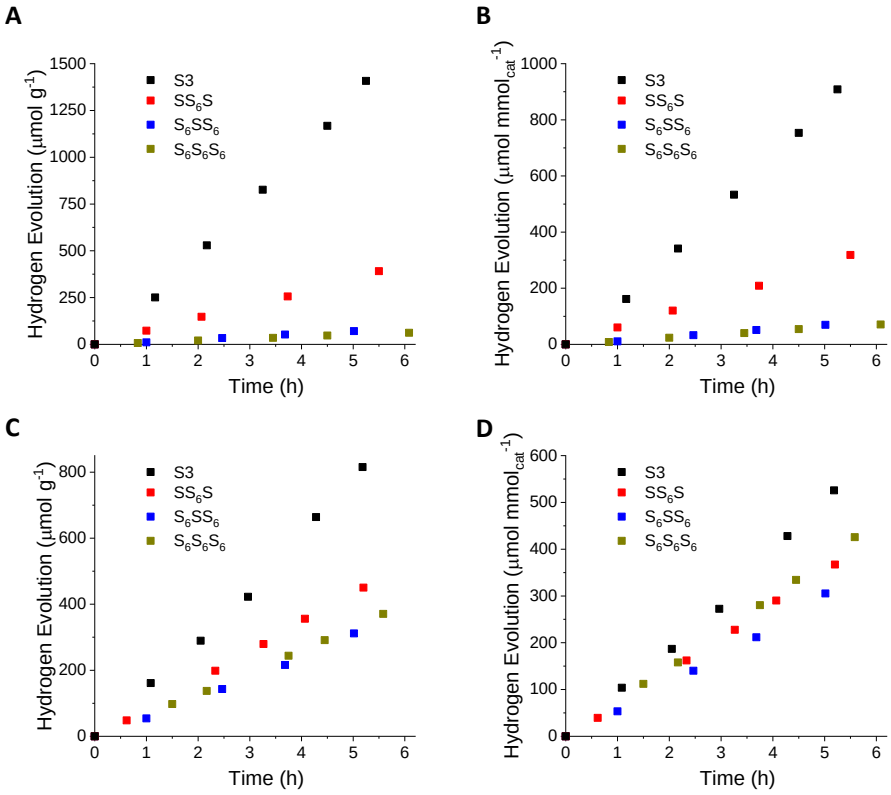

Figure 46: Photocatalytic hydrogen evolution of **S3** and the hexylated oligomers (25 mg) suspended in $Na_2S_{(aq)}$ (0.35 M) / $Na_2SO_{3(aq)}$ (0.2 M) (25 mL), 300 W Xe light source, using a $\lambda >$ 295 nm filter (A and B) and using a $275 < \lambda < 400$ nm filter (C and D). Amounts of hydrogen normalised to the mass of the catalyst (A and C) compared to the moles of catalyst (B and D).

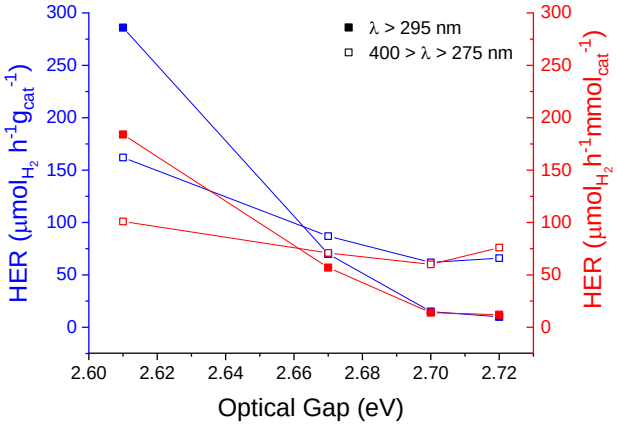

Figure 47: Hydrogen evolution rate normalised to the mass of catalyst (blue) or normalised to the moles of catalyst (red) of **S3** and the hexylated oligomers plotted against their optical gaps. Hydrogen evolution rate from illumination by a 300 W Xe light source, using a $\lambda > 295$ nm filter (solid squares) and using a $275 < \lambda < 400$ nm filter (open squares).

Unlike the oligomers, **P7** and **P7$_6$** were both insoluble in the TEA/MeOH/Water mixture and so these materials were tested using this scavenger system (Figure 48). The TEA/MeOH/Water scavenger system is less polar than the fully aqueous system used for the oligomers and one may therefore expect the increased hydrophobicity of **P7$_6$** to be less significant. Under visible light ($\lambda > 420$ nm filter) **P7** displayed a HER of 1533 μmol h^{-1} g^{-1} similar to previous reports[31] whilst **P7$_6$** was significantly less active with a HER of 121 μmol h^{-1} g^{-1}. Even converting to per mole rates the hexylated polymer is significantly less active with a HER of 52 μmol h^{-1} mmol$_{cat}$$^{-1}$compared to 445 μmol h^{-1} mmol$_{cat}$$^{-1}$ for **P7**. When using broad spectrum irradiation ($\lambda > 295$ nm filter) the activity of **P7** increased by 91% to 2926 μmol h^{-1} g^{-1} (849 μmol h^{-1} mmol$_{cat}$$^{-1}$) whilst **P7$_6$** increased by 412% to 619 μmol h^{-1} g^{-1} (266 μmol h^{-1} mmol$_{cat}$$^{-1}$) reflecting the larger proportion of the latter's absorption spectrum that lies at wavelengths less than 420 nm. Using solely UV light ($400 > \lambda > 275$ nm filter) the rates of hydrogen evolution of **P7** and **P7$_6$** were even more similar at 594 and 332 μmol h^{-1} g^{-1} respectively, equivalent to 172 and 143 μmol h^{-1} mmol$_{cat}$$^{-1}$. As above, it appears that the majority of the reduction in activity for the hexylated material is due to its reduced light absorption, although another factor could be its lower residual palladium content of 0.21 wt.% compared to 0.37 wt% measured for **P7**.

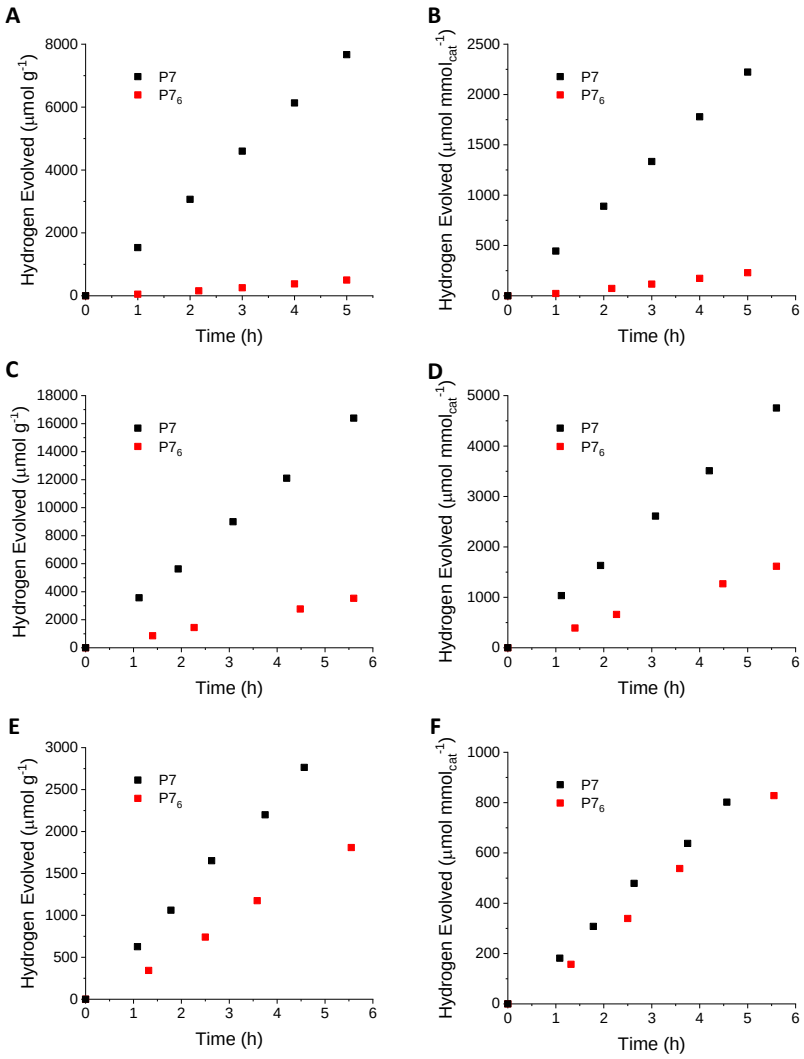

Figure 48: Photocatalytic hydrogen evolution of **P7** and **P7$_6$** (25 mg) suspended in (1:1:1) water/methanol/triethylamine mixtures (25 mL), 300 W Xe light source, using a $\lambda > 420$ nm filter (A and B), a $\lambda > 295$ nm filter (B and C) and using a $275 < \lambda < 400$ nm filter (D and E). Amounts of hydrogen normalised to the mass of the catalyst (A, C and E) compared to the moles of catalyst (B, D and F).

3.8 Effect of Pd on P10

In the light of the results of section 3.4 it was thought that the relationship between palladium content and activity should also be investigated in the polymer analogue of **S1-3**, **P10**. The increased magnitude of the TAS signal for this material also allowed for further analysis of the kinetics of the photoexcited states.

3.8.1 Synthesis and characterisation

P10 was synthesised *via* Suzuki coupling of 3,7-dibromodibenzo[*b*,*d*]thiophene sulfone and 3,7-bis(4,4,5,5-tetramethyl-1,3,2-dioxaborolan-2-yl)dibenzo[*b*,*d*]thiophene sulfone monomers in dimethlyformamide (see section 3.10.2 for full details). Batches with variable palladium contents were produced by using different amounts of the tetrakis(triphenylphosphine)palladium (0) cross coupling catalysts in synthesis. After work up this gave batches of **P10** with 0.2, 0.7 and 2.7 wt. % residual Pd, as measured by ICP-MS, hereafter referred to as **P10$_{0.2}$**, **P10$_{0.7}$** and **P10$_{2.7}$**. In addition, a batch of **P10** was synthesised by Yamamoto homo-coupling, of the dibrominated monomer using a nickel(0) catalyst to obtain a Pd-free sample, referred to as **P10Y** (section 3.10.2 for full protocol). Whilst **P10Y** had Pd levels below the 10 ppm detection limit of the ICP-MS instrument, it was found to contain 0.4 wt. % residual Ni from synthesis.

3.8.2 Photophysical properties

One concern when altering the cross-coupling catalysts used for synthesis is that polymerisation may occur more or less efficiently resulting in samples with different chain lengths. As **P10** is insoluble in all common organic solvents and is not stable to mass spectrometry ionisation techniques, determining chain length accurately is not simple. However, the solid-state absorption spectra (Figure 49) gives an indication of chain length as longer chains would be expected to give smaller optical gaps. It appears that there are some small differences in degree of polymerisation between **P10** batches as the absorption onset shifts 16 nm on moving from **P10Y**, the most redshifted sample, to **P10$_{2.7}$**, the least. This indicates shorter chain lengths in the samples where more Pd was used in synthesis. The emission spectra show larger differences between the samples with emission maxima at 520, 508, 471 and 436 nm with increasing Pd content.

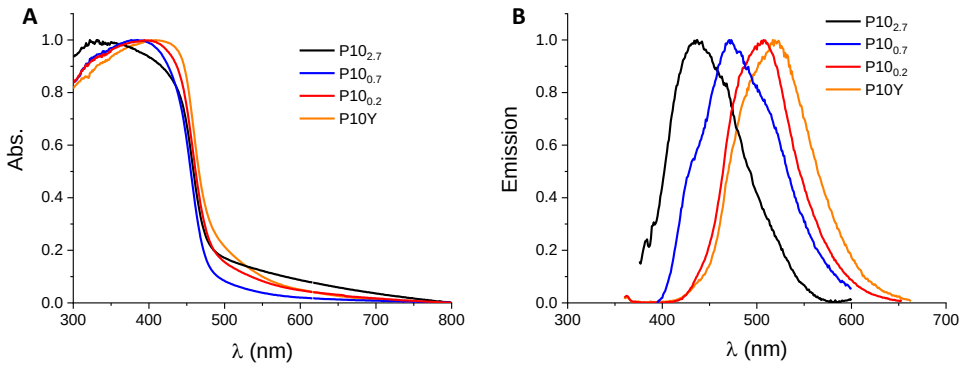

Figure 49: Normalised solid-state UV-Vis DRS (A) and fluorescence emission spectra (B) of **P10** polymers. An excitation wavelength of 400 nm was used for fluorescence measurements.

The fluorescence magnitude of the **P10** batches suspended in water was also measured. In general batches with more palladium had weaker emission indicating some quenching of excitons by Pd in water suspension (Figure 50A). This could also be influenced by the suspension absorption and scattering effects from differences in the polymers dispersibility. All batches showed significant fluorescence quenching upon addition of TEA, indicating hole scavenging occurs (Figure 50, dotted lines).

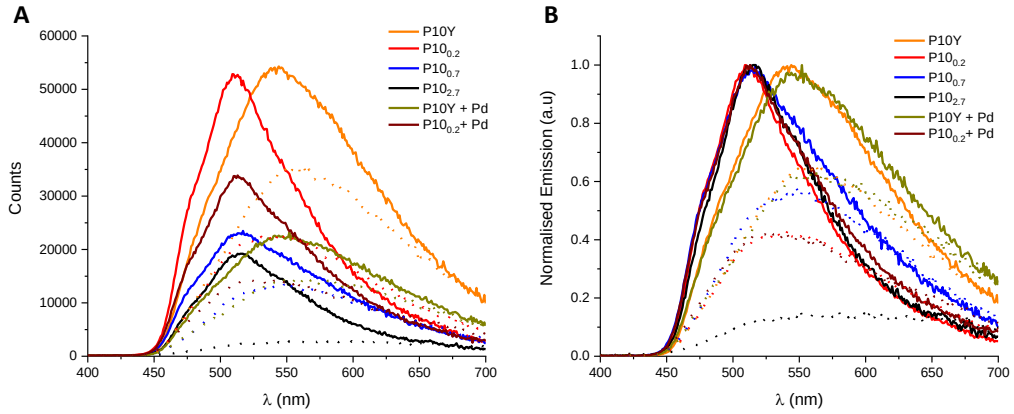

Figure 50: Emission TCSPC spectra of the **P10** polymers (2mg) suspended in water (4 mL) pre (solid lines) and post (dotted lines) addition of TEA (50 µL). Raw data (A) and normalised to the emission magnitude of each suspension pre TEA addition (B). Excited at 375 nm.

As with the **S** oligomers, it appears that Pd-content has a limited effect on exciton lifetime as measured by TCSPC (Figure 51). **P10$_{0.2}$**, **P10$_{0.7}$** and **P10$_{2.7}$** had τ_{Av} values of 0.79, 0.64 and 0.58 ns whilst **P10Y** had a value of 1.23 ns. However, samples of **P10$_{0.2}$** and **P10Y** loaded with Pd by photodeposition were almost identical to the pristine samples (τ_{Av} = 0.79 and 1.25 ns respectively) indicating the changes in lifetime between batches may be partially caused by some other inter-batch variation.

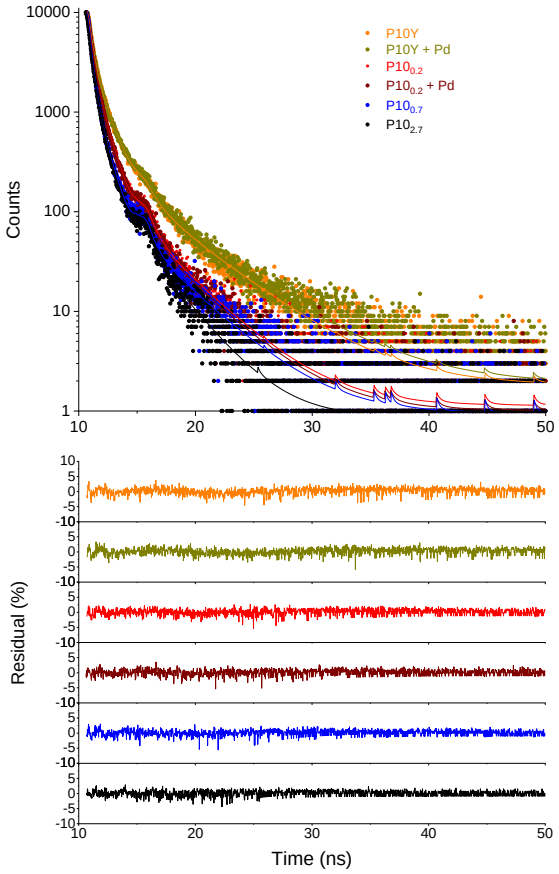

Figure 51: TCSPC spectra of the **P10** polymers (2 mg) suspended in water (4 mL), data (circles), fit (lines) and residuals (bottom). Samples were excited with a 375 nm laser and emission was measured from the emission maxima of each suspension as shown in Figure 48.

Interestingly, the TCSPC lifetimes of the polymers in suspension were only found to reduce very slightly upon addition of triethylamine hole scavenger (Figure 52). The averaged lifetimes in this case were 0.69 and 0.63 ns for samples of pristine **P10$_{0.2}$** and **P10$_{0.2}$** + Pd compared to 0.79 ns before TEA addition. Taken together with the large reduction in the fluorescence magnitude shown in Figure 50, this suggests that hole quenching by the TEA scavenger may occur on a quicker timescale than is measurable by TCSPC (order of ns) but that interaction with the scavenger is not 100% efficient. The lifetimes measured thus represent mostly the excitons that do not interact with the scavenger, perhaps due to being further from the particle surface.

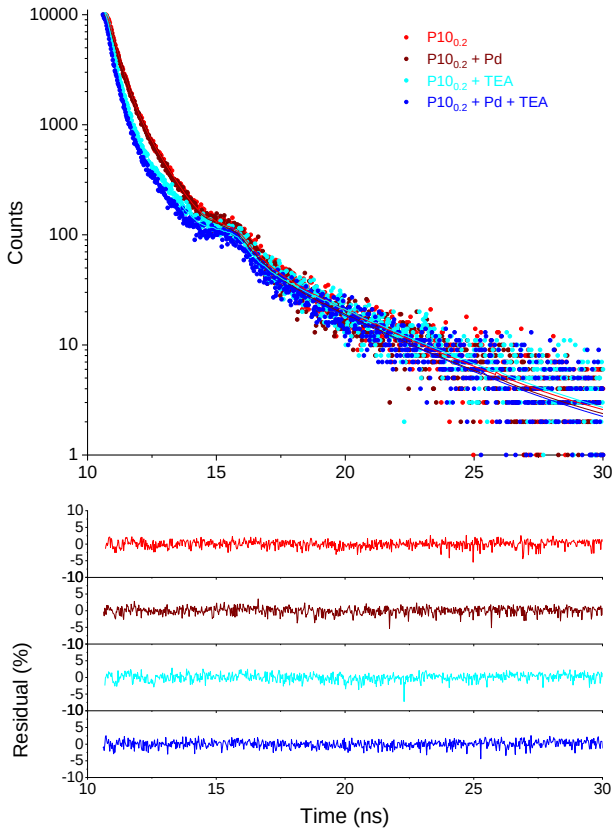

Figure 52: TCSPC spectra of the **P10$_{0.2}$** (2 mg) with and without Pd loading, suspended in water (4 mL) before and after the addition of TEA (50 µL). Data (circles), fit (lines) and residuals (bottom) Samples were excited with a 375 nm laser and emission was measured at 511 nm.

As discussed above, it has been previously shown that the TAS spectra of **P10** in the presence of a triethylamine electron donor, shows a long-lived absorption feature at 630 nm assigned to a polymer-based electron polaron. All batches of **P10** tested here were also found to have 630 nm features in their transient spectra (Figure 53D) when suspended in the TEA/MeOH/Water mixture and probed at 10 µs following a 355 nm excitation. There was some variation in the magnitude of the 630 nm features, but this is thought to reflect differences in the suspension's absorption at the excitation wavelength (Figure 53A) rather than differing polaron yield. More significantly, when the decay kinetics of these features were measured a large decrease in polaron lifetime was found with increasing Pd content (Figure 53C) indicating palladium plays a role in polaron quenching.

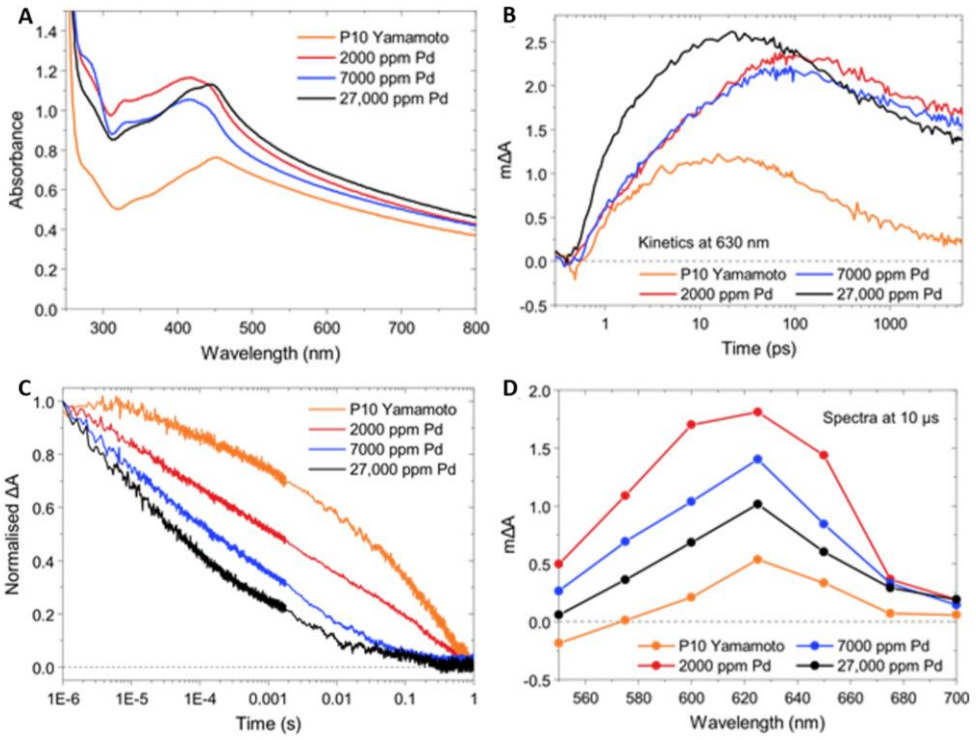

Figure 53: Steady-state absorbance and transient data on P10 particles with different Pd content, obtained in a solvent mixture consisting of equal volumes of H_2O/MeOH/TEA; Steady state absorbance spectra in H_2O/MeOH/TEA (A). Transient absorption decay kinetics probed at 630 nm following 355 nm excitation on the fs – early ns timescale using a fluence of 0.08 mJ cm^{-2} (C) and over longer ns – s timescale using a fluence of 0.32 mJ cm^{-2} (B). Transient absorption spectra in probed at 10 µs following nm following 355 nm excitation using a fluence of 0.32 mJ cm^{-2} (D). All samples were prepared with a polymer concentration of 0.24 g L^{-1}. Note that the charge yield on the ps – ns timescale largely reflects the absorbance differences at the excitation wavelength between the different samples.

3.8.3 Photocatalytic hydrogen evolution

The activity of the different **P10** batches was then tested for photocatalytic activity in the TEA/MeOH/Water system (Figure 54). HER increases from 2825 µmol h^{-1} g^{-1} for $\mathbf{P10_{0.2}}$ to 5332 µmol h^{-1} g^{-1} for $\mathbf{P10_{0.7}}$ then remained similar at 4906 µmol h^{-1} g^{-1} for $\mathbf{P10_{2.7}}$. This is consistent with the accelerated polaron decay observed by TAS and indicates faster transfer of photoinduced polarons to Pd active sites at higher Pd contents results in increased hydrogen evolution rates. To confirm this activity change was a result of Pd content rather than other sample differences $\mathbf{P10_{0.2}}$ was also measured with the addition of 2 wt. % Pd by photodeposition of $[Pd(NH_4)_2Cl_4]$. This sample had the highest rate of all measured samples (5718 µmol h^{-1} g^{-1}) and was found by ICP-MS to have a Pd content of 1.7 wt. %.

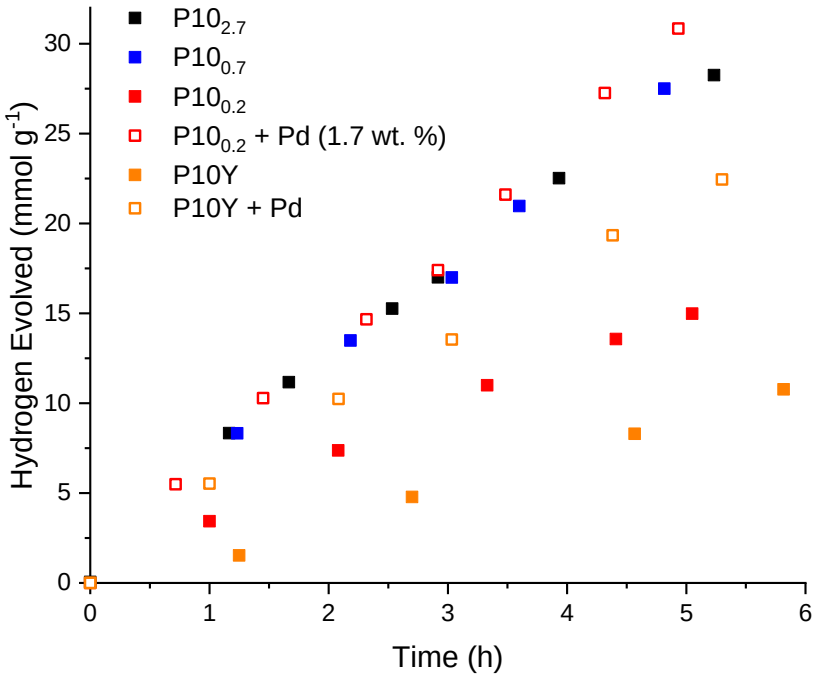

Figure 54: Photocatalytic hydrogen production of the **P10** polymers (25 mg) suspended in (1:1:1) water/methanol/triethylamine mixtures (25 mL), 300 W Xe light source, using a $\lambda > 420$

P10Y also shows moderate hydrogen evolution activity with a rate of 1897 µmol h^{-1} g^{-1} indicating perhaps that Ni may also act as active site for proton reduction. Considering the large difference in polaron lifetime, the **P10Y**s rate is perhaps surprisingly close to that of **P10$_{0.2}$**. This could be due to slow formation of the Ni active species. Photocatalysis experiments are conducted over five hours under highly reducing, de-oxygenated conditions. It was noted that after the first hour of irradiation the **P10Y** sample had changed from bright yellow/orange to a yellow/green and by the end of the experiment was dark yellow/green, perhaps indicating the slow formation of Ni(0). After the 6-hour experiment was ended and the sample was exposed to air, the colour returned to yellow/orange within 30 seconds suggesting the Ni species formed during photolysis is oxygen sensitive (Figure 55).

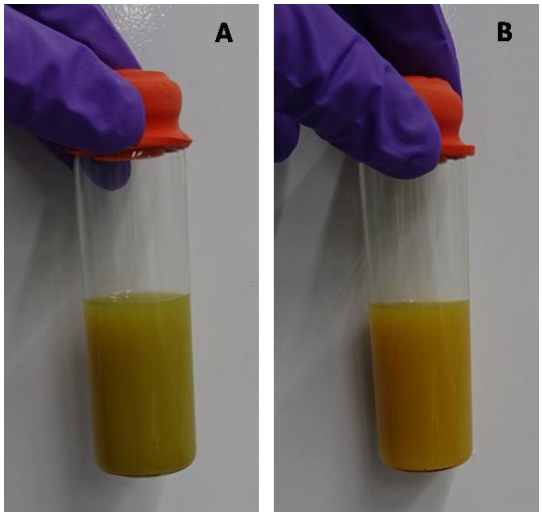

Figure 55: Photographs of **P10Y** (25 mg) suspended in (1:1:1) water/methanol/triethylamine mixture (25 mL), after photolysis under nitrogen (A) and 30 seconds after exposure to air (B).

TAS experiments, while conducted under de-oxygenated conditions, may not provide sufficient time or photons to form Ni(0) and thus the polaron decay rates shown in Figure 53C may represent a sample with limited sites for polaron quenching. Slow formation of Ni(0) would also be consistent with the induction period observed in photocatalytic testing. The initial HER over the first 75 minutes of the experiment was 1226 µmol h^{-1} g^{-1} compared to 2004 µmol h^{-1} g^{-1} for the subsequent five hours.

P10Y was also tested with the addition of 2 wt. % Pd by photodeposition of $[Pd(NH_4)_2Cl_4]$. Again, the addition of Pd resulted in an increase in HER to 4005 µmol h^{-1} g^{-1}. ICP analysis of this sample showed 1.9 wt. % Pd in addition to the 0.4 wt. % Ni from synthesis. Whilst this sample had a lower 5 h rate than the equivalent **P10$_{0.2}$** experiment, the rate over the first hour of photolysis was very similar (5527 µmol h^{-1} g^{-1}). The slight slowing of the rate after this point could be due to a an overloading of metal centres as Ni(0) forms on the polymer in addition to Pd. This would result in a total metal content of 2.3 wt. %, which is perhaps in excess of the optimal loading, or could result in Ni(0) competing with Pd but being less efficient at the final proton reduction step.

STEM analysis showed that residual Pd from synthesis on **P10$_{0.2}$**, **P10$_{0.7}$** and **P10$_{2.7}$** formed a polydisperse mixture of 5 to 30 nm sized particles (Figure 56A-C and Figure 57). The samples of **P10$_{0.2}$** and **P10Y** with Pd added by photodeposition showed similarly sized Pd particles, well distributed across the surface of the polymer (Figure 56E-G and 58E-G). This is consistent with **P10$_{0.2}$ + 2wt. % Pd**'s similar HER compared to **P10$_{0.7}$** and **P10$_{2.7}$**. Similarly sized Ni particles of 7 – 20 nm were observed on **P10Y** collected post

photocatalysis (Figure 58A-C) indicating these may be the active site for proton reduction in this material. Whilst these metal particles are visible by STEM, this does not rule out the possibility that smaller Pd/Ni particles or clusters are also present on the materials. Analysis by high resolution TEM would be required in this case.

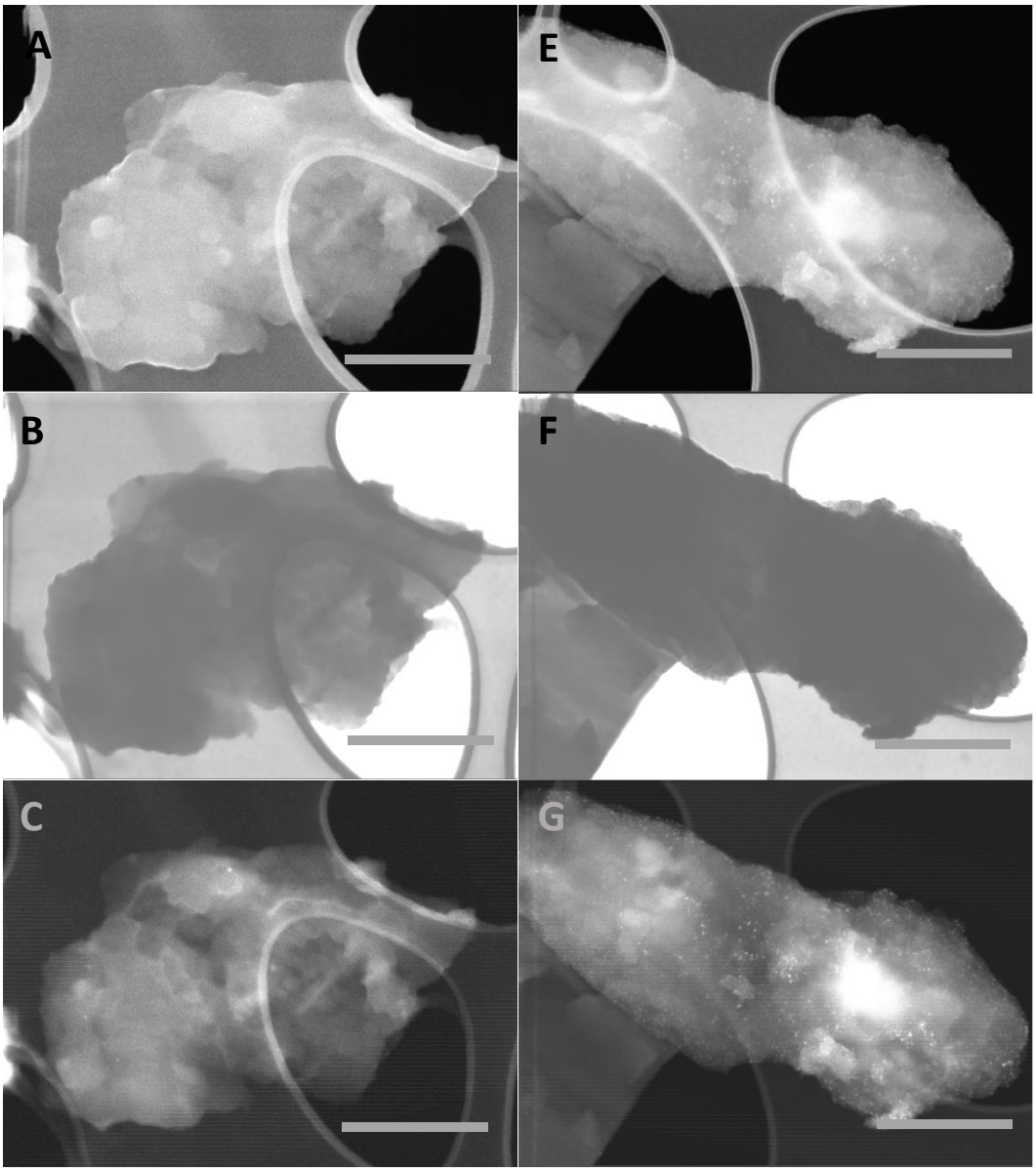

Figure 56: **P10$_{0.2}$** by SEM (A) and STEM in BF mode (B) and HADF mode (C). **P10$_{0.2}$** + Pd by SEM (E) and STEM in BF mode (F) and HADF mode (G). Scale bars are 500 nm

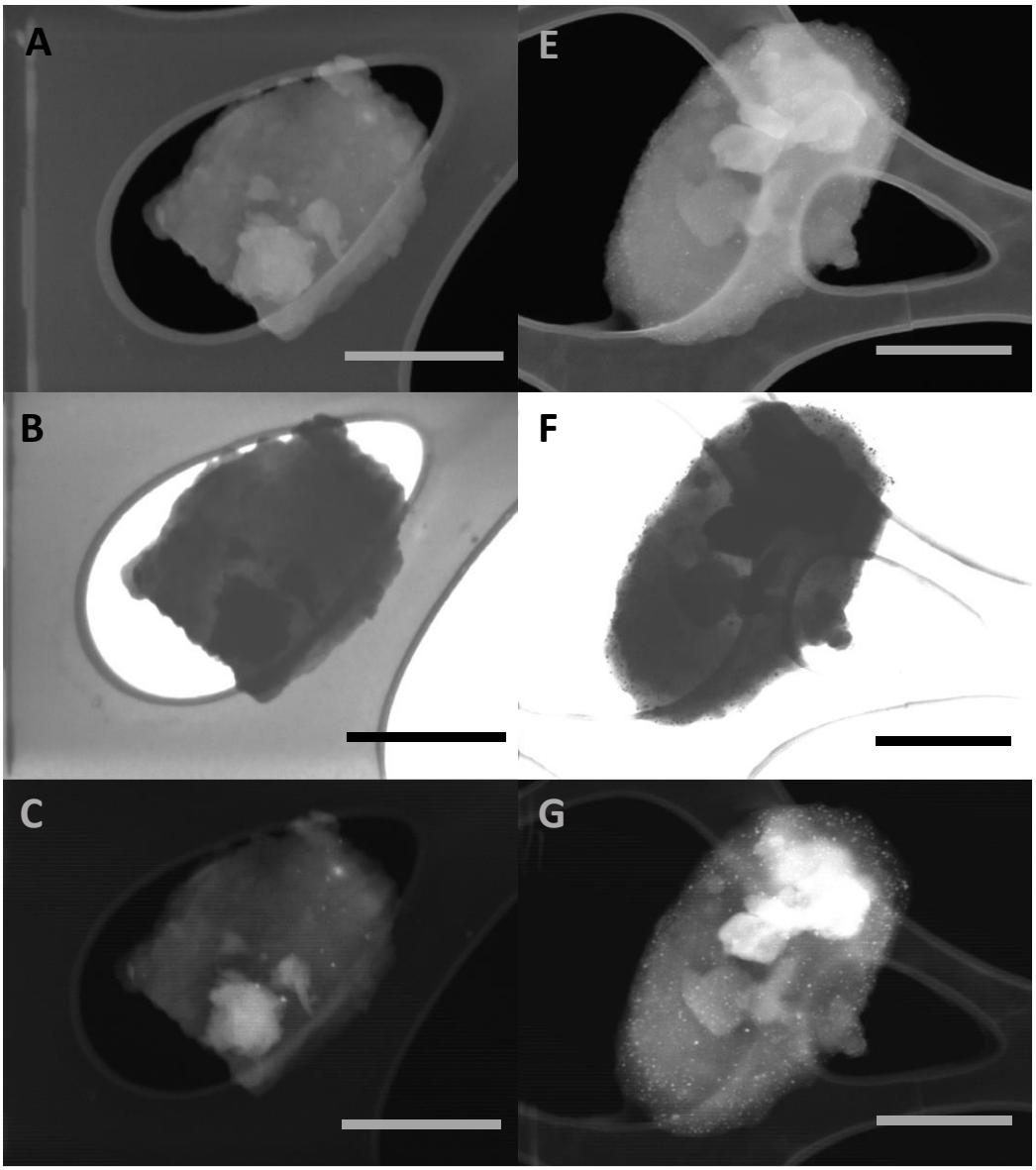

Figure 57: **P10$_{0.7}$** by SEM (A) and STEM in BF mode (B) and HADF mode (C). **P10$_{2.7}$** by SEM (E) and STEM in BF mode (F) and HADF mode (G). Scale bars are 500 nm

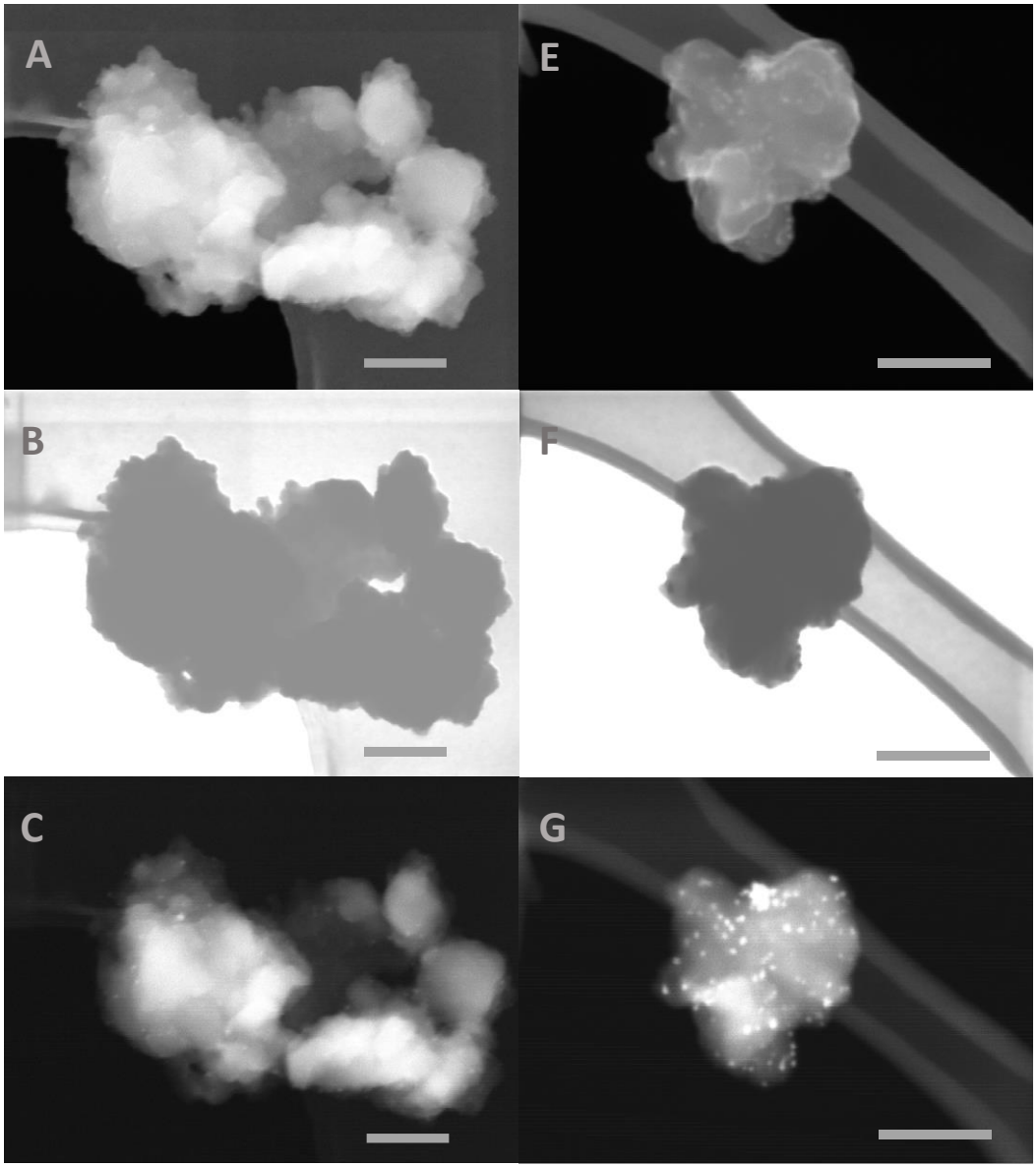

Figure 58: **P10Y** by SEM (A) and STEM in BF mode (B) and HADF mode (C). **P10Y** + Pd by SEM (E) and STEM in BF mode (F) and HADF mode (G). Scale bars are 200 nm.

.

3.9 Conclusions

The investigation into these series of oligomers and polymers has enabled a number of conclusions to be drawn. Whilst light absorption appeared to be the dominant factor in the activity of most of the systems investigated, the **MeF1-3** oligomers showed that, in some cases, decreasing chain length can provide sufficient improvements to other factors to outweigh reduced light absorption. Precisely what these other factors are, though, is still somewhat unclear. Driving force most likely plays a role as widening the optical gap increases the overpotential for the two redox half reactions. However, the trend in activity with chain length was not consistent when the electron donor was altered, indicating the kinetics of hole scavenging and, hence, how excited state lifetimes vary with chain length must also be considered.

The behaviour of the **S** oligomers was quite different to the **MeF** oligomers, highlighting the difficulty of developing general rules for structure-activity relationships between different conjugated organic materials. Activity was found to increase rapidly on moving from **S1** to **S2** to **S3** with the latter displaying HER not far from the polymer analogue. This was found to primarily be a function of the rapid increase of conjugation length with oligomer length and subsequent improved absorption properties. TAS and TCSPC measurements both showed a decrease in exciton lifetime with increasing chain length, but this did not seem to be a dominant factor in regulating photocatalytic activity, possibly due to the speed of hole scavenging. TAS measurement of **S2** and **S3** also indicated that scavenger assisted charge separation occurs similarly in short chain lengths to those in polymers, although the magnitude of polaron yield was found to be significantly lower for shorter chain lengths.

Whilst the number of units in the oligomer backbone is clearly important to optical properties and photocatalytic activity, the planarity of said backbone is equally important. Phenyl and mesityl substitution of fused ring cores were found to give very different molecular conformation and packing in the solid state. As a result, the more twisted mesityl substituted oligomers had significantly reduced light absorption properties which manifested in lower photocatalytic activity under broad spectrum irradiation. This was reversed when using solely UV light indicating this twisting did not negatively alter non-absorption properties. This was consistent with the behaviour of the series of hexylated oligomers and the $\mathbf{P7_6}$ polymer where increasing alkylation gave more blueshifted light absorption and thus low photocatalytic activity at longer wavelengths, but similar activity under UV light. This was not the case for the monomer, $\mathbf{S_6}$ where absorption properties and activity were similar to **S1**, again indicating that it is a backbone twisting effect that disrupts the oligomers. This is pertinent to the growing field of organic-solvent-soluble alkylated polymers for hydrogen

evolution, and further studies into the effect of substitution positions on backbone twisting may be useful.

Overall, it appears that materials with longer effective conjugation lengths are primarily more active due to their superior absorption properties. The search for new organic photocatalytic materials therefore need not be limited to polymers with particularly extended conjugation or indeed to polymers in general, as long as aromatic units with sufficiently red-shifted absorption profiles and high oscillator strengths are incorporated.

It is widely assumed that the active site for proton reduction on polymer photocatalysts is a metal co-catalyst; commonly Pt added after synthesis or residual Pd present from synthesis by cross-coupling. Previous work has suggested that aside from acting as the active site for proton reduction, hydrogen evolution rate is highly dependent on Pd concentration because Pd particles can help to prevent exciton recombination by separating charges. The relative independence of the dibenzothiophene sulfone materials' exciton lifetime to palladium content, and the large variation in activity observed at Pd contents above 0.1 wt. % are not consistent with this theory. The accumulation of polarons on **S2** and **S3** as shown by PIAS, as well as the large decrease in polaron lifetime of the **P10** batches with higher Pd contents instead suggests that the rate limiting step for these materials is transfer of an electron polaron from the polymer to a Pd active site.

The fact that polaron lifetime decreases dramatically when the diffusion distance required to reach a Pd centre is reduced indicates that charge carrier mobility in these materials may be lower than organic materials commonly used for electronic applications. Further work could therefore aim to measure and optimise the conductivity of these materials. This may be a difficult task as the component that is thought to make **S1-3** and **P10** good hydrogen evolution photocatalysts is the highly polar sulfone group, but monomers containing similar, large-dipole-inducing, groups have been found to give reduced charge carrier mobilities.[68–70] In addition, high charge carrier mobility is commonly achieved by increasing crystallinity[29,30] but the fact that **S2**, a polycrystalline material, shows similar behaviour to its longer chain analogues indicates this may not be an effective strategy for these materials. Similarly, minimising twisting of polymer backbones is thought to increase charge carrier mobility[71,72] but **S2** and **S3**'s crystal structures indicate dibenzothiophene sulfone units most likely already adopt a highly planar conformation. Other strategies could be to introduce extra conductive components into the material. For example increases in photocatalytic activity have been found by adding conducting graphene or reduced graphene oxides layers to polymer semiconductors.[73,74] An alternative approach would to be to start from materials

that are known to be highly conductive, such as polythiophene based materials,[29] and to add in dibenzothiophene sulfone units.

3.10 Experimental

3.10.1 General Procedures

CHNS microanalysis, solution state NMR, ICP-MS, UV-Vis and fluorescence spectroscopy, static light scattering, thermogravimetric analysis and hydrogen evolution experiments were conducted as described in Chapter 2.

Solid-state Nuclear Magnetic Resonance Spectroscopy

Solid-state NMR experiments were performed on a 9.4 T Bruker DSX solid-state NMR spectrometer 4 mm HXY triple-resonance MAS probe in double resonance mode tuned to ^{1}H at $n_0(^{1}H)$ = 399.98 MHz and the X channel tuned to ^{13}C at $n_0(^{13}C)$ = 100.56 MHz. Experiments were performed at room temperature under MAS at n_r = 12.5 kHz. ^{1}H pulses and SPINAL-64 heteronuclear decoupling[75] were performed at a radiofrequency (rf) field amplitude of 83 kHz. ^{1}H-^{13}C cross polarization (CP) MAS experiments were obtained with a ^{13}C rf field of 55 kHz, while the ^{1}H rf field amplitude was ramped to obtain maximum signal at a ^{1}H rf field of approximately 60 kHz, at a contact time of 2 ms for 16384 and 8192 scans for **S2** and **S3** respectively at a recycle delay corresponding to $1.3*T_1(^{1}H)$. The ^{13}C chemical shifts were referenced to the CH carbon of adamantane at 29.45 ppm.[76] Samples were packed in a zirconia rotor with a KelF cap, and NMR data were obtained and analysed using TopSpin 3.2.

Mass Spectrometry

High resolution mass spectrometry of **MeF2**, **MeF3**, **PSP**, **MSM** and all intermediates was performed on an Agilent Technologies 6530B accuratemass QTOF mixed ESI/APCI mass spectrometer (capillary voltage 4000 V, fragmentor 225 V) in positive-ion detection mode. **PFP** was measured in chloroform solution on an Agilent 7890B GC-MS. High resolution mass spectrometry of **MFM**, **S2** and **S3** was performed at the National Mass Spectrometry Facility on an Xevo G2-S Atmospheric Solids Analysis Probe in positive ion detection mode.

Fourier Transformed Infra-Red Spectroscopy

Transmission FT-IR spectra were recorded on a Bruker Tensor 27 at room temperature; samples were prepared as pressed KBr pellets.

Powder X-ray Diffraction

PXRD measurements were performed on a Panalytical Empyrean diffractometer, with a Cu X-ray source (λ = 1.5418 Å, Cu-Kα), used in high throughput transmission mode with Kα focusing mirror and PIXcel 3D detector.

Single crystal X-ray Diffraction

SC-XRD data sets were measured on a Rigaku MicroMax-007 HF rotating anode diffractometer (Mo-Kα radiation, λ = 0.71073 Å, Kappa 4-circle goniometer, Rigaku Saturn724+ detector); or at beamline I19, Diamond Light Source, Didcot, UK using silicon double crystal monochromated synchrotron radiation (λ = 0.6889 Å, Pilatus 2M detector). Absorption corrections, using the multi-scan method, were performed with the program SADABS.[77,78] For synchrotron X-ray data, collected at Diamond Light Source (λ = 0.6889Å) data reduction and absorption corrections were performed with xia2.[79] Structures were solved with SHELXT,[80] or by direct methods using SHELXS,[81] and refined by full-matrix least squares on $|F|^2$ by SHELXL,[82] interfaced through the programme OLEX2.[83] All H-atoms were fixed in geometrically estimated positions and refined using the riding model. For full refinement details, see Tables S1-3.

Scanning (Transmission) Electron Microscopy

Imaging of the oligomer morphology was achieved on a Tescan S8000G with secondary electron, backscatter and transmission detectors. SEM samples were dropped as powder onto conductive carbon and coated with chromium using a sputter coater. SEM images recorded at 3 keV with a beam current of 26 pA. STEM samples were dropped onto Agar Scientific holey carbon / Cu TEM grids from water suspensions. Unless otherwise stated images were recorded at 20 keV with a current of 125 pA. Images were recorded in both Bright Field (BF) mode and High Angle Dark Field (HADF) mode.

Time Correlated Single Photon Counting

TCSPC experiments were performed on an Edinburgh Instruments LS980-D2S2-STM spectrometer equipped with picosecond pulsed LED excitation sources and a R928 detector, with a stop count rate below 3%. An EPL-295 diodide (λ = 300.4 nm, instrument response 100 ps, fwhm) or an EPL-375 diode (λ = 370.5 nm, instrument response 100 ps, fwhm) were used as the light source. Oligomers were measured in the solid state and in chloroform solution. Polymers were measured in water suspensions. The instrument response was measured with colloidal silica (LUDOX HS-40, Sigma-Aldrich) at the excitation wavelength. Decay times were fitted in the FAST software using suggested lifetime estimates.

Transient Absorption Spectroscopy

Measurements were conducted as described previously.[84]

External Quantum Efficiency

EQEs were measured using a 420 nm (± 10 nm, fwhm) LED. S2 or S3 (12 mg) were suspended in water/TEA/MeOH (1:1:1, 8 mL) by sonication. The mixture was transferred into a quartz cell, sealed with a septum and degassed for 30 minutes before illuminating with the LED. Light intensity was measured at the front of the cell using a ThorLabs probe and the hydrogen produced was measured as above. Efficiency was calculated as the incident photon to hydrogen conversion yield. Path length was 1 cm, illuminated area was 8 cm and light intensity varied from 15-19 W m^{-2} between experiments.

3.10.2 Synthesis

All reagents including **MeF1** and **S1** were obtained from Sigma-Aldrich, TCI, or Fluorochem and used as received. Reactions were carried out under nitrogen atmosphere using standard Schlenk techniques. 3,7-dibromodibenzo[*b*,*d*]thiophene sulfone and 3,7-dibenzo[*b*,*d*]thiophene sulfone diboronic acid bis(pinacol) ester were prepared as described in Chapter 2.

3-Bromodibenzo[b,d]thiophene sulfone

Dibenzo[*b*,*d*]thiophene sulfone (20.0 g, 102.4 mmol) was dissolved in concentrated H_2SO_4 (500 mL). *N*-Bromosuccinimide (36.0 g, 202.2 mmol) was added in several portions over 3 hours and the mixture was stirred overnight at room temperature. The mixture was poured into ice-cold water (5000 mL) and stirred for 10 minutes. The solid was filtered off and washed repeatedly with water to give a mixture of 3,7-dibromodibezo[*b*,*d*]thiophene sulfone and 3-bromodibezo[*b*,*d*]thiophene sulfone. The mono brominated product was purified by column chromatography of the residue material (DCM : *n*-hexane (40:60)) to give white crystals of 3-bromodibezo[*b*,*d*]thiophene sulfone (0.71 g, 2.41 mmol, 2.4%). ^{1}H NMR (400 MHz, $CDCl_3$): δ(ppm) = 7.95 (d, *J* = 2.0 Hz, 2H), 7.83 (d, *J* = 7.5 Hz, 2H), 7.79 (d, *J* = 7.5 Hz, 2H), 7.77 (dd, *J* = 8.0 and 2.0 Hz, 2H), 7.67 (d, *J* = 8.0 Hz, 2H), 7.67 (t, *J* = 7.5, 2H), 7.57 (t, *J* = 7.5, 2H). ^{13}C {^{1}H} NMR (75 MHz, $CDCl_3$): δ(ppm) = 139.22 (quaternary), 137.46 (quaternary), 136.93, 134.14, 130.74 (quaternary), 130.72, 130.49 (quaternary), 125.48, 124.24 (quaternary), 122.95, 122.34, 121.16. Anal. Calcd for $C_{12}H_7BrO_2S$: C, 48.83; H, 2.39; S, 10.86 %; Found: C, 48.82; H, 2.49; S, 10.96 %. HR-MS Calcd for $[C_{12}H_7BrO_2S + Na]^+$: m/z = 316.9248, 318.9227 ; Found: m/z = 316.9243, 318.9222.3-Dibenzo[b,d]thiophene sulfone boronic acid (pinacol) ester

3-Bromodibezo[*b*,*d*]thiophene sulfone (147 mg, 0.5 mmol), diboron pinacol ester (152 mg, 0.6 mmol), potassium acetate (293 mg, 3.0 mmol) and Pd(dppf)Cl_2 (4.8 mg, 6.5 µmols 1.3 mol%) were added to a dry flask, dried under vacuum for 5 mins and then purged with N_2. *N*,*N*-Dimethylformamide (4 mL) was added via a syringe and the solution was stirred under nitrogen at 90 °C overnight. The solution was addedto water (20 mL) and the product extracted with ethyl acetate. The crude product was recrystallized from acetonitrile to give brown crystals of 3-dibenzo[*b*,*d*]thiophene sulfone boronic acid (pinacol) ester (129 mg, 0.37 mmol, 72%). ^{1}H NMR (400 MHz, $CDCl_3$): δ(ppm) = 8.29 (s, 1H), 8.05 (d, *J* = 7.5 Hz, 1H), 7.83 (m, 2H), 7.79 (d, *J* = 7.5 Hz, 1H), 7.65 (t, *J* = 7.5, 1H), 7.55 (t, *J* = 7.5, 1H), 1.36 (s, 12H). ^{13}C {^{1}H} NMR (75 MHz, $CDCl_3$): δ(ppm) = 140.14, 138.17 (quaternary), 137.18 (quaternary), 133.80(s), 131.63(2C, quaternary), 130.77, 128.42, 122.3, 121.91, 120.73, 84.58 (quaternary), 24.89. Signals for carbons bonded to boron were not observed due to C-B coupling. Anal. Calcd for $C_{18}H_{19}BO_4S$: C, 63.18; H, 5.60; S, 9.37 %; Found: C, 62.63; H, 5.45; S, 9.11 %. HR-MS Calcd for $[C_{18}H_{19}BO_4S + Na]^+$: m/z = 365.0995; found: m/z = 365.0995.

*9,9,9',9'-Tetramethyl bifluorene (**MeF2**)*

A flask was charged with 9,9-dimethylfluoren-2-yl boronic acid pinacol ester (320 mg, 1 mmol), 2-bromo-9,9-dimethylfluorene (273 mg, 1 mmol), toluene (10 mL), sodium carbonate solution (2 M, 5 mL) and Starks' catalyst (1 drop) and was degassed via nitrogen bubbling for 30 minutes. $[Pd(PPh_3)_4]$ (17.3 mg, 0.015 mmol, 1.5 mol%) was added and the mixture was degassed for further 10 minutes before refluxing at 110 °C for 48 hours. The mixture was allowed to cool to room temperature before being poured into water (30 mL). The organic phase was extracted with chloroform (30 mL), washed with brine (20 mL) and dried with magnesium sulfate, filtered, and the solvents were removed under reduced pressure. The crude product was recrystallized using a two-solvents mixture of dichloromethane/*n*-hexane to give 9,9,9',9'-tetramethyl bifluorene as white crystals (298 mg, 77%). ^{1}H NMR (400 MHz, $CDCl_3$): δ(ppm) =1.52-1.53 (m, 12H), 7.31-7.39 (m, 4H), 7.47 (dd, *J* = 7.0, 1.5 Hz, 2H), 7.64 (dd, *J* = 7.0, 2.0 Hz, 2H), 7.70 (s, 2H), 7.76 (dd, *J* = 7.0, 1.5 Hz, 2H), 7.81 (d, *J* = 7.0Hz, 2H). ^{13}C{^{1}H} NMR (75 MHz, $CDCl_3$): δ (ppm) = 27.6, 47.1, 120.4, 121.5, 122.8, 126.4, 127.2, 127.4, 138.5, 139.0, 140.9, 154.0, 154.4, 120.2. Anal. Calcd (for $C_{15}H_{13}$): C, 93.22; H, 6.78%; Found: C, 91.52; H, 6.64%. HR-MS Calcd for $[C_{30}H_{26}]^+$: m/z = 386.2035; found: m/z = 386.2028.

*9,9,9',9',9'',9''-Hexamethyl terfluorene (**MeF3**)*

A flask was charged with 2,7-dibromo-9,9-dimethylfluorene (353 mg, 1 mmol), 2-(9,9-dimethylfluoren-yl boronic acid pinacol ester (640 mg, 2 mmol), toluene (20 mL), sodium carbonate solution (2 M, 10 mL) and Starks' catalyst (1 drop) and was degassed via nitrogen

bubbling for 30 minutes. $[Pd(PPh_3)_4]$ (17.3 mg, 0.015 mmol, 1.5 mol%) was added and the mixture was degassed for further 10 minutes before refluxing at 110 °C for 48 hours. The mixture was allowed to cool to room temperature before being poured into water (60 mL). The organic phase was extracted with chloroform (60 mL), washed with brine (20 mL) and dried with magnesium sulfate, filtered, and the solvents were removed under reduced pressure. The crude product was recrystallized using a two-solvents mixture of dichloromethane/ *n*-hexane to give the pure product as white crystals (521mg, 0.901 mmol, 90%). ^{1}H NMR (400 MHz, $CDCl_3$): δ(ppm) = 7.84 (d, *J* = 8.0 Hz, 2H), 7.81(d, J 8.0 Hz, 2H), 7.77 (dd, *J* = 6.5, 1.5 Hz, 2H), 7.72 (dd, *J* = 4.0, 1.5 Hz, 4H), 7.65-7.68 (m, 4H), 7.47 (dd, *J* = 6.5, 1.5 Hz, 2H), 7.31-7.39 (m, 4H), 1.65 (s, 6H), 1.58 (s, 12H). ^{13}C{^{1}H} NMR (75 MHz, $CDCl_3$): δ (ppm) = 154.6, 154.3, 153.9, 140.8 (2x), 138.9, 138.4, 138.1, 127.2, 127.0, 126.4, 126.3, 122.6, 121.4, 120.4, 120.3, 120.1, 47.1, 47.0, 27.4, 27.3. Anal. Calcd (for $C_{45}H_{38}$): C, 93.38; H, 6.62%; Found: C, 92.55; H, 6.52%. HR-MS Calcd for $[C_{45}H_{38}]^+$: m/z = 578.2974; Found: m/z = 578.2969.

*3,7-Diphenyldibenzo[b,d]thiophene sulfone (**PSP**)*

A flask was charged with the 3,7-dibromodibenzo[*b*,*d*]thiophene sulfone (374 mg, 1.0 mmol), phenylboronic acid (366 mg, 3 mmol), Starks' catalyst (2 drops), toluene (50 mL), aqueous K_2CO_3 (25 mL, 2 M) and the mixture was degassed with nitrogen. Then $[Pd(PPh_3)_4]$ (35 mg, 3 mol%) was added and the reaction was heated to 110 °C for 2 days. After cooling to room temperature the layers were separated, and the aqueous phase was extracted with toluene. The combined organic phases were filtered over a plug of SiO_2 and the plug was thoroughly washed with dichloromethane. The combined organic phases were reduced to around 20 mL and the filters that formed were filtered off giving the product as white crystals in 76% yield (280 mg). ^{1}H NMR (400 MHz, $CDCl_3$): δ (ppm) = 8.06 (s, 2 H), 7.88 (d, *J* = 1.0 Hz, 4H), 7.65 (d, *J* = 7.5 Hz, 4H), 7.50 (t, *J* = 7.5 Hz, 4H), 7.44 (t, *J* = 7.5 Hz, 2H). ^{13}C{^{1}H} NMR (75 MHz, $CDCl_3$): δ (ppm) = 143.8, 138.8, 138.7, 132.6, 130.2, 129.2, 128.6, 127.1, 121.9, 120.8. Anal. Calcd for $C_{24}H_{16}O_2S$: C, 78.24; H, 4.38; O, 8.68; S, 8.70%; Found: C, 77.48; H, 4.35; S, 8.64%. HR-MS Calcd for $[C_{24}H_{16}O_2S+Na]^+$: m/z = 391.0769; Found: m/z = 391.0767.

*3,7-Dimesityldibenzo[b,d]thiophene sulfone (**MSM**)*

A flask was charged with mesitylboronic acid (328 mg, 2 mmol), 3,7-dibromodibenzo[*b*,*d*]thiophene sulfone (374 mg, 1 mmol), toluene (20 mL), potassium carbonate solution (2 M, 7 mL) and Starks' catalyst (1 drop) and was degassed via nitrogen bubbling for 30 minutes. $[Pd(PPh_3)_4]$ (15 mg) was added and the mixture was degassed for further 10 minutes before refluxing at 110 °C for 48 hours. The mixture was allowed to cool to room temperature before being poured into water (50 mL). The organic phase was

extracted with chloroform (50 mL), washed with brine (40 mL) and dried with magnesium sulfate, filtered, and the solvents were removed under reduced pressure. The crude product was purified by column chromatography in light petroleum ether : ethyl acetate (75:25 gradient to 30:70) and was then recrystallized using a two-solvents mixture of dichloromethane/methanol to give the pure product as white crystals (201 mg, 44%). ^{1}H NMR (400 MHz, $CDCl_3$): δ (ppm) = 7.88 (d, *J* = 7.5 Hz, 2H), 7.63 (d, *J* = 1.0 Hz, 2H), 7.44 (dd, *J* = 7.5 and 1.0 Hz, 2H), 6.97 (s, 4H), 2.35 (s, 6H), 2.04 (s, 12H). ^{13}C{^{1}H} NMR (75 MHz, $CDCl_3$): δ (ppm) = 144.0, 138.4, 137.7, 136.6, 135.7, 135.2, 130.1, 128.5, 123.1, 121.6, 21.1, 20.8. Anal. Calcd (for $C_{30}H_{28}O_2S$): C, 79.61; H, 6.24; O, 7.07; S, 7.08%; Found: C, 79.01; H, 6.14; S, 6.98%. HR-MS Calcd for $[C_{30}H_{28}O_2S + Na]^+$: m/z = 475.1708; Found: m/z = 475.1707.

*3,7-Diphenylfluorene (**PFP**)*

A flask was charged with the 2,7-dibromo-9*H*-fluorene (1.22 g, 3.77 mmol), phenylboronic acid (1.38 g, 11.31 mmol), Starks' catalyst (2 drops), toluene (50 mL), aqueous K_2CO_3 (25 mL, 2 M) and the mixture was degassed with nitrogen. Then $[Pd(PPh_3)_4]$ (35 mg, 3 mol%) was added and the reaction was heated to 110 °C for 2 days. After cooling to room temperature the layers were separated, and the aqueous phase was extracted with chloroform. The combined organic phases were filtered over a plug of SiO_2 and the plug was thoroughly washed with chloroform. The combined organic phases were evaporated to dryness and the product recrystallized from toluene to give the product as white crystals in 74% yield (888 mg). ^{1}H NMR (400 MHz, $CDCl_3$): δ (ppm) = 7.87 (d, *J* = 7.5 Hz, 2H), 7.80 (d, *J* = 1.5 Hz, 2H), 7.67 (dd, *J* = 1.5 and 7.5 Hz, 4H), 7.64 (d, *J* = 7.5 Hz, 2H), 7.47 (t, J 7.5 Hz, 4H) 7.36 (tt, *J* = 7.5 and 1.5 Hz, 2H) 4.03 (s, 2H). ^{13}C{^{1}H} NMR (75 MHz, $CDCl_3$): δ (ppm) = 144.2, 141.5, 140.6, 139.9, 128.8, 127.2, 127.1, 126.1, 123.8, 120.2, 37.2. Anal. Calcd for $C_{25}H_{18}$: C, 94.30; H, 5.70%; Found: C, 94.46; H, 5.72%. GC-MS Calcd for $[C_{25}H_{18}]^+$: m/z = 318; found: m/z = 318.

*3,7-Dimesitylfluorene (**MFM**)*

A flask was charged with the 2,7-dibromo-9*H*-fluorene (972 mg, 3.0 mmol), 2,4,6-trimethylphenylboronic acid (1.48 g, 9 mmol), Starks' catalyst (3 drops), toluene (150 mL), aqueous K_2CO_3 (75 mL, 2 M) and the mixture was degassed with nitrogen. Then $[Pd(PPh_3)_4]$ (105 mg, 3 mol%) was added and the reaction was heated to 110 °C for 2 days. After cooling to room temperature, the layers were separated, and the aqueous phase was extracted with toluene. The combined organic phases were dried over $MgSO_4$, filtered, and the solvents were removed under reduced pressure. The crude product was then recrystallized from acetonitrile to give the product as light brown crystals in 48% yield (653 mg). ^{1}H NMR

(400 MHz, $CDCl_3$): δ (ppm) = 7.85 (d, *J* = 7.5 Hz, 2H), 7.32 (s, 2H), 7.16 (d, *J* = 7.5 Hz, 2H), 6.97 (s, 4H), 3.98 (s, 2H) 2.35 (s, 6H), 2.05 (s, 12H). $^{13}C\{^1H\}$ NMR (75 MHz, $CDCl_3$): δ (ppm) = 143.6, 140.0, 139.6, 139.4, 136.5, 136.2, 128.1, 128.0, 125.9, 119.7, 37.1, 21.1, 20.8.Anal. Calcd for $C_{31}H_{30}$: C, 92.49; H, 7.51%; Found: C, 91.88; H, 7.60%. HR-MS Calcd for $[C_{31}H_{30}+H]^+$: m/z = 404.2426, 404.2460; found: m/z = 403.2422, 404.2457.

*Bis-dibenzo[b,d]thiophene sulfone (**S2**)*

3-Bromodibenzo[*b,d*]thiophene sulfone (147 mg, 0.5 mmol), 3-dibenzo[*b,d*]thiophene sulfone boronic acid (pinacol) ester (179 mg, 0.5 mmol), toluene (10 mL), sodium carbonate solution (2 M, 5 mL) and Starks' catalyst (1 drop) and was degassed via nitrogen bubbling for 30 minutes. $[Pd(PPh_3)_4]$ (8 mg, 0.007 mmol, 1.4 mol%) was added and the mixture was degassed for further 10 minutes before refluxing at 110°C for 48 hours. The mixture was allowed to cool to room temperature before pouring into methanol (150 mL). The precipitate was collected by filtration and washed with methanol, water and chloroform to give bis-dibenzo[*b,d*]thiophene sulfone as an off-white powder (198 mg, 0.46 mmol, 92%).^{1}H NMR (400 MHz, $C_2D_2Cl_4$, 373 K): δ(ppm) = 8.11 (s, 2H), 7.99 – 7.88 (unresolved m, 8H), 7.74 (t, *J* = 7.5 Hz, 2H), 7.63 (t, *J* = 7.5 Hz, 2H). ^{13}C NMR in solution was not possible due to poor solubility. Solid state ^{13}C $\{^1H\}$ NMR: δ(ppm) = 137.3 (C_1, C_3, C_8), 134.0 (C_{11}), 131.9 (C_4), 130.4 (C_6, C_7), 129.2 (C_5), 125.0 (C_2), 123.1 (C_{12}), 120.3 (C_{10}), 116.7 (C_9). HR-MS Calcd for $[C_{12}H_7O_2S+H]^+$: m/z = 431.0412; found: m/z = 431.0415. Anal. Calcd for $C_{12}H_7O_2S$: C, 66.96; H, 3.28; O, 14.87; S, 14.89%; Found: C, 66.10; H, 3.54; S, 14.81%.

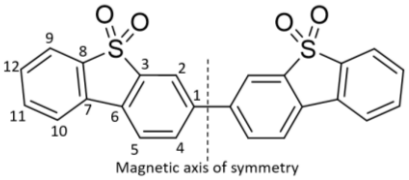

*Tris-dibenzo[b,d]thiophene sulfone (**S3**)*

3-Bromodibezo[*b,d*]thiophene sulfone (147 mg, 0.5 mmol), 3,7-dibezo[*b,d*]thiophene sulfone diboronic acid bis(pinacol) ester (117 mg, 0.25 mmol), toluene (10 mL), sodium carbonate solution (2 M, 5 mL) and Starks' catalyst (1 drop) and was degassed via nitrogen bubbling for 30 minutes. $[Pd(PPh_3)_4]$ (8 mg, 0.007 mmol, 1.4 mol%) was added and the mixture was degassed for further 10 minutes before refluxing at 110 °C for 48 hours. The mixture was allowed to cool to room temperature before pouring into methanol (150 mL). The precipitate was collected by filtration and washed with methanol and water. Purification by Soxhlet extraction using methanol, followed by chloroform gave tris-dibenzo[*b,d*]thiophene sulfone as a green-yellow powder (143 mg, 0.22 mmol, 89%). NMR in solution was not possible due to poor solubility in chloroform, DMSO and

tetrachloroethane. Solid state ^{13}C {^{1}H} NMR: δ(ppm) = 140.1 ($C_{5,}$ C_{15}), 139.8 (C_8), 136.8 ($C_{1,}$ C_{13}), 133.3 (C_{11}), 131.5 ($C_{4,}$ $C_{7,}$ C_{16}), 130.3 (C_5, C_6, C_{17}, C_{18}), 124.5 ($C_{2,}$ C_{14}), 122.3 (C_{12}), 120.5 (C_{10}), 116.5 (C_9). HR-MS Calcd for $[C_{36}H_{20}O_6S_3+H]^+$: m/z = 645.0500; found: m/z = 645.0509. Anal. Calcd for $C_{36}H_{20}O_6S_3$: C, 67.07; H, 3.13; O, 14.89; S, 14.92%; Found: C, 65.81; H, 3.23; S, 14.58%.

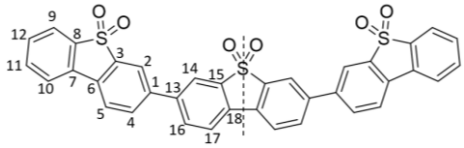

*Homopolymer of dibenzo[b,d]thiophene sulfone by Suzuki coupling (**P10$_{0.2}$**, **P10$_{0.7}$**, **P10$_{2.7}$**)*

P10 was synthesized following a previously reported synthetic procedure:[44] 3,7-dibromodibenzo[*b*,*d*]thiophene sulfone (187 mg, 0.5 mmol), 3,7-bis(4,4,5,5-tetramethyl-1,3,2-dioxaborolan-2-yl)dibenzo[*b*,*d*]thiophene sulfone (234 mg, 0.5 mmol), *N*,*N*-dimethylformamide (25 mL) and K_2CO_3 (aq., 2 M, 5 mL) were added to a flask and degassed by N_2 bubbling for 30 minutes. Tetrakis(triphenylphosphine)palladium(0) (6, 23 or 69 mg; corresponding to 0.5, 2 or 6 mol. %) was added and the mixtures were degassed for a further 10 minutes. The reactions were refluxed at 140 °C for 48 hours under a nitrogen atmosphere. After cooling to room temperature, the reaction mixtures were poured into water (400 mL) and stirred for 30 minutes. The yellow-green solids were collected by filtration and washed with water (100 mL) and methanol (100 mL). The polymers were purified by Soxhlet extraction in methanol and chloroform before drying the solids under vacuum. The polymers were ground before use to give free flowing yellow-green powders (207, 214 or 211 mg, 97-100 %). Anal. Calcd for $C_{12}H_6O_2S_3$: C, 67.29; H, 2.83; S, 14.94%; Found **P10$_{0.2}$**: C, 60.77; H, 3.02; S, 13.76%. Found **P10$_{0.7}$**: C, 58.16; H, 3.00; S, 13.16%. Found **P10$_{2.7}$**: C, 58.99; H, 3.03; S, 13.42%.

*Homopolymer of dibenzo[b,d]thiophene sulfone by Yamamoto coupling (**P10$_Y$**)*

P10 was prepared via Yamamoto coupling following a previously reported protocol:[44] A flame-dried Schlenk flask was charged with 3,7-dibromodibenzo[*b*,*d*]thiophene sulfone (374 mg, 1.00 mmol), 2,2′-bipyridine (344 mg, 2.20 mmol), and transferred into a nitrogen glove-box. Inside the glove-box the flask was charged with bis(cyclooctadiene)nickel(0) (660 mg, 2.40 mmol). Outside the glove-box 1,5-cyclooctadiene (338 mg, 2.20 mmol) and *N*,*N*-dimethylformamide (anhydrous, 20 mL) were added and the resulting suspension was heated to 80 °C under nitrogen for 2 days. After

cooling to room temperature hydrochloric acid was added (conc., 20 mL) and the polymer was filtered off. The polymer was washed with water until neutral, and then methanol and tetrahydrofuran. Further purification of the polymer was carried out by Soxhlet extraction in chloroform before drying the solids under vacuum. The polymer was ground before use to give a free-flowing yellow powder (190 mg, 84 %). Anal. Calcd for $C_{12}H_6O_2S_3$: C, 67.29; H, 2.83; S, 14.94%; Found: C, 62.05; H, 3.83; S, 12.25%

2,8-Dibromodibenzothiophene

A solution of dibenzothiophene (10.0 g, 54.2 mmol) in chloroform (30 mL), connected to a sodium sulfite/sodium hydroxide scrubber (2 eq of sodium hydroxide: 1 eq sodium sulfite), was cooled to 0°C and bromine (6.2 mL, 121 mmol) was added drop wise. The reaction was stirred overnight under nitrogen before filtering. The residue was washed with more of the scrubber solution (10 mL) and methanol (10 mL) to give the 2,8-dibromothiophene as a white powder (18.1 g, 52.9 mmol, 98%). ^{1}H NMR (400 MHz, $CDCl_3$): δ (ppm) = 8.22 (s, 2H), 7.70 (d, J = 8.0 Hz, 2H), 7.57 (d, J = 8.0 Hz, 2H). $^{13}C\{^1H\}$ NMR (75 MHz, $CDCl_3$): δ (ppm) = 138.6 (quarternary), 136.2 (quarternary), 130.3, 124.7, 124.2, 118.6 (quarternary).

*2,8-Dihexyldibenzo[b,d]thiophene sulfone (**S_6**)*

A flask was purged with nitrogen and charged with 2,8-dibromodibenzothiophene (10.0 g, 29.3 mmol) and dry THF (200 mL) and the solution was cooled to -78°C using dry ice/acetone. Hexyl-lithium in hexane (28 mL, 2.3 M, 64.4 mmol) was added dropwise and the solution was stirred for 3h. 1-bromohexane (10 mL, 7.12 mmol) was added and the solution was allowed to warm to room temperature and stirred for 12 hours. Water (20 mL) was added and the mixture was stirred for 2h. The product was extracted with diethyl ether, washed with water and dried with magnesium sulphate. The solvent was removed under reduced pressure to give the product as a yellow oil.

The oil was dissolved in acetic acid (50 mL, hydrogen peroxide (30% in water, 15 mL) was carefully added and the solution was heated with stirring at 140 °C for 2 hours. More hydrogen peroxide (10 mL) was added and the solution was heated for a further 16h. After cooling, water (150 mL) was added and the product was extracted with chloroform, washed with water and dried over magnesium sulphate to give a yellow oil. The crude product was recrystallized from ethanol in the freezer to yield a the product as a white solid (5.88 g, 15.3 mmol, 52%) ^{1}H NMR (400 MHz, $CDCl_3$): δ (ppm) = 7.68 (d, *J* = 7.9 Hz, 2H), 7.56 (d, *J* = 0.9 Hz, 2H), 7.29 (dd, *J* = 7.9, 1.4 Hz, 2H), 2.77-2.60 (m, 4H), 1.72-1.59 (m, 4H), 1.45-1.24 (m, 12H), 0.88 (dd, *J* = 8.9, 5.2 Hz, 6H). $^{13}C\{^1H\}$ NMR (75 MHz, $CDCl_3$): δ (ppm) = 149.9, 136.0, 132.3, 130.6, 122.2, 121.5, 36.5, 31.9, 31.4, 29.1, 22.8, 14.3. HR-MS Calcd for

$[C_{24}H_{32}O_2S+Na]^+$: m/z = 407.2015; found: m/z = 407.2019. Anal. Calcd for $C_{24}H_{32}O_2S$: C, 74.96; H, 8.39; O, 8.32; S, 8.34%; Found: C, 73.60; H, 7.97; S, 8.27%.

2,8-Dihexyl-3,7-dibromodibenzo[b,d]thiophene sulfone and 2,8-Dihexyl-3-bromodibenzo[b,d]thiophene sulfone

2,8-Dihexyldibenzothiophene sulfone, (2.5 g, 6.5 mmol) and sulfuric acid (150 mL) were heated in a nitrogen purged flask to 70°C. Under dark conditions N-bromosuccinimide (2.6 g, 14.6 mmol) was added in portions and the solution stirred for 24h. The mixture was carefully added to water with cooling and then extracted with chloroform, washed with water and dried with magnesium sulphate. The di- and monobrominated products was isolated by column chromatography eluting with *n*-hexane: DCM (1:1).

2,8-Dihexyl-3,7-dibromodibenzo[*b*,*d*]thiophene sulfone (780 mg, 1.44 mmol, 57.5%) ^{1}H NMR (400 MHz, $CDCl_3$): δ (ppm) = 7.91 (s, 2H), 7.56 (s, 2H), 2.85-2.74 (m, 4H), 1.74-1.57 (m, 4H), 1.47-1.26 (m, 12H), 0.89 (dd, J 9.5, 4.7 Hz, 6H). $^{13}C\{^1H\}$ NMR (75 MHz, $CDCl_3$): δ (ppm) = 149.2, 136.8, 130.5, 126.8, 126.4, 122.8, 77.6, 77.2, 76.9, 37.1, 31.8, 29.9, 29.3, 22.8, 14.3.

2,8-Dihexyl-3-bromodibenzo[*b*,*d*]thiophene sulfone (372 mg, 0.80 mmol, 12.3%). ^{1}H NMR (400 MHz, $CDCl_3$): δ (ppm) = 7.92 (s, 1H), 7.67 (d, J 7.9 Hz, 1H), 7.60-7.52 (m, 2H), 7.31 (dd, J 7.9, 1.4 Hz, 1H), 2.88-2.75 (m, 2H), 2.75-2.65 (m, 2H), 1.73-1.57 (m, 4H), 1.49-1.19 (m, 12H), 0.98-0.76 (m, 6H). $^{13}C\{^1H\}$ NMR (75 MHz, $CDCl_3$): δ (ppm) = δ 150.27, 148.82, 137.20, 135.54, 131.47, 131.26, 130.85, 126.63, 125.99, 122.90, 122.32, 121.54, 37.04, 36.47, 31.83, 31.79, 31.40, 29.88, 29.28, 29.07, 22.78, 22.77, 14.28, 14.27.

3-(2,8-Dihexyldibenzo[b,d]thiophene sulfone) boronic acid (pinacol) ester

2,8-Dihexyl-3-bromodibenzo[*b*,*d*]thiophene sulfone (231 mg, 0.50 mmol), diboronpinacol ester (152 mg, 0.6 mmol), potassium acetate (293 mg, 3.0 mmol) and [Pd(dppf)Cl_2] (4.8 mg, 6.5 µmols, 1.3 mol%) were added to a dry flask, dried under vaccum for 5 mins and then purged with N_2. DMF (4 mL) was added *via* syringe and the solution was stirred under nitrogen at 90 °C overnight. The solution was added to water (20 mL) and the product extracted with ethyl acetate. The crude product was recrystallised from acetonitrile to give brown crystals of the product (166 mg, 0.33 mmol, 65%). ^{1}H NMR (400 MHz, $CDCl_3$): δ (ppm) = 8.25 (s, 1H), 7.71 (d, J 7.5 Hz, 1H), 7.83 (m, 4H), 7.60 (s, 1H), 7.55 (s, 1H), 7.32 (d, J 7.5, 1H), 2.96-3.00 (m, 2H), 2.70-2.75 (m, 2H), 1.54 -1.71 (m, 4H), 1.49-1.19 (m, 12H), 0.87-0.93 (m, 6H).

*2',8''-Dihexyl- tris-dibenzo[b,d]thiophene sulfone (**SS_6S**)*

A flask was charged with 2,8-dihexyl-3,7-dibromodibenzo[*b*,*d*]thiophene sulfone (109 mg, 0.2 mmol), 3-dibenzo[*b*,*d*]thiophene sulfone) boronic acid (pinacol) ester (137 mg, 0.4 mmol), toluene (5 mL), sodium carbonate solution (2 M, 2.5 mL) and Starks' catalyst (1 drop) and was degassed via nitrogen bubbling for 30 minutes. $[Pd(PPh_3)_4]$ (6 mg, 0.006 mmol, 1.5 mol%) was added and the mixture was degassed for a further 10 minutes before refluxing at 110 °C for 48 hours. The mixture was allowed to cool before being poured into water (60 mL). The organic phase was extracted with chloroform (60 mL), washed with brine (20 mL) and dried with magnesium sulfate before removing the solvent under vacuum. The product was re-crystallised from DCM : methanol to give a white powder (150 mg, 0.19 mmol, 93%). ^{1}H NMR (400 MHz, CDCl3): δ(ppm) = 7.84 (d, J = 7.8 Hz, 2H), 7.80 (d, J = 8 Hz, 4H), 7.73 (s, 4 H), 7.63 (t, J = 8 Hz, 2H), 7.62 (s, 2H), 7.54 (t, J = 8 Hz, 2H), 7.51 (d, J = 8 Hz, 2H), 2.64 (t, J = 8 Hz, 4H), 1.47 -1.54 (m, 4H), 1.12-1.22 (m, 12H), 0.76 (t, J = 8 Hz, 6H). $^{13}C\{^1H\}$ NMR (75 MHz, $CDCl_3$): δ (ppm) = 147.5, 142.3, 141.8, 138.3, 138.0, 136.1, 134.6, 134.1, 131.3, 131.3, 131.1, 130.7, 123.5, 122.7, 122,6, 122.4, 121.8, 121.8, 33.6, 31.4, 31.2, 29.0, 22.5, 14.0. Anal. Calcd for $C_{48}H_{44}O_6S_3$: C, 70.91; H, 5.45; O, 11.81; S, 11.83%; Found: C, 69.84; H, 5.01; S, 10.10%.

*2,2'',8,8''-Tetrahexyl- tris-dibenzo[b,d]thiophene sulfone (**S_6SS_6**)*

A flask was charged with 2,8-dihexyl-3- bromodibenzo[*b*,*d*]thiophene sulfone (256.5 mg, 0.56 mmol), 3,7-dibezothiophene sulfone diboronic acid bis(pinacol) ester (130 mg, 0.28 mmol), toluene (10 mL), sodium carbonate solution (2 M, 5 mL) and Starks' catalyst (1 drop) and was degassed via nitrogen bubbling for 30 minutes. $[Pd(PPh_3)_4]$ (8 mg, 0.007 mmol, 1.4 mol%) was added and the mixture was degassed for a further 10 minutes before refluxing at 110°C for 48h. The mixture was allowed to cool before being poured into water (60 mL). The organic phase was extracted with chloroform (60 mL), washed with brine (20 mL) and dried with magnesium sulphate before removing the solvent under vacuum. The product was re-crystalised from DCM : methanol to give an off-white powder (250 mg, 0.25 mmol, 91%). ^{1}H NMR (400 MHz, $CDCl_3$): δ (ppm) = 7.96 (d, J 8.0 Hz, 2H), 7.82 (s, 2H), 7.72-7.77 (m, 4H), 7.63-7.69 (m, 6H), 7.34 (d, J 8.0 Hz, 2H), 2.66-2.79 (m, 8H), 1.19-1.74 (m, 24H), 0.82-0.93 (m, 12H). $^{13}C\{^1H\}$ NMR (75 MHz, $CDCl_3$): δ (ppm) = 150.1, 147.3, 142.7, 141.4, 138.5, 136.1, 135.7, 134.7, 131.9, 131.5, 130.8, 130.7, 123.3, 122.8, 122.5, 122.2, 122.0, 121.6, 36.29, 33.61, 31.7, 31.4, 31.3, 31.2, 29.0, 28.9, 22.6, 22.5, 14.1, 14.0.

Anal. Calcd for $C_{60}H_{68}O_6S_3$: C, 73.43; H, 6.98; O, 9.78; S, 9.80%; Found: C, 72.33; H, 6.92; S, 9.04%.

*2,2',2'',8,8',8''-Hexahexyl- tris-dibenzo[b,d]thiophene sulfone (**$S_6S_6S_6$**)*

A flask was charged with 2,8-dihexyl-3,7-dibromodibenzo[*b*,*d*]thiophene sulfone (54 mg, 0.10 mmol), 3-(2,8-dihexyldibenzo[*b*,*d*]thiophene sulfone) boronic acid (pinacol) ester (100 mg, 0.20 mmol), toluene (5 mL), sodium carbonate solution (2 M, 2.5 mL) and Starks' catalyst (1 drop) and was degassed via nitrogen bubbling for 30 minutes. $[Pd(PPh_3)_4]$ (3 mg, 0.003 mmol, 1.5 mol%) was added and the mixture was degassed for a further 10 minutes before refluxing at 110°C for 48h. The mixture was allowed to cool before being poured into water (60 mL). The organic phase was extracted with chloroform (60 mL), washed with brine (20 mL) and dried with magnesium sulfate before removing the solvent under vacuum. The product was re-crystalised from DCM : methanol to give a white powder (101 mg, 0.088 mmol, 88%). ^{1}H NMR (400 MHz, CDCl3): δ(ppm) = 7.81 (s, 2H), 7.76 (s, 2H), 7.48 (d, J 7.0 Hz, 2H), 7.66 (2, 2H), 7.59 (s, 2H), 7.55 (s, 2H), 7.36 (d, J 7.0 Hz, 2H), 2.76 (t, 4H), 2.40-2.57 (m, 8H), 1.70 (t, 4H), 1.49-1.60 (m, 8H), 1.31-1.42 (m, 12H), 1.18-1.28 (m, 24H), 0.89-0.93 (m, 6H), 0.80-0.85 (m, 12H). $^{13}C\{^1H\}$ NMR (75 MHz, $CDCl_3$): δ (ppm)= 149.9, 147.2, 142.8, 141.5, 138.9, 136.5, 136.1, 131.9, 131.5, 130.7, 130.5, 123.3, 123.2, 122.8, 122.4, 122.1, , 121.8, 121.4, 36.2, 33.7, 33.6, 31.6, 31.4, 31.3, 31.1, 31.0, 29.0, 28.9, 28.8, 22.4, 22.3, 22.34, 22.32, 13.9, 13.79, 13.77. HR-MS Calcd for $[C_{72}H_{92}O_6S_3+Na]^+$: m/z = 1171.5948; found: m/z = 1171.5937. Anal. Calcd for $C_{72}H_{92}O_6S_3$: C, 75.22; H, 8.07; O, 8.07; S, 8.37%; Found: C, 71.72; H, 7.64; S, 7.75%.

*Copolymer of 1,4-Benzenediboronic acid bis(pinacol)ester and 3,7-Dibromodibenzo[b,d]thiophene sulfone (**P7**)*

3,7-Dibromodibenzo[*b*,d]thiophene sulfone (748 mg, 2.0 mmol) and 1,4-benzenediboronic acid bis(pinacol)ester (660 mg, 2.0 mmol) were loaded in a N_2 purged flask. DMF (40 mL) and aqueous sodium carbonate (2 M, 8 mL) were added and the mixture was degassed by N_2 bubbling for 30 minutes. $[Pd(PPh_3)_4]$ (34 mg, 0.015 mmol, 1.5 mol%) was added and degassing continued for 30 minutes before heating to 140 °C for 48 hours. The mixture was cooled to room temperature and poured into water. The precipitate was collected by filtration and washed with H_2O and methanol. The polymers were purified by Soxhlet extraction in methanol and chloroform before drying the solids under vacuum. The polymer was ground before use to give free flowing light green powder (572 mg, 99%). Anal. Calcd for $C_{18}H_{10}O_2S$: C, 74.46; H, 3.47; S, 11.04%; Found: C, 69.20; H, 3.73; S, 10.55%.

*Copolymer of 1,4-Benzenediboronic acid bis(pinacol)ester and 2,8-dihexyl-3,7-dibromodibenzo[b,d]thiophene sulfone (**P7$_6$**)*

3,7-Dibromo-2,8-dihexyldibenzo[*b*,d]thiophene sulfone (543 mg, 1.0 mmol) and 1,4-benzenediboronic acid bis(pinacol)ester (330 mg, 1.0 mmol) were loaded in a N_2 purged flask. DMF (20 mL) and aqueous sodium carbonate (2 M, 4 mL) were added and the mixture was degassed by N_2 bubbling for 30 minutes. [$Pd(PPh_3)_4$] (17 mg, 0.015 mmol, 1.5 mol%) was added and degassing continued for 30 minutes before heating to 140 °C for 48 hours. The mixture was cooled to room temperature and poured into water. The precipitate was collected by filtration and washed with H_2O and methanol. The polymers were purified by Soxhlet extraction in methanol and chloroform before drying the solids under vacuum. The polymer was ground before use to give free flowing green powder (398 mg, 87%). Anal. Calcd for $C_{30}H_{36}O_2S$: C, 78.22; H, 7.88; S, 6.96%; Found: C, 63.50; H, 6.14; S, 4.82%.

3.10.3 Definitions and Measurement of Optical Properties

Molar extinction coefficients (ε_{Molar}) were calculated using Equation 1 below, with absorption (A) recorded at the maxima for each material in chloroform, at a range of different concentrations (c), in a cell of path length (l) 1 cm. Values were calculated from a concentration / absorption graph with at least 4 points and R^2 values of over 0.99.

$$\varepsilon_{Molar} = \frac{A}{lc} \qquad \text{(Equation 1.)}$$

Average extinction coefficients (*Average* ε_{Molar}) were calculated by averaging of absorption values over the 275-400 nm range (values collected every 0.5 nm) for each concentration. Values were calculated from a concentration / average absorption graph with at least 4 points and R^2 values of over 0.99.

Mass extinction coefficients (ε_{Mass}) were calculated by dividing the molar extinction coefficients (ε_{Molar}) by the molar mass (m_r) of each material, Equation 2, and represents the absorption of the oligomers per unit mass (m).

$$\varepsilon_{Mass} = \frac{\varepsilon_{Molar}}{m_r} = \frac{A}{lcm_r} = \frac{AV}{l\,m} \qquad \text{(Equation 2.)}$$

Average mass extinction coefficients (*Average* ε_{Mass}) were calculated by dividing the average molar extinction coefficients (*Average* ε_{Molar}) by the molar mass (m_r) of each material.

Photoluminescent quantum yields (Φ) were calculated using standard techniques,[85] Equation 3 using the quantum yield of a standard (Φ_s), the integrated fluorescence emission of the oligomers (I_x) and the standard (I_s), the absorption of the oligomers (A_x) and the standard (A_s) at the excitation wavelength and the refractive index of the solvent used for the oligomers

(η_x) and the standard (η_s). The oligomers were measured in chloroform (η_x = 1.46),[86] a quinine sulfate standard in $H_2SO_{4(aq)}$ (0.5 M) was used (Φ_s = 0.546, η_s = 1.346),[85] and values were calculated from the gradient of an absorption / emission graph with at least 4 points and R^2 values over 0.99. The uncertainty in the absorption/emission slope was used to estimate percentage errors for the quantum yield value.

$$\Phi = \frac{No.photons\ emitted}{No.photons\ absorbed} \times (100\%) = \Phi_s \frac{I_x A_s}{A_x I_s}\left(\frac{\eta_x^2}{\eta_s^2}\right) \times (100\%) \quad \text{(Equation 3.)}$$

Absorption corrected activity (ACA) values, Equation 4, were calculated by dividing the hydrogen evolution rates (HER) of the oligomers in μmol h^{-1} g^{-1}, by the average mass extinction coefficients in cm^2 g^{-1}.

$$ACA = \frac{HER}{Average\ \varepsilon_{Mass}} \quad \text{(Equation 4.)}$$

3.10.4 Single Crystal X-ray Diffraction

Table 4. Single crystal X-ray refinement details for MeF1, MeF2, and MeF3.

	MeF1	MeF2	MeF3[a]
Crystallisation Conditions	Received from supplier as crystalline sample	DCM / *n*-hexane	DCM / *n*-hexane
Space Group	$I4_1/a$	$P\bar{1}$	$P2_1/n$
Wavelength [Å]	Mo-Kα	Mo-Kα	Mo-Kα
Collection Temperature	100 K	100 K	298 K
Formula	$C_{15}H_{14}$	$2(C_{30}H_{26})$	$2(C_{45}H_{38})$
Mr	194.26	773.01	1157.5
Crystal Size (mm)	0.53 x 0.43 x 0.32	0.28 x 0.09 x 0.04	0.41 x 0.29 x 0.09
Crystal System	Tetragonal	Triclinic	Monoclinic
a [Å]	21.5488(14)	8.3173(13)	19.5956(5)
b [Å]		9.6055(17)	22.8016(4)
c [Å]	9.6725(6)	13.200(2)	16.5804(4)
α [°]		100.545(5)	
β [°]		92.275(4)	109.790(3)
γ [°]		90.001(5)	
V [Å^3]	4491.4(6)	1035.9(3)	6970.8(3)
Z	16	1	4
D_{calcd} [g cm^{-3}]	1.149	1.239	1.103
μ [mm^{-1}]	0.065	0.070	0.062
F(000)	1664	412	2464
2θ range [°]	3.78 – 61.98	4.31 – 46.61	4.77 – 52.74
Reflections collected	25139	11415	145548
Independent reflections, R_{int}	3576, 0.0572	2982, 0.1043	14055, 0.0544
Obs. Data [$I > 2\sigma$]	2650	412	7267
Data / restraints / parameters	3576 / 0 / 138	2982 / 0 / 352	14055 / 1309 / 1077
Final R1 values ($I > 2\sigma(I)$)	0.0478	0.0700	0.0955
Final R1 values (all data)	0.0671	0.1297	0.1680
Final wR(F^2) values (all data)	0.1338	0.2008	0.2548
Goodness-of-fit on F^2	1.049	1.033	1.572
Largest difference peak and hole [e.A^{-3}]	0.153 / -0.247	0.183 / -0.225	0.693 / -0.244
CCDC	1999752	1999748	1999755

[a] In the crystal structure of MeF3, one of the fluorene trimers was disordered over two position (50:50 occupancy split) and both parts were refined with constrained aromatic geometries (AFIX 66 in SHELX) and bond distance restraints (DFIX in SHELX). In addition, due to disordered, the structure was refined with a rigid bond restraint (RIGU in SHELX).

Table 5. Single crystal X-ray refinement details for PSP, PFP, MSM, and MFM.

	PSP[a]	PFP[b]	MSM[c]	MFM
Crystallisation Conditions	DCM / toluene	toluene	DCM / *n*-hexane	acetonitrile
Space Group	$P2_1/n$	$P2_1/n$	*Ia*	$P\bar{1}$
Wavelength [Å]	Mo-Kα	Mo-Kα	Mo-Kα	Mo-Kα
Collection Temperature	293 K	150 K	150 K	100 K
Formula	$C_{24}H_{16}O_2S$	$C_{25}H_{18}$	$2(C_{30}H_{28}O_2S)$	$2(C_{31}H_{30})$
Mr	368.43	318.39	905.16	805.10
Crystal Size (mm)	0.14 x 0.05 x 0.03	0.45 x 0.11 x 0.04	0.10 x 0.08 x 0.02	0.27 x 0.04 x 0.04
Crystal System	Monoclinic	Monoclinic	Monoclinic	Triclinic
a [Å]	9.362(3)	7.9704(15)	15.642(5)	8.5024(8)
b [Å]	9.511(2)	5.7466(10)	17.335(3)	11.1377(10)
c [Å]	20.202(5)	36.314(7)	18.046(3)	26.180(2)
α [°]				83.462(7)
β [°]	99.403(11)	95.924(4)	98.641(5)	84.924(7)
γ [°]				89.341(7)
V [Å^3]	1774.6(8)	1654.4(5)	4837.7(19)	2453.4(4)
Z	4	4	4	2
D_{calcd} [g cm^{-3}]	1.379	1.278	1.243	1.090
μ [mm^{-1}]	0.199	0.072	0.159	0.061
F(000)	768	672	1920	864
2θ range [°]	4.08 – 46.48	4.51 – 52.76	3.28 – 43.93	3.68 – 46.51
Reflections collected				30026
Independent reflections, R_{int}	2755, 0.0789	3387, 0.0412	5280	7071, 0.1343
Obs. Data [$I > 2\sigma$]	2012	2863	4007	3474
Data / restraints / parameters	2755 / 0 / 245	3387 / 0 / 227	5280 / 578 / 608	7071 / 3 / 571
Final R1 values ($I > 2\sigma(I)$)	0.0814	0.0524	0.0883	0.0682
Final R1 values (all data)	0.1240	0.0636	0.1178	0.1666
Final wR(F^2) values (all data)	0.1573	0.1309	0.2131	0.1792
Goodness-of-fit on F^2	1.208	1.065	1.046	0.994
Largest difference peak and hole [e.A^{-3}]	0.298 / -0.391	0.219 / -0.206	0.753 / -0.409	0.194 / -0.203
CCDC	1999749	1999747	1999756	1999753

[a] X-ray data for PSP was refined as a 2-component twin (HKLF 5) with the BASF refined to 0.504(3), after scaling the X-ray data in TWINABS. [b] X-ray data for PFP was refined as a 2-component twin (HKLF 5) with the BASF refined to 0.667(2), after scaling the X-ray data in TWINABS. [c] X-ray diffraction data for MSM was weakly diffracting and twinned. X-ray data was detwinned using the TwinRotMat function in Platon and refined as a 2-component twin (HKLF 5) with the BASF refined to 0.337(7). Due to disorder, a 0.95 Å resolution limit was applied during refinement and structure was refined with a rigid-bond restraint (RIGU in SHELX).

Table 6. Single crystal X-ray refinement details for S1, S2, and S3.

	S1	S2[a]	S3
Crystallisation Conditions	Received from supplier as crystalline sample	sublimation	sublimation
Space Group	*C*2/*c*	$P\bar{1}$	$P\bar{1}$
Wavelength [Å]	Mo-Kα	Mo-Kα	0.6889
Collection Temperature	298 K	298 K	298 K
Formula	$C_{12}H_8O_2S$	$2(C_{24}H_{14}O_4S_2)$	$2(C_{36}H_{20}O_6S_3)$
Mr	216.24	860.94	1289.40
Crystal Size (mm)	0.12 x 0.06 x 0.04	0.09 x 0.06 x 0.01	0.09 x 0.03 x 0.006
Crystal System	Monoclinic	Triclinic	Triclinic
a [Å]	10.1221(8)	7.3833(13)	7.6704(19)
b [Å]	13.8377(11)	8.4946(16)	16.878(3)
c [Å]	7.1345(5)	15.020(3)	23.693(5)
α [°]		94.371(5)	71.258(16)
β [°]	91.650(2)	93.590(6)	84.16(2)
γ [°]		90.853(5)	78.786(18)
V [Å^3]	998.89(13)	937.3(3)	2846.6(11)
Z	4	1	2
D_{calcd} [g cm^{-3}]	1.438	1.525	1.504
μ [mm^{-1}]	0.296	0.316	0.283
F(000)	448	444	1328
2θ range [°]	4.99 – 58.30	4.81 – 52.80	2.50 – 51.69
Reflections collected	6680		37013
Independent reflections, R_{int}	1349, 0.0374	3813	11880, 0.1731
Obs. Data [$I > 2\sigma$]	1139	2510	5372
Data / restraints / parameters	1349 / 0 / 69	3813 / 0 / 272	11880 / 0 / 811
Final R1 values ($I > 2\sigma(I)$)	0.0454	0.0653	0.0854
Final R1 values (all data)	0.0518	0.1041	0.1546
Final wR(F^2) values (all data)	0.1401	0.1804	0.2427
Goodness-of-fit on F^2	1.088	1.057	0.945
Largest difference peak and hole [e.A^{-3}]	0.316 / -0.332	0.306 / -0.413	0.596 / -0.354
CCDC	1999750	1999751	1999754

[a] X-ray data for S2 was detwinned using the TwinRotMat function in Platon and refined as a 2-component twin (HKLF 5) with the BASF refined to 0.198(3).

3.10.5 Analysis of S1 Breakdown Product

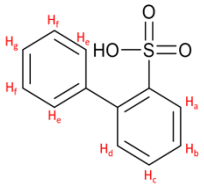

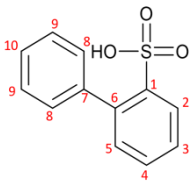

^{1}H NMR (400 MHz, $CDCl_3$): δ(ppm) = 8.08 (H_a, dd, J = 7.5, 1.5 Hz, 1H), 7.55 (H_e, d, J = 7.5 Hz, 2H), 7.45 (H_b, td, J = 7.5, 1.5 Hz, 1H,), 7.40 -7.30 (H_c, H_f, H_g, m, 4H), 7.23 (H_d dd, J = 7.5, 1.5 Hz, 1H). $^{13}C\{^{1}H\}$ NMR ($CDCl_3$): δ(ppm) = 154.07 (C_1), 139.94 (C_6), 139.80 (C_7), 130.17 (C_8), 130.05 (C_5), 129.15 (C_4), 127.84 (C_3), 127.78 (C_9), 127.04 (C_{10}), 121.81 (C_2). HR-MS Calcd for $[C_{12}H_9O_3S]^-$: m/z = 233.0278; found: m/z = 233.0274.

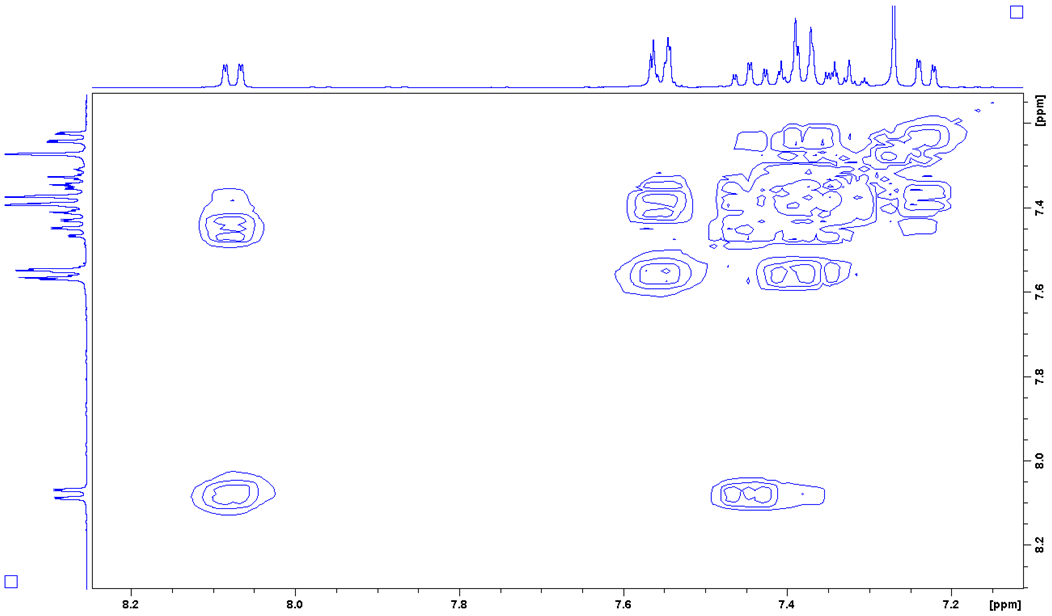

Figure 59: ^{1}H-COSY NMR spectrum of **S1** breakdown product (400 MHz, $CDCl_3$).

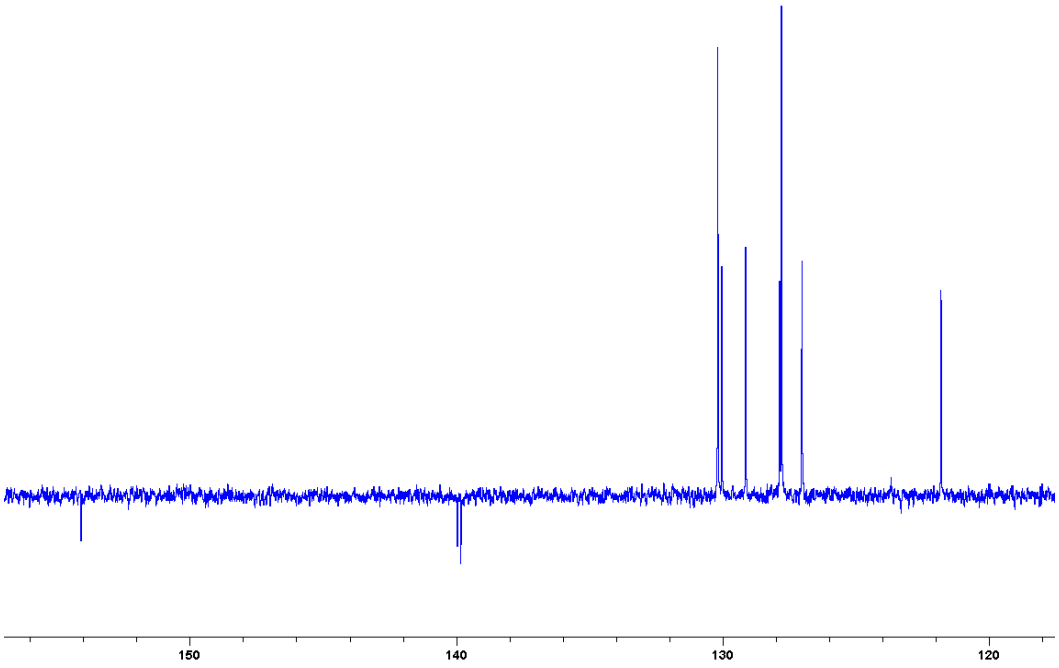

Figure 60: ^{13}C-NMR ATP spectrum of S1 breakdown product in $CDCl_3$. X-axis displays chemical shift in ppm.

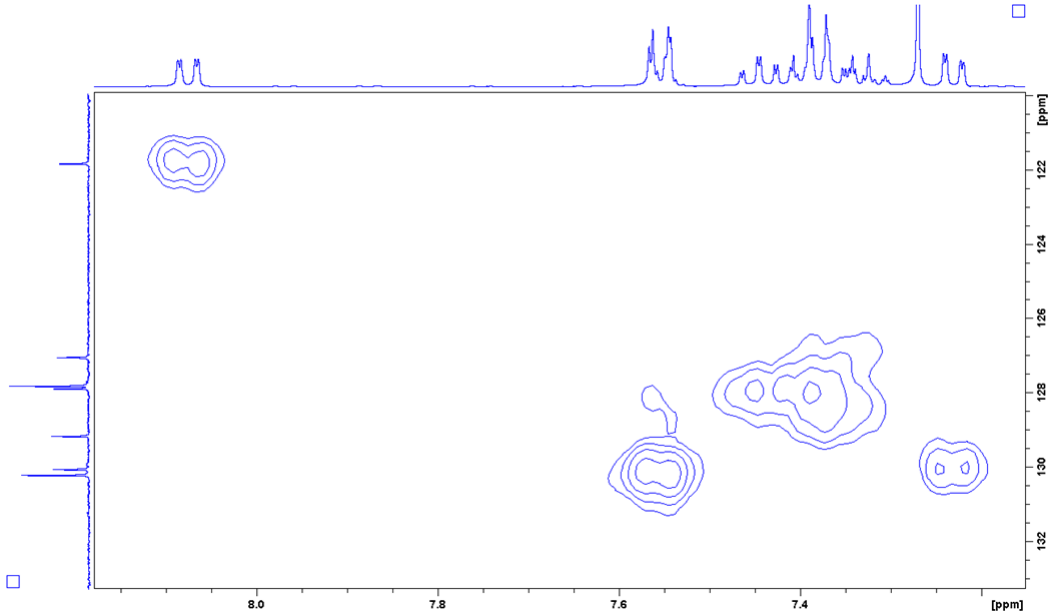

Figure 61: HSQC NMR spectra of S1 breakdown product in $CDCl_3$.

3.10.6 Summary of Photocatalytic Testing

Table 7: Summary of HERs

Material	Pd[a] (wt. %)	HER (µmol h^{-1} g^{-1}) TEA/MeOH/Water[b] λ > 295 nm filter[c]	HER (µmol h^{-1} g^{-1}) TEA/MeOH/Water[b] 400 > λ > 275 nm filter[c]	HER (µmol h^{-1} g^{-1}) Na_2S / Na_2SO_3 (aq)[d] λ > 295 nm filter	HER (µmol h^{-1} g^{-1}) Na_2S / Na_2SO_3 (aq)[d] 400 > λ > 275 nm filter[c]	HER (µmol h^{-1} g^{-1}) Homogeneous[e] 400 > λ > 275 nm filter[c]
PSP	< 0.001[f]			24.1 ± 0.8	29.6 ± 0.4	14 ± 0.5
MSM	0.002			5.5 ± 0.2	20.4 ± 0.7	44 ± 4[h]
PFP	0.003			13.8 ± 0.8	8.7 ± 0.3	120 ± 13
MFM	0.014			4.8 ± 0.4	10.0 ± 0.5	13 ± 1
MeF1	< 0.001[f]	4.7 ± 0.2[g]	2.6 ± 0.3[g]	4.1 ± 0.3	6.5 ± 0.6	107 ± 8
MeF2	0.011	12.9 ± 0.4	4.3 ± 0.3	3.4 ± 0.2	4.4 ± 0.2	93 ± 5
MeF3	0.017	37 ± 1	28 ± 1	10.1 ± 0.3	6.6 ± 0.3	30 ± 1
MeF1+ 0.02 % Pd	0.016	9.6 ± 0.5	4.9 ± 0.3	14.2 ± 0.3	28 ± 1	**HER (µmol h^{-1} g^{-1}) TEA/MeOH/Water[b] λ > 420 nm filter[c]**
S1	< 0.001[f]	26 ± 3[g,h]	20.1 ± 0.4[g,h]	8.1 ± 0.8	25.4 ± 0.2	< 0.1

S2	0.22	414 ± 9	101 ± 1	81 ± 2	50 ± 1	26 ± 1
S3	0.26	2073 ± 82	526 ± 9	286 ± 4	162 ± 6	1125 ± 9
S1 + 0.4 % Pd	0.36			14.7 ± 0.5	33 ± 0.7	< 0.1
S1+ 3 wt. % Pd	-[j]	43 ± 3[g,h]				
S2[i]	0.008	306 ± 9				
S2 + 3 wt. % Pd	2.1	1369 ± 24				
S3 + 3 wt. % Pd	2.5	6550 ± 150				
S_6	< 0.001[f]			5.1 ± 0.5	18 ± 0.4	
$S_6S_6S_6$	0.43			10 ± 0.2	66 ± 0.7	
S_6SS_6	0.33			15 ± 0.4	62 ± 2	
SS_6S	0.34			70 ± 4	87 ± 0.7	
P7	0.37	2926 ± 80	594 ± 12			1533 ± 100
$P7_6$	0.21	619 ± 40	332 ± 12			121 ± 9
$P10_{0.2}$	0.2					2825 ± 130

$P10_{0.7}$	0.7		5332 ± 180
$P10_{2.7}$	2.7		4906 ± 200
P10Y	< 0.001(0.4 Ni)		1897 ± 74
$P10_{0.2}$ + 2 wt. % Pd	1.7		5718 ± 170
P10Y + 2 wt. % Pd	1.9		4005 ± 180

[a] Measured by ICP-MS after microwave digestion with HNO_3, present from$[Pd(PPh_3)_4]$ used in synthesis via Suzuki-Miayura coupling or loaded by photodepostion using $[Pd(NH_4)_2Cl_4]$; [b] Photocatalyst (1 mg mL^{-1}) suspended in TEA/MeOH/Water (1:1:1), rate calculated as linear regression fit over 5 hours; [c] See appendix for full filter characteristics. [d] Photocatalyst (1 mg mL^{-1}) suspended in Na_2S / Na_2SO_3 (aq) (0.2 M / 0.35 M, 25 mL), rate calculated as linear regression fit over 5 hours; [e] Photocatalyst (5 mg) dissolved in THF (22.5 mL), TEA (1.25 mL) and water (1.25 mL), rate calculated as linear regression fit over 5 hours; [f] Pd level below the baseline of the instrument; [g] Catalyst partially soluble in mixture used for photocatalysis experiment; [h] Rate determined as linear regression fit less than 5 hours due to non-linearity; [i] Photocatalyst washed with sodium *N,N*-diethyldithiocarbamate. [j] Accurate Pd deposition could not be determined due to dissolution of the photocatalyst.

3.11 References

1 Z. Zhou, Y. Zhang, Y. Shen, S. Liu and Y. Zhang, *Chem. Soc. Rev.*, 2018, **47**, 2298–2321.

2 D. J. Martin, K. Qiu, S. A. Shevlin, A. D. Handoko, X. Chen, Z. Guo and J. Tang, *Angew. Chemie - Int. Ed.*, 2014, **53**, 9240–9245.

3 Z. Mo, X. She, Y. Li, L. Liu, L. Huang, Z. Chen, Q. Zhang, H. Xu and H. Li, *RSC Adv.*, 2015, **5**, 101552–101562.

4 J. Wang, Y. Shen, Y. Li, S. Liu and Y. Zhang, *Chem. - A Eur. J.*, 2016, **22**, 12449–12454.

5 X. H. Li, J. Zhang, X. Chen, A. Fischer, A. Thomas, M. Antonietti and X. Wang, *Chem. Mater.*, 2011, **23**, 4344–4348.

6 L. Lin, H. Ou, Y. Zhang and X. Wang, *ACS Catal.*, 2016, **6**, 3921–3931.

7 G. Zhang, L. Lin, G. Li, Y. Zhang, A. Savateev, S. Zafeiratos, X. Wang and M. Antonietti, *Angew. Chemie - Int. Ed.*, 2018, **57**, 9372–9376.

8 G. Zhang, G. Li, Z.-A. Lan, L. Lin, A. Savateev, T. Heil, S. Zafeiratos, X. Wang and M. Antonietti, *Angew. Chemie - Int. Ed.*, 2017, **56**, 13445–13449.

9 W. J. Ong, L. L. Tan, Y. H. Ng, S. T. Yong and S. P. Chai, *Chem. Rev.*, 2016, 116, 7159–7329.

10 J. Xu and M. Antonietti, *J. Am. Chem. Soc.*, 2017, **139**, 6026–6029.

11 V. W. Lau, I. Moudrakovski, T. Botari, S. Weinberger, M. B. Mesch, V. Duppel, J. Senker, V. Blum and B. V. Lotsch, *Nat. Commun.*, 2016, **7**, 12165.

12 V. W. H. Lau, M. B. Mesch, V. Duppel, V. Blum, J. Senker and B. V. Lotsch, *J. Am. Chem. Soc.*, 2015, **137**, 1064–1072.

13 S. Yanagida, A. Kabumoto, K. Mizumoto, C. Pac and K. Yoshino, *J. Chem. Soc. Chem. Commun.*, 1985, 474–475.

14 S. Matsuoka, H. Fujii, T. Yamada, C. Pac, a Ishida, S. Takamuku, M. Kusaba, N. Nakashima, S. Yanagida, K. Hashimoto and T. Sakata, *J. Phys. Chem.*, 1991, **95**, 5802–5808.

15 L. Wang, W. Huang, R. Li, D. Gehrig, P. W. M. Blom, K. Landfester and K. A. I. Zhang, *Angew. Chemie - Int. Ed.*, 2016, **55**, 9783–9787.

16 D. Ravelli, M. Fagnoni, A. Albini, X. Gong, W. Hu, J.-P. Fouassier and C.-H. Tan, *Chem. Soc. Rev.*, 2013, **42**, 97–113.

17 C. D. McTiernan, S. P. Pitre and J. C. Scaiano, *ACS Catal.*, 2014, **4**, 4034–4039.

18 N. A. Romero and D. A. Nicewicz, *Chem. Rev.*, 2016, **116**, 10075–10166.

19 M. Neumann, S. Füldner, B. König and K. Zeitler, *Angew. Chemie Int. Ed.*, 2011, **50**, 951–954.

20 Y. Lin, Y. Li, X. Zhan, Y. Qu, Z. Xie, D. Yan, Y. Geng, F. Wang, J.-L. Brédas, M. D. McGehee, A. Sellinger, M. Drees, L. Jiang, C. Shu and C. Wang, *Chem. Soc. Rev.*, 2012, **41**, 4245.

21 A. Mishra and P. Bäuerle, *Angew. Chemie - Int. Ed.*, 2012, **51**, 2020–2067.

22 K. Schwinghammer, S. Hug, M. B. Mesch, J. Senker and B. V. Lotsch, *Energy Environ. Sci.*, 2015, **8**, 3345–3353.

23 C. Ru, Q. Wei, W. Chen, Q. Guan, Q. Zhang, Y. Ling, C. Tao, D. Qin, J. Wu and X. Pan, *ACS Energy Lett.*, 2020, **5**, 669–675.

24 X. Yang, Z. Hu, Q. Yin, C. Shu, X. Jiang, J. Zhang, X. Wang, J. Jiang, F. Huang and Y. Cao, *Adv. Funct. Mater.*, 2019, 1808156.

25 K. Schwinghammer, M. B. Mesch, V. Duppel, C. Ziegler, J. Senker and B. V. Lotsch, *J. Am. Chem. Soc.*, 2014, **136**, 1730–1733.

26 S. Kuecken, A. Acharjya, L. Zhi, M. Schwarze, R. Schomäcker and A. Thomas, *Chem. Commun.*, 2017, **53**, 5854–5857.

27 V. S. Vyas, F. Haase, L. Stegbauer, G. Savasci, F. Podjaski, C. Ochsenfeld and B. V. Lotsch, *Nat. Commun.*, 2015, **6**, 8508.

28 X. Wang, L. Chen, S. Y. Chong, M. A. Little, Y. Wu, W.-H. Zhu, R. Clowes, Y. Yan, M. A. Zwijnenburg, R. S. Sprick and A. I. Cooper, *Nat. Chem.*, 2018, **10**, 1180–1189.

29 I. McCulloch, M. Heeney, C. Bailey, K. Genevicius, I. MacDonald, M. Shkunov, D. Sparrowe, S. Tierney, R. Wagner, W. Zhang, M. L. Chabinyc, R. J. Kline, M. D. McGehee and M. F. Toney, *Nat. Mater.*, 2006, **5**, 328.

30 R. Noriega, J. Rivnay, K. Vandewal, F. P. V Koch, N. Stingelin, P. Smith, M. F. Toney and A. Salleo, *Nat. Mater.*, 2013, **12**, 1038-1044.

31 R. S. Sprick, B. Bonillo, R. Clowes, P.

Guiglion, N. J. Brownbill, B. J. Slater, F. Blanc, M. A. Zwijnenburg, D. J. Adams and A. I. Cooper, *Angew. Chemie - Int. Ed.*, 2016, **55**, 1792–1796.

32 L. Y. Ting, J. Jayakumar, C. L. Chang, W. C. Lin, M. H. Elsayed and H. H. Chou, *J. Mater. Chem. A*, 2019, **7**, 22924–22929.

33 A. Vogel, M. Forster, L. Wilbraham, C. L. Smith, A. J. Cowan, M. A. Zwijnenburg, R. S. Sprick and A. I. Cooper, *Faraday Discuss.*, 2019, **215**, 84–97.

34 L. Wang, R. Fernández-Terán, L. Zhang, D. L. A. Fernandes, L. Tian, H. Chen and H. Tian, *Angew. Chemie - Int. Ed.*, 2016, **55**, 12306–12310.

35 Y. Bai, L. Wilbraham, B. J. Slater, M. A. Zwijnenburg, R. S. Sprick and A. I. Cooper, *J. Am. Chem. Soc.*, 2019, **141**, 9063–9071.

36 L. Wilbraham, E. Berardo, L. Turcani, K. E. Jelfs and M. A. Zwijnenburg, *J. Chem. Inf. Model.*, 2018, **58**, 2450–2459.

37 J. Kosco, M. Sachs, R. Godin, M. Kirkus, L. Francas, M. Bidwell, M. Qureshi, D. Anjum, J. R. Durrant and I. McCulloch, *Adv. Energy Mater.*, 2018, **8**, 1802181.

38 R. S. Sprick, Y. Bai, A. A. Y. Guilbert, M. Zbiri, C. M. Aitchison, L. Wilbraham, Y. Yan, D. J. Woods, M. A. Zwijnenburg and A. I. Cooper, *Chem. Mater.*, 2019, **31**, 305–313.

39 M. Z. Rahman, M. G. Kibria and C. B. Mullins, *Chem. Soc. Rev.*, 2020, **49**, 1887-1931.

40 M. Leclerc, *J. Polym. Sci. Part A Polym. Chem.*, 2001, **39**, 2867–2873.

41 R. M. Gadirov, R. R. Valiev, L. G. Samsonova, K. M. Degtyarenko, N. V. Izmailova, A. V. Odod, S. S. Krasnikova, I. K. Yakushchenko and T. N. Kopylova, *Chem. Phys. Lett.*, 2019, **717**, 53–58.

42 C. Fan, C. Duan, Y. Wei, D. Ding, H. Xu and W. Huang, *Chem. Mater.*, 2015, **27**, 5131–5140.

43 J. T. Petroff, K. N. Skubic, C. K. Arnatt and R. D. McCulla, *J. Org. Chem.*, 2018, **83**, 14063–14068.

44 M. Sachs, R. S. Sprick, D. Pearce, S. A. J. Hillman, A. Monti, A. A. Y. Guilbert, N. J. Brownbill, S. Dimitrov, X. Shi, F. Blanc, M. A. Zwijnenburg, J. Nelson, J. R. Durrant and A. I. Cooper, *Nat. Commun.*, 2018, **9**, 4968.

45 L. Li, Z. Cai, Q. Wu, W.-Y. Lo, N. Zhang, L. X. Chen and L. Yu, *J. Am. Chem. Soc*, 2016, **138**, 58.

46 J. Kosco, M. Sachs, R. Godin, M. Kirkus, L. Francas, M. Bidwell, M. Qureshi, D. Anjum, J. R. Durrant and I. McCulloch, *Adv. Energy Mater.*, 2018, **8**, 1802181.

47 A. Bree and R. Zwarich, *J. Chem. Phys.*, 1969, **51**, 903–912.

48 T. G. Pavlopoulos, *Spectrochim. Acta Part A Mol. Spectrosc.*, 1986, **42**, 1307–1310.

49 M. Kreyenschmidt, G. Klaerner, T. Fuhrer, J. Ashenhurst, S. Karg, W. D. Chen, V. Y. Lee, J. C. Scott and R. D. Miller, *Macromolecules*, 1998, **31**, 1099–1103.

50 T. Jafari, E. Moharreri, A. Amin, R. Miao, W. Song and S. Suib, *Molecules*, 2016, **21**, 900.

51 M. Sachs, R. S. Sprick, D. Pearce, S. A. J. Hillman, A. Monti, A. A. Y. Guilbert, N. J. Brownbill, S. Dimitrov, X. Shi, F. Blanc, M. A. Zwijnenburg, J. Nelson, J. R. Durrant, A. I. Cooper, *Nat. Commun.*, 2018, **9**, 4968.

52 B. Rn Kobin, S. Behren, B. Braun-Cula and S. Hecht, *J. Phys. Chem. A*, 2016, **120**, 5474-5480.

53 F. Waiblinger, J. Keck, A. P. Fluegge, H. E. A. Kramer, D. Leppard and G. Rytz, *J. Pho J. Photoch. Photobio. A*,1999, ***126***, 43-49.

54 M. Salvador, N. Gasparini, J. Darí O Perea, S. H. Paleti, A. Distler, L. N. Inasaridze, P. A. Troshin, L. Lü, H.-J. Egelhaaf and C. Brabec, *Energy Environ. Sci*, 2017, **10**, 2005-2016.

55 P. Hapiot, C. Lagrost and F. Le Floch, *Macromolecules*, 2012, **17**, 2003–2012.

56 K. Maeda, X. Wang, Y. Nishihara, D. Lu, M. Antonietti and K. Domen, *J. Phys. Chem. C.*, 2009, **113**, 4940-4947.

57 J. Kosco, M. Bidwell, H. Cha, T. Martin, C. T. Howells, M. Sachs, D. H. Anjum, S. Gonzalez Lopez, L. Zou, A. Wadsworth, W. Zhang, L. Zhang, J. Tellam, R. Sougrat, F. Laquai, D. M. DeLongchamp, J. R. Durrant and I. McCulloch, *Nat. Mater.*, 2020, **19**, 559-565.

58 L. Li, Z. Cai, Q. Wu, W.-Y. Lo, N. Zhang, L. X. Chen and L. Yu, *J. Am. Chem. Soc.*, 2016, **138**, 7681–7686.

59 R. S. Sprick, C. M. Aitchison, E. Berardo, L. Turcani, L. Wilbraham, B. M. Alston, K. E. Jelfs, M. A. Zwijnenburg and A. I. Cooper, *J. Mater. Chem. A*, 2018, **6**, 11994–12003.

60 S. G. Bratsch, *J. Phys. Chem. Ref. Data*, 1989, **18**, 1–21.

61 I. Mills, T. Cvitas, K. Homann, N. Kallay and K. Kuchitsu, *Quantities, Units and Symbols in Physical Chemistry*, , *International Union Of Pure And Applied Chemistry*, Blackwell Science, Oxford, 2nd edn., 1993.

62 M. Grundmann, *The Physics of Semiconductors*, Springer Science and Business Media LLC, Heidelberg, 2016.

63 R. S. Sprick, B. Bonillo, R. Clowes, P. Guiglion, N. J. Brownbill, B. J. Slater, F. Blanc, M. A. Zwijnenburg, D. J. Adams and A. I. Cooper, *Angew. Chemie Int. Ed.*, 2016, **55**, 1792–1796.

64 R. S. Sprick, B. Bonillo, M. Sachs, R. Clowes, J. R. Durrant, D. J. Adams and A. I. Cooper, *Chem. Commun.*, 2016, **52**, 10008–10011.

65 Y. Kan, Y. Zhu, Z. Liu, L. Zhang, J. Chen and Y. Cao, *Macromol. Rapid Commun.*, 2015, **36**, 1393–1401.

66 Y. Xu and D. Jiang, *Chem. Commun. Chem. Commun*, 2014, **50**, 2781–2783.

67 H. Kisch, *Angew. Chemie - Int. Ed.*, 2010, **49**, 9588–9589.

68 P. Friederich, V. Meded, A. Poschlad, T. Neumann, V. Rodin, V. Stehr, F. Symalla, D. Danilov, G. Lüdemann, R. F. Fink, I. Kondov, F. von Wrochem and W. Wenzel, *Adv. Funct. Mater.*, 2016, **26**, 5757–5763.

69 P. Friederich, V. Gómez, C. Sprau, V. Meded, T. Strunk, M. Jenne, A. Magri, F. Symalla, A. Colsmann, M. Ruben and W. Wenzel, *Adv. Mater.*, 2017, **29**, 1703505.

70 P. M. Borsenberger and H. Bässler, *J. Chem. Phys*, 1991, **95**, 5327.

71 W. Zhang, J. Smith, R. Hamilton, M. Heeney, J. Kirkpatrick, K. Song, S. E. Watkins, T. Anthopoulos and I. Mcculloch, *J. Am. Chem. Soc*, 2009, **131**, 33.

72 A. Wadsworth, H. Chen, K. J. Thorley, C. Cendra, M. Nikolka, H. Bristow, M. Moser, A. Salleo, T. D. Anthopoulos, H. Sirringhaus and I. McCulloch, *J. Am. Chem. Soc.*, 2020, **142**, 652-664.

73 Q. Xiang, J. Yu and M. Jaroniec, *J. Phys. Chem. C*, 2011, **115**, 7355–7363.

74 L. Wang, X. Zheng, L. Chen, Y. Xiong and H. Xu, *Angew. Chemie - Int. Ed.*, 2018, **57**, 3454–3458.

75 B. M. Fung, A. K. Khitrin and K. Ermolaev, *J. Magn. Reson.*, 2000, **142**, 97–101.

76 C. R. Morcombe and K. W. Zilm, *J. Magn. Reson.*, 2003, **162**, 479–86.

77 G. M. Sheldrick, *SADABS, Programs Scaling Absorpt. Correct. Area Detect. Data*, 2008, University of Göttingen: Göttingen, Germany.

78 L. Krause, R. Herbst-Irmer, G. M. Sheldrick and D. Stalke, *J. Appl. Crystallogr.*, 2015, **48**, 3-10.

79 G. Winter, D. G. Waterman, J. M. Parkhurst, A. S. Brewster, R. J. Gildea, M. Gerstel, L. Fuentes-Montero, M. Vollmar, T. Michels-Clark, I. D. Young, N. K. Sauter and G. Evans, *Acta Crystallogr. Sect. D*, 2018, **74**, 85-97.

80 G. M. Sheldrick, *Acta Crystallogr. Sect. A*, 2015, **71**, 3-8.

82 G. M. Sheldrick, *Acta Crystallogr. Sect. C.*, 2015, **71**, 3-8.

83 O. V. Dolomanov, L. J. Bourhis, R. J. Gildea, J. A. K. Howard and H. Puschmann, *J. Appl. Crystallogr.*, 2009, **42**, 339-341.

84 M. Sachs, C. Hyojung, J. Kosco, C. M. Aitchison, L. Francas, S. Corby, C.-L. Chiang, A. A. Wilson, R. Godin, A. Fahey-Williams, A. I. Cooper, R. S. Sprick, I. McCulloch and J. R. Durrant, *J. Am. Chem. Soc.*, 2020, Advanced article.

85 G. A. Crosby and J. N. Demas, *J. Phys. Chem.*, 1971, **75**, 991–1024.

86 A. Samoc, *J. Appl. Phys.*, 2003, **94**, 6167–6174.

87 C. M Aitchison, M. Sachs, M. A. Little, L. Wilbraham, N. J. Brownbill, C. M. Kane, F, Blanc, M. A. Zwijnenburg, J. R. Durrant, R. S. Sprick, A. I. Cooper, *Chem. Sci.*, 2020, advance article.

Chapter 4: Hydrogen-bonded Organic Frameworks for Photocatalytic Hydrogen Production

All materials in this chapter were synthesised by the author except for **TPhP**, which was prepared by Dr. Christopher Kane. Dr. Marc Little amorphised **TBAP** and performed single crystal X-ray diffraction analysis. Thermogravimetric analysis and carbon monoxide production experiments were performed by Dr. Reiner Sebastian Sprick and sorption analysis was performed by Dr. Marc Little, Rob Clowes, and Michael Brand. (TD)-DFT calculations were performed by Dr. Liam Wilbraham and Dr. Martijn Zwijnenburg. All other materials characterisation and testing were carried out by the author.

4.1. Introduction

Porous hydrogen-bonded organic frameworks (HOFs) are a class of molecular crystals that are stabilised by hydrogen-bonding interaction between molecules, and which possess permanent porosity. It is the retention of porosity upon solvent removal that distinguishes porous molecular crystals (including HOFs) from other pore-containing molecular crystals. Inclusion crystals[1–3] and molecular zeolitic structures[4–8] have been studied since the 1950s and can efficiently contain and exchange guest molecules within their open frameworks, but these classes of materials are not typically self-supporting and the structures collapse upon guest removal. In contrast, in 2005 Sozzani *et. al* showed a framework of tris-*o*-phenylenedioxycyclotriphosphazene molecules (Figure 1) could retain open pores under complete removal of solvent. This material shows significant gas sorption with CO_2 uptake of over 1 mol mol^{-1}, corresponding to more than two guest molecules per unit cell.[9]

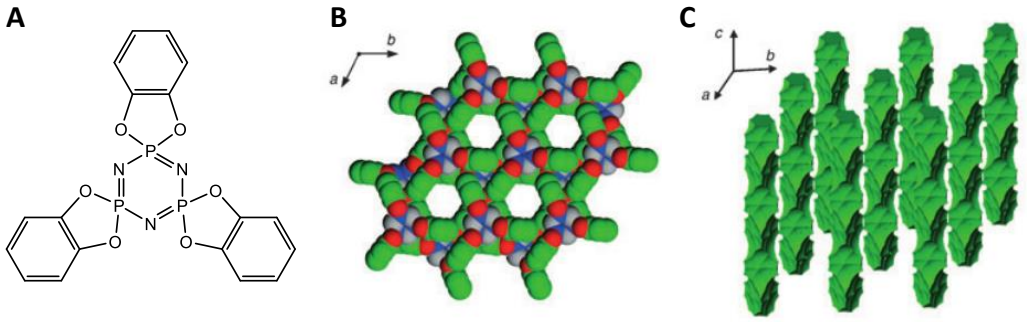

Figure 1: Molecular structure of tris-*o*-phenylenedioxycyclotriphosphazene (A) and the porous crystal structure of tris-*o*-phenylenedioxycyclotriphosphazene (B and C). *Adapted, with permission from reference [9].*

The term HOF was first coined in 2011 by He and co-workers.[10] Their material, HOF-1, is a crystalline phase of the molecule shown in Figure 2A and was the first example of a hydrogen-bonded molecular crystal with proven permanent porosity, although in fact the structure was first reported by Wuest over a decade earlier,[11] who also showed the phase was stable to desolvation. In HOF-1, (Figure 2B) a tetraphenylmethane core is substituted with four 2,4-diaminotriazine groups. Each of these groups forms two hydrogen bonds to a neighbouring molecule to give a body centred cubic network (Figure 2C). The rigid nature of the molecular tecton[12] prevents the involvement of the further eight hydrogen bonding positions, as the molecules cannot interpenetrate. This is in contrast to more flexible analogues of this molecule[13] (Figure 2D) where increased conformational freedom results in a less open framework with the fulfilment of all sixteen possible hydrogen bonding positions.

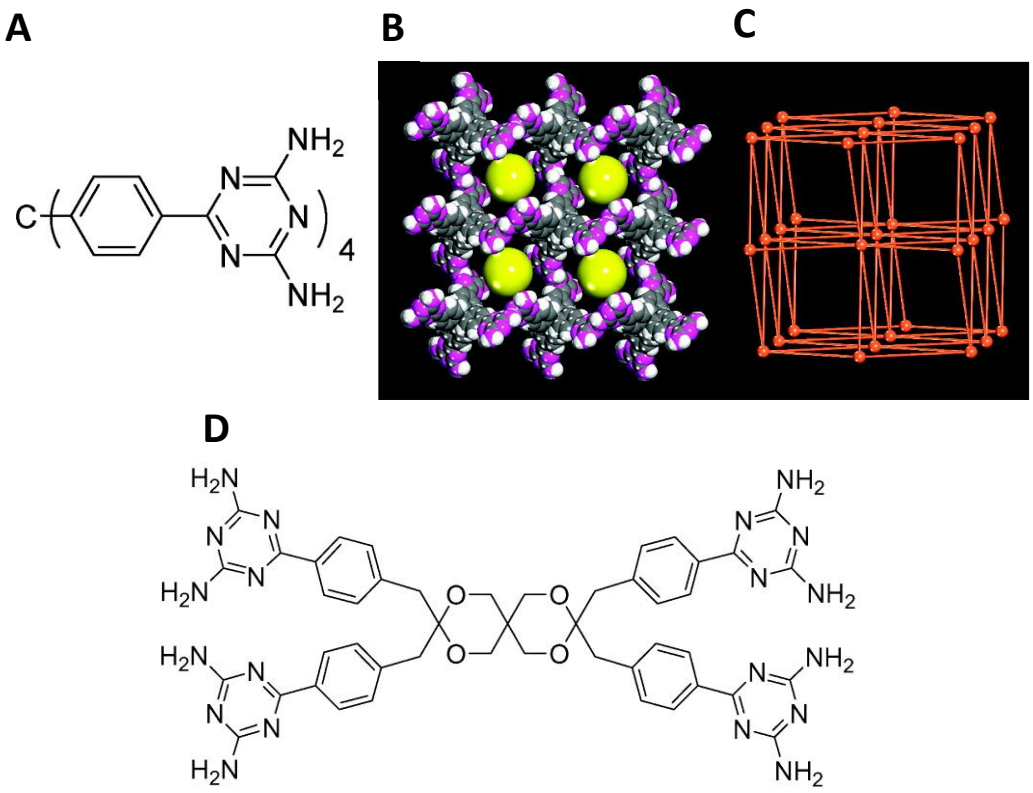

Figure 2: (A) Molecular structure of HOF-1. X-ray crystal structure of HOF-1 featuring (B) one-dimensional channels along the c axis with a size of ~8.2 Å (yellow spheres) and (C) three-dimensional body-centered cubic network topology. *Adapted with permission from reference [10]* (D) Molecular structure of flexible 2,4-diaminotriazine analogue with an 2,4,8,10-tetraoxaspiro[*5,5*]undecyl cores.

The diamino triazine groups in HOF-1 are a commonly used[14–17] hydrogen-bonding 'synthon'[12] in HOFs, and along with carboxylic acids[18–22] and azole motifs,[23,24] utilise strong O/N–H interactions to thermodynamically stabilise the formation of low-density phases. Hydrogen-bonding alone is often insufficient to maintain the large open pore structures in HOFs that can be stabilised by covalent or coordination bonding in COFs[25,26] and MOFs[27,28], respectively. Secondary intermolecular interactions, such as π-π stacking or van der Waals forces, are thus frequently crucial for stabilising the extended packing in HOFs and maintaining their porosity.[29]

Carboxylic acid pairs form 1-dimensional hydrogen-bonding synthons and thus planar tecton cores such as pyrene[30] and triphenylene[31] exclusively give sheets where hydrogen bonding occurs in the same plane as the core. These then stack to give layered structures held together by π-π interactions. Carboxylic acid-bearing tectons with non-planar cores such as biphenylene[20] and hexaazatriphenylene,[32] or indeed sp^3 centres[33] show 3D networks held

together by linear hydrogen bonds. Other hydrogen bonding groups form more complex synthons and so can give a diversity of structures. One example of this is the triptycene trisbenzimidazolone material in Figure 3, where a triptycene core and peripheral urea groups give a C_3 symmetric molecule where the tecton has a 'sideways' rotational plane perpendicular to its π systems. Mastalerz *et. al* first found that this molecule could form a HOF structure where the rigid triptycene cores stack perpendicularly with almost no aromatic ring overlap.[34] Instead, each molecule relies on a network of hydrogen bonds with molecules in adjacent stacks above and below its own plane. Cooper, Day and co-workers subsequently found three further polymorphs of the same molecule, one of which (T2-γ), is the lowest density molecular crystals to date with a BET surface area of 3425 m^2g^{-1}.[35]

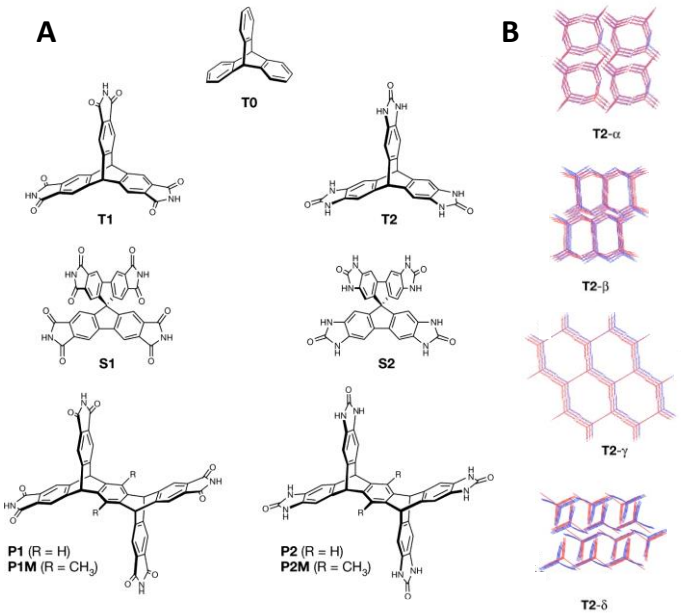

Figure 3: (A) Molecular structure of triptycene trisbenzimidazolone (T2) and related candidates for HOF porous crystal formation. (B) Predicted (red) and experimental (blue) structures of several polymorphs of T2. *Adapted with permission from reference [35].*

HOFs have primarily been studied for their gas sorption properties. There are now many examples of HOFs showing high CO_2 uptake and selectivity versus N_2[36–38] and as well as uptake of various hydrocarbons and chlorofluorocarbons.[10,23] These are important properties for greenhouse gas capture technologies. There are also a growing number of materials with considerable H_2 and methane uptake,[34,35,39] which indicate HOFs could be used for fuel storage applications. HOFs have also been shown to have potential for various separations. They have been widely studied for simple hydrocarbon separation,[10,14,20,40] but others have developed chiral HOFs[15] or HOFs with very large pores[41] to generate more niche selectivity for alcohol enantiomers and fullerene, respectively. Whilst the 'weak' H-bond or Van der

Waals interactions between HOFs and guests give good reversibility and guest release properties, the lack of 'strong' binding sites, such as open metal centres in MOFs, somewhat limits the potential of HOFs for molecular recognition.

HOFs are also becoming a material of interest for proton conduction membranes. The low-density and high concentration of proton carriers inherent to HOFs mean they are obvious candidates for fuel cell technologies. HOFs containing neutral tectons, such as a diamino triazine bearing porphyrin,[42] have been shown to have moderate proton conductivities but HOFs formed of charged guanidinium and sulfonate-bearing tectons[43] and porous salts formed from various diamines and tetra acids[44] appear to show more promise, with proton conductivities comparable to MOFS.

The above applications take advantage of HOFs vesicular structure but a newer area for HOF studies is their use in optical applications. The highly conjugated rigid molecules commonly used as HOF tectons, often have highly favourable absorption and emission properties. In recent years there have been several examples of HOF structures exhibiting interesting emissive behaviour, distinct from that of their component molecules. Douhal and co-workers found that a HOF based on the widely studied 'phenylene triangle' core of 5,6,11,12,17,18-hexadehydrotribenzo[*a,e,i*]cyclododecene had an allowed $S_0 \rightarrow S_1$ transition forbidden in the solution state of the molecule, as well an emission associated with charge transfer and a red-shifted emission thought to be due to species with proton transfer element.[45] These three components are thought to show the significant effects i) tecton conformation, ii) π-stacking and iii) hydrogen bonding can have on the electronic states of molecules confined within HOF structures. It has also been shown that the generation of crystalline HOF structures can be used to increase the fluorescence yields of HOF tectons compared to the solutions state,[46] increase the efficiency and lifetime of phosphorescent materials[47] and give highly anisotropic emissive behaviour.[32,48] HOFs have also been shown to be suitable for fluorescence-quenching-based sensing of nitroaromatics,[49] silver ions,[50] and acids.[51]

One of the least explored properties of HOFs is their ability to act as semi-conductors. HOFs are highly ordered materials based on extended aromatic groups and often contain extensive π-stacking interactions. These are all beneficial properties for forming organic electronics with high charge carrier mobilities. The band structures of HOFs also mean they may be useful for photoredox applications but thus far the only examples involve a 1,3,6,8-tetrakis(*p*-benzoic acid)pyrene (**TBAP**) HOF (discussed further below), which Liu and Cao showed to be capable of singlet oxygen generation for photodynamic therapy[30] and which was later shown to be capable of photooxidation of a mustard gas simulant.[52]

The high crystallinity and often the hydrophilic groups inherent to HOFs are highly attractive properties for a photocatalyst but HOFs are not an obvious choice for water splitting as they were initially found to be unstable in hydrogen bonding solvents, such as water. There are, however, now several examples of more robust HOFs that utilise strong intermolecular interactions and allow retention of the framework under harsh conditions such as boiling water and strong acids and bases. Previously, the lack of an extended covalent network may also have been expected to prevent HOFs from acting as effective hydrogen production catalysts but in light of the results in Chapter 3 it cannot be assumed that longer chain lengths are necessarily required for good photocatalytic activity. The fact that HOFs are molecular materials with weaker non-covalent interactions than COFs also give them the highly desirable feature of being solution-processable. This allows for the formation of single crystalline materials, allowing for easy characterisation and a complete picture of material structure. It also bestows the potential for framework regeneration and the formation of nanostructured architectures.

4.2 TBAP-α and Amorphous TBAP

At room temperature and atmospheric pressure, pyrene forms a stable $P2_1/a$ polymorph with herringbone style packing and limited π-π interactions between molecules.[53] However, at pressures greater than 0.3 GPa, a high density phase has been observed.[54] In the high pressure polymorph, extended columns of stacked pyrene units are stabilised by strong π-π interactions with significant overlap and small 3.85 Å distances between layers. This aromatic ring stacking [55–58]motif is present in a number of recently reported COF crystal structures with high activity for photocatalytic hydrogen production from water. In 2018 Lotsch and co-workers reported a pyrene based COF with a HER of 98 μmol h^{-1} g^{-1} with a TeOA scavenger, under AM 1.5 G.[59] This was a similar activity to previously reported amorphous pyrene based networks[60] but their material did show high photocurrents of 6 μA cm^{-2} and the authors attribute this high conductivity to through-layer interactions between the closely stacked, small offset layers. There is evidence of layered 2D sheet structures in less ordered organic photocatalysts, such as CTFs[61] and carbon nitrides[62] as well, and these are often targeted to give improved charge transfer properties. HOFs combine such structures with a much higher degree of accessible crystallinity making them ideal candidates for investigation. HOF structures of **TBAP** (Figure 4) combine π-stacking with good visible light absorption, porosity, hydrophilic groups, and a suitable band structure (discussed below) meaning it possesses many of the properties outlined in Chapter 1 as beneficial for photocatalysis.

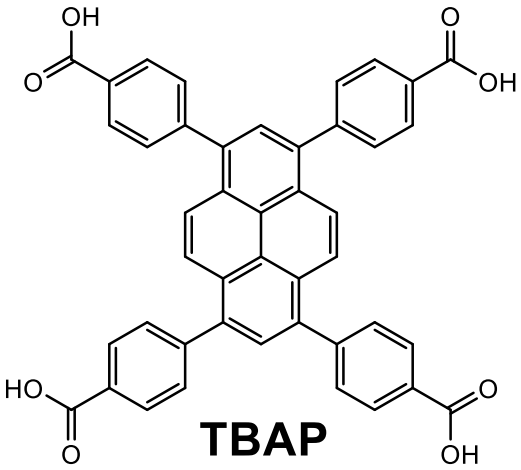

Figure 4: Chemical structure of **TBAP**

4.2.1 Synthesis and Characterisation.

TBAP was synthesised according to a literature method[63] and crystallised in batches by vapour diffusion of $CHCl_3$ into DMF solution (see experimental section 4.8.1 for details). After the formation of yellow crystals, the crystallisation solvent was exchanged with acetone over several days before drying under vacuum at 120 °C. Desolvation of the crystal pores was verified by the lack of solvent peak in the ^{1}H NMR spectrum (Figure 5B) and by TGA. At 400 °C, the desolvated material had lost less than 2 wt.% (Figure 5A). This contrasts with the material isolated directly from chloroform/DMF which lost more than 20 wt.% up to 400 °C.

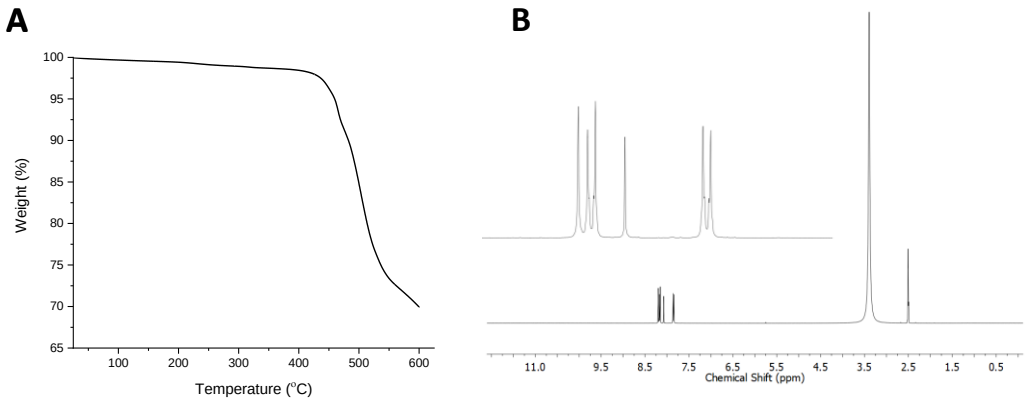

Figure 5: Thermogravimetric trace (A) and ^{1}H NMR (400 MHz, DMSO-d_6) spectra (B) of thermally activated **TBAP-*α***.

The single crystal structure of the desolvated material, **TBAP-α**, is shown in Figure 6. The structure has *C*2/*c* symmetry, with 2-dimensional sheets of **TBAP** molecules held in an open framework structure by two hydrogen bonds from each of the four benzoic acid groups to four neighbouring molecules. These layers are stacked with a slight offset to form infinite columns of overlapping pyrene units, as shown in Figure 6A, with a distance of 3.93 Å between the **TBAP** layers. The rhombohedral voids of each layer also overlap to give open channels running perpendicular to the **TBAP** sheets. The structure is in good agreement with that obtained by Cao *et al*.[30]

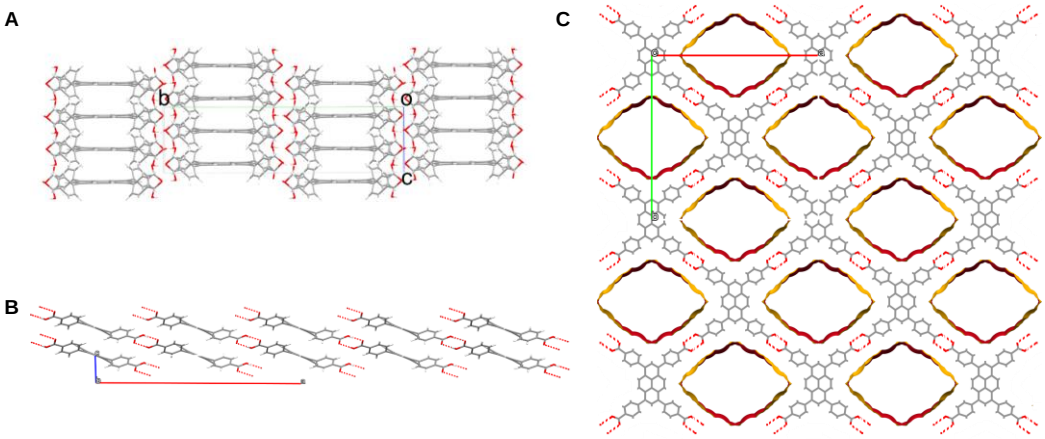

Figure 6: Structure of **TBAP-α** as determined by single crystal XRD. Viewed down the crystallographic *a* (A), *b* (B) and *c* (C) axes.

The PXRD spectra of three batches of **TBAP-α** are shown in Figure 7. These batches gave BET surface areas of 2001, 2270 and 2074 m^2 g^{-1}, respectively, consistent with the literature value.[30]

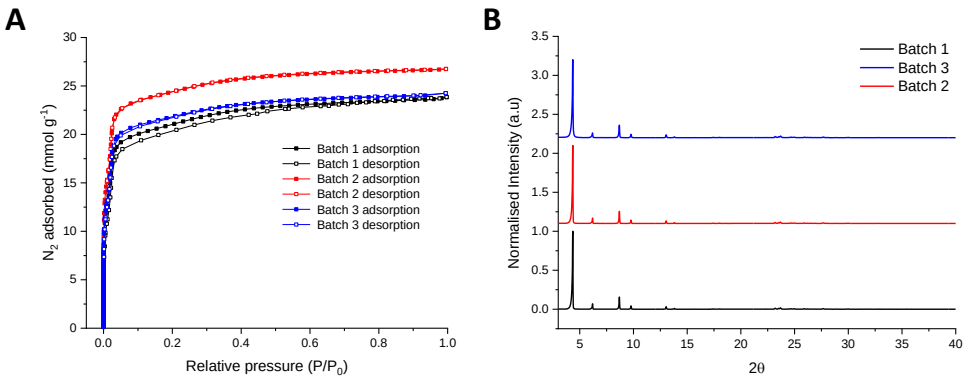

Figure 7: Nitrogen sorption isotherm at 77 K (A) and PXRD spectra (B) of batches of **TBAP-α**.

An amorphous version of **TBAP** was prepared by rapid acidification of a solution of **TBAP** dissolved in $KOH_{(aq)}$ (see experimental for full details). This material was analysed by PXRD (Figure 8A), which showed complete loss of crystallinity, and nitrogen sorption (Figure 8B), which showed complete loss of porosity with a nominal BET surface area of just 4.9 m^2 g^{-1}.

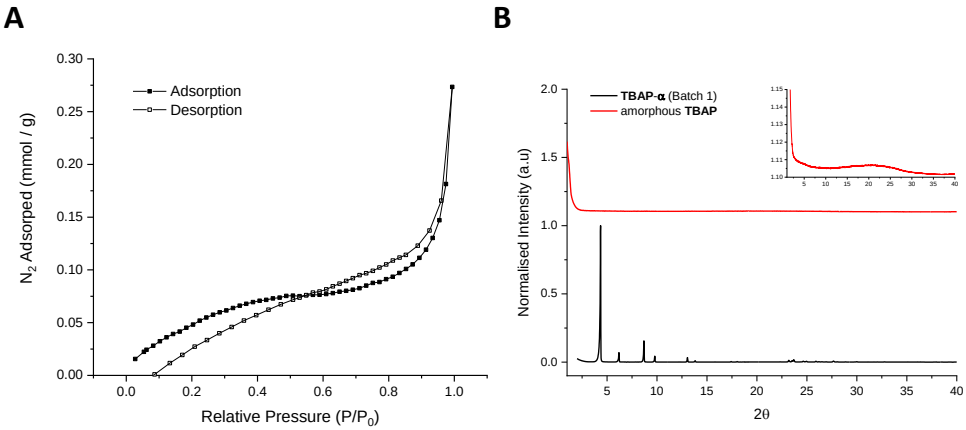

Figure 8: Nitrogen sorption isotherm (A) and PXRD spectra (B) of amorphous **TBAP**. Inset in B shows expanded PXRD spectra of amorphous **TBAP**.

Aside from this, the amorphous material showed very similar properties to the crystalline samples; The particle sizes of the amorphous **TBAP** were found to be similar to those of the crystalline batches, by SLS (Figure 9A and B). Suspensions of the crystalline batches in water gave particle size distributions with Sauter mean diameters of 15.5, 11.0, and 9.3 µm, whilst the amorphous material had an intermediate Sauter mean diameter of 11.9 µm. Similarly, turbidity measurements of **TBAP-α** and amorphous **TBAP** suspended in water (Figure 9C), showed similar light transmission over time, indicating they have comparable dispersibilities.

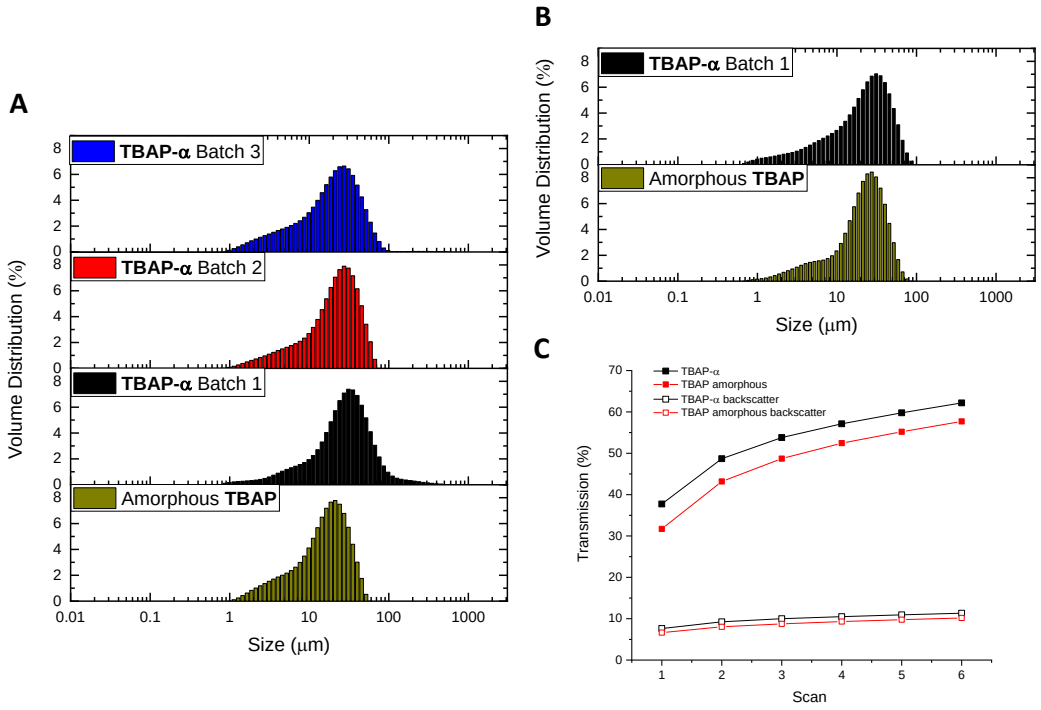

Figure 9: SLS spectra of **TBAP** materials in water (A) and ascorbic acid (0.1 M) (B). Light transmission measurements of materials dispersed in water over time (C), scans were recorded every 30 mins with scan 1 occurring at t = 0 mins.

Interestingly, water sorption isotherms for both amorphous **TBAP** and **TBAP-α** showed limited (< 10 wt. %) water uptake at low (< 0.6) relative pressures (Figure 10A), suggesting the pores of **TBAP-α** may not be easily wetted. **TBAP-α** does show up to 25 wt. % uptake at higher pressures, but this would be consistent with water condensing on the surface of the crystals. This is in contrast to other highly porous organic materials used as photocatalysts where water uptake can reach more than 50 wt.% at relative pressures of 0.6.[55,64] One reason for this difference may be the hydrophobicity of the pore wall in **TBAP-α**. Although **TBAP** molecules contain four hydrophilic carboxylic acid groups, in the HOF the hydrogen-bonding capability of these groups is fully saturated, limiting the interaction possible with solvent molecules. The pore walls themselves are primarily hydrophobic aromatic groups. This is different from a previously studied highly-wettable material, FS-COF, which has polar sulfone groups lining the pore walls.[55]

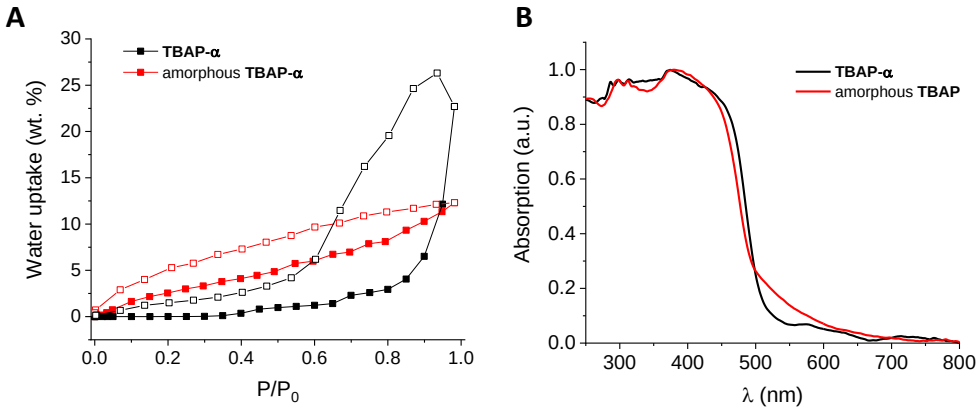

Figure 10: Water uptake measurements (A) and UV-Vis absorption spectra (B) of the **TBAP** materials.

The absorption profiles of the crystalline and amorphous materials were also similar. Figure 10B shows the solid-state UV-Vis diffuse reflectance spectra of **TBAP-α** and amorphous **TBAP** which have absorption onsets of 507 and 497 nm, respectively. This indicates that the solid-state packing of **TBAP** units has a limited effect on the optical gap of the material. This is consistent with the band structures as predicted by DFT calculations (Figure 11). In previous chapters, DFT calculations have been performed on the lowest energy conformers of single molecules in the gas phase. To account for the differences in secondary structure between **TBAP-α** and amorphous **TBAP**, calculations were performed for both an isolated **TBAP** molecule optimised in the gas phase (Figure 11, I), an isolated **TBAP** molecule taken from a DFT optimised **TBAP-α** crystal structure (Figure 11, II), a **TBAP** molecule taken from a DFT optimised **TBAP-α** crystal structure with a neighbouring molecule above and below it (Figure 11, III) and finally a **TBAP** molecule taken from a DFT optimised **TBAP-α** crystal structure with four neighbouring molecules above and four below it (Figure 11, IV). These calculations suggest that the extended stacking structures observed in **TBAP-α** (approximated by case IV) do not significantly affect the substrates overpotentials for proton reduction and scavenger oxidation in comparison to the amorphous material (approximated by case I or II). These calculations also indicate that both materials should have sufficient thermodynamic driving force for proton reduction, as in all cases the substrate EA lies greater than 1.5 V above the proton reduction potential. As the benzoic acid groups in **TBAP** are susceptible to deprotonation at high pHs, an acidic sacrificial electron donor, ascorbic acid, was used for photocatalytic testing. Therefore, the proton reduction potentials shown in Figure 11 are at pH 2.6, the likely pH of a 0.1 M ascorbic acid solution.[55] Whilst all cases described above have reasonable (> 0.5 V) driving force for the overall oxidation of ascorbic acid, the driving forces for the initial one-hole oxidation of ascorbic acid are significantly

smaller (although all still represent a thermodynamically favourable reaction) indicating this may act as a kinetic barrier to hydrogen evolution.

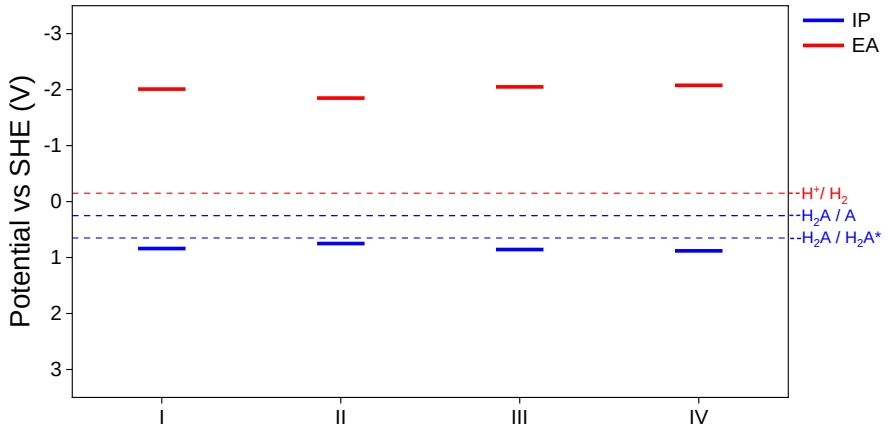

Figure 11: Comparison of the IP and EA values of **TBAP** based on an isolated **TBAP** molecule optimized in the gas-phase (I), an isolated **TBAP** molecule taken from the DFT optimized **TBAP-α** crystal structure (II), a **TBAP** single molecule taken from the DFT optimized **TBAP-α** crystal structure surrounded by a molecule above and below it, as well as the phenyl groups of the laterally adjacent molecules (III), and the analogous tetramer case (IV). Solution potentials for the reduction of protons and oxidation of ascorbic acid at pH 2.6, the likely pH of a 0.1 M ascorbic acid solution.

The excited state lifetimes of the two materials were studied by TCSPC (Figure 12). In water suspensions, the fluorescence lifetime spectra of amorphous **TBAP** and **TBAP-α** are almost identical and very similar to a solution of **TBAP** dissolved in DMSO (Figure 12A). All spectra were best fitted by multicomponent exponential decay curves and **TBAP-α** and amorphous **TBAP** and had τ_{Av} values of 1.86 and 1.94 ns, whilst in DMSO solution **TBAP** had a τ_{Av} value of 1.80 ns. This indicates that exciton formation and decay, are not significantly affected by differences in solid state packing in these materials. Equally, neither material showed a large change in the fluorescence lifetime spectra upon addition of Pt by photodeposition with similar 1.79 and 1.88 ns. This suggests limited exciton quenching by Pt in these materials. When the suspension medium was changed from water to 0.1 M ascorbic acid, however, both materials show a significant decrease in fluorescence lifetime; τ_{Av} decreased to 0.58 ns **TBAP-α** in 0.1 M ascorbic acid, and to 0.85 ns for amorphous **TBAP** in 0.1 M ascorbic acid, with similar decreases to 0.69 and 0.80 ns for the platinised analogues. This indicates that ascorbic acid is an effective hole scavenger for both the crystalline and amorphous versions of this material and is independent of platinisation.

Analysis of material collected post catalytic testing (section 4.2.2.3) rule out chemical or structural changes to **TBAP-α** as the source of these lifetime changes.

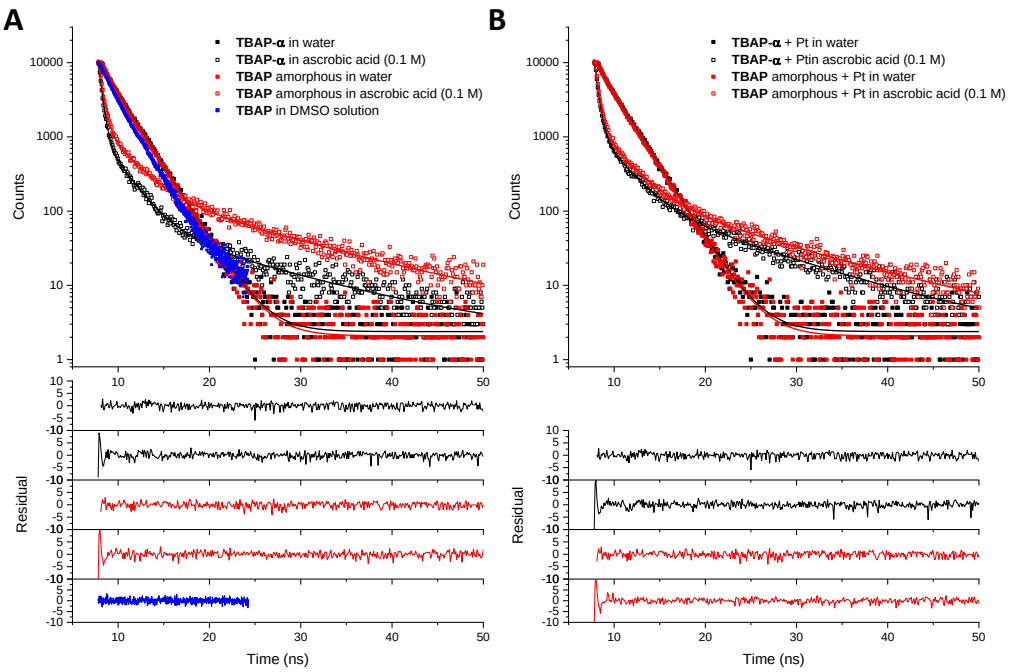

Figure 12: TCSPC fluorescence lifetime measurements of **TBAP** materials in suspension. Raw data (squares), fit (lines) and residuals (bottom). λ_{ex} = 370 nm, λ_{em} = 509 nm.

4.2.2 Photocatalysis Experiments

4.2.2.1 Co-catalyst loading

The materials were first tested for hydrogen production in 0.1 M ascorbic acid as a sacrificial electron donor with 4 wt. % Pt as co-catalyst, loaded by photodeposition of H_2PtCl_6. Using a 420 nm filter (300 W Xe lamp) batches 1-3 of **TBAP-α** produced hydrogen at rates of 591, 837, and 829 µmol h^{-1} g^{-1} over 6 hours of irradiation, demonstrating reproducibility between batches (Figure 13C). In contrast, no hydrogen was detected from the amorphous sample over 6 hours. The catalysts were collected by filtration after photolysis and the platinum contents determined by ICP-MS. Analysis indicated that photodeposition of the Pt co-catalysts had occurred at low yields; The crystalline batches had Pt contents of 1.54, 1.01 and 1.12 wt.% respectively whilst the amorphous sample had 1.27 wt.%. STEM imaging (Figure 14) showed the formation of 2 - 15 nm sized Pt nanoparticles, which were well dispersed across the **TBAP** particles and indeed covered a high proportion of the surface. It has been shown previously that overloading of Pt co-catalysts can hinder hydrogen evolution, possibly by reducing light absorption or increasing

recombination[65,66] and it is noted that Batch 1, which had the lowest HER, had a 38 – 52 % higher Pt content than the other batches.

As such, a sample of **TBAP-α** and an amorphous sample were then tested adding only 1 wt.% Pt (Figure 13A and B). Again, deposition occurred in low yield with Pt contents for the amorphous and crystalline samples of 0.24 and 0.48 wt.% by ICP-MS. Under these conditions both materials were more active; the amorphous sample produced hydrogen evolution at a rate of 6 µmol h^{-1} g^{-1} whilst the HER of **TBAP-α** increased to 1293 µmol h^{-1} g^{-1}.

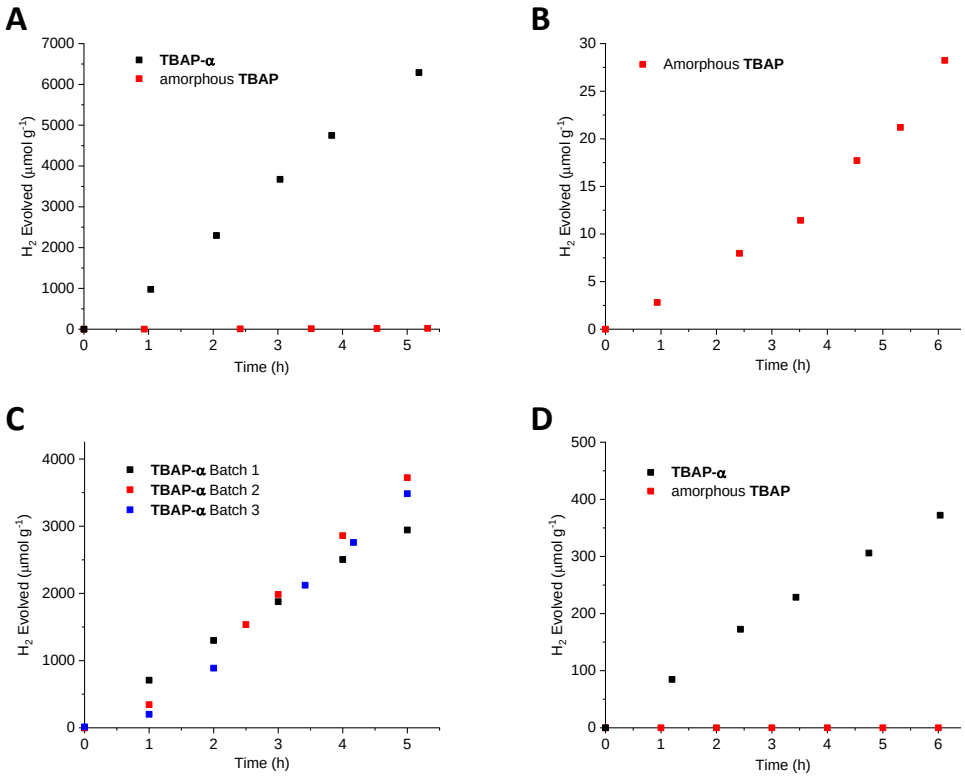

Figure 13: Hydrogen evolution of **TBAP-α** and amorphous **TBAP** (25 mg) loaded with 1 wt.% (A and B (where, (B) shows an expanded view of (A)), or 4 wt.% (C) Pt, from photodeposition of H_2PtCl_6, or with no Pt added (D), dispersed in ascorbic acid solution (25 mL, 0.1 M) illuminated with a 300 W Xe light source fitted with a $\lambda > 420$ nm cut off filter.

With no Pt co-catalysts added, activity was dramatically reduced; the amorphous sample produced no measurable hydrogen whilst **TBAP-α** had a rate of just 59 µmol h^{-1} g^{-1}. Although no Pt was added to these samples, **TBAP** was synthesised using Pd-catalysed Suzuki coupling so it is not sensible to suggest that **TBAP-α** is acting as a completely metal-free catalyst; Pd levels were lower than could be detected by ICP-MS (10 ppm = 0.001 wt.%) but even very low levels of Pd have been found to be sufficient to give limited photocatalytic activity for hydrogen production.[67] Whilst the kinetics of this material are not

studied in detail in this work, the large variation in rate with Pt content suggests it is crucial to photocatalysis and may act as the active centre for proton reduction.

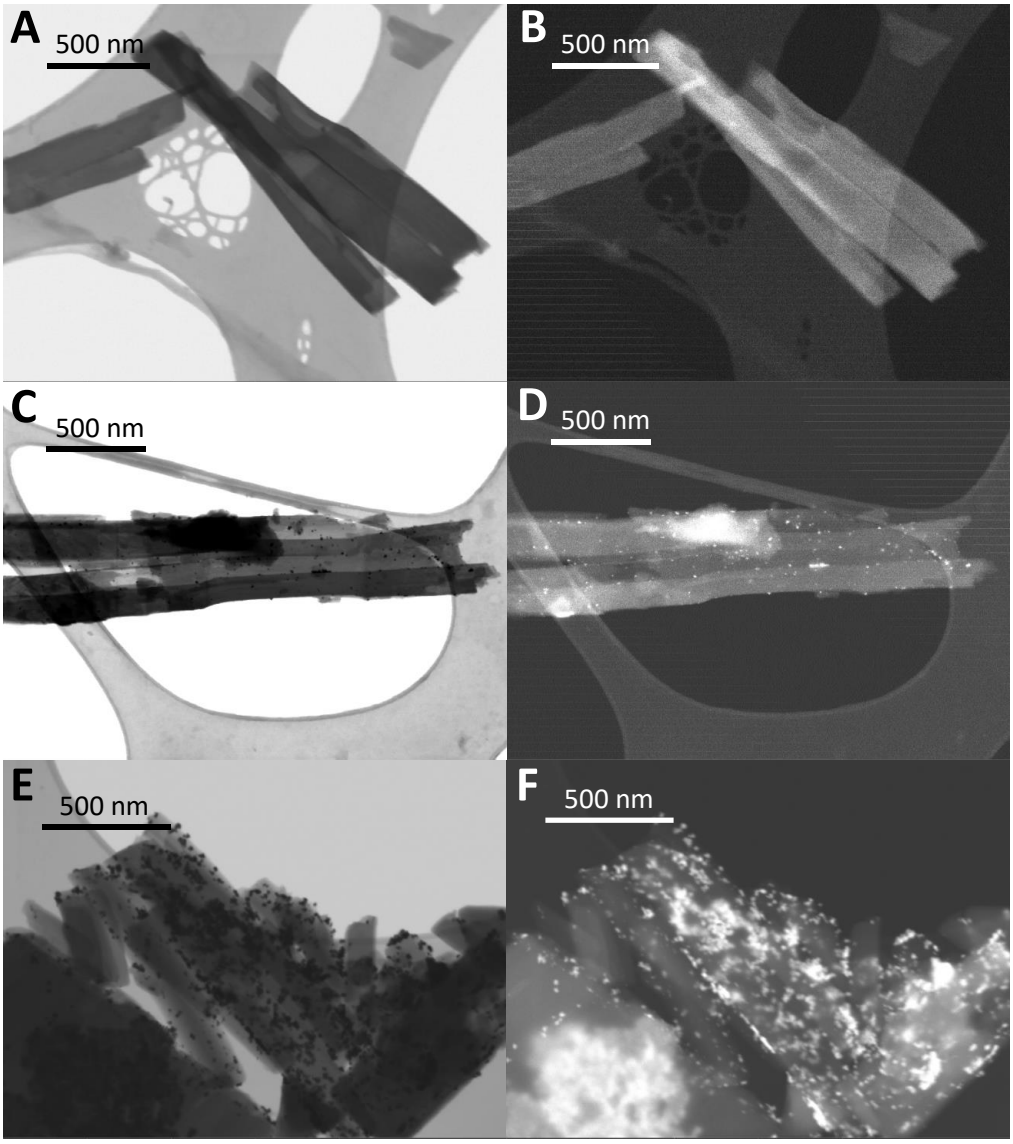

Figure 14: STEM images of **TBAP-α** collected post photocatalysis with no (A and B), 1 wt.% (C and D) or 4 wt.% (E and F) Pt loaded by photodeposition of H_2PtCl_6. Images were recorded in bright field (BF) mode (left) and High Angle Dark Field (HADF) mode (right).

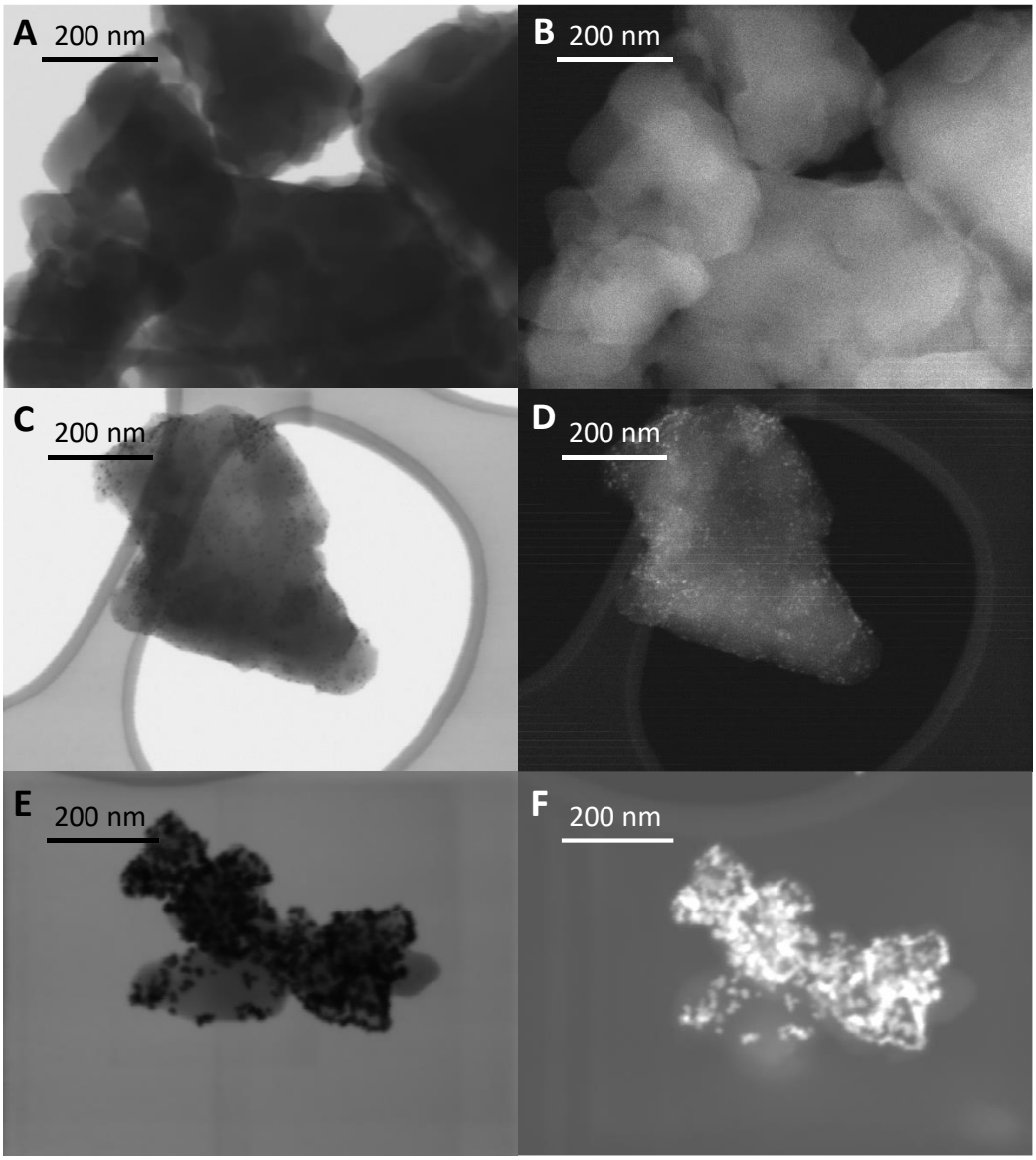

Figure 15: STEM images of amorphous **TBAP** collected post photocatalysis with no (A and B), 1 wt.% (C and D) or 4 wt.% (E and F) Pt loaded by photodeposition of H_2PtCl_6. Images were recorded in bright field (BF) mode (left) and High Angle Dark Field (HADF) mode (right).

Given the high BET surface area of **TBAP-α** and that photons can typically penetrate *ca.* 100 nm into organic materials[68] photodeposition of PtH_2Cl_6 could theoretically occur inside the 1.9 × 2.1 nm pores wide pores of **TBAP-α**. Indeed, it has been previously shown that using the same Pt photodeposition method, small 3 nm Pt particles form within the pores of a dibenzothiophene sulfone-based COF (FS-COF) and it is suggested that this is partially responsible for the materials very high proton reduction activity.[55] However, as mentioned above, the pores of this material are both larger and more hydrophilic than **TBAP-α** and so the behaviour of the two materials may be different. A combination of SEM and STEM

imaging suggested Pt nanoparticles were located predominantly on the surface of **TBAP-α** crystals (Figure 16).

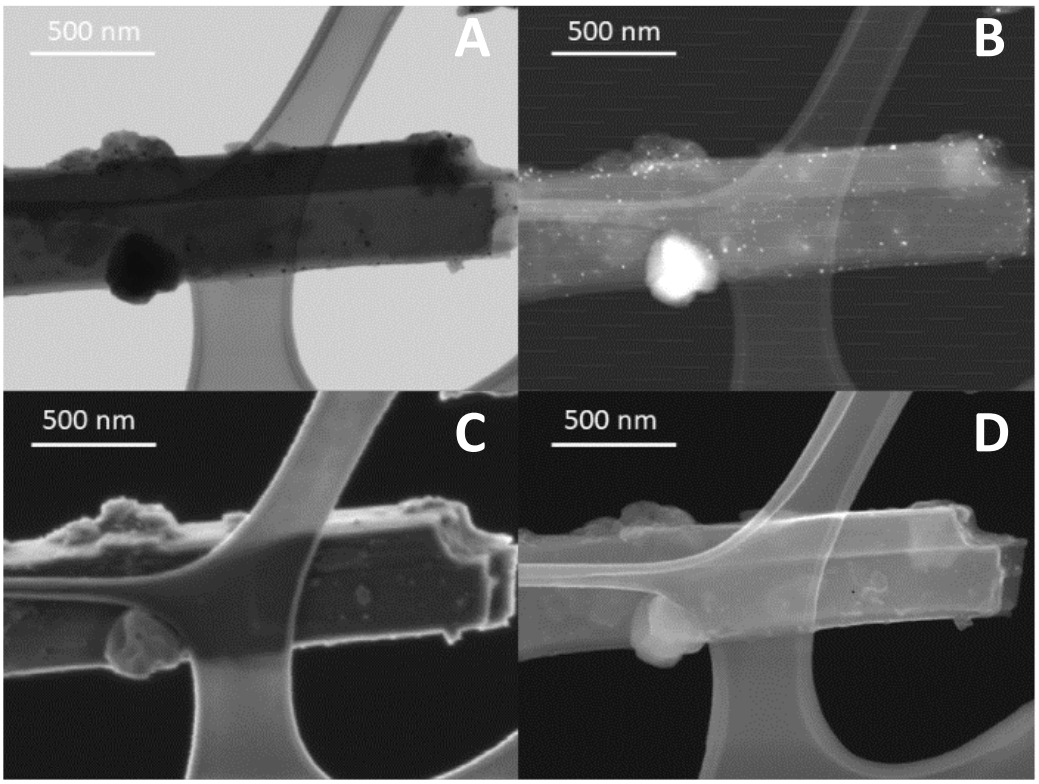

Figure 16: TBAP-α with 1 wt. % Pt, STEM images in BF mode (A) and HADF mode (B) and SEM images at 1 KeV (C) and 30 KeV (D).

To study this further, large pre-made Pt nanoparticles were loaded onto **TBAP-α** and the material tested for photocatalytic activity. These particles were synthesised by the reduction of PtH_2Cl_6 by $NaBH_4$ to give particles with hydrodynamic diameters from 4 to 40 nm and a Z_{av} of 13 nm by DLS (Figure 17A), too large to fit inside the 1.9 × 2.1 nm pores of **TBAP-α**. To load, **TBAP-α** was sonicated with the Pt nanoparticles in water for 30 minutes followed by evaporation of the water under vacuum. This gave a sample with a loading of 0.46 wt.% Pt by ICP-MS. Whilst, the sample with large pre-made nanoparticles produced hydrogen at a rate of 813 μmol h^{-1} g^{-1}, 37% lower than the sample with Pt from photodeposition (Figure 17C), this small drop in HER is not consistent with the orders of magnitude drop in active surface area that would result from moving from a system were pores are fully coated with Pt active sites to one where they are not. STEM imaging of the sample with pre-made Pt nanoparticles showed a less even distribution of Pt (Figure 18) and the "higher stress" preparation of this sample likely causes some delamination of the crystalline sample, which would both be expected to reduce the effectiveness of the photocatalyst. Taken together

these results suggest proton reduction is primarily occurring at the surface of the crystals, rather than within the pores.

An amorphous sample loaded with the same, large pre-made nanoparticles had a HER of 50 μmol h^{-1} g^{-1}, higher than the photodeposited sample (Figure 17D) but still significantly lower than the crystalline sample under the same conditions (813 μmol h^{-1} g^{-1}). This could be a result of its slightly higher Pt content, which was measured to be 0.55 wt.% by ICP-MS (compared to 0.24 wt.% for the photodeposited sample).

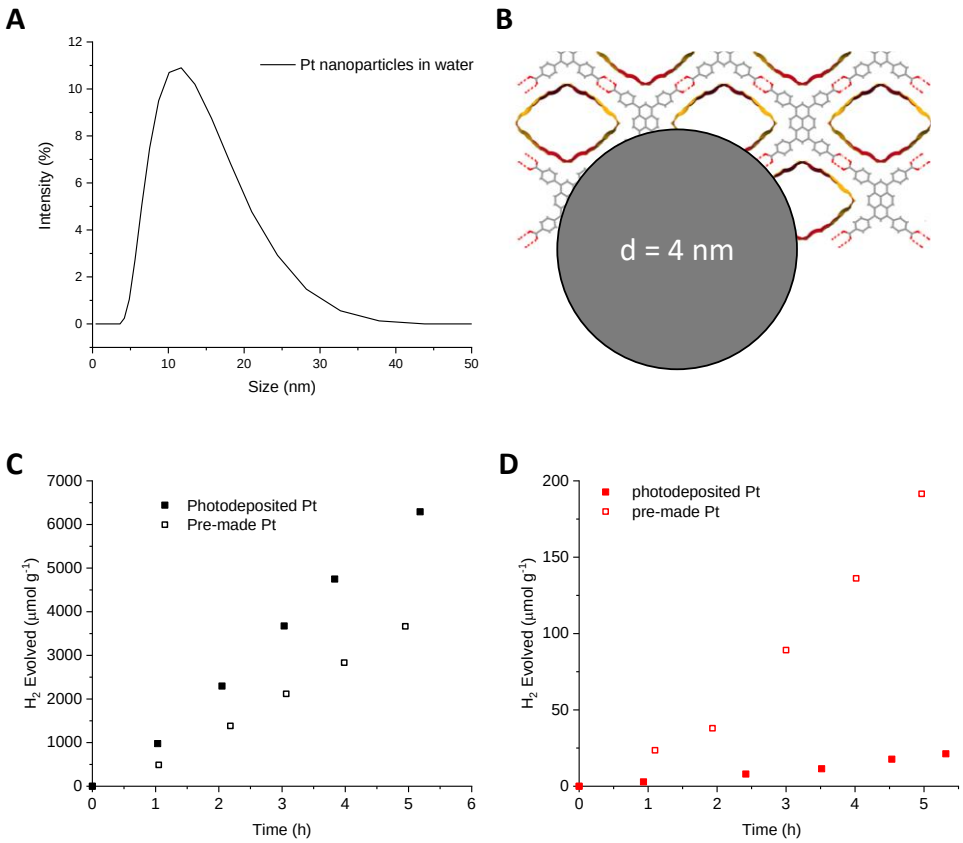

Figure 17: DLS spectra of the 'pre-made' Pt nanoparticles (A). To scale cartoon of the minimum particle size and the pores of **TBAP-α** (B). Hydrogen evolution of **TBAP-α** (C) and amorphous **TBAP** (D) (25 mg) loaded with 'pre-made' Pt nanoparticles or Pt from photodeposition of H_2PtCl_6, dispersed in ascorbic acid solution (25 mL, 0.1 M) illuminated with a 300 W Xe light source fitted with a λ > 420 nm cut off filter.

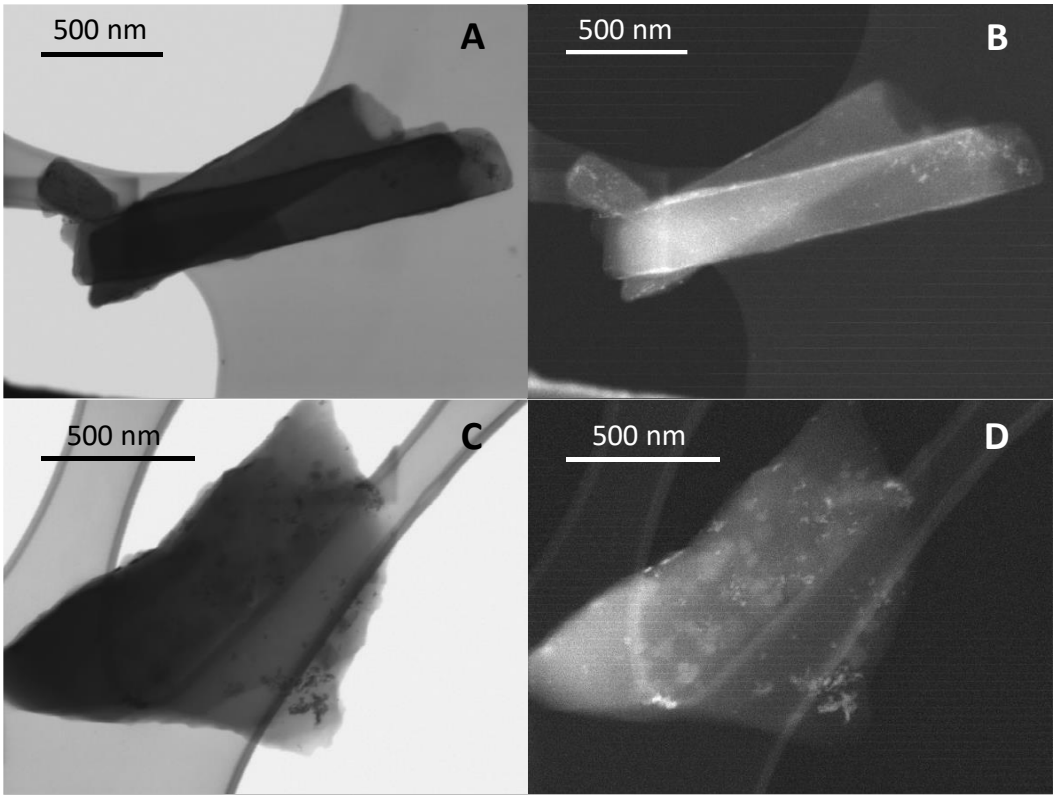

Figure 18: STEM images of **TBAP-α** (A and B) and amorphous **TBAP** (C and D) collected post photocatalysis with 'pre-made' Pt nanoparticles. Images were recorded in bright field (BF) mode (left) and high angle dark field (HADF) mode (right).

4.2.2.2 EQE and control reactions.

The external quantum efficiency of **TBAP-α** (Batch 1, 1 wt.% Pt added, suspended in ascorbic acid (0.1M)) upon illumination at 420 nm was estimated to be 4.1%, dropping to 1.2% at 470 nm and below detection levels at 595 nm, in line with the absorption profile of the material (Figure 19A). A sample of **TBAP- α**, loaded with Pt and stirred in the ascorbic acid scavenger solution, in the dark, produced no detectable hydrogen over 6 hours. These experiments indicate hydrogen is being produced in a light-driven process.

When **TBAP-α** was suspended in a 0.1 M solution of ascorbic acid in D_2O and illuminated (300 W Xe light source, $\lambda > 420$ nm filter) sustained D_2 production was measured over a four-hour period (Figure 19B). This suggests hydrogen production is a catalytic process rather than the result of the degradation of **TBAP** molecules. A small amount of H_2 was also produced, which is thought to be due to H-D exchange between D_2O solvent and non-deuterated ascorbic acid scavenger.

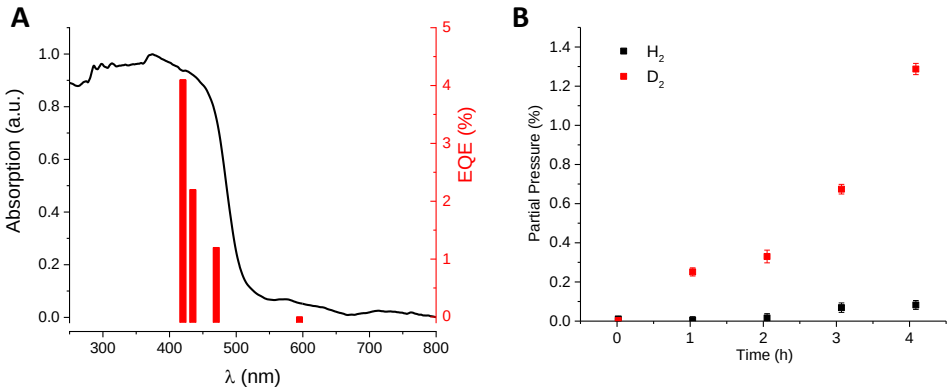

Figure 19: EQE values of **TBAP-α** measured at various wavelengths overlying the materials UV-Vis absorption spectra (A). D_2 and H_2 production of **TBAP-α** (25 mg) dispersed in D_2O (25 mL) with ascorbic acid (440 mg) illuminated with a 300 W Xe light source fitted with a $\lambda > 420$ nm cut off filter. Low levels of H_2 production are consistent with hydrogen/deuterium exchange between the non-deuterated ascorbic acid scavenger and the D_2O solvent.

In addition, very low levels of CO were detected from suspensions of **TBAP-α** in normal (non-deuterated) water / ascorbic acid solutions without (Figure 20A) and with (Figure 20B) the addition of 1 wt.% Pt, upon illumination for 5 hours (AAA Solar simulator, 1 sun). Significant hydrogen evolution, on the other hand, was observed with the pristine and platinated samples producing 2.8 and 33.0 µmol of hydrogen respectively.

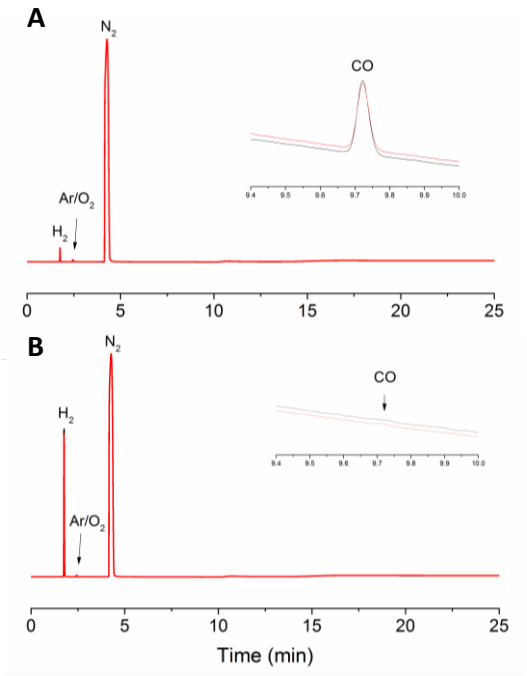

Figure 20: GC chromatograms photocatalysis experiments of **TBAP-α**. The photocatalyst (5 mg) loaded without (A) and with (B) 1 wt.% Pt in ascorbic acid solution (0.1 M, 5 mL) was illuminated for 5 hours with a solar simulator (AAA solar simulator, 1 Sun). Each trace shows two repeat experiments. Inset shows spectrum expanded > 100 x to show very low amounts of CO produced.

4.2.2.3 Long term stability

The stability of **TBAP-α** under photocatalytic conditions was also tested over 110 hours (0.1 M ascorbic acid, 1 wt.% Pt from photodepostion, λ > 420 nm) (Figure 21A). **TBAP** was found to be chemically stable by NMR and solution state UV and PL (Figure 22). However, the secondary structure, the hydrogen-bonded framework, was not stable under these conditions. Samples collected after 6, 40, and 110 hours had decreasing crystallinity, shown through a reduction in the peak intensity by PXRD (Figure 21B). This reduction in crystallinity was accompanied by a gradual decrease in photocatalytic activity over time. HER dropped from 1293 µmol h^{-1} g^{-1} over hours 1-6, to 653 µmol h^{-1} g^{-1} after 20 hours, to 369 µmol h^{-1} g^{-1} after 60 hours and 156 µmol h^{-1} g^{-1} after 110 hours and thus was tending to the behaviour of the amorphous sample in terms of activity and crystallinity. This, along with the very low activity of the amorphous sample discussed above, is a strong indication that the high activity of **TBAP-α** is a direct consequence of its secondary HOF structure.

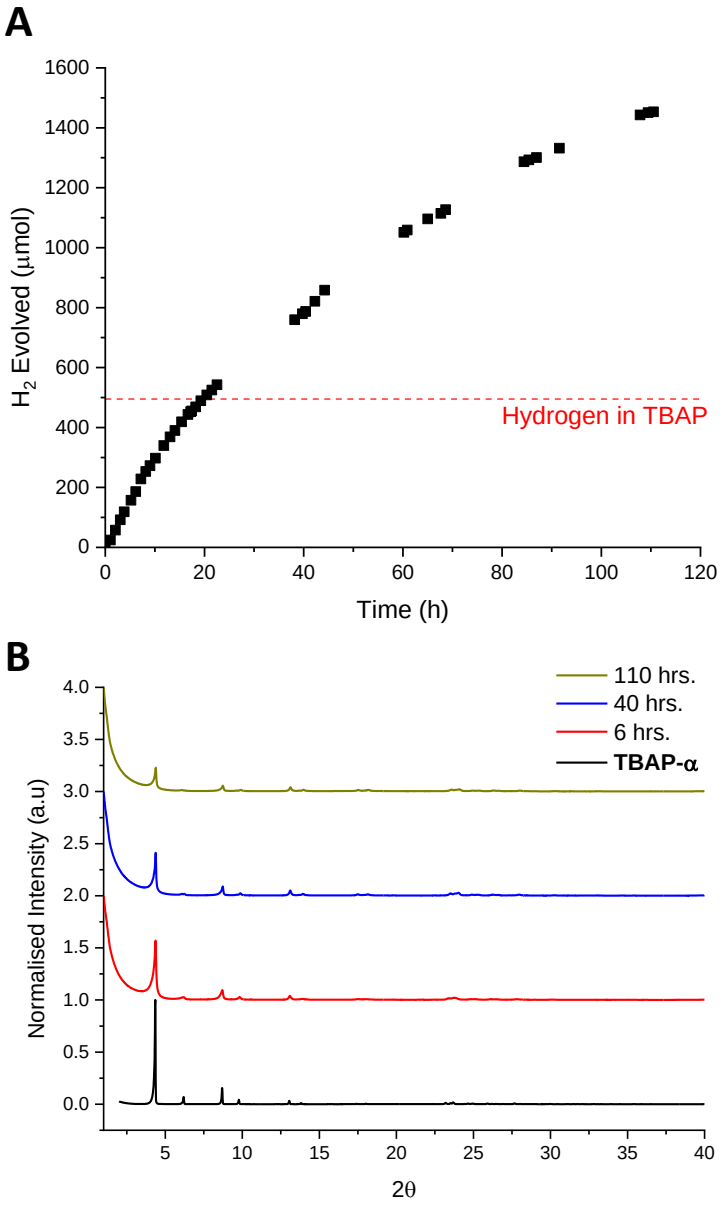

Figure 21: Hydrogen evolution of **TBAP-α** over an extended photocatalysis experiment (A) and PXRD spectra of the material collected pre and post 6, 40 or 110 hours of photolysis (B). Photocatalysis conditions were **TBAP- α** (25 mg) with 1 wt.% Pt, from photodeposition of H_2PtCl_6, dispersed in ascorbic acid solution (25 mL, 0.1 M) illuminated with a 300 W Xe light source fitted with a $\lambda > 420$ nm cut off filter. Red line in (A) shows the amount of hydrogen present in the chemical structure of the photocatalyst.

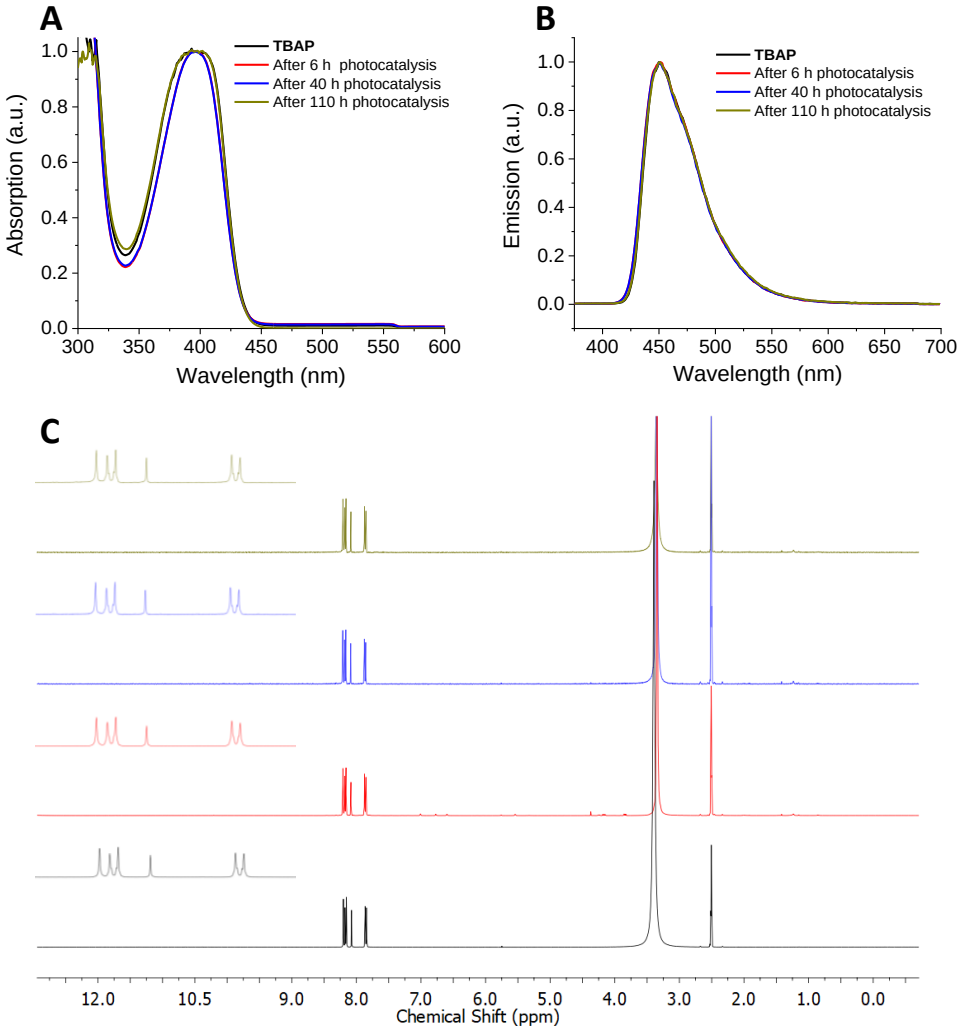

Figure 22: UV-Vis (A), PL (B) and ^{1}H NMR (400 MHz, DMSO-d6) (C) spectra of **TBAP-α** in DMSO solution collected pre and post 6, 40 or 110 hours of photolysis (ascorbic acid solution (0.1 M), 1 wt.% Pt co-catalyst, from photodeposition of H_2PtCl_6, illuminated by a 300 W Xe light source fitted with a $\lambda > 420$ nm cut off filter).

HOF structures are often unstable in water due to solvent molecules competing for hydrogen bonding interactions with the framework.[16] Without these interactions the π-stacked columns of aromatic units are no longer energetically favourable, leading to delamination and collapse of the framework into a high-density amorphous phase. Whilst **TBAP-α** can sustain hydrogen production over similar timescales to many organic photocatalysts in the literature[69–72] it was thought the process of amorphisation of **TBAP-α** crystals, and thus the drop in activity, may be slowed by using a dispersant solvent with a lower concentration of hydrogen bonding groups. **TBAP-α** was therefore also tested suspended in a solution of ascorbic acid (0.1 M) in an acetonitrile : water (9 : 1) mixture. With the addition of 1 wt.% Pt and using a 420 nm filter (300 W, Xe light source) **TBAP-α** produced hydrogen at a rate

of 358 µmol h^{-1} g^{-1} across the first 6 hours of testing. In contrast to the fully aqueous system, hydrogen evolution remained approximately linear over 118 hours (Figure 23A) with a HER of 347 µmol g^{-1} h^{-1} over the final 16 hours of the experiment, very close to the initial rate. PXRD analysis of the sample collected at 6, 62, and 118 hours (Figure 23B) showed a much slower decrease in peak intensity than in the aqueous system (Figure 21B) suggesting the non-hydrogen-bonding acetonitrile component was suppressing degradation of the ordered network.

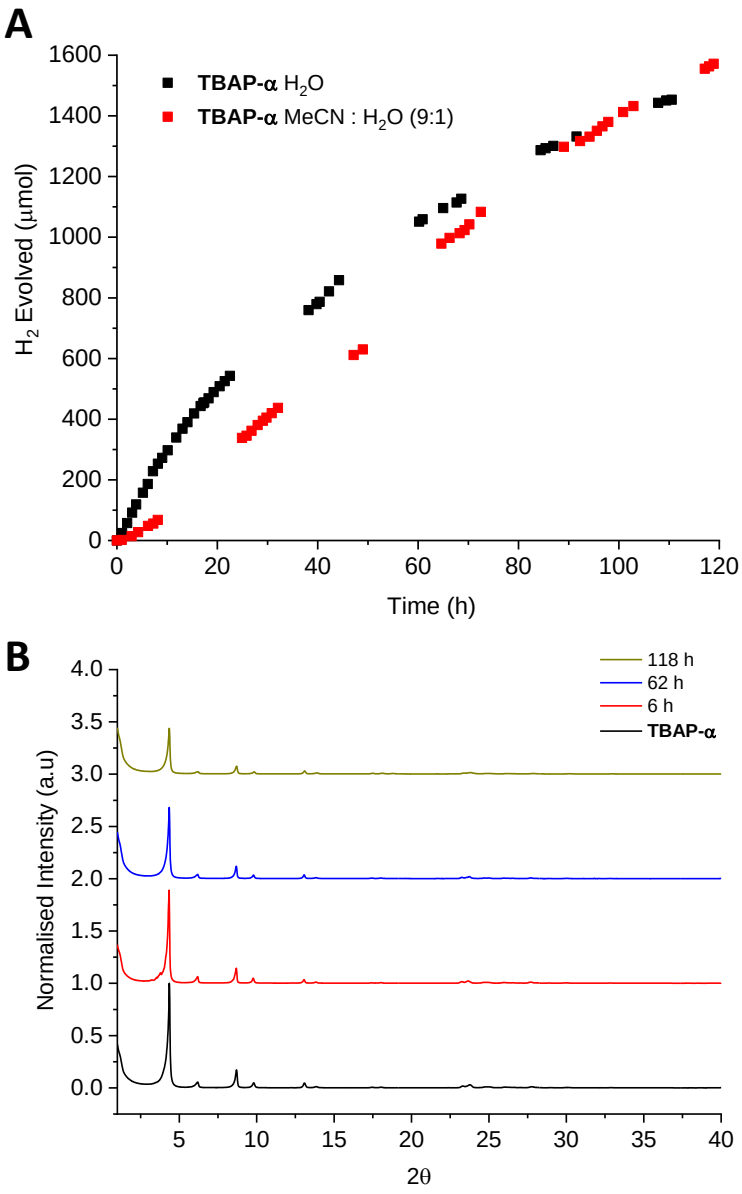

Figure 23: (A) Hydrogen evolution of **TBAP-α** over extended photocatalysis experiments dispersed in either aqueous ascorbic acid or ascorbic acid dissolved in MeCN:H_2O (9:1). (B). PXRD spectra of the material collected pre and post 6, 62 or 118 hours of photolysis under MeCN conditions.

The lower initial HER of **TBAP-α** in the acetonitrile : water dispersant compared to the aqueous system could be a consequence of the smaller driving force for scavenger oxidation expected in this system. The lower rate could also be a result of lower Pt content as photodeposition was found to occur much less efficiently in this system, with only 0.05 wt.% measured for the sample collected post photolysis by ICP-MS.

To circumvent the poor photodeposition yields found in the acetonitrile: water system a sample of **TBAP-α** was pre-loaded with Pt by photodeposition in fully aqueous ascorbic acid solution. Irradiation for 1 hour (λ > 295 nm, 300 W Xe light source, the sample was kept as cool as possible with a fan) resulted in a material with 0.15 wt.% Pt by ICP-MS. Although PXRD peak intensity did decrease somewhat over the photodeposition process (Figure 24) the material was still found to be highly crystalline and, when redispersed in the acetonitrile: water system, the sample produced hydrogen at a rate of 911 μmol g^{-1} h^{-1} much closer to the activity of the fully aqueous system.

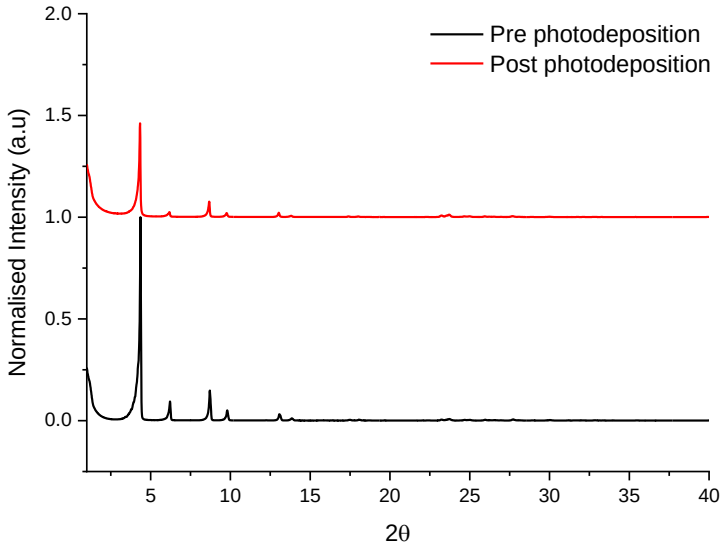

Figure 24: PXRD spectra of **TBAP-α** pre and post photodeposition of 1 wt.% Pt, from H_2PtCl_6, by 1 hour of irradiation in fully aqueous ascorbic acid (0.1 M), illuminated by a 300 W Xe light source fitted with a λ > 295 nm cut off filter).

4.2.2.4 Influence of Driving Force and pH

As discussed in section 4.2.1, **TBAP** is predicted to have a large driving force for proton reduction, but oxidation of ascorbic acid scavenger is thermodynamically less favourable and thus is perhaps rate limiting. Ideally, we could investigate this using a scavenger, such as TEA, that has a less positive oxidation potential, however **TBAP** dissolves under alkaline conditions and thus a buffered system of 5 vol.% TEA in water adjusted to pH 7 by the

addition of (HCl, 1 M) was used as the photolysis dispersant. Under these conditions no measurable hydrogen was produced by **TBAP-α** over 6 hours of irradiation (1 wt.% Pt, λ > 420 nm filter, 300 W Xe light source) which is consistent with previous studies that indicate triethylamine ceases to function as an effective electron donor at low pH.[73] Instead the photocatalytic activity of **TBAP-α** and amorphous **TBAP** were investigated in suspensions of ascorbic acid (0.1 M), buffered to pH 7 by the addition of $NaOH_{(aq)}$ (1 M) (Figure 25). In this system the potentials of the substrate will remain constant but the decreased proton concentration from neutral pH will result in a shift of the proton reduction and scavenger oxidation potentials to more negative values. This leads to a decrease in driving force for proton reduction but an increase in driving force for scavenger oxidation.

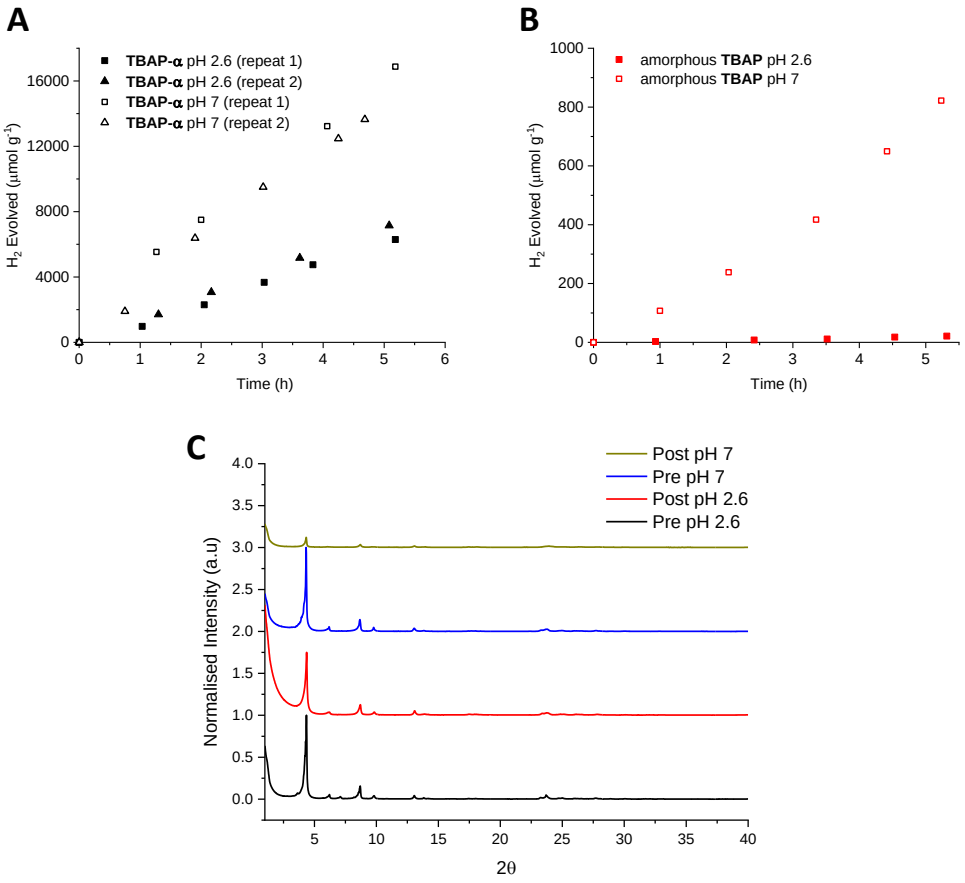

Figure 25: Hydrogen evolution of **TBAP-α** (A) and amorphous **TBAP** (B) at different pHs and PXRD spectra (C) of the samples collected before and after 6 hours of catalysis. Photolysis conditions were **TBAP** (25 mg) with 1 wt.% Pt, from photodeposition of H_2PtCl_6, dispersed in ascorbic acid solution (25 mL, 0.1 M) illuminated with a 300 W Xe light source fitted with a λ > 420 nm cut off filter. Samples at pH 7 were buffered by the addition of NaOH.

Under these conditions (1 wt.% Pt, λ > 420 nm filter, 300 W Xe light source) the HER of **TBAP-α** was 3108 μmol g^{-1} h^{-1} an increase of 240 % relative to equivalent measurements at

pH 2.6. This increase suggests that the small driving force for ascorbic acid oxidation at low pH is limiting hydrogen evolution rate, and that the larger driving force at higher pH outweighs the decrease in driving force for proton reduction. This is explained by the fact that even at higher pH the reduction overpotential remains large (> 1.5 V). Whilst HER of **TBAP-α** at pH 2.6 was approximately linear over 6 hours, it is apparent in the buffered sample (and a repeat also shown in Figure 25A with a rate of 2945 μmol g^{-1} h^{-1}) that hydrogen evolution slows over 6 hours. This corresponded to a more rapid decrease in PXRD peak intensity than at pH 2.6 (Figure 25C) presumably due to loss of the ordered HOF structure occurring more rapidly at higher pH. This is thought to be due to a more significant population of deprotonated **TBAP** molecules at pH 7, further disrupting the hydrogen bond network.

Amorphous **TBAP** also had an increase in rate under neutral conditions. HER increased to 156 μmol g^{-1} h^{-1}, an increase of 2200% relative to pH 2.6 (Figure 15B). The Pt contents of the amorphous and crystalline materials collected post aqueous buffered measurements were found to be very similar with Pt contents of 0.31 and 0.37 wt.% respectively. The relatively larger improvement of the amorphous material perhaps indicates that amorphous **TBAP** has a slightly raised IP relative to **TBAP-α** and thus, moving from pH 2.6 to pH 7 represents a larger relative increase in the driving force for scavenger oxidation for amorphous **TBAP** than for **TBAP-α**. Even with this larger improvement the activity of the amorphous sample remains 20 times lower than that of the crystalline, indicating the HOFs secondary structure is the dominant factor dictating activity.

The increase in rate with pH was also found in the acetonitrile : water (9:1) dispersants. In this case, at pH 7 **TBAP-α** had a HER 792 μmol g^{-1} h^{-1}, 2.2 times the pH 2.6 experiment with similar, very low Pt deposition (0.04 wt.%) (Figure 26A). Figure 26B shows the sample of **TBAP-α** with Pt pre-loaded by 1 hour of photodeposition in water, which was initially tested in unbuffered ascorbic acid in acetonitrile : water (as discussed above), but after 6 hours, NaOH (aq) (625 μL, 4 M) was added to bring the dispersant to neutral pH. This, as with the low Pt samples, resulted in an increase in rate. HER over the first 6 hours at pH 2.6 was 911 μmol g^{-1} h^{-1}, whilst the HER across two hours following NaOH addition was 2305 μmol g^{-1} h^{-1}.

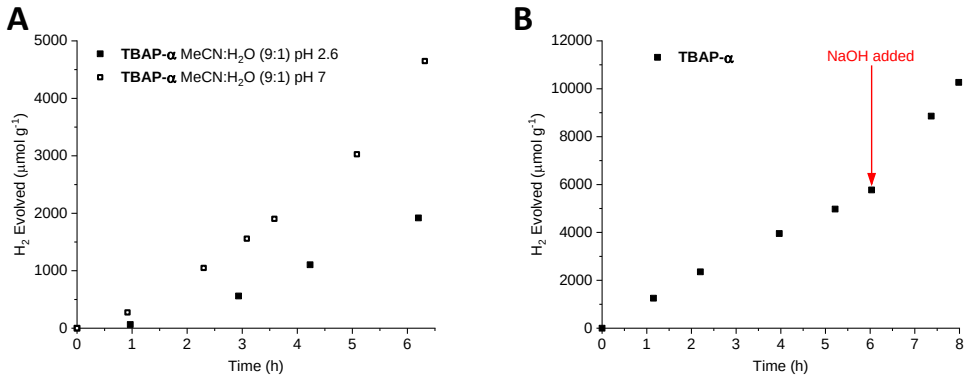

Figure 26: Hydrogen evolution of **TBAP-α** (25 mg) at different pHs with 1 wt.% Pt, from photodeposition of H_2PtCl_6 *in situ* (A) or pre-loaded by 1 hour of irradiation in fully aqueous ascorbic acid (0.1 M), at $\lambda > 295$ nm (B). The samples were dispersed in ascorbic acid dissolved in MeCN:H_2O (9:1) (25 mL) illuminated with a 300 W Xe light source fitted with a $\lambda > 420$ nm cut off filter. Samples at pH 7 were buffered by the addition of NaOH.

4.3 Phenyl and Pyridyl Analogues

4.3.1 Synthesis and Characterisation

To better analyse what features of the **TBAP-α** HOF contributed most to its high photocatalytic activity, the material was compared to a number of pyrene-based analogues. The first these replace the four benzoic acid groups in **TBAP** with phenyl and pyridyl groups to give 1,3,6,8-tetraphenylpyrene (**TPhP**) and 1,3,6,8-tetrapyridin-4-yl pyrene (**TPyP**), respectively (Figure 27). These materials were synthesised in one step by Suzuki coupling of 1,3,6,8-tetrabromopyrene with phenyl boronic acid or 4-pyridyl boronic acid in DMF solution. After work up, the amorphous powders were crystallised by sublimation at 425 °C (**TPhP**) or 450 °C (**TPyP**) and pressures of 5×10^{-4} hPa. Figure 28 shows the structures of the crystalline materials **TPhP-α** and **TPyP-α** as determined by SCXRD.

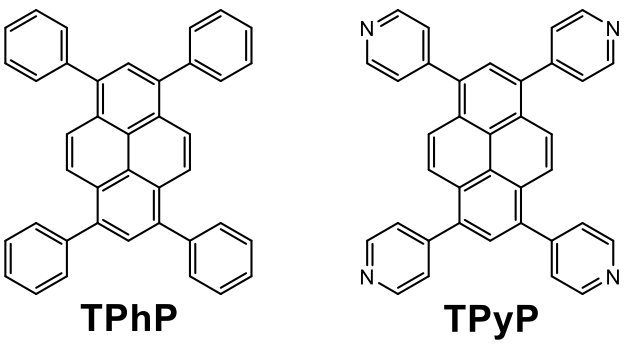

Figure 27: Chemical structures of **TPhP** and **TPyP**.

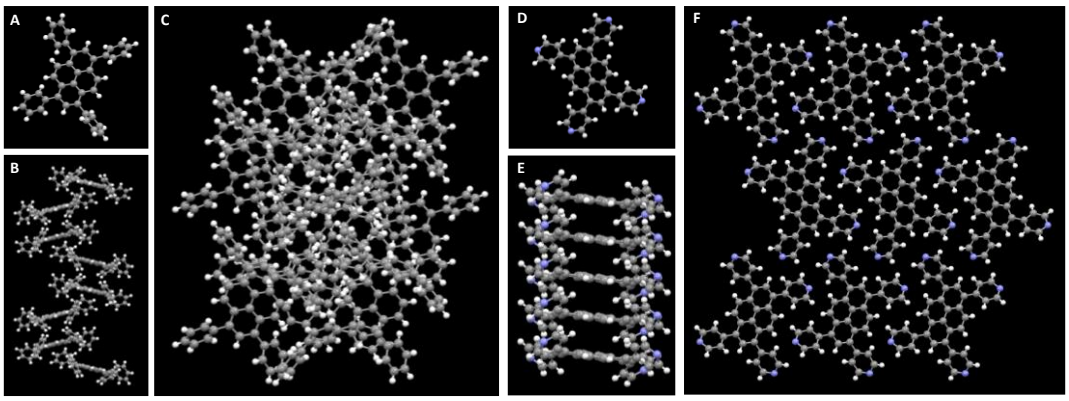

Figure 28: Structures of **TPhP-α** (A-C) and **TPyP-α** (D-F) as determined by single crystal XRD.

The π-stacked pyrene columns found in **TBAP-α** are stabilised by hydrogen-bonding interactions within the perpendicular 2D layers. Without such hydrogen bonding groups, **TPhP-α** does not contain extended π-stacking interactions or contain pores (Figure 28B and C), but forms a dense $P2_12_12_1$ polymorph which has previously been observed from crystallisation of **TPhP** in CH_2Cl_2 / hexane.[74]

In contrast, **TPyP-α** was found to crystallise in the monoclinic space group $P2_1/n$ with extended columns of **TPyP** molecules stacked 3.95 Å apart (Figure 28E), very similar to the 3.93 Å packing distance observed in **TBAP-α**. Whilst **TPyP** does not contain any conventional hydrogen-bonding groups,[75] labile C–H···N bonding interactions have been found to have significant effect in many chemical and biological structures[76] and have been shown to direct crystal packing in 4-pyridyl functionalised molecules before.[77] It is therefore thought that interactions between pyridyl lone pairs and hydrogen atoms on neighbouring **TPyP** molecules (Figure 28F) help to stabilise the observed crystal structure. In **TPyP-α** these C–H···N interactions have N···H distances as low as 2.58 Å, slightly longer than the 1.5 - 2.2 Å observed for a 'normal' hydrogen bond[75,78] (H-bond length in **TBAP-α** is 1.79 Å) but still sufficient to contribute to lattice stabilisation. One significant difference between **TPyP-α** and **TBAP-α** is that the former contains interdigitated stacks of **TPyP** molecules creating a non-porous structure with a negligible internal surface area.

The particle sizes of **TPhP-α** and **TPyP-α** suspended in water were measured by SLS (Figure 29A). Whilst **TPhP-α** had large particles of several hundred micrometres, perhaps indicating the lack of polar groups does somewhat limit dispersibility, it also had a significant population of particles from 500 nm to 50 μm. This was reflected in the Sauter mean diameter (D[3,2]) of 9.17 μm, smaller than all **TBAP-α** batches. This was also the case when **TPhP-α** was measured as a suspension in ascorbic acid (0.1 M) where a Sauter mean diameter of 7.86 μm was measured compared to **TBAP-α**'s 10.13 μm. **TPyP-α** had by far

the smallest particles with material from 300 nm to 40 µm when suspended in water and a Sauter mean diameter of 2.63 µm. Turbidity measurements correlated well with particle sizes as measured by SLS with **TPyP-α** suspended in water showing low light transmission over several hours compared to **TPhP-α** and **TBAP-α** (Figure 29C). The turbidity and SLS measurements indicate dispersibility in these materials is not solely dictated by the presence, or lack, of hydrophilic groups. Instead, this may be dependent on the primary crystal sizes of the materials and thus on the differing methods used for crystallisation; sublimation or solution growth. In either case, it appears that both **TPhP-α** and **TPyP-α** have higher external surface areas in contact with water or scavenger than **TBAP-α**.

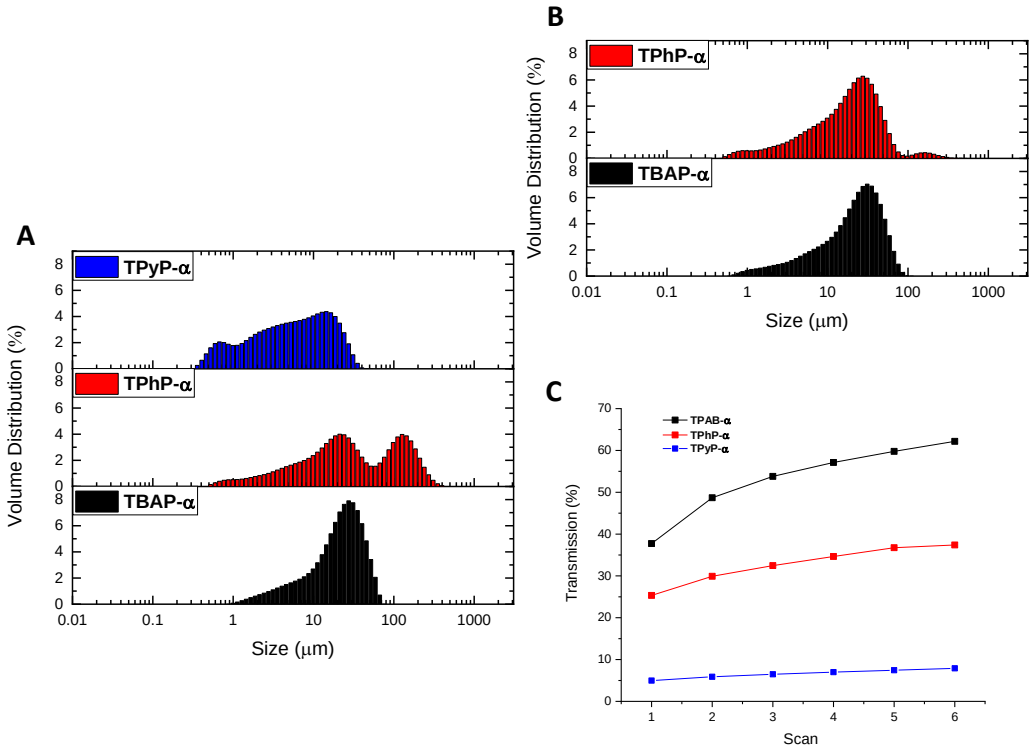

Figure 29: SLS spectra of materials in water (A) and ascorbic acid (0.1 M) (B). Light transmission measurements of materials dispersed in water over time (C), scans were recorded every 30 mins with scan 1 occurring at t = 0 mins.

The absorption profiles of **TPhP-α** and **TPyP-α** were blue-shifted with respect to **TBAP-α** (Figure 30) but both still show absorption well into the visible region with onsets of 453 and 477 nm respectively.

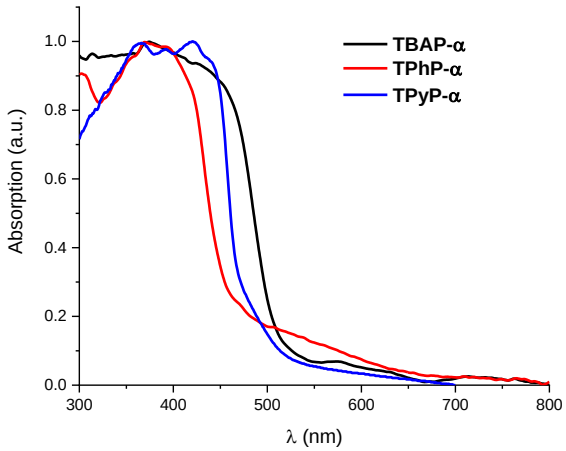

Figure 30: UV-Vis diffuse reflectance spectra of the materials in the solid state.

As in previous sections, the band structures of the **TPhP** and **TPyP** were predicted by TD-DFT calculations using gas phase energy minimised structures (Figure 31). Like **TBAP** both materials had a high EA and were predicted to have large (> 1 V) driving force for proton reduction at pHs from 2.6 up to 11.5 (applicable for TEA scavenger, see next section). The IP of both materials lie below the potential for overall oxidation of ascorbic acid and for overall oxidation of TEA (to diethylamine and acetaldehyde) suggesting hydrogen production is thermodynamically favourable using both these scavengers.

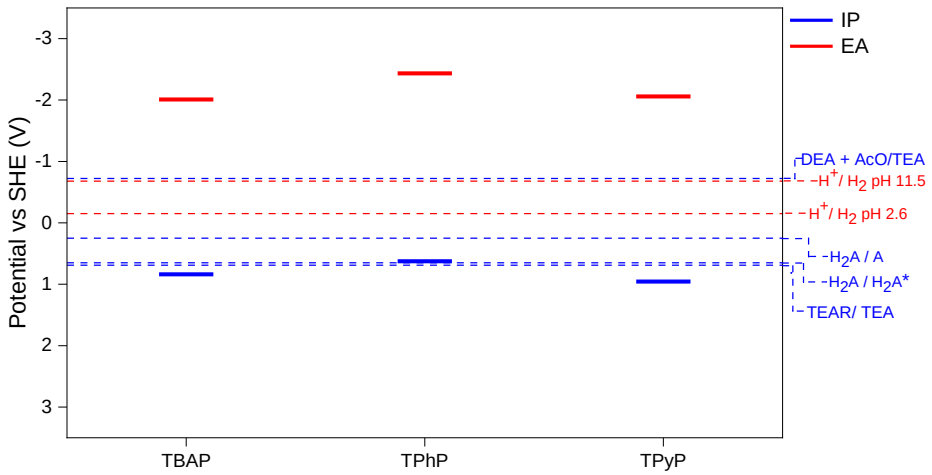

Figure 31: Comparison of the IP and EA values of the materials based on isolated molecules optimized in the gas-phase.

In **TPhP** though, the overpotential for two-hole ascorbic acid oxidation is reduced to less than 0.5 V and the initial 1-hole oxidation potential is thermodynamically disfavoured and could thus provide a kinetic bottleneck to hydrogen production rates overall. **TPyP** is predicted to have the largest driving force for all of the various scavenger oxidation reactions as its IP lies 0.11 V below that of **TBAP**.

TBAP, in both its amorphous and crystalline forms, showed a significant reduction of fluorescence lifetime upon introduction of ascorbic acid, suggesting efficient hole scavenging occurs. In contrast, **TPhP-α** shows minimal changes in fluorescence lifetime as measured by TCSPC on moving from a water suspension to a suspension of ascorbic acid (0.1 M). Average fluorescence lifetimes moved from 0.95 ns in water to 0.87 ns in ascorbic acid, with similar behaviour for a platinated **TPhP-α** sample, where τ_{Av} values of 0.90 and 0.83 ns were measured. Equally TCSPC measurements in 5 vol% triethylamine suspensions showed very similar behaviour to those in water (Figure 32) with τ_{Av} values of 0.83 and 0.86 ns for the pristine and platinated samples.

TPyP-α also showed little change in fluorescence lifetime in water (τ_{Av} = 7.22 ns) compared to 5 vol.% TEA (τ_{Av} = 7.52 ns) and again behaviour seemed to be mostly unaffected by platinization (Figure 32A). These results could indicate that hole scavenging is not occurring efficiently in **TPhP-α** and **TPyP-α** but it was shown in Chapter 3 Section 3.8 that triethylamine does not appear to reduce fluorescence lifetimes as measured by TCSPC even in highly active materials, possibly because scavenging occurs on too fast a timescale to be measured. To examine this further the fluorescence intensities were also measured. Whereas the highly active materials discussed in Chapter 3 Section 3.8 showed a large reduction in fluorescence intensity upon addition of TEA, **TPyP-α** did not (Figure 33A). This is strong evidence that hole scavenging does not occur efficiently in this system. This is in contrast to **TPhP-α** where an 80% reduction in the maximum peak intensity is observed upon addition of 5 vol. % TEA suggesting that, as in previous chapters, hole scavenging does occur but perhaps on a timescale that is too fast to observe by TCSPC. This also suggests that, although the initial 1-hole oxidation of TEA lies below the EA of **TPhP**, initial electron donation by TEA is possible in this system. This perhaps indicates the large driving force for overall TEA oxidation is sufficient to drive the disfavoured initial step for this particular scavenger. Figure 33B shows the significant drop in emission peak intensity of **TBAP-α** suspended in water upon addition of ascorbic acid, which is further evidence that efficient hole scavenging occurs in this system as well.

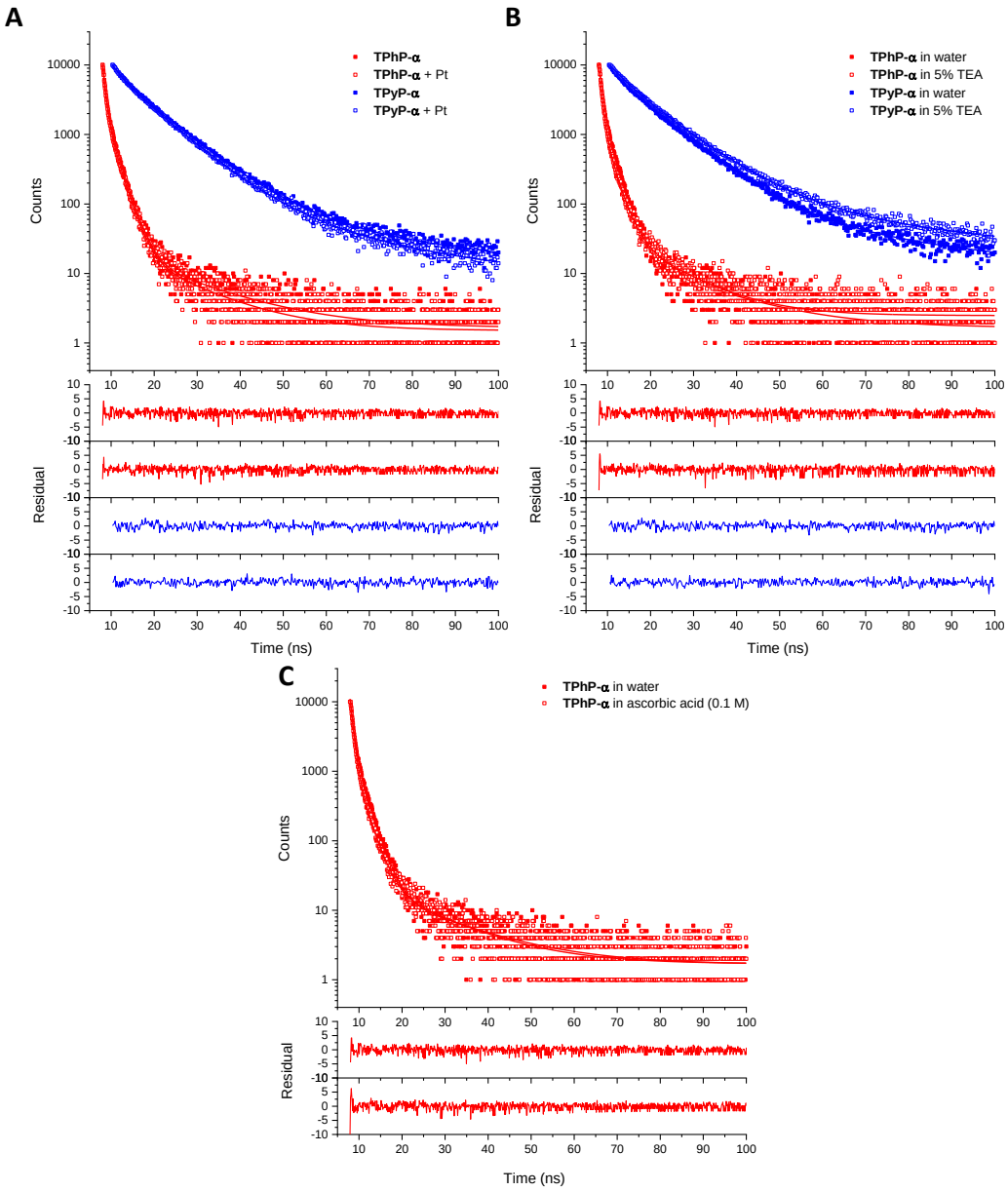

Figure 32: TCSPC fluorescence lifetime measurements of the materials in suspension. Raw data (squares), fit (lines) and residuals (bottom). λ_{ex} = 370 nm, emission was measured at each materials maxima.

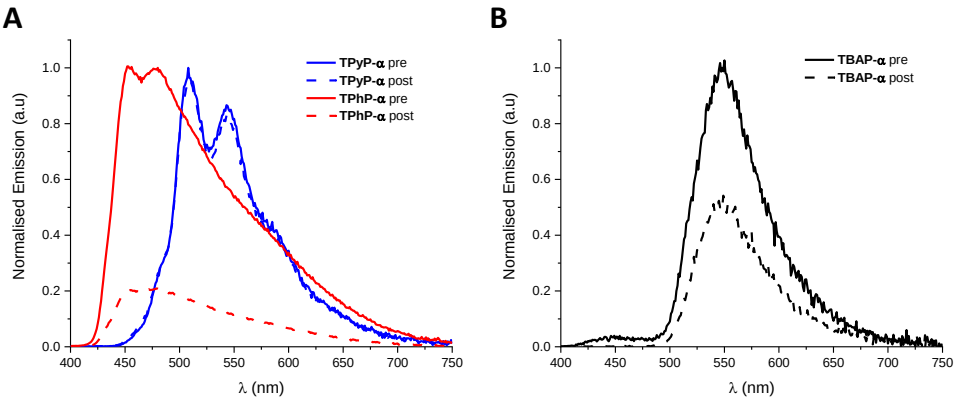

Figure 33: Emission spectra of the materials (3 mg) in aqueous suspension (3 mL) before and after the addition of TEA (150 µL) (A) or ascorbic acid (300 µL, 1 M) (B). Materials were excited at 380 nm.

4.3.2 Photocatalysis Experiments

Photocatalysis measurements were first conducted in 0.1 M ascorbic acid with 1 wt.% Pt added by photodeposition (Figure 34). **TPhP-α** was the least active material under these conditions, with a HER of 2 µmol $h^{-1}g^{-1}$. **TPyP-α** partially dissolves under these conditions, presumably due to protonation of the basic pyridyl groups, but after an induction period produced hydrogen with a rate of 18 µmol $h^{-1}g^{-1}$. ICP-MS analysis of **TPhP-α** indicated 0.54 wt.% Pt, similar to the levels measured for **TBAP-α** under equivalent conditions (0.48 wt.%). Less than 50 wt.% **TPyP-α** could be collected by filtration of the photocatalysis mixture and therefore accurate Pt photodeposition levels could not be determined. These rates are just 0.2 and 1.4 % of the HER of **TBAP-α** under equivalent conditions.

For **TPyP-α** it was thought that protonation and dissolution of the substrate may be partially responsible for the reduced activity and thus the materials were also tested in ascorbic acid buffered to pH 7 (as described in section 4.2.2). Under these conditions, **TPyP-α** and **TPhP-α** were stable as crystalline solids and showed reasonable photodeposition yields of 0.60 and 0.91 wt.% Pt. The HER of **TPhP-α** increased to 3 µmol $h^{-1}g^{-1}$, similar to the behaviour of the **TBAP-α** on moving from acidic to neutral conditions. Interestingly, **TPyP-α** produced no detectable hydrogen over 24 hours of irradiation under these conditions. This reduction in activity is surprising given the relatively higher driving force for ascorbic acid oxidation at pH 7. It should be noted that protonation of the substrate at low pH may alter the substrate electronics and that the presence of a significant amount of dissolved catalyst will alter interaction with both water and scavenger meaning the two systems should not be directly compared.

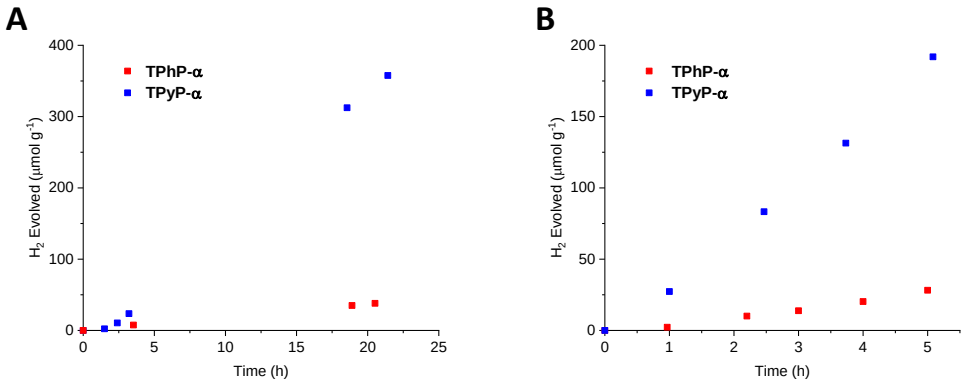

Figure 34: Hydrogen evolution of **TPhP-α** and **TPyP-α** (25 mg) loaded with 1 wt.% Pt, from photodeposition of H_2PtCl_6, dispersed in ascorbic acid solution (25 mL, 0.1 M) (A) or TEA in water (5 vol.%, 25 mL) (B) illuminated with a 300 W Xe light source fitted with a $\lambda > 420$ nm cut off filter.

As with **TBAP-α**, a buffered system of 5 vol. % TEA in water adjusted to pH 7 by the addition of $HCl_{(aq)}$ was not found to be an effective electron donor system for **TPhP-α** or **TPyP-α** (1 wt.% Pt added, 0.89 and 1.01 wt.% by ICP-MS), with neither material producing hydrogen under illumination. However, both **TPhP-α** and **TPyP-α** are insoluble in basic solutions and so could be tested in un-buffered 5. vol % TEA in water. Photodeposition yields were high under these conditions with 0.99 and 0.94 wt. % Pt measured for **TPhP-α** and **TPyP-α** respectively. The activity of both materials was higher than in the ascorbic acid systems with HERs of 6 and 40 μmol $h^{-1}g^{-1}$ (Figure 34B), consistent with the larger driving force for overall triethylamine oxidation than for ascorbic acid oxidation (Figure 31). **TBAP-α** tested under the same conditions fully dissolved and produced no hydrogen under irradiation, again suggesting the materials solid state packing is crucial to its high activity under heterogeneous conditions.

The crystallinity of both **TPhP-α** and **TPyP-α** were mostly preserved during photocatalysis in the TEA systems (Figure 35, blue) and NMR analysis (Figure 36, blue) suggests that both materials are also chemically stable. **TPhP-α** and **TPyP-α** collected post catalysts in ascorbic acid, were also chemically stable by NMR (Figure 36, red). Whilst the pyridyl bearing material partially dissolves at low pH, Figure 36 (red) shows the PXRD spectra of **TPhP-α** and **TPyP-α** collected post catalysts in ascorbic acid buffered to pH 7. Under these conditions both materials show preservation of their **α** polymorphs.

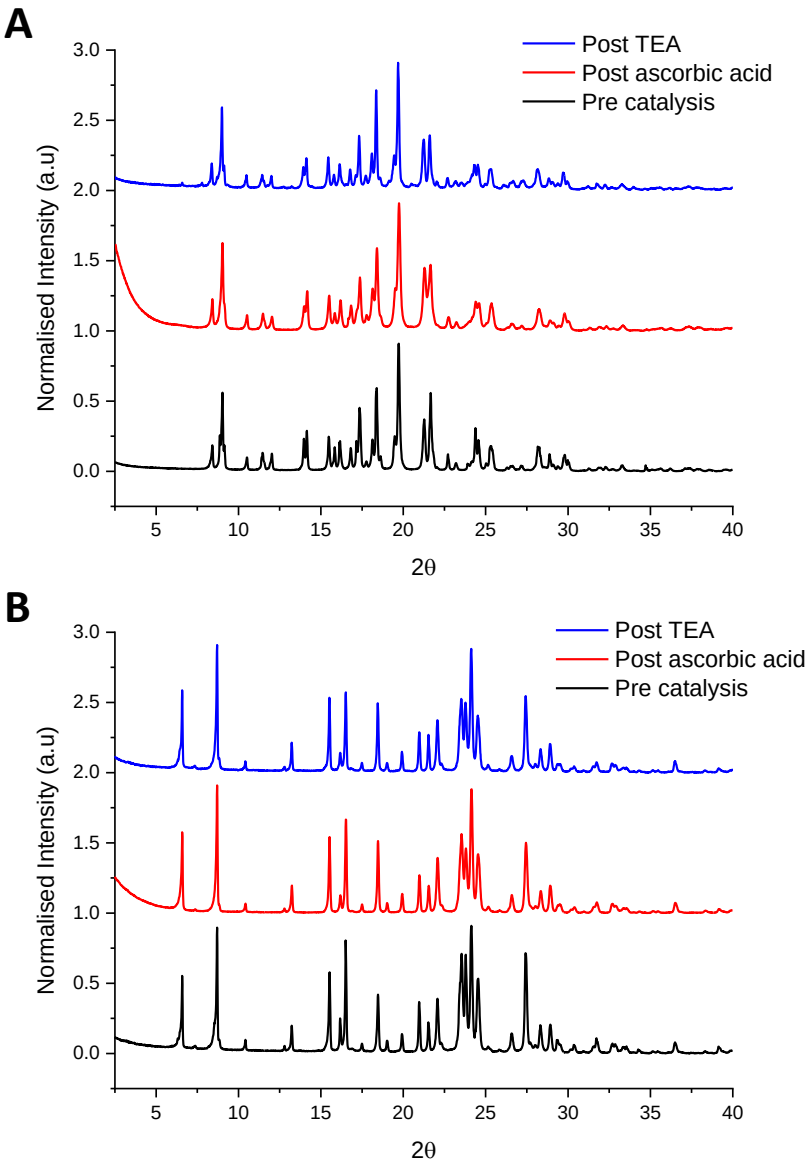

Figure 35: PXRD spectra of **TPhP-α** and **TPyP-α** pre and post photocatalysis in either buffered ascorbic acid solution (25 mL, 0.1 M) or TEA in water (5 vol.%, 25 mL).

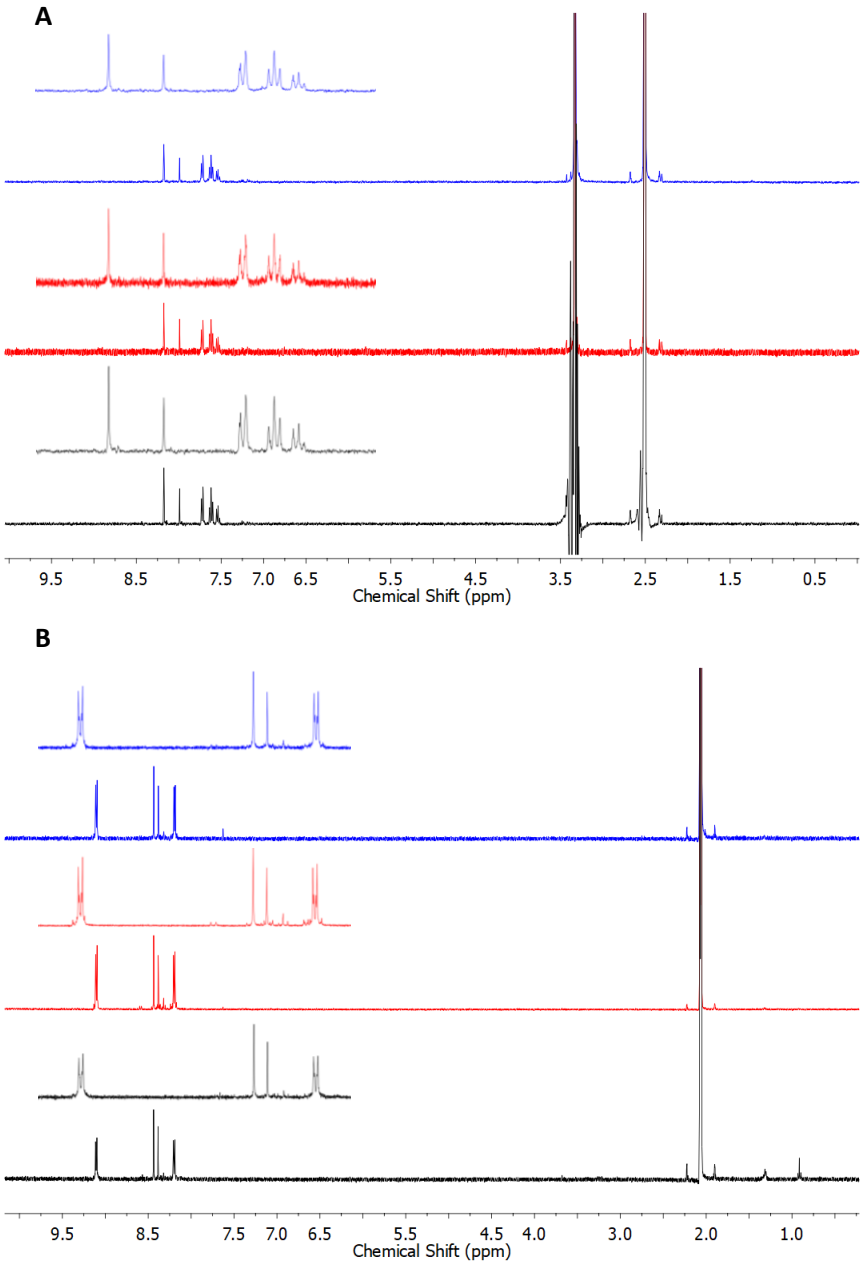

Figure 36: ^{1}H NMR (400 MHz) spectra of **TPhP** in DMSO-d_6 **(**A) and **TPyP** in acetic acid-d_4 (B)**,** recorded pre (black) and post photocatalysis in ascorbic acid solution (25 mL, 0.1 M) (red) or TEA in water (5 vol.%, 25 mL) (blue).

4.4 Other Pyrene based HOF candidates

4.4.1 Synthesis and Characterisation

The above experiments indicate the high activity of **TBAP-α** is directly related to its crystal structure and its good interaction with the ascorbic acid sacrificial electron donor. It was thought that other pyrene-based materials containing similar hydrogen bonding groups, may

encourage the formation of analogous HOF structures and give similar affinity for the electron donor.

In 2002 a large-scale study of several hundred crystal structures determined average $H\cdots O_{Water}$ distances between H-bond donor groups and water of 1.99 Å for CONH (amide) donors compared to 1.63 Å for COOH (carboxylic acid) donors.[78] This indicated that amide groups tend to be weaker hydrogen bond donors than carboxylic acids due to their less electronegative N atoms. Despite this, hydrogen bonding between amide groups has been shown to stabilise some of the most porous HOFs in the literature[34,35] suggesting an amide analogue of **TBAP**, **TPAP** shown in Figure 37, may be a promising candidate for HOF formation. Amide groups also have significantly higher pKa's than equivalent carboxylic acids. The more rapid loss in crystallinity of **TBAP-α** observed at high pH indicates that deprotonation of the substrate reduces the HOFs water stability. A **TPAP** based HOF, which contains less labile protons, may therefore show higher water stability.

In addition to **TPAP**, a biphenyl bearing analogue of **TBAP**, **1** shown in Figure 37, was prepared. This molecule, with its longer linkers, has the potential to form structures with larger pores than **TBAP-α**, which could enable the, as yet unclear, relationship between porosity and activity to be further studied. A final naphthalene bearing analogue, **2** shown in Figure 37, was also thought to be a promising candidate for both HOF formation and photocatalytic activity. The naphthalene 'arms' of this molecule provide an intermediate linker length for comparison with **TBAP** and **1** but could also provide additional π-stacking interactions. Like pyrene, crystalline naphthalene does not readily form structures with extended columns of π-stacked molecules. However, naphthalene-based materials with hydrogen bonding groups, particularly naphthalene diimides, are some of the most widely utilised units in non-covalent supramolecular structures for organic electronic applications due to their propensity to form π-stacks in the solid state.[79] Naphthalene is also predicted to have considerably stronger stabilisation energies for slip stacked structures than benzene[80,81] and may therefore provide increased interlayer interaction in **2** compared to **TBAP**. Such interactions could be beneficial for i) HOF stability and ii) charge transport between layers.

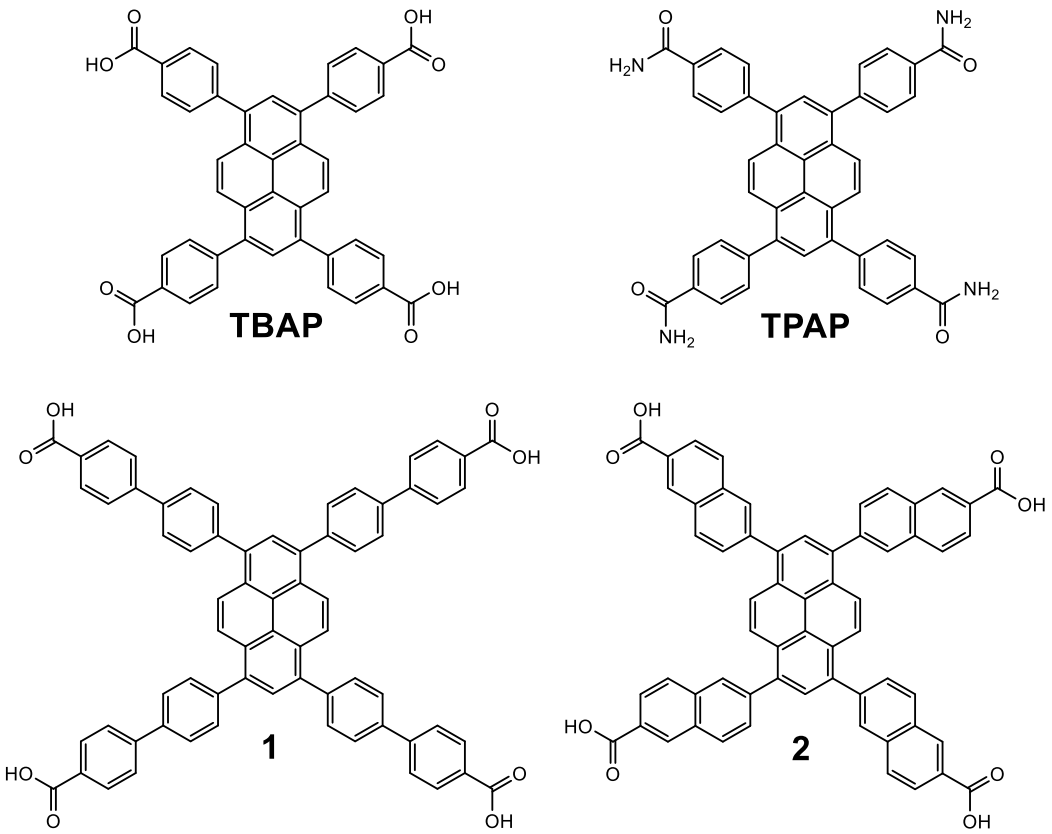

Figure 37: Chemical structures of **TBAP**, **TPAP**, **1** and **2**.

TPAP, **1** and **2** were synthesised by Pd(0)-catalysed Suzuki coupling of 1,3,6,8-tetrabromopyrene with (4-carbamoylphenyl)boronic acid, (4'-(methoxycarbonyl)-[1,1'-biphenyl]-4-yl)boronic acid and 6-(methyl 2-naphthoate) boronic acid pinacol ester respectively. The last of these is not commercially available and so was synthesised by Miyaura borylation of methyl 6-bromo-2-naphthoate, see section 4.8 for full details. The two ester bearing molecules were deprotected and all three materials were then crystallised from DMF/chloroform or DMSO/chloroform.

TPAP material obtained from DMF/chloroform (**TPAP-α**) had formed elongated yellow/green needles of several mm in length. However, closer inspection revealed these needles were highly disordered polycrystallites that were not suitable for analysis by single crystal XRD. Powder XRD spectra also showed low levels of order in the material with only broad, low intensity peaks present. It did appear that the 2θ values of these peaks roughly corresponded to those of **TBAP-α** (Figure 43) suggesting the material may contain some areas of short-range order with an analogous structure. Solvent exchange with acetone and drying under vacuum at 120 °C gave no significant change in the sample PXRD and nitrogen sorption measurements of this material indicated very low porosity compared to **TBAP-α** with a BET surface area of 51 $m^2 g^{-1}$ (Figure 41).

TPAP material obtained from DMSO/chloroform (**TPAP-β**) was comprised of smaller more plate-like yellow/green crystals that were suitable for SCXRD. The obtained structure is shown in Figure 38 and, whilst not analogous to **TBAP-α**, does show hydrogen bonding interaction between layers of **TPAP** molecules. Molecules are somewhat interdigitated however, resulting in smaller bimodal voids between **TPAP** units which, in the solvated structure, are occupied by DMSO and chloroform (Figure 38C). As in **TBAP-α** layers are packed to give extended columns of π-stacked pyrene units, however the offset of these layers in greater in **TPAP-β** resulting in larger 5.32 Å distance between pyrene units (Figure 38B). Desolvation by acetone exchange and vacuum drying resulted in fragmentation of the **TPAP-β** crystals precluding the collection of a desolvated **TPAP-β** structure. PXRD analysis of the desolvated material indicated retention of crystallinity with sharp peaks at 2θ values of 6.8 and 13.7 which match the predicted powder pattern for the solvated structure. The BET surface area of this **TBAP-β** phase from nitrogen adsorption was measured to be 604 m^2g^{-1} indicating the material retains a porous framework structure throughout desolvation.

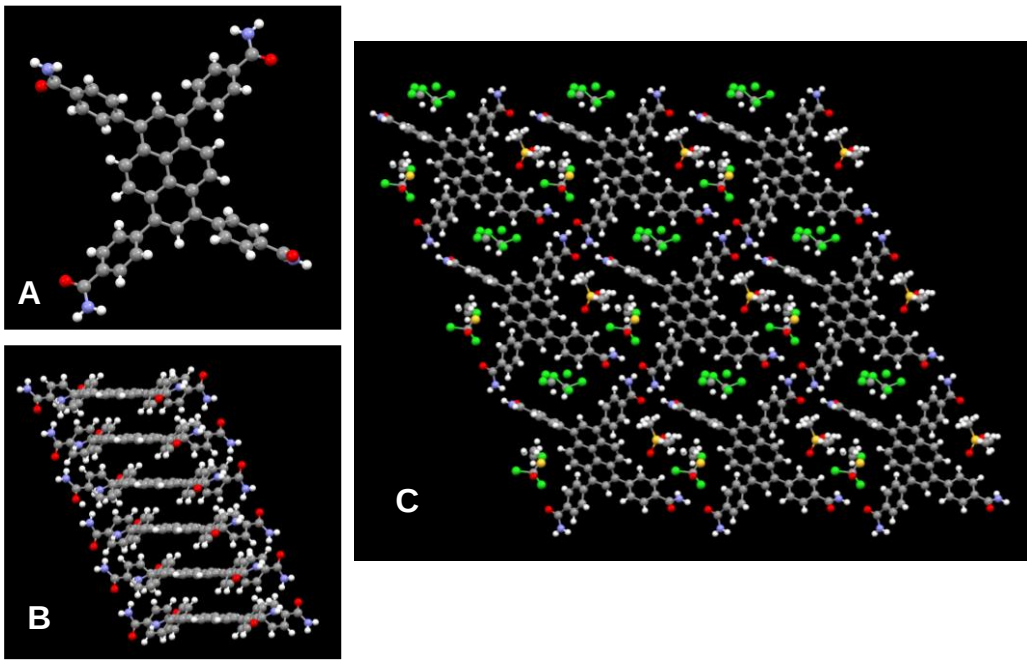

Figure 38: Structure of solvated **TPAP-β** as determined by single crystal XRD. Solvent molecules are removed in (A) and (B) for clarity.

Compound **1** crystallised from DMF/chloroform (**1-α**) was found to form an ordered solvate. The molecules of **1** in this structure showed minimal π-stacking and there was no evidence of hydrogen bonding interactions between molecules meaning desolvation does not lead to the formation of a HOF. Nitrogen adsorption of the material after solvent exchange with

acetone and drying at 120 °C under vacuum still showed significant gas uptake with a BET sorption isotherm of 668 m^2g^{-1} (Figure 41). This suggests pores persist in the crystalline material isolated after thermally removing the solvent from the crystal structure.

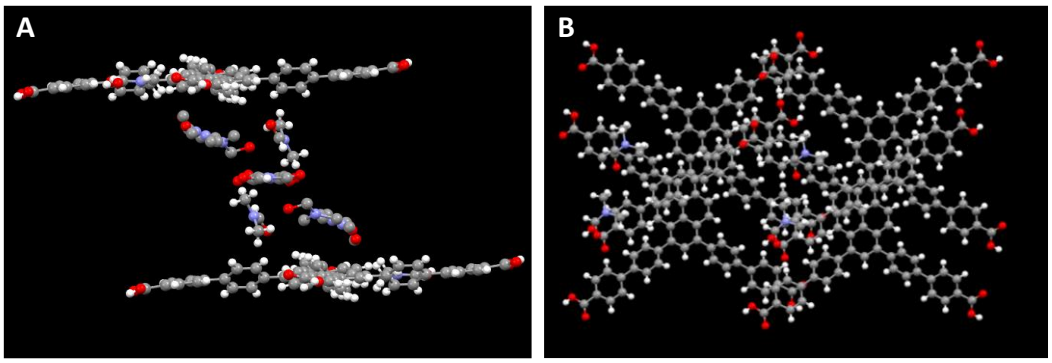

Figure 39: Structure of solvated **1-α** as determined by single crystal XRD. The desolvated crystals were too disordered for analysis.

2 showed crystallisation behaviour similar to **TBAP**, forming elongate yellow crystals from DMF/$CHCl_3$ (**2-α**) but these were not found to be of sufficient quality for SCXRD. PXRD analysis of the **2-α** sample following acetone exchange and drying (Figure 45C) indicated the sample retained crystallinity upon removal of the solvent and this was further supported by the high BET surface area of 1,740 m^2g^{-1} as measured by nitrogen sorption (Figure 41). The PXRD peaks of **2-α** at 2θ values of 3.6, 5.1, 7.2, 8.2 and 10.9 match well with a crystal structure of this molecule recently reported recently by Ma *et al*, which was determined by Pawley refinement of the PXRD signal.[52] The literature structure, shown in Figure 40, is analogous to that found for **TBAP-α** with 2-dimensional sheets of **2** molecules held in an open framework structure by two hydrogen bonds from each of the four benzoic acid groups to four neighbouring molecules. The layers are stacked to form extended columns of overlapping pyrene units, with a distance of 3.71 Å between the layers. The, in this case, 2.5 by 3.0 nm voids within each layer overlap to give open channels running perpendicular to the **2** sheets.

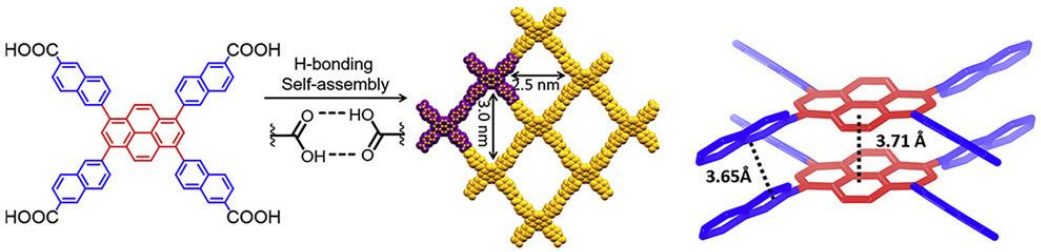

Figure 40: Literature structure of **2** which shows the same PXRD peaks as the **2-α** sample. *Reproduced with permission from reference [52]*

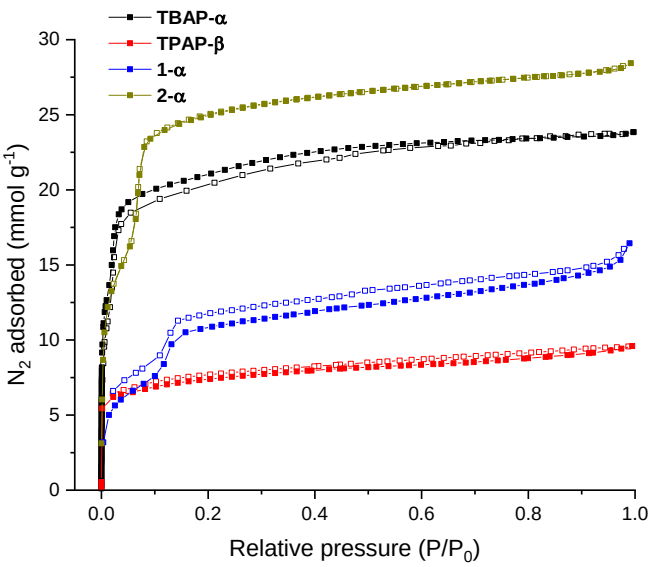

Figure 41: Nitrogen sorption isotherms of the materials at 77 K.

The UV-Vis spectra of the materials were measured in the solid state and dissolved in DMSO (Figure 42A and B). Under solution conditions, all materials had absorption profiles with multiple peaks corresponding to excitation of the pyrene and linker (phenyl, biphenyl or napthyl) respectively. **TPAP** had a similar solution spectra to **TBAP** with slightly blue-shifted maxima at 391 and 305 nm (compared to the maxima at 397 and 307 nm observed for **TBAP**) but the solid state absorption spectra of **TPAP-β** had an absorption onset of 520 nm, redshifted 13 nm in comparison to **TBAP-α**. The emission spectra (Figure 42C and D) showed larger differences between the materials; **TPAP-β** in the solid state and dissolved in DMSO had emission maxima at 528 nm and 441 nm respectively, compared to 548 nm and 450 nm observed for **TBAP-α** under the same conditions. **1** and **2** showed slightly more redshifted absorption in solution, consistent with the greater conjugation lengths possible through their extended linkers. The pyrene-based absorption maxima were at 404 and 408 nm, with an additional biphenyl-based absorption at 320 nm and a broad naphthalene-based absorption at 313 nm for **1** and **2** respectively. The emission spectra of **1** and **2** were almost identical with maxima at 461 and 462 nm respectively. The solid-state absorption spectra of **1-α** and **2-α** were also similar, with materials showing absorption onsets of 515 nm whilst the solid-state emission maxima were at 534 and 526 nm respectively. Overall, it appears that the materials' different linkers do not have a strong effect on absorption or emission properties and that all materials should be able to interact with visible wavelengths.

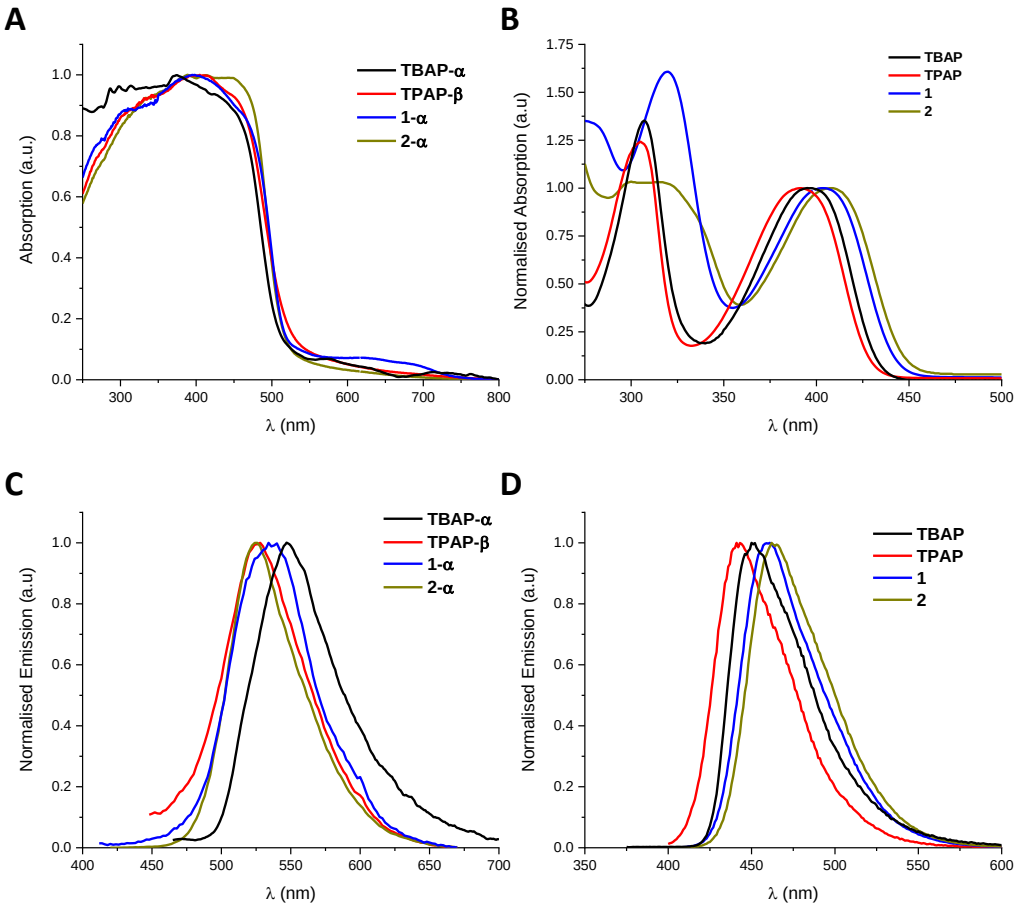

Figure 42: UV-Vis spectra of the materials in the solid state (A) and in DMSO solution (B) and fluorescence spectra of the materials in the solid state (C) and in DMSO solution (D).

4.4.2 Photocatalytic Testing

Both **TPAP-α** (from DMF/$CHCl_3$) and **TPAP-β** (from DMSO/$CHCl_3$) were tested for photocatalysis using λ > 420 nm, 1 wt. % Pt co-catalyst and an ascorbic acid scavenger (0.1 M) (Figure 43 A). Despite its very low crystallinity and porosity, **TPAP-α** produced hydrogen at a moderate rate of 302 μmol h^{-1} g^{-1} over the first 6 hours and, as shown in Figure 43B, continued to produce hydrogen with a slight drop in rate over 70 hours. ICP-MS analysis of the sample collected post photolysis verified Pt photodeposition with a content of 0.53 wt.% As well as a gradual broadening and drop in intensity of the PXRD peaks **TPAP-α** collected after 33 and 70 hours of photolysis showed the development of several extra peaks, indicating the formation of a second polymorph. This contrasts with **TBAP-α** and indicates the weaker hydrogen bonds of the amide result in a smaller kinetic barrier to transitions between polymorphs or a larger distribution of meta-stable polymorphs with similar energies.

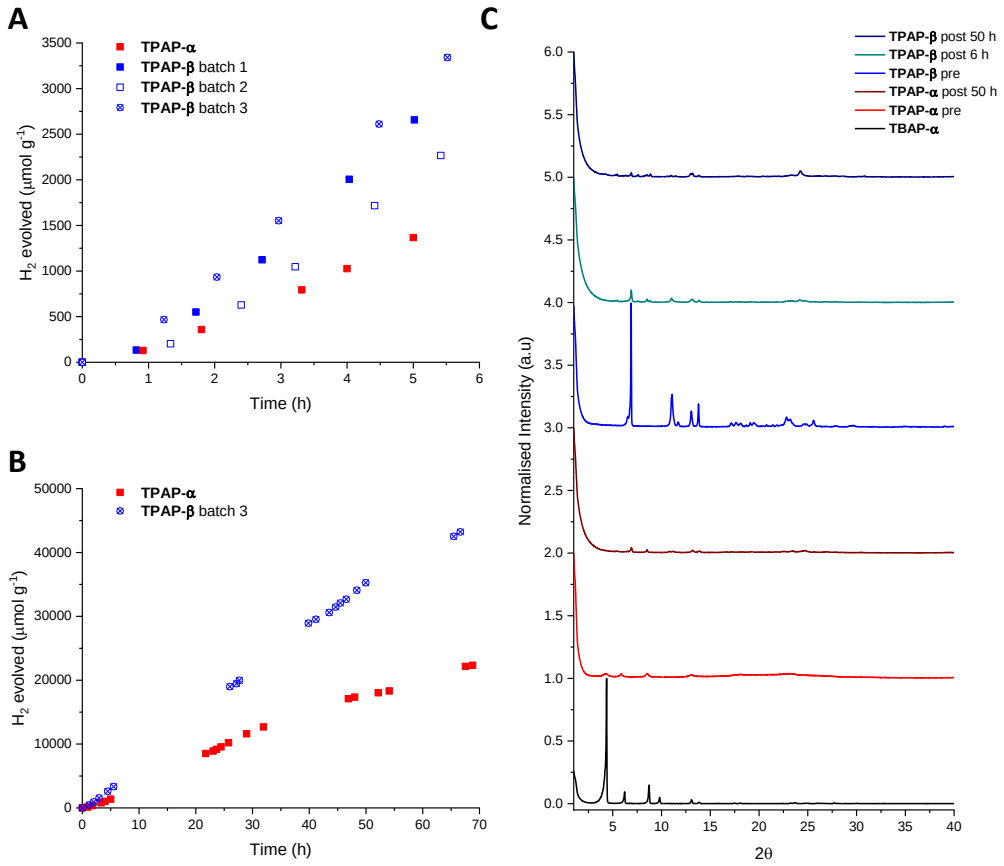

Figure 43: Hydrogen evolution of **TPAP-α** and **TPAP-β** (25 mg) loaded with 1 wt.% Pt, from photodeposition of H_2PtCl_6, dispersed in ascorbic acid solution (25 mL, 0.1 M) illuminated with a 300 W Xe light source fitted with a λ > 420 nm cut off filter (A and B). PXRD spectra of **TPAP-α** and **TPAP-β** collected pre and post photolysis compared to **TBAP-α** (C).

The **TPAP-β** sample, isolated from DMSO/$CHCl_3$, showed twice the activity of the **α**-sample, with a HER of 609 μmol $h^{-1}g^{-1}$ and similar retention of activity over 70 hours. The increased activity is primarily thought to be due this materials' higher crystallinity compared to the **α**-sample. Two further batches of **TPAP-β** showed similar rates of 645 and 513 μmol $h^{-1}g^{-1}$ (Figure 43A) with Pt contents of 0.64 and 0.76 wt. % by ICP-MS compared to 0.57 wt.% measured for the first batch. Like the **α**-sample, a **TPAP-β** collected after just 6 hours of photolysis showed evidence of a secondary polymorph as well as an overall loss in crystallinity.

It has been previously shown that amides and acid groups can form strong hydrogen bonds between molecules and form similar synthons to the dual acid-acid hydrogen bonds found in **TBAP-α**.[82,83] However, attempts to generate a **TBAP/TPAP** co-crystal resulted in only disordered materials, with lower activity than either single component.

1-α was significantly less active than either **TPAP** phase with a HER of just 43 µmol $h^{-1}g^{-1}$ (Figure 44). The sample collected post six hours of photocatalysis had 1.03 wt.% Pt by ICP-MS and showed a loss in PXRD peak intensity compared to the material pre-photocatalysis and no observable secondary peaks. This low activity suggests the absence of any extended columnar π-stacking observed in the solvated structure of **1-α** limits the activity of the materialcompared to **TBAP-α** or either **TPAP** phase. It appears that porosity alone is not sufficient to impart high activity as **1-α** has a relatively high, 668 m^2 g^{-1}, BET surface area but less than 1/7 of the activity of the almost non-porous **TPAP-α** phase, which had a BET surface area of 51 m^2 g^{-1}. It is possible, although unlikely, that the substitution of phenyl linkers with biphenyl significantly alters the substrate IP and EA of **1** in comparison to **TBAP**. DFT calculations would be required to determine whether this is a likely factor in the two materials differing activities.

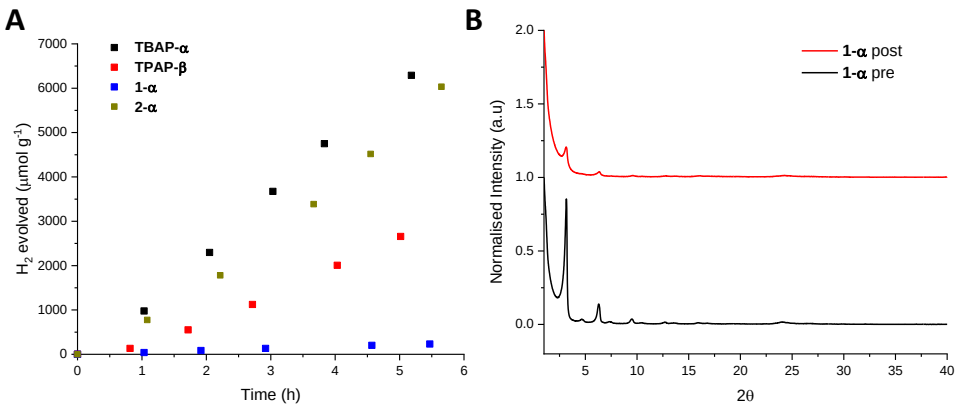

Figure 44: Hydrogen evolution of **1-α** compared to the other materials (25 mg) loaded with 1 wt. % Pt, from photodeposition of H_2PtCl_6, dispersed in ascorbic acid solution (25 mL, 0.1 M) illuminated with a 300 W Xe light source fitted with a λ > 420 nm cut off filter (A). PXRD spectra of **1-α** collected pre and post photolysis (B).

2-α, which has similar porosity and π-stacking to **TBAP-α**, also shows very similar activity for hydrogen evolution. Over the first 6 hours of photocatalysis **2-α** produced hydrogen at a rate of 1151 µmol $h^{-1}g^{-1}$ and a second batch had a HER of 1286 µmol h^{-1} g^{-1} (Figure 45) with both samples measured to have low Pt deposition yields, with 0.21 and 0.24 wt. % Pt by ICP-MS. **2-α** appeared to show a more rapid drop in PXRD peak intensity than **TBAP-α** under equivalent conditions and this was reflected in a more rapid drop off in activity over an extended run (Figure 45B). After 10 hours **2-α** had a HER of just 317 µmol $h^{-1}g^{-1}$, 28% of its initial rate, whilst **TBAP-α** retained 75% activity over the same time frame. Like, **TBAP-α**, the initial HER of **2-α** tested at pH 7 was higher than under acidic conditions indicating a small overpotential for scavenger oxidation may limit activity in this material as well.

However, the high (2052 µmol g^{-1} h^{-1}) HE of the pH 7 sample over the first hour decreased very quickly, such that over a 6 hour test it had produced a similar amount of hydrogen to the acidic sample. This was consistent with a more rapid loss in crystallinity of the pH 7 sample as measured by PXRD (Figure 45C). It is unclear why the **2-α** framework appears to be less stable in water than **TBAP-α** but these experiments indicate the extended aromatic linkers do not provide the desired π-stacking stabilisation.

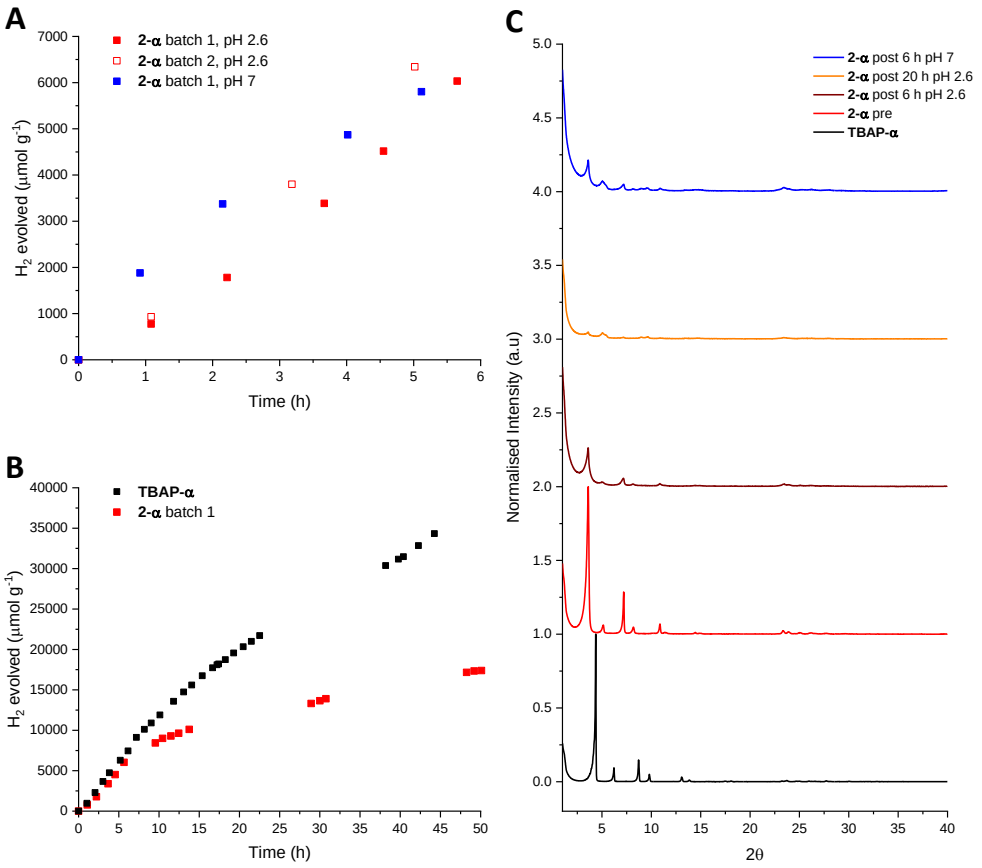

Figure 45: Hydrogen evolution of **2-α** (25 mg) loaded with 1 wt.% Pt, from photodeposition of H_2PtCl_6, dispersed in ascorbic acid solution (25 mL, 0.1 M) illuminated with a 300 W Xe light source fitted with a λ > 420 nm cut off filter (A) and long term stability compared to **TBAP-α** (B). PXRD spectra of **2-α** collected pre and post photolysis compared to **TBAP-α** (C).

4.5 Other HOF candidates

This chapter has focused on pyrene based photocatalysts but a diverse range of different aromatic groups have been used to generate hydrogen-bonded organic frameworks.[16,29] Initial investigations into several pyrene-free materials were also conducted to explore the potential of alternative aromatic 'core' units for HOF formation and photocatalytic activity.

A recent high-throughput study found that co-polymers of triphenylene with dibenzo[*b*,d]thiophene sulfone, 1,4-difluorophenylene or 3,7-benzo[b,d]dithiophene had very high activity with EQEs at 420 nm of up to 15.1%[84] so it was thought to be an interesting central unit for investigation. Extended triphenylene molecules have been previously utilised in the formation of HOFs with small triangular pores of circa 8.5 Å,[31] however small C_3 symmetric carboxylic acids, such as trimesic acid, have been found to form lower density honeycomb sheets with larger pore sizes[85] and so the triphenylene analogue, **3**, shown in Figure 46 was chosen for analysis.

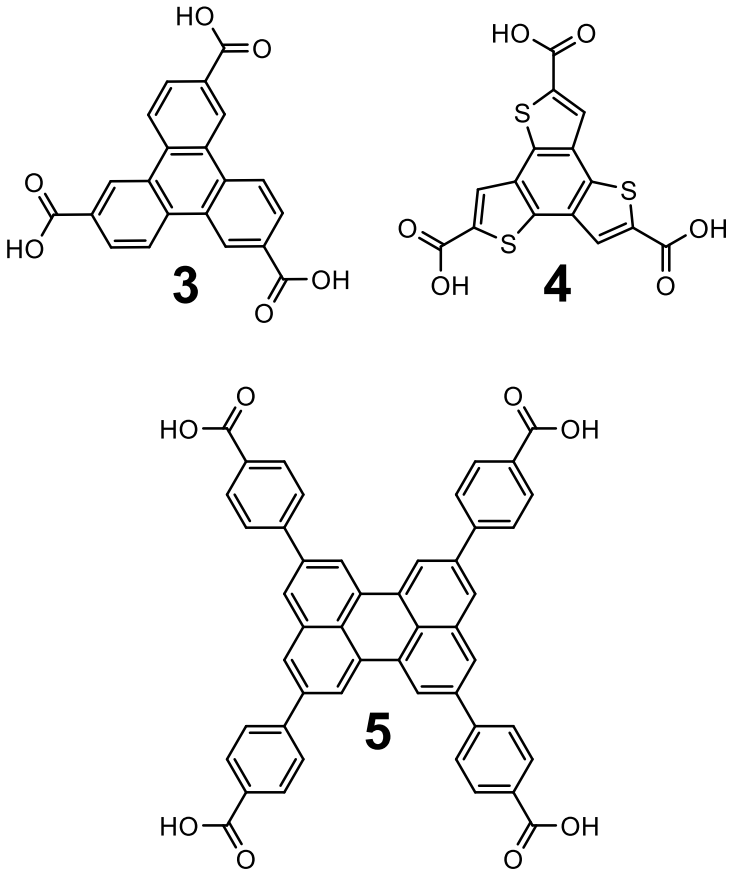

Figure 46: Chemical structures of **3**, **4** and **5**.

To date, there have been few examples of HOFs containing heterocycles which, aside from hydrogen bonding groups, have mostly been hydrocarbon based. This is in contrast to the organic materials usually studied for photoactive or electronic applications, where heteroatom incorporation is used to promote a variety of electronic and physical material properties.[86–88] Thiophenes have been very widely studied for photoelectronic applications due to their strong donor properties and ability to form materials with high conductivity and red-shifted absorption spectra. More recently, the C_3 symmetric benzotrithiophene (BTT) unit has been used across a number of supercapcitor,[89] photovoltaic,[90] electrochemical[91] and

photocatalytic[92] applications, which primarily attribute high material performance to the favourable conductivity properties provided by BTT units. Indeed, BTT based materials have been shown to form supramolecular,[93] liquid crystalline[94,95] and COF[89] structures with highly overlapped, columnar π-stacks that are thought to be beneficial to charge transport. The carboxylic acid functionalised BTT molecule, **4**, was therefore thought to be a promising candidate for HOF formation and photocatalytic activity.

The perylene analogue of **TBAP**, **5**, was also selected due to its large aromatic system. It was thought this would help to extend the materials absorption spectra further into the visible region, allowing a greater percentage of solar light to be utilised, and may provide stronger π-stacking interactions[96] that could aid in HOF stability. Like naphthalene, bisimides of perylene have become ubiquitous as photoactive components and easily form π-π stacking architectures[97] but **5** provides an example of an ortho functionalised perylene substituted at the 2,5,8 and 11 positions, which are far less widely studied and may provide a more suitable symmetry for porous HOF formation. Perylene been previously utilised as a monomer in moderately active polymeric photocatalysts for hydrogen production[98] but studies on molecular materials have primarily focused on perylene diimide derivatives which have been shown to be active hydrogen production photo(electro)catalysts in supramolecular 'nanobelt' or nanoribbon structures[99,100] and to act as an efficient photosensitizers when combined with carbon nitride.[101]

4.5.1 Synthesis and Characterisation

3 was synthesised via a modified literature route shown in Scheme 1.[102] Full synthetic procedures can be found in the experimental section 4.8.2 . Briefly methlcyclohexanone was dehydrated with zirconium tetrachloride to form 2,6,10-trimethyl-dodecahydrotriphenylene, followed by aromatisation using palladium on carbon to give 2,6,10-trimethyltriphenylene. This material was fully oxidised to the tri-carboxylic acid using sodium dichromate.

2,4,6-Trichlorobenzene-1,3,5-tricarbaldehyde was synthesised by Friedel crafts substitution of 1,3,5-trichlorobenzene with dichloromethane to yield 1,3,5-trichloro-2,4,6-tris(dichloromethyl)benzene, followed by oxidation to the tri-aldehyde with fuming sulfuric acid.[89] **4** was then synthesised by the reaction of trichlorobenzene-1,3,5-tricarbaldehyde with ethylmercapto acetate,[103] followed by ester deprotection with $NaOH_{(aq)}$.

5, was synthesised in an analgous manner to the pyrene-based materials; 2,5,8,11-perylenetetraboronic acid tetra pinacol ester was synthesised from perylene and bis(pinacolato)diboron using a (1,5-cyclooctadiene)(methoxy)iridium(I) dimer C-H activation catalyst.[98] This was then coupled to ethyl 4-bromobenzoate *via* Pd catalysed Suzuki coupling in DMF, followed by ester deprotection to give **5**.

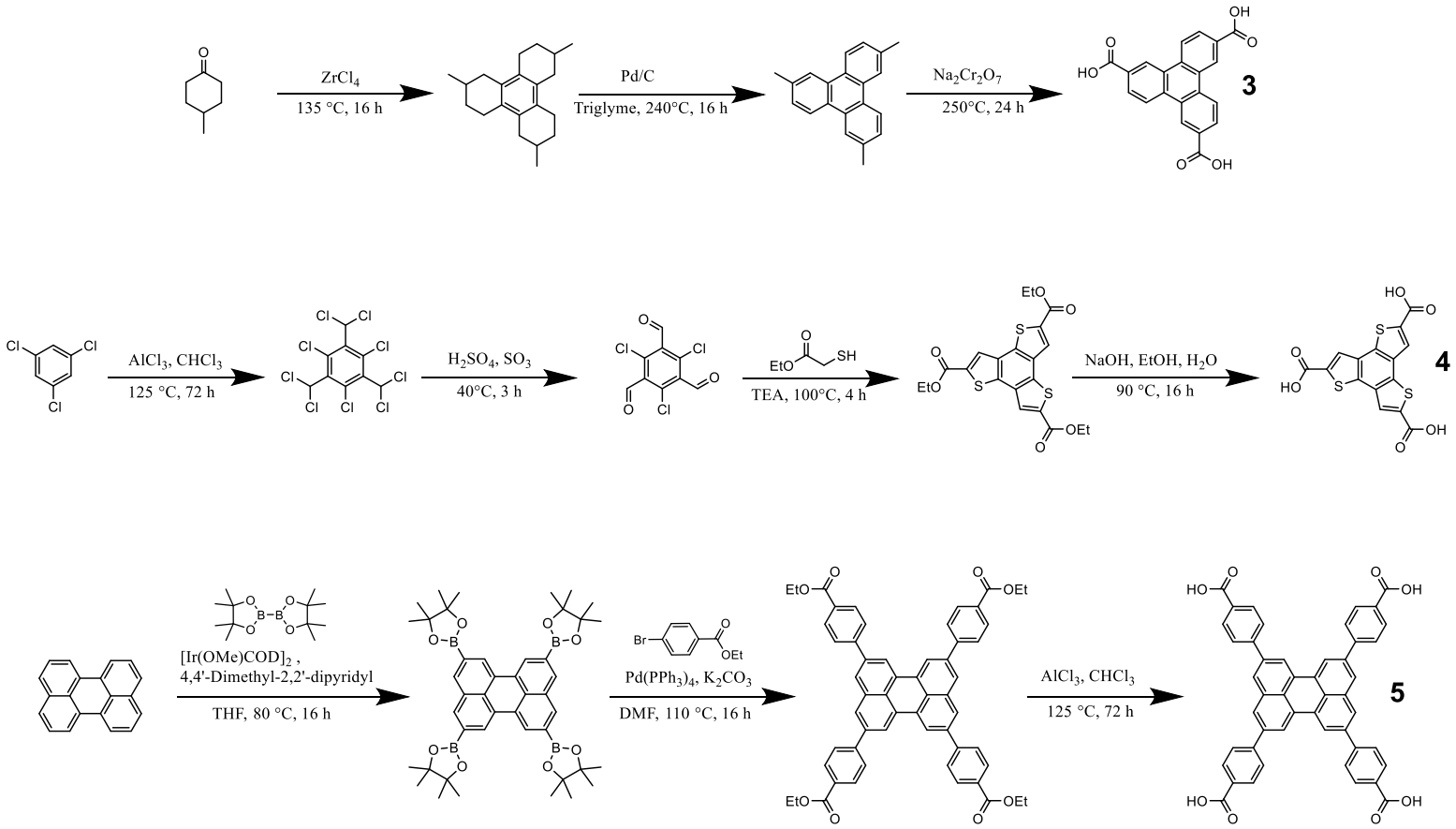

Scheme 1: Synthesis of **3**, **4** and **5**.

Initial attempts to crystallise the materials were conducted in DMF or DMSO solutions by vapour diffusion of chloroform. The samples of **3** and **5** isolated from DMSO/chloroform (**4-α** and **5-α**) showed high crystallinity by PXRD (Figures 48B and D) although the crystal sizes were too small to analyse by SCXRD. In contrast, both samples of **4** were comprised of amorphous powder. A screen of further crystallising conditions for **3** with hydrogen bonding solvents (DMF, DMSO and NMP) coupled with precipitating co-solvents (chloroform, acetone and ethyl acetate) yielded primarily amorphous or semi-crystalline samples. The PXRD spectra of the sample isolated from DMSO/acetone, **4-α**, is shown in Figure 48C. This was the most crystalline of the samples and so was used for photocatalytic testing.

The UV-vis and PL emission spectra of **3**, **4**, and **5** dissolved in DMSO are shown in Figure 47 and demonstrate the range of absorption properties that can be achieved through varying the aromatic core of HOF candidates. In solution, **3** and **4** only absorb in the UV region with maxima at 278 and 291 nm. **5** also showed an absorption peak in the UV region corresponding to the molecules' benzoic acid linkers, as well as three absorption maxima at 404, 428 and 456 nm typical of perylene bearing materials. When excited at these wavelengths, the emission spectra of **5** also showed peaks corresponding to the perylene core at 467, 494 and 530 nm. **4** had a blue-shifted emission spectrum in comparison, with a maximum at 416 nm whilst **3** emits at even shorter wavelengths with a maximum at 382 nm. The absorption properties of **3-α**, **4-α** and **5-α** were also measured in the solid state. The diffuse reflectance spectra are shown in Figure 47A. **3-α** has more redshifted absorption spectra than **3** in solution but the onset is still just outside of the visible region at 394 nm. **4-α** shows a more complex profile with the main onset at 439 nm and a shoulder onset further into the visible at 661 nm, this represents a significant difference from the solution spectra indicating solid state packing may be increasing conjugation length through intermolecular interaction. **5-α** absorbs up to 800 nm but has a sharper onset at 645 nm. **3-α** and **4-α** retain their fluorescence in the solid state with emission maxima at 452 and 469 nm, but **5-α** showed only baseline fluorescence when excited at a range of wavelengths from 300 to 500 nm. "Aggregate-caused quenching" (ACQ) is common in organic chromophores[104] as planar aromatic rings allow for the formation of π-stacking structures, which can facilitate intermolecular energy transfer and result in non-radiative decay of excited states. As such, it is common for perylene based materials to have lower photoluminescent quantum yields in the solid state than in solution[97,105,106] but the absence of emissive behaviour is somewhat surprising. Whilst emissive behaviour is not known to be essential to photocatalytic activity, if the reduction in emissive behaviour is accompanied by a more rapid decay of excited states or leads to non-accessible trap states, this could limit activity.

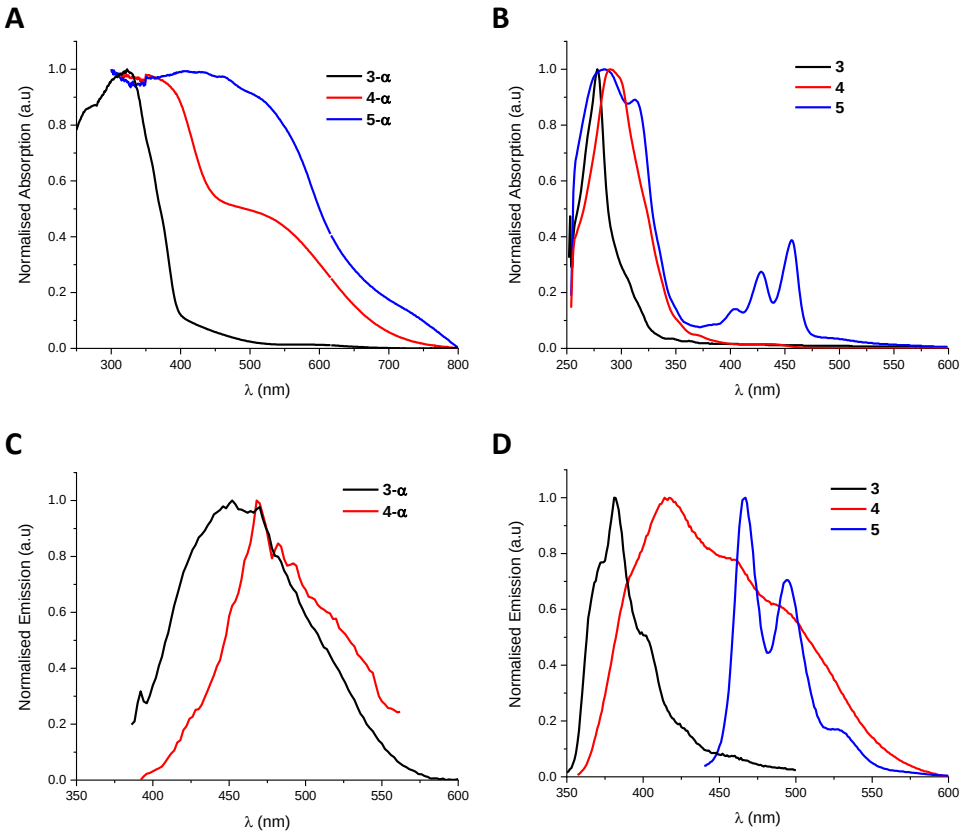

Figure 47: UV-Vis spectra of the materials in the solid state (A) and in DMSO solution (B) and fluorescence spectra of the materials in the solid state (C) and in DMSO solution (D).

4.5.2 Photocatalytic Testing

Due to the more limited absorption profile of **3-α**, the three materials were tested for photocatalytic activity using a λ > 295 nm filter (ascorbic acid (0.1 M) and 1 wt. % Pt co-catalyst). As synthesised **3** produced no measurable hydrogen over 6 hours of irradiation but the crystalline sample **3-α** showed sustained hydrogen production of 98 µmol $h^{-1}g^{-1}$ under the same conditions. Analysis of the **3-α** material collected post photocatalysis however showed an almost complete loss in crystallinity suggesting any HOF structure that forms is not stable in water. As synthesised **4** showed moderate hydrogen activity with a HER of 571 µmol $h^{-1}g^{-1}$, slightly lower than the crystallised **4-α** sample which had a rate of 766 µmol $h^{-1}g^{-1}$. Examining the PXRD patterns of the materials, the relatively high activity of **4** is not surprising; Whilst the as synthesised **4**, does have fewer and less well-defined diffraction peaks than **4-α**, it has a strong peak at 2θ value of 26.8° which corresponds to spacings of 3.32 Å. This would be consistent with the presence of π-stacked BTT units[94] and is slightly smaller than the inter-layer distances observed in **TBAP-α** (3.93 Å) and thus may enhance charge transport in a similar manner.

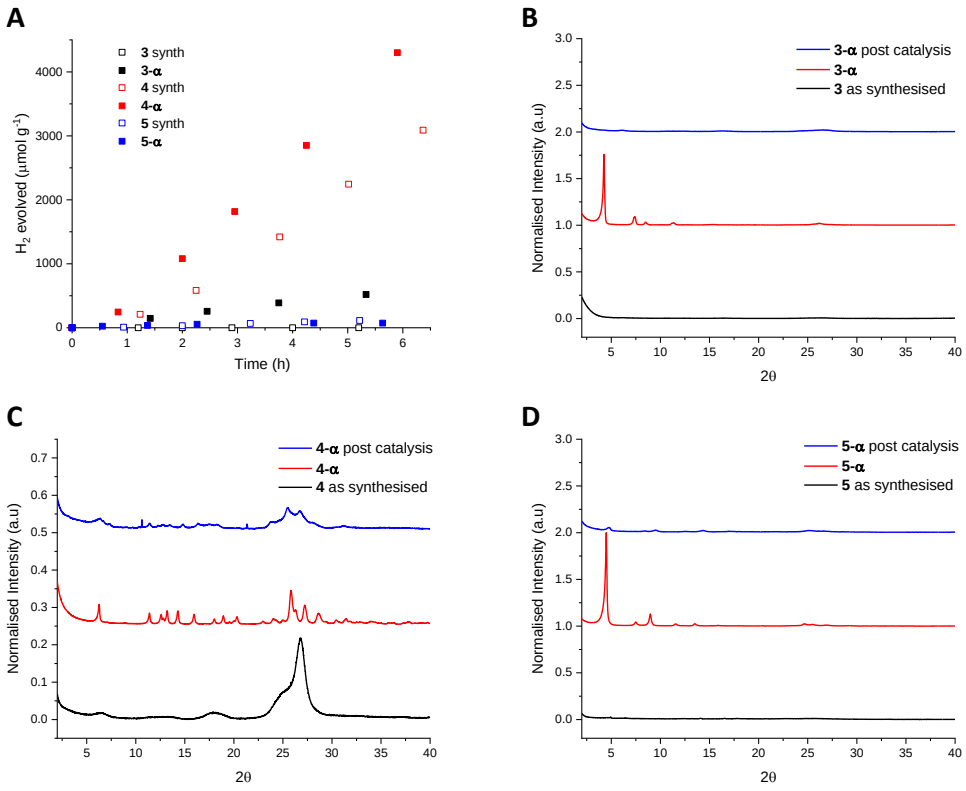

Figure 48: Hydrogen evolution of the materials (10 mg) loaded with 1 wt.% Pt, from photodeposition of H_2PtCl_6, dispersed in ascorbic acid solution (25 mL, 0.1 M) illuminated with a 300 W Xe light source fitted with a $\lambda > 295$ nm cut off filter (A). PXRD spectra of **3-α** (B), **4-α** (C) and **5-α** (D) collected pre and post photolysis.

5 and **5-α** showed the lowest activity with HER of 25 and 12 μmol $h^{-1}g^{-1}$, respectively. **5-α**'s low activity may be due to immediate loss in crystallinity as the PXRD spectra of the material collected post photocatalysis showed a significant loss in peak intensity. It is also possible that the aforementioned ACQ prevents efficient generation or extraction of charge carriers. Equally, the reduced band gap of **5** could result in a loss of driving force for either proton reduction of scavenger oxidation, thermodynamically limiting hydrogen production. DFT calculations to predict the IP and EA of this material would be useful in checking this.

Further studies into the crystal structures of these materials are required to confirm HOF formation but the lack of water stability of the **3-α** and **5-α** structures does not make them ideal candidates for further photocatalytic study. **4-α** on the other hand retains a degree of crystallinity throughout catalysis. Optimising the crystallisation of this phase to give single crystals for XRD analysis would be a valuable course of action as it would give further insight into the structure of the material and potentially generate a more active, fully crystalline phase.

4.6 Discussion

TBAP-α and amorphous **TBAP** are chemically identical, the only differences between the samples being the secondary structures of the materials. This is one of the first examples to provide strong evidence of a cause-effect relationship between intermolecular packing and photocatalytic activity, both in terms of the differences between the amorphous and crystalline samples' initial behaviour as well as the gradual loss in activity of **TBAP-α** as it slowly converts to the amorphous phase. What, precisely, it is about the HOF structure that causes such different photocatalytic activity to the amorphous sample is difficult to deconvolute. UV-Vis measurements and DFT-calculations suggest the different structures do not significantly alter the orbital energies of the materials and thus each materials ability to absorb light and to provide overpotential to drive photocatalytic reaction. The similarity in the two materials PL emission and lifetime can be taken as evidence that exciton formation and (at least radiative) decay occurs similarly in both cases. Both materials also show significant PL quenching in the presence of ascorbic acid indicating efficient hole scavenging by the electron donor.

Light scattering and transmission measurements indicate the particle sizes and dispersibility of the two materials in the photolysis medium are also broadly comparable and thus external surface area is unlikely to be the cause of their differing activities. On the other hand, the two materials do have dramatically different levels of porosity and so a large internal surface area could be available for reaction in **TBAP-α**, but not the amorphous sample. This hypothesis is not, however, supported by water uptake measurements, which indicate the pores of **TBAP-α** are not particularly wettable. S(T)EM imaging and experiments using larger, Pt nanoparticle co-catalysts also indicate catalysis occurs primarily at the surface of **TBAP-α** crystals and thus the HOFs porosity may not be crucial to its high photocatalytic activity.

The final difference between the two materials, and what seems most likely to cause their differing photocatalytic activities, is crystallinity. As discussed in sections 3.1 and 4.1 it is frequently claimed that highly crystalline materials possess high photocatalytic activities because of their molecular packing, and that improved charge transport through more ordered structures is responsible for this. In the case of **TBAP-α**, it is thought that particular features of the crystal structure, namely the presence of extended columns of close packed, highly overlapped pyrene units, may result in increased charge transport properties. This would enable more efficient migration of wholly or partially separated charges, from the area of initial exciton formation to the surface of the crystal before decay. Assuming an unwetted pore and that Pt is the active site for proton reduction, this would increase the

proportion of photon-induced excitations that result in scavenger oxidation and/or transfer onto a Pt active site, and thus the overall efficiency of hydrogen production.

Experiments using the alternative, acetonitrile-based, dispersant further corroborate the integral relationship between the crystal structure and photocatalytic activity as extended HOF stability correlated with extended longevity of hydrogen production.

The large changes in catalytic activity observed at higher pHs are also interesting, as they show that the thermodynamic driving force can be an important factor in these systems. Particularly in the case of the amorphous sample, it appears that increasing the driving force for scavenger oxidation can substantially increase activity with a 20-fold increase in HER on moving from pH 2.6 to 7. Despite this, **TBAP-α** in the lower overpotential conditions (pH 2.6, driving force for 1 hole ascorbic acid oxidation predicted to be 0.23 V) still outperforms amorphous **TBAP** at the higher overpotential conditions (pH 7, driving force for 1 hole ascorbic acid oxidation predicted to be 0.51 V) by a factor of 8. This suggests that, whilst thermodynamics play a role in activity, the differing kinetics or charge transport of the two structures is the overriding factor dictating photocatalytic activity.

Comparing **TBAP-α** with the phenyl and pyridyl analogues **TPhP-α** and **TPyP-α** gives further insight into the relationship between crystal structure and photocatalytic activity. **TPhP-α** does have slightly blueshifted light absorption onset and a smaller driving force for scavenger oxidation compared to **TBAP-α** but this seems inadequate to explain the 650-fold difference in their photocatalytic activity. It is possible the polar groups present in **TBAP** make **TBAP-α** more hydrophilic and this improved interaction with water aids with photocatalysis. However this is not represented in the external surface areas of the two samples as measured by SLS particle sizing, as **TPhP-α** has the smaller $D[3,2]$ value. Light transmission measurements also indicated **TPhP-α** maintained high suspension opacity over several hours and was equally, if not more, dispersible than **TBAP-α**. These results are surprising when compared to polymer photocatalysts, where there is often a strong correlation between small particle size and hydrophilic groups.[107–109] It is possible the distribution of particle sizes measured for suspensions of **TBAP-α**, **TPhP-α** and the other HOF samples is determined predominately by the primary crystal size, resulting in substantially different behaviour to amorphous polymers. Whilst the TCSPC fluorescence lifetime of **TPhP-α** is largely unaffected by the addition of a hole scavenger, the magnitude of fluorescence emission is reduced significantly, suggesting quenching of the excited state by the sacrificial electron donor.

It does not appear that the activity of **TPhP-α** should be hindered by any of the aforementioned properties severely enough to explain the disparity with **TBAP-α** and it

could thus be concluded that, although **TPhP-α** is a fully crystalline material, its ordered structure does not impart the same beneficial properties as that of **TBAP-α**. This is primarily attributed to the lack of extended π-stacking columns present in **TPhP-α** which is thought to benefit charge transfer. In contrast **TPyP-α** contains very similar π-stacked pyrene units, with comparable overlap and stacking distance between layers, to those found in **TBAP-α**. This, along with **TPyP-α**'s similar UV-Vis absorption, driving force, particle size and dispersibility properties, might be expected to give high activity, akin to **TBAP-α**. High activity was not observed, however, and the reasons for this are not entirely clear. The lack of porosity in **TPyP-α** could play a role but, as mentioned above, this is not supported by experimental measurement. The other significant difference between the two materials is the emission behaviour upon exposure to a sacrificial electron donor. **TPyP-α** does not show the same fluorescence quenching as **TBAP-α** indicating poor interaction with the hole scavenger and a higher proportion of exciton recombination. Inefficient hole quenching in **TPyP-α** could prevent efficient formation of catalytically active polarons from excitons.[110] This would render any crystal-structure-dependant increase in charge-carrier mobility less relevant as the concentration of polarons present in the material is very low.

The generally higher activity of the other pyrene-based HOFs (section 4.3) suggests carboxylic acid or amide groups, similar to those in **TBAP-α**, may help to give good interaction between the substrate and hole scavengers. The structures obtained from **TPAP** and **2** suggest it might be possible to form molecular crystals containing hydrogen-bond directed pyrene stacks from a range of different aromatic linkers and directing groups. Although the lack of HOF formation in **1** suggests highly extended units may result in low density phases becoming energetically disfavoured. A recent report certainly found a negative correlation between measured surface area and the thermal stability of HOFs, but it is not clear whether this is causal as the number, strength and orientation of hydrogen bonding groups, as well as overall structural symmetry will also play a role.[29] Larger crystallisation screens and crystal structure prediction[35,111] could be useful to investigate this further.

The high activity of the π-stacking **TPAP** and **2-α** samples in comparison to **1-α**, which was not found to contain extended pyrene stacks, provides further evidence that these crystal structure motives are beneficial to photocatalytic activity. **TPAP**'s different polymorphs indicate the distance, and overlap, between these stacked layers may also significantly alter activity. **TPAP-β**, which has a large 5.32 Å gap between layers and an overlap of less than 0.5, displayed around half the rate of **TBAP-α**, whilst the poorly crystalline **TPAP-α** sample (which may have a more similar stacking structure to **TBAP-α**) had a surprisingly high activity given it's low degree of order. There did not appear to be a strong correlation

between porosity and activity in these materials, again suggesting catalysis is occurring primarily at the crystal surface.

The water stability of the HOFs varied significantly between materials. Surprisingly, the naphthalene-bearing **2-α** appears to show more rapid HOF degradation in aqueous suspension (as measured by both PXRD and loss in catalytic activity) than **TBAP-α** despite similar π-stacking interactions in terms of interlayer distances and overlap. On the other hand, both **TPAP** samples showed somewhat better longevity of photocatalytic activity than **TBAP-α**. This was not reflected in the retention of PXRD peak intensity across the materials spectra but the **TPAP-β** sample did maintain a peak at $2\theta = 24.2°$ which could correspond to interlayer distances of 3.67 Å. This could explain the materials longer-lived catalytic activity as it indicates stacking may be somewhat preserved over small domain sizes.

3, **4** and **5** are examples of the breadth of different aromatic core units that can be used to form hydrogen-bonded organic frameworks, but the rapid loss in crystallinity of **3-α** and **5-α** under photocatalytic conditions also demonstrates the challenge water instability presents to this class of materials for solar fuels applications. The relatively high activity of the polycrystalline **4-α** sample indicates order, even across very short length scales, can give significant hydrogen evolution rates and make **4** a good candidate for further study. The strong red-shift in the absorption behaviour of **4** on moving from solution to solid state also highlights the fact that molecular UV-only absorbers can form supramolecular structures that absorb well into the visible region and thus should not be ruled out as photocatalyst candidates.

It seems likely that the low activity of **5-α** is related to its lack of fluorescence behaviour in the solid state. This underlines the potential of ACQ to inhibit photocatalysis in HOF materials and the need to consider negative effects of π-stacking when designing new materials.

4.7 Conclusions

These initial investigations into HOFs indicate they are a promising new class of materials for hydrogen production photocatalysis. **TBAP-α** is a highly active proton reduction photocatalyst with a high EQE of 4.1% at 420 nm, higher than many polymeric materials,[72] and interestingly almost ten times higher than a crystalline pyrene-based COF with similar stacking.[112] Whilst catalytic longevity needs to be improved, this first study shows HOFs can produce hydrogen over multi-day time periods, similar to many recently published organic photocatalysts.[55,57,113,114] Along with the oligomers studied in chapter 3, these molecular

materials contradict the assumption that only polymers can give efficient and robust hydrogen production.

This work is also useful in terms of understanding the properties and features that make a good photocatalyst. **TBAP-α** and amorphous **TBAP** represent a rare comparison of two materials that are chemically identical and that differ only in secondary structure. This allows the relationship between molecular packing and activity to be deconvoluted from that of molecular structure and activity. Comparison between these two and the analogous materials strongly suggests crystal structures with columnar π-stacks are beneficial to photocatalytic activity. This is likely due to increased charge carrier mobility but further conductivity measurements on these samples would be required to confirm this. Growing single crystalline films suitable for conductivity measurements by impedance spectroscopy[115] could be challenging but the conductivity of particulate materials can also be determined using time-resolved microwave conductivity[116–118] which may be a more viable method for HOF materials.

There is a large diversity of aromatic units that have the potential to form photocatalytically active HOFs. Materials that are known to form supramolecular stacking structures with high conductivity would seem worthwhile candidates for photocatalytic testing.[119] Pyrene is a strong absorber in the blue region, but there are a wealth of different donor-acceptor cores that have the potential to form HOFs with improved charge separation or with redshifted absorption spectra that could extend photocatalytic activity into the near-IR. Aside from modifying the framework molecular structure, another route to improving light absorption could be dye-loading. The pores of **TBAP-α** do not seem to be particularly accessible to water, but the solvated **TBAP-α** structure indicates less polar solvents such as chloroform and acetone may be able to enter the pores. This would enable efficient loading of dyes[120] as well as other beneficial components such as molecular or small particle oxygen evolution co-catalysts.[121]

Of course, HOFs with fully wettable pores would be highly valuable in terms of increased catalytically active surface area. Developing materials with more polar linkers is therefore an obvious route for investigation. For example, an analogue of **TBAP** with dibenzothiophene sulfone linkers replacing phenyl, could give a HOF with a hydrophilic pore wall, a donor acceptor structure, and the benefits of close-packed dibenzothiophene sulfone units observed in **S1-S3**.

The effect of pore wetting on HOF stability is not easily predicted. It could be argued that the inaccessibility of **TBAP-α**'s pores to water molecules may in fact be one of the reasons that the HOF structure remains relatively stable in water suspension. One of the few HOF

papers to measure water uptake, showed that a very water stable pyrazole-based HOF was also highly hydrophobic.[23] If water were to saturate the pores of the material, it may accelerate crystallinity loss by competing with the substrate for hydrogen bonding interactions. Reducing the potential for **TBAP**-dispersant hydrogen bonding interactions by using the acetonitrile solvent system, certainly seemed to improve HOF stability.

Whilst the introduction of organic components to the dispersant mix is interesting for examining the mechanism of HOF breakdown it does not represent a viable solution to the stability issues associated with HOFs. Moving away from 'low energy' salt or waste-water suspensions towards more complex organic dispersants is not a feasible direction of travel for renewable energy systems. Alternative strategies for HOF stabilisation would involve modification of the molecular structure. Maximising the strength of intermolecular interactions, whether that be hydrogen bonds or π-π stacking, is clearly crucial and thus using larger or less homogeneous aromatic units as well as stronger and more H-bonding groups might be beneficial. For example, one of the most stable HOFs to date relies on six strong hydrogen-bonding carboxylic acid groups per molecule and an aromatic core of 30 π electrons.[122] Within this, it is important to retain a degree of solubility in organic solvents as controlled crystallisation is often crucial for HOF formation.

Another approach could be to look at co-crystals and forming HOFs with more than one molecular component.[37] Charge assisted hydrogen bonding may provide stronger framework interactions[78] although the extreme of this is porous molecular salts that, whilst able to form crystalline layered structures,[43,44,123] are unlikely to have the desired optical and conductivity properties for photocatalysis. Aside from H-bonding strength, π-π interactions are often stronger between heterogeneous aromatic units, with fully eclipsed packing common between electron rich and electron poor rings.[23] In addition to improving stability, it has been suggested similar interactions are behind the overall watersplitting capability of 'Van-der Waals heterostructures' where a donor/acceptor layered structure leads to improved charge separation.[124]

As outlined in section 4.1, HOFs have been shown to be stable for numerous desolvated applications and ultimately it may be more feasible to use these materials for solar fuels photocatalysis that can be done in the gas phase. Photocatalytic hydrogen production from water is not generally conducted in the gas phase as HERs often decrease with temperature and the formation and conduction of adsorbed protons can be slow.[125] HOFs may be better suited to photocatalytic CO_2 reduction. Although CO_2 reduction for solar fuels applications has primarily been investigated in solid-solution[126,127] or fully dissolved systems[128,129] investigations into heterogeneous solid / gas systems[130–133] are thought to be promising as

they sidestep the problem of poor CO_2 water solubility. Several HOF materials have been shown to have very high CO_2 uptakes and selectivity and so, if used for photocatalysis, solid-gas systems might be able to utilise the porosity of HOFs more effectively than in solution, as well as improving HOF stability.

4.8 Experimental

4.8.1 General Procedures

CHNS microanalysis, nuclear magnetic resonance spectroscopy, thermogravimetric analysis, PXRD, inductively coupled plasma mass spectrometry, static light scattering, scanning (transmission) electron microscopy, time correlated single photon counting, hydrogen evolution experiments and external quantum efficiencies were performed as described in Chapters 2 and 3.

Mass Spectrometry

Mass spectrometry of **1**, **2** and **5** was performed by matrix-assisted laser desorption/ionisation time-of-flight mass spectrometry (MALDI-TOF MS) which was performed on a Bruker Autoflex Speed MALDI ToF Mass Spectrometer (λ = 355 nm laser) in linear (negative) mode, referencing against CsI cluster ions. All other high resolution mass spectrometry was performed at the National Mass Spectrometry Facility on an Xevo G2-S Atmospheric Solids Analysis Probe in positive ion detection mode (**TBAP**, **TPyP**, **TPhP**, and **TPAP**) or on an LTQ Orbitrap XL in negative ion detection mode (**3**).

Powder X-ray Diffraction

PXRD patterns were collected in transmission mode on samples held on thin Mylar film in aluminum well plates on a Panalytical Empyrean diffractometer, equipped with a high throughput screening (HTS) XYZ stage, X-ray focusing mirror, and PIXcel detector, using Cu-Kα (λ = 1.541 Å) radiation. Diffraction patterns were measured over 2θ range in 0.013° steps, for 15-60 minutes. For indexing, samples were loaded into borosilicate glass capillaries and PXRD patterns were recorded in transmission mode on a Panalytical Empyrean diffractometer, equipped with a sample spinner to improve powder averaging.

Single crystal X-ray Diffraction

Single crystal X-ray data sets were measured on a Rigaku MicroMax-007 HF rotating anode diffractometer (Mo-Kα radiation, λ = 0.71073 Å, Kappa 4-circle goniometer, Rigaku Saturn724+ detector); at beamline 11.3.1, Advanced Light Source, Berkeley, USA, using silicon monochromated synchrotron radiation (λ = 0.7749 Å, PHOTON II CMOS detector); or at beamline I19, Diamond Light Source, Didcot, UK using silicon double crystal monochromated synchrotron radiation (λ = 0.6889 Å, Pilatus 2M detector). Rigaku frames

were converted to Bruker compatible frames using the programme ECLIPSE.[134] Absorption corrections, using the multi-scan method, were performed with the program SADABS.[135,136] For synchrotron X-ray data, collected at Diamond Light Source (λ = 0.6889Å) data reduction and absorption corrections were performed with xia2. Structures were solved with SHELXD,[137] SHELXT,[138] or by direct methods using SHELXS, and refined by full-matrix least squares on $|F|^2$ by SHELXL,[139] interfaced through the programme OLEX2.[140] Unless stated, all non-H atoms were refined anisotropically, and unless stated H-atoms were fixed in geometrically estimated positions and refined using the riding model.

Sorption Analysis

Surface areas were measured by nitrogen adsorption and desorption at 77.3 K. Powder samples were degassed offline at 110 °C for 15 hours under dynamic vacuum (10-5 bar) before analysis. Isotherms were measured using Micromeritics 2420 volumetric adsorption analyser. Surface areas were calculated in the relative pressure (P/P_0) range from 0.07 to 0.35 of the adsorption branch. Water vapor isotherms were determined at 293 K using an IGA gravimetric adsorption apparatus (Hiden Isochema) with an anti-condensation system carried out in an ultrahigh vacuum system equipped with a diaphragm and turbo pumps.

UV-Visible Absorption Spectroscopy

The UV-Visible absorption spectra of the materials as solutions in DMSO or acetic acid and the diffuse reflectance spectra of the materials in the solid state were recorded, at room temperature on a Cary 5000 UV-Vis spectrometer.

Fluorescence Spectroscopy

The fluorescence spectra of the materials were measured with a Shimadzu RF-5301PC fluorescence spectrometer at room temperature in the solid state and as solutions in DMSO or acetic acid.

Carbon Monoxide Production Experiments

Borosilicate crimp top vials (Agilent Technologies, 10 mL, 23 × 46 mm) were charged with 5 mg of the photocatalyst and transferred to a Chemspeed Accelerator SWING platform for liquid transfer. Degassed aqueous ascorbic acid solution (0.1 mL) and degassed stock solution of H_2PtCl_6 were loaded into the system and the whole system was flushed with nitrogen for 4 hours. Liquids were automatically dispensed into the vials and the vials were capped under inert conditions by the system. The vials were then ultrasonicated for 10 minutes before illumination with an Oriel Solar Simulator 94123A (1 Sun, classification IEC 60904-9 2007 spectral match A, uniformity classification A, temporal stability A, 1600 W Xenon lamp, 12 × 12 in. output beam, Air ass 1.5G filter, 350-1000 nm) and continuous dispersion of the photocatalyst on a Stuart roller bar SRT9.. After photocatalysis, the

samples were measured on a Shimadzu GC-2010 plus equipped with a BID detector using a HS-20 headspace auto-sampler and sampling from the headspace of the vial. Helium was used as the carrier-gas and the gases were separated on a 5 Å Molseive capillary column. The gas amounts were calculated by referencing against standard gases with known concentrations of hydrogen and CO. Hydrogen and CO dissolved in the reaction mixture was not measured and the pressure increase generated by the evolved hydrogen and CO was neglected in the calculations.

Deuterium Labelling Experiments

Ascorbic acid (440 mg) was dissolved in D_2O (25 mL). **TBAP-α** (25 mg) was dispersed in this solution by ultrasonication before degassing thoroughly by N_2 bubbling for 30 minutes. The mixture was placed in a quartz vessel and sealed in a reactor under nitrogen. The sample was illuminated with a 300 W Newport Xe light source (Model: 6258, Ozone free) for the time specified at a fixed distance under atmospheric pressure. The Xe light source was cooled by water circulating through a metal jacket. Gas samples from the 1.3 mL headspace of the reactor were analysed at the time periods specified by a customized HPR-70 batch sampling system from Hiden Analytical using a HAL3F/301 triple filter Mass Spectrometer with a Faraday detector for analysis.

Crystallisation Experiments

HOF candidates were dissolved in DMF or DMSO (0.5 – 10 mg mL^{-1}) by bath sonication at 40 °C (1 hour). Any undissolved material was removed by passing solutions through hydrophilic Nylon syringe filters (0.2 µm pore size) into large vials. Added volumes were less than ¼ of the total vial volumes. Vials were capped with a septum that had been pierced using a needle and these vials were placed in a sealed chamber containing chloroform (or other precipitating solvent. Vapour diffusion of chloroform into the candidate solutions was carried out for 2-5 days until the vials were full of solvent. Most of the solvent was then removed via syringe, leaving the precipitate on the edges of the vial until the level of solvent was just above the precipitate. For solvent exchange, acetone was then injected into the solution and subsequently removed via syringe. This process was repeated twice more, and enough acetone was then added to fill the vial completely. This solvent was removed and then replenished every 12 hours for 2-5 days, which yielded the solvent exchanged materials. This was filtered off and allowed to dry under ambient conditions before evacuation at 110 °C for 12 hours.

4.8.2 Synthesis

All reagents were obtained from Sigma-Aldrich, TCI, or Fluorochem and used as received. Reactions were carried out under nitrogen atmosphere using standard Schlenk techniques.

*1,3,6,8-Tetra(p-benzoic acid)pyrene (**TBAP**)*

TBAP was synthesized according to a modified literature route.[63] 1,3,6,8-Tetrabromopyrene (1.04 g, 2.0 mmol), (4-(methoxycarbonyl)phenyl)boronic acid (1.44 g, 8.0 mmol), K_2CO_3 (2.5 g) and anhydrous N,N-dimethylformamide (50 mL) were added to a dry flask and the mixture was degassed by N_2 bubbling for 30 minutes. $Pd(PPh_3)_4$ (45 mg) was added and the mixture was degassed for a further 10 minutes before heating to 110 °C for 16 hours. The mixture was allowed to cool to room temperature before pouring into water (500 mL) and stirring for 1 hour. The formed precipitate was collected by filtration and washed with water (100 mL) and methanol (100 mL) to give tetramethyl 4,4',4",4"'-(pyrene-1,3,6,8-tetrayl)tetrabenzoate (1.39 g, 1.88 mmol, 94%). ^{1}H NMR (400 MHz, $CDCl_3$): δ(ppm) = 8.23 (d, J = 8.5 Hz, 8H), 8.15 (s, 4H), 8.01 (s, 2H), 7.75 (d, J = 8.5 Hz, 8H), 3.99 (s, 12 H).

Tetramethyl 4,4',4",4"'-(pyrene-1,3,6,8-tetrayl)tetrabenzoate (500 mg, 0.68 mmol) methanol (20 mL), THF (20 mL) and $NaOH_{(aq)}$ (4 M, 20 mL) were refluxed at 70 °C overnight. The mixture was filtered and the solids washed repeatedly with water until the filtrate was colourless. The combined filtrates were acidified by excess HCl (1 M). The formed yellow precipitate was collected by filtration, washed repeatedly with water and dried under vacuum to yield the product (450 mg, 0.66 mmol, 97%).^{1}H NMR (400 MHz, DMSO-d_6): δ(ppm) = 8.20 (s, 4H), 8.15 (d, 8H, J 8.0 Hz), 8.07 (s, 2H), 7.84 (d, 8H, J 8.0 Hz). ^{13}C{^{1}H} NMR (75 MHz, DMSO-d_6): δ(ppm) = 167.7, 144.7, 136.8, 131.3, 130.5, 130.1, 128.1. 125.9, 125.7. Anal. Calcd for $C_{44}H_{26}O_8$: C, 77.41; H, 3.84; Found: C, 76.06; H, 3.80. HR-MS Calcd for $[C_{44}H_{26}O_8 + H]^+$: m/z = 683.1706, 684.1740, 685.1771; found: m/z = 683.1716, 684.1752, 685.1779.

*1,3,6,8-Tetraphenylpyrene (**TPhP**)*

TPhP was synthesised according to literature procedure.[74] ^{1}H NMR (400 MHz, DMSO-d_6): δ(ppm) = 8.18 (s, 4H), 7.99 (s, 2H), 7.72 (d, J 7.5 Hz, 8H), 7.62 (t, J 7.5 Hz, 8H), 7.54 (t, J 7.5 Hz, 4H). ^{13}C{^{1}H} NMR ($CDCl_3$): δ(ppm) = 141.21, 137.3, 130.6 (2C), 129.4, 128.3, 128.2, 127.2, 126.0, 125.3. Anal. Calcd for $C_{40}H_{26}$: C, 94.83; H, 5.17; Found: C, 94.36; H, 5.04. HR-MS Calcd for $[C_{40}H_{26} + H]^+$: m/z = 507.2113, 508.2147, 509.2180; found: m/z = 507.2109, 508.2144, 509.2180.

*1,3,6,8-Tetra(pyridin-4-yl)pyrene (**TPyP**)*

1,3,6,8-Tetrabromopyrene (1.04 g, 2 mmol), 4-pyridinylboronic acid (983 mg, 8 mmol), DMF (200 mL) and $K_2CO_{3(aq)}$ (50 mL, 2 M) were added to a flask and degassed by N_2 bubbling for 30 minutes. $Pd(PPh_3)_4$ (40 mg, 0.035 mmol) was added and the solution was degassed for a further 10 minutes before heating to 145 °C for 48 hours. After cooling, the mixture was poured into water (1 L) and stirred for 30 minutes. The precipitate was

collected by filtration and washed with, water (100 mL), methanol (100 mL) and dichloromethane (100 mL) before drying under vacuum. The product was obtained as a green solid (986 mg, 1.92 mmol, 96 %). ^{1}H NMR (400 MHz, Acetic acid-d_4): δ(ppm) = 9.08 (d, J 6.0 Hz, 8H), 8.41 (s, 4H), 8.36 (s, 2H), 8.17 (d, J 6.0 Hz, 8H). The solubility of **TPyP** in acetic acid was too low to conduct ^{13}C NMR. Anal. Calcd for $C_{36}H_{22}N_4$: C, 84.68; H, 4.34; N, 10.97; Found: C, 84.37; H, 4.31; N, 10.73. . HR-MS Calcd for $[C_{36}H_{22}N_4 + H]^+$: m/z =511.1923, 512.1954, 513.1985; found: m/z = 511.1922, 512.1957, 513.1993.

Synthesis of Pt Nanoparticles

Pt nanoparticles were synthesized according to a modified literature procedure.[141] H_2PtCl_6 (0.9 mL, 8 wt. % solution) was added to water (36 mL). Water (464 mL) was heated to 95 °C and the H_2PtCl_6 solution was added with stirring followed by 0.05 wt. % citric acid / 1 wt. % trisodium citrate dihydrate aqueous solution (11 mL) followed by sodium borohydride (37 mg) in 0.05 wt.% citric acid / 1 wt. % trisodium citrate dihydrate aqueous solution (11 mL). The solution was stirred at 100 °C for 10 minutes before cooling to room temperature.

*1,3,6,8-Tetra(p-benzamide)pyrene (**TPAP**)*

1,3,6,8-tetrabromopyrene (2.0 g, 3.9 mmol), (4-carbamoylphenyl)boronic acid (3.19 g, 19.3 mmol), K_2CO_3 (5.0 g) and anhydrous N,N-dimethylformamide (100 mL) were added to a dry flask and the mixture was degassed by N_2 bubbling for 30 minutes. $Pd(PPh_3)_4$ (90 mg) was added and the mixture was degassed for a further 10 minutes before heating to 110 °C for 16 hours. The mixture was allowed to cool to room temperature before pouring into water (1 L) and stirring for 1 hour. The formed precipitate was collected by filtration and washed with water (200 mL) and methanol (200 mL) and THF (200 mL). ^{1}H NMR (400 MHz, DMSO-d_6): δ(ppm) = 8.20 (s, 4H), 8.14 (bs, 1H), 8.18 (d, J = 8.5 Hz, 8H), 8.06 (s, 2H), 7.81 (d, J = 8.5 Hz, 8H), 7.48 (bs, 1H). ^{13}C{^{1}H} NMR (DMSO-d_6: δ(ppm) = 168.2, 143.2, 136.9, 133.9, 130.9, 128.3, 128.1, 125.8, 125.7. Anal. Calcd for $C_{44}H_{30}N_4O_4$: C, 77.86; H, 4.46; N, 8.25; Found: C, 74.59; H, 5.07; N, 6.92. HR-MS Calcd for $[C_{44}H_{30}N_4O_4 + H]^+$: m/z = 679.2346, 680.2377, 681.2408; found: m/z = 679.2355, 680.2413, 681.2555.

*4',4''',4'''''',4''''''''-(pyrene-1,3,6,8-tetrayl)tetrakis(([1,1'-biphenyl]-4-carboxylic acid))(**1**)*

1,3,6,8-tetrabromopyrene (1.04 g, 2.0 mmol), (4'-(methoxycarbonyl)-[1,1'-biphenyl]-4-yl)boronic acid (2.05 g, 8.0 mmol), K_2CO_3 (2.5 g) and anhydrous N,N-dimethylformamide (50 mL) were added to a dry flask and the mixture was degassed by N_2 bubbling for 30 minutes. $Pd(PPh_3)_4$ (45 mg) was added and the mixture was degassed for a further 10 minutes before heating to 110 °C for 16 hours. The mixture was allowed to cool to room temperature before pouring into water (500 mL) and stirring for 1 hour. The formed

precipitate was collected by filtration and washed with water (100 mL) and methanol (100 mL) to give tetramethyl 4',4''',4'''',4'''''-(pyrene-1,3,6,8-tetrayl)tetrakis([1,1'-biphenyl]-4-carboxylate) (2.00 g, 1.92 mmol, 96%). ^{1}H NMR (400 MHz, $CDCl_3$): δ(ppm) = 8.29 (s, 8H), 8.17 (d, J = 8.5 Hz, 16H), 8.19 (s, 2H), 7.78-7.84 (m, 24 H).

Tetramethyl-4',4''',4'''',4'''''-(pyrene-1,3,6,8-tetrayl)tetrakis([1,1'-biphenyl]-4-carboxylate) (300 mg, 0.29 mmol), methanol (20 mL), THF (20 mL) and $NaOH_{(aq)}$ (4 M, 20 mL) were refluxed at 70 °C overnight. The mixture was filtered and the solids washed repeatedly with water until the filtrate was colourless. The combined filtrates were acidified by excess HCl (1 M). The formed yellow precipitate was collected by filtration, washed repeatedly with water and dried under vacuum to yield the product (274 mg, 0.28 mmol, 96%). ^{1}H NMR (400 MHz, DMSO-d_6): δ(ppm) = 8.26 (s, 4H), 8.06-8.09 (m, 10H), 7.90-7.97 (m, 16H), 7.82 (d, J = 8.0 Hz, 8H). This material was too insoluble in DMSO-d_6 to conduct ^{13}C NMR. Anal. Calcd for $C_{68}H_{42}O_8$: C, 82.74; H, 4.29; Found: C, 72.64; H, 4.31. MALDI-MS Calcd for $[C_{68}H_{42}O_8]^-$: m/z = 986.29, 987.29; found: m/z = 986.39, 987.39.

*1,3,6,8-Tetra(2-napthoic acid)pyrene (**2**)*

methyl 6-bromo-2-naphthoate (4.5 g, 17.0 mmol), bispinacolatodiboron (4.7 g, 18.5 mmol), potassium acetate (5 g), and 1,1′-Bis(diphenylphosphino)ferrocene]dichloropalladium(II) (400 mg) were placed under nitrogen and dry DMSO (30 mL) was added. The mixture was heated under nitrogen at 90 °C for 16 hours. After cooling the mixture was poured in water (100 mL), extracted with ethyl acetate, washed with dilute HCl (1 M) and brine, dried with magnesium sulfate and the solvent removed under vacuum. Hot hexane (300 mL) was added to the brown residue and the mixture was passed through a celite plug. Hexane was removed under reduced pressure to yield methyl 6-(4,4,5,5-tetramethyl-1,3,2-dioxaborolan-2-yl)-2-naphthoate as an off white powder (3.3 g, 10.6 mmol, 62%). ^{1}H NMR (400 MHz, $CDCl_3$): δ(ppm) = 8.60 (s, 1H), 8.39 (s, 1H), 8.05 (d, J = 8.5 Hz, 1H), 7.89- 7.95 (m, 3H), 3.98 (s, 3H), 1.19 (s, 12H).

methyl 6-(4,4,5,5-tetramethyl-1,3,2-dioxaborolan-2-yl)-2-naphthoate (1.50 g, 4.81 mmol) 1,3,6,8-tetrabromopyrene (518 mg, 1.0 mmol) trihydro-potassium phosphate (2.0 g) and toluene (50 mL) were added to a dry flask and degassed by nitrogen bubbling for 30 minutes. $Pd(PPh_3)_4$ (50 mg) was added and the solution was degassed for a further 10 minutes before heating to 110 °C for 16 hours. After cooling the mixture was poured into methanol (500 mL) and stirred for 30 minutes. The precipitate was collected by filtration and recrystallized from DCM : hexane to yield tetramethyl 6,6',6'',6'''-(pyrene-1,3,6,8-tetrayl)tetrakis(2-naphthoate) (836 mg, 0.89 mmol, 89 %). ^{1}H NMR (400 MHz, $CDCl_3$):

δ(ppm) = 8.73 (s, 4H), 8.27 (s, 4H), 8.23 (s, 2H), 8.21 (s 4H), 8.14 (m, 8H), 7.98 (d, J = 8.5 Hz, 4H), 7.92 (d, J = 8.5 Hz, 4H) 4.02 (s, 12H).

tetramethyl 6,6',6",6"'-(pyrene-1,3,6,8-tetrayl)tetrakis(2-naphthoate) (270 mg, 0.29 mmol), methanol (20 mL), THF (20 mL) and $NaOH_{(aq)}$ (4 M, 20 mL) were refluxed at 70 °C overnight. The mixture was filtered and the solids washed repeatedly with water until the filtrate was colourless. The combined filtrates were acidified by excess HCl (1 M). The formed yellow precipitate was collected by filtration, washed repeatedly with water and dried under vacuum to yield the product (230 mg, 0.26 mmol, 90%). ^{1}H NMR (400 MHz, DMSO-d_6): δ(ppm) = 8.72 (s, 4H), 8.36 (s, 4H), 8.31 (d, J = 8 Hz, 4H), 8.27 (s, 2H), 8.26 (s, 4H), 8.10 (d, J = 8 Hz, 4H), 8.03 (d, J = 8 Hz, 4H), 7.96 (d, J = 8 Hz, 4H). ^{13}C NMR (400 MHz, DMSO-d_6: δ(ppm) = 167.9, 140.3, 137.2, 135.5, 131.9, 130.9, 130.6, 130.0, 129.9, 129.6, 129.0, 128.9, 128.2, 126.2, 126.0, 125.8. Anal. Calcd for $C_{60}H_{34}O_8$: C, 81.62; H, 3.88; Found: C, 80.78; H, 3.84. MALDI-MS Calcd for$[C_{60}H_{34}O_8]^-$: m/z = 882.23, 883.23; found: m/z = 882.20, 883.18.

2,6,10-Trimethyltriphenylene

2,6,10-Trimethyltriphenylene was synthesised according to a modified literature procedure.[102] Methylcyclohexanone (40.0 g, 0.35 mol) and zirconium tetrachloride (4.0 g, 17 mmol) were heated at 135° C overnight under a nitrogen. The mixture was allowed to cool to 70° C before hot chloroform (100 mL) was added. The mixture was stirred before 5 minutes before the solids were filtered off. Ethanol (20 mL) was added to the hot filtrate and the solution was allowed to cool to room temperature and then in the fridge overnight. The formed white crystals were collected by filtration and dried under vacuum to give 2,6,10-trimethyl-dodecahydrotriphenylene (12.5 g, 44.3 mmol, 38%). ^{1}H NMR (400 MHz, $CDCl_3$): δ(ppm) = 2.41-2.84 (m, 9H), 2.00-2.16 (m 3H), 1.67-1.95 (m, 6H), 1.23-1.41 (m, 3H), 1.06-1.10 (m, 9H).

2,6,10-trimethyl-dodecahydrotriphenylene (3.0 g, 10.1 mmol), Palladium on carbon (10 wt.% Pd, 0.30 g) and triglyme (10 mL) were refluxed at 240° C (sand bath) overnight . After cooling to 70° C chloroform (50 mL) was added to re-dissolve the partially precipitated product. The mixture was filtered, and the chloroform removed from the filtrate under vacuum. Water (5 mL) was added and the white precipitate collected by filtration and dried. The product was recrystallized from DCM/hexane. (2.6 g, 9.6 mmol, 95%). ^{1}H NMR (400 MHz, $CDCl_3$): δ(ppm) = 8.52 (d, J = 8.0 Hz, 3H), 8.40 (s, 3H), 7.44 (d, J = 8.0 Hz, 3H), 2.61 (s, 9H). ^{13}C NMR ($CDCl_3$): δ(ppm) = 136.6 (quaternary), 13.0 (quarternary), 128.2, 127.1 (quarternary), 123.2, 123.1, 21.9.

*Triphenylene-2,6,10-tricarboxylic acid (**3**)*

2,6,10-Trimethyltriphenylene (1.20 g, 4.44 mmol) was suspended in water (56 mL) and added to a 125 mL Parr vessel. Sodium dichromate dihydrate (5.29 g, 17.8 mmol) was added in portions with stirring. The Parr vessel was sealed and heated with sitrring at 250 °C (sand bath) for 24 hours. After cooling to room temperature, the vessel contents were washed out with water, the green chromium salts were filtered off and the formed triphenylene-2,6,10-tricarboxylic acid was precipitated by addition of excess HCl (12 M). The product was filtered off and washed with water repeatedly before drying under vaccum. The crude product was crystallised from DMSO/Chloroform to give a white powder (810 mg, 2.25 mmol, 51%). ^{1}H NMR (400 MHz, DMSO-d_6: δ(ppm) = 9.35 (s, 3H), 8.98 (d, J = 10 Hz, 3H), 8.31 (d, J = 10 Hz, 3H). ^{13}C NMR (DMSO-d_6: δ(ppm) = 167.2 (quarternary), 132.7, 130.3, 128.9 (quarternary), 128.4, 125.6 (quarternary), 124.5 (quarternary). Anal. Calcd for $C_{21}H_{12}O_6$: C, 70.00; H, 3.26; O, 26.64; Found: C, 68.31; H, 3.86. HR-MS Calcd for $[C_{21}H_{12}O_6 - H]^-$: m/z = 359.0561, 360.0595; found: m/z = 359.0562, 360.0596.

2,4,6-trichlorobenzene-1,3,5-tricarbaldehyde

2,4,6-trichlorobenzene-1,3,5-tricarbaldehyde was synthesised according to a modified literature procedure.[89] 1,3,5-trichlorobenzene (3.0 g , 16.6 mmol), $AlCl_3$ (2.6 g , 19.6 mmol), and $CHCl_3$ (60 ml) were added to a Parr vessel (125 ml), which was heated with stirring at 125°C (sand bath) for 72 h. During the heating period, the autoclave was cooled to room temperature twice at 6 h and 18 h after the reaction started and opened to release the pressure. After 72 h, the reaction was cooled to room temperature, $CHCl_3$ (60 mL) was added, and the reaction mixture was poured into concentrated HCl/ice and stirred for 1 h. The organic layer was separated and washed with $NaHCO_3$, brine, and dried over $MgSO_4$. The solvent was removed under vacuum, the brown solid suspended in hexane and filtered through a silica plug before solvent removal to give 1,3,5-trichloro-2,4,6-tris(dichloromethyl)benzene (5.0 g, 11.6 mmol, 70%). ^{1}H NMR (400 MHz, $CDCl_3$: δ(ppm) = 7.75 (s, 2H), 7.63 (s, 1H). Hindered roation around the $C_{Benzene}$ –C_{CHCl2} bond causes two distinct proton environemnts in a 2: 1 ratio.[103]

Fuming sulfuric acid (20% SO_3) (18 mL) was added to 1,3,5-trichloro-2,4,6-tris(dichloromethyl)benzene (2.5 g, 5.8 mmol) and stirred at 40°C for 3 hours. The reaction mixture was poured onto ice (500 g) in a large (2 L) beaker and $NaHCO_3$ (20g, 0.24 mmol) was **slowly** added. The formed precipitate was filtered off, washed with water, and purified silica gel column chromatography eluting with DCM : Hexane (60 : 40) to give the product as off white crystals. (600 mg, 2.26 mmol, 39%). ^{1}H NMR (400 MHz, $CDCl_3$: δ(ppm) = 10.42 (s, 3H).

*Benzo[1,2-b:3,4-b':5,6-b"]trithiophene-2,5,8-tricarboxylic acid (**4**)*

Benzo[1,2-b:3,4-b':5,6-b"]trithiophene-2,5,8-tricarboxylic acid was synthesised according to a modified literature procedure.[103] Triethylamine (20 mL) was added to 2,4,6-trichlorobenzene-1,3,5-tricarbaldehyde (500 mg, 1.88 mmol), under nitrogen and the mixture cooled to 0 °C. Ethylmercaptoacetate (900 mg, 7.50 mmol), was added dropwise before refluxing at 100 °C for 4 hours. After cooling to room temperature methanol (10 mL) was added and the light brown precipitate was collected by filtration, washed with methanol and dried to give benzo[1,2-b:3,4-b':5,6-b"]trithiophene-2,5,8-tricarboxylic acid triethyl ester (650 mg, 1.40 mmol, 76%). ^{1}H NMR (400 MHz, $CDCl_3$): δ(ppm) = 8.32 (s, 3H), 4.47 (q, J = 7.2 Hz, 6H), 1.47 (t, J = 7.2 Hz, 9H).

benzo[1,2-b:3,4-b':5,6-b"]trithiophene-2,5,8-tricarboxylic acid triethyl ester (250 mg, 0.54 mmol), NaOH (1 g), ethanol (25 mL) and water (25 mL) were refluxed at 90°C overnight. After cooling, more water (50 mL) was added and the mixture filtered to remove any unreacted ester. The filtrate was acidified by the addition of excess HCl (1 M), the precipitate was collected by vacuum filtration and washed with water (3 x 100 mL) before drying under vacuum to give the product as a pink powder (190 mg, 0.50 mmol, 93%). ^{1}H NMR (400 MHz, DMSO-d_6: δ(ppm) = 8.35 (s, 3H). ^{13}C NMR (DMSO-d_6: δ(ppm) = 163.5 (quarternary), 137.5 (quarternary), 136.1 (quarternary), 130.8, 126.84 (quarternary). Anal. Calcd for $C_{15}H_6O_6S_3$: C, 47.61; H, 1.60; O, 25.37; S, 25.42. Found: C, 45.13; H, 2.25; S, 23.76.

2,5,8,11-tetrakis(4,4,5,5-tetramethyl-1,3,2-dioxaborolan-2-yl)perylene

Was synthesised via a modified literature procedure.[98] Perylene (1.26 g, 5.0 mmol), bispinacolato diboron (5.08 g, 20.0 mmol) 4,4'-dimethyl-2,2'-bipyridyl (27 mg, 0.1 mmol), and $[Ir(OMe)COD]_2$ (33 mg, 0.05 mmol) were added to a dry flask and placed under nitrogen. Dry THF (40 mL) was added and the solution was heated at 80 °C for 16 hours. The reaction was cooled to room temperature and poured onto methanol (100 mL). The precipitate was collected by filtration and washed with methanol to give the product as a light yellow solid (3.30 g, 4.4 mmol, 87%). ^{1}H NMR (400 MHz, $CDCl_3$): δ(ppm) = 8.63 (s, 4H), 8.25 (s, 4H), 1.43 (s, 48H).

*2,5,8,11-Tetra(p-benzoic acid)perylene (**5**)*

2,5,8,11-tetrakis(4,4,5,5-tetramethyl-1,3,2-dioxaborolan-2-yl)perylene (1.51 g, 2.0 mmol), ethyl 4-bromobenzoate (1.83 g, 8.0 mmol), K_2CO_3 (2.5 g) and anhydrous N,N-dimethylformamide (50 mL) were added to a dry flask and the mixture was degassed by N_2 bubbling for 30 minutes. $Pd(PPh_3)_4$ (45 mg) was added and the mixture was degassed for a further 10 minutes before heating to 110 °C for 16 hours. The mixture was allowed to cool

to room temperature before pouring into water (500 mL) and stirring for 1 hour. The formed precipitate was collected by filtration and washed with water (100 mL) and methanol (100 mL) to give 2,5,8,11-Tetra(*p*-benzoic acid ethyl ester)perylene (1.10 g, 1.30 mmol, 65%). ^{1}H NMR (400 MHz, $CDCl_3$): δ(ppm) = 8.55 (s, 4H), 8.23 (d, J = 8.2 Hz, 8H), 8.05 (s, 4H), 7.88 (d, J = 8.2 Hz, 8H).

2,5,8,11-Tetra(*p*-benzoic acid ethyl ester)perylene (500 mg, 0.59 mmol), methanol (20 mL), THF (20 mL) and $NaOH_{(aq)}$ (4 M, 20 mL) were refluxed at 70 °C overnight. The mixture was filtered and the solids washed repeatedly with water until the filtrate was colourless. The combined filtrates were acidified by excess HCl (1 M). The red precipitate was collected by filtration, washed repeatedly with water and dried under vacuum to yield the product (360 mg, 0.48 mmol, 83%). ^{1}H NMR (400 MHz, DMSO-d_6): δ(ppm) = 8.77 (s, 4H), 8.23 (s, 4H), 8.06-8.12 (m, 16 H). This material was too insoluble in DMSO-d_6 to conduct ^{13}C NMR. Anal. Calcd for $C_{48}H_{28}O_4$: C, 78.68; H, 3.85; O, 17.47; Found: C, 74.87; H, 3.81. MALDI-MS Calcd for $[C_{48}H_{28}O_4]^-$: m/z = 732.2, 733.2, 734.2; found: m/z = 732.3, 733.3, 734.3.

4.9 References

1 S. G. Frank, *J. Pharm. Sci.*, 1975, **64**, 1585–1604.

2 A. E. Smith, *Acta Crystallogr.*, 1952, **5**, 224–235.

3 M. E. Brown and M. D. Hollingsworth, *Nature*, 1995, **376**, 323–327.

4 D. Venkataraman, S. Lee, J. Zhang and J. S. Moore, *Nature*, 1994, **371**, 591–593.

5 K. Endo, T. Sawaki, M. Koyanagi, K. Kobayashi, H. Masuda and Y. Aoyama, *J. Am. Chem. Soc.*, 1995, **117**, 8341-8352.

6 J. P. Hill, W. Jin, A. Kosaka, T. Fukushima, H. Ichihara, T. Shimomura, K. Ito, T. Hashizume, N. Ishii and T. Aida, *Science*, 2004, **304**, 1481-1483.

7 X. Wang, M. Simard and J. D. Wuest, *J. Am. Chem. Soc.*, 1994, **116**, 12119–12120.

8 R. M. Barrer, and V. H. Shanson, *J. C. S. Chem. Comm*, 1976, 333-334.

9 P. Sozzani, S. Bracco, A. Comotti, L. Ferretti and R. Simonutti, *Angew. Chemie Int. Ed.*, 2005, **44**, 1816–1820.

10 Y. He, S. Xiang and B. Chen, *J. Am. Chem. Soc.*, 2011, **133**, 14570–14573.

11 P. Brunet, M. Simard and J. D. Wuest, *J. Am. Chem. Soc.*, 1997, **119**, 2737-2738.

12 J. L. Atwood and J. W. Steed, *Encyclopedia of supramolecular chemistry*, M. Dekker, 2004.

13 H. Sauriat-Dorizon, T. Maris, J. D. Wuest and G. D. Enright, *J. Org. Chem.*, 2003, **68**, 240–246.

14 P. Li, Y. He, Y. Zhao, L. Weng, H. Wang, R. Krishna, H. Wu, W. Zhou, M. O'Keeffe, Y. Han and B. Chen, *Angew. Chemie Int. Ed.*, 2014, **54**, 574-577 .

15 P. Li, Y. He, J. Guang, L. Weng, J. Cong, G. Zhao, S. Xiang and B. Chen, *J. Am. Chem. Soc*, 2014, **136**, 547–549.

16 R.-B. Lin, Y. He, P. Li, H. Wang, W. Zhou and B. Chen, *Chem. Soc. Rev.*, 2019, **48**, 1362–1389.

17 K. E. Maly, E. Gagnon, T. Maris and J. D. Wuest, *J. Am. Chem. Soc.*, 2007, **129**, 4306–4322.

18 C. A. Zentner, H. W. H. Lai, J. T. Greenfield, R. A. Wiscons, M. Zeller, C. F. Campana, O. Talu, S. A. Fitzgerald and J. L. C. Rowsell, *Chem. Commun.*, 2015, **51**, 11642–11645.

19 I. Hisaki, S. Nakagawa, N. Tohnai and M. Miyata, *Angew. Chemie Int. Ed.*, 2015, **54**, 3008–3012.

20 F. Hu, C. Liu, M. Wu, J. Pang, F. Jiang, D.

Yuan and M. Hong, *Angew. Chemie Int. Ed.*, 2017, **56**, 2101–2104.

21 P. Li, P. Li, M. R. Ryder, Z. Liu, C. L. Stern, O. K. Farha and J. F. Stoddart, *Angew. Chemie Int. Ed.*, 2019, **58**, 1664–1669.

22 I. Hisaki, *J. Incl. Phenom. Macrocycl. Chem.*, 2020, **96**, 215–231.

23 T.-H. Chen, I. Popov, W. Kaveevivitchai, Y.-C. Chuang, Y.-S. Chen, O. Daugulis, A. J. Jacobson, and O. S. Miljanic, *Nat. Commun.*, 2014, **5**, 5131.

24 M. I. Hashim, H. T. M. Le, T. H. Chen, Y. S. Chen, O. Daugulis, C. W. Hsu, A. J. Jacobson, W. Kaveevivitchai, X. Liang, T. Makarenko, O. Miljanić, I. Popovs, H. V. Tran, X. Wang, C. H. Wu and J. I. Wu, *J. Am. Chem. Soc.*, 2018, **140**, 6014–6026.

25 A. P. Côté, A. I. Benin, N. W. Ockwig, M. O'Keeffe, A. J. Matzger and O. M. Yaghi, *Science.*, 2005, **310**, 1166–1170.

26 C. S. Diercks and O. M. Yaghi, *Science*, 2017, **355**, eaal1585.

27 O. M. Yaghi, G. Li and H. Li, *Nature*, 1995, **378**, 703–706.

28 H. C. Zhou, J. R. Long and O. M. Yaghi, *Chem. Rev.*, 2012, **112**, 673–674.

29 I. Hisaki, C. Xin, K. Takahashi and T. Nakamura, *Angew. Chemie Int. Ed.*, 2019, **58**, 11160–11170.

30 Q. Yin, P. Zhao, R.-J. Sa, G.-C. Chen, J. Lü, T.-F. Liu and R. Cao, *Angew. Chemie Int. Ed.*, 2018, **57**, 7691–7696.

31 I. Hisaki, S. Nakagawa, N. Ikenaka, Y. Imamura, M. Katouda, M. Tashiro, H. Tsuchida, T. Ogoshi, H. Sato, N. Tohnai and M. Miyata, *J. Am. Chem. Soc.*, 2016, **138**, 6617-6628.

32 I. Hisaki, N. Ikenaka, E. Gomez, B. Cohen, N. Tohnai and A. Douhal, *Chem. - A Eur. J.*, 2017, **23**, 11611–11619.

33 I. Bassanetti, S. Bracco, A. Comotti, M. Negroni, C. Bezuidenhout, S. Canossa, P. P. Mazzeo, L. Marchió and P. Sozzani, *J. Mater. Chem. A*, 2018, **6**, 14231–14239.

34 M. Mastalerz and I. M. Oppel, *Angew. Chemie Int. Ed.*, 2012, **51**, 5252–5255.

35 A. Pulido, L. Chen, T. Kaczorowski, D. Holden, M. A. Little, S. Y. Chong, B. J. Slater, D. P. McMahon, B. Bonillo, C. J. Stackhouse, A. Stephenson, C. M. Kane, R. Clowes, T. Hasell, A. I. Cooper and G. M. Day, *Nature*, 2017, **543**, 657–664.

36 H. Wang, B. Li, H. Wu, T. L. Hu, Z. Yao, W. Zhou, S. Xiang and B. Chen, *J. Am. Chem. Soc.*, 2015, **137**, 9963–9970.

37 J. Lü, C. Perez-Krap, M. Suyetin, N. H. Alsmail, Y. Yan, S. Yang, W. Lewis, E. Bichoutskaia, C. C. Tang, A. J. Blake, R. Cao and M. Schrö, *J. Am. Chem. Soc*, 2014, **136**, 12828-12831.

38 S. Nandi, D. Chakraborty and R. Vaidhyanathan, *Chem. Commun.*, 2016, **52**, 7249–7252.

39 W. Yang, A. Greenaway, X. Lin, R. Matsuda, A. J. Blake, C. Wilson, W. Lewis, P. Hubberstey, S. Kitagawa, N. R. Champness and M. Schröder, *J. Am. Chem. Soc.*, 2010, **132**, 14457–14469.

40 T. U. Yoon, S. Bin Baek, D. Kim, E. J. Kim, W. G. Lee, B. K. Singh, M. S. Lah, Y. S. Bae and K. S. Kim, *Chem. Commun.*, 2018, **54**, 9360–9363.

41 W. Yan, X. Yu, T. Yan, D. Wu, E. Ning, Y. Qi, Y.-F. Han, Q. Li, R. Li, *Chem. Commun*, 2017, **53**, 3677–3680.

42 W. Yang, F. Yang, T. L. Hu, S. C. King, H. Wang, H. Wu, W. Zhou, J. R. Li, H. D. Arman and B. Chen, *Cryst. Growth Des.*, 2016, **16**, 5831–5835.

43 A. Karmakar, R. Illathvalappil, B. Anothumakkool, A. Sen, P. Samanta, A. V. Desai, S. Kurungot and S. K. Ghosh, *Angew. Chemie Int. Ed.*, 2016, **55**, 10667–10671.

44 G. Xing, T. Yan, S. Das, T. Ben and S. Qiu, *Angew. Chemie Int. Ed.*, 2018, **57**, 5345–5349.

45 E. Gomez, M. Gutiérrez, B. Cohen, I. Hisaki and A. Douhal, *J. Mater. Chem. C*, 2018, **6**, 6929–6939.

46 I. Hisaki, N. Ikenaka, S. Tsuzuki and N. Tohnai, *Mater. Chem. Front.*, 2018, **2**, 338–346.

47 L. Bian, H. Shi, X. Wang, K. Ling, H. Ma, M. Li, Z. Cheng, C. Ma, S. Cai, Q. Wu, N. Gan, X. Xu, Z. An and W. Huang, *J. Am. Chem. Soc.*, 2018, **140**, 10734–10739.

48 I. Hisaki, Y. Suzuki, E. Gomez, B. Cohen, N. Tohnai and A. Douhal, *Angew. Chemie Int. Ed.*, 2018, **57**, 12650–12655.

49 Z. Sun, Y. Li, L. Chen, X. Jing and Z. Xie, *Cryst. Growth Des.*, 2015, **15**, 542–545.

50 H. Wang, Z. Bao, H. Wu, R. B. Lin, W. Zhou, T. L. Hu, B. Li, J. C. G. Zhao and B. Chen, *Chem. Commun.*, 2017, **53**, 11150–11153.

51 I. Hisaki, Y. Suzuki, E. Gomez, Q. Ji, N. Tohnai, T. Nakamura and A. Douhal, *J. Am. Chem. Soc.*, 2019, **141**, 2111-2121.

52 K. Ma, P. Li, H. John, R. R. Maldonado, R. Q. Snurr, O. K. Farha, K. Ma, P. Li, J. H. Xin, Y. Chen, Z. Chen and S. Goswami, *Cell Reports Phys. Sci.*, 2020, **1**, 100024.

53 A. Camerman and J. Trotter, *Acta Crystallogr.*, 1965, **18**, 636–643.

54 F. P. A. Fabbiani, D. R. Allan, S. Parsons and C. R. Pulham, *Acta Crystallogr. Sect. B*, 2006, **62**, 826-842.

55 X. Wang, L. Chen, S. Y. Chong, M. A. Little, Y. Wu, W.-H. Zhu, R. Clowes, Y. Yan, M. A. Zwijnenburg, R. S. Sprick and A. I. Cooper, *Nat. Chem.*, 2018, **10**, 1180–1189.

56 V. S. Vyas, F. Haase, L. Stegbauer, G. Savasci, F. Podjaski, C. Ochsenfeld and B. V. Lotsch, *Nat. Commun.*, 2015, **6**, 8508.

57 B. P. Biswal, H. A. Vignolo-González, T. Banerjee, L. Grunenberg, G. Savasci, K. Gottschling, J. Nuss, C. Ochsenfeld and B. V. Lotsch, *J. Am. Chem. Soc.*, 2019, **141**, 11082-11092.

58 S. Bi, C. Yang, W. Zhang, J. Xu, L. Liu, D. Wu, X. Wang, Y. Han, Q. Liang and F. Zhang, *Nat. Commun.*, 2019, **10**, 1–10.

59 L. Stegbauer, S. Zech, G. Savasci, T. Banerjee, F. Podjaski, K. Schwinghammer, C. Ochsenfeld and B. V. Lotsch, *Adv. Energy Mater.*, 2018, **8**, 1703278.

60 R. S. Sprick, J. X. Jiang, B. Bonillo, S. Ren, T. Ratvijitvech, P. Guiglion, M. A. Zwijnenburg, D. J. Adams and A. I. Cooper, *J. Am. Chem. Soc.*, 2015, **137**, 3265–3270.

61 M. Liu, Q. Huang, S. Wang, Z. Li, B. Li, S. Jin and B. Tan, *Angew. Chemie Int. Ed.*, 2018, **57**, 11968–11972.

62 G. Zhang, G. Li, Z. A. Lan, L. Lin, A. Savateev, T. Heil, S. Zafeiratos, X. Wang and M. Antonietti, *Angew. Chemie - Int. Ed.*, 2017, **56**, 13445–13449.

63 K. C. Stylianou, R. Heck, S. Y. Chong, J. Bacsa, J. T. A. Jones, Y. Z. Khimyak, D. Bradshaw and M. J. Rosseinsky, *J. Am. Chem. Soc.*, 2010, **132**, 4119–4130.

64 R. S. Sprick, Y. Bai, A. A. Y. Guilbert, M. Zbiri, C. M. Aitchison, L. Wilbraham, Y. Yan, D. J. Woods, M. A. Zwijnenburg and A. I. Cooper, *Chem. Mater.*, 2019, **31**, 305–313.

65 K. Maeda, X. Wang, Y. Nishihara, D. Lu, M. Antonietti and K. Domen, *J. Phys. Chem. C*, 2009, **113**, 4940–4947.

66 B. Ohtani, K. Iwai, S.-I. Nishimoto and S. Sato, *J. Phys. Chem. B.*, 1997, **101**, 3349-3359.

67 J. Kosco, M. Sachs, R. Godin, M. Kirkus, L. Francas, M. Bidwell, M. Qureshi, D. Anjum, J. R. Durrant and I. McCulloch, *Adv. Energy Mater.*, 2018, **8**, 1802181.

68 J. Ulanski, B. Luszczynska and K. Matyjaszewski, *Solution-Processable Components for Organic Electronic Devices*, Wiley, 2019.

69 P. B. Pati, G. Damas, L. Tian, D. L. A. Fernandes, L. Zhang, I. B. Pehlivan, T. Edvinsson, C. M. Araujo and H. Tian, *Energy Environ. Sci.*, 2017, **10**, 1372–1376.

70 P.-J. Tseng, C.-L. Chang, Y.-H. Chan, L.-Y. Ting, P.-Y. Chen, C.-H. Liao, M.-L. Tsai and H.-H. Chou, *ACS Catal.*, 2018, **8**, 7766–7772.

71 V. S. Vyas, F. Haase, L. Stegbauer, G. Savasci, F. Podjaski, C. Ochsenfeld and B. V. Lotsch, *Nat. Commun.*, 2015, **6**, 1–9.

72 Y. Wang, A. Vogel, M. Sachs, R. S. Sprick, L. Wilbraham, S. J. A. Moniz, R. Godin, M. A. Zwijnenburg, J. R. Durrant, A. I. Cooper and J. Tang, *Nat. Energy*, 2019, **4**, 746–760.

73 Y. Pellegrin and F. Odobel, *Comptes Rendus Chim.*, 2017, **20**, 283–295.

74 X. Feng, H. Tomiyasu, J. Y. Hu, X. Wei, C. Redshaw, M. R. J. Elsegood, L. Horsburgh, S. J. Teat and T. Yamato, *J. Org. Chem.*, 2015, **80**, 10973–10978.

75 G. A. Jeffrey, *An Introduction to Hydrogen Bonding*, Oxford University Press, New York, 1997.

76 Desiraju, Gautam, Steiner, Thomas, *The Weak Hydrogen Bond: In Structural Chemistry and Biology*, Oxford University Press, 2001.

77 H. Yamagishi, H. Sato, A. Hori, Y. Sato, R. Matsuda, K. Kato and T. Aida, *Science*, 2018, **361**, 1242 – 1246.

78 T. Steiner, *Angew. Chemie - Int. Ed.*, 2002, **41**, 48–76.

79 S. V. Bhosale, C. H. Jani and S. J. Langford, *Chem. Soc. Rev.*, 2008, **37**, 331–342.

80 N. J. Silva, F. B. C. Machado, H. Lischka and A. J. A. Aquino, *Phys. Chem. Chem. Phys.*, 2016, **18**, 22300–22310.

81 E. M. Cabaleiro-Lago and J. Rodríguez-Otero, *ACS Omega*, 2018, **3**, 9348–9359.

82 P. L. Wash, E. Maverick, J. Chiefari and D. A. Lightner, *J. Am. Chem. Soc.*, 1997,

119, 3802–3806.

83 S. Saha and G. R. Desiraju, *J. Am. Chem. Soc.*, 2018, **140**, 6361–6373.

84 Y. Bai, L. Wilbraham, B. J. Slater, M. A. Zwijnenburg, R. S. Sprick and A. I. Cooper, *J. Am. Chem. Soc.*, 2019, **141**, 9063–9071.

85 F. H. Herbstein, M. Kapon and G. M. Reisner, *J. Inclusion Phen.*, 1987, **5**, 211-214.

86 W. Jiang, Y. Li and Z. Wang, *Chem. Soc. Rev.*, 2013, **42**, 6113–6127.

87 W. Zhang, Y. Liu and G. Yu, *Adv. Mater.*, 2014, **26**, 6898–6904.

88 X. Wang, G. Sun, P. Routh, D. H. Kim, W. Huang and P. Chen, *Chem. Soc. Rev.*, 2014, 43, 7067–7098.

89 H. Wei, J. Ning, X. Cao, X. Li and L. Hao, *J. Am. Chem. Soc*, 2018, **140**, 34.

90 A. Molina-Ontoria, I. Zimmermann, I. Garcia-Benito, P. Gratia, C. Roldán-Carmona, S. Aghazada, M. Graetzel, M. K. Nazeeruddin and N. Martín, *Angew. Chemie Int. Ed.*, 2016, **55**, 6270–6274.

91 C. Gu, N. Huang, Y. Chen, L. Qin, H. Xu, S. Zhang, F. Li, Y. Ma and D. Jiang, *Angew. Chemie Int. Ed.*, 2015, **54**, 13594–13598.

92 Y. S. Kochergin, D. Schwarz, A. Acharjya, A. Ichangi, R. Kulkarni, P. Eliášová, J. Vacek, J. Schmidt, A. Thomas and M. J. Bojdys, *Angew. Chemie Int. Ed.*, 2018, **57**, 14188–14192.

93 T. Ikeda, H. Adachi, H. Fueno, K. Tanaka and T. Haino, *J. Org. Chem.*, 2017, **82**, 10062-10069.

94 A. Demenev, S. H. Eichhorn, T. Taerum, D. F. Perepichka, S. Patwardhan, F. C. Grozema, L. D. A. Siebbeles and R. Klenkler, *Chem. Mater.*, 2010, **22**, 1420–1428.

95 Q. Xiao, T. Sakurai, T. Fukino, K. Akaike, Y. Honsho, A. Saeki, S. Seki, K. Kato, M. Takata and T. Aida, *J. Am. Chem. Soc.*, 2013, **135**, 18268–18271.

96 E. M. Cabaleiro-Lago and L. X. Avda Alfonso El Sabio, *ACS Omega*, 2018, **3**, 9348-9359.

97 F. Würthner, *Chem. Commun.*, 2004, **4**, 1564–1579.

98 Y. Xu, N. Mao, S. Feng, C. Zhang, F. Wang, Y. Chen, J. Zeng and J. X. Jiang, *Macromol. Chem. Phys.*, 2017, **218**, 1700049.

99 K. Kong, S. Zhang, Y. Chu, Y. Hu, F. Yu, H. Ye, H. Ding and J. Hua, *Chem. Commun.*, 2019, **55**, 8090-8093.

100 L. Yang, M. Wang, P. M. Slattum, B. R. Bunes, Y. Wang, C. Wang and L. Zang, *ACS Appl. Mater. Interfaces*, 2018, **10**, 19764–19772.

101 F. Yu, Z. Wang, S. Zhang, K. Yun, H. Ye, X. Gong, J. Hua and H. Tian, *Appl. Catal. B Environ.*, 2018, **237**, 32–42.

102 H. Bock, M. Rajaoarivelo, S. Clavaguera and É. Grelet, *European J. Org. Chem.*, 2006, 2889–2893.

103 T. Taerum, O. Lukoyanova, R. G. Wylie and D. F. Perepichka, *Org. Lett.*, 2009, **11**, 3230–3233.

104 J. B. Birks, *Photophysics of aromatic molecules*, Wiley-Interscience, London, 1970.

105 F. Zhang, Y. Ma, Y. Chi, H. Yu, Y. Li, T. Jiang, X. Wei and J. Shi, *Sci. Rep.*, 2018, **8**, 8208.

106 Y. Huang, J. Xing, Q. Gong, L.-C. Chen, G. Liu, C. Yao, Z. Wang, H.-L. Zhang, Z. Chen and Q. Zhang, *Nat. Commun.*, 2019, **10**, 169.

107 Y. Bai, L. Wilbraham, B. J. Slater, M. A. Zwijnenburg, R. S. Sprick and A. I. Cooper, *J. Am. Chem. Soc.*, 2019, **141**, 9063-9071.

108 R. S. Sprick, Y. Bai, A. A. Y. Guilbert, M. Zbiri, C. M. Aitchison, L. Wilbraham, Y. Yan, D. J. Woods, M. A. Zwijnenburg and A. I. Cooper, *Chem. Mater.*, 2019, **31**, 305–313.

109 C. M. Aitchison, R. S. Sprick and A. I. Cooper, *J. Mater. Chem. A*, 2019, **7**, 2490–2496.

110 M. Sachs, R. S. Sprick, D. Pearce, S. A. J. Hillman, A. Monti, A. A. Y. Guilbert, N. J. Brownbill, S. Dimitrov, X. Shi, F. Blanc, M. A. Zwijnenburg, J. Nelson, J. R. Durrant, A. I. Cooper, *Nat. Commun.*, 2018, **9**, 4968.

111 C. M. Aitchison, C. M. Kane, D. P. McMahon, P. R. Spackman, A. Pulido, X. Wang, L. Wilbraham, L. Chen, R. Clowes, M. A. Zwijnenburg, R. S. Sprick, M. A. Little, G. M. Day and A. I. Cooper, *J. Mater. Chem. A*, 2020, **8**, 7158–7170.

112 E. Jin, Z. Lan, Q. Jiang, K. Geng, G. Li, X. Wang and D. Jiang, *Chem*, 2019, **5**, 1632–1647.

113 J. Kosco, M. Bidwell, H. Cha, T. Martin, C. T. Howells, M. Sachs, D. H. Anjum, S. Gonzalez Lopez, L. Zou, A. Wadsworth,

W. Zhang, L. Zhang, J. Tellam, R. Sougrat, F. Laquai, D. M. DeLongchamp, J. R. Durrant and I. McCulloch, *Nat. Mater.*, 2020, **19**, 559-565.

114 M. Z. Rahman, M. G. Kibria and C. B. Mullins, *Chem. Soc. Rev.*, 2020, **49**, 1887-1931.

115 J. F. Rubinson and Y. P. Kayinamura, *Chem. Soc. Rev.*, 2009, **38**, 3339–3347.

116 S. Wan, F. Gándara, A. Asano, H. Furukawa, A. Saeki, S. K. Dey, L. Liao, M. W. Ambrogio, Y. Y. Botros, X. Duan, S. Seki, J. F. Stoddart and O. M. Yaghi, *Chem. Mater.*, 2011, **23**, 4094–4097.

117 S. Wang, X. Hai, X. Ding, S. Jin, Y. Xiang, P. Wang, B. Jiang, F. Ichihara, M. Oshikiri, X. Meng, Y. Li, W. Matsuda, J. Ma, S. Seki, X. Wang, H. Huang, Y. Wada, H. Chen and J. Ye, *Nat. Commun.*, 2020, **11**, 1–9.

118 S. Tiwari and · N C Greenham, *Opt Quant Electron*, 2009, **41**, 69–89.

119 M. Hasegawa and M. Iyoda, *Chem. Soc. Rev.*, 2010, **39**, 2420–2427.

120 X. Zhang, T. Peng and S. Song, *J. Mater. Chem. A*, 2016, **4**, 2365–2402.

121 S. Chen, T. Takata and K. Domen, *Nat. Rev. Mater.*, 2017, **2**, 17050.

122 I. Hisaki, Y. Suzuki, E. Gomez, Q. Ji, N. Tohnai, T. Nakamura and A. Douhal, *J. Am. Chem. Soc.*, 2019, **141**, 2111–2121.

123 W. Xiao, C. Hu and M. D. Ward, *J. Am. Chem. Soc.*, 2014, **136**, 14200–14206.

124 L. Wang, X. Zheng, L. Chen, Y. Xiong and H. Xu, *Angew. Chemie Int. Ed.*, 2018, **57**, 3454–3458.

125 F. Dionigi, P. C. K. Vesborg, T. Pedersen, O. Hansen, S. Dahl, A. Xiong, K. Maeda, K. Domen and I. Chorkendorff, *Energy Environ. Sci.*, 2011, **4**, 2937–2942.

126 T. Inoue, A. Fujishima, S. Konishi and K. Honda, *Nature*, 1979, **277**, 637–638.

127 J. L. White, M. F. Baruch, J. E. Pander, Y. Hu, I. C. Fortmeyer, J. E. Park, T. Zhang, K. Liao, J. Gu, Y. Yan, T. W. Shaw, E. Abelev and A. B. Bocarsly, *Chem. Rev.*, 2015, **115**, 12888–12935.

128 S. Berardi, S. Drouet, L. Francàs, C. Gimbert-Suriñach, M. Guttentag, C. Richmond, T. Stoll and A. Llobet, *Chem. Soc. Rev.*, 2014, **43**, 7501–7519.

129 N. Mie Elgrishi, M. B. Chambers, X. Wang and M. Fontecave, *Chem. Soc. Rev*, 2017, **46**, 761.

130 S. Wang, M. Xu, T. Peng, C. Zhang, T. Li, I. Hussain, J. Wang and B. Tan, *Nat. Commun.*, 2019, **10**, 1–10.

131 L. B. Hoch, T. E. Wood, P. G. O'Brien, K. Liao, L. M. Reyes, C. A. Mims and G. A. Ozin, *Adv. Sci.*, 2014, **1**, 1400013.

132 S. Sorcar, Y. Hwang, J. Lee, H. Kim, K. M. Grimes, C. A. Grimes, J.-W. Jung, C.-H. Cho, T. Majima, M. R. Hoffmann and S.-I. In, *Energy Environ. Sci*, 2019, **12**, 2685.

133 A. Li, Q. Cao, G. Zhou, B. V. K. J. Schmidt, W. Zhu, X. Yuan, H. Huo, J. Gong and M. Antonietti, *Angew. Chemie Int. Ed.*, 2019, **58**, 14549–14555.

134 S. Parsons, *ECLIPSE*, 2004, University of Edinburgh.

135 Bruker, *APEX II*, 2009

136 L. Krause, R. Herbst-Irmer, G. M. Sheldrick and D. Stalke, *J. Appl. Crystallogr.*, 2015, **48**, 3-10.

137 G. M. Sheldrick, *Acta Crystallogr. Sect. D.*, 2010, **66**, 479-485.

138 A. L. Spek, *Acta Crystallogr. Sect. C.*, 2015, **71**, 9–18.

139 G. M. Sheldrick, *Acta Crystallogr. Sect. A*, 2015, **71**, 3-8.

140 O. V. Dolomanov, L. J. Bourhis, R. J. Gildea, J. A. K. Howard and H. Puschmann, *J. Appl. Crystallogr.*, 2009, **42**, 339-341.

141 N. C. Bigall, T. Härtling, M. Klose, P. Simon, L. M. Eng and A. Eychmüller, *Nano Lett.*, 2008, **8**, 4588-4592.

Chapter 5: Conclusions and Future Work

5.1 Conclusions and Future Work

The overall aim of this project was to understand the effect of structural features of organic photocatalysts and their hydrogen production rates. Whilst a clear correlation between HER and external polymer surface was found for the materials in Chapter 1, ultimately emulsion derived materials may not be ideal candidates for studying the relationship between particle size and activity, or to determine the optimal size of polymer photocatalysts. This is because changes to particle size can only be achieved through altering polymer synthesis conditions, which in turn appear to affect chain length and other polymer properties, and this affects HER in a way that is difficult to deconvolute. Nanoprecipitation of organic solvent-soluble polymers may be better suited to further investigations into this area.

In general, however, emulsion polymerisation was found to be an effective method for generating small particle analogues of otherwise unprocessable polymer photocatalysts. **P10-e** displays very high hydrogen evolution rates, with an EQE of 20.4% at 420 nm and substantially higher catalyst longevity than existing nanoparticle systems. This is significantly higher than the bulk sample and suggests emulsion polymerisation could be used to generate more active versions of other insoluble polymer photocatalysts. For example, a recent high throughput study[1] identified several linear copolymers, shown in Figure 1, with higher activity than bulk **P10** and it would therefore be interesting to synthesise versions of these materials by emulsion polymerisation.

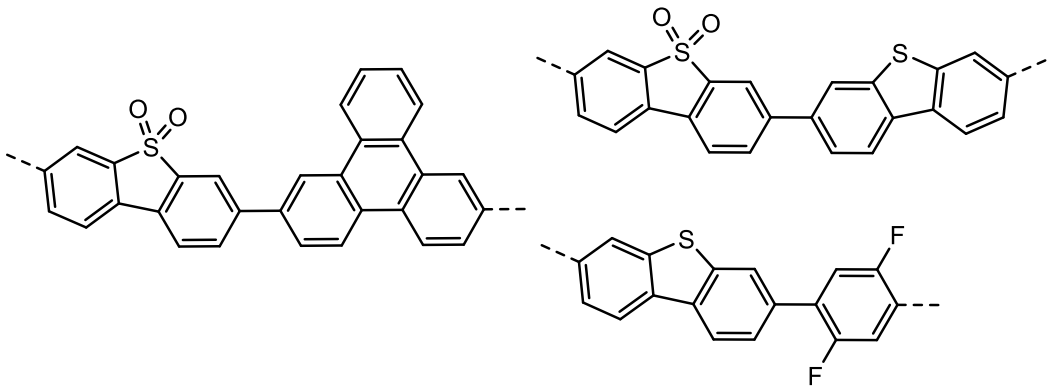

Figure 1: Linear polymer photocatalysts with high activity as hydrogen producing photocatalysts.

Previously, the shorter chain lengths that appear to be accessible through emulsion polymerisation might have been regarded as a serious issue with this method. However, the oligomeric and monomeric photocatalysts studied in Chapters 3 and 4 indicate that long polymer chain lengths are not necessarily required for high hydrogen production rates so long as the material band gap is sufficiently narrowed to allow visible light absorption.

This is perhaps the most significant discovery of Chapter 3; oligomeric materials, with as few as three repeat units can act as highly efficient heterogeneous catalysts for hydrogen production and display EQEs higher than many polymeric materials. Increasing activity with chain length was observed for the **S** family of oligomers but this was found to be in large part due to the redshifted absorption onset of the longer oligomers and smaller differences in activity were found when using UV wavelengths. Time-resolved spectroscopy indicated charge separation and polaron formation occurred similarly in **S3** to **P10**, and that photocatalytic activity in both materials was limited by transfer of polarons from the oligomer to Pd active sites for proton reduction. However, polaron yield was lower in the shorter chain length materials indicating the lower HERs of the **S1–3** could be due to less efficient separation of charges. The relationship between chain length and photocatalytic activity was less clear in the **MeF** oligomers with the monomer showing the highest activity under some conditions. This was particularly interesting given the significantly more blueshifted absorption of **MeF1**, it certainly does not appear that increasing chain length always gives an inherent advantage to photocatalytic activity.

Testing of the materials substituted with alkyl and mesityl groups indicated that twisting of the oligomer backbone can negatively influence hydrogen production rates highlighting the significance of effective conjugation length, as opposed to the number of repeat units in a molecular structure. The difference in activity between planar and twisted materials was found to be smaller under UV irradiation, indicating that the blueshifted absorption onset of the latter is the primary reason for their poorer activity under visible wavelengths. Substitution with bulky groups clearly causes changes to molecular conformation and conjugation length but also affects molecular packing. The crystal structures of the more active unsubstituted oligomers were found to contain more π-stacking interactions, and it is possible this also plays a role in activity differences, perhaps resulting in more efficient energy transfer. Similarly, closely packed, highly overlapping aromatic units were also thought to be essential in the high photocatalytic activity of materials studied in Chapter 4. Comparison of **TBAP-α** and its amorphous analogue provided convincing evidence that the packing of molecular units has a strong effect on photocatalytic activity and can give orders of magnitude variation in HER. Further work is needed to clarify the cause of the variation, but this work suggests that the difference in porosity between the HOF and the amorphous sample may not be a significant factor. Instead the high activity of **TBAP-α** is attributed to improved exciton or charge carrier mobility through extended columnar pyrene stacks. This was supported by the relatively high proton reduction activity of **TPAP**, **2-α** and **4-α** all of which also showed evidence of π-stacking interactions.

As well as providing insight into structure-activity relationships, Chapter 4 also introduces a new class of organic photocatalysts for hydrogen production; **TBAP-α** is believed to be the first HOF proven to be capable of light-driven proton reduction. The high EQE and competitive catalytic lifetime of this HOF warrants further investigation into this class of materials. Initial attempts to form HOF photocatalysts with increased structural diversity (sections 4.4 and 4.5) indicate that predicting the formation of new, stable HOFs is not straightforward. Crystal structure prediction could aid with the discovery of new structures, but a valuable area of investigation may also be to screen the now significant number of HOF structures reported in literature[2] for photocatalytic activity. Given the apparent importance of π stacking motifs in the pyrene HOFs, of particular interest are literature HOFs with planar aromatic units which show eclipsed layered stacking or at least significant overlap. For example, carboxyphenyl-substituted hexaazatrinaphthylene derivative (CPHATN, Figure 2a) forms a hexagonal network of hydrogen bonded sheets which stack with small 2.89 to 3.13 Å distances between layers with some overlap between the substituted trinapthylene cores (CPHATN-1a Figure 2b and c).[3] This HOF is also reported to be stable in water as well as acid, making it a good candidate for photocatalytic proton reduction. The band structure of CPHATN and other potential molecules could be predicted using TD-DFT to rule out candidates with EA and IP potentials inconsistent with hydrogen production and scavenger (or water) oxidation.

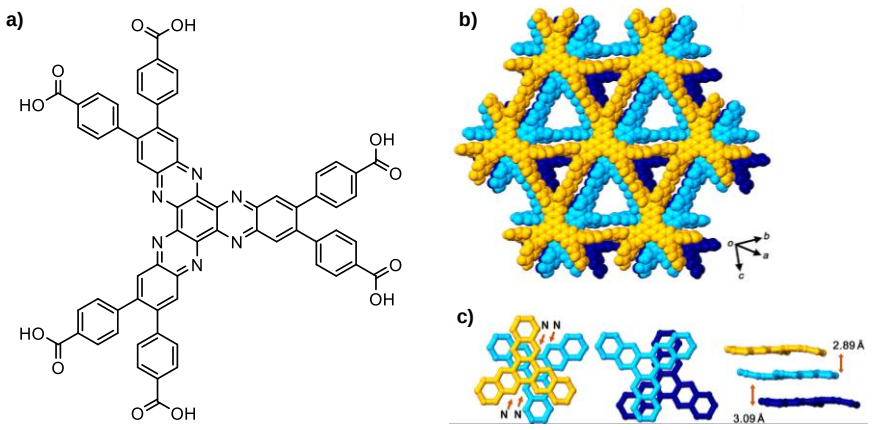

Figure 2: a) Molecular structure of CPHATN and (b and c) crystal structure of CPHATN-1a HOF. *Adapted with permission from reference [3], Copyright (2019) American Chemical Society*.

Carboxylic acids and other hydrogen bonding groups increase photocatalyst wettability, impart good solubility in polar solvents and are frequently cited as crucial in stabilising low-density structures,[2] but many non-HOFs also show extended columnar π-stacking.[4] Furthermore, the most active molecular material studied in this work, **S3**, has a close packed structure indicating this approach need not be confined to porous organic crystals. Screening

crystal structure databases for suitable packing motifs in combination with band structure prediction could be used to identify known structures that are good candidates for photocatalytic testing. For example, N-heteropentacenes, such as those shown in Figure 3, are known to form extended slipped stacked structures with similar interlayer distances to **TBAP-α**.[5] These have already been shown to have high charge carrier mobility and absorption onsets well into the visible and energy levels consistent with driving proton reduction and thus may be suitable materials for study.

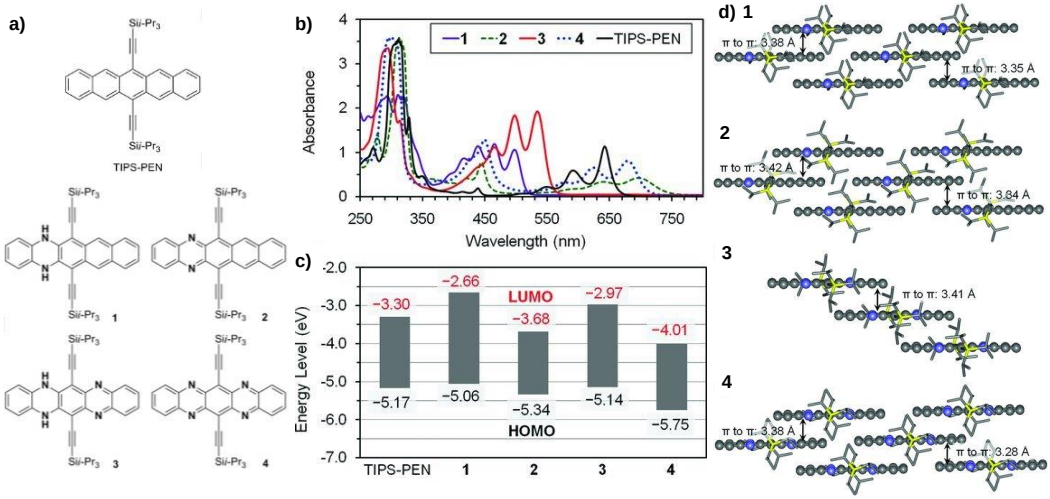

Figure 3: a) Molecular structure, (b) UV-vis absorption in CH_2Cl_2 , c) HOMO and LUMO energy levels and (d) crystal structures of N-heteropentacenes. *Adapted with permission from reference [5].*

Overall, the results in Chapters 3 and 4 indicate the search for new organic photocatalysts for hydrogen production should be expanded to include oligomers and molecular crystals, opening up a potentially large and new area of study. Further suggestions for study of emulsion polymerisation-derived, oligomeric and HOF photocatalysts are also included in sections 2.3, 3.9 and 4.7 respectively but considerations for future work in the context of overall water splitting are discussed below.

Time resolved spectroscopic measurements in Chapter 3 suggest that hydrogen production in dibenzothiophene sulfone-based materials is limited by diffusion of polarons to Pd active sites for proton reduction. Whilst overcoming this post-charge-separation kinetic bottleneck would likely give higher HERs, this work also highlights a potential flaw in using sacrificial donor systems as model systems for overall water splitting. The most active family of materials studied here, **S1-3** and **P10**, are found to have hydrogen evolution rates that appear to be independent of exciton lifetime. This means that extensive work on these and other

related materials may be optimising organic semi-conductors for a fast hole scavenging regime that is not representative of the kinetically slow process of water oxidation.[6]

The **TPyP** material investigated in Chapter 4 also highlights the importance of interaction between SED and the semiconductor substrate. In this particular system, it appears that hydrogen production is limited by inefficient quenching of excitons by the ascorbic acid electron hole scavenger. This could pose an issue for studies under sacrificial conditions as similar photocatalysts tested for hydrogen production using SEDs may be omitted as potential 'hits' for hybrid or Z-scheme OWS systems when in fact their low activity is due to poor interaction with one particular hole scavenger – a component that must ultimately be removed. Future studies under sacrificial conditions should aim to test each photocatalyst with a number of different SEDs, (preferably organic and inorganic with a range of oxidation potentials, surface charges and molecular sizes) in order to minimise this possibility. Candidates could be 'judged' on the basis of activity across a number of SEDs rather than focusing on a particularly high rate with just one SED. This may improve the likelihood that, with optimisation and suitable cocatalysts, a material's ability to oxidise scavengers can be translated into the ability to oxidise water. The results of Chapters 3 and 4 suggest that quenching of photocatalyst fluorescence intensity in suspension by the addition of SEDs may be useful as a quick screening test for successful scavenger oxidation and could reduce the need for time- and resource-consuming photocatalytic hydrogen production tests.

These are valid concerns when pursuing single component organic semiconductors where charge separation of photogenerated excitons is unlikely to occur spontaneously. In these cases, the short singlet exciton lifetimes of organic semi-conductors may hinder OWS. A more promising approach is to move towards multicomponent systems that enable the separation of charges.[7] One way this could be achieved is through redox shuttles which, in a similar way to SEDs/SEAs, quench excitons and facilitate the formation of charge separated polarons. Unlike sacrificial scavengers, these can be cycled between HEP and OEP components and are thus not consumed by the system. Initial experiments with the HEPs covered in this work would be to see if photocatalytic hydrogen production occurs in the presence of Fe^{II} or I^-. These oxidise to Fe^{III} and IO_3^- respectively and have been shown to acts as reversible redox shuttles in inorganic Z-scheme systems.[8] If hydrogen production does occur with these or other redox shuttles then screening experiments that couple the HEPs with known OEPs, such as WO_3, should be conducted. Such studies have already started on the dibenzothiophene sulfone homopolymer **P10**, which was recently shown to be capable of hydrogen production in the presence of an Fe^{II} SED and could form an overall water splitting Z-scheme when coupled with $BiVO_4$ and the Fe^{II} / Fe^{III} redox couple.[9] It would be worth

investigating whether the trimer, **S3**, could replace **P10** in this system. **S3** has a lower IP than **P10** and thus would provide a slightly larger driving force for Fe^{II} oxidation which could improve the rate of OWS. Similar experiments should also be conducted on the active HOF materials in Chapter 4. The IP of **TBAP-α** lies above the water oxidation potential but should be sufficient to drive Fe^{II} oxidation and thus it is feasible that it could be incorporated into an analogous Z-scheme.

An alternative approach would be to attempt heterojunction-based charge separation. Here, the processability of the materials studied in this work would be particularly beneficial. Heterojunctions rely on physical contact between two materials whose offset band/orbital structures mean that exciton separation into charged species is thermodynamically favourable at the contact between a donor and an acceptor. The large surface area of **P10-e** could be ideally suited to forming such a heterostructure. The **P10-e** coated silica microparticles in Chapter 2 appeared to work favourably as a hydrogen evolution photocatalyst; the same method could be used to generate particles of $BiVO_4$ OEP coated in **P10-e**. The nanoscale dimensions of the emulsion-derived material would minimise the diffusion length required for excitons in **P10-e** to reach the interface with the OEP increasing the likelihood of charge separation before recombination. The silica particles in Chapter 2 were coated by sonication of the two components in water followed by filtration. The simple fabrication process and the large number of inorganic OEPs that could be incorporated into such a hybrid, mean this would be suited to high throughput screening approach. Emulsion-derived materials could also be used in three component systems utilising HEP particles and OEP particles adhered to a conducting electron mediator sheet. Sheet systems using similarly sized particles to **P10-e** have been shown to form some of the most active OWS Z-schemes in literature.[10]

As well as particle size, charge separation across heterojunction interfaces is also thought to be dependent on crystalline order. The ability to grow single crystals of the oligomeric and HOF photocatalysts in Chapter 3 and 4 opens up the possibility of generating single crystal heterojunctions. These consist of single crystals of two distinct organic molecules grown from a crystal surface or intermixed by lamination.[11] Layering organic crystals containing ‘acceptor’ units such as dibenzothiophene sulfone with ‘donor’ crystals such as oligothiophenes could form such a heterojunction and encourage charge separation as well as introducing a light absorber with a more red-shifted onset. Whilst thin single crystals of organic conjugated molecules are known to adhere to a variety of surfaces,[12] stronger electrostatic interactions may be required to adhere crystals together in aqueous suspension. In this case, materials with similar unit cells may provide stronger epitaxial interaction between crystals; modification of an existing structure with electron donating or accepting

groups could provide the desired offset band structures whilst retaining similar packing. For instance, an analogue of **TBAP** with fluorinated phenyl linkers (Figure 4a) might be expected to have a lowered LUMO energy whilst an analogue with a methoxy substituted pyrene core (Figure 4b) might be expected to have a raised HOMO energy. Both molecules could pack to form HOFs with similar structures to **TBAP-α** and could be used as the acceptor and donor phases respectively of a single crystal heterojunction. Band structure calculations and CSP would be useful to determine the feasibility of specific molecules and their combinations.

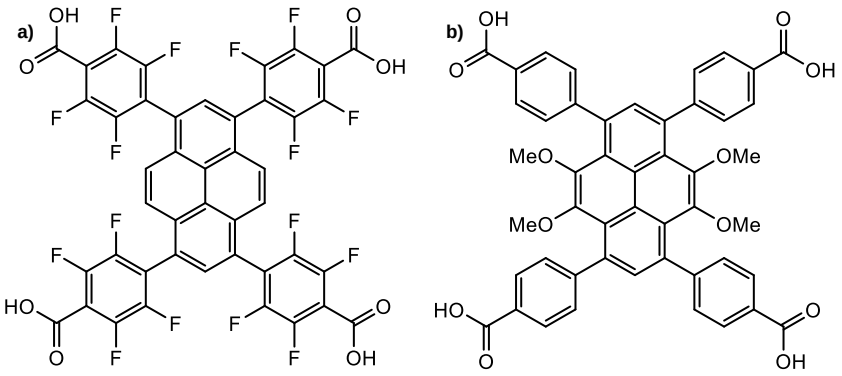

Figure 4: Potential acceptor (a) and donor (b) structures for a crystalline heterojunction photocatalyst.

5.2 References

1 Y. Bai, L. Wilbraham, B. J. Slater, M. A. Zwijnenburg, R. S. Sprick and A. I. Cooper, 2019, **141**, 9063-9071.

2 R.-B. Lin, Y. He, P. Li, H. Wang, W. Zhou and B. Chen, *Chem. Soc. Rev.*, 2019, **48**, 1362–1389.

3 I. Hisaki, Y. Suzuki, E. Gomez, Q. Ji, N. Tohnai, T. Nakamura and A. Douhal, *J. Am. Chem. Soc.*, 2019, **141**, 2111-2121.

4 Z. F. Yao, J. Y. Wang and J. Pei, *Cryst. Growth Des.*, 2018, **18**, 7–15.

5 Z. Liang, Q. Tang, J. Xu and Q. Miao, *Adv. Mater.*, 2011, **23**, 1535–1539.

6 J. Tang, J. R. Durrant and D. R. Klug, *J. Am. Chem. Soc.*, 2008, **130**, 13885–13891.

7 A. A. Bakulin, A. Rao, V. G. Pavelyev, P. H. M. Van Loosdrecht, M. S. Pshenichnikov, D. Niedzialek, J. Cornil, D. Beljonne and R. H. Friend, *Science.*, 2012, **335**, 1340–1344.

8 S. Chen, T. Takata and K. Domen, *Nat. Rev. Mater.*, 2017, **2**, 17050.

9 Y. Bai, K. Nakagawa, A. Cowan, C. M. Aitchison, Y. Yamaguchi, M. Zwijnenburg, A. Kudo, R. S. Sprick and A. Cooper, *J. Mater. Chem. A*, 2020, **6**, 4883–5230.

10 Q. Wang, T. Hisatomi, Q. Jia, H. Tokudome, M. Zhong, C. Wang, Z. Pan, T. Takata, M. Nakabayashi, N. Shibata, Y. Li, I. D. Sharp, A. Kudo, T. Yamada and K. Domen, *Nat. Mater.*, 2016, **15**, 611–615.

11 J. Wu, Q. Li, G. Xue, H. Chen and H. Li, *Adv. Mater.*, 2017, **29**, 1606101.

12 H. Alves, A. S. Molinari, H. Xie and A. F. Morpurgo, *Nat. Mater.*, 2008, **7**, 574–580.

6. Appendix

6.1 Additional NMR spectra

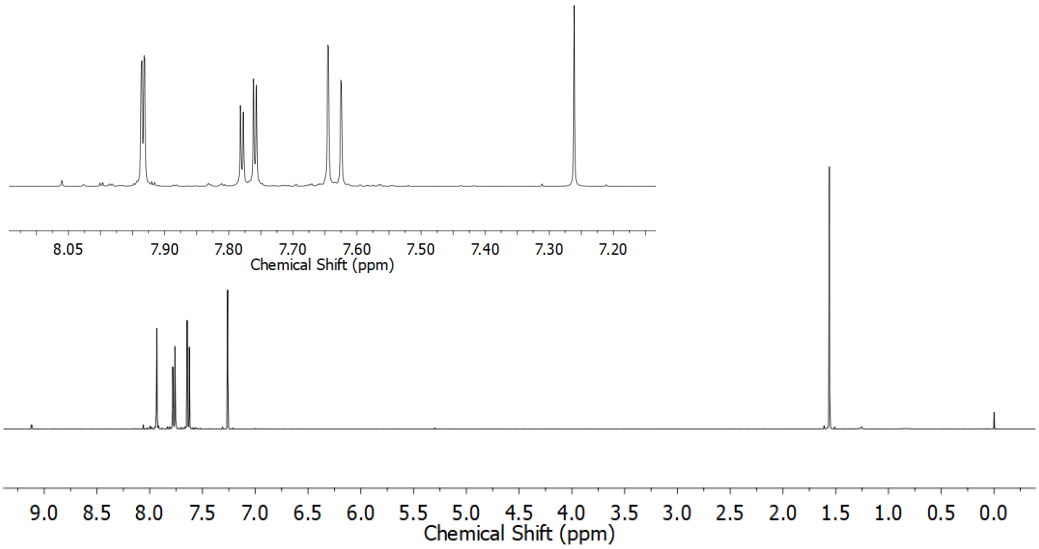

Figure 1: NMR spectra of 3,7-dibromodibenzo[*b,d*]thiophene sulfone in $CDCl_3$. Inset shows expanded spectra of the aromatic region.

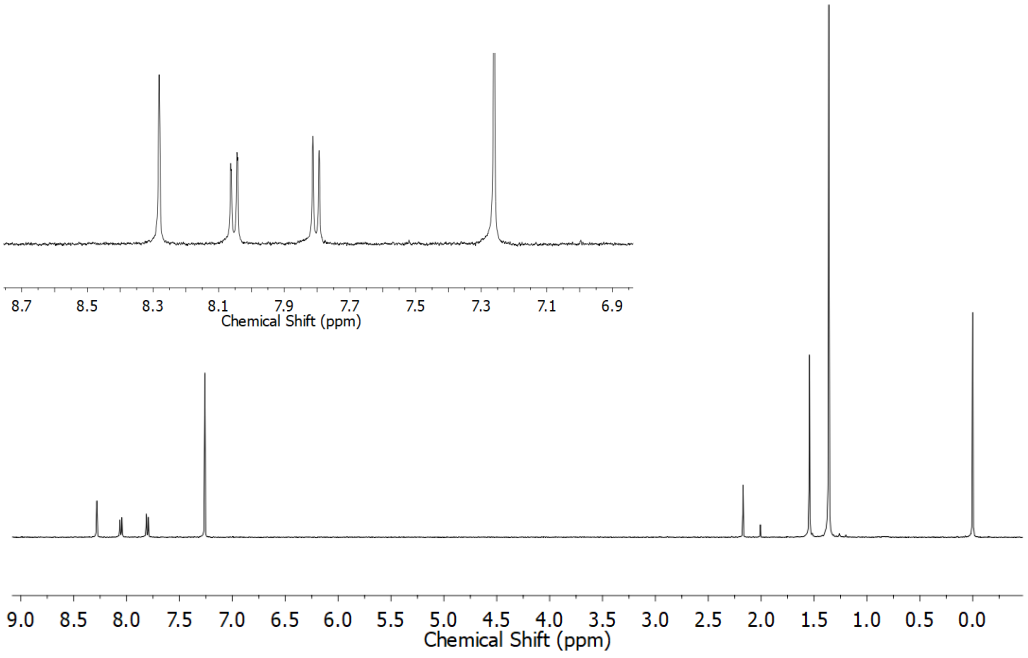

Figure 2: NMR spectra of 3,7-dibenzo[*b,d*]thiophene sulfone diboronic acid bis(pinacol) ester in $CDCl_3$. Inset shows expanded spectra of the aromatic region.

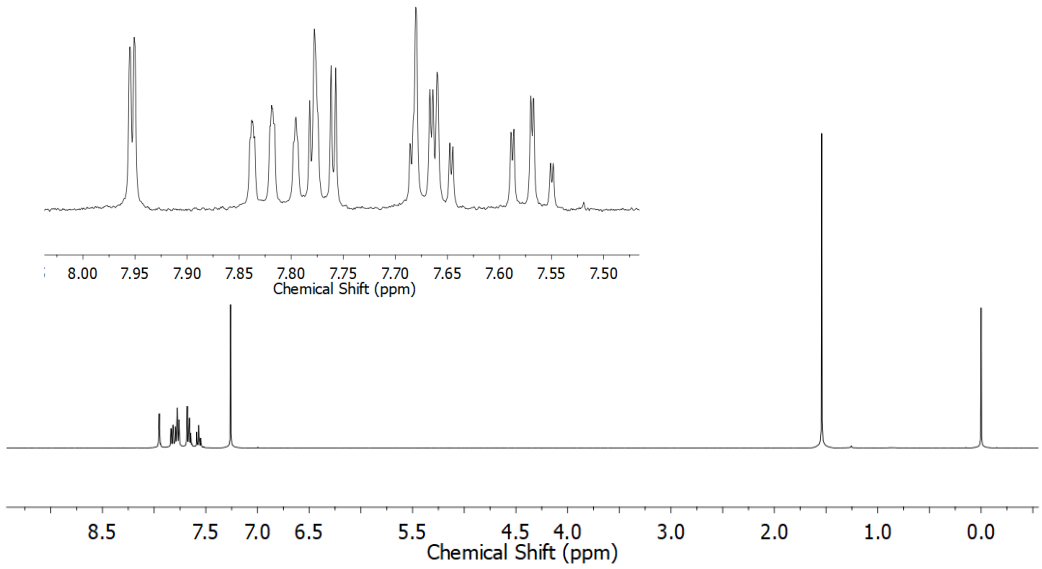

Figure 3: NMR spectra of 3-bromodibenzo[*b*,*d*]thiophene sulfone in $CDCl_3$. Inset shows expanded spectra of the aromatic region.

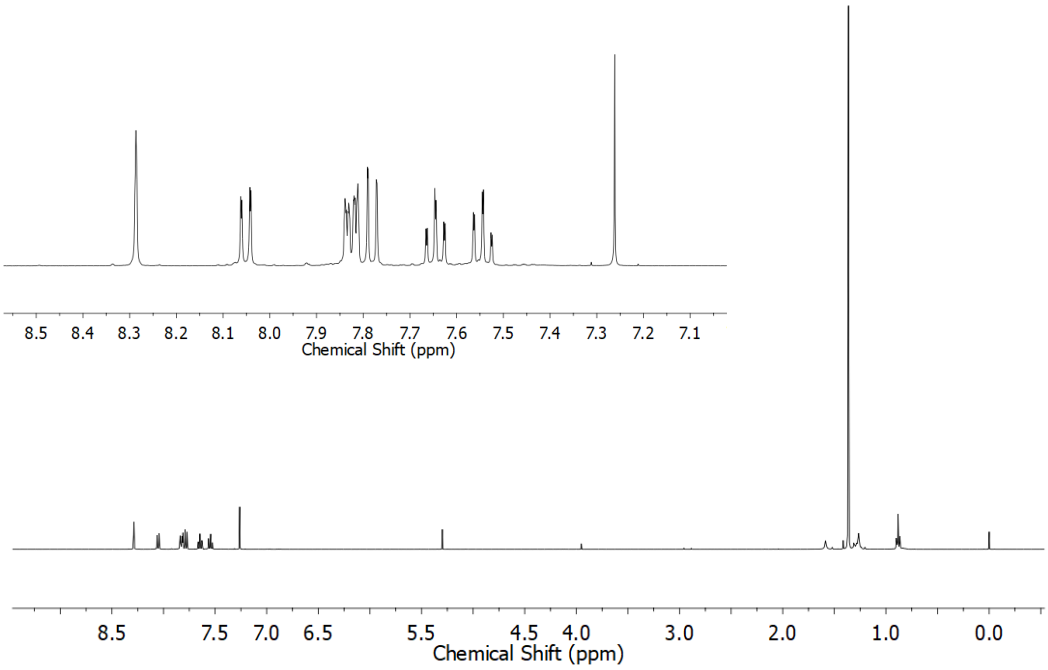

Figure 4: NMR spectra of 3-dibenzo[*b*,*d*]thiophene sulfone boronic acid pinacol ester in $CDCl_3$. Inset shows expanded spectra of the aromatic region.

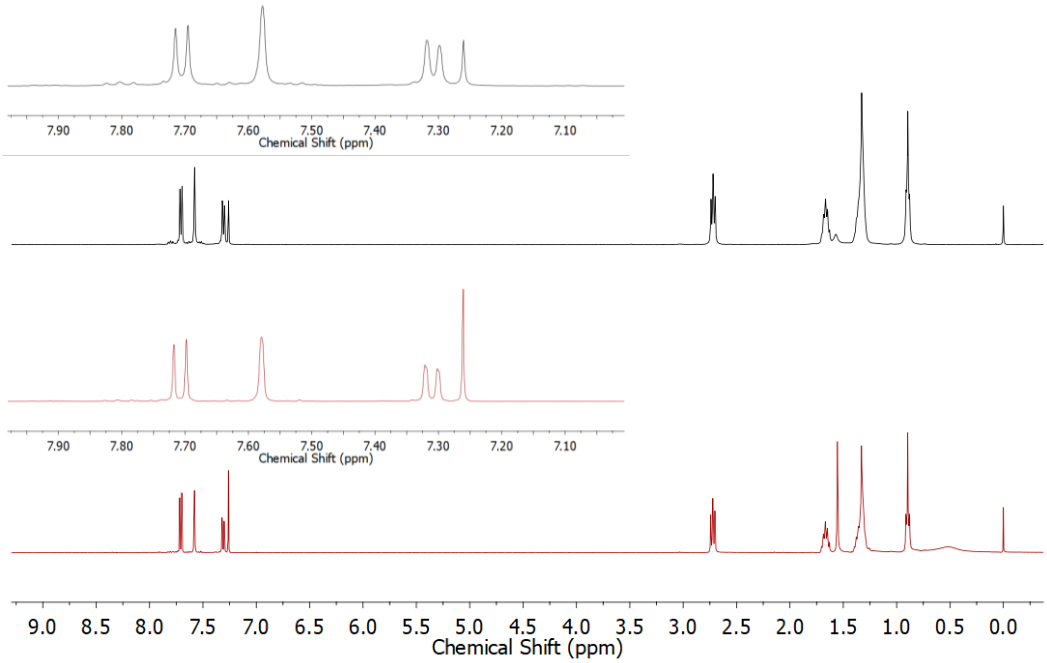

Figure 5: NMR spectra of 2,8-dihexyldibenzo[*b*,*d*]thiophene sulfone in $CDCl_3$. Pre (black) and post (red) photocatalysis. Inset shows expanded spectra of the aromatic region.

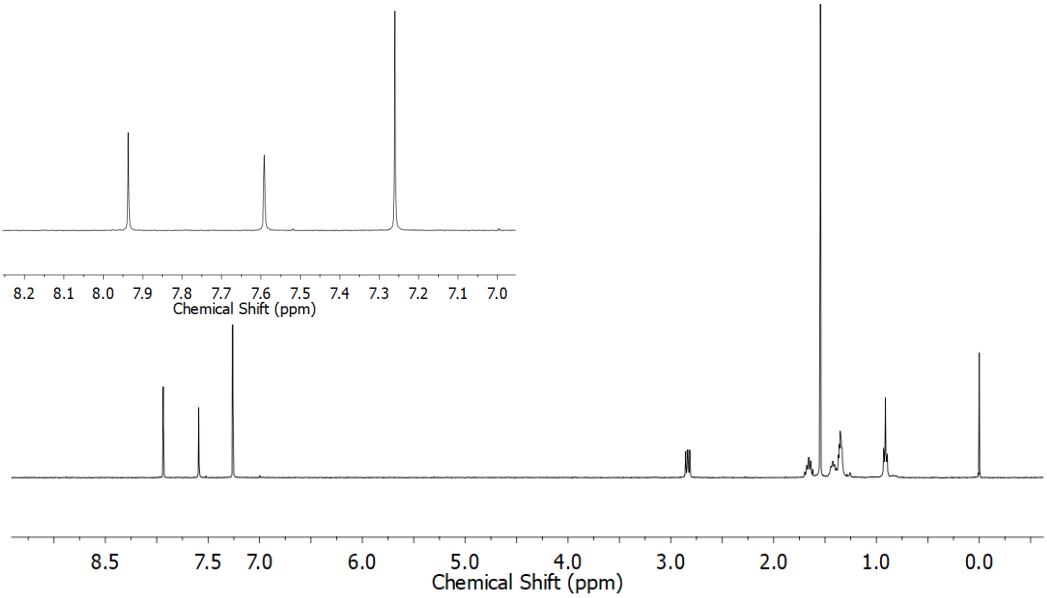

Figure 6: NMR spectra of 2,8-dihexyl-3,7-dibromodibenzo[*b*,*d*]thiophene sulfone in $CDCl_3$. Inset shows expanded spectra of the aromatic region.

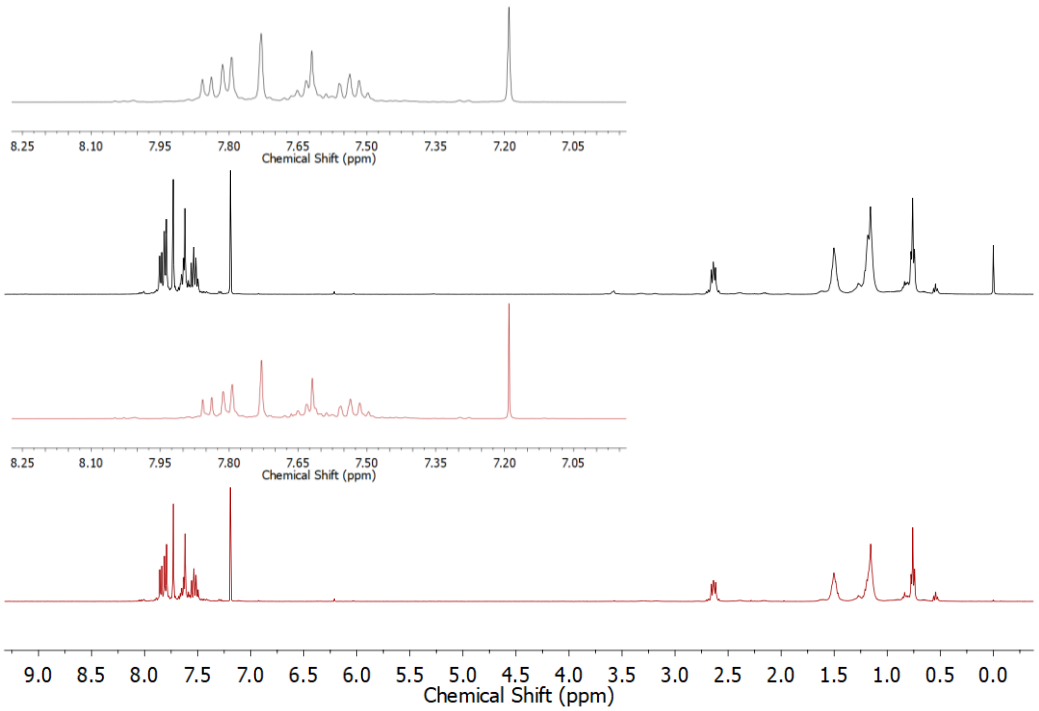

Figure 7: NMR spectra of **SS_6S** in $CDCl_3$. Pre (black) and post (red) photocatalysis. Inset shows expanded spectra of the aromatic region.

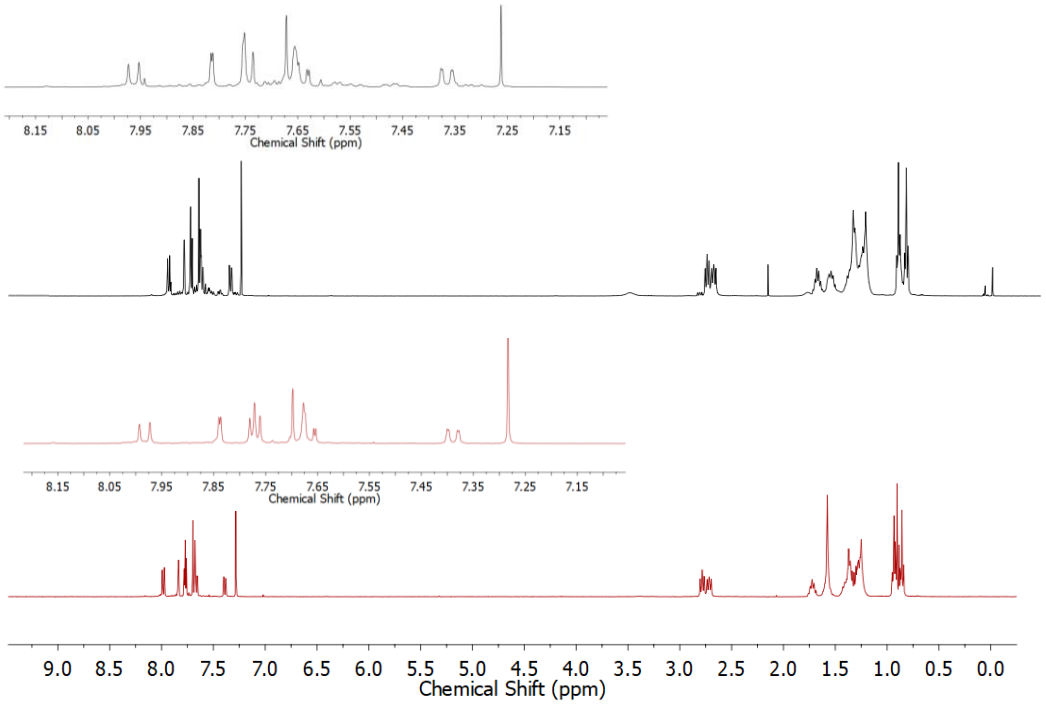

Figure 8: NMR spectra of **S_6S_6 S_6** in $CDCl_3$. Pre (black) and post (red) photocatalysis. Inset shows expanded spectra of the aromatic region.

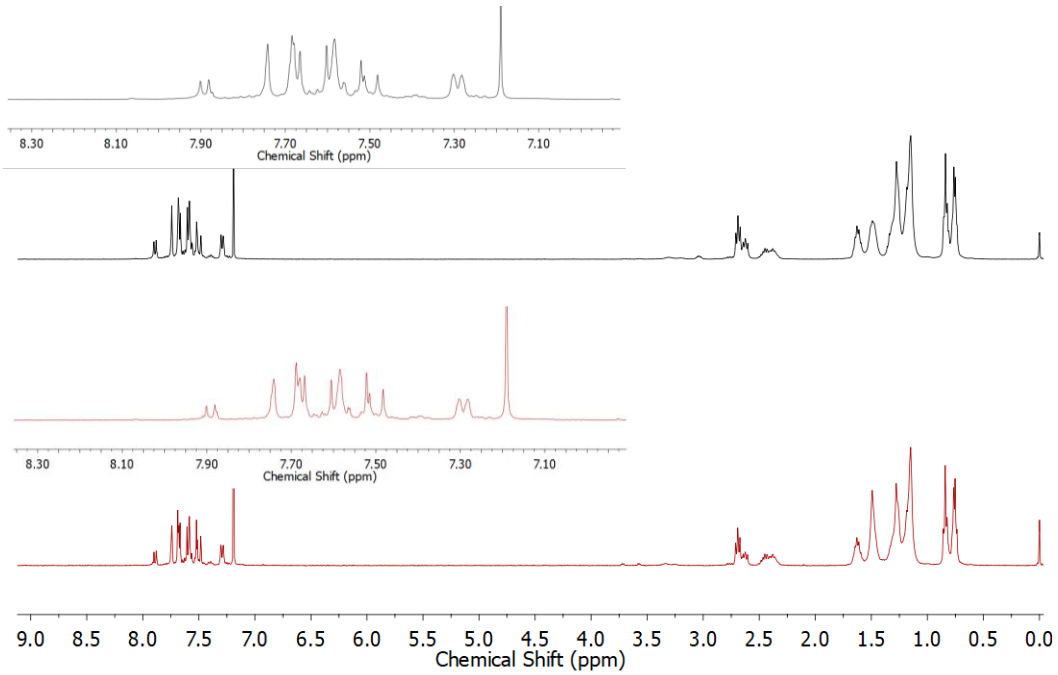

Figure 9: NMR spectra of **S_6S_6 S_6** in $CDCl_3$. Pre (black) and post (red) photocatalysis. Inset shows expanded spectra of the aromatic region.

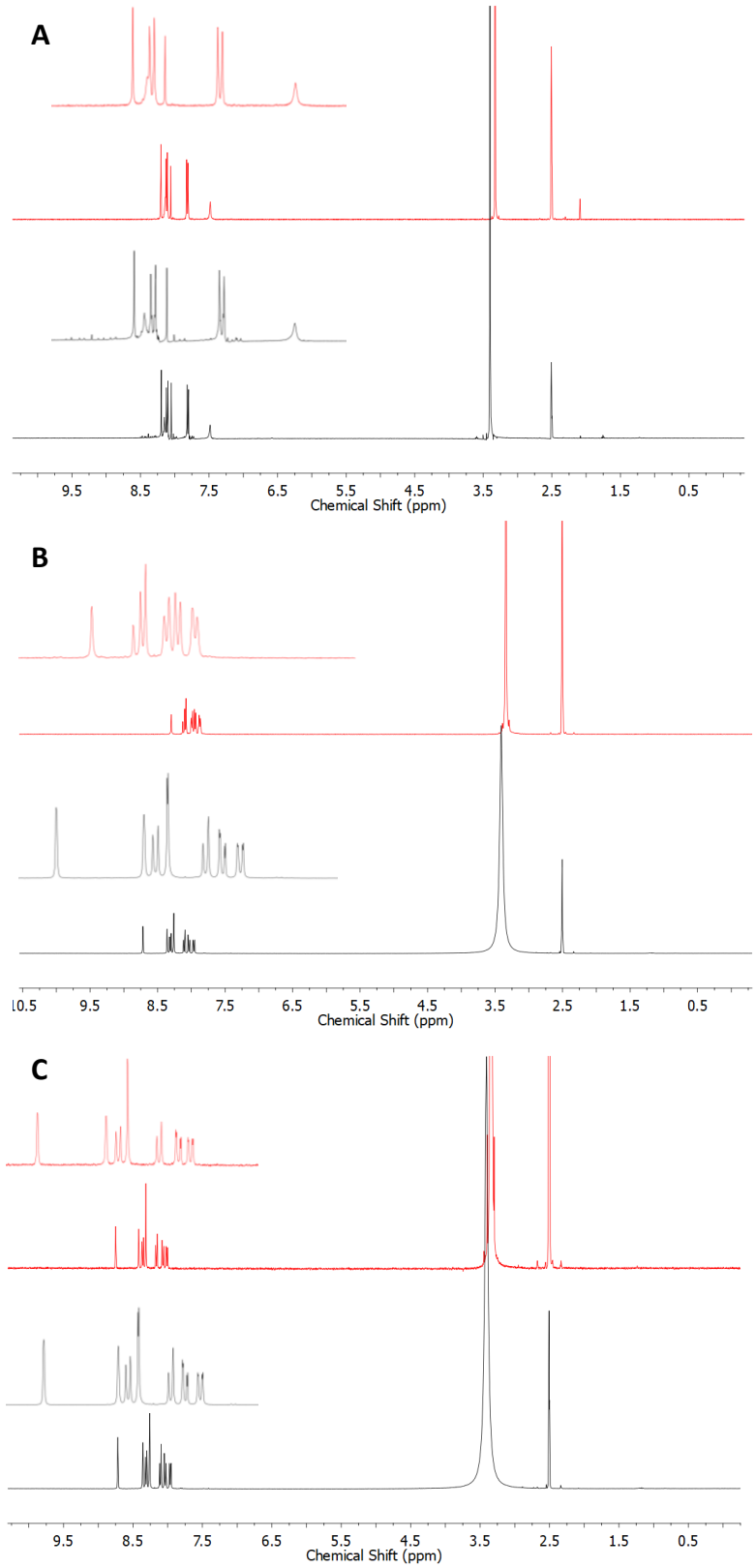

Figure 10: NMR spectra of **TPAP** (A), **1** (B) and **2** (C) pre (black) and post (red) photocatalysis. Inset shows expanded spectra of the aromatic region.

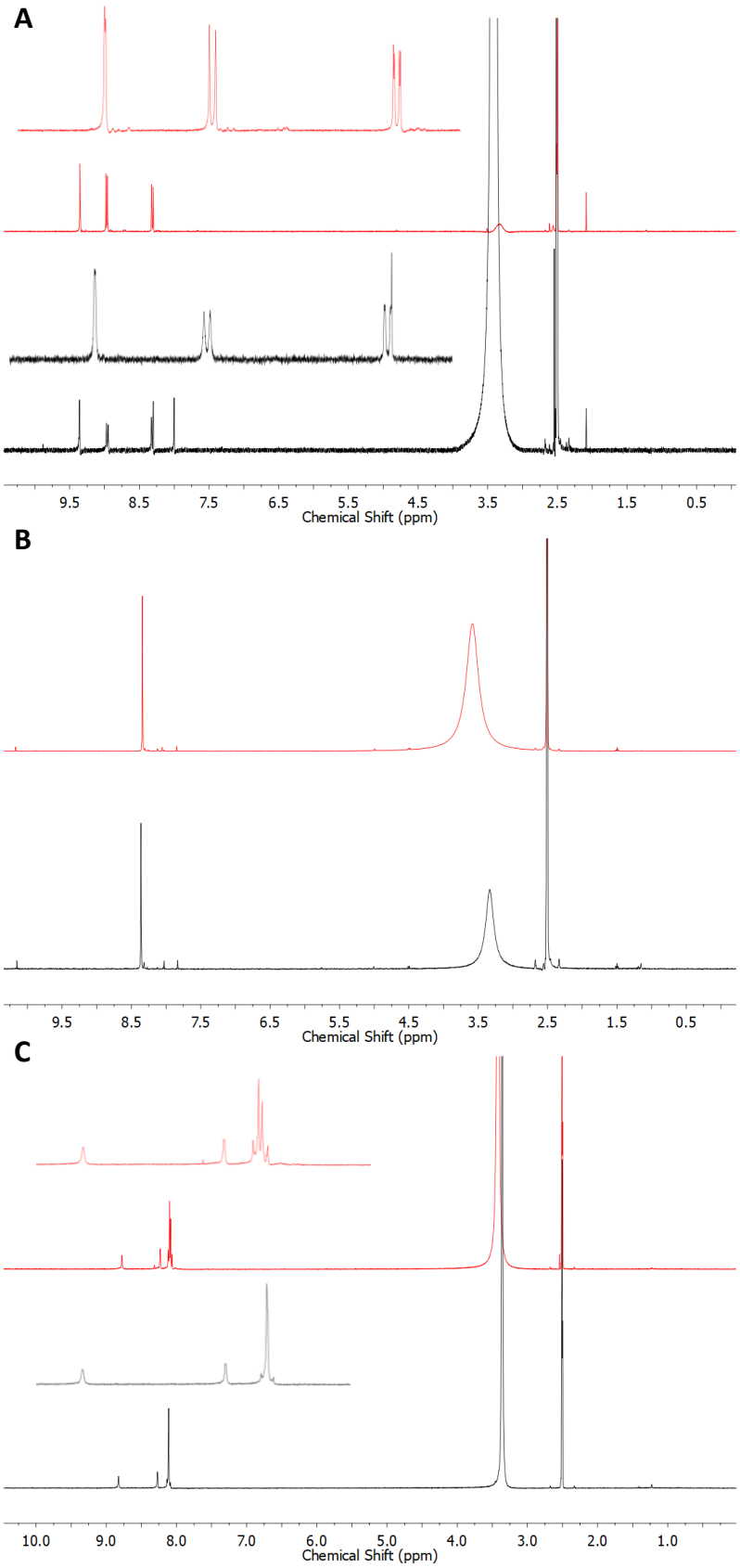

Figure 11: NMR spectra of **3** (A), **4** (B) and **5** (C) pre (black) and post (red) photocatalysis. Inset shows expanded spectra of the aromatic region.

6.2 Additional UV-Vis Spectra

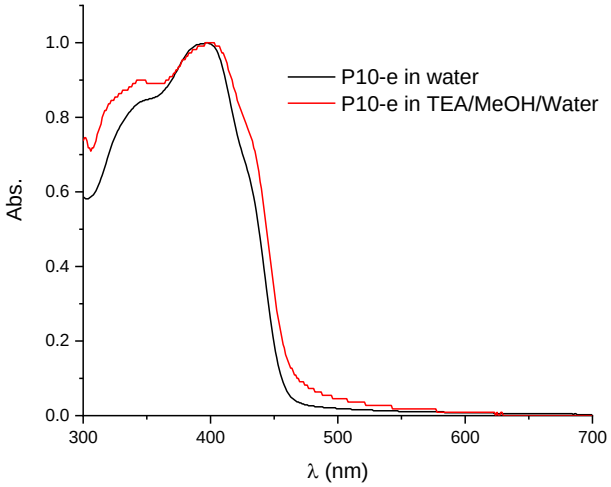

Figure 12: Normalised UV-Vis spectra of **P10-e** (0.01 mg mL^{-1}) suspended in water (black) or TEA/MeOH/Water (red).

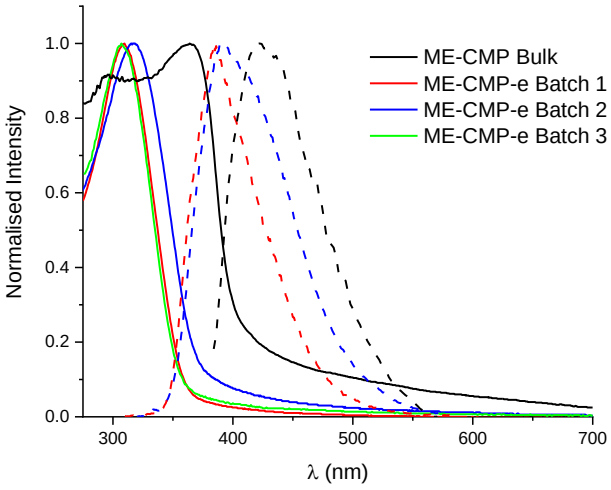

Figure 13: Spectra of **ME-CMP** and batches of **ME-CMP-e**. Normalised absorption (solid lines) and normalised emission (λ_{ex} = 325 nm, dashed lines), Bulk measured in the solid state emulsion derived particles measured in water suspension (0.006 mg mL^{-1})

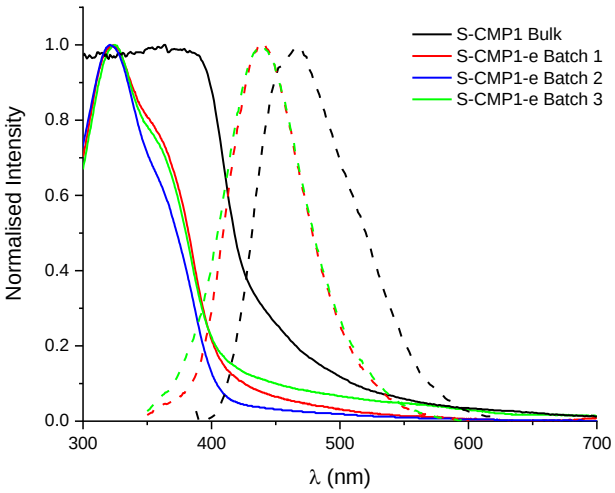

Figure 14: Spectra of **S-CMP1** and batches of **S-CMP1-e**. Normalised absorption (solid lines) and normalised emission (λ_{ex} = 325 nm, dashed lines), Bulk measured in the solid state emulsion derived particles measured in water suspension (0.007 mg mL^{-1})

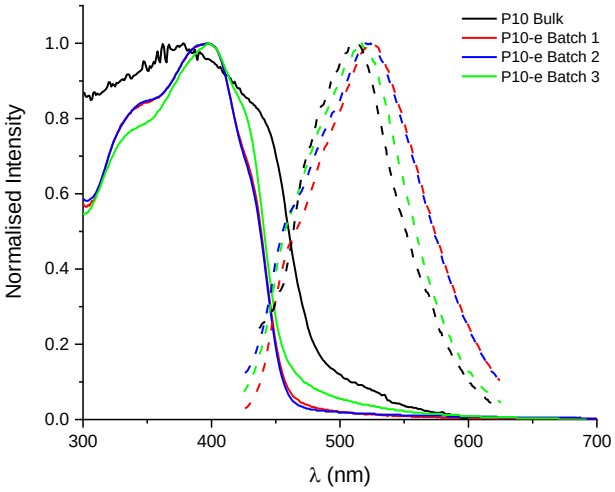

Figure 15: Spectra of **P10** and batches of **P10-e**. Normalised absorption (solid lines) and normalised emission (λ_{ex} = 325 nm, dashed lines), Bulk measured in the solid state emulsion derived particles measured in water suspension (0.01 mg mL^{-1})

6.3 Light Source and Filter Characteristics

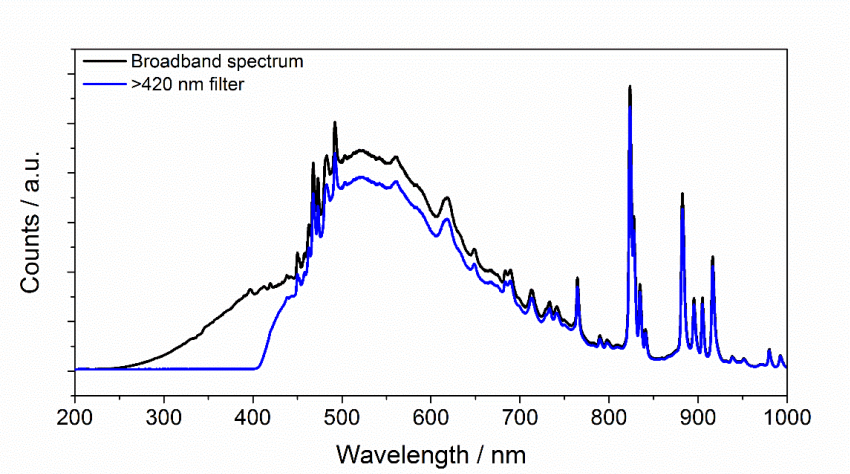

Figure 16: Output of the Xe light source used in this work.

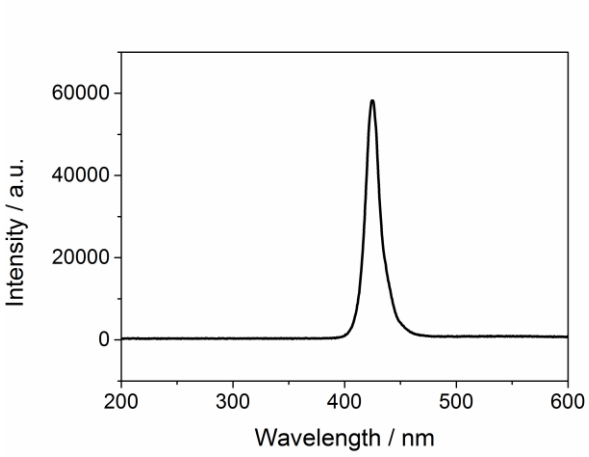

Figure 17: Output of the 420 nm LED used in this work.

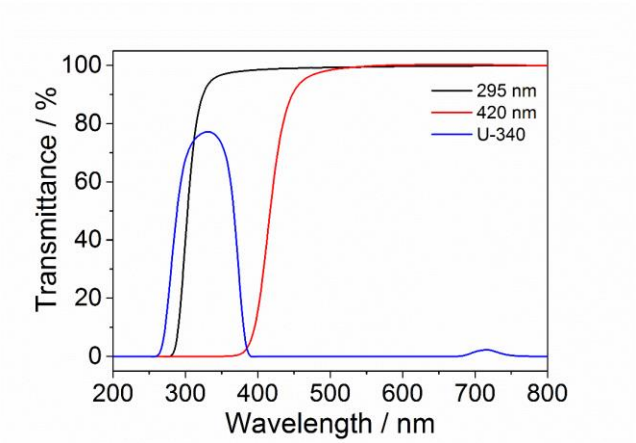

Figure 18: Transmission characteristics of the filters used in this work.

6.4 Additional Photocatalysis Measurements

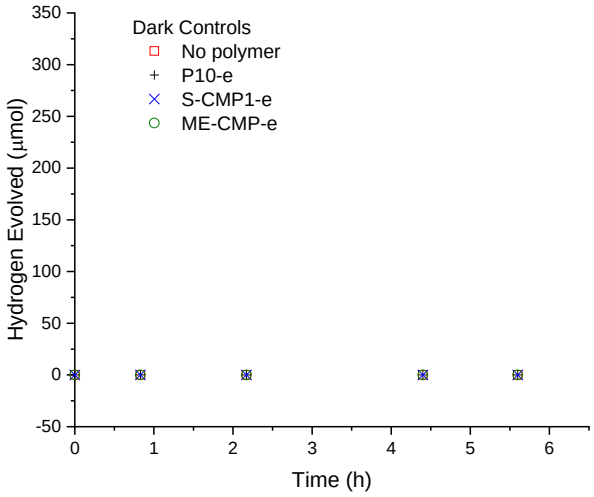

Figure 19: Control measurements of photocatalysts suspended in TEA/MeOH/Water and stirred in the dark.

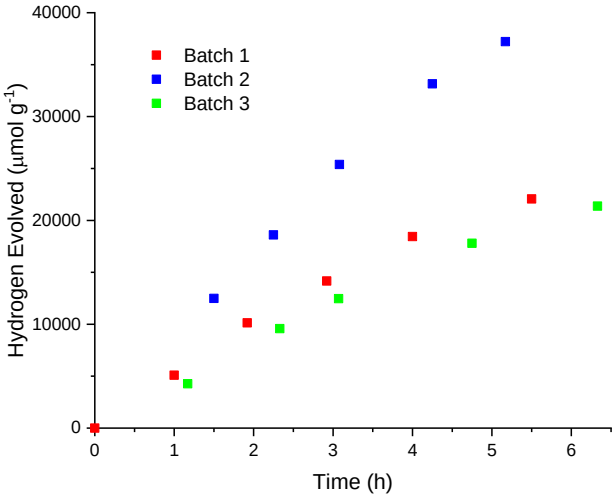

Figure 20: Hydrogen evolution of batches of **ME-CMP-e** (0.06 mg mL^{-1}) in 25 mL aqueous/methanol/triethylamine (1:1:1) (aqueous phase containing water: toluene (9:1), SDS surfactant 10 mg mL^{-1} and Na_2CO_3 3.5 mg mL^{-1}) illuminated using $\lambda > 295$ nm.

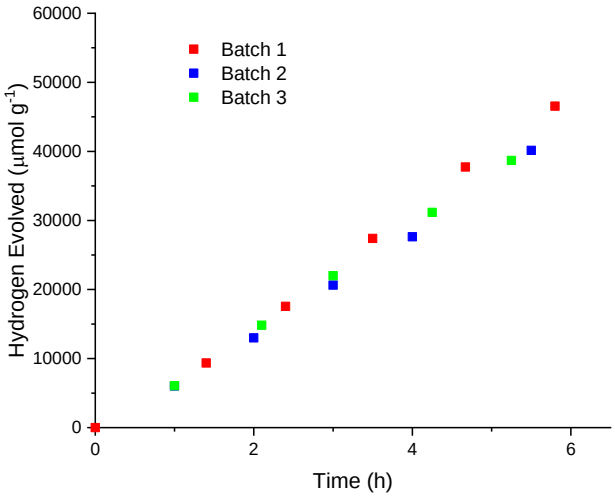

Figure 21: Hydrogen evolution of batches of **S-CMP1-e** (0.07 mg mL^{-1}) in 25 mL aqueous/methanol/triethylamine (1:1:1) (aqueous phase containing water: toluene (9:1), SDS surfactant 10 mg mL^{-1} and Na_2CO_3 3.5 mg mL^{-1}) illuminated using $\lambda > 295$ nm.

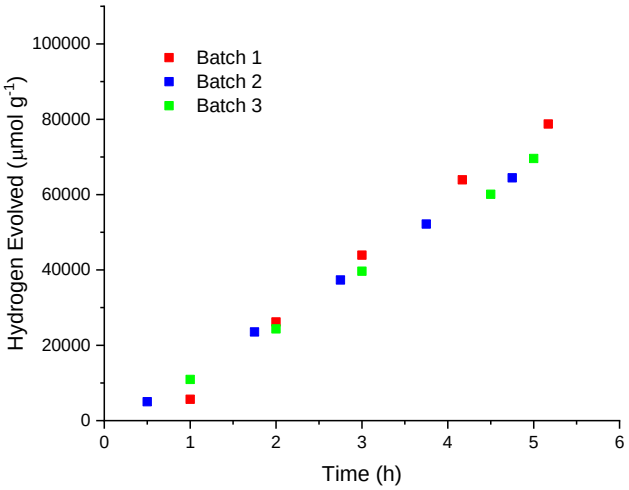

Figure 22: Hydrogen evolution of batches of **P10-e** (0.1 mg mL^{-1}) in 25 mL aqueous/methanol/triethylamine (1:1:1) (aqueous phase containing water: toluene (9:1), SDS surfactant 10 mg mL^{-1} and Na_2CO_3 3.5 mg mL^{-1}) illuminated using $\lambda > 420$ nm.

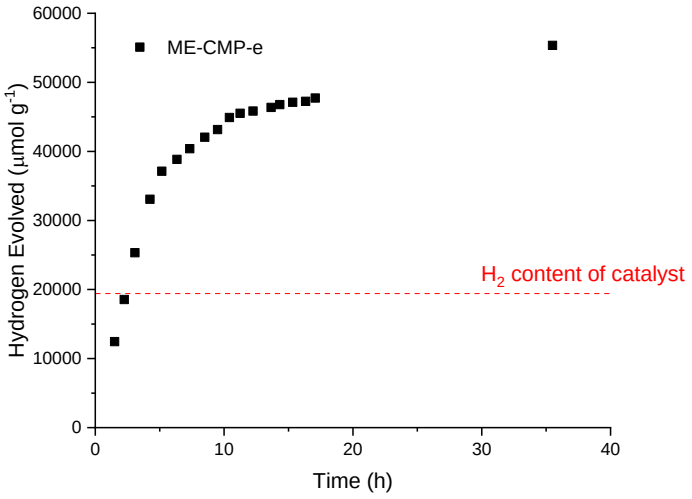

Figure 23: Extended hydrogen evolution **ME-CMP-e** (0.06 mg mL^{-1}) in 25 mL aqueous/methanol/triethylamine (1:1:1) (aqueous phase containing water: toluene (9:1), SDS surfactant 10 mg mL^{-1} and Na_2CO_3 3.5 mg mL^{-1}) illuminated using $\lambda > 295$ nm.

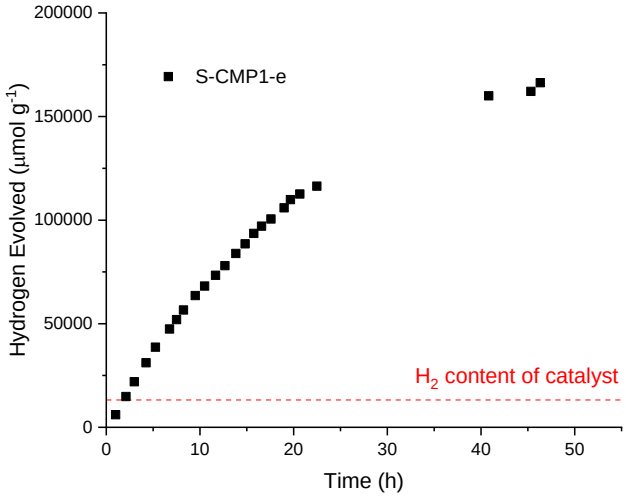

Figure 24: Extended hydrogen evolution **S-CMP1-e** (0.07 mg mL^{-1}) in 25 mL aqueous/methanol/triethylamine (1:1:1) (aqueous phase containing water: toluene (9:1), SDS surfactant 10 mg mL^{-1} and Na_2CO_3 3.5 mg mL^{-1}) illuminated using $\lambda > 295$ nm.